UILU-ENG.-71-2019

CIVIL ENGINEERING STUDIES
STRUCTURAL RESEARCH SERIES NO. 380

SHEAR STRENGTH OF END SLABS WITH AND WITHOUT PENETRATIONS IN PRESTRESSED CONCRETE REACTOR VESSELS

by

B. I. KARLSSON
and
M. A. SOZEN

JULY 1971

Subcontract No. 2906
Under Contract No. W-7405-eng-26

A Report on an Investigation
carried out as part of the
Prestressed Concrete Reactor Vessel Program
of the
Oak Ridge National Laboratory
Operated by
UNION CARBIDE CORPORATION
for the
U. S. ATOMIC ENERGY COMMISSION

UNIVERSITY OF ILLINOIS
URBANA, ILLINOIS

SHEAR STRENGTH OF END SLABS WITH AND WITHOUT PENETRATIONS IN PRESTRESSED CONCRETE REACTOR VESSELS

By

B. I. Karlsson
and
M. A. Sozen

JULY 1971

Subcontract No. 2906
Under Contract No. W-7405-eng-26

A Report on an Investigation
carried out as part of the
Prestressed Concrete Reactor Vessel Program
of the
Oak Ridge National Laboratory

Operated by
Union Carbide Corporation
for the
U. S. Atomic Energy Commission

University of Illinois
Urbana, Illinois

ACKNOWLEDGMENT

The reported work was carried out at the Structural Research Laboratory of the Civil Engineering Department, University of Illinois, Urbana, as part of the Prestressed Concrete Reactor Vessel Program of the Oak Ridge National Laboratory Sponsored by the U. S. Atomic Energy Commission. The program is coordinated by G. D. Whitman of the Oak Ridge National Laboratory. Additional financial support was provided by Gulf General Atomic.

Thanks are due to the following people who have assisted in various aspects of this investigation:

W. C. Schnobrich, Professor of Civil Engineering

S. L. Paul, Assistant Professor of Civil Engineering

A. K. Gupta, Research Assistant in Civil Engineering

M. H. Salem, Research Assistant in Civil Engineering

This report was based on a thesis written by B. I. Karlsson under the direction of M. A. Sozen.

TABLE OF CONTENTS

Page

LIST OF TABLES

LIST OF FIGURES

Figure Page

Figure Page

1. INTRODUCTION

An investigation of the response and strength of prestressed concrete reactor vessels has been in progress at the University of Illinois Department of Civil Engineering since 1967. The purpose has been to investigate the different modes of failure and to develop general design criteria for vessels consisting of a cylinder bounded by flat end slabs.

The experimental part of the project consisted of the testing of 21 small-scale specimens. The specimens were not models of any particular full-scale vessel. A simple geometrical shape was chosen so that generally applicable information of the response and strength of concrete vessels would be obtained. The major variables were ratio of the thickness of the end slab to the interior diameter of the vessel, penetrations in the end slab and the longitudinal and circumferential prestressing forces.

Two types of structural failures were observed in the end slab: flexural failures characterized by fracture of the circumferential reinforcement, and shear failures resulting from the development of inclined cracks. A third type of failure was leakage of the seal because of cracks in the side wall leading to a slow loss of pressure.

In a previous report the experimental results for the first 16 vessels were presented (Paul et al., 1969). The different types of failure were discussed and a method to calculate the flexural strength of the end slab was presented.

The possibility of using the lumped-parameter model to predict the response and mode of failure of pressure vessels has been investigated (Echeverria Gomez, Schnobrich, 1968; Higashionna, Schnobrich, 1970). The response in the elastic range and part of the nonelastic range up to and including the initiation of the shear crack has been successfully predicted.

However, the lack of explicit criteria to define the cracking of the end slab and its subsequent failure under a complex state of stresses, has made the development of an elaborate computer program, with excessive computer capacity demand, unjustified in order to predict the shear strength of the end slab.

This report presents the results of six tests of pressure vessels, conducted primarily to investigate the shear strength of the end slab and the effect of penetrations on the shear strength. Observations have indicated that the end slab fails in shear as a result of the following mechanism: A critical inclined crack develops tending to transform the end slab into a dome. Collapse occurs by failure of the concrete in the dome. A method was developed to estimate the shape of the dome and the failure load, based on finite-element analyses of the end slab and a failure criterion for concrete subjected to triaxial stresses.

2. SUMMARY OF TESTS AND TEST RESULTS

2.1 The Test Specimens

The geometrical shapes of the six test vessels were identical except for the penetrations in the end slab. The material properties and the prestressing forces were comparable for all vessels.

The vessel configuration was one half of a cylindrical vessel with a flat end slab (Fig. 2.1). The dimensions were 40 in. diameter by 40 in. high. The interior diameter was 25 in. and the slab thickness was 10 in. The open end of the vessel was sealed by a 4 in. steel plate.

The circumferential prestress was provided by high tensile strength wire wrapped around the vessel. The wire had 0.25-in. diameter and was wrapped continuously, at a pitch equal to the wire diameter.

The longitudinal prestress was provided by sixty 0.75-in. Stressteel rods running through the wall.

The end slab was cast without any reinforcement in the concrete. Forty No. 4 bars were located vertically in the side wall to prevent cracking during circumferential prestressing.

Five vessels had penetrations located in the end slab. The penetrations were sealed by steel plates placed in indentations on the inside face of the slab.

2.2 Test Variables

Several of the vessels that were tested in the earlier phase of the project failed in shear or responded in a manner indicating that they were close to failing in shear. One of the vessels, PV16, that failed in shear was chosen as a yardstick for the vessels with penetrations, and the experimental results for vessel PV16 are repeated in this report. Five vessels, designated PV17 to PV21, with penetrations were tested. The

six vessels were similar except for the following variables:

(a) Location of penetrations in the end slab.

(b) Number of penetrations in the end slab.

(c) Size of penetrations in the end slab.

The locations of the penetrations were determined in view of the crack propagation leading to a shear failure. The shear failure is initiated by the formation of an inclined crack near the mid-height of the slab and at a slope of about 45 degrees (Fig. 2.2). The crack propagates upwards to the edge of the anchorage plate of the longitudinal reinforcement. It propagates downwards toward the inside face of the slab at a gradually decreasing slope, ultimately carving out a dome in the slab (Fig. 2.3). A shear failure is characterized by a failure of the dome under a combination of compressive stresses and shear stresses (Fig. 2.4). There are two critical stages in the development of a shear failure:

(1) The initation of the inclined crack occurs near the edge of the slab. If penetrations are introduced in this section, the formation of the inclined crack is precipitated. However, if this section is not the one at which the dome in the corresponding solid slab failed, the penetrations may not affect the ultimate strength of the dome unless a certain minimum amount of the section is removed.

(2) The dome in vessel PV16 failed near the center of the slab. If penetrations are introduced in this section, the formation of the inclined crack will not be affected but the strength of the dome once it is formed may be reduced.

To test the first assumption, four of the vessels (PV17, PV18, PV20 and PV21) were cast with penetrations 8 in. from the center of the slab. Two of the vessels (PV17 and PV21) had 25 percent of the perimeter removed

at a radius of 8 in., while 50 percent of the perimeter was removed in the other two vessels (PV18 and PV20). Two of the vessels (PV17 and PV18) had 4-in. penetrations while the other two vessels (PV20 and PV21) had 2-in. penetrations. The pertinent data are given in Fig. 2.5 and Table 2.1.

To test the second assumption, one vessel, PV19, was cast with penetrations 4 in. from the center of the slab. The six penetrations removed 50 percent of the perimeter at a radius of 4 in. (Fig. 2.6 and Table 2.1)

2.3 Test Results

The test setup and material properties are described in Appendix A. To pressurize the vessel it was necessary to seal the penetrations by applying steel plates to the inside face of the slab. In evaluating the test results the influence of the steel plates on the strength of the vessels has to be considered. The vessels can be divided into two groups by the location of the penetrations:

(1) Four of the vessels had penetrations located 8 in. from the center of the slab. The test of vessel PV16 indicated that the radial strains were small on the inside face of the slab at this section. A small modification of the geometry at this section and the presence of steel plates would have a negligible influence on the specimen. Indentations in the form of 1x1-in. tori were formed around the penetrations and the steel plates were placed in these (Fig. 2.7).

(2) Test vessel PV19 had penetrations located 4 in. from the center of the slab. The concrete along the inside face of the slab at this section is subjected to high compression in the radial direction, especially after the formation of the dome. It was not considered suitable to form indentations for the steel plates, because the extra concrete that would be removed might exaggerate the effect of penetrations. The steel plates were supported

on the inside face of the slab (Fig. 2.7). However, because of friction between the steel plates and the concrete, some of the stresses were transferred by the steel plates and they acted as reinforcement. The effect of penetrations was reduced and may even have been reversed by the presence of the steel plates.

The vessels were pressurized internally. Deflections were measured along the outside of the vessel. The concrete strains were measured on the inside and outside faces of the slab. Strains were measured in the circumferential prestressing wire and in the longitudinal rods. All test data are reported in Appendix B.

The vessels were pressurized using a test setup that allowed the usage of either oil or gas. At low internal pressures the vessels were pressurized hydraulically. When the pressure was increased the test vessels developed leaks. If the leakage exceeded the capacity of the oil pumps a switch to pneumatic pressurizing was made. Four of the vessels, PV16, PV17, PV20 and PV21, failed explosively while the vessels were pressurized with gas. The measured trajectories of the inclined cracks and the failure surfaces are shown in Fig. 2.8 to 2.11. The three vessels with penetrations failed in the sections where the penetrations were located at internal pressures between 3000 and 3300 psi (Table 2.1).

Test vessel PV18 was subjected to hydraulic pressure up to 3000 psi, at which pressure the leakage exceeded the capacity of the oil pumps. To preserve the end slab in order to study the crack development the test was aborted at this point. The slab was cut and the trajectory of the inclined crack was determined. The inclined crack had propagated to the center of the slab carving out a complete dome (Fig. 2.12). However, the boundary of the cryptodome was not well defined near the center of the slab.

Test vessel PV19 was pressurized hydraulically when at 3500 psi a sudden drop in internal pressure occurred. It was not possible to regain the lost pressure either with oil or gas. The slab was cut and the crack development was studied. The cracks indicated that the failure pressure had been reached but that the use of oil prevented a violent failure or the formation of an easily recognized failure plane (Fig. 2.13).

3. OBSERVED RESPONSE OF THE TEST VESSEL WITH A SOLID END SLAB

3.1 Introductory Remarks

This chapter is concerned with phenomena observed in the tests of vessels with solid end slabs. It refers primarily to the test of vessel PV16 (Fig. 2.1) which was tested to provide a standard for the evaluation of the response of the five test vessels (PV17-PV21) with penetrations in the end slabs. However, information from the tests of other vessels with solid end slabs is also used.

The chapter is divided into five sections. The first section discusses strains measured in the linear range of response, before the development of cracks. Conditions leading to, and subsequent to, the formation of three different types of cracks are considered in the following three sections. In these experiments it was not possible to study the crack development directly, because some cracks developed inside the slab. Even the cracks on the surface could not be studied closely because of the explosive failures that were expected. An effort has been made to relate the strain readings to the crack configuration. The failure mechanism is described in the fifth section.

In discussing the development of the inclined crack and the failure of the end slab, test results from an earlier phase of the project are included (Paul et al., 1969).

The discussion of the causes and effects of cracking is based on solutions of the stress conditions using the finite-element model. The axisymmetric finite element was used to represent the vessel (Mohraz, Schnobrich, Gupta, 1969). The solutions have certain limitations. First, the effects of the various types of cracks were evaluated separately rather than simultaneously as they may occur in the actual test. Second, the effects of a

given type of crack were analyzed at a specific internal pressure and at an arbitrarily specified extent of cracking rather than calculating the development of the cracks with increase in pressure. The analyses are intended to indicate the directions in which strains and stresses will change with cracking and are not intended to show progressive changes in the end slab as cracking develops.

Stress and strain conditions have been analyzed at zero internal pressure (with full prestress as indicated in Table 2.1 for PV16) and at an internal pressure of 3200 psi, the choice of the latter pressure being arbitrary. The primary function of the calculated strain changes is to interpret the variations in strain measured in the test.

All the strain readings for vessel PV16 that are shown in the figures of this chapter are compared with calculated strains obtained using the finite-element model and assuming a linear force-deformation relationship for concrete.

3.2 Initial Response and Initiation of Cracking

The vessels were prestressed by longitudinal rods and by wire wrapped around the outside cylindrical surface (Fig. 2.1). The wire prestresses the slab and the wall in the radial and tangential directions. The longitudinal rods prestress the wall in the vertical direction.

At a low internal pressure the concrete stresses in the entire vessel are small in relation to its strength so that a linear stress-strain relationship can be assumed. At this stage, the state of stress can be predicted using the finite-element or the lumped-parameter methods with a linear force-deformation function. A lumped-parameter analysis has been used to predict the response of vessel PV16 before cracking occurs (Paul et al., 1969). With a few exceptions the analysis and strain readings

compare well, the exceptions being the gages close to the joint between the side wall and the end slab where the analysis cannot simulate the high stress gradient, and the gages close to the anchor plate of the longitudinal rods where it is difficult to simulate the boundary condition correctly. Some of the gages on the inside face of the end slab do not compare favorably with the analysis and the discrepancy is discussed in Appendix C.

As the internal pressure is increased, the compression due to prestress will eventually be overcome in certain locations and cracks will develop.

The types of cracks affecting the response of the end slab can be divided into three categories (Fig. 3.1). One type is a conical crack starting at the joint between the end slab and the wall (the reentrant corner) and propagating outwards and upwards through the vessel. The second type is flexural cracking, a term which will be used to define the radial cracks originating at the top surface of the slab. The third type is an inclined conical crack corresponding to a shear crack in a beam. These three types of cracks and how they would influence the behavior of the vessel if occurring isolated from each other are discussed in the next three sections.

3.3 Effect of Cracking at the Reentrant Corner

(a) Introduction

In its uncracked state the vessel can be viewed as a circular slab attached along its edge to a cylinder. The cylinder provides the slab with stiffness against rotation along the edge and may introduce an edge moment because of the external prestressing forces and internal pressure acting on the cylinder. The internal pressure results in a tensile stress at the reentrant corner eventually leading to a crack which occurs on a plane slightly inclined to the horizontal. The crack at the reentrant corner reduces the restraint provided by the cylinder.

(b) Calculated Effects of a Crack at the Reentrant Corner

The change in behavior of the vessel caused by a crack at the reentrant corner was investigated using the finite-element method (Fig. 3.2). It was assumed that the rest of the vessel remained uncracked during the development of the crack so that its influence could be isolated.

The stress gradient is very high near the reentrant corner, making it difficult to predict the internal pressure at which cracking occurs and to compare the strain gage readings with the calculated strains. There are three reasons for these difficulties. First, the high stress gradient makes the accuracy of the calculations questionable. The size and locations of the finite elements influence the calculations. Second, the tensile strength of concrete is not well defined for the case of multiaxial stresses and a high stress gradient. Third, a small error in the location of a strain gage causes a large difference in the measured strain.

The radial and tangential strains, respectively, are calculated for the following three conditions:

(1) Prestress only, no cracks.

(2) Prestress + 3200 psi internal pressure, no cracks.

(3) Prestress + 3200 psi internal pressure, a crack at the reentrant corner (Fig. 3.2).

Figures 3.3 and 3.4 show that, as a result of the introduction of the crack at the reentrant corner, both the radial and the tangential strains increase in the central portion of the slab, the change being more noticeable at the bottom than at the top because the strains at the top are larger before cracking. The increase in strain at the top makes it likely that flexural cracking, if it has not already started, will start when the crack at the reentrant corner develops. The strain increase is more accentuated at the

bottom surface at the center but it may be difficult to distinguish on the basis of the strain gage readings as other types of cracking also increase the strain at this location.

The uncracked slab has a circle of inflection (or, more correctly, a circle of zero change in strain) that is about 6 in. from the center of the slab at the inside surface and about 10 in. from the center on the outside surface. The crack at the reentrant corner reduces the stiffness of the joint between the end slab and the side wall, increasing the radius of the circle of inflection. When the circle of inflection shifts, the strain gages nearby will record distinct changes in strain, some of them indicating a change from tension to compression. Consequently, the development of the crack at the reentrant corner can easily be detected by strain gages located on the inside surface but not too close to the center of the slab. The change in radius of the circle of inflection on the outside surface is small, because of the restrictions imposed by the longitudinal rods.

The propagation of the crack at the reentrant corner could be expected to cause an increase in the force in the longitudinal prestressing rods because the crack may permit increased vertical deflection of the slab. However, because of the stiffness of the end slab the increased vertical deflection will be small and the rod force will increase only slightly if no additional radial cracking occurs. The finite-element solution indicates an increase in force for a rod in the inner row of 694 lb/1000 psi of internal pressure if the slab is uncracked. If a crack as the one in Fig. 3.2 exists, the corresponding value is 913 lb/1000 psi internal pressure, i.e. the increase is only about 30 percent.

(c) Discussion of Measured Strains

The development of the crack at the reentrant corner can be studied

using the strain readings obtained from PV16. Figure 3.5 shows the radial strain 1 in. from the reentrant corner. There is a decrease in tension between 1200 and 1600 psi reflecting the initiation of the crack. After 2000 psi the tension increases again which indicates that cracking at some other location overshadows the effect of the further development, if any, of the crack at the reentrant corner.

Figure 3.6 shows the strain read 3-1/8 in. from the reentrant corner. These readings confirm results obtained from the gages 1 in. from the reentrant corner but the changes are not as noticeable, the gages being further away from the crack.

The circumferential strains indicated by gages located 1/2 in. from the reentrant corner as well as those 3-1/8 in. from the corner (Fig. 3.7 and 3.8) also show the initiation of the crack although for these gages other types of cracking would give the same effect making it impossible to deduce the existence of the crack from these gages alone. The rest of the gages on the inside of the slab are located closer to the center and do not show any significant changes in strain due to the crack at the reentrant corner.

Of the gages on the outside of the slab, the ones close to the middle show a decrease in strain after 1200 psi (Fig. 3.9) which shows that flexural cracking starts at about the same pressure as the crack at the reentrant corner. The opening of the flexural cracks could have been influenced by the opening of the crack at the reentrant corner.

The strain curve for the inner row of rods (Fig. 3.10) does not show any significant increase due to the initiation of the crack.

3.4 Effect of Flexural Cracking in the End Slab

(a) Introduction

The circumferential prestress compresses the concrete in the slab in

the radial and tangential directions. The internal pressure generates bending in the slab leading to cracking on the outside face at the center of the slab. At the center of the slab, the radial and tangential strains are equal but at a distance from the center the tangential strain is larger so the flexural cracking consists of radial cracks.

(b) Calculated Effect of Flexural Cracking in the End Slab

To simulate a case of flexural cracking with no other cracks occurring, a finite-element analysis was obtained for the crack configuration shown in Fig. 3.11. The calculated radial and tangential strains are shown in Fig. 3.12 and 3.13. On the inside surface the strains are affected very little by the cracking, except at the area close to the center. At the center the strain increases significantly but the change is in the same sense and of the same magnitude as the change caused by cracking at the reentrant corner and by inclined cracks.

The introduction of the flexural cracks cause a considerable change in the calculated strains at the outside surface. The strain drops to zero and the strain gages can be expected to show tensile strains which are equal to the initial compressive prestress. The radial strains further out from the center are compressive as a result of flexural cracking.

The calculated tangential strains, which are averages at each section and include the width of the radial cracks, increase because of flexural cracking. The actual strain in the concrete between the cracks can be expected to be zero.

The calculations did not indicate any change of force in the longitudinal rods as a result of the flexural cracking.

(c) Discussion of Measured Strains

There were no tangential strain gages mounted on the outside of the slab

of PV16, so the propagation of the radial cracks has to be traced from strain gages in the radial direction only. Both gages at the center of the outside face (Fig. 3.9) indicated cracking between 1200 and 1600 psi. It is reasonable to assume that flexural cracking started at an internal pressure just below 1600 psi. If that is the case, the cracking occurred at a strain change of about 0.0004. This value was not recorded but it has to be remembered that strain was recorded at selected load steps and the maximum strain was most likely never recorded. After cracking the strain decreased to 0.00024 which is close to the initial level of prestress, indicating that the concrete cracked at a strain of about 0.00016. The finite-element analysis indicates a prestrain of 0.00016 which is slightly less than the 0.00024 deduced from the test.

The gages at 3-1/8 in. and 6-1/4 in. radius (Fig. 3.14 and 3.15) also indicate cracking at about 1600 psi which implies rapid propagation of the radial crack.

The strain readings of gages at 9-3/8 in. radius (Fig. 3.16) change from tension to compression after 1600 psi conforming to the change predicted by the finite-element analysis.

The gages at 12 in. radius show a faster increase of compression after 1600 psi (Fig. 3.17) which also conforms to the analysis. The change in slope at 1600 psi may partly be due to the simultaneous development of the crack at the reentrant corner, the development of which causes a change in the same direction (Fig. 3.3).

3.5 Effect of Development of an Inclined Crack in the End Slab

(a) Introduction

The trajectory of the inclined crack to be introduced into the finite-element model should be as close to the actual one as possible in order to

obtain meaningful results from the analysis. Because the inclined crack forms within the slab, it has been difficult to follow its development in vessels with solid end slabs. Consequently, the assumed trajectory has been based on the following observations and complementary analyses.

The analyses show that the shear stress in the end slab is distributed parabolically through the depth of the slab causing the principal tensile stresses to reach their maximum values near the mid-height of the slab. The vertical and radial stresses are of about the same size and smaller than the shear stress close to mid-height of the slab resulting in a direction of the maximum tensile stress of about 45 degrees to the horizontal.

The shear stress along the mid-height of the slab is zero at the center of the slab and increases continuously with the distance from the center up to the vicinity of the connection with the wall. The maximum tensile stress varies in approximately the same way, so the first inclined crack can be expected to develop at the mid-height of the slab, close to the wall and at approximately 45 degrees with the horizontal. However, a crack close to the wall (crack 1 in Fig. 3.18) cannot propagate far in either direction because it is bounded by areas in triaxial compression, and will have a negligible influence on the stress condition. More inclined cracks may develop further away from the wall as the internal pressure is increased. The first crack of importance is the one that propagates in the direction of the edge of the anchorage plate of the longitudinal rods (crack 2 in Fig. 3.18) because this crack is not hindered from continuing to the top surface of the slab. The direction of the principal tensile stress being about 45 degrees with the horizontal, the crack is initiated at about half the slab thickness from the edge of the anchorage plate. In one case it was possible to observe the inclined crack in its initial stage. The test of vessel PV13 was terminated

by leakage in the wall and the intact slab was cut along a diameter after the test. The embryo of an inclined crack, about 5 in. long and close to the predicted location could be seen (Fig. 3.19). The crack did not reach the top of the slab and could not have been discovered without cutting the vessel. An inclined crack may exist in the end slab without there being any way to discover it without disturbing the structure.

The inclined crack propagates in both directions. It propagates toward the edge of the anchorage plate of the longitudinal rods and simultaneously toward the inner surface of the slab but at a slower rate because of compressive stresses in both the radial and vertical directions. Due to bending, the radial compressive stress is high close to the inside surface and the slope of the crack decreases as it approaches the inside surface. This was illustrated in the case of PV12, a vessel which failed because of leakage through the wall. The slab was cut (Fig. 3.20) revealing an inclined crack that extended from the edge of the anchorage plate to a point 5-1/2 in. from the center and 2 in. from the bottom of the slab. It can also be seen that near the bottom of the slab the slope of the crack was less.

(b) Calculated Effect of an Inclined Crack in the End Slab

To investigate the effect on stresses and strains of the initiation of an inclined crack, a finite-element analysis was run for the case of a 5-1/4 in. long inclined crack extending 3-1/2 in. above and 1-3/4 in. below the mid-depth of the slab (Fig. 3.21). The calculated change in strain at the bottom and top surfaces of the slab was hardly observable, and consequently is not shown graphically.

Figure 3.22 shows the stresses through the depth of the slab at radii of 7-1/2 in. and 8-3/4 in. (sections A-A and B-B in Fig. 3.21). The size of the elements in the analysis was 1-1/4 by 1-1/4 in. Only the elements

adjoining the crack were noticeably affected by the crack. Consequently, the initiation of the crack cannot be observed from the strain readings obtained from gages applied on the surface of the slab or on the prestressing steel.

Figure 3.23 shows an inclined crack that has propagated to the top surface of the slab. The crack changes the load carrying mechanism of the slab in that the pressure is carried by "dome action." The structure, cracked as shown in Fig. 3.23, was analyzed using the finite-element model. The radial strains at the bottom and top surfaces of the slab is shown in Fig. 3.24. The radial strain at the outside surface was reduced considerably from the center of the slab to the intersection of the inclined crack with the top surface. This is reasonable, because that portion of the slab bounded by the crack has lost most of its structural usefulness. At the inside surface the circle of inflection changed location only slightly, the most noteworthy change being the increase in the magnitude of strain.

The calculated tangential strains are shown in Fig. 3.25. On the inside surface of the slab there is an increase in strain similar to the increase in radial strain. On the outside surface inside of the inclined crack the tangential strain is reduced considerably, making the likelihood of further flexural cracking small once the inclined crack has developed.

The propagation of the inclined crack to the outside surface can be detected by studying the strain readings from the strain gages on the outside surface of the slab. The strain gages just inside the anchorage plate can be expected to show only the residual strain caused by the prestressing when the crack reaches the outside surface.

(c) Discussion of Measured Strains

The radial strain recorded at the outside surface and 11-1/2 in. from

the center of the slab is shown in Fig. 3.17. At about 2500 psi, a decrease in compressive strain was recorded. The decrease cannot be explained by flexural cracking or the crack at the reentrant corner but must be entirely due to the inclined crack, indicating that the crack reached the top surface at a pressure of about 2500 psi. A corresponding change at the same pressure is shown by the gages at 9-3/8 in. distance from the center (Fig. 3.16). Because of the removal of the precompression caused by prestress both sets of gages indicate tensile strains at higher pressures.

These observations and the analyses described in the preceding section indicate that the development but not the initiation of inclined cracking can be sensed by the radial strain gages on the outside surface of the slab and near the anchorages of the longitudinal reinforcement.

3.6 Development of the Cryptodome and Failure of the End Slab

(a) The Failure Mechanism

The development of an inclined crack in a reinforced concrete beam changes the load-carrying mechanism from "beam action" to "arch action" a change which may lead to immediate failure. A deep beam resists the load as an arch even before an inclined crack develops. The main effect of the development of an inclined crack is to introduce geometric restrictions on the arch rib that carries the normal and shear stresses. The behavior of a deep slab is analogous to that of a deep beam. The stress distribution in the slab, even at low internal pressures, can be compared to that of a dome. The development of the inclined crack reduces the thickness of the slab and imposes restrictions on the configuration of the dome.

The inclined crack initiates at the neutral axis and at about half the slab thickness from the edge of the anchorage plate of the longitudinal rods. It propagates toward the edge of the anchorage plate of the longitudinal rods.

The crack propagates also toward the inside surface of the slab at a decreasing slope. The change in slope is caused by the high radial compressive stress close to the inside surface of the slab.

At this stage failure may occur through three mechanisms:

(1) The section of concrete between the tip of the inclined crack and the inside surface of the slab decreases continuously, causing increasing radial and shear stresses. This stress combination may cause a shear failure at the extreme point of penetration of the crack (Fig. 3.26).

(2) The inclined crack may propagate to the center of the slab at a continuously decreasing slope, carving out a plug similar to a segment of a sphere. A complete cryptodome, bounded by the inclined crack, is formed inside the slab (Fig. 3.27). The cryptodome may be able to resist a further increase of internal pressure. Ultimately the dome fails because of a combination of high normal and shear stresses (Fig. 3.28).

(3) The horizontal support of the dome is provided by the circumferential prestressing wire. At any stage during or after the development of the cryptodome the wire may fail. This type of failure is precipitated by rapidly increasing deflection of the slab due to yielding of the wire and rotation of the slab at the edge and is classified as a flexural failure (Paul et al., 1969).

The stress conditions in the cryptodome are complex for all three mechanisms of failure. The stresses are multiaxial and extremely high. The strain gages on the inside surface indicate strains on the order of 0.002 while the internal pressure is still increasing. It is clear that the strength and deformation characteristics of the concrete in the cryptodome cannot be expressed on the basis of information from cylinder tests under uniaxial compression. The properties of concrete under triaxial stress are discussed in Chapters 5 and 6.

(b) Failure Planes

Sections of the failure surfaces for three vessels failing in shear are shown in Fig. 3.29. In a diametral section, the failure surface consisted ideally of two plane portions. Plane I started at the edge of the anchorage plate and proceeded downward making an angle of about 45 degrees with the vertical. The concrete surfaces along Plane I were examined after the tests and showed rough surfaces confirming that no shearing had occurred along this plane and that the cracking was indeed caused by tensile stresses. Plane II made a smaller angle with the vertical. The concrete surfaces along Plane II were smooth indicating that the failures were caused by shear.

The inclination of the two planes varied around the vessel. The maximum and minimum inclinations are given in parentheses in Fig. 3.29. For Plane I the average angles between the vertical and the surface were between 43 and 44 degrees for the three specimens in spite of their differeng geometrical shapes. For Plane II, the average angles varied between 15 and 25 degrees with the vertical. A photograph of vessel PV16 after failing in shear is shown in Fig. 2.8.

4. OBSERVED RESPONSE OF THE TEST VESSELS WITH PENETRATIONS IN THE END SLAB

4.1 Introduction

In this chapter the observed phenomena in the tests of four vessels with penetrations 8 in. from the center of the end slab and one vessel with penetrations 4 in. from the center of the end slab are discussed in relation to the response of vessels with solid end slabs. In designing the test vessels with penetrations, it was desired to locate the series of penetrations in a position that would be most critical for the shear strength of the end slab.

It was observed in the test of vessel PV16 with a solid end slab that inclined cracking initiated at mid-height of the slab on an 8-in. radius from the center. To have a direct influence on the development of the inclined crack, it was decided to place the penetrations in four of the vessels symmetrically along a circle with an 8-in. radius.

There were two variables in the design of these four vessels: the number and the size of the penetrations. Two of the vessels were cast with penetrations of 4-in. diameter while the other two had 2-in. penetrations. In two vessels, PV18 and PV20, the penetrations removed 50 percent of the slab section along a circle of 8-in. radius. The other two vessels, PV17 and PV21, had half as many penetrations removing 25 percent of the concrete along a circle of 8-in. radius (Table 2.1 and Fig. 2.5).

The dome which was formed in the end slab of vessel PV16 failed about 4-1/2 in. from the center of the slab. To investigate if penetrations in this section would influence the shear strength of the end slab, vessel PV19 was cast with penetrations located 4 in. from the center of the slab, removing 50 percent of the slab section along a circle of 8-in. radius (Fig. 2.6). It was shown in Chapter 2 that the effect of penetrations may have been curtailed by the presence of sealing plates and it is unwise to draw conclusions based

on the experimental results. However, the analytical results for this vessel are shown.

The following section of this chapter develops an analytical model for the vessels with penetrations. It is shown that a simple model based on axisymmetry of the structure supplemented by idealized assumptions regarding the influence of penetrations can be used instead of resorting to a three-dimensional model. The model is used for comparison of the vessels with each other as well as with the vessel with a solid end slab and in the interpretation of the test results.

In section 4.3, the initiation and propagation of the inclined cracks are discussed. Strain gages were mounted on the concrete inside the penetrations in the area where the inclined crack was initiated. Thus the initiation of the inclined crack could be studied, which was not possible for vessels with solid end slabs.

In sections 4.4 and 4.5 the crack at the reentrant corner and flexural cracking as observed in the tests of the vessels with penetrations are discussed.

Observations of the failure mode of the vessels are discussed in section 4.6.

4.2 Calculated Influence of Penetrations

A vessel with penetrations in the end slab is not an axisymmetric structure. The finite-element solution presented in Chapter 3 cannot be used in evaluating the stress condition in such a vessel. It could be analyzed using a three-dimensional solution but such an approach would be unwieldy and expensive and may not lead to a substantially better result than a modified two-dimensional solution.

In this section a simple approach is described based on the following

two assumptions about the stress condition in the neighborhood of the penetrations.

The tangential strains at the same distance from the center of the slab as the penetrations are small. If there are several penetrations within a torus (Fig. 4.1) the tangential stress in the torus approaches zero. The more penetrations there are, the better is this assumption. Furthermore, it is preferred to overestimate rather than underestimate the influence of the penetrations because the correct solution is then bounded by the solutions for a vessel with a solid end slab and for a vessel with penetrations in the end slab.

If the assumption is made that the tangential stress is zero in the area between the penetrations, the slab can be considered as consisting of a solid cylinder inside a thick-walled cylinder, the two interacting through springs (Fig. 4.2). The springs transfer normal and shear stresses in the radial-vertical plane. The stiffness of the springs is determined by the amount of concrete remaining between the penetrations.

The calculated effect on radial and tangential stresses of penetrations in a slab subjected to uniform pressure in the radial direction is shown in Fig. 4.3. The approximations described above have been used to simulate the effect of the penetrations. If 50 percent of the concrete is removed (Fig. 4.3a) the radial stress will reach a maximum of more than twice that in a solid slab.

The changes in the tangential stress resulting from the introduction of the penetrations can be estimated directly from the conditions of equilibrium. For a given external pressure, the integral of the tangential stresses along a diameter has to remain constant. If the penetration removes a certain portion of the diameter, the stresses in the remaining portions increase. In the solid

end slab, the tangential stress would have been unity.

The approximations described above have to be incorporated into the finite-element program because of the complicated geometrical shape and loading condition of the vessels. The finite-element tori that are cut by penetrations are modified in the way described above by setting the modulus of elasticity in the tangential direction to zero and by reducing the modulus of elasticity in the radial-vertical plane in proportion to the amount of concrete that is removed by the penetrations in each torus.

Solutions have been obtained for all vessels with penetrations using the approximations described above. The solution for PV16 has been used as a standard of comparison. The material properties and the prestressing levels do not differ very much between the vessels (Table 2.1). To evaluate the influence of the penetrations properly, the material properties and prestressing level of PV16 have been used in the solutions for all vessels, thus making the size, number and location of the penetrations the only variables.

In comparing the finite-element solutions with the solution in Fig. 4.3 the strains at mid-height of the slab are most appropriate to use since the influence of bending is small at that level. Figure 4.4 shows the radial strains at mid-height of the slab under the influence of the prestressing forces. A comparison of the radial strains for vessels PV16, PV17 and PV18 (vessels with 0, 25 and 50 percent, respectively, of the slab section removed at a distance of 8 in. from the center) shows that the magnitude of the strain varies with the amount of section removed in the same way for both the finite-element solution and the solution in Fig. 4.3.

Figure 4.5 shows the tangential strains at mid-height of the slab due to prestress. These results also compare favorably with the results in Fig. 4.3.

Finite values of the strains at penetrations refer to average deformations of the tori containing the penetrations. The stress at these locations is zero because, in the finite-element solution, the modulus of elasticity of the elements contained in those particular tori has been assumed to be zero.

Figures 4.6 and 4.7 show the radial and tangential strains at mid-height of the vessels at 3200 psi internal pressure with the strain due to prestress subtracted. The vessel is assumed to be uncracked. These results can be compared directly with the initial slope of the strain readings obtained in the tests. A comparison between calculated strains at mid-height for different vessels show that throughout the slab they are related in about the same way as for the case of prestress only. Evidently the radial and tangential strains at mid-height of the vessel are only slightly affected by bending and are mainly due to changing stress in the circumferential wire.

The corresponding results for strains at the outside and inside surfaces of the slab are shown in Fig. 4.8 through 4.15. These results can be compared with strain readings obtained from gages mounted on the surface of the slab during the tests of the vessels.

The most important indication of the finite-element solutions is that the strains, except at locations close to the penetrations, are not sensitive to the number and size of the penetrations in the test vessels. The differences are too small to be confirmed by strain gage readings or to be of major importance to the behavior of the vessel.

4.3 Initiation and Propagation of the Inclined Crack

In the vessels with solid end slabs the condition leading to an inclined crack and the initiation of the inclined crack could not be measured directly (Chapter 3). The conclusions drawn were based upon the post-test inspections of some slabs that did not fail structurally and on the analysis of the stress

condition in the end slab.

The introduction of penetrations through the slab made it possible to record the initiation of the crack. The inclined crack is assumed to start at mid-height of the slab and at half the slab thickness from the edge of the anchorage plate. Strain gage rosettes, measuring the vertical, diagonal and horizontal strains, were mounted at mid-height of some of the penetrations in an effort to determine the initiation of the inclined crack.

(a) Initiation of the Inclined Crack

The measured radial strains in the penetrations of vessels PV17, PV18, PV20 and PV21 are shown in Fig. 4.16 through 4.19. The radial strains indicated by the finite-element solutions are also shown in the figures. In general, the agreement between the calculated and measured strains is satisfactory until cracking is initiated. In the area where the penetrations are located, the axisymmetric finite-element solution appears to estimate the radial strains correctly.

The vertical strains at mid-height of the slabs inside the penetrations are shown in Fig. 4.20 through 4.23. These measurements also compare well with the finite-element solutions.

The radial and vertical strains calculated for the case of internal pressure only by using the finite-element model agree well with the strain gage readings. It is therefore assumed that the radial strains for the case of prestressing load are evaluated equally well by the finite-element method for known forces in the prestressing wire and rods. The vertical strains in the end slab related to prestressing are very small.

The shear strains at mid-height of the slab and inside the penetrations as calculated from the multiaxial strain readings are shown in Fig. 4.24 through 4.27. In all cases the finite-element solutions indicate shear strains smaller than those measured.

The discrepancy in calculating the shear strain is due to the size of the elements. The effect of element size on the shear strain for the case of PV20 with 2-in. penetrations is illustrated in Fig. 4.28. In the finite-element model used, the radial dimension of the element was 1 in. Thus, elements located between circles with radii 7 and 8 in. were used. These elements are tangent to the center of the penetrations as well as the circumference. The effect of the penetrations is averaged in the elements. In the section between radii 7 and 8 in., an average of 40 percent of the concrete was removed so the modulus of elasticity used in the analysis is reduced to 60 percent of the value used in the rest of the vessel. However, at a radius of 8 in. 50 percent of the concrete is removed. Thus, the calculated shear strain at a radius of 8 in. is increased by only 67 percent instead of 100 percent. This could be corrected by using smaller elements which represent the penetrations more accurately. However, it is not warranted to use smaller elements because the shear force along any circumference is uniquely determined by equilibrium and is independent of the force-deformation relationship. A good estimation is obtained if the shear strain calculated from the finite-element solution for PV16, increased in proportion to the slab section removed at a radius of 8 in., is used as a comparison. The results of this estimate are shown by the broken lines in Fig. 4.24-4.27.

The size of the elements, which led to the disparity between calculated and measured shear strains, does not seem to have adversely affected the calculations of vertical and radial strains as they show good agreement with the strain gage readings.

In Chapter 3 it was shown that the initiation of an inclined crack in a solid slab affects the strain in the concrete only locally. Before the crack propagates to the top surface only those gages bridging the crack or very close

to it can be expected to record the crack. There is no reason to assume this to be different in a slab with penetrations. Although the gages were located where the crack is believed to have started, all of them cannot be expected to record the event. For this reason the initiation of the crack is assumed to have occurred at the internal pressure at which any one of the gages at mid-height indicates cracking. Therefore, the inclined crack is assumed to have started between internal pressures of 1250 and 1500 psi in PV17 (Fig. 4.20) and between 1400 and 1600 psi in PV18 (Fig. 4.17 and 4.21).

To determine the internal pressures corresponding to the initiation of the inclined cracks in PV20 and PV21 from individual strain gage measurements proved futile. The strain gages do not record any appreciable deviation before internal pressures of 2000 psi. Such a late development of the inclined crack is very unlikely in view of the cracking pressures for the other vessels and cannot be accepted as being correct without further investigation.

The rosette gages mounted in the penetrations at mid-height of the slabs measured strains in three directions in the radial-vertical plane. These readings made it possible to calculate the strain in the horizontal-vertical plane in polar coordinates so that the strain in any direction could be obtained. Figure 4.29 shows in polar coordinates the strains measured by a particular rosette gage located at mid-height in one of the penetrations in the end slab of vessel PV17. This particular gage was chosen for discussion because the indicated strains represented median values of those measured at comparable locations.

To evaluate the significance of the strains in Fig. 4.29 the influence of the prestressing has to be known. The vertical and radial strains due to prestress can be obtained from the finite-element solutions (Fig. 4.4 and 4.5). The shear strain around the penetrations due to prestress is very small so any

inaccuracy in the finite-element solution can be neglected. The strains in polar coordinates due to prestress are shown in Fig. 4.30. Two more curves are drawn, showing tensile strains of 0.00015 and 0.00030 which are reasonable bounds to the cracking strain of concrete.

Figure 4.31 shows Fig. 4.30 superimposed on Fig. 4.29. According to this interpretation a net tensile strain is developed before an internal pressure of 500 psi is reached. If a cracking strain of 0.0003 is assumed, cracking can be expected to occur an an internal pressure of 1250 psi and at an angle of about 45 degrees with the horizontal. This is a reasonable inclination of the crack and the stimated cracking load is consistent with the previous mentioned way of determining the cracking load.

Even after a net tensile strain of 0.0003 is reached, the strain continues to increase smoothly (Fig. 4.31). Some gages have recorded net tensile strains of 0.0006, which is much higher than any reasonable assumption of the cracking strain of concrete. The reason for the high measured strain is that initially an inclined crack, located within a solid body and fairly short, is very fine. It does not break a strain gage that spans it, but only increases the average strain that is recorded by the strain gage. Not until the crack is longer, perhaps extended to the top surface, is it wide enough to manifest itself through the strain gage readings as a crack.

Using the method illustrated in Fig. 4.31, the internal pressures corresponding to the initiation of the inclined crack in the other vessels were estimated to 1350 psi for PV18 (Fig. 4.32), 1400 psi for PV20 (Fig. 4.33) and 1500 psi for PV21 (Fig. 4.34). The variation in the internal pressure at which the inclined crack was initiated is small even though the number and size of penetrations varied considerably.

The observed variation in the cracking pressure was considerably less than

the reduction of the perimeter through the centers of the penetrations. This result is related to the mechanism of cracking. Consider a hypothetical end slab made of concrete that has no tensile strength. The strain leading to cracking can be considered to be the sum of a compressive strain caused by prestressing, ε_o, and a tensile strain caused by the internal pressure, ε_g:

$$\varepsilon_o = A\sigma_o \tag{4.1}$$

$$\varepsilon_g = B\sigma_g \tag{4.2}$$

Cracking occurs when ε_g exceeds ε_o. When penetrations are introduced the constants A and B are changed. However, it was found using the finite-element solutions that the ratio A/B remained almost constant. Thus, the internal pressure at which cracking is initiated can be expected not to vary when penetrations are introduced into the hypothetical end slab.

But the concrete has some tensile strength which has to be taken into account. Equation 4.1 has to be changed so that the tensile strain at cracking, ε_t, is included in ε_o

$$\varepsilon_o = A\sigma_o + \varepsilon_t \tag{4.3}$$

To determine the influence of the penetrations on the cracking pressure the relation

$$\frac{\varepsilon_o}{\varepsilon_g} = \frac{A\sigma_o + \varepsilon_t}{B\sigma_g} \tag{4.4}$$

has to be studied. For the solid slab, the terms $A\sigma_o$ and ε_t in Eq. 4.4 were comparable.

The variable β is defined as the solid perimeter divided by the total

perimeter at any section. If it is assumed that A and B vary inversely with β (meaning, for example, that if the penetrations reduce the perimeter by 50 percent the strains are doubled) and that the terms $A\sigma_o$ and ε_t are identical for a solid slab, Eq. 4.4 reduces to

$$\frac{\varepsilon_o}{\varepsilon_g} = \frac{\frac{1}{\beta} + 1}{\frac{c\sigma_g}{\beta}} \tag{4.5}$$

Cracking is assumed to occur when Eq. 4.5 is equal to unity, which occurs at an internal pressure of

$$\sigma_g = \frac{1 + \beta}{c} \tag{4.6}$$

It follows that in going from the end slabs with β equal to 0.75 to those with β equal to 0.50, the reduction in cracking pressure is only 0.14.

In view of the scatter to be expected as a result of concrete strength, of cracking at other locations, and of measuring inaccuracies, it is not surprising that no consistent trend was observed in the measured cracking pressures for the end slabs with different numbers and sizes of penetrations.

(c) Propagation of the Inclined Crack

It was shown in Chapter 3 that the emergence of the inclined crack at the top surface of the slab can be sensed by gages mounted in the radial direction on the top surface of the slab.

Vessels PV17 and PV18 had 4-in. penetrations. Gages were mounted in the penetrations at radii 6 and 10 in. from the center of the slab so that the development of the inclined crack could be recorded at two more points along its trajectory.

According to the method of observation described in the previous section, the inclined crack in vessel PV17 initiated at 1250 psi. Gage C44 (Fig. 4.35), located 10 in. from the center of the slab inside the penetration and just

below the expected trajectory of the crack, recorded an increase in the rate of compressive strain after 1500 psi internal pressure, indicating increased "dome-action" because of the development of the inclined crack.

The inclined crack affected the radial strains along the outside surface after 2250 psi (Fig. 4.36). Evidently the compressive radial stress at the top surface restrained the propagation of the inclined crack.

The propagation of the inclined crack toward the inside face of the end slab should be sensed by gages mounted inside the penetrations at the location shown in Fig. 4.37. Gage C65, which is close to the expected path of the inclined crack, recorded tensile strains on the order of 0.0006 (the compressive prestrain plus the net tensile strain) at a pressure of approximately 2500 psi indicating that the crack reached this level.

Gages were mounted in corresponding locations in vessel PV18. The inclined crack initiated at about 1350 psi. The gage 10 in. from the center of the slab recorded the crack after 1400 psi (Fig. 4.38) and it reached the top surface after 2100 psi (Fig. 4.39). In propagating downwards the crack crossed the strain gage mounted 6 in. from the center of the slab and 2-1/2 in. from the bottom surface at 2500 psi (Fig. 4.40).

Vessels PV20 and PV21 did not have any gages in the penetrations besides the one at 8 in. from the center of the slab. The only information about the propagation of the inclined crack is derived from the radial gages at the top surface of the slab. In the test of vessel PV20, the inclined crack reached the top surface at 2000 psi internal pressure (Fig. 4.41), while in vessel PV21 the same event took place at a slightly higher pressure, 2250 psi (Fig. 4.42).

For vessel PV19, which had penetrations located 4 in. from the center of the slab, the formation of the inclined crack could not be traced. The

gages on the outside face of the slab first recorded the inclined crack at a pressure of about 2700 psi (Fig. 4.43).

The following conclusions can be drawn from observations of the propagation of the inclined crack:

(a) The inclined crack was initiated at about mid-height of the slab at an angle of approximately 45 degrees with the horizontal.

(b) The crack propagated first toward the outer surface of the end slab while its propagation toward the inside surface is almost negligible.

(c) The propagation of the crack toward the outer surface was slow due to the restraining effect of the radial compressive stress close to the anchorage plate of the longitudinal prestressing rods.

(d) Downward propagation of the crack was not recorded until after the inclined crack had reached the top surface. This is attributable to the redistribution of shear stresses occurring when the inclined crack reaches the top surface. The entire shear force then has to be transferred by the concrete section between the tip of the inclined crack and the inside surface of the slab (Fig. 4.44).

(e) The rate of progress of the inclined crack toward the outer surface of the slab was faster in the slabs having penetrations.

4.4 Crack at the Reentrant Corner

The stress gradient is very high at the reentrant corner making it difficult to determine the absolute stresses. However, a comparison between the finite-element solutions for the different vessels shows the influence of penetrations on the stresses at the reentrant corner. The radial, vertical and shear stresses at the reentrant corner have to be studied as they are all very high. The radial compression caused by the prestressing is lower in vessels with penetrations than in a vessel with a solid slab, Fig. 4.8.

Furthermore, the additional tensile strain caused by the internal pressure is slightly higher in a vessel with penetrations in the end slab compared to a solid one, Fig. 4.10. Therefore, the net tensile radial strain can be expected to be slightly higher if the slab has penetrations. The vertical strain is of about the same size as the radial strain but the variation caused by penetrations is almost zero. Also the shear strain, which is very large, is virtually unaffected by the presence of penetrations. The composite effect of the three stresses is that the initiation of the crack at the reentrant corner is almost independent of penetrations in the end slab.

It was shown in Chapter 3 that the crack at the reentrant corner would affect the radial gages close to the crack. In PV16 the crack is believed to have been initiated between 1200 and 1600 psi internal pressure.

The crack can be detected by the same method in the vessels with penetrations. It is believed to have initiated at about 1250 psi in PV17 (Fig. 4.45), between 1000 and 1200 psi in PV18 (Fig. 4.46) and between 1200 and 1400 psi in PV20 (Fig. 4.47). In PV21 there were no radial gages close to the reentrant corner but circumferential gages indicate cracking between 1250 and 1500 psi (Fig. 4.48).

In vessel PV19 the crack was initiated between 1500 and 1750 psi internal pressure (Fig. 4.49).

Usually the initiation of the crack at the reentrant corner is manifested by a very distinct reversal in the radial strain. This is not the case for PV18 (Fig. 4.46), in which the increase in strain only stagnates. The reason for this may be a circumferential crack connecting the penetrations on the inside of the slab. The crack was discovered after the test but it is not possible to determine at what pressure it developed.

To determine the internal pressure at which cracking is initiated at the

reentrant corner the load steps should have been smaller. The only conclusion that can be drawn is that the crack initiated at about the same internal pressure in all vessels and seems to have been independent of the penetrations.

4.5 Flexural Cracking

(a) Introduction

Before cracking, the solid end slab resists the load primarily in flexure. If penetrations are introduced, one section of the slab is made weaker but the internal pressure is still resisted by bending as long as the concrete is intact. The main difference is that the strains in the concrete between the penetrations is higher than they would be in a solid slab.

(b) Observed Response

The calculated change in radial strains at the outside of the slab caused by the internal pressure only is shown in Fig. 4.14. It can be seen that the slabs with 4-in. penetrations can be expected to have a slightly larger strain at the center of the slab than the slabs with 2-in. penetrations which in their turn can be expected to have a larger strain than the solid slab. The difference between the two extreme values is less than 20 percent.

The strain measured at the center of the outside face of the end slab of vessel PV16 is shown in Fig. 3.9. The rate of strain increase was slightly smaller than predicted by the finite-element solution. The rates of strain increase measured in PV17 (Fig. 4.50) and PV20 (Fig. 4.51) were almost the same as that measured in PV16. In PV18 (Fig. 4.52) and PV21 (Fig. 4.53) the measured rates of strain increase were slightly higher than in the other vessels. However, the differences are very small and do not correlate with the finite-element solutions.

The radial strains were also measured at a distance of about 6-1/2 in. from the center of the slab. According to the analysis, the effect of pene-

trations should be noticed on these gages through increased radial strains. However, no noticeable increases were recorded by the gages on PV17 and PV21, the slabs that had 25 percent of the concrete removed along a circular section 8 in. from the center. For PV18 and PV20, the measured strains (Fig. 4.54 and 4.41) were significantly larger than the strains measured at the same radius in the solid slab (Fig. 3.15).

To determine the internal pressure corresponding to the initiation of flexural cracking the strains caused by the prestressing forces and by internal pressure have to be evaluated. According to the finite-element solution the strain due to prestress on the outer surface at the center of the slab is slightly higher in vessels with penetrations than in vessels with solid end slabs (Fig. 4.12). However, in all slabs the prestressing level at the top surface was very small compared with the expected strains caused by the internal pressure. The strains caused by internal pressure were larger between the penetrations than they were in the same section in a solid end slab. The measured strains for PV18 (Fig. 4.52 and 4.54) show that the rate of strain increase at the center of the slab and at a distance of 6-1/4 in. from the center were almost the same. Therefore, two types of flexural cracking were possible: (a) radial cracks originating at the center of the slab and (b) a circumferential crack passing through the penetrations. In PV18, both types of cracking were observed after the test. The circumferential crack penetrated about 6 in. below the top surface of the slab and about 2 in. below the level of the inclined crack (Fig. 2.12). Presumably, that part of the crack which fell between the inclined crack and the inside surface of the slab closed at higher internal pressures under the influence of the thrust in the cryptodome.

It was not possible to determine if circumferential cracks developed in

the slabs of the other vessels because the slabs were badly damaged at the end of the test as a result of explosive failures.

The calculated radial strain along the outside face of vessel PV19 had its maximum value between the penetrations (Fig. 4.14). A circular crack developed connecting the penetrations (Gage C49 in Fig. 4.43) and relieving the strains in the center part of the slab (Fig. 4.55).

The internal pressure at which flexural cracking initiated varied between vessels. The internal pressures after which flexural cracking occurred were 500 psi for PV19 (Fig. 4.55), 750 psi for PV21 (Fig. 4.53), 1000 psi for PV17 (Fig. 4.50) and PV18 (Fig. 4.52) and 1200 psi for PV20 (Fig. 4.51) as compared with 1250 psi for PV16 (Fig. 3.9). There is a tendency for flexural cracking to develop earlier in a slab with penetrations. Except for vessel PV19 the difference is small enough to be attributable to variations in material properties and prestressing level.

4.6 Failure of the End Slab

In the previous sections the similarities in crack patterns and crack development between vessels with and without penetrations have been pointed out. It is then not surprising to find that the type of failure and the failure load are only slightly affected by the introduction of penetrations in the end slab (Table 2.1).

Because of the explosive failures a positive description of the failure characteristics is not possible. However, by combining the information from the five vessels with penetrations a general idea of what actually happened can be obtained. Vessels PV18 and PV19, which did not fail structurally, show the formation of the cryptodome while the other vessels show the location of the failure plane.

Figure 2.12 shows a diametral cut of the slab of vessel PV18 with the

inclined crack marked with black dye. The slope of the inclined crack is initially 45 degrees. The location of the crack is clearly visible up to a distance of 5 in. from the center line of the slab. In the central portion of the slab, about 2 in. from the inside surface, horizontal cracks can be seen indicating that the cryptodome is formed even if the boundary is not clearly defined.

In vessel PV19, the flexural crack that connects the penetrations propagated downward carving out a narrow but deep (about 7 in.) plug. The inclined crack formed but it cannot be confirmed if it propagated to the center of the slab or ended at the penetrations (Fig. 2.13).

The failure planes for the three vessels failing in shear are shown in Fig. 2.9 to 2.11. The inclined cracks of these vessels had initial slopes that were about 45 degrees. The failure planes were located 8 in. from the center of the slabs, i.e. through the section where the penetrations were. The planes made angles with the vertical of about 20 degrees. If vessel PV18 had failed structurally, the failure plane would probably have been similar to that of the other vessels.

It is likely that the cryptodome was fully developed in all four vessels with penetrations 8 in. from the center, as they all reached the maximum pressure of PV18. The failure occurred in the section where the most dangerous stress combination was developed, which for all vessels, probably PV18 too, was the section with penetrations.

The failure pressures were influenced very little by the penetrations, it was 3200 for PV16 while it varied between 3000 and 3300 psi for the vessels with penetrations 8 in. from the center. Vessel PV19 with penetrations 4 in. from the center failed at an internal pressure of 3500 psi. This variation is small enough to be attributable to varying material properties and prestress

levels as well as to the penetrations.

The tests showed that a limited number of penetrations did not lower the maximum internal pressure. If still more penetrations are introduced a point can undoubtedly be reached where the strength of the slab is adversely affected.

5. REVIEW OF FAILURE THEORIES FOR CONCRETE

5.1 Introduction

The propagation of the inclined crack leads to the formation of the cryptodome in the end slab. The failure of the concrete in the cryptodome is likely to occur under a complex state of multiaxial stresses. There is as yet no generally accepted or confirmed failure criterion for concrete subjected to stresses in three directions. The following sections review various methods for predicting the failure of concrete in order to describe explicitly the considerations involved in the selection of the failure criterion used in calculating the strength of the end slab.

The failure criterion refers to the effects of stress at room temperature. Its selection was guided by three factors:

1. The theory should make possible an accurate prediction of the failure stresses. To judge the reliability of the theory, its predictions have to be compared with test results. However, different researchers have often reached widely different failure loads for what was believed to have been the same loading condition. Therefore, it is also necessary to evaluate the available test results.

2. The failure criterion to be used should be as simple as possible and certainly no more complicated than is warranted by its accuracy and scope in relation to the supporting data.

3. The stress combinations considered are limited to cases where none of the principal stresses is tensile.

5.2 The Octahedral Shearing Stress Theory

In using the octahedral shearing stress theory, the normal and shearing stresses on an octahedral plane, relative to the principal planes, are calculated.

$$\tau_{oct} = 1/2\ [(\sigma_1 - \sigma_2)^2 + (\sigma_2 - \sigma_3)^2 + (\sigma_3 - \sigma_1)^2]^{1/2} \qquad (5.1)$$

$$\sigma_{oct} = 1/3(\sigma_1 + \sigma_2 + \sigma_3) \qquad (5.2)$$

Failure is predicted by relating the octahedral normal stress to the octahedral shearing stress

$$\tau_{oct} = f(\sigma_{oct}) \qquad (5.3)$$

Bresler and Pister (1957 and 1958) performed combined compression and torsion tests on hollow cylinders. Thus they created a biaxial state of stress with one of the principal stresses compressive and the other tensile. They found a consistent and nearly linear relationship between τ_{oct} and σ_{oct} but they stated that their results could not be extended to either biaxial compression or to triaxial compression.

Bellamy (1961) performed tests on hollow cylinders which failed under either triaxial or biaxial compression. He compared the octahedral shearing stress with the octahedral normal stress determined in his tests as well as in tests by Richart, Brandtzaeg and Brown (1928), and Balmer (1949). However, for low values of σ_{oct}/f_{cu}, a large scatter was obtained and no correlation could be found. For higher values of σ_{oct}/f_{cu} the correlation obtained was good.

All these test data are from triaxial compression tests where the two smallest stresses are equal. For this case the Eq. 5.1 and 5.2 are simplified to

$$\tau_{oct} = 2/3(\sigma_1 - \sigma_2) \qquad (5.4)$$

$$\sigma_{oct} = 1/3(\sigma_1 + 2\sigma_2) \qquad (5.5)$$

If these equations are combined with Eq. 5.3 the following relationship is obtained

$$\sigma_1 = f(\sigma_2) \tag{5.6}$$

Equation 5.6 leads to a failure criterion that is identical to the one based on Mohr's stress circles and which is described in section 6 of this chapter. Consequently, for the case of triaxial compression when $\sigma_2 = \sigma_3$ the octahedral shearing stress theory is not better than the criterion based on Mohr's stress circles.

The only advantage the octahedral shearing stress theory may have is its possible capability to predict the failure load of concrete subjected to three principal stresses of different magnitude. However, for cases of triaxial compression other than $\sigma_1 > \sigma_2 = \sigma_3$* there are no reliable experimental results. Therefore, there is no justification for using the octahedral shearing stress theory for an arbitrary stress combination. Indeed, there are reasons to suggest that this theory may indicate as safe certain stress combinations which will cause failure. Figure 5.1 shows a relation between σ_{oct} and τ_{oct} calculated from test data for the case $\sigma_1 > \sigma_2 = \sigma_3$ reported by Balmer (1949). The data show a smooth and consistent relationship. Any stress combination which is represented by a point below these data would be called admissible according to the octahedral shearing stress theory. Two particular stress combinations are considered below to check the applicability of this hypothesis.

Consider a stress combination with $\sigma_1 = \sigma_2 = 5f_{cu}$ and $\sigma_3 = 0.1f_{cu}$. This is essentially a biaxial stress condition and should be unsafe because it is not plausible to expect that the third principal stress of $0.1f_{cu}$ would increase the strength in the other two directions from approximately $1.2f_{cu}$ for $\sigma_3 = 0$

---

*These inequalities are written with respect to the absolute magnitudes of the stresses.

(Kupfer, Hilsdorf, Rusch, 1969) to $5f_{cu}$ for $\sigma_3 = 0.1f_{cu}$. However, the octahedral shear and normal stresses for this stress condition locate it at a point below the limiting stress combination (Fig. 5.1). A similar result is obtained for $\sigma_1 = \sigma_2 = 10f_{cu}$ and $\sigma_3 = f_{cu}$ (Fig. 5.1).

From the preceding discussion, it follows that the octahedral shearing stress theory is neither accurate nor safe for general use.

5.3 The Maximum Distortion Energy Theory

The maximum distortion energy theory, also called the von Mises yield criterion, is strictly applicable to a material which remains linearly elastic up to the yielding stress. However, it does provide a scheme for incorporating the effects of combined stresses on the strength of concrete.

The energy of a material subject to stresses consists of energy due to volume change and energy due to distortion. The energy due to distortion, chosen as a criterion for failure, can be expressed as

$$U_{distortion} = \frac{1}{12G}\left[(\sigma_1 - \sigma_2)^2 + (\sigma_2 - \sigma_3)^2 + (\sigma_3 - \sigma_1)^2\right] \tag{5.7}$$

For an unconfined compression test, Eq. 5.7 becomes

$$U_{distortion} = \frac{2}{12G}(f_{cu})^2 \tag{5.8}$$

The failure criterion obtained is then

$$(\sigma_1 - \sigma_2)^2 + (\sigma_2 - \sigma_3)^2 + (\sigma_3 - \sigma_1)^2 = 2(f_{cu})^2 \tag{5.9}$$

If Eq. 5.9 is compared with Eq. 5.1 to 5.3 it is evident that the maximum distortion energy theory is a special case of the octahedral shearing stress theory for which Eq. 5.3 is

$$\tau_{oct} = \text{constant} \tag{5.10}$$

It is then clear that the maximum distortion energy theory has the same drawbacks and limitations as the octahedral shearing stress theory.

For a triaxial test where $\sigma_1 > \sigma_2 = \sigma_3$, Eq. 5.9 is simplified to:

$$(\sigma_1 - \sigma_2)^2 = (f_{cu})^2 \tag{5.11}$$

This relationship is plotted in Fig. 5.2 for different values of σ_1, and σ_2. As it is evident from the figure, the basis for Eq. 5.11 is a constant limiting shear stress. However, existing data (Richart, Brandtzaeg and Brown, 1928) show convincingly that for higher compressive stresses in the principal directions, higher shear stresses can be carried. This criterion is therefore not suitable as a general failure criterion for concrete.

5.4 The Limiting Tensile Strain Criterion

The limiting tensile strain criterion is based on the notion that the material fails when the tensile strain in any direction reaches a limiting value. If $\sigma_1 \geq \sigma_2 \geq \sigma_3$ the limiting tensile strain is

$$\varepsilon_3 = -\frac{\sigma_1 \nu_1}{E_1} - \frac{\sigma_2 \nu_2}{E_2} + \frac{\sigma_3}{E_3} \tag{5.12}$$

where

$E_i = \frac{\text{average stress}}{\text{average strain}}$ at this particular stress combination

ν_i = Poisson's ratio corresponding to E_i

Several problems arise in applying this criterion to concrete.

The limiting strain varies. Different values of the limiting strain have been obtained for different concrete mixes and different types of loading (Anson, 1964). A value frequently used is 0.0001, but even twice that value can easily be justified.

The value of E_i varies with the stresses. In tests with triaxial compression it can decrease to 1/5 or less of its initial value (Balmer, 1949; Richart, Brandtzaeg and Brown, 1928).

Poisson's ratio is often assumed to be 0.15. However, at higher stresses internal cracks will develop and the apparent value of ν_i will increase considerably.

Anson (1964) and Baker (1970) have used the limiting strain criterion in order to determine the strength of concrete under complex states of stress. Concrete was assumed to be essentially a two-phase material consisting of aggregate surrounded by softened mortar. This structure was simulated as a lattice with the joints at the center of the pieces of aggregate. The stiffnesses of the different components of the lattice were chosen to simulate the behavior of concrete. The structure was loaded and the strains in the different members calculated. A failure criterion for the components was obtained by assuming a limiting tensile strain. It could then be demonstrated that E and ν change as the load is increased. However, the lattice structure had to be kept simple and the method provided qualitative rather than quantitative results.

To use Eq. 5.12 properly under all loading conditions, it is necessary to have information on the variations of E and ν under all levels and combinations of stress. This is not possible today and it is doubtful if it will be possible within the foreseeable future.

5.5 Failure Criterion Proposed by Hannant and Frederick

In determining the combination of stresses causing failure, Hannant and Frederick (1968) used a three-dimensional stress space with the principal stresses σ_1, σ_2 and σ_3 plotted along the axes (Fig. 5.3). Only one-eighth of the stress space, where all stresses are compressive, was considered. A failure surface was defined as the limit of the safe domain of stress combi-

nations not leading to failure and consisted of two main surfaces A and B and a transition surface C. The failure surface was obtained by compiling and plotting available data on stress combinations causing failure.

(a) Surface A

This surface represents the condition of biaxial compression. Much confusion prevails for this loading case as different authors have reached widely varying results (Kupfer, Hilsdorf and Rusch, 1969; Vile, 1968; Fumagalli, 1965; Iyengar, Chandrashekhara and Krishnaswamy, 1965). The biaxial strength found has varied from four times to less than the uniaxial compressive strength. Hannant and Frederick believed that the credible tests were those which indicated the biaxial compressive strength to be slightly higher than the uniaxial compressive strength and chose a square criterion such that

$$\sigma_1 \leq f_{cu}$$

$$\sigma_2 \leq f_{cu} \qquad (5.13)$$

$$\sigma_3 = 0$$

(b) Surface B

Surface B represents one of the boundaries of the safe domain for conditions with all three principal stresses compressive. Test data have been reported only for the conditions $\sigma_1 > \sigma_2 = \sigma_3$ and $\sigma_1 = \sigma_2 > \sigma_3$.

The condition $\sigma_1 = \sigma_2 > \sigma_3$ has been treated by Richart, Brandtzaeg and Brown (1928) and Chinn and Zimmerman (1965). The former recognized that the results they obtained were not reliable. Frederick and Hannant thought that the results by Chinn and Zimmerman did not agree with accepted results obtained for biaxial compression and could not be used.

The only case for which reliable data have been obtained is $\sigma_1 > \sigma_2 = \sigma_3$.

Hannant and Frederick used data from Richart, Brandtzaeg and Brown (1928), Chinn and Zimmerman (1965) and Balmer (1949) to obtain

$$\sigma_1 = f_{cu} + 4\sigma_3 \qquad \sigma_2 = \sigma_3 \tag{5.14}$$

if $\sigma_1 < 4f_{cu}$.

Equation 5.14 gives the line closest to the σ_1 axis. Lines for σ_2 and σ_3 are obtained similarly.

The data available locate only three lines in the stress space. The failure surface was obtained by letting three planes pass through the three lines.

(c) Transition Plane C

The boundary of surface A will not coincide with surface B. To obtain a continuous surface a transition is needed. An arbitrary transition surface was obtained using the von Mises yield criterion

$$\sigma_j - \sigma_i \leq f_{cu} \qquad i, j = 1, 2, 3 \tag{5.15}$$

The method described above gives a good geometrical picture of the stress condition and it is easy to relate any combination of principal stresses to the failure surface.

Because of the limited amount of data available, surface B gives only a rough approximation of the actual failure surface. However, a refinement can be effected by extrapolating existing data. The strength is known for the case $\sigma_1 > \sigma_2 = \sigma_3$, i.e. the intermediate stress is equal to the minimum stress. It is safe to assume that by increasing the intermediate stress the overall strength is not decreased. By doing this a lower bound for the condition $\sigma_1 = \sigma_2 > \sigma_3$ can be obtained from Eq. 5.14

$$\sigma_1 = f_{cu} + 4\sigma_3 \qquad \sigma_2 = \sigma_1 \tag{5.16}$$

Equation 5.16 gives a line that is close to the $\sigma_1 - \sigma_2$ plane. Two more lines can be obtained using similar relationships.

Equations 5.14 and 5.16 give six lines in stress space. A new surface B can be obtained by letting six planes pass through these six lines, a cross section of this is shown in Fig. 5.4. This surface coincides with the boundary of surface A and a transition surface is not needed. The new failure surface is

Surface A:

$$\begin{aligned} \sigma_1 &< f_{cu} \\ \sigma_2 &< f_{cu} \\ \sigma_3 &= 0 \end{aligned} \tag{5.17}$$

Surface B:

$$\sigma_i - 4\sigma_j = f_{cu} \qquad i, j = 1, 2, 3 \tag{5.18}$$

By comparing Eq. 5.18 with the results in the next section obtained using Mohr's stress circles it is seen that they are identical. Consequently, the failure surface proposed by Hannant and Frederick is more conservative than the failure criterion based on Mohr's stress circles.

5.6 Failure Criterion Based on Mohr's Stress Circles

Figure 5.5 shows Mohr's stress circles for different cases of triaxial compressive stress with $\sigma_1 > \sigma_2 = \sigma_3$. Generally, for the condition $\sigma_1 > \sigma_2 = \sigma_3$, the strength has been described by the relationship:

$$\sigma_1 = f_{cu} + f(\sigma_3) \tag{5.19}$$

The form of the function $f(\sigma_3)$ has been investigated by Richart, Brandtzaeg and Brown (1928), Balmer (1949) and Chinn and Zimmerman (1965). A comparison of their results (Hannant and Frederick, 1968) shows good

consistency and makes it reasonable to assume that if $\sigma_2 < f_{cu}$ then

$$\sigma_1 = f_{cu} + 4\sigma_3 \qquad \sigma_2 = \sigma_3 \tag{5.20}$$

To assume the function $f(\sigma_3)$ in Eq. 5.19 to vary linearly is an approximation which is valid only within a limited range of σ_3. It is known that for high stresses the curve will flatten out (Balmer, 1949) and it may ultimately be horizontal conforming to the maximum distortion energy theory. Furthermore, the slope of the envelope may vary depending on the composition of the concrete. Tests by Smee (1967) indicated that the slope will vary with the uniaxial compressive strength of the concrete and with the maximum aggregate size used in the mix. However, for the mix used in the pressure vessel tests and at confining stresses less than the uniaxial compressive strength of the concrete, the coefficient used in Eq. 5.20 to indicate the rate of increase of σ_1 with σ_3 is acceptable.

The Mohr's circles constructed according to Eq. 5.20 are the extreme stress conditions attainable before failure. The failure envelope can be constructed as shown in Fig. 5.5.

The Mohr's failure envelope does not recognize the intermediate principal stress. The failure envelope in Fig. 5.5 has been constructed for the conditions $\sigma_1 > \sigma_2 = \sigma_3$. If σ_2 is increased so that $\sigma_1 > \sigma_2 > \sigma_3$, the envelope has to be constructed using σ_1 and σ_3. Any strength increase which may be caused by the increase in σ_2 cannot be accounted for.

An estimate of the strength increase due to the increase of σ_2 can be obtained with the help of results from biaxial tests. Figure 5.6 shows the strength of concrete under biaxial compression as reported by Kupfer, Hilsdorf and Rusch (1969). The maximum value of σ_1/f_{cu} when σ_2 is varied is $1.27f_{cu}$. Accordingly for the case $\sigma_1 > \sigma_2 > \sigma_3 = 0$, variation of σ_2 can cause a

variation in σ_1 of 27 percent. No similar test results exist for the case of $\sigma_3 \neq 0$. However, it is plausible to assume that a variation of σ_2 does not cause a change in σ_1 of more than about 25 percent. If this assumption is true, Mohr's envelope based on Eq. 5.20 can be considered to provide a safe and not unduly conservative criterion for the failure of concrete under triaxial compression.

5.7 Conclusions

A generally successful failure criterion for concrete is yet to be developed. Regarding the different criteria presented here, the following conclusions can be made.

For the case of triaxial compression, there are no tests supporting the octahedral shearing stress theory. Furthermore, it is suspected that the theory gives results on the unsafe side for certain stress combinations.

The maximum distortion energy theory assumes a limiting shear stress as failure criterion. It has been shown that this does not apply to concrete.

The limiting tensile strain criterion is very sensitive to the determination of the values of E_i and ν_i in a triaxial stress state. Before a considerable improvement can be made in this, it is difficult to evaluate the theory fairly.

The failure surface proposed by Hannant and Frederick is too conservative in its present state. However, it gives a good geometrical picture of admissible stress combinations and may be very attractive if modified by test results for more stress combinations.

Mohr's failure criterion is considered to be the most reliable in spite of its simplicity. It is considered a drawback that it does not take the intermediate principal stress into account, but its results are still as accurate as those of any other criterion for triaxial compression. Equation

5.20 is considered to give a good approximation of the failure envelope for the concrete mix that was used and for the stress range to be encountered in the tested pressure vessels.

6. ANALYSIS OF THE STRESS CONDITIONS AT FAILURE IN A SOLID END SLAB

6.1 Introduction

In this chapter a method is presented to calculate the stress conditions in the end slab at the internal pressure at which collapse occurs. The stress conditions in vessel PV16 are analyzed in detail to determine the parameters which have strong influences on the concrete stresses, and the magnitude and distribution of stresses under which fracture occurs.

A description of the analysis for the case of linear response of the concrete is provided in the next section. A cryptodome limited by an inclined crack with a shape similar to the actual crack in vessel PV16 is used as an example. The stresses calculated in this particular cryptodome are described in section 6.3 leading to a quantitative discussion of the application of the failure criterion of concrete (Eq. 5.20) to the problem of determining the shear strength of the end slab.

In section 6.4 the stress conditions are calculated for three cryptodomes with different shapes to demonstrate the effect of the shape on calculated stresses.

The concrete is subjected to high triaxial compressive stresses in some parts of the cryptodome. The force-deformation relationship of concrete under these conditions is discussed in section 6.5 and the calculated influence of inelasticity on the stress conditions is shown with some examples.

The last section contains a summary of the chapter.

6.2 Description of Analysis

The axisymmetric finite-element model that was introduced in Chapter 3 is used to calculate the stresses in the end slab. At the failure pressure the behavior of the slab has changed greatly because of tensile cracking of the concrete and probably also by inelasticity of the concrete under the influence

of high compressive stresses. The extent of cracking at the failure pressure is known with good accuracy and is included by modifying the geometrical properties of the vessel in the analysis. The extent of inelasticity of the concrete because of high compressive stresses is not known and initially it is assumed that a linear force-deformation relationship can be used. Figure 6.1 shows the finite-element model with the geometrical modifications introduced.

The crack originating at the reentrant corner has propagated through most of the wall at the failure pressure (Fig. 3.1). Vertical stresses can still be transmitted close to the exterior wall surface but only small shear stresses can be carried over the area of concrete that is left. Therefore, the entire wall is ignored in the analysis and the slab is considered to be simply supported along its edge.

The inclined crack has propagated to the centerline of the slab carving out a cryptodome. The concrete above the inclined crack is separated from the rest of the structure and does not influence the stresses in the dome.

The flexural cracking consists of radial cracks which are deep at the centerline and become shallower as they approach the edge of the slab. The inclined crack isolates most of the area in which radial cracks have developed. Only shallow radial cracks below the anchorage plate of the longitudinal reinforcement occur within the cryptodome. In the initial analysis the radial cracks are disregarded.

The location of part of the inclined crack and the failure surface of vessel PV16 could be measured after the test (Fig. 2.8). The initial slope of the inclined crack was about 45 degrees to the vertical, as also observed in the other test vessels in which inclined cracks were detected. The observed failure plane was located about 4-1/2 in. from the centerline and had a depth of approximately 1-1/2 in.

For the initial analysis, the assumed shape of the cryptodome (Fig. 6.2) differed from the one that was observed. The initial slope of the assumed inclined crack is 45 degrees which agrees well with the observed slope. The depth of the cryptodome at the centerline was made slightly larger than that implied by the observed depth of the failure surface.

6.3 Stresses in the Assumed Cryptodome for Linear Response of Concrete

Figure 6.3 shows the calculated stresses along the inside face of the slab. The maximum compressive stress is 26,000 psi which corresponds to a strain of 0.0054 for $E = 4.0 \times 10^6$ psi and $\nu = 0.15$. The high stresses indicate that inelastic deformations occur but in this section of the chapter elastic properties are assumed. It should also be noted that the calculated radial stress is compressive from the center to the reentrant corner. The calculated radial strain is compressive inside a radius of 11 in. This does not completely agree with the values recorded by the strain gages as the ones at a radius of 9-3/8 in. showed small tensile strains (Fig. 3.6) at the failure pressure.

The observed failure occurred in the radial-vertical plane, the only plane in which shear stresses act if the test vessel can be considered to be axisymmetric. To be compatible with the failure criterion, this condition would require the tangential stress to be the intermediate principal stress. The following discussion shows that the average calculated stresses at vertical sections in the vicinity of the failure plane satisfied this condition, even though it was violated at the inside face of the slab.

The principal stresses plotted in Fig. 6.4 have been calculated from the average radial, tangential, vertical, and shear stresses on sections of the cryptodome. The tangential stress is the intermediate principal stress at all sections where failure of the cryptodome is likely.

In the following evaluations of stress conditions leading to failure

using the failure criterion, the tangential stress has been ignored.

The stress circles at a radius of 2 in. and at different distances from the inside face of the slab are shown in Fig. 6.5. The magnitude of the stresses is highest close to the inside of the slab. However, a comparison with the failure envelope (Eq. 5.20) shows that the concrete at all nodes is very close to failure.

At a radius of 5 in. the thrust surface is not close to the inside face of the slab and the stresses are distributed differently. At the inside face, the two principal stresses are of about the same magnitude. The stress circle is small and considerably below the failure envelope (Fig. 6.6). The concrete close to the upper surface has a stress combination that leads to failure according to the failure criterion.

The likelihood of material failure at a point is indicated by the relative position of the stress circle to the failure envelope. Ideally, failure occurs if the failure envelope is tangent to or crosses the stress circle. This condition can be evaluated by a single numerical factor α defined as

$$\alpha = \frac{\sigma_1}{f_{cu} + 4\sigma_3} \tag{6.1}$$

The factor α is a failure index in that it indicates whether the assumed failure criterion has been violated at a point. Stress circles for the maximum values of α at different vertical sections of the cryptodome are plotted in Fig. 6.7. The corresponding values of α are plotted in Fig. 6.8. In plotting these figures the stress conditions at nodes along the upper and lower surfaces have been ignored because they do not satisfy the boundary conditions completely. Plots of the failure index are preferable to the stress circles because more exact comparisons can be made and more stress combinations can be included in one figure.

The values of α close to the center of the slab are irregular because of a decrease in the vertical stress along the inside face of the slab. There is no reason to expect this decrease, because the vertical stress should be equal to the internal pressure. It is probably caused by the mathematical model that is used, and the value of α close to the centerline is ignored in subsequent figures. There are values of α larger than 1.0 from the center to a radius of 8 in. and the failure could conceivably have occurred in any section within this radius. The maximum value of α was 1.23 and was calculated at a radius of 4 in.

If the failure index, α, exceeds 1.0 at a node, collapse of the cryptodome may occur. However, if the stresses at one node reach a failure condition comparatively large deformations would occur and part of the stresses may be redistributed to other nodes along the same section enabling the cryptodome to resist further load. At a radius of 2 in., all the nodes have stresses close to the failure condition (Fig. 6.5). If one node reaches a failure condition the other nodes have small capacity to relieve it and collapse of the cryptodome follows. In the section 5 in. from the centerline (Fig. 6.6), the nodes close to the inclined crack have severe stress combinations but the other nodes have considerable reserve capacity. To calculate the redistribution of stresses to the other nodes requires knowledge of the force-deformation characteristics of the concrete. Information on the force-deformation response of concrete subjected to triaxial stresses of different magnitudes is nonexistent. However, the reserve capacity can be estimated by calculating the average stresses at each vertical section and the corresponding failure index, α.

The values of α, based on average stresses, decrease with the distance from the center (Fig. 6.9). If the magnitude of α, based on average stresses, was accepted as the only criterion for failure, failure of this particular cryptodome would have been predicted to occur at the center of the dome and at

an internal pressure of about 3200 psi.

Instead of calculating the average stresses, the stresses at mid-height of the cryptodome can be used, which gives approximately the same value for α at most of the sections (Fig. 6.9).

In evaluating the possibility of failure, the different methods of calculating the index α can be used to provide upper and lower bounds. If α does not exceed unity at any single node, then failure is unlikely for the cryptodome assumed. If α based on average stresses exceeds unity, failure is quite likely.

6.4 The Shape of the Cryptodome

In the previous section the stress conditions in a cryptodome of a certain preselected shape were discussed. In this section the variations of the stresses with the shape of the cryptodome are treated. For this purpose the stress conditions of two additional cryptodomes with different shapes have been analyzed, one with a thick dome (Fig. 6.10) and one with a thin dome (Fig. 6.11), as compared with the dome previously analyzed (Fig. 6.2). These domes provide no limits for the shape the cryptodome of vessel PV16 may actually have had.

The radial stresses along the inside faces of the slabs of the three cryptodomes are shown in Fig. 6.12. The more slender the dome is, the higher is the stress gradient along the inside face and the higher is the compressive stress at the center. This relationship is true at any level inside the domes. The bending moment and the thrust cause higher stresses in a thin dome than in a thick one.

The value of the failure index, α, for the worst stress combination at each section varies considerably among the three domes (Fig. 6.13). For the thick

dome the value is not larger than 0.95 at any section indicating collapse to be unlikely. For the thin dome a maximum value of 1.45 at a radius of 3 in. is calculated.

The failure index, α, calculated from the average stresses at each section varies less for the three domes (Fig. 6.14). The thinner the dome is, the higher is the failure index. At a radius of more than 7 in. the thicknesses of the three domes are identical and the failure indices are also the same.

The values of α at mid-height of each section varied more than for α based on average stresses (Fig. 6.15). These values of α are sensitive to the location of the thrust surface, which explains the peak at a radius of 3 in. for the thin dome.

It is apparent that the stress conditions in the dome are sensitive to the shape of the cryptodome.

6.5 Nonlinear Response of Concrete and its Effects

The calculated radial stresses along the inside face of the slab for different shapes of the cryptodome with elastic material properties are shown in Fig. 6.12. The compressive stress at the center of the thickest dome is about 20,000 psi. Because the confining vertical pressure is only 3200 psi, the concrete in this area is about to fail according to the failure criterion. The assumption of elastic behavior of concrete is then doubtful and it becomes necessary to investigate the effect of inelasticity. The force-deformation relationship of concrete subjected to multi-axial compression is not known. On the basis of limited available data, a force-deformation relationship is assumed for concrete, which makes it possible to recognize the effect of inelasticity even if the magnitude of the calculated stresses is inaccurate.

The strain gage readings from the test specimens do not confirm that the concrete deformed inelasticly. The calculated stress combination mentioned

in the previous paragraph corresponds to a radial strain of 0.0042. This is considerably larger than was recorded by any strain gage located on the inside face of the slab. Inelastic conditions would lead to still higher calculated strains. However, it has been shown that the strain gages on the inside face did not record the strains correctly at low internal pressures (Appendix C) so it is possible that the recorded strains at the failure load are not correct.

Another source of inelasticity in the overall response of the cryptodome is introduced by radial cracks near the anchorage plate of the longitudinal rods providing the vertical reaction to the cryptodome.

(a) Force-Deformation Relationship of Concrete

The stress-strain relationship of concrete subjected to uniaxial compression is readily determined. The relationship can be assumed to be parabolic up to the maximum stress (Hognestad, 1951)

$$\sigma = f_{cu}[\frac{2\varepsilon}{\varepsilon_o} - (\frac{\varepsilon}{\varepsilon_o})^2] \qquad (6.2)$$

In using this equation either the modulus of elasticity at very low stresses, E, or the strain at the maximum stress, ε_o, can be selected. They cannot be varied independently because Eq. 6.2 defines the following relationship between them

$$E = \frac{2f_{cu}}{\varepsilon_o} \qquad (6.3)$$

This is not a serious drawback because the properties of concrete are satisfied approximately by Eq. 6.3. The stress-strain curve of the concrete used in PV16 has been compared with Eq. 6.2 (Fig. 6.16).

A less accurate but more versatile method of representing the stress-strain curve is to use two straight lines. The first line represents the

modulus of elasticity at low stresses, E, and is valid up to a stress of 75 percent of the failure stress. The second line intersects the first line at a stress of 0.75 f_{cu} and goes through the point f_{cu}/ε_o (Fig. 6.16). This does not give as good an approximation of the actual stress-strain curve as the parabolic representation. However, it makes it possible to select values E and ε_o that are independent of each other. The two straight lines are represented by

$$\varepsilon = \frac{\sigma}{E} \qquad \sigma \leq 0.75\ f_{cu} \tag{6.4}$$

$$\varepsilon = \varepsilon_o \left(\frac{4\sigma}{f_{cu}} - 3\right) + \frac{3}{E}(f_{cu} - \sigma) \qquad \sigma \geq 0.75\ f_{cu} \tag{6.5}$$

At each point along the assumed stress-strain curve a secant modulus of elasticity E_a is defined

$$E_a = \frac{\sigma}{\varepsilon} \tag{6.6}$$

If the parabolic stress-strain curve is used, the value of E_a is equal to E at low stresses and decreases continuously to E/2. If two straight lines are used to represent the stress-strain curve the value of E_a is equal to E initially (Eq. 6.4). The value of E_a at the maximum stress is dependent on the selection of the value of ε_o.

There are no data on the force-deformation relationship of concrete subjected to compressive stresses of different magnitude in the three principal directions. However, for the simplified loading case of $\sigma_1 > \sigma_2 = \sigma_3$ some stress-strain relationships in the σ_1 direction have been reported (Richart, Brandtzaeg and Brown, 1928; Balmer, 1949). The observed results have not been synthesized, but two trends can be seen. First, the higher the confining pressure ($\sigma_2 = \sigma_3$) is, the higher is the stress in the σ_1-direction

at which the value of E_a starts to deviate considerably from E. Second, the higher the confining pressure is, the lower is the value of E_a at the maximum stress in the σ_1-direction.

Using these observations the stress-strain relationship in the σ_1-direction for the loading condition $\sigma_1 > \sigma_2 = \sigma_3$ can be estimated, but not determined accurately. A parabolic curve cannot be used because the value of E_a at the maximum stress would then be independent of the confining pressure. The representation by two straight lines has to be used. It is assumed that $E_a = E$ up to a stress of

$$\sigma_E = 0.75 f_{cu} + 2\sigma_3 \tag{6.7}$$

From the point σ_E/ε_E a line is drawn to the point σ_M/ε_M. σ_M and ε_M represent the maximum stress and the corresponding strain. The value of σ_M is obtained using the failure criterion

$$\sigma_M = f_{cu} + 4\sigma_3 \tag{6.8}$$

The value of ε_M is set to

$$\varepsilon_M = \frac{\sigma_M}{E}\left(2 + \frac{\sigma_3}{4000}\right), \qquad \sigma_3 < 4000 \tag{6.9}$$

Equation 6.9 implies that the value of E_a at the maximum stress is set to be 0.5E for the unconfined loading case and linearly decreases to 0.25E for a confining pressure of 4000 psi. The calculated confining pressure did not exceed the internal gas pressure (3200 psi) at any point in the dome. Sample stress-strain curves have been calculated for concrete with $f_{cu} = 7450$ psi and $E = 4.0 \times 10^6$ psi and are shown in Fig. 6.17.

To account for the cracking under the anchorage plate, a radial crack is introduced if the tangential stress in an element exceeds a tension of $4\sqrt{f_{cu}}$.

In the finite-element analysis an iterative method has been used to recognize the effects of inelasticity in the concrete. First a solution of the stress condition is obtained assuming that the force-deformation relationship is linear. Thereafter the stresses in each single element are compared and the value of the force-deformation relationship changed whenever required. A new solution is then obtained and the stresses are compared again. The number of steps is determined by the degree of convergence that is sought.

The force-deformation relationship is determined by the stress combination in each element. However, this relationship has been discussed only for the case of the two smallest stresses being equal. Furthermore, Eq. 6.7-6.9 are only estimates of the real relationship. Therefore, the following simplified method is used to determine the value of E_a.

The three principal stresses are calculated and the confining pressure, σ_3, is defined by the smallest principal stress. If it is tensile the confining pressure is set to zero. The confining pressure determines Eq. 6.7 to 6.9 uniquely and a stress-strain curve is obtained.

The tangential stress, σ_t, which is a principal stress, and the stress-strain curve give the tangential strain ε_t. By using Eq. 6.6 a value of E_a for the tangential direction is obtained.

Ideally two different values of E_a should be obtained for the radial-vertical plane because it contains two principal stresses. This would lead to practical difficulties in the analysis and in view of the approximations already involved it is considered sufficient to use one value of E_a which is calculated as described in the previous paragraph with the difference that σ_t is substituted by either σ_r or σ_z, whichever is the higher compressive stress.

The value of Poisson's ratio, ν, is not varied.

To determine if inelasticity of concrete in the cryptodome has to be considered in evaluating the stress condition, a comparison is made in the

last part of this section between a solution assuming elastic properties and a solution assuming inelastic properties.

(b) The Effect of Inelasticity

The assumption of a nonlinear force-deformation relationship for the concrete changes the calculated stresses in the cryptodome. To evaluate the relative effects of inelasticity, the dome configuration in Fig. 6.2 is analyzed for assumed elastic and inelastic material properties.

The radial stresses along the inside face of the slab (Fig. 6.18) deviate in two major respects if inelastic instead of elastic material properties are assumed. First, the stresses at a radius of less than 9 in. are reduced considerably. Second, at a radius of about 6 in. the radial stress is tensile. This is compatible with the lower secant moduli of elasticity in the areas of high compressive stresses, leading to increased deflection at the center of the dome (Fig. 6.19). The load at the center of the dome cannot be resisted by dome action then, but has to be carried by bending. This causes large bending stresses in the area where the slope of the inclined crack changes and tensile stresses occur on the inside face of the slab. The appearance of tensile stresses can be counteracted in the analytical model by increasing the thickness of the dome or by increasing the assumed slope of the force-deformation relationship of concrete. Since the strain gages in this area did not record tensile stresses it has to be concluded that either the assumed shape of the dome or the force-deformation relationship is incorrect in this example. However, the discrepancy may be small and the example can still be used to illustrate the stress condition in the dome.

The values of the failure index, α, for the worst stress condition at each section and for assumed elastic and inelastic material properties are shown in Fig. 6.20. The maximum value of α is reduced very little but the

distribution is changed so that the peak value may occur at any radius smaller than 8 in.

The values of the failure index, α, based on the average stresses at each section are shown in Fig. 6.21. The values of α close to the center of the dome, where the concrete is affected most by the decreased secant modulus of elasticity, drop substantially creating a peak at a radius of 3 in., but remain almost unchanged at larger radii. The location of the peak of the curve can be changed by altering the force-deformation relationship of the material.

The values of the failure index, α, for the stress combinations at mid-height are similar to the values of α based on average stresses (Fig. 6.22).

The calculated radial stresses along the inside face of the slab for the three different domes with inelastic material properties are shown in Fig. 6.23. Tensile stresses are calculated at a radius of 6 in. for the two thinner domes. The amount of bending may be changed considerably by a small change of the shape of the assumed cryptodome and its effect is amplified by the inelastic material properties.

6.6 Conclusions

The primary objective of the studies described in this chapter was to reconcile the observed strength of the end slab with the failure criterion developed in Chapter 5. This requires three critical steps: (1) the assumption of a cryptodome shape, (2) the calculation of stresses in the cryptodome and (3) comparison of these stresses with the failure criterion (Fig. 6.24). It has not yet been possible to develop a method that accurately and simply defines the path of the particular crack which establishes the boundary of the cryptodome. Within the realm of available methods of analysis, the choice of the cryptodome will depend on judgment and require a trial-and-error

solution. To execute step (2) the force-deformation relationship of concrete subjected to multiaxial stresses of different magnitudes has to be known. There are no data reported that would establish this relationship and it has not been within the scope of this investigation to study it experimentally. A force-deformation relationship was developed on the basis of limited data obtained under a particular stress combination of $\sigma_1 > \sigma_2 = \sigma_3$. Compared with the first two steps the failure criterion adopted for concrete can be considered as relatively accurate, but it is difficult to apply because the failure occurs along a plane that has a very steep stress gradient.

The assumptions mentioned above are discussed separately in the following.

(a) Shape of the Cryptodome

The shape of the cryptodome could conceivably be obtained by employing an analytical model that traces the development of the crack which controls the shape of the cryptodome as the pressure is increased (Higashionna and Schnobrich, 1970). However, using this method only the initial slope of the inclined crack has been determined. It has not been possible to determine the shape of the crack close to the center of the slab, a parameter that is essential in calculating the stresses in the area in which failure occurred.

In the case of the test vessels, the shape of the cryptodome could be obtained experimentally by studying the vessel after failure. This gives a general picture of the shape, but it may not be too reliable in the neighborhood of the center or at the failure plane because of the structural damage caused by the collapse.

In this chapter three different domes have been analyzed with both elastic and inelastic material properties assumed. The calculated stresses vary considerably with the shape of the dome, emphasizing the necessity of defining the correct shape of the dome. By studying the calculated stresses,

it is possible to determine the bounds within which the actual shape of the dome has to lie.

The trajectory of the critical crack which defines the shape of the cryptodome can be estimated by considering it in two parts: the section between the mid-height and the outside face of the slab, and the section between the mid-height and the inside face of the slab.

Analyses of the end slab (Higashionna and Schnobrich, 1970) have shown that initially there is a tendency to develop a multitude of individual cracks, each at approximately 45 degrees, in the vicinity of and at the mid-height of the slab. On the basis of this information, it is plausible to put the critical crack at an angle of 45 degrees and to assume that it extends from the edge of the anchorage plate to the mid-height of the vessel. Parallel cracks at locations closer to the center of the slab would result in stronger cryptodomes.

After the portion of the crack described above is formed, the load cannot be carried by bending alone. Instead the internal pressure is resisted primarily by dome action. The direction of the maximum compressive stress in the dome is defined by the thrust surface. Normal to the thrust surface tensile strains develop. The propagation of the inclined crack towards the center is defined by the direction of the tensile strains. Thus the crack is parallel to the thrust surface and has the shape of a dome. It can then be expected that a minimum of bending occurs and that the internal pressure is resisted primarily by the thrust in the dome.

Figure 6.25 shows the calculated radial strains along the inside face of the slab for three different domes and inelastic material properties. For two of the domes tensile strains are calculated at a radius of about 5 in., indicating considerable bending to occur in the dome. According to the

discussion above this is unlikely to occur in the actual slab and these two shapes of the cryptodome are not realistic. If the assumed material properties are correct, only the thickest of the domes has a realistic shape. These assumptions are supported by the test results as the strain gages at a radius of 6-1/4 in. show compression at the failure pressure (Fig. 6.26).

A reasonable upper bound of the shape of the cryptodome can also be determined by studying the calculated strains in the different domes. The critical inclined crack is assumed to propagate through the points with the largest tensile strains and parallel to the thrust surface. The calculated maximum principal strains (elastic) at three different radii for the dome shown in Fig. 6.2 are plotted in Fig. 6.27. The strains increase with the depth and have their maximum values at the boundary shaped by the inclined crack. This indicates that the assumed shape of the inclined crack is in or below the area of maximum principal strains. As a comparison the maximum principal strains in a very thick dome (Fig. 6.28) have been calculated (Fig. 6.29). The strains have their highest value below the inclined crack indicating that the assumed shape of the dome is too thick.

Thus the bounds of the shape of the cryptodome can be found if correct material properties are assumed.

(b) Force-Deformation Relationship of Concrete

In the preceding sections two different force-deformation relationships of concrete, one linear and one nonlinear, were used. The nonlinear relationship was defined by Eq. 6.7 through 6.9. There are no experimental data to check the accuracy of the assumed relationship.

The comparison of the calculated stresses based on elastic and inelastic material properties shows that the failure index, α, is not affected critically. The largest effect occurs at points close to the center where the high compressive

stresses are reduced if inelasticity of concrete is assumed.

The radial stresses along the inside face of the slab are influenced by the force-deformation relationship. Since these stresses can be used in appraising the bounds of the actual shape of the dome, the assumption of a force-deformation relationship may influence the final results.

(c) Application of the Failure Index

To facilitate the comparisons of the stress combination at each node with the failure criterion for concrete, a special failure index was defined (Eq. 6.1). This avoids the cumbersome method of drawing stress circles and comparing them with the failure envelope.

If the shape of the dome and a perfect force-deformation relationship for the concrete were given, the calculation of the maximum internal pressure and of the pressure corresponding to collapse would be straightforward. Not having a confirmed force-deformation relationship, it becomes necessary to use judgment in interpreting the results of the stresses calculated in relation to the failure criterion. The failure index, α, makes it possible to survey the likelihood of failure at several nodes in a concise manner. It has been based on three different definitions of critical stress:

(1) By stating that the failure index has to be less than unity at each single node a lower bound of the strength of the dome is obtained. Collapse cannot occur if the concrete in the dome is not subjected to a stress combination that exceeds the failure condition at at least one node.

(2) If a failure condition is reached at a node, the large deformations will cause redistribution of the stresses and failure will probably not occur. To estimate the possibility of redistribution of stresses the average stresses were calculated at each vertical section. The failure indices were then based on the average stresses. If the index as calculated exceeds unity at any

section, there is no capacity left for redistribution of stresses and failure will occur. Thus an upper bound of the strength of the dome is obtained.

(3) The failure index can be based on the stress at mid-height of the dome. This gives results that are about the same as if the average stresses were used.

The stresses in the slabs with penetrations have to be analyzed before it is possible to evaluate more closely the different methods of calculating the failure index.

7. ANALYSIS OF THE STRESS CONDITIONS AT FAILURE IN AN END SLAB WITH PENETRATIONS

7.1 Introduction

In this chapter a method is presented to calculate the stresses in a cryptodome forming in an end slab with penetrations in order to determine the extent to which penetrations affect the shear strength of the end slab. Vessel PV16 which had a solid end slab is used as a yardstick for comparison of stresses and the strength.

In section 7.2 it is shown that for the purpose of calculating the critical stresses and the failure pressure, the slabs with penetrations can be represented by an axisymmetric model. This model is used in section 7.3 to calculate the stresses in the vessels with penetrations. The obtained results are discussed and general observations regarding the location of penetrations are presented in the last section.

7.2 Analytical Model

Vessel PV18 had 6 penetrations in the end slab, each with a diameter of 4 in. The penetrations removed 50 percent of the perimeter along a circle with a radius of 8 in. and 15.3 percent of the inside area of the end slab (Table 2.1). Compared with the other vessels, the effect of penetrations can be expected to be largest in PV18 so the dome of this vessel was chosen for the comparison of the three-dimensional finite-element model to the axisymmetric one. The shape of the dome is the same as the one shown in Fig. 6.2.

(a) Three-Dimensional Finite-Element Model

The three-dimensional finite-element program uses an isoparametric finite element, which can accommodate a varying number of nodes. The minimum number of nodes connected to an element is eight, one in each corner, but up to

twenty-four nodes can be used by defining additional ones along the edges of the elements.*

Using the three-dimensional element, the stresses can be calculated with approximately the same accuracy as with the axisymmetric element. In the three-dimensional program relatively few elements can be used because of the large number of unknown displacements that are generated. This is counteracted by the high accuracy of the three-dimensional elements. The axisymmetric element is derived assuming constant strains while the three-dimensional element has linearly varying strains or strains of still higher order depending on the number of nodes it is connected to. In the three-dimensional program a very fine grid was used in the vicinity of the penetration which made it necessary to use a coarse grid in the remaining parts of the dome (Fig. 7.1). Three rows of finite-elements are defined by dividing the depth of the dome into three equal distances (Fig. 7.2).

The three-dimensional program assumes the material to have a linear force-deformation relationship so elastic material properties have to be used in both models to make the comparison relevant.

(b) The Axisymmetric Finite-Element Model

A method to modify the axisymmetric finite-element program so that it can be used for vessels with penetrations was described in Chapter 4. A similar method is used here. The modulus of elasticity for the concrete in each torus is reduced in proportion to the amount of material that is removed by penetrations. Contrary to the method described in Chapter 4, radial cracks were not introduced in the tori that were cut by the penetrations. It was found that the tangential stresses between the penetrations

---

*This program was developed by A. K. Gupta and will be described in his doctoral dissertation to be submitted to the Graduate College of the University of Illinois, Urbana, in 1971.

were reduced very little by the penetrations and that the reduction was sufficiently accounted for by the reduced modulus of elasticity. However, the introduction of radial cracks affects the calculated stresses little, and either assumption can be used.

(c) Comparison of the Two Finite-Element Programs

The stresses and displacements that were calculated using the three-dimensional finite-element model are plotted in Fig. 7.3-7.10 as functions of the radius. The stresses and displacements also vary with the tangential location. Consequently, the stresses and displacements are identified in three groups according to the locations of the nodes as shown in Fig. 7.1 and described below:

(A) Nodes along the uninterrupted radius that is located symmetrically between the penetrations ($\theta = 30°$ in Fig. 7.1).

(B) Nodes along the radius that passes through the center of a penetration ($\theta = 0°$) and including the nodes along the periphery of the penetration.

(C) Nodes located between the penetration and the uninterrupted radius.

In the three-dimensional model, it was not feasible to simulate the stiffnesses of the circumferential prestressing wire or the longitudinal rods. Only forces could be specified along the boundary. To account for the stiffness of the reinforcement, the prestressing forces had to be chosen so that they represented the values at the failure pressure. This was achieved by comparing the calculated stresses, along the boundaries of the slab at which the prestressing forces were applied, for the axisymmetric solution and the three-dimensional solution. The increase in boundary forces was less than 15 percent of the initial force.

The calculated vertical deflections along the inside face of the slab for the two different finite-element solutions are shown in Fig. 7.3.

The calculated radial stresses along the inside face of the slab are plotted in Fig. 7.4. The stresses calculated using the axisymmetric model represent the stresses calculated by the three-dimensional model reasonably.

The depth of the cryptodome was represented by three isoparametric elements in the analysis of the end slab with penetrations. The stresses calculated at the intersection of two of these element layers at one third of the depth from the critical inclined crack (Fig. 7.2) are plotted in Fig. 7.5-7.8.

Figure 7.5 compares the radial stresses. The radial stresses at the same radius but at different tangential locations varied widely but based on the axisymmetric solution stresses at all radii were between the extreme values.

The vertical stresses varied less with the tangential location than the radial stresses. The axisymmetric solution predicted stresses that agreed well with the three-dimensional solution (Fig. 7.6). Also in predicting the shear stresses, the axisymmetric solution proved to be reliable (Fig. 7.7).

The tangential stresses calculated by the axisymmetric program were smaller than the ones calculated by the three-dimensional program (Fig. 7.8). The difference is probably caused by the boundary condition and the size of the elements and may be eliminated by changing these. The difference is of minor importance since the tangential stress is assumed to be the intermediate principal stress and does not affect the predicted strength of the dome.

It appears that the stresses obtained using the modified axisymmetric model were representative for the stresses predicted using the three-dimensional model, and that each stress obtained from the axisymmetric model can be

considered to be an average stress for the particular radial and vertical location at which it is defined. Considering that the failure plane is axisymmetric, the "average" stresses calculated by the axisymmetric model may be as accurate to use in predicting the failure pressure, as the stresses that are calculated using the three-dimensional model. In using the three-dimensional model, very high stresses are calculated at a few nodes. It can be assumed that as the failure pressure is approached and large deformations occur, some redistribution of stresses will occur from the nodes with very high stresses to nodes with smaller stresses. By using the axisymmetric model a portion of the redistribution is incorporated in the analysis. The redistribution of stresses that is assumed in using the axisymmetric model is smaller than the actual redistribution that occurs and the assumption is conservative.

By calculating the failure indices, at a distance of 1/3 of the depth of the dome below the inclined crack using the two finite-element models, the amount of redistribution of stresses that is predicted as the failure pressure is approached can be illustrated (Fig. 7.9). The failure indices based on the calculated stresses using the three-dimensional model, are widely scattered for nodes at approximately the same radii. The maximum value of α is 2.10 and occurs at a radius of 8 in. and at the periphery of the penetration. If the axisymmetric solution is used, the maximum value of α is reduced to 1.37. Both these values would be higher if there were nodes located closer to the inclined crack for which α could be calculated. In the following sections it is shown that even the stresses calculated using the modified axisymmetric model have to be redistributed considerably to be compatible with the real strength of the slabs with penetrations.

Consequently, the redistribution of stresses that is implicitly assumed

in using the axisymmetric model is conservative, because it underestimates the stress redistribution that occurs in the actual slab.

7.3 Comparison of the Calculated Stress Conditions in the Cryptodomes of the Different Vessels

The influence of penetrations on the stress conditions in the cryptodome is described in this section. The modified axisymmetric model is used to obtain the stresses in the cryptodomes formed in the different vessels. The prestressing forces, the concrete properties and the maximum internal pressure were specified to be the same for all vessels so that the location, size, and number of penetrations were the only variables. The variations between the properties of the different test vessels were insignificant and the calculated stresses can be compared directly with the experimental results.

In the previous chapter it was shown that the calculated stresses in a cryptodome without penetrations were insensitive to the force-deformation relationship of concrete. The effect of inelasticity in a cryptodome with penetrations is more important because of the high stresses in the concrete between the penetrations. However, considering the uncertainty in the accuracy of the assumed nonlinear force-deformation relationship, it is relevant to compare the stresses in the domes of the different vessels assuming a linear relationship.

The propagation of the inclined crack and thus the shape of the dome is determined by the thrust surface. Because the stresses in the slab are influenced by the penetrations, differently shaped domes were formed in the different vessels. In the previous chapter the calculated radial strains along the inside face of the slab were used in determining one of the limits of the shape of the dome. The calculated radial strains along the inside faces of vessels PV16, PV18 and PV20 for identically shaped cryptodomes are

shown in Fig. 7.10. The strains are nearly the same for all vessels, the main difference occurring at a distance of 6 to 8 in. from the center of the slab where the penetrations are located. This suggests that the domes in the different slabs were of similar shapes and in the following comparison identical domes as defined by Fig. 6.2 are used.

(a) Vessels with Penetrations 8 in. from the Center of the Slab

Four of the vessels (PV17, PV18, PV20 and PV21) had penetrations at a distance of 8 in. from the centerline (Table 2.1). In the following the calculated stresses in the domes of these vessels and of vessel PV16 are compared.

In the three vessels PV16, PV17 and PV18, penetrations removed 0, 25 and 50 percent, respectively, of the slab section along a circle of 8 in. radius.

Vessel PV20 had 50 percent of the slab section along a circle of 8 in. radius removed by penetrations but it was obtained by using twice as many penetrations of half the diameter as compared to vessel PV18. This means that the penetrations in PV20 removed less of the concrete volume in the slab than the penetrations in PV18.

To make the figures easy to read the stresses calculated for PV21 are not included. These stresses are easy to estimate because PV21 relates to PV20 as PV17 relates to PV18.

The stress conditions in the domes of the different vessels can be compared by plotting the radial, vertical and shear stresses at mid-height of the domes (Fig. 7.11 to 7.13). The penetrations have a similar influence on the stresses at other levels of the domes. The following conclusions about the effect of the penetrations can be drawn from the comparison:

(1) The stresses in the sections without penetrations are affected very little.

(2) The stresses are increased in the section in which the penetrations are located. If β is defined as the solid perimeter at any radius divided by the total perimeter at the same radius, then the stress is approximately inversely proportional to β.

(3) The vertical stress at mid-height of the dome of vessel PV16 has its maximum value at a radius of 6-1/2 in. This radius is within the section where the penetrations are located in the other slabs. Therefore, the maximum value of the vertical stress is increased considerably by the presence of penetrations. The radial and shear stresses at mid-height of the dome of vessel PV16 have their maxima nearer the center of the slab.

The calculated radial, vertical, and shear stresses increased approximately at the same rate in the section where the penetrations are located. This caused a proportional increase in the principal stresses leading to a larger value of the failure index (Fig. 7.14). The increase in the value of the failure index is larger if the smallest principal stress has a low value.

The failure indices, based on the stresses at mid-height of the domes of the different vessels are shown in Fig. 7.15. The penetrations cause an increase in the failure indices in the section where they are located that is approximately inversely proportional to β. The failure indices calculated for vessel PV16 are small in the section between radii 6 in. and 10 in. compared to the values close to the center. The penetrations cause a substantial increase in the failure indices, but they still do not exceed appreciably the values calculated close to the center of the dome of vessel PV16.

The failure indices based on average stresses at each section (Fig. 7.16) were approximately the same as the failure indices based on stresses at mid-height of the dome.

The failure indices based on the worst stress condition at each section are shown in Fig. 7.17. The failure index of the dome of vessel PV16 has its maximum value, 1.23, at a radius of 4 in. and decreases gradually with increasing radius. At a radius of 8 in. the value of α is still 1.00. The penetrations in the vessels cause an increase in the failure index that is approximately inversely proportional to β, which generates values of α considerably higher than was calculated for PV16. Even PV17, with only 25 percent of the concrete along the perimeter at a radius of 8 in. removed by penetrations, had a maximum value of the failure index of 1.33 as compared with 1.23 for PV16.

(b) Vessel with Penetrations 4 in. from the Center of the Slab

Vessel PV19 had 6 penetrations, each with a diameter of 2 in., located 4 in. from the center of the slab. The penetrations removed 50 percent of the concrete along a perimeter with a radius of 4 in.

The calculated radial, vertical and shear stresses at mid-height of the domes of vessels PV16 and PV19 are shown in Fig. 7.18 to 7.20. The radial and shear stresses in the dome of PV16 are higher at a radius of 4 in. than at 8 in. The penetrations in PV19 caused higher stresses than were calculated for any other vessel. The failure index based on the stresses at mid-height of the dome reflects the high stresses (Fig. 7.21). The penetrations in PV19 cause an increase in the failure index that is compatible with the increase caused by penetrations in the other vessels. However, the increase occurs at a radius where the failure index for a solid dome is high and the failure index for PV19 reaches a peak that substantially surpasses the maximum values that were calculated for the other vessels. The maximum values of the failure index based on the average stresses at each section (Fig. 7.22) and on the worst stress condition (Fig. 7.23) are also extremely high because of the location of the penetrations.

The penetrations in all vessels were sealed by steel plates. The steel plates in the vessels with penetrations 8 in. from the center of the slab were located in an area of very low radial strains and their influence on the ultimate strength of the vessels were negligible. The steel plates used in PV19 were located 4 in. from the center of the slab in an area of very high radial compression. It is likely that these plates had a reinforcing effect on the dome so that the stresses that have been calculated did not occur in the concrete in the actual vessel. It is therefore not possible to draw strong conclusions from the test of this vessel (Chapter 2).

7.4 Conclusions

(a) Failure Index

Three different sets of failure indices have been calculated by basing them on different stresses. Two of these sets, the ones based on average stresses at each section and on stresses at mid-height of the domes, yield similar results indicating that either can be used.

The failure index relates directly to the strength of concrete and should explain both the ultimate capacity of a dome and the location of the failure plane. None of the failure indices that have been used fulfills both these requirements. However, it is possible to use a combination of the two failure indices each satisfying one of the criteria.

The failure index based on average stress at each section has for all vessels a maximum of about 1.0 at the center of the slab (Fig. 7.16). It decreases as the radius is increased. For the vessels with penetrations at a radius of 8 in., it increases considerably in the section where the penetrations are located but it does not exceed unity. Using the failure index based on the average stresses at each section and stating that failure occurs if it exceeds unity is compatible with the observed strength of the vessels.

This would also indicate that vessels PV18 and PV20 had the maximum number of penetrations that is possible without adversely affecting the strength of the slab.

The failure index based on the worst stress condition at each section has for vessel PV16 a maximum value at a radius of 4 in. (Fig. 7.17), which is close to the location of the actual failure plane. For vessels PV17, PV20 and PV21 with penetrations 8 in. from the center of the slab the maximum values occur between 7 and 7-1/2 in. from the center of the slab which agrees with the observed locations of the failure planes (vessel PV18 did not fail structurally because of leakage). It is therefore concluded that the failure index based on the worst stress condition at each section indicates the location of the failure plane.

The results from the test of vessel PV19 are distorted because of the reinforcing effect of the sealing plates. The calculations indicate that if it had not been for the sealing plates this vessel would have failed at a lower internal pressure than any of the other vessels.

(b) Influence of Penetrations

In all the test vessels reported here, the observed failure sequence has been the formation of a cryptodome followed by a shear failure in the cryptodome. The analysis and the conclusions that are drawn are limited to this type of failure.

The penetrations cause an increase in stresses in the radial-vertical plane and in the failure indices in the sections where the penetrations are located. A reasonable upper bound of the stresses and the failure indices is obtained if it is assumed that the increase, compared to a solid dome, is inversely proportional to β, which is the solid perimeter divided by the total perimeter at each section.

The influence of penetrations can be estimated by plotting the failure index based on the average stresses at each section as a function of the radius. In a solid slab, this failure index has its maximum value near the center. The tests indicate that if the penetrations do not cause an increase in the maximum value of this failure index, they would not impair the strength of the slab. This implies that penetrations close to the edge of the slab where the failure index is low can be expected to have less influence on the strength of the cryptodome than penetrations nearer the center.

8. CALCULATION OF THE INTERNAL PRESSURE AT WHICH THE INCLINED CRACK IS INITIATED

The initiation of the inclined cracks in the test specimens as interpreted from the measurements was discussed in Chapters 3 and 4. In this chapter quantitative information is presented that can be used in calculating the cracking pressure in vessels with flat end slabs.

The problem of determining the cracking pressure is twofold. First, a suitable cracking criterion for concrete subjected to multiaxial stresses has to be chosen. It has not been within the scope of this investigation to do any testing to evaluate possible cracking criteria for concrete but it is suggested that either a maximum stress or a maximum strain criterion will suffice. Second, the stresses have to be calculated in the area where the inclined crack is likely to occur. This problem is discussed in the following.

Several inclined cracks are initiated near the mid-height of the slab and at a slope of about 45 degrees. Cracks that are close to the wall remain limited in length because they are bounded by areas of concrete that are in triaxial compression (Fig. 3.18). The critical inclined crack is the one that propagates toward the edge of the anchorage plate of the longitudinal reinforcement. The idealized location at which this crack is initiated is at mid-height of the slab and at a distance of half the slab thickness from the edge of the anchorage plate.

Flexural cracking and the conical crack at the reentrant corner are initiated at about the same internal pressure as the inclined crack and influence the stresses in the area where the inclined crack is located. To properly account for different types of cracking and to accurately determine the internal pressure at which the inclined crack is initiated, a lumped-parameter or finite-element model with a cracking criterion included can be

used (Higashionna and Schnobrich, 1970). As an alternative to this approach, approximate equations of the governing stresses are presented in this chapter.

If the initiation of the inclined crack occurs in an intact end slab, the internal pressure at which it occurs can be calculated using an axisymmetric finite-element model (Chapter 3) that assumes elastic behavior. If flexural cracking and the crack at the reentrant corner occur first, the stresses at mid-height of the slab are increased, and the initiation of the inclined crack is hastened. However, extensive cracking is necessary before the effect is conspicuous. In most vessels, especially the ones with penetrations aggravating the conditions leading to the inclined crack, the effect of cracking in other areas can be neglected in determining the internal pressure at which the inclined crack is initiated. It is then possible to determine the cracking pressure from a finite-element model that assumes a linear force-deformation relationship. The following equations were found to provide a good approximation of the stresses calculated with the finite-element model at the point where the inclined crack is assumed to initiate

$$\sigma_r = - [\sigma_o + (\sigma_o - \sigma_g) \frac{t}{d} \tan 20°]/\beta \tag{8.1}$$

$$\sigma_z = - \frac{1}{3} \sigma_g \sqrt{\frac{1}{\beta}} \tag{8.2}$$

$$\tau = - \frac{3}{4} \frac{r}{d} \sigma_g \frac{1}{\beta} \tag{8.3}$$

$$\sigma_t = \sigma_r \tag{8.4}$$

The slab is stiffer than the wall in the radial direction, and some of the prestress and internal pressure exerted on the wall flows into the slab (Fig. 8.1), which is represented by the second term in Eq. 8.1.

The vertical stress (Eq. 8.2) is assumed to vary parabolically through the depth of the slab and to be 1/3 of the internal pressure at mid-height of the slab (Fig. 8.2).

The shear stress (Eq. 8.3) is obtained by assuming that the radial stress varies linearly through the depth of the slab.

If a maximum stress criterion is used to determine the internal pressure at which the inclined crack is initiated, the tangential stress does not have to be known. If a maximum strain criterion is used, the tangential stress can be assumed to be equal to the radial stress.

9. CALCULATION OF THE INTERNAL PRESSURE AT FAILURE

9.1 Introduction

In the following sections, a procedure is presented for obtaining a conservative estimate of the internal pressure corresponding to the failure of the end slab in shear. The procedure comprises a sequence of calculations performed with the use of an axisymmetric finite-element model of the end slab based on linear response. The suggested calculations are performed for vessels PV16 to PV21 as well as for PV9, PV13 and PV15. The properties of the latter three vessels were reported earlier (Paul et al., 1969) and are summarized in Table 9.1.

9.2 Vessel with a Solid End Slab

The calculation of the strength of the end slab is divided into three parts to be performed consecutively: (a) the internal pressure at which the inclined crack is initiated, (b) the shape of the cryptodome and (c) the strength of the cryptodome.

(a) The Initiation of the Inclined Crack

The initiation of the inclined crack is the first significant event in the sequence leading to a shear failure. The internal pressure and the location at which it occurs can be determined using the method described in Chapter 8.

(b) The Shape of the Cryptodome

The inclined crack will propagate from point A (Fig. 8.1) where it initiated to the edge of the anchorage plate of the longitudinal reinforcement. This part of the inclined crack is not changed in the following calculations. The shape of the center part of the cryptodome can be determined by studying the calculated strains in the dome. In Chapter 6 it was shown that the strains at the failure pressure should satisfy two conditions:

(I) The calculated radial strains along the inside face of the slab should be compressive. If tensile strains are calculated it would indicate a high bending moment in the dome. This criterion has two drawbacks. First, it is necessary to estimate the force-deformation relationship for concrete accurately. Second, depending on the internal pressure used in the calculations, differently shaped domes would be deemed acceptable.

(II) The maximum tensile strains at any vertical section of the dome should have their largest value at the inclined crack and decrease toward the inside face of the slab. If this condition is not satisfied for an assumed shape of the dome, a thinner dome should be tried. The value of this criterion is realized if the following three observations are considered:

(1) If elastic material properties are assumed, the variation of the calculated maximum tensile strains through the depth of the dome will be insensitive to the internal pressure. This is exemplified by calculating the strains at internal pressures of 1900 psi and 3200 psi in the dome shown in Fig. 9.1. The maximum principal strains are of different magnitude but the variation with depth is similar at the two pressures (Fig. 9.2).

(2) If inelastic material properties are assumed, the variation of the strains will change with the internal pressure (Fig. 9.2). However, inelasticity caused by high compressive stresses occurs only if the internal pressure is close to the failure pressure. The inclined crack, or at least the major part of the crack, develops at an internal pressure at which the effect of inelasticity is negligible. Therefore, in evaluating the strain condition in the dome for the purpose of determining the shape of the dome, inelasticity of the concrete does not have to be accounted for and the variation of the strains is virtually independent of the internal pressure.

(3) If the shape of the dome is changed inside any radius r_o, the strains

at radii greater than r_o will remain almost unchanged. The shape of the two domes in Fig. 9.3 are identical outside a radius of 4 in. The strains are different at a radius of 2 in. but almost the same at radii greater than 4 in. (Fig. 9.4). If a shape of the dome is found that is satisfactory outside a certain radius, r_o, only the center part of the dome, inside the radius r_o, has to be varied in the further investigation.

These observations justify the following method of determining the shape of the part of the dome that is inside point A:

(1) Assume a shape of the inclined crack from r = 0 to r = r_A (Fig. 9.5). The inclined crack has to be horizontal at the centerline. At r = r_A the location and the slope of the crack have to be continuous with the part that is located at radii greater than r_A. The crack has to be concave upwards inside r = r_A.

(2) Divide the dome with an arbitrary number of vertical lines, which do not have to be equidistant. Number them in sequence with the line going through point A called zero (Fig. 9.5).

(3) Calculate the strains in the dome using the axisymmetric finite-element model and assuming a linear force-deformation relationship for concrete, at the internal pressure corresponding to the initiation of the inclined crack. If the strains along the vertical line designated 1 satisfy condition II above, make the dome thicker. If they do not satisfy the condition make the dome thinner. Recalculate the strains in the dome. Continue this process until the differences in the comparable stresses for two consecutive calculations become negligible.

(4) The depth of the dome at vertical 1 is now fixed. Repeat the above calculations for the strains at vertical 2 without changing the depth of the dome at vertical 1.

(5) Continue until the entire shape of the dome is determined.

In the slabs with a large span width-to-depth ratio (PV9 and PV15) these calculations led to domes that were extremely thin at the center. At larger radii, in the "stock" of the dome where a shear failure would occur, the location of the crack was reasonable but the crack did not flatten out sufficiently near the center. There may be several reasons for this. First, the calculations are sensitive to the assumed value of Poisson's ratio. Second, if a slab is close to a flexural failure when the inclined crack is propagating, which was the case for these two vessels, the concrete may deform inelastically. This cannot be taken into account without a better knowledge than is currently available of the force-deformation characteristics of concrete. The effect of inelasticity would be most noticeable in the formation of the center part of the inclined crack because this part develops at the highest internal pressure and is subject to the largest stresses. Third, the concrete located above the inclined crack is ignored in the analysis but may have had a stiffening influence on the center part of the dome.

Because the determination of the shape of the center portion of the dome involves uncertainties and because these uncertainties affect the calculated stresses directly, it is necessary to be conservative in evaluating the consequences of the stresses in the dome.

(c) The Strength of the Cryptodome

The stress condition in the dome is analyzed using the axisymmetric finite-element model. To evaluate the stress condition, the failure indices (Chapters 6 and 7) are calculated. Two different evaluations of the failure index were used: (a) α_w which represents the worst stress condition at a vertical section and is defined as the maximum value of α at each section,

excluding the nodes at the two boundaries, (b) α_a which is obtained from the average stresses at each vertical section.

The value of the failure index usually increases at the nodes very close to the centerline (Fig. 9.6). This is caused by imperfections in the finite-element model. The actual vertical stress along the inside face of the slab is equal to the applied internal pressure. However, the calculated vertical stress close to the centerline is smaller than the internal pressure (Fig. 9.6). This leads to an increase in the failure index because the vertical stress is the confining pressure. In the examples in the next section, the values of the failure index inside a radius of 1 in. have been ignored.

The calculation of the strength of a given cryptodome was, for three reasons, based on elastic response:

(a) The force-deformation relationship for triaxially stressed concrete is not well defined beyond the linear range.

(b) The tests did not demonstrate clearly that inelastic deformation of concrete subjected to triaxial compression occurred to a significant extent.

(c) If inelastic material properties are assumed, the calculated value of the failure index α_a will be insensitive to the applied internal pressure at the center of the dome where it has its maximum value (Fig. 9.7). This could lead to overestimation of the strength of the dome.

A twofold condition has been chosen as the failure criterion. If both of the following conditions are satisfied at a certain internal pressure, failure is predicted to have occurred (Fig. 9.8):

$$\alpha_a > 1.0 \quad \text{at locations with} \quad r < r_b \tag{9.1}$$

$$\alpha_w > 1.0 \quad \text{at locations with} \quad r_b - d < r < r_b \tag{9.2}$$

This dual condition was prompted by the uncertainties in the determination of the shape of the dome, the force-deformation relationship of concrete and the failure criterion for concrete. However, the following rationale can be given:

(1) For all vessels failing in shear, the observed failure plane was located in the stock of the dome. The inclined crack has an initial slope of about 45 degrees and the stock can be assumed to be limited to $r > r_b - d$ (Fig. 9.8). For shear failure to occur the value of α_w has to exceed unity at at least one node in the stock (Eq. 9.2).

(2) Due to redistribution of stresses as the failure pressure is approached, the average stresses at one section have to reach a failure condition. This does not have to occur in the stock (Eq. 9.1).

If only Eq. 9.1 had been chosen as the failure criterion, the strength of the vessels with a high spanwidth-to-depth ratio (PV9 and PV15) would have been underestimated considerably. This is caused by the very thin domes that are obtained by using the method described above. If it can be shown that the dome is thicker and if a more accurate criterion to determine the shape of the dome is found, it is possible that Eq. 9.1 would suffice as a failure criterion.

If only Eq. 9.2 had been chosen as the failure criterion the strength of the vessels with penetrations would have been underestimated and it could not have been explained why the vessels with penetrations (PV17 to PV21) carried the same internal pressure as vessel PV16 with a solid end slab.

9.3 Examples

(a) Vessel PV16

Using a tensile stress of $4\sqrt{f_{cu}}$ as the cracking criterion, the inclined crack is calculated to have started at 1900 psi internal pressure, 8 in. from

the centerline and at mid-height of the slab. This pressure is used in determining the shape of the cryptodome.

The inclined crack is defined by an equation of the third order between radii 0 in. and 8 in.

$$z = ar^3 + br^2 + cr + d \tag{9.3}$$

The variable z is the vertical location of the crack counted from the inside face of the slab. By specifying the crack to go through point A (r = 8 in., z = 5 in.) and to be horizontal at the centerline and have a slope of 45 degrees at point A, the following equation is obtained

$$z = \frac{\delta - 1}{256} r^3 + \frac{7 - 3\delta}{64} r^2 + \delta \tag{9.4}$$

The only constant left is δ, which is the depth of the dome at the centerline. By varying δ the thickness of the dome can be varied. For all values of δ less than 2.33 the inclined crack is concave upwards. The strains were calculated in domes that were from 1 in. to 2 in. thick at the centerline (Fig. 9.9). In the first step the strains at a radius of 4 in. was studied (Fig. 9.10). The calculated strains at the nodes along the two boundaries are ignored because they often seem to be incompatible with the strains at the other nodes. The dome with a value of 1-1/2 in. for δ is the thickest one for which the strains at a radius of 4 in. increase continuously from one boundary to the other. The part of the dome that is outside a radius of 4 in. is now fixed.

In the second step the dome inside a radius of 4 in. was studied. A cubic equation was used to define this part of the dome, too. The strains were studied at a radius of 1 in. instead of at the centerline because of the discontinuities obtained at the centerline. The dome in Fig. 9.11 with a thickness of 0.85 in. at the centerline satisfied the strain criterion. The calculated strains at different radii in this dome, at an internal pressure

of 1900 psi, are shown in Fig. 9.12.

The defined limit of the stock of the dome is shown by the broken line in Fig. 9.11. Equation 9.2 has to be satisfied at radii greater than 3 in. The calculated values of the failure indices at an internal pressure of 1900 psi are lower than the limits specified by Eq. 9.1 and 9.2 (Fig. 9.13). The failure indices are then calculated for an internal pressure of 2850 psi (Fig. 9.14) for the same dome. The value of α_w has a maximum value of 1.06 at a radius of 3 in. and α_a is 0.97 at a radius of 1-1/4 in. The maximum internal pressure that vessel PV16 can resist in shear is therefore determined to be just above 2850 psi as compared to an experimental result of 3200 psi.

(b) Vessel PV13

The calculated cracking pressure is 3500 psi at a radius of 6-3/4 in. Domes with depths from 1.0 to 4.0 in. were analyzed using a cubic equation to define the shape of the crack (Fig. 9.15). Only one step was used in defining the shape of the crack because of the low spanwidth-to-depth ratio. The dome that is 2 in. thick at the centerline satisfies the strain condition at all radii (Fig. 9.16) and is a conservative (thin) estimate of the shape of the dome.

At an internal pressure of 3500 psi the maximum values of the failure indices are 0.57 for α_a and 0.66 for α_w (Fig. 9.17). The calculated internal pressure at which this vessel would fail in shear is considerably greater than 3500 psi. As this vessel reached a pressure of 3450 psi without failing in shear, the calculations are in accord with the test results.

(c) Vessel PV9

The cracking pressure was calculated to be 810 psi. For determining the shape of the dome, the part inside point A was divided into four subsections because of the high spanwidth-to-depth ratio. Each section was defined by a

cubic equation. It was found that the center of the dome would be very thin (Fig. 9.18) and that the calculated strength of the dome would be determined by the maximum value of α_w in the stock (Eq. 9.2). It was therefore not necessary to try to satisfy the strain condition inside the stock of the dome (Fig. 9.19). At an internal pressure of 810 psi the calculated maximum value of α_w is 0.76 at a radius of 6-1/2 in. which is the defined boundary of the stock (Fig. 9.20). The internal pressure was increased to 1000 psi but the value of α_w was still less than 1.0 in the stock (Fig. 9.21). This agrees with the test results, because the vessel failed in flexure at 887 psi.

(d) Vessel PV15

The calculated cracking pressure is 1200 psi. Also for this vessel an extremely thin dome would have been obtained if the strain condition was stringently satisfied. A dome (Fig. 9.22) was chosen that was sufficiently thin to make Eq. 9.2 the critical condition and that satisfied the strain condition in the stock (Fig. 9.23). The maximum value of α_w at 1200 psi internal pressure is 0.86 at a radius of 6 in. (Fig. 9.24). At an internal pressure of 1500 psi the value of α_w exceeded 1.0 slightly, making the calculated shear strength of the slab about 1500 psi. The test vessel failed in shear at an internal pressure of 2300 psi so the design method was unnecessarily conservative for this vessel.

9.4 Vessel with Penetrations in the End Slab

(a) Idealization of Penetrations

In determining the shape of the dome, the penetrations can be ignored and the slab analyzed as a solid slab. The influence of penetrations on the shape of the dome is minor.

The penetrations influence the magnitude of the failure indices. Two different methods can be chosen to calculate the failure indices:

(1) The axisymmetric finite-element is modified where the penetrations are located (Chapter 7). The modulus of elasticity for each element is reduced in proportion to the amount of concrete that is removed by the penetrations. Thereafter, the failure indices are calculated.

(2) The failure indices are calculated as if the slab was solid. Then, the failure indices at the radii where the penetrations are located are divided by β, which is defined as the solid perimeter at any radius divided by the total perimeter at the same radius. This method is simpler but more conservative than the first method.

After the failure indices have been calculated, Eq. 9.1 and 9.2 are used to determine if a failure condition exists.

(b) Examples

For test vessel PV16 the calculated maximum values are located at 1-in. radius for α_a and at 3-in. radius for α_w (Fig. 9.14). Both values are about 1.0 at the calculated failure pressure. The penetrations do not lower the calculated failure pressure unless the maximum values of both α_a and α_w are increased.

Vessels PV17, PV18, PV20 and PV21 had penetrations located at a radius of 8 in. The value of α_w for PV16 is 0.86 at a radius of 8 in. and only a few penetrations have to be introduced before it exceeds unity. However, α_a is only 0.50 at this radius and 50 percent of the section has to be removed before it exceeds unity. The calculated failure pressure is therefore 2850 psi for all these vessels and for vessel PV16, and the penetrations have not had any effect on the calculated shear strength of the vessels. This agrees with the test results.

Vessel PV19 had penetrations at a radius of 4 in. For vessel PV16 the value of α_w is about 1.0 at this section while the value of α_a is 0.65.

Consequently, 35 percent of this section could be removed without affecting the calculated shear strength of the slab. In vessel PV19 penetrations removed 50 percent of the section and a decrease in strength was expected. That this effect did not materialize is probably due to the sealing plates for the penetrations (section 2.3).

10. SUMMARY

(a) Object and Scope

The object with this investigation was to study the shear strength of end slabs of prestressed concrete reactor vessels. The configuration of the vessels was that of a cylinder bounded by two flat slabs. The vessels were prestressed circumferentially and longitudinally and subjected to an internal pressure. Vessels with solid end slabs and vessels with penetrations in the end slabs were studied.

Six pressure vessels were tested. The only systematically varied variables were the amount and location of penetrations in the end slabs. The vessels failed at internal pressures between 3000 psi and 3500 psi with no apparent relation between the failure pressures and the amount and location of penetrations.

(b) Initiation of the Inclined Crack

A set of equations have been presented that predicts the internal pressure at which the inclined crack is initiated. The equations are accurate if only a small amount of cracking occurs in other areas of the slab before the inclined crack is initiated. Extensive flexural cracking may precipitate the development of the inclined crack.

(c) Shear Strength of the End Slab

The end slab and the wall of the pressure vessel are almost separated as the failure pressure is approached, and the end slab can be analyzed separately. There are two stages involved in analyzing the shear strength of the end slab: (1) determining the shape of the cryptodome that is carrying the internal pressure and (2) calculating the stress condition in the cryptodome.

(1) The shape of the cryptodome was determined by assuming that the

inclined crack passed through the points at which the principal tensile strains had their maximum values. This assumption proved successful in determining the major part of the inclined crack. However, sometimes it leads to an underestimation of the thickness at the center of the dome.

(2) The stresses in the cryptodome were calculated assuming the concrete to have a linear force-deformation relationship in compression. The calculated stresses were compared by using a failure criterion based on Mohr's stress circles.

(d) Influence of Penetrations

Penetrations that are located in the section in which the inclined crack is initiated, precipitate the formation of the crack. This effect is included in the equations that were suggested for predicting the initiation of the inclined crack.

In the experiments that were performed, the penetrations did not affect the strength of the vessels. However, it has not been possible to give a "rule of thumb" of the amount of penetrations that can be introduced without affecting the strength of the slab. The design method that has been developed indicates that, depending on the geometrical shape of the vessel and the location of penetrations, even a few penetrations may reduce the strength of the slab. When the effect of penetrations in the end slab is being considered, the calculations presented in Chapter 9 have to be carried out.

(e) Conclusions

The following may be concluded from the tests and analyses of the pressure vessels with and without penetrations in the end slab.

About the development of cracks:

- Cracking at the reentrant corner changes the distribution and magnitude of radial strains on the inside face of the end slab. The propagation of the

reentrant-corner crack is associated with a reduction in the end restraint on the slab.

- Cracking at the reentrant corner increases the tensile strains on the outside face of the end slab, thus hastening the initiation of flexural cracks.

- Calculations indicated that initiation of inclined cracking near the mid-height of the end slab would not be sensed by strain measurements on the inside and outside surfaces of the end slab. This was not refuted by the experimental measurements.

- Experimental observations indicated that, after initiation near the mid-height of the end slab, the inclined crack propagated in both directions, extending toward the outside face at a faster rate than toward the inside face. The inclined crack tended to carve a dome out of the end slab, called the "cryptodome" in this report.

- Measurable changes occurred in the end-slab strains when the inclined crack reached the outside surface. These changes indicated that the internal pressure was being resisted primarily through dome action.

- End slabs with penetrations developed flexural cracks at the outside surface at a slightly lower pressure than solid end slabs.

- It was possible to observe the initiation of the inclined crack in end slabs with penetrations through the use of strain gages. These observations led to no significant difference between inclined-cracking pressures in vessels with increased number or size of penetrations in the critical cracking region despite the indication from calculations that the difference would be approximately 14 percent. It was not possible to make direct comparisons of the cracking load for a solid end slab with that for one with penetrations on the basis of the experimental observations.

About the shear strength of the end slab:

- Collapse of the end slab resulted from failure of the concrete in the cryptodome under the influence of high compressive and shear stresses.
- In end slabs with penetrations, failure occurred in the concrete between the penetrations.
- Although the penetrations in some test vessels removed up to half of the circumference on which they were located, the reduction in shear strength of the end slab was not significant.

About analysis:

- The pressure at initiation of the inclined crack could be estimated on the basis of an elastic analysis of the end slab using a tensile stress of $4\sqrt{f_{cu}}$ as the criterion for cracking.
- It was found by comparing the results of two- and three-dimensional analyses that the stresses in end slabs with penetrations could be evaluated through the use of axisymmetric analyses with simple modifications.
- A failure criterion based on Mohr's stress circles was found most suitable to evaluate the significance with respect to failure of the multi-axial stress conditions in the dome.
- Using a nonlinear force-deformation relationship for concrete did not affect the calculated critical stresses in a given cryptodome.
- If average stresses are calculated at each vertical section, the tangential stress is the intermediate principal stress, which is compatible with the fact that failure occurs in the radial-vertical plane.
- The shape of the cryptodome can be determined by specifying that the maximum tensile strains at any vertical section should have their maximum value at the trajectory of the inclined crack.
- The distribution of maximum tensile stresses in any vertical section was found insensitive to the applied internal pressure.

- A method was developed which can be used for obtaining a safe lower bound to the shear strength of a flat end slab. This included (a) the calculation of the pressure corresponding to inclined cracking, (b) the determination of the dimensions of the cryptodome, and (c) evaluation of the stresses in the cryptodome.

LIST OF REFERENCES

Anson, M. "An Investigation into a Hypothetical Deformation and Failure Mechanism for Concrete," Magazine of Concrete Research, V. 16, No. 47, June 1964, pp. 73-82.

Baker, A. L. L., "A Criterion of Concrete Failure," The Institution of Civil Engineers, Proceedings, V. 45, February 1970, pp. 269-278.

Balmer, G. G., "Shearing Strength of Concrete under High Triaxial Stress," Laboratory Report No. SP-23, U. S. Department of the Interior, Bureau of Reclamation, October 1949.

Bellamy, C. J., "Strength of Concrete under Combined Stress," ACI Journal, Proceedings, V. 58, No. 4, October 1961, pp. 367-381.

Bresler, B., and Pister, K. S., "Failure of Plain Concrete under Combined Stresses," Transactions, ASCE, V. 122, 1957, pp. 1049-1068.

Bresler, B., and Pister, K. S., "Strength of Concrete under Combined Stresses," ACI Journal, Proceedings, V. 55, No. 3, September 1958, pp. 321-345.

Echeverria, G. A., and Schnobrich, W. C., "Lumped-Parameter Analysis of Cylindrical Prestressed Concrete Reactor Vessels," University of Illinois, Civil Engineering Studies, Structural Research Series No. 340, Urbana, December 1968.

Fumagalli, E., "Strength of Concrete under Biaxial Compression," ACI Journal, Proceedings, V. 62, No. 9, September 1965, pp. 1187-1188.

Hannant, D. J., and Frederick, C. O., "Failure Criteria for Concrete in Compression," Magazine of Concrete Research, V. 20, No. 64, September 1968, pp. 137-144.

Higashionna, R., and Schnobrich, W. C., "Lumped-Parameter Analysis for Shear Failure in the End Slab of Cylindrical Prestressed Concrete Pressure Vessels," University of Illinois, Civil Engineering Studies, Structural Research Series No. 363, Urbana, August 1970.

Hognestad, E., "A Study of Combined Bending and Axial Load in Reinforced Concrete Members," Bulletin No. 399, University of Illinois, Engineering Experimental Station, November 1951.

Iyengar, K. T. S. R., Chandrashekhara, K., and Krishnaswamy, K. T., "Strength of Concrete under Biaxial Compression," ACI Journal, Proceedings, V. 62, No. 2, February 1965, pp. 239-250.

Kupfer, H., Hilsdorf, H. K., and Rusch, H., "Behavior of Concrete under Biaxial Stresses," ACI Journal, Proceedings, V. 66, No. 8, August 1969, pp. 656-666.

McHenry, D., and Karni, J., "Strength of Concrete under Combined Tensile and Compressive Stress," ACI Journal, Proceedings, V. 54, No. 10, April 1958, pp. 829-839.

Mohraz, B., Schnobrich, W. C., and Gupta, A. K., "A Finite Element Method for the Analysis of Nozzle Openings in Shells of Revolution," University of Illinois, Civil Engineering Studies, Structural Research Series No. 355, Urbana, December 1969.

Paul, S. L., Sozen, M. A., Schnobrich, W. C., Karlsson, B. I., and Zimmer, A., "Strength and Behavior of Prestressed Concrete Vessels for Nuclear Reactors - Volume 1," University of Illinois, Civil Engineering Studies, Structural Research Series No. 346, Urbana, July 1969.

Richart, F. E., Brandtzaeg, A., and Brown, R. L., "A Study of the Failure of Concrete under Combined Compressive Stresses," Bulletin No. 185, University of Illinois, Engineering Experiment Station, November 1928.

Smee, D. J., "The Effect of Aggregate Size and Concrete Strength on the Failure of Concrete under Triaxial Compression," The Civil Engineering Transactions, The Institute of Engineers in Australia, October 1967, pp. 339-343.

Vile, G. W. D., "The Strength of Concrete under Short-term Static Biaxial Stress," The Structure of Concrete; Proceedings of an International Conference, London, 1965, Cement and Concrete Association, 1968.

TABLE 2.1

PROPERTIES OF TEST VESSELS

Mark	Number and Diameter of Penetrations	Distance from Center of Slab	Percent of Perimeter Removed[a]	β[b]	Percent of Slab Removed[c]	Circumf. Prestress[d]	Total Longitudinal Prestressing Force	f_{cu}	Maximum Internal Pressure
		in.				psi	kips	psi	psi
16	-	-	-	100	-	1206	1995	7450	3200
17	3 x 4"	8	25	75	7.7	1265	2080	7180	3000
18	6 x 4"	8	50	50	15.3	1188	1818	7590	3000
19	6 x 2"	4	50	50	3.8	1170	2300	7470	3500
20	12 x 2"	8	50	50	7.7	1155	2140	6890	3300
21	6 x 2"	8	25	75	3.8	1130	2300	7400	3300

(a) Length of perimeter removed divided by total perimeter along the circle that passes through the centers of the penetrations.

(b) Solid perimeter divided by total perimeter along circle that goes through the center of the penetrations.

(c) Horizontal area of penetrations divided by inside area of slab ($\pi \times 12.5^2$).

(d) Equivalent radial pressure.

TABLE 9.1

PROPERTIES OF THREE VESSELS WITH SOLID END SLABS

Vessel	Vessel Diameter	Slab Thickness	Wall Thickness	Circumf.* Prestress	Long. Prestress	Concrete f_{cu}	Max. Internal Pressure	Failure
	in.	in.	in.	psi	kips	psi	psi	
PV9	40	9	5	615	750	7140	887	Flexural
PV13	40	12.5	7.5	1145	1356	6750	3450	Wall
PV15	40	7.5	7.5	1292	1200	7340	2300	Shear

* Equivalent radial pressure

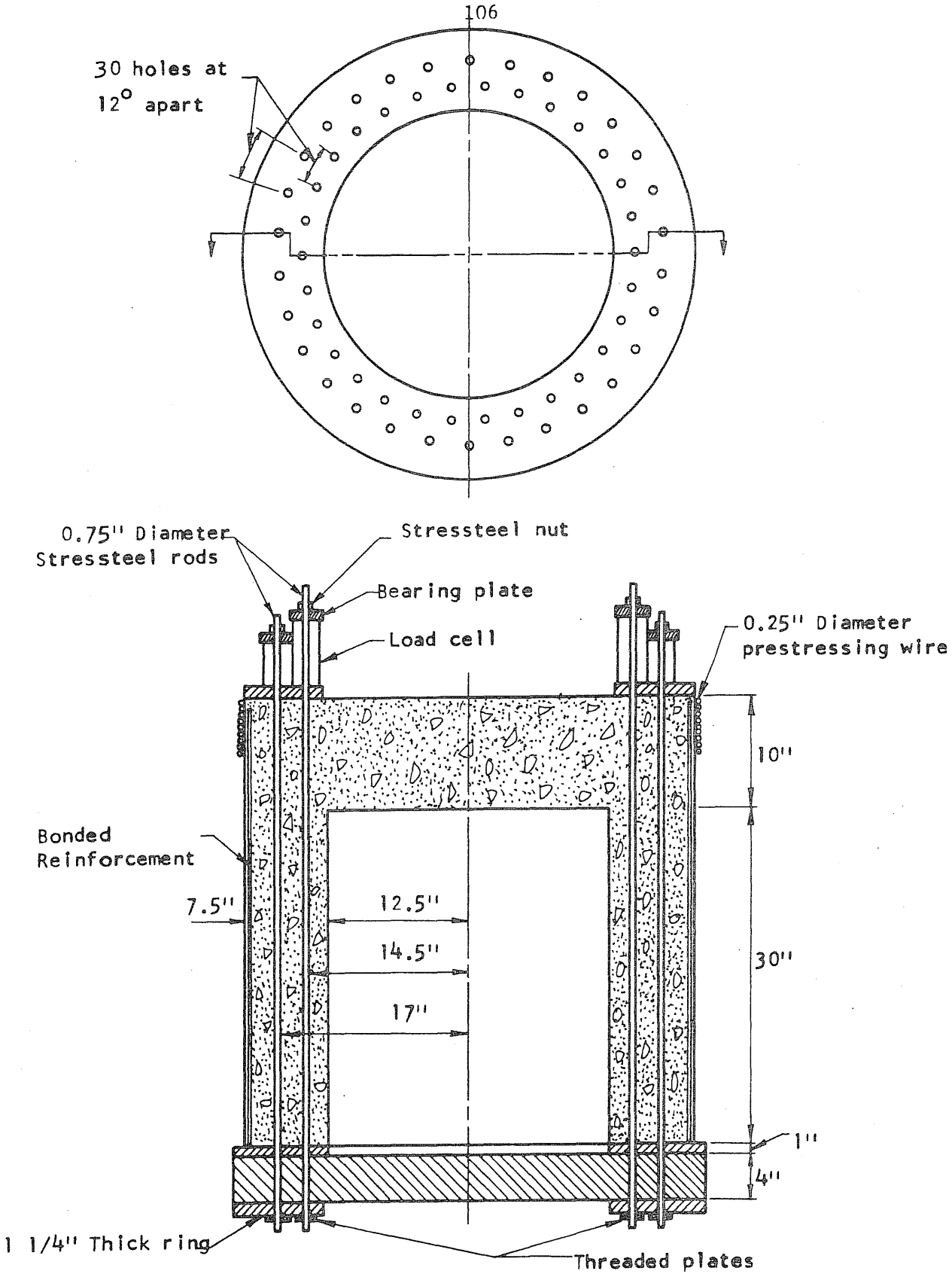

FIG. 2.1 DIMENSIONS OF TEST VESSELS

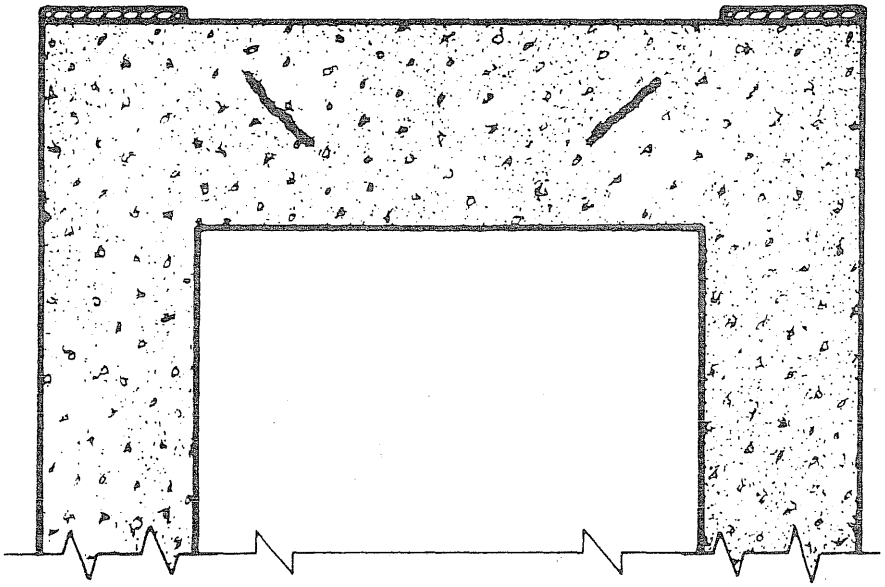

FIG. 2.2 THE INCLINED CRACK AFTER INITIATION

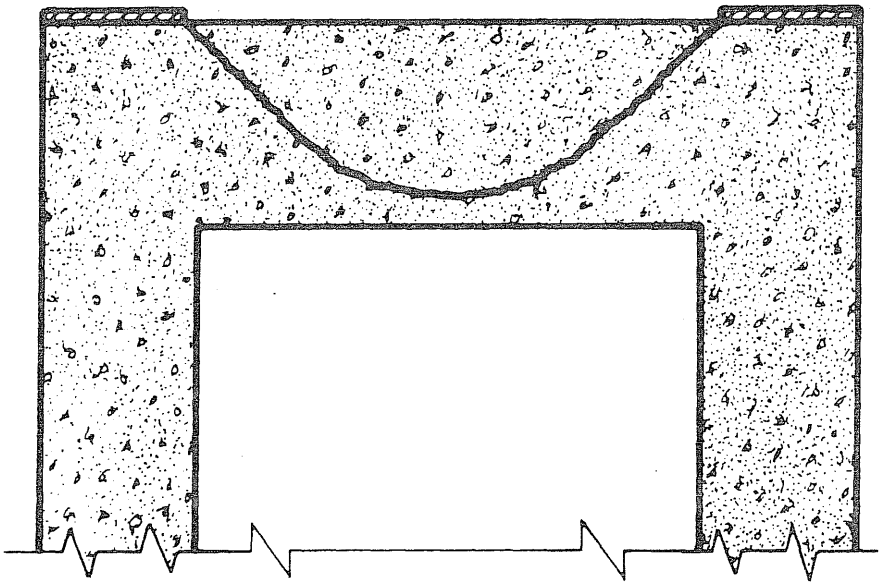

FIG. 2.3 THE CRYPTODOME THAT IS CARVED OUT BY THE INCLINED CRACK

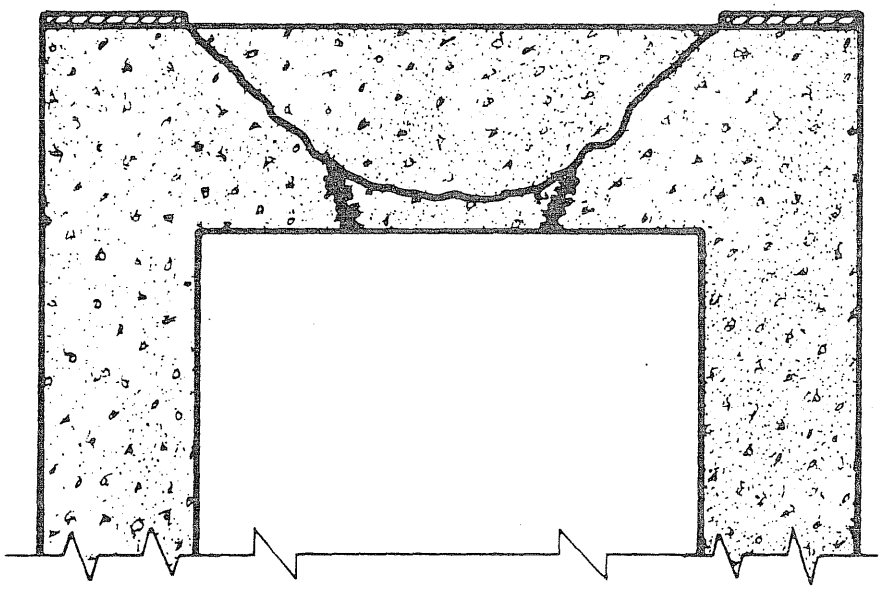

FIG. 2.4 THE FAILURE PLANE IN THE CRYPTODOME

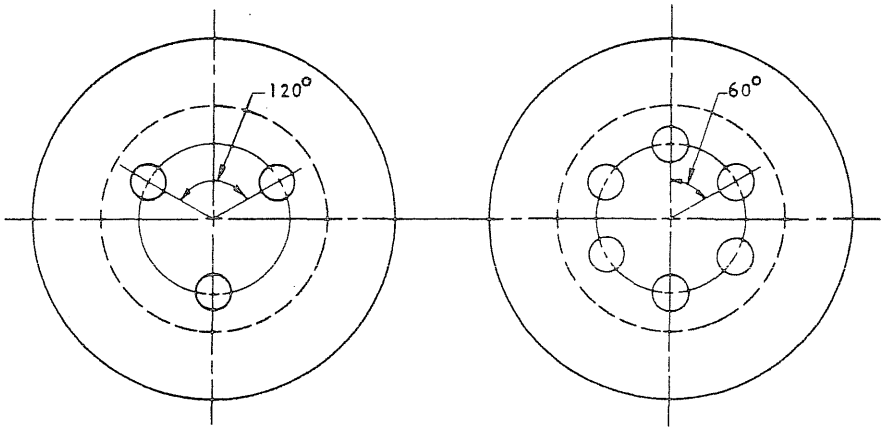

PV17 (3 x 4-in.)

PV18 (6 x 4-in.)

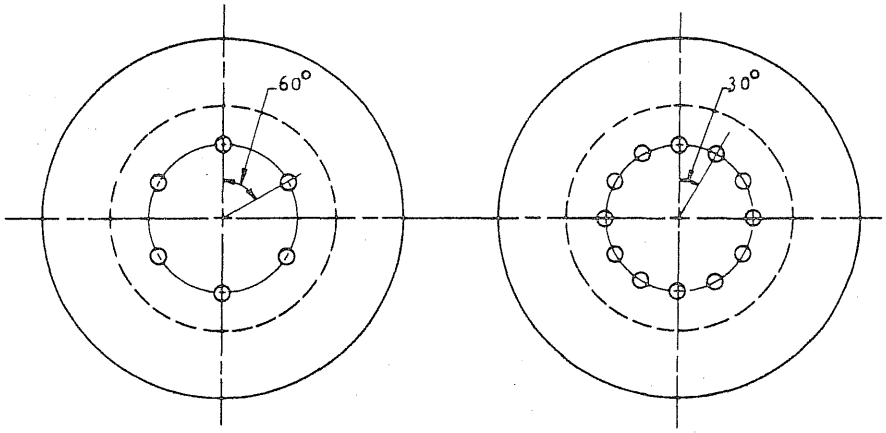

PV21 (6 x 2-in.)

PV20 (12 x 2-in.)

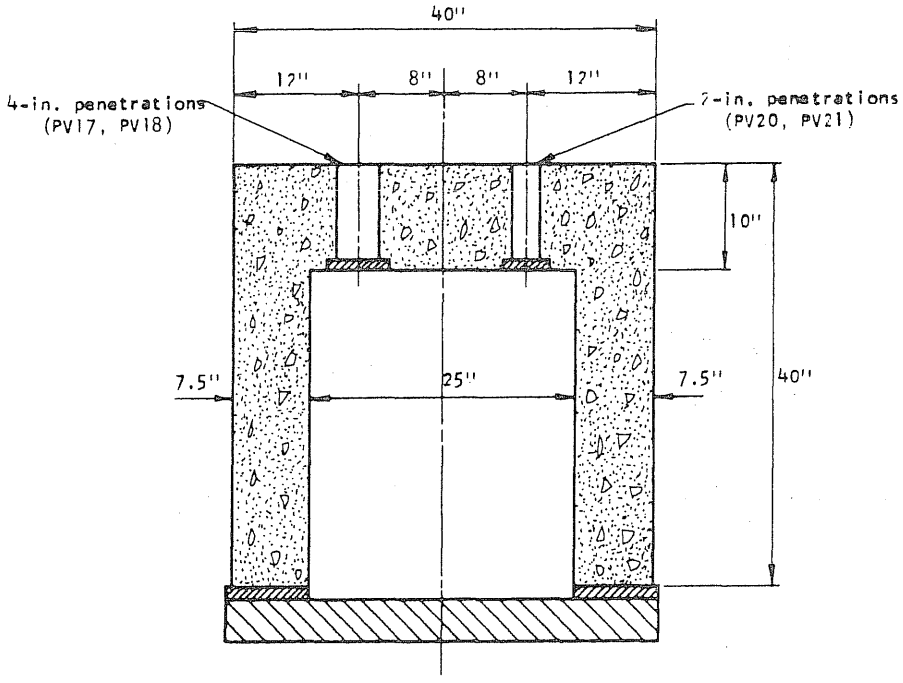

FIG. 2.5 VESSELS WITH PENETRATIONS 8 in. FROM THE CENTER OF THE SLAB

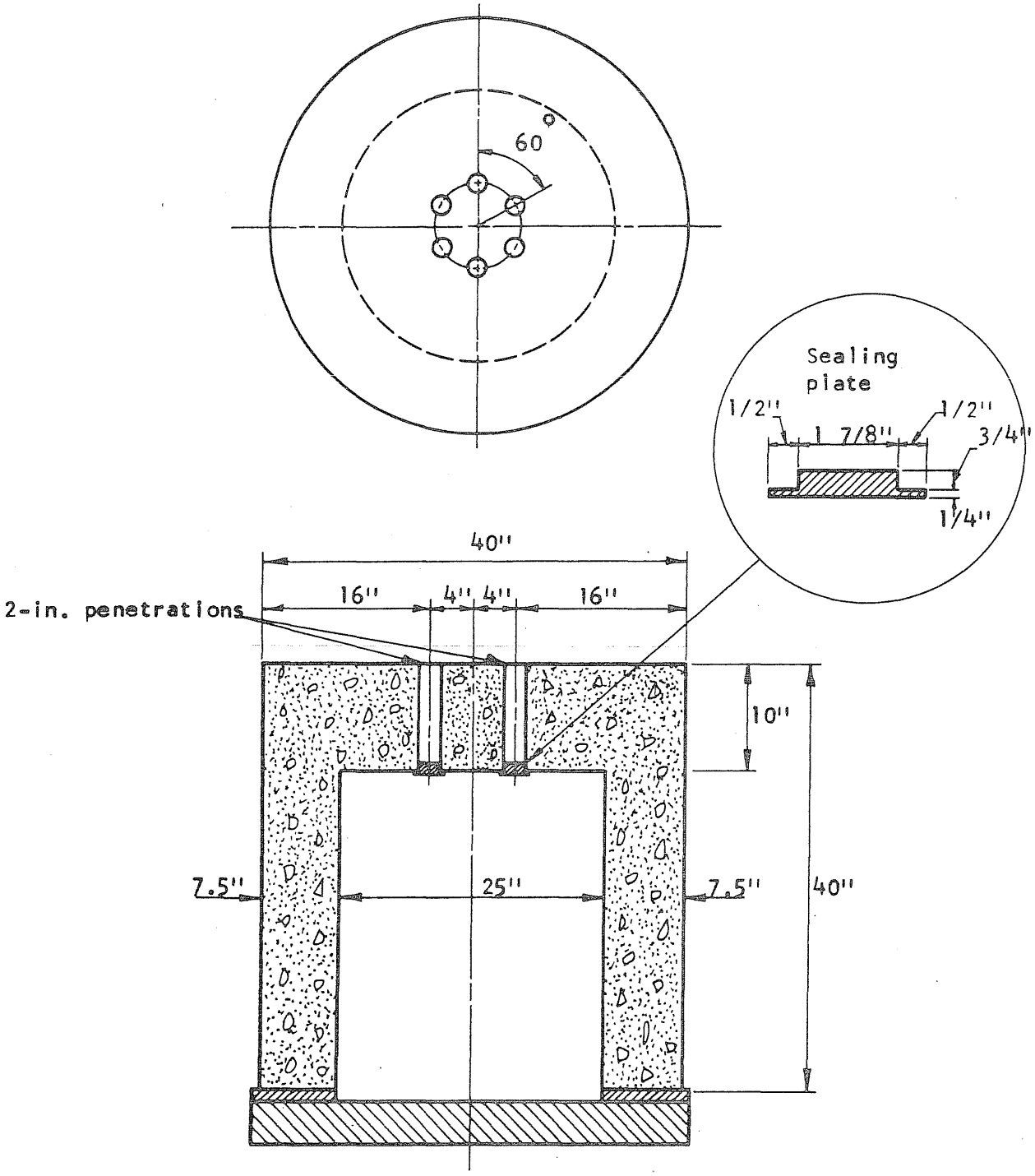

FIG. 2.6 VESSEL WITH PENETRATIONS 4 in. FROM THE CENTER OF THE SLAB

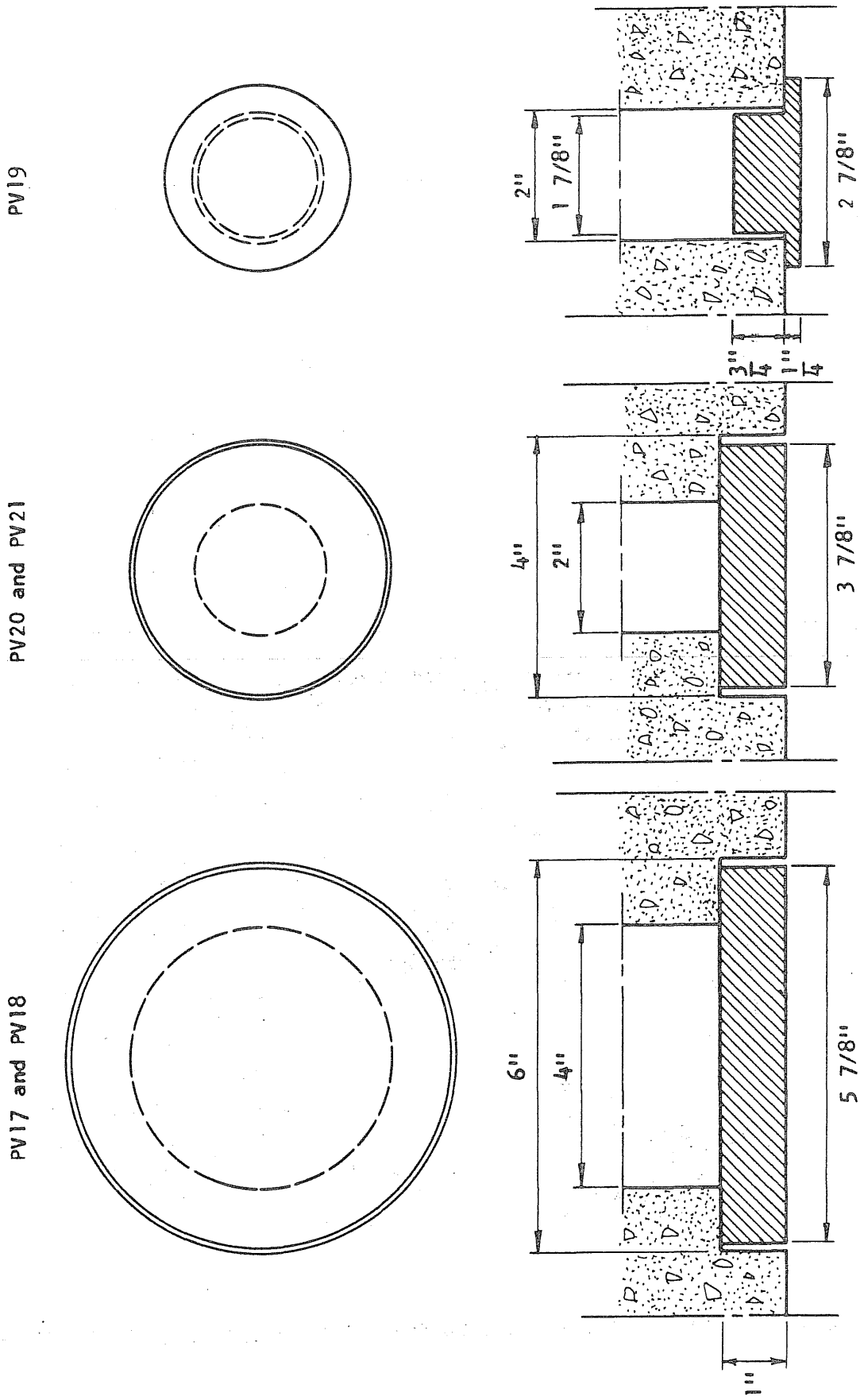

FIG. 2.7 DETAIL OF SEALING OF THE PENETRATIONS

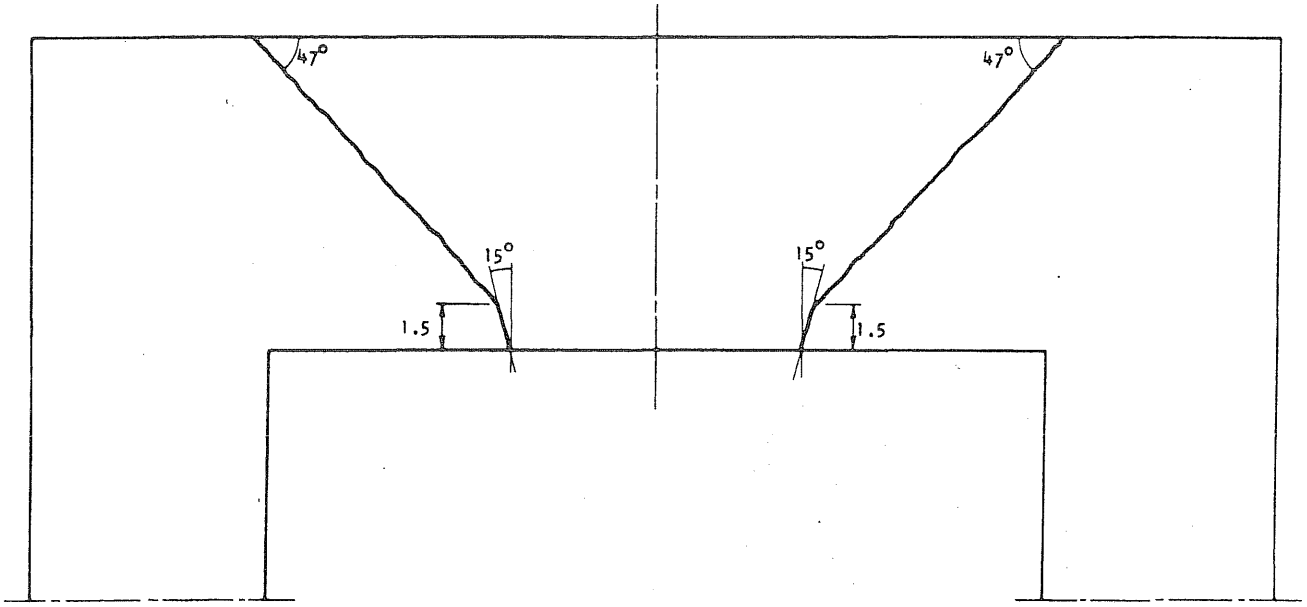

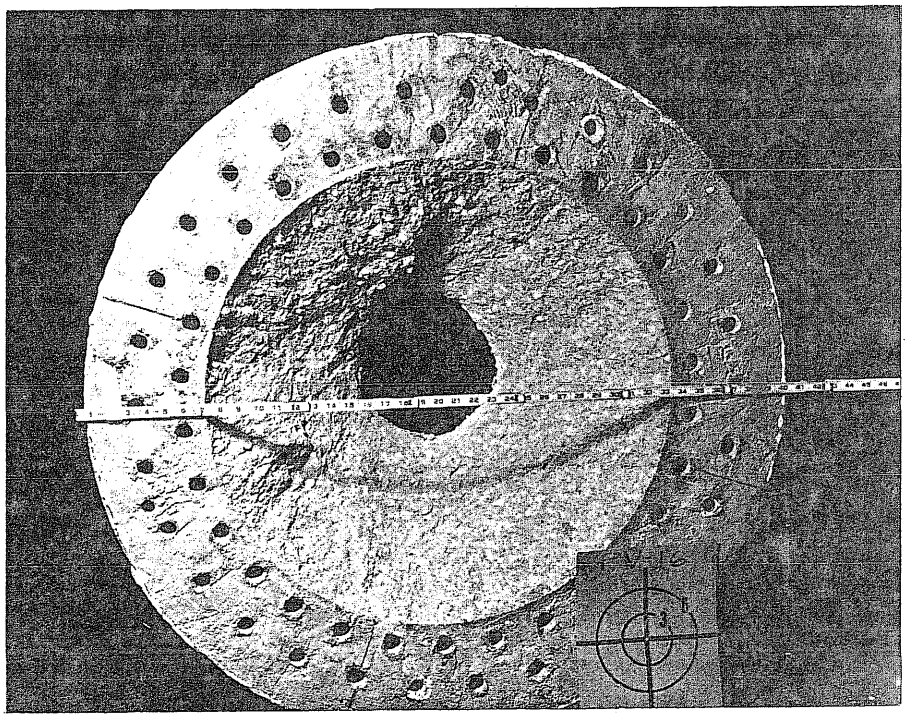

FIG. 2.8 TRAJECTORY OF THE INCLINED CRACK AND FAILURE SURFACE IN VESSEL PV16

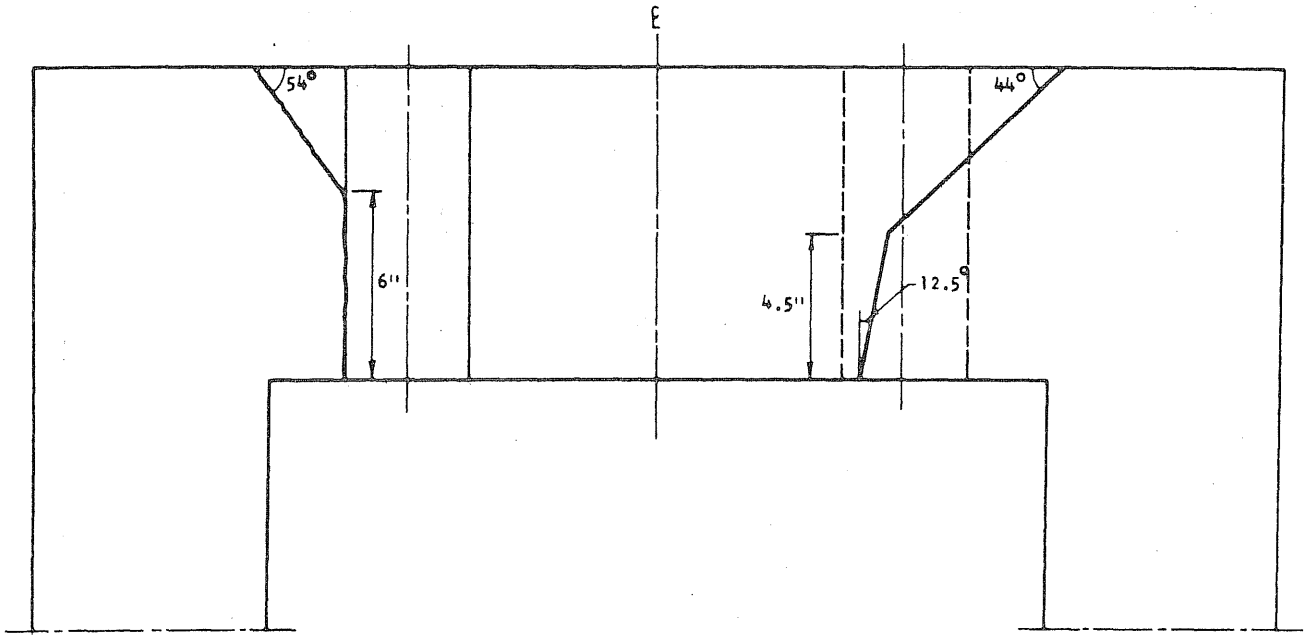

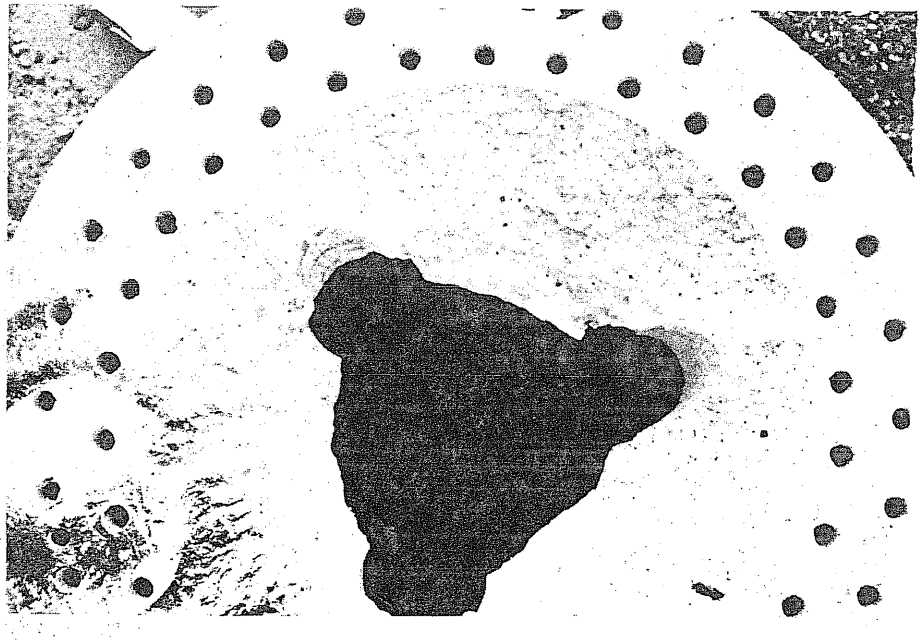

FIG. 2.9 TRAJECTORY OF THE INCLINED CRACK AND FAILURE SURFACE IN VESSEL PV17

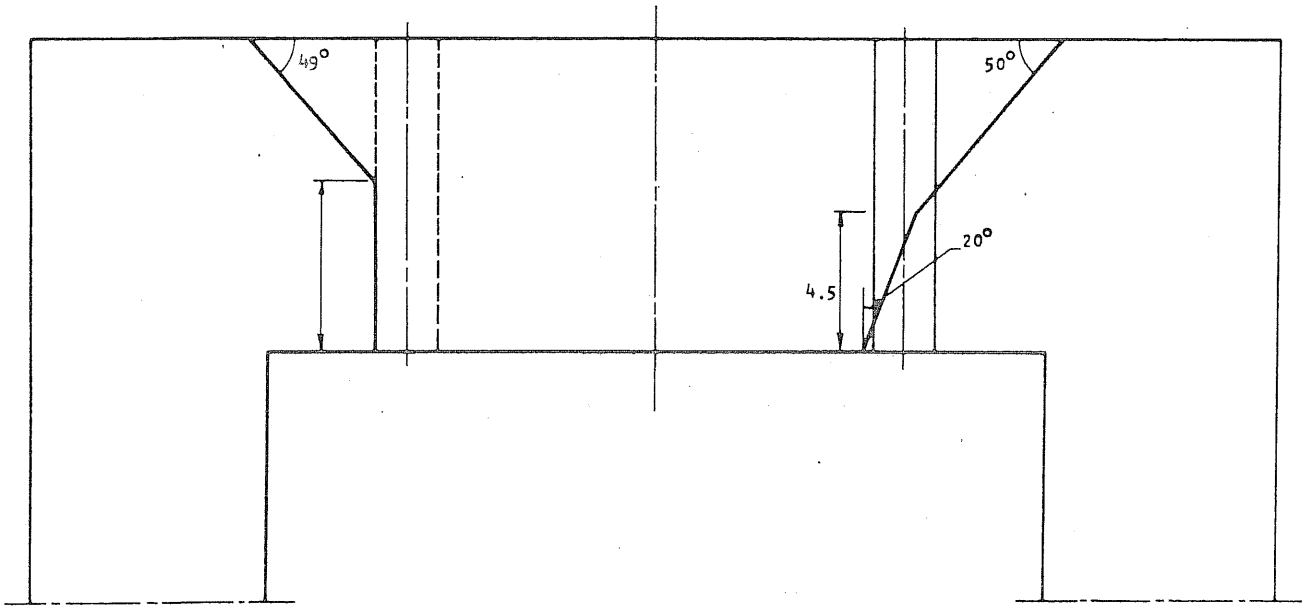

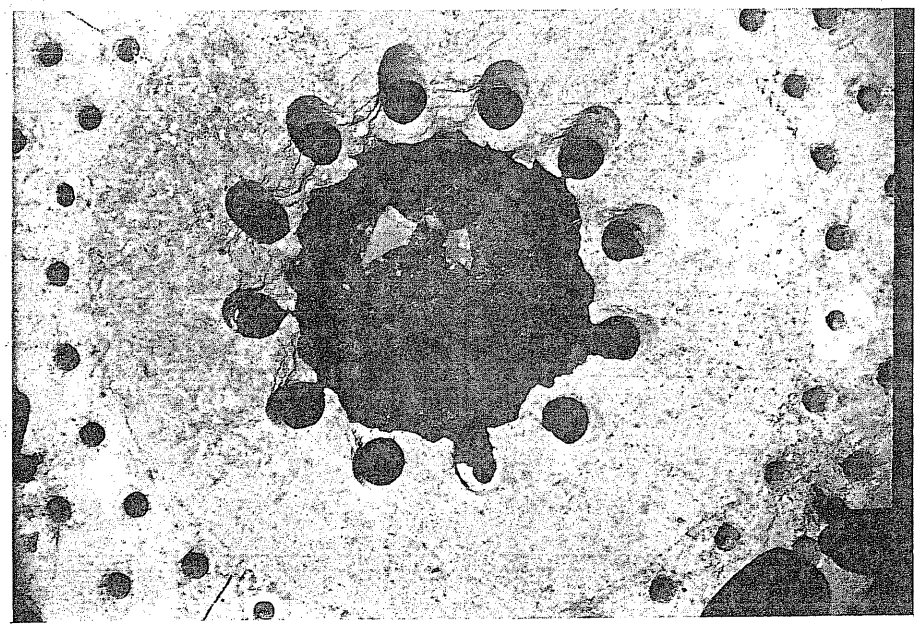

FIG. 2.10 TRAJECTORY OF THE INCLINED CRACK AND FAILURE SURFACE IN VESSEL PV20

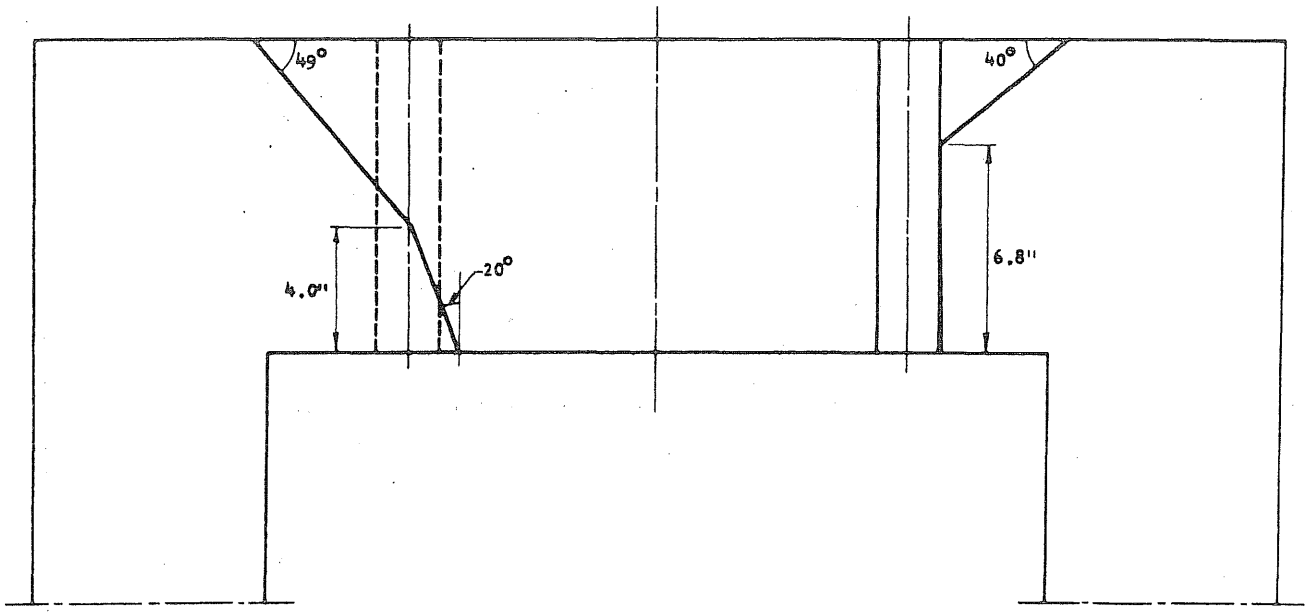

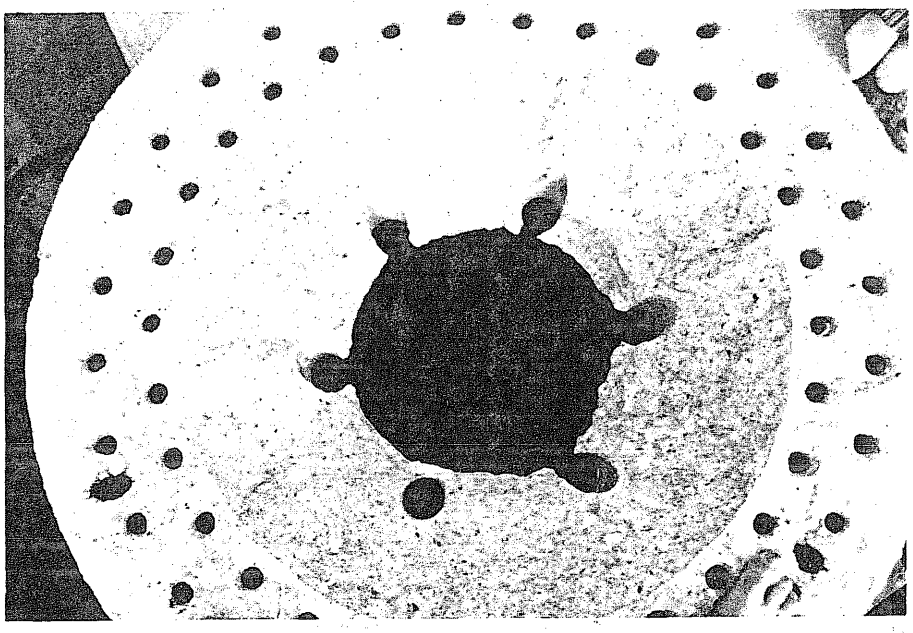

FIG. 2.11 TRAJECTORY OF THE INCLINED CRACK AND FAILURE SURFACE IN VESSEL PV21

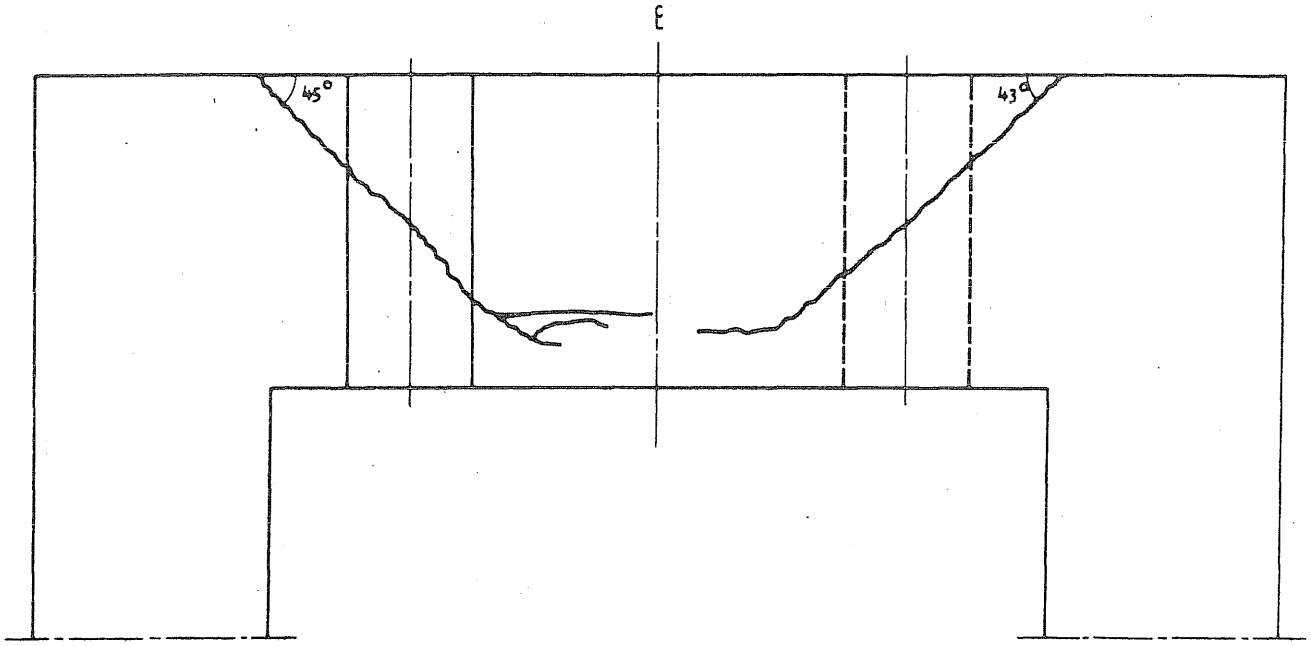

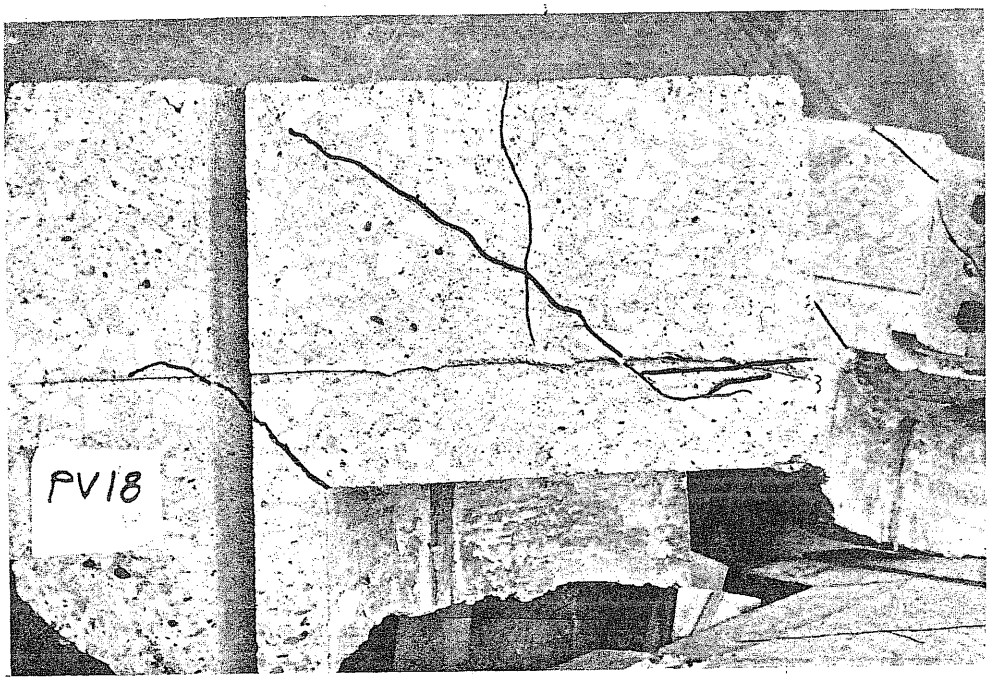

FIG. 2.12 TRAJECTORY OF THE INCLINED CRACK IN VESSEL PV18

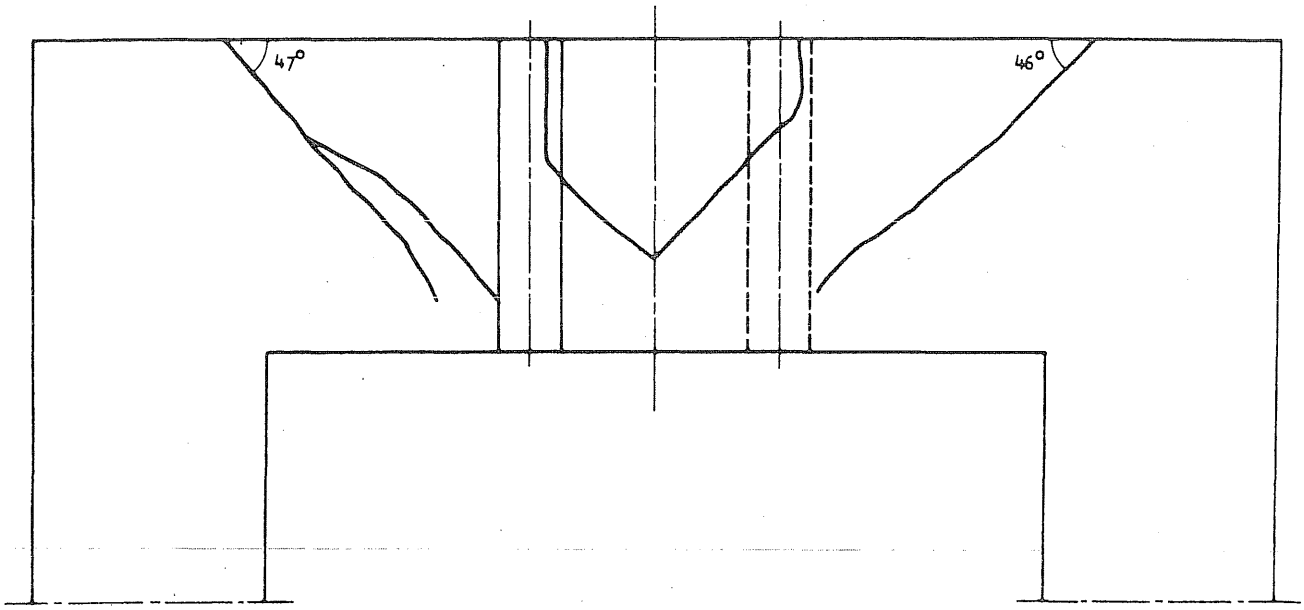

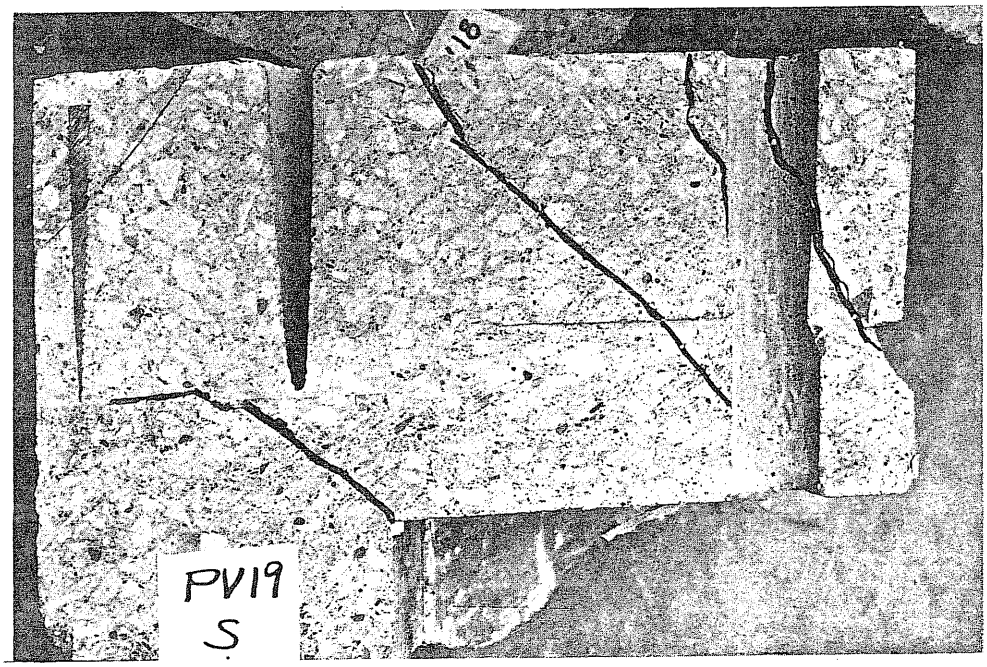

FIG. 2.13 TRAJECTORY OF THE INCLINED CRACK IN VESSEL PV19

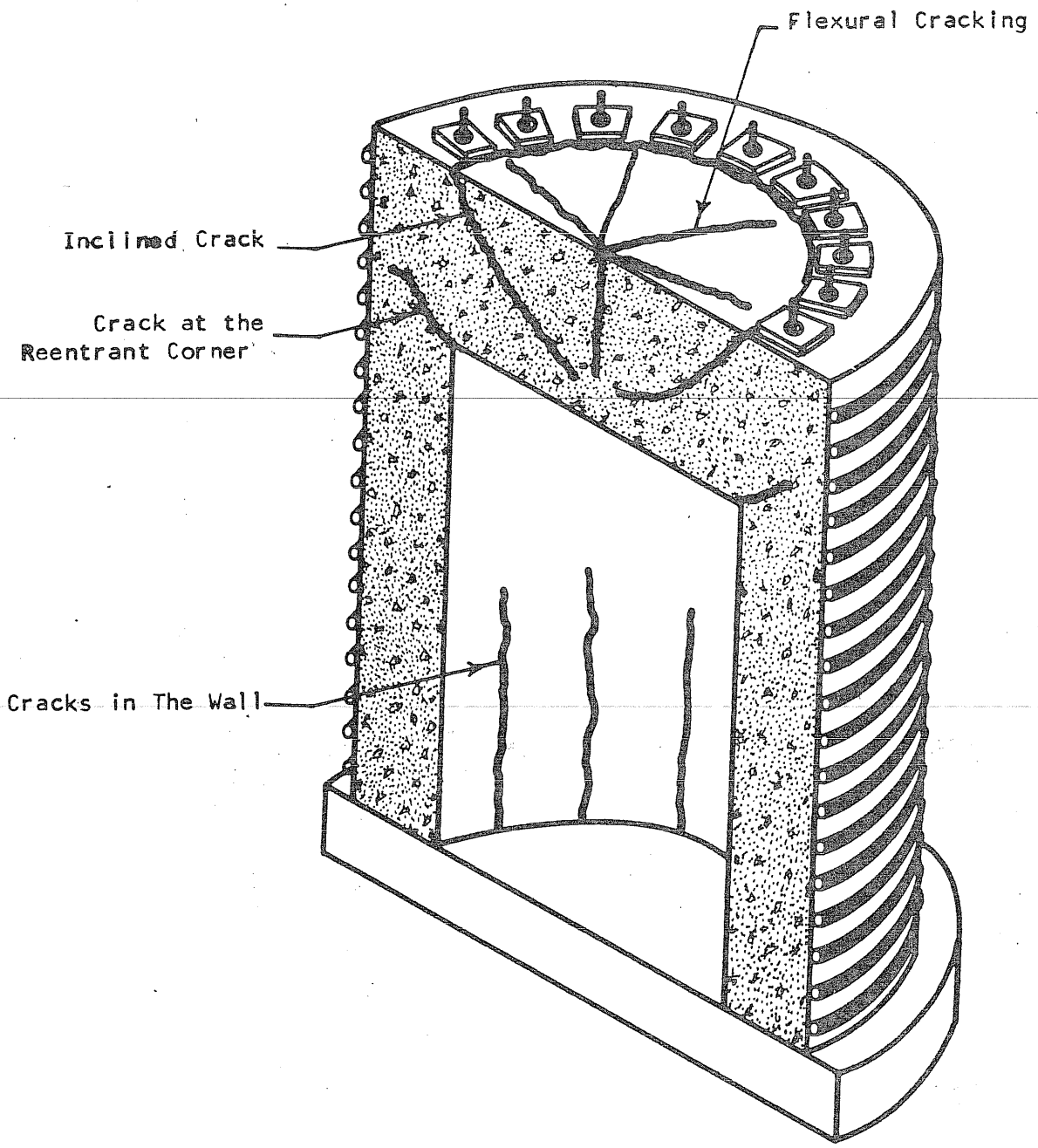

FIG. 3.1 IDEALIZED PRESTRESSING ARRANGEMENT AND DIFFERENT TYPES OF CRACKS OBSERVED IN THE VESSELS

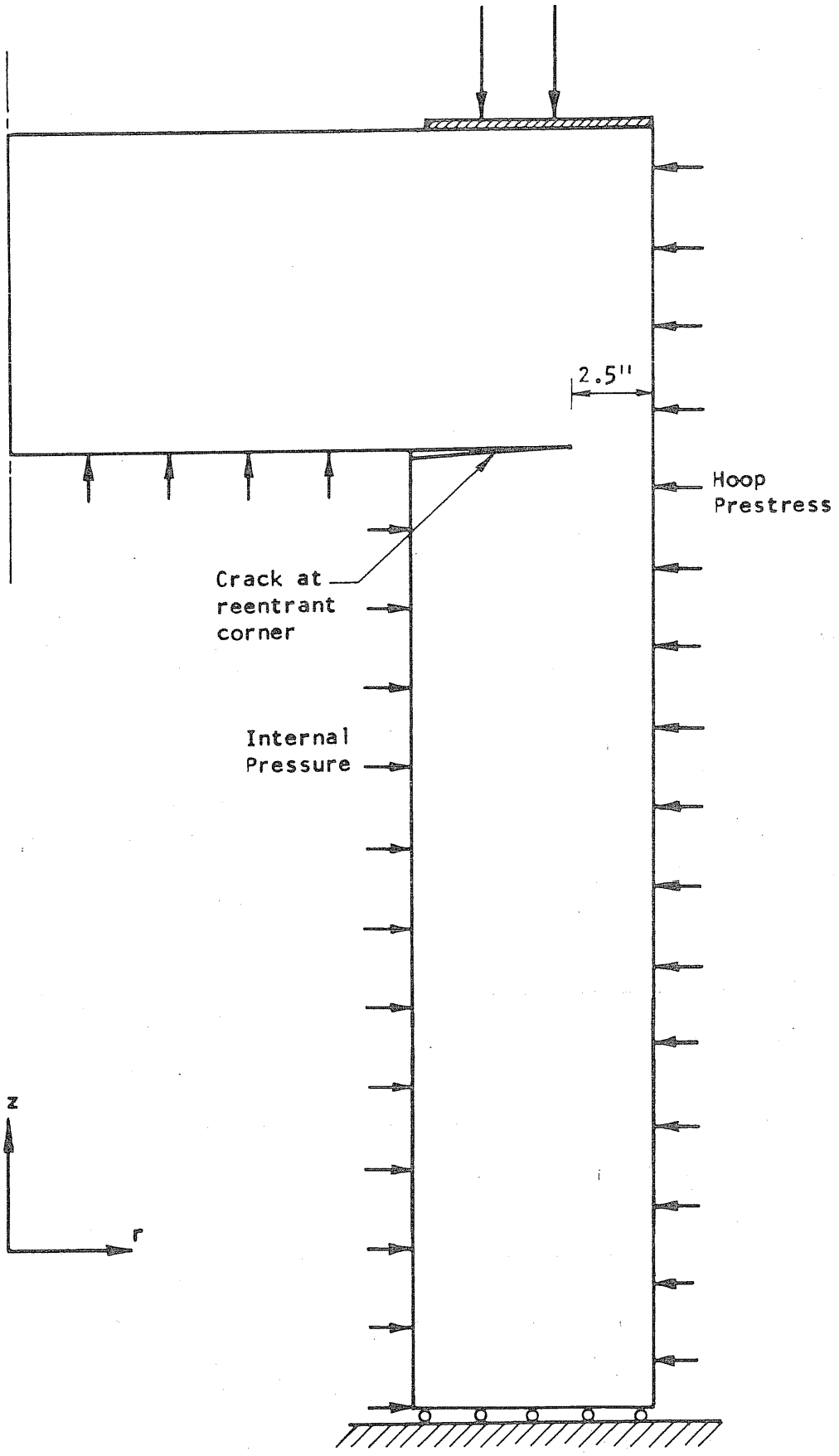

FIG. 3.2 CRACK AT THE REENTRANT CORNER THAT WAS INTRODUCED IN THE FINITE-ELEMENT MODEL

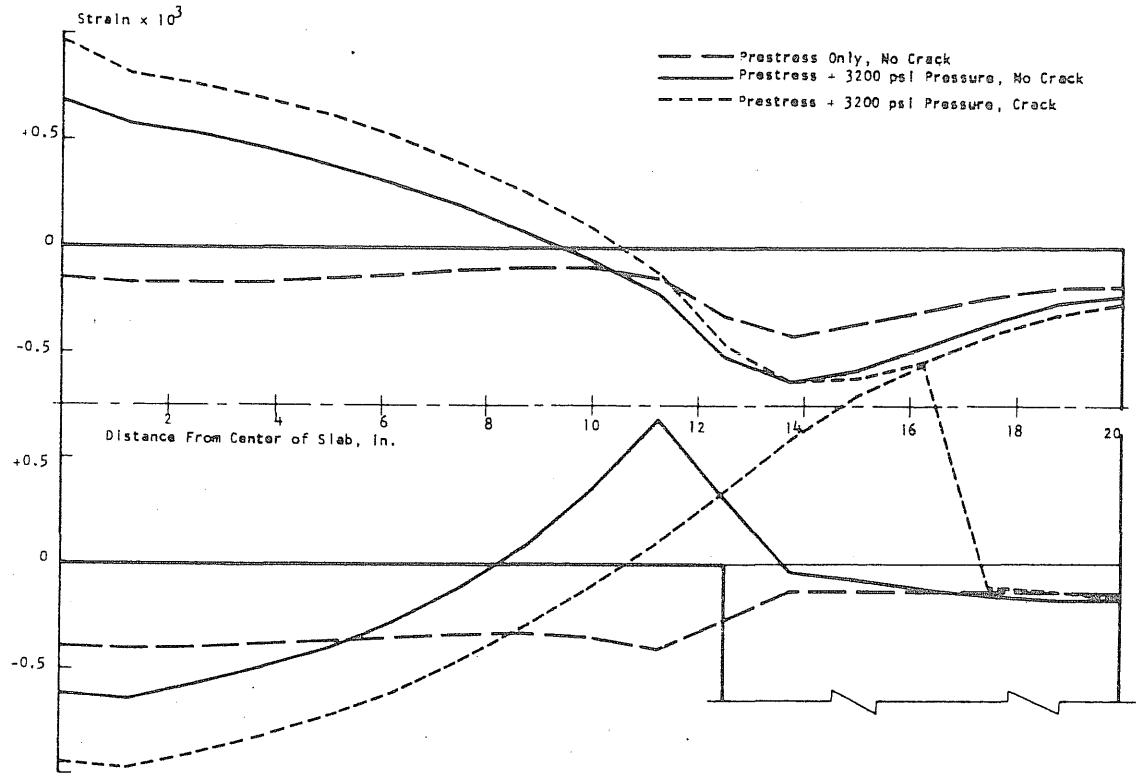

FIG. 3.3 CALCULATED RADIAL STRAINS ALONG TWO HORIZONTAL PLANES IN VESSEL PV16, INDICATING INFLUENCE OF A CRACK AT THE REENTRANT CORNER

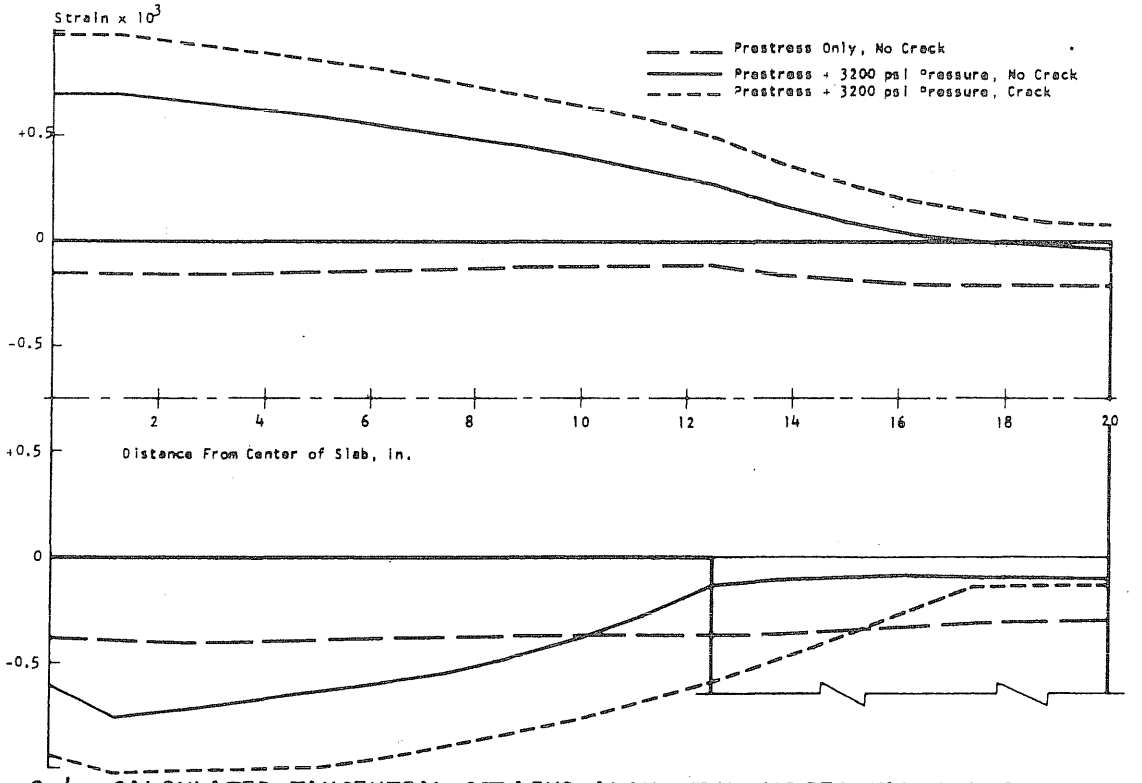

FIG. 3.4 CALCULATED TANGENTIAL STRAINS ALONG TWO HORIZONTAL PLANES IN VESSEL PV16, INDICATING INFLUENCE OF A CRACK AT THE REENTRANT CORNER

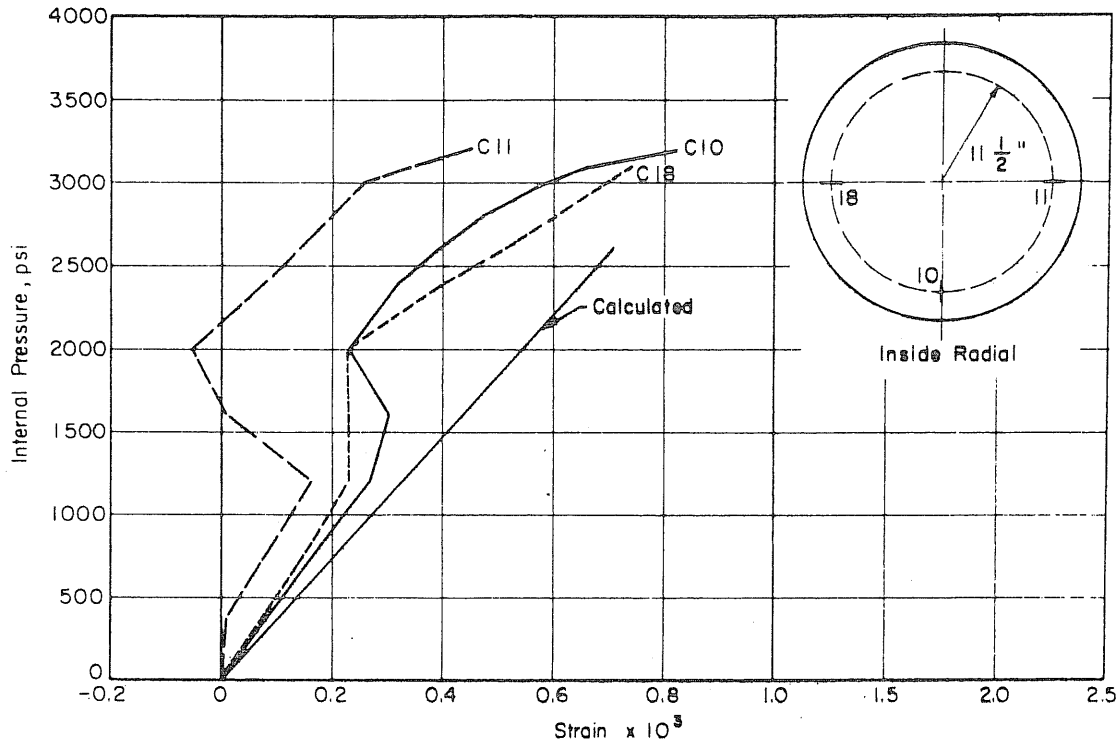

FIG. 3.5 MEASURED RADIAL STRAINS ON INSIDE FACE OF THE SLAB OF VESSEL PV16, 11-1/2 in. FROM THE CENTER

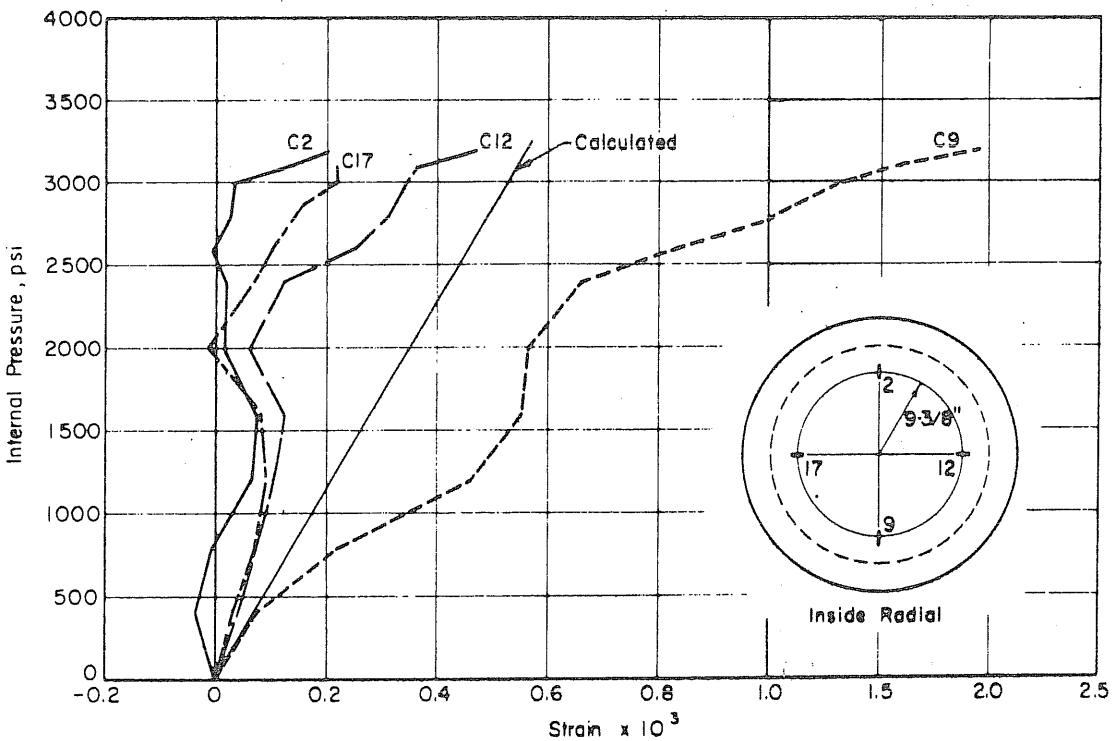

FIG. 3.6 MEASURED RADIAL STRAINS ON INSIDE FACE OF THE SLAB OF VESSEL PV16, 9-3/8 in. FROM THE CENTER

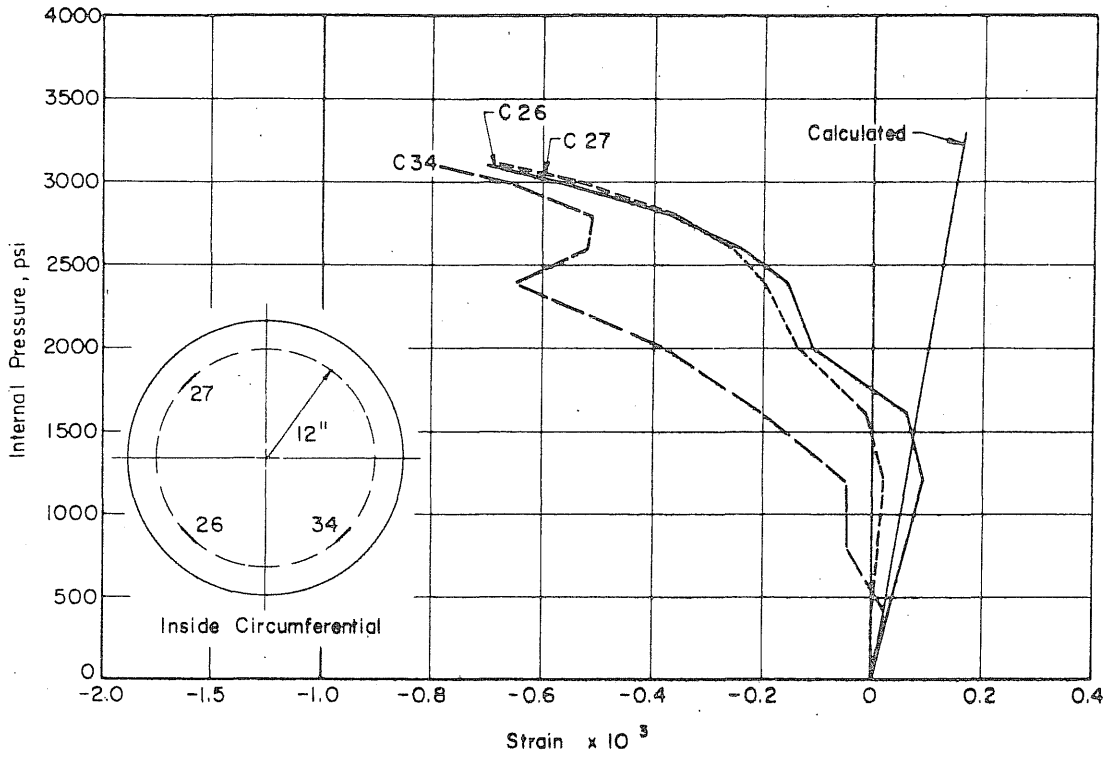

FIG. 3.7 MEASURED CIRCUMFERENTIAL STRAINS ON INSIDE FACE OF THE SLAB OF VESSEL PV16, 12 in. FROM THE CENTER

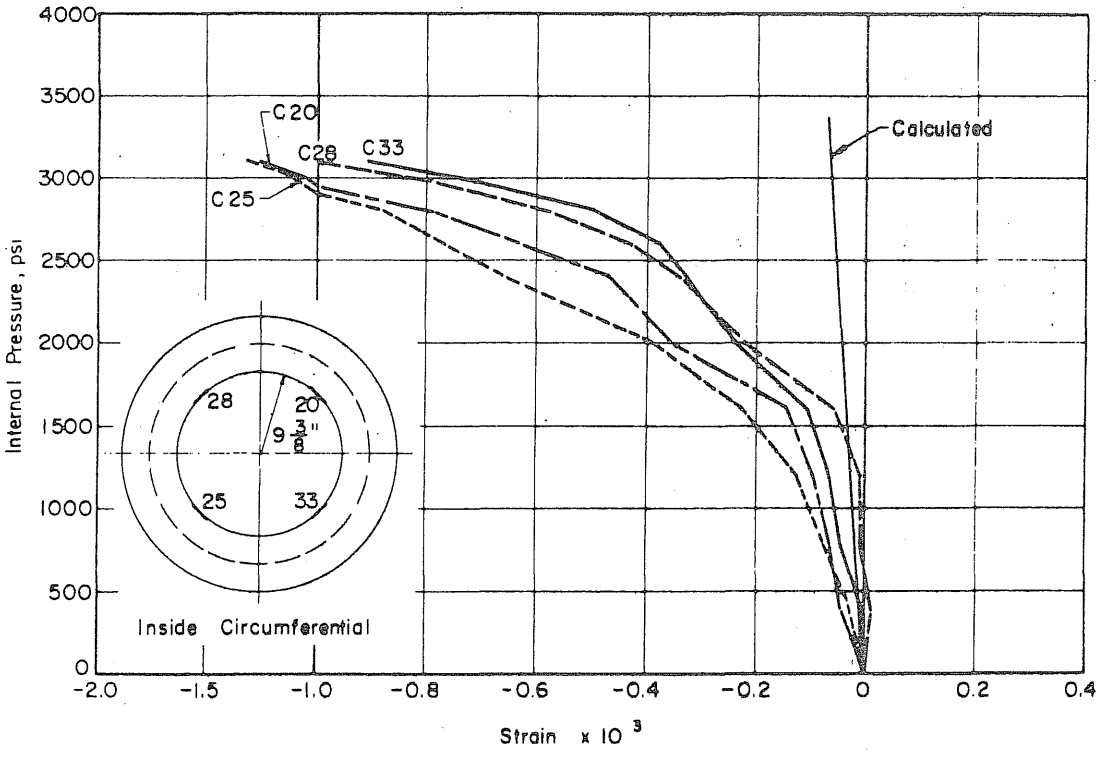

FIG. 3.8 MEASURED CIRCUMFERENTIAL STRAINS ON INSIDE FACE OF THE SLAB OF VESSEL PV16, 9-3/8 in. FROM THE CENTER

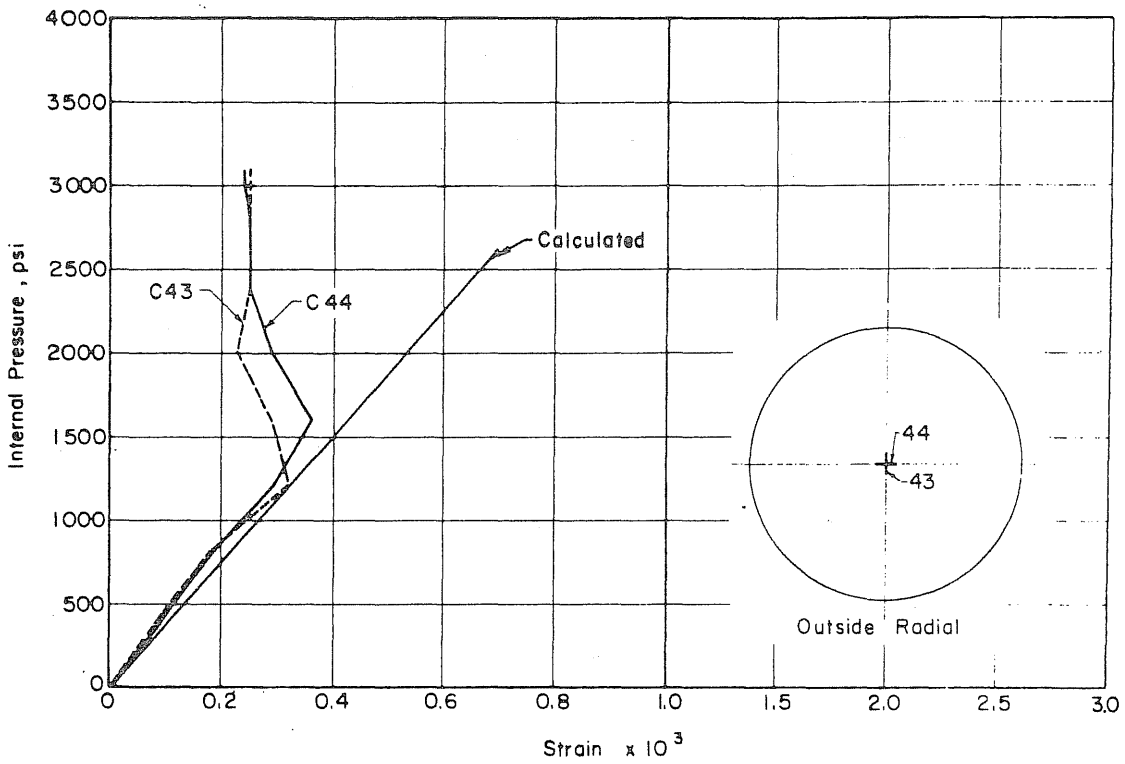

FIG. 3.9 MEASURED STRAINS AT THE CENTER OF THE OUTSIDE FACE OF THE SLAB OF VESSEL PV16

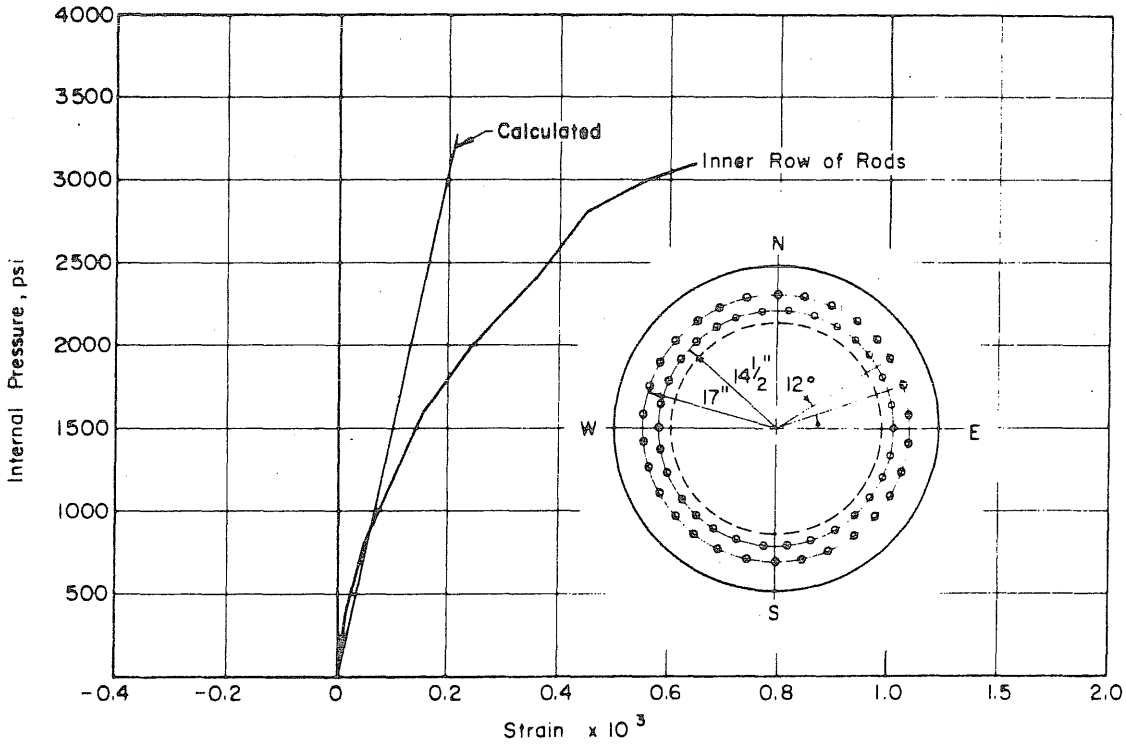

FIG. 3.10 MEASURED AVERAGE STRAINS IN THE INSIDE ROW OF THE PRESTRESSING RODS

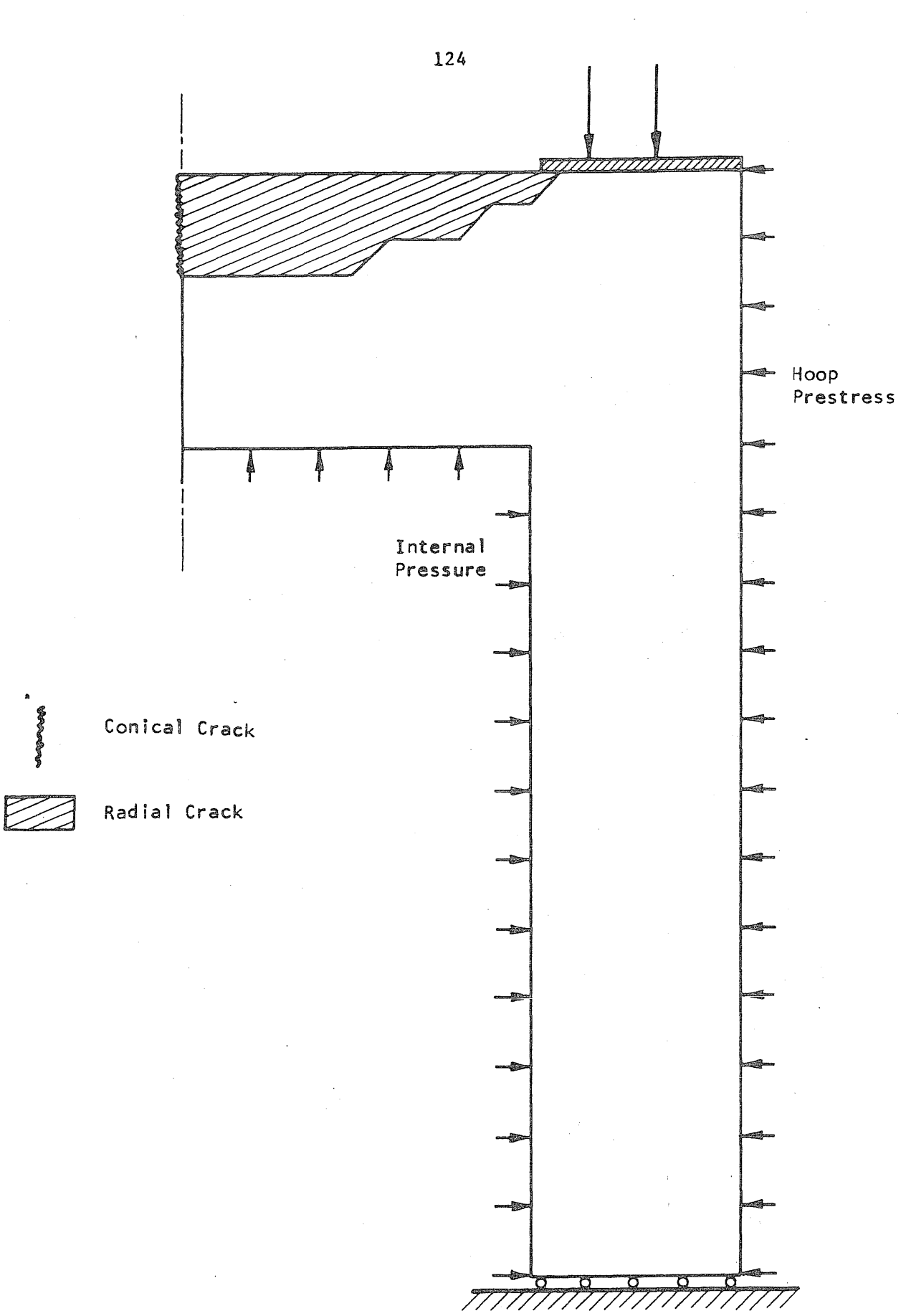

FIG. 3.11 EXTENT OF FLEXURAL CRACKING THAT WAS INTRODUCED IN THE FINITE-ELEMENT MODEL

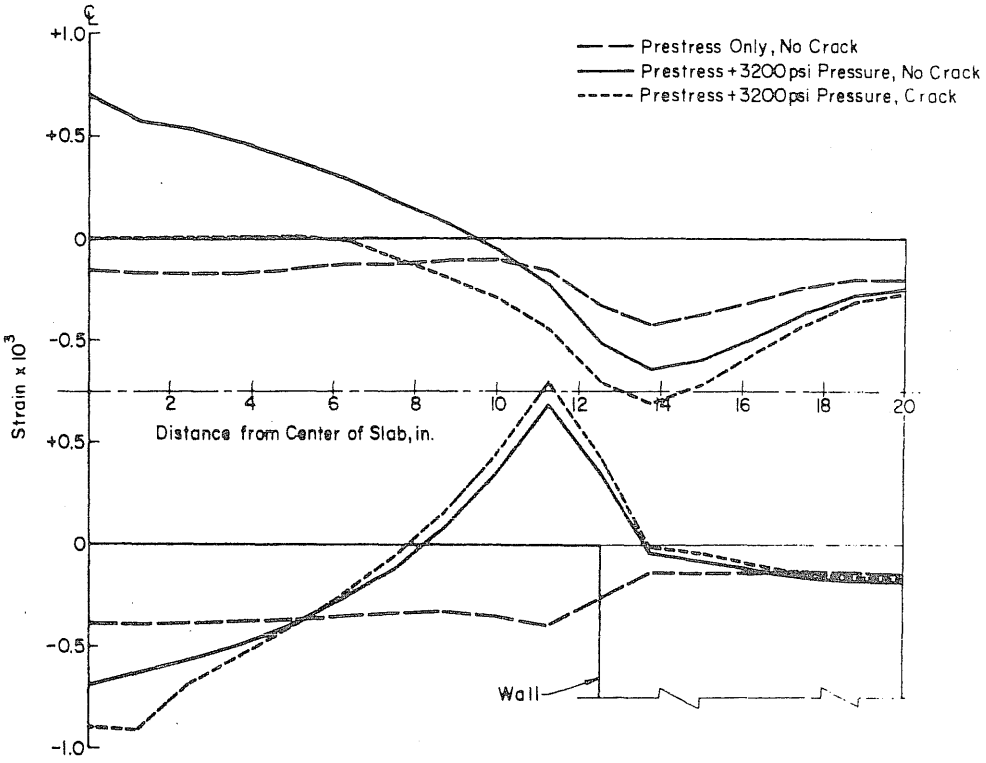

FIG. 3.12 CALCULATED RADIAL STRAINS ALONG TWO HORIZONTAL PLANES IN VESSEL PV16, INDICATING INFLUENCE OF EEEXURAL CRACKING

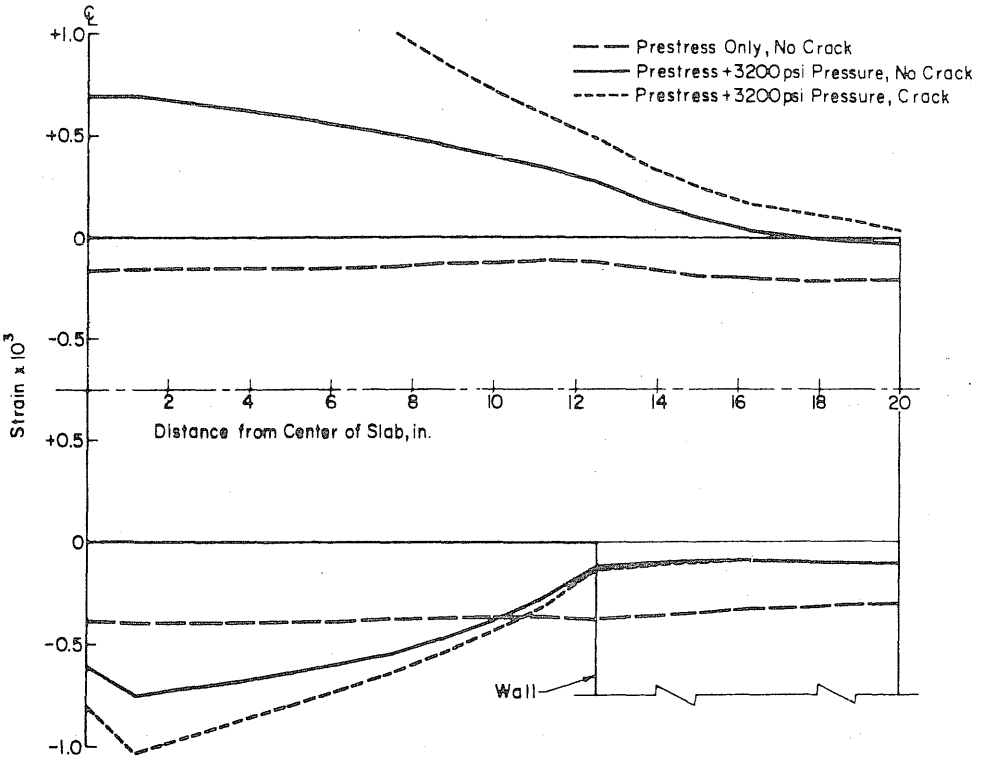

FIG. 3.13 CALCULATED TANGENTIAL STRAINS ALONG TWO HORIZONTAL PLANES IN VESSEL PV16, INDICATING INFLUENCE OF FLEXURAL CRACKING

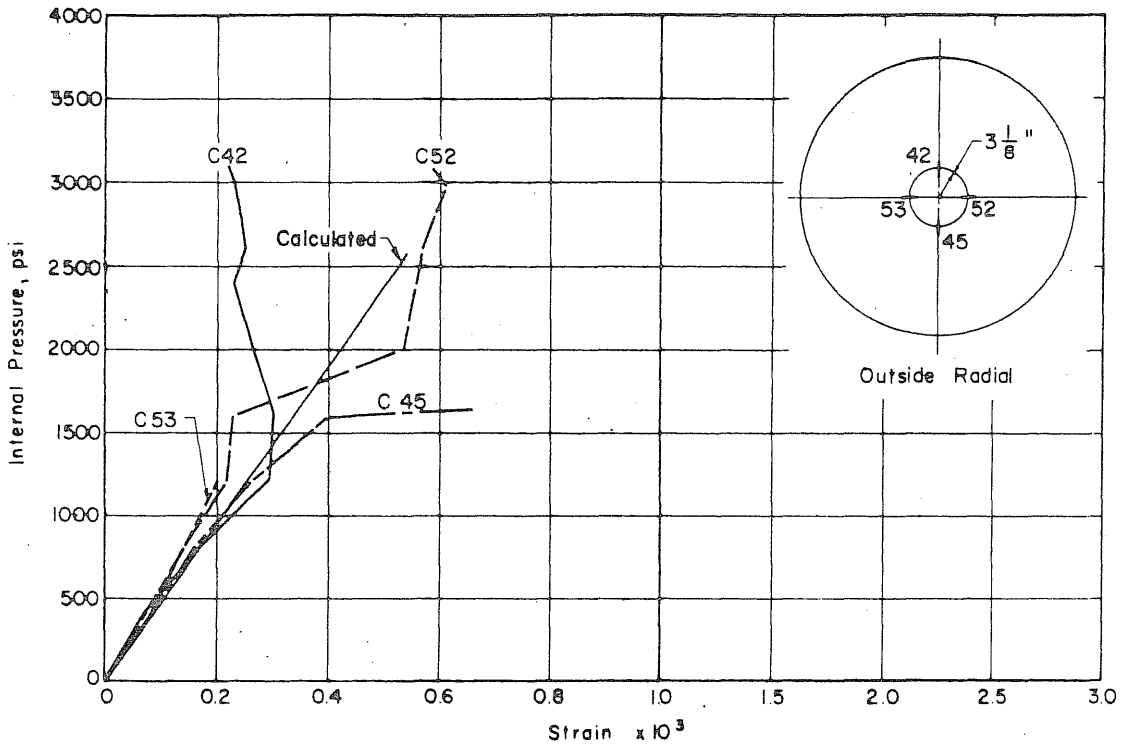

FIG. 3.14 MEASURED STRAINS ON THE OUTSIDE FACE OF THE SLAB OF VESSEL PV16, 3-1/8 in. FROM THE CENTER

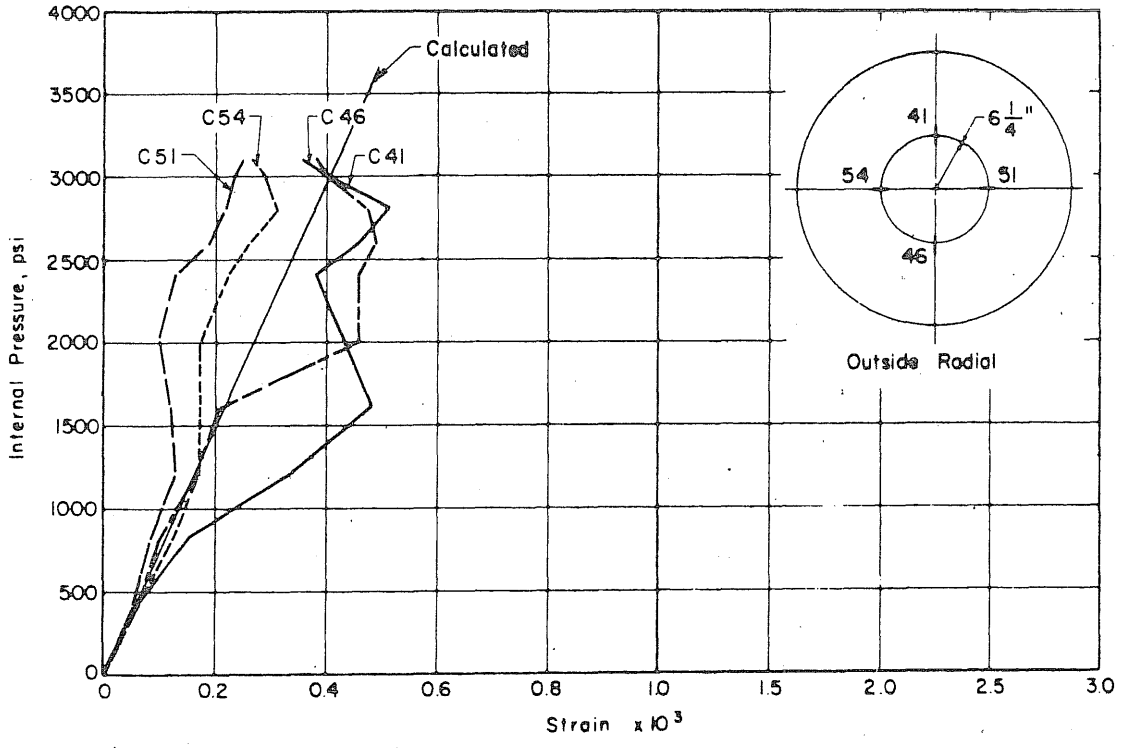

FIG. 3.15 MEASURED STRAINS ON THE OUTSIDE FACE OF THE SLAB OF VESSEL PV16, 6-1/4 in. FROM THE CENTER

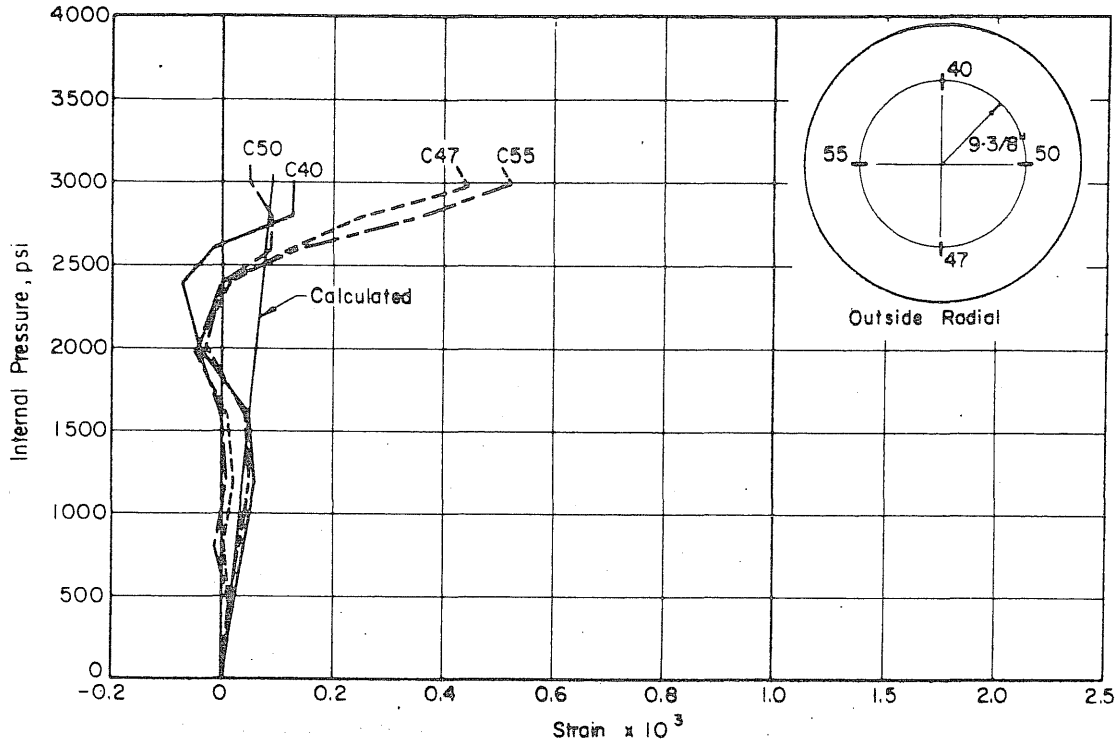

FIG. 3.16 MEASURED RADIAL STRAINS ON THE OUTSIDE FACE OF THE SLAB OF VESSEL PV16, 9-3/8 In. FROM THE CENTER

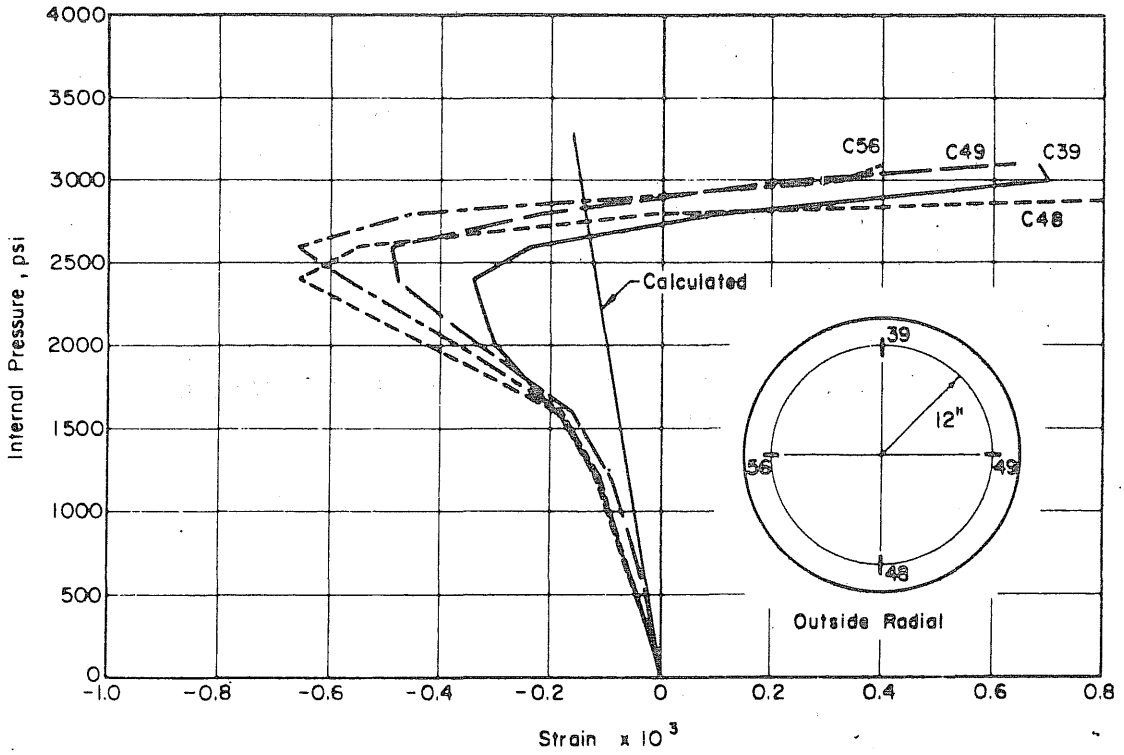

FIG. 3.17 MEASURED RADIAL STRAINS ON THE OUTSIDE FACE OF THE SLAB OF VESSEL PV16, 12 In. FROM THE CENTER

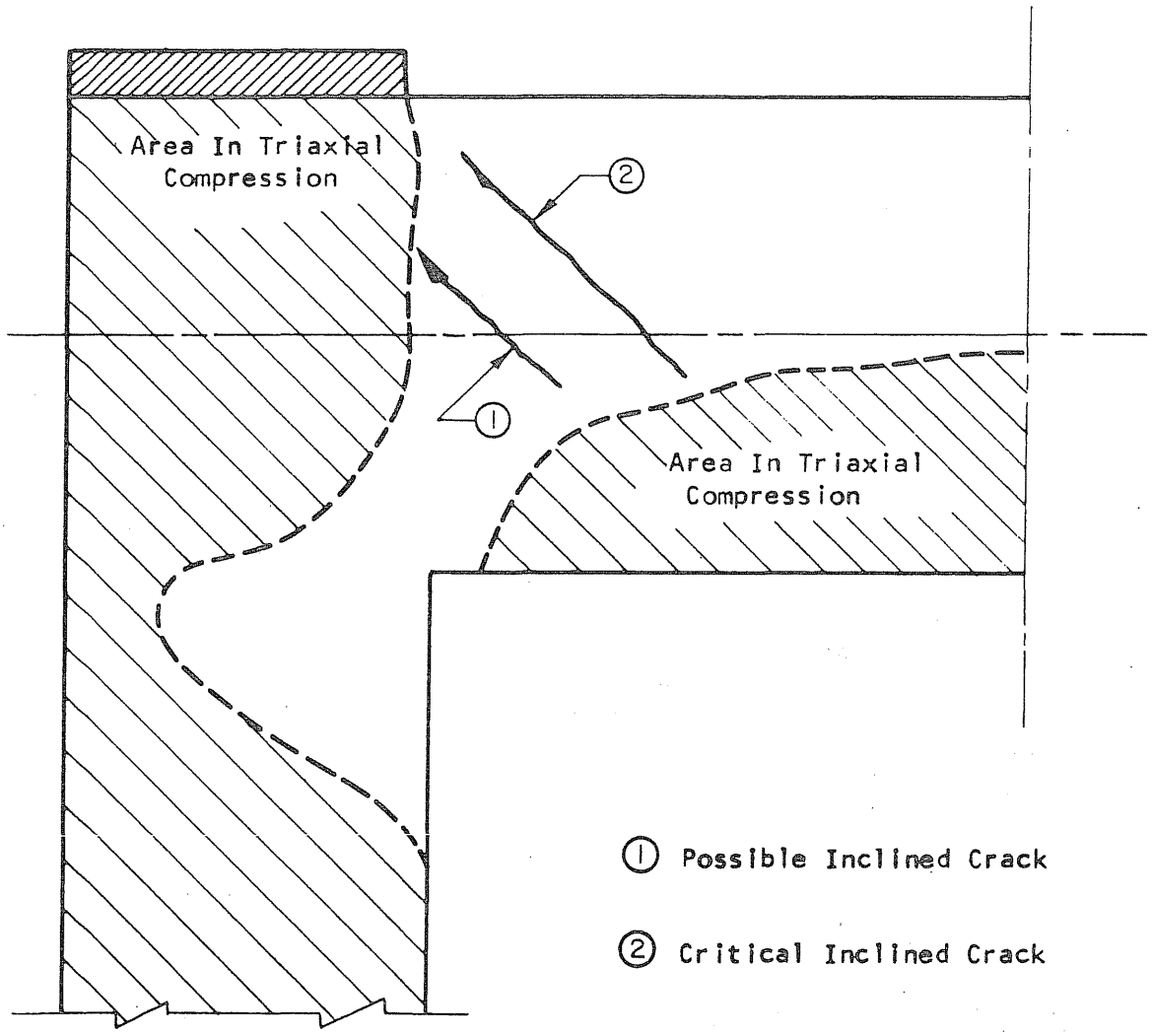

FIG. 3.18 THE INITIATION OF INCLINED CRACKS AND SCHEMATIC STRESS CONDITION

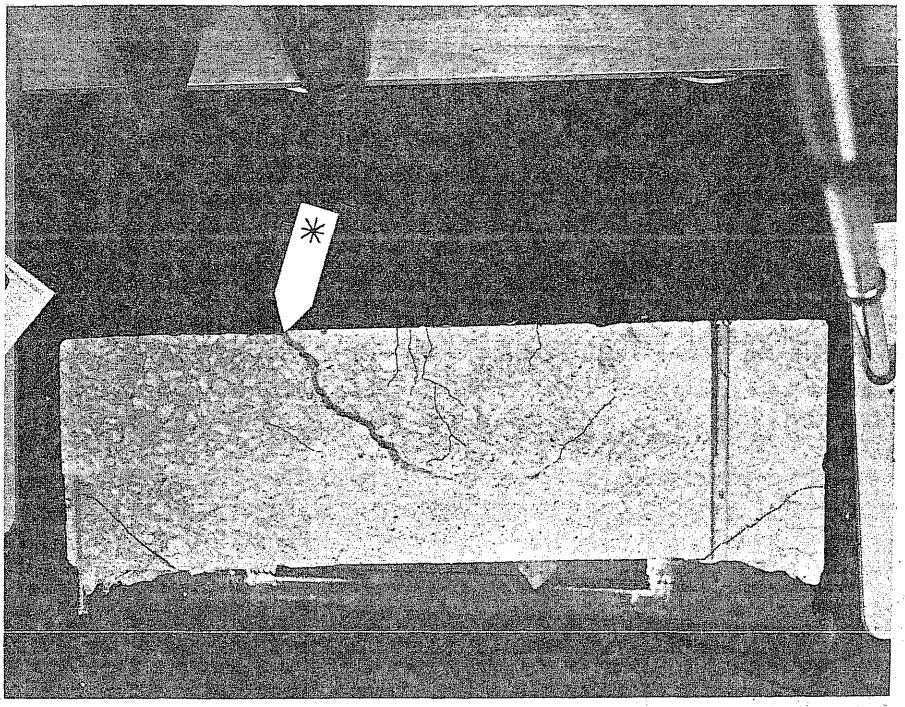

*This is not a crack but a fault caused by an uneven cut. The cracks are marked with black dye.

FIG. 3.19 DIAMETRAL CUT THROUGH THE END SLAB OF VESSEL PV13

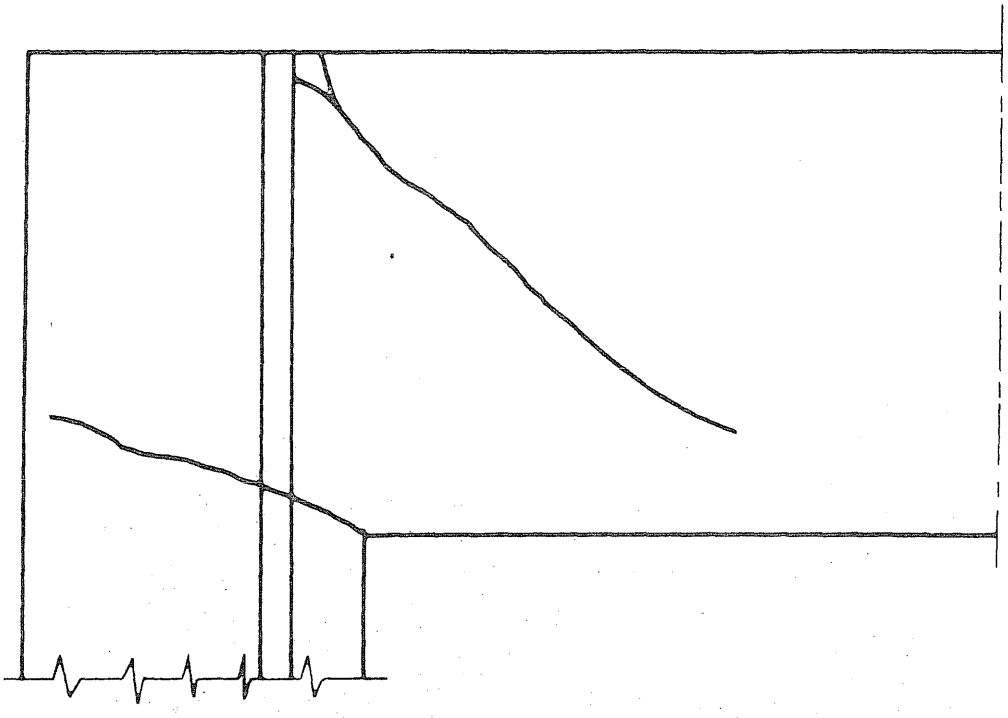

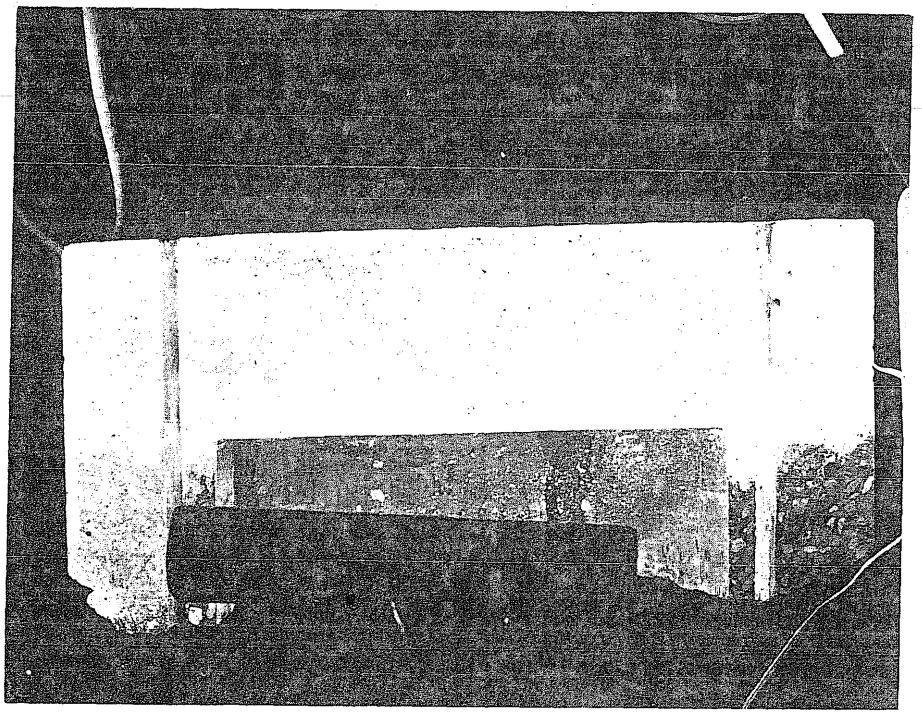

FIG. 3.20 PHOTOGRAPH AND SKETCH SHOWING LOCATION OF CRACKS IN SLAB OF VESSEL PV12

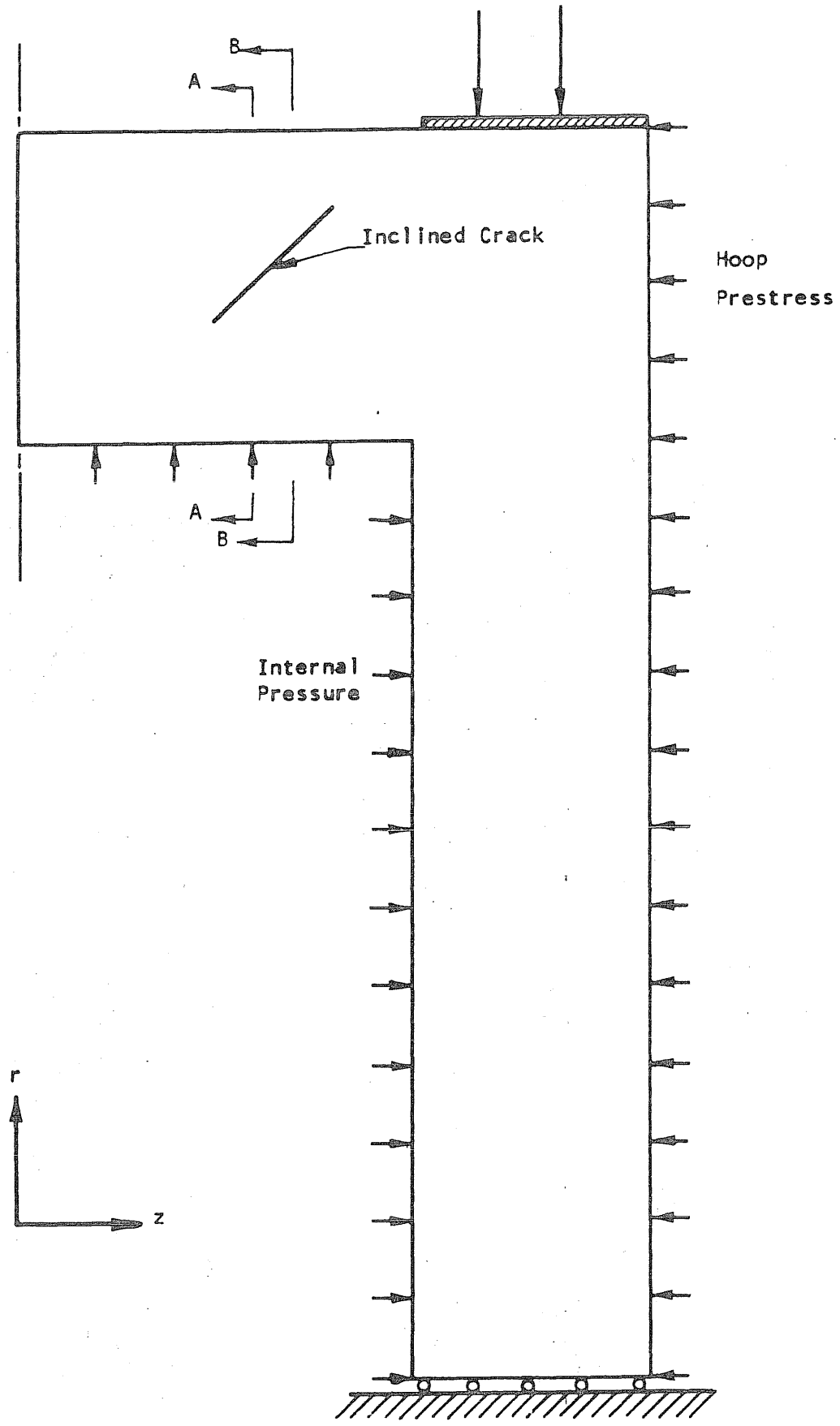

FIG. 3.21 SHORT INCLINED CRACK THAT WAS INTRODUCED IN THE FINITE-ELEMENT MODEL

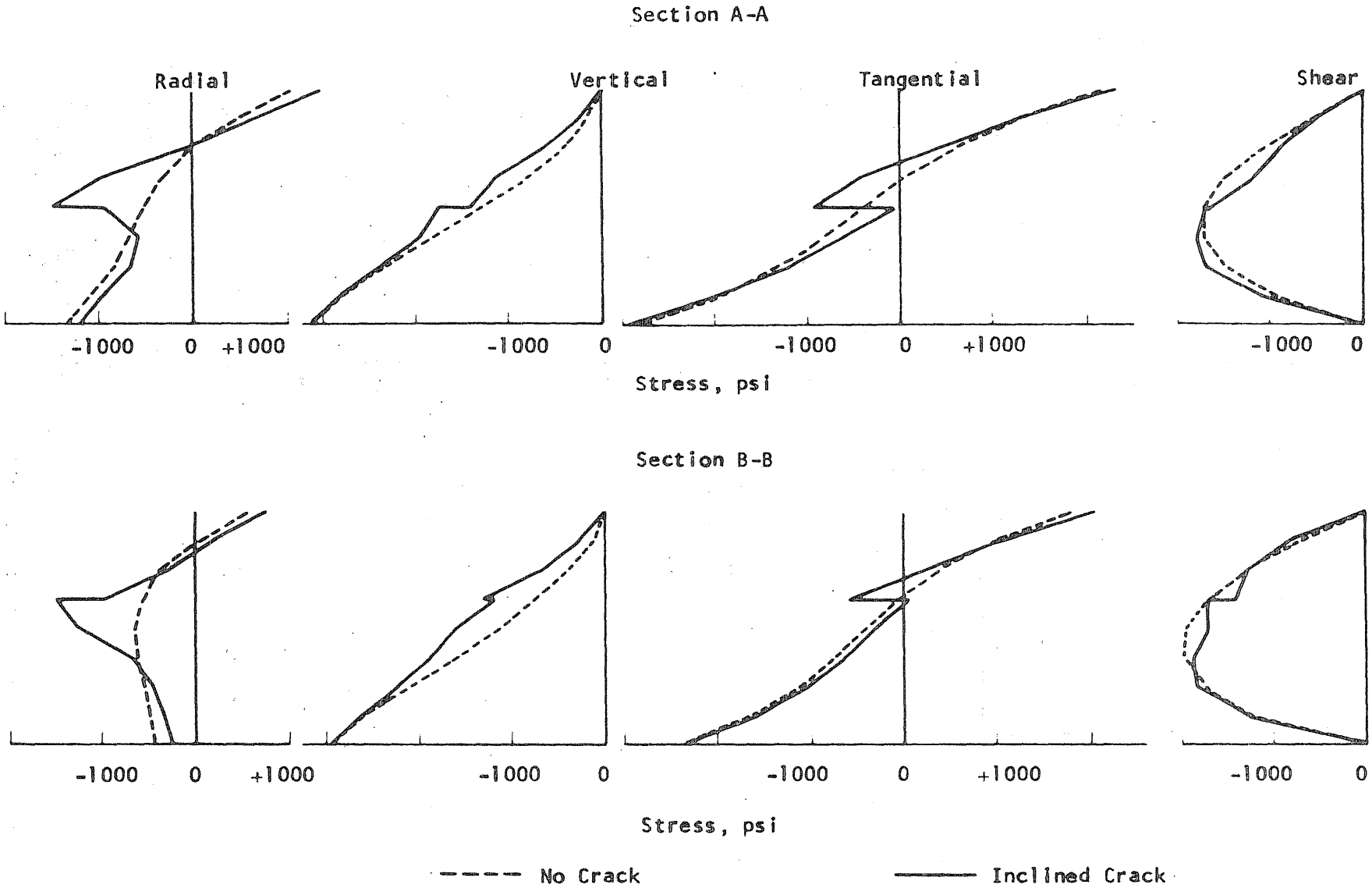

FIG. 3.22 DISTRIBUTION OF STRESSES ALONG TWO VERTICAL PLANES, INDICATING INFLUENCE OF A SHORT INCLINED CRACK

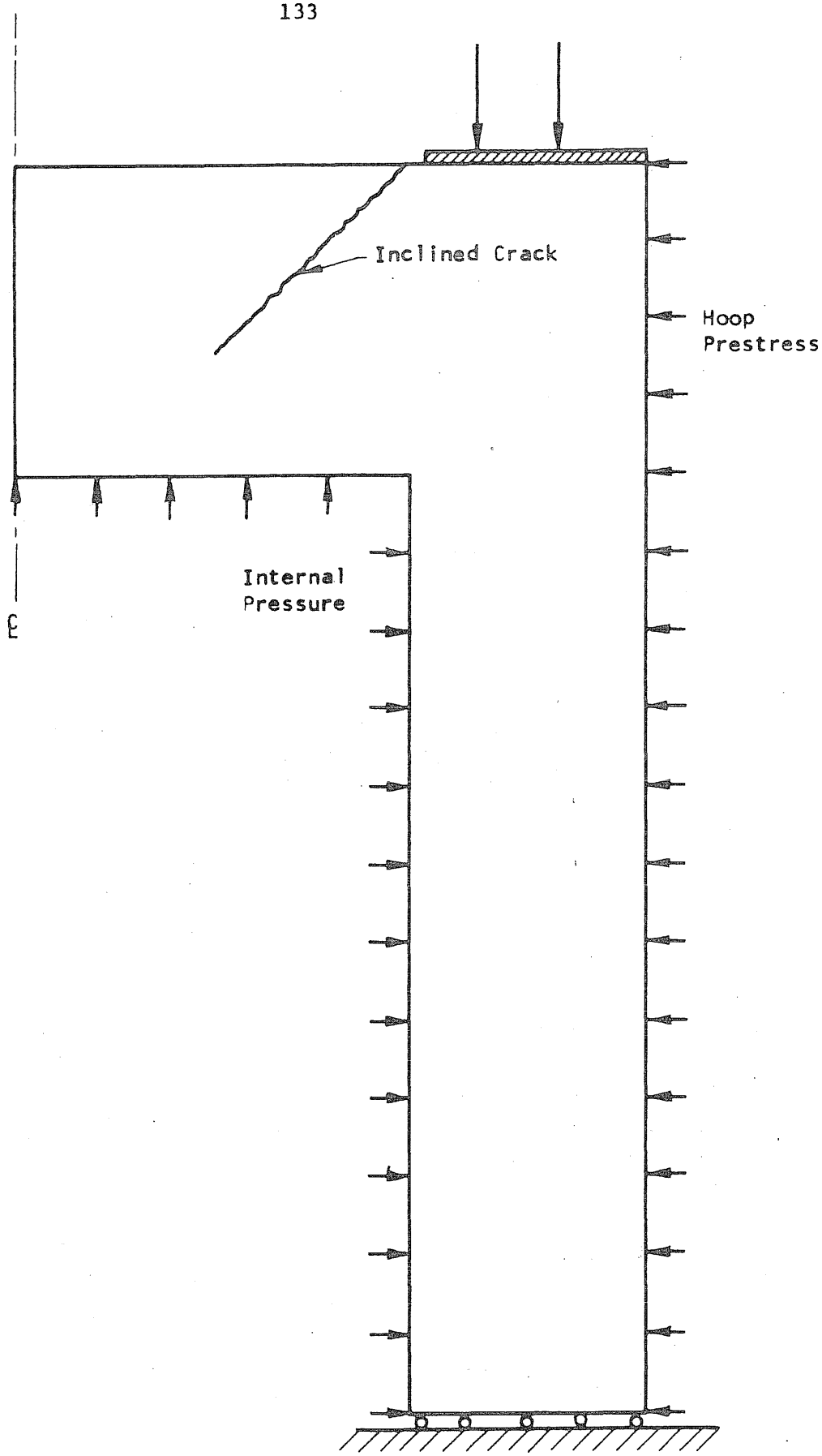

FIG. 3.23 LONG INCLINED CRACK THAT WAS INTRODUCED IN THE FINITE-ELEMENT MODEL

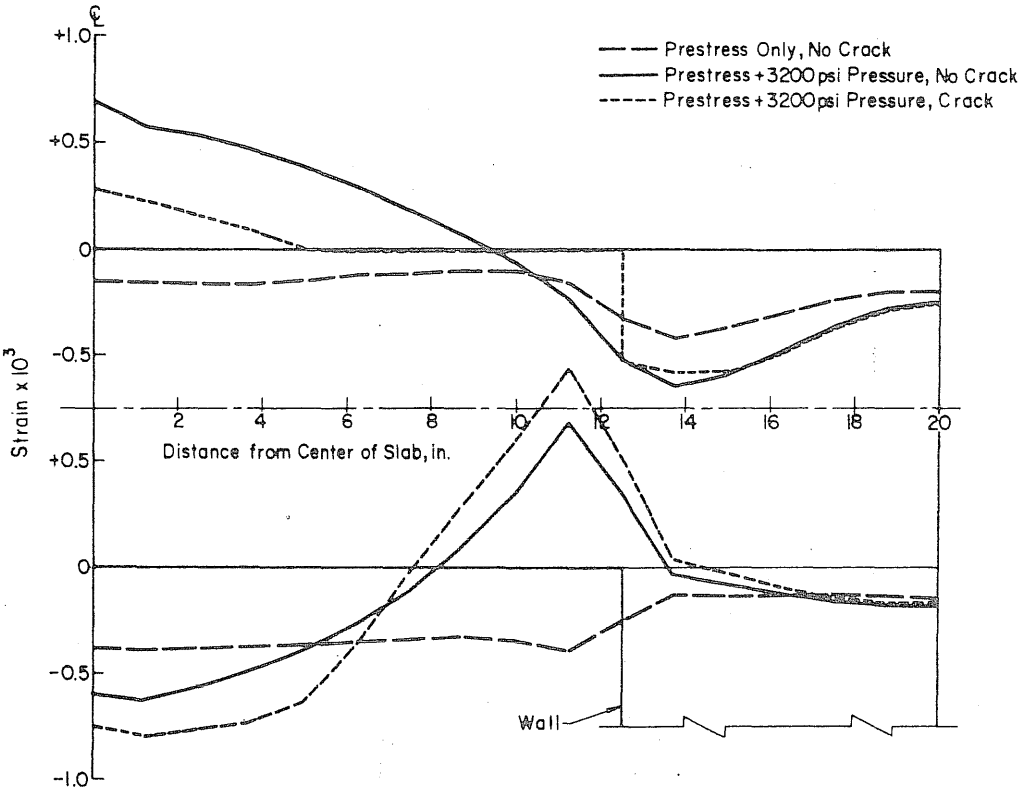

FIG. 3.24 CALCULATED RADIAL STRAINS ALONG TWO HORIZONTAL PLANES IN VESSEL PV16, INDICATING INFLUENCE OF THE LONG INCLINED CRACK

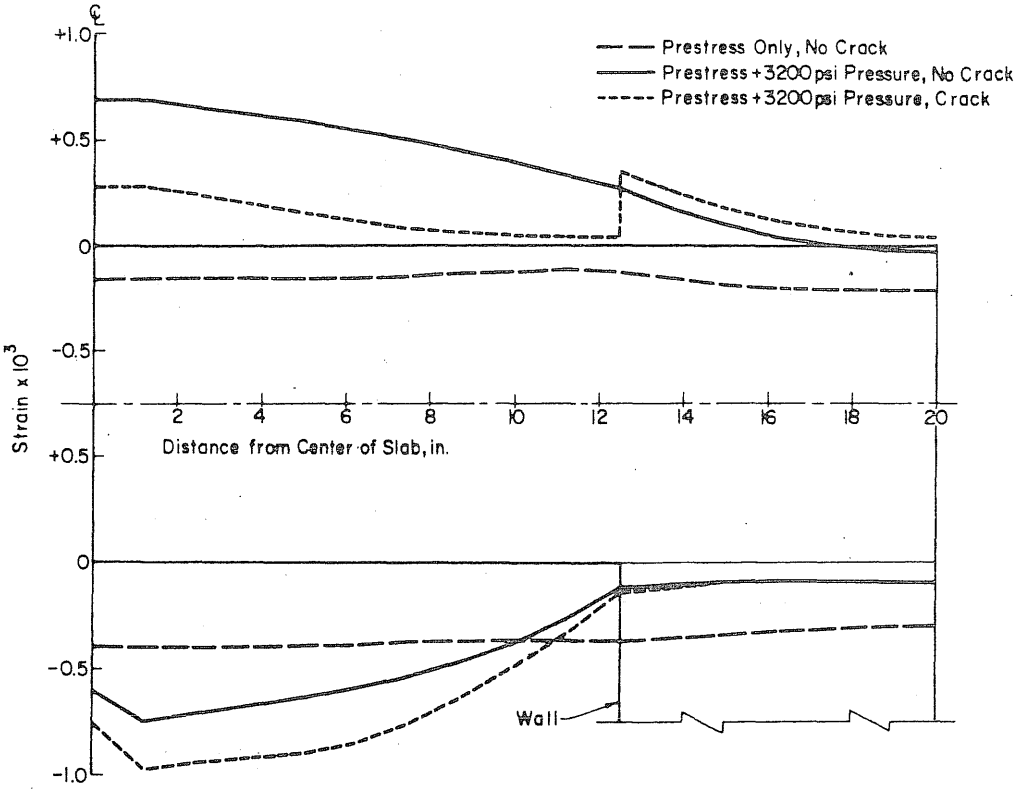

FIG. 3.25 CALCULATED RADIAL STRAINS ALONG TWO HORIZONTAL PLANES IN VESSEL PV16, INDICATING INFLUENCE OF THE LONG INCLINED CRACK.

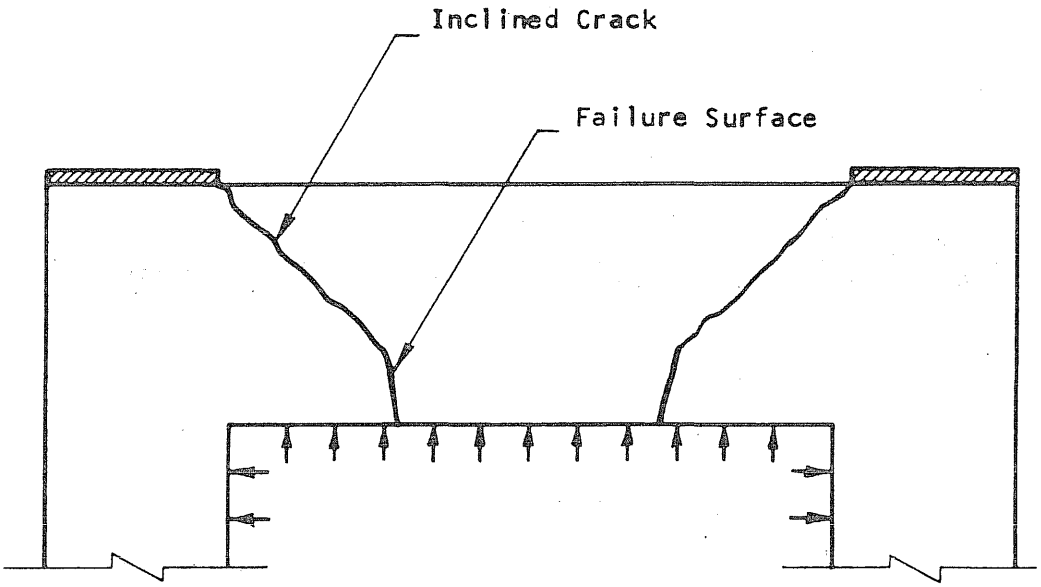

FIG. 3.26 SHEAR FAILURE OCCURRING BEFORE THE COMPLETION OF THE CRYPTODOME

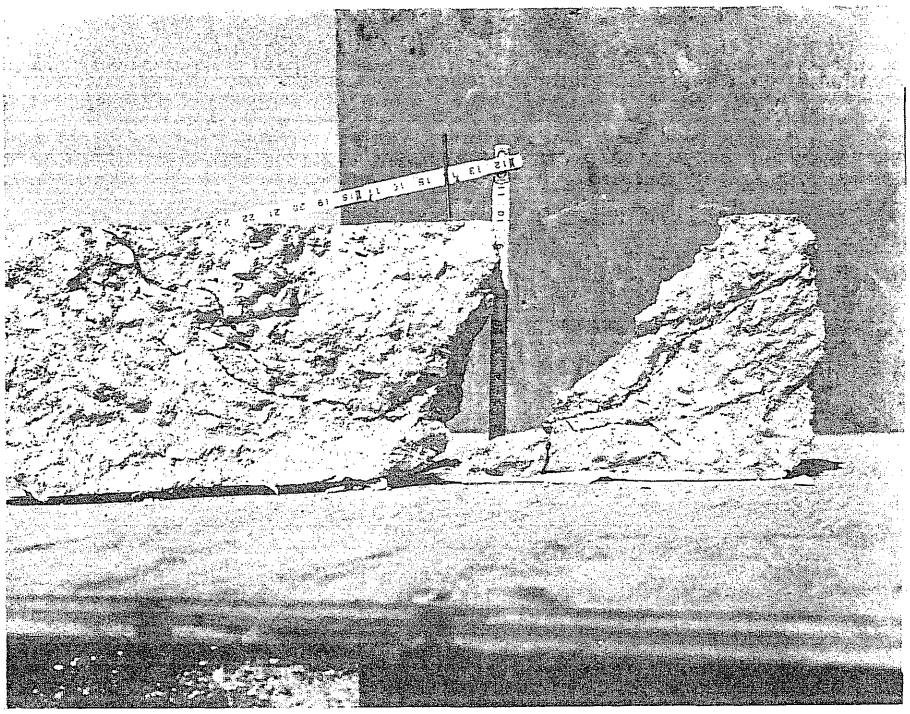

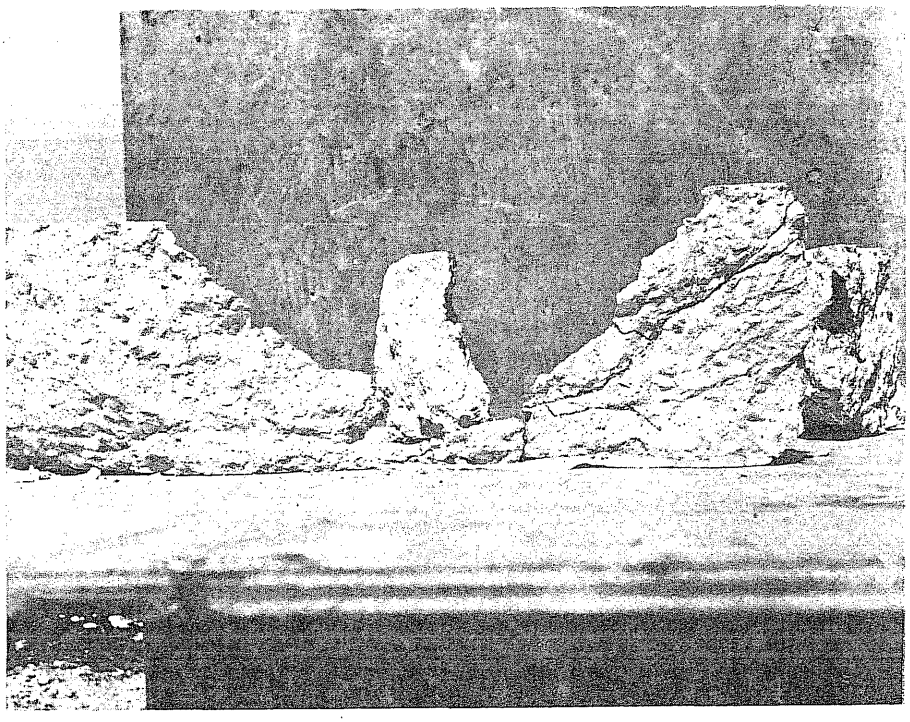

FIG. 3.27 PIECES FROM THE END SLAB OF VESSEL PV9

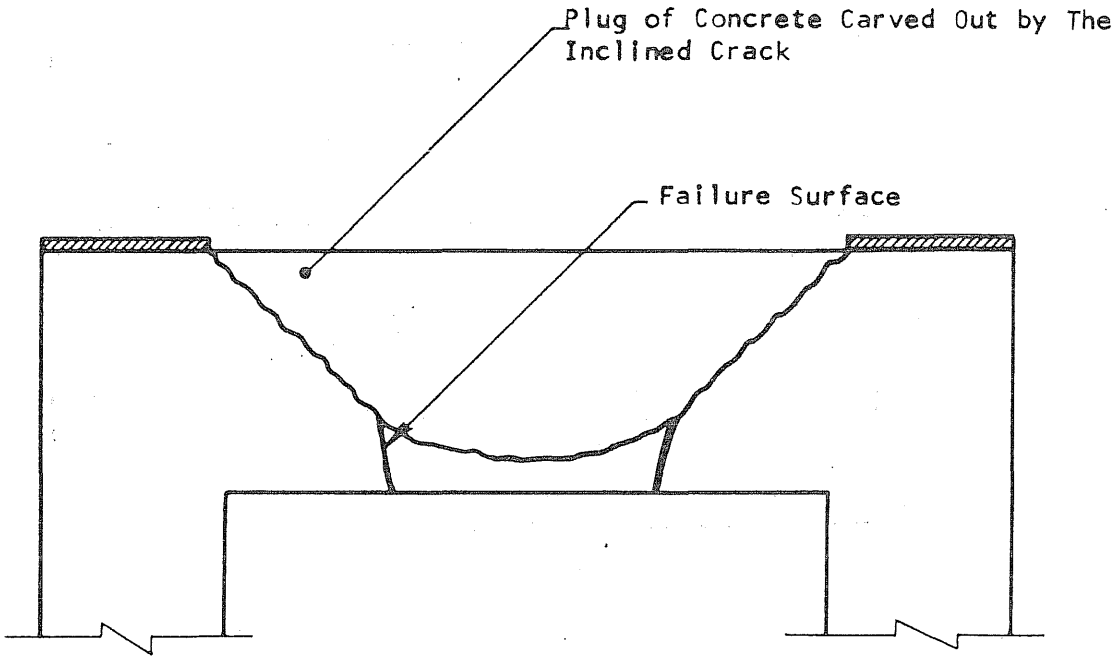

FIG. 3.28 CRYPTODOME SHAPED BY THE INCLINED CRACK AND THE FAILURE SURFACE

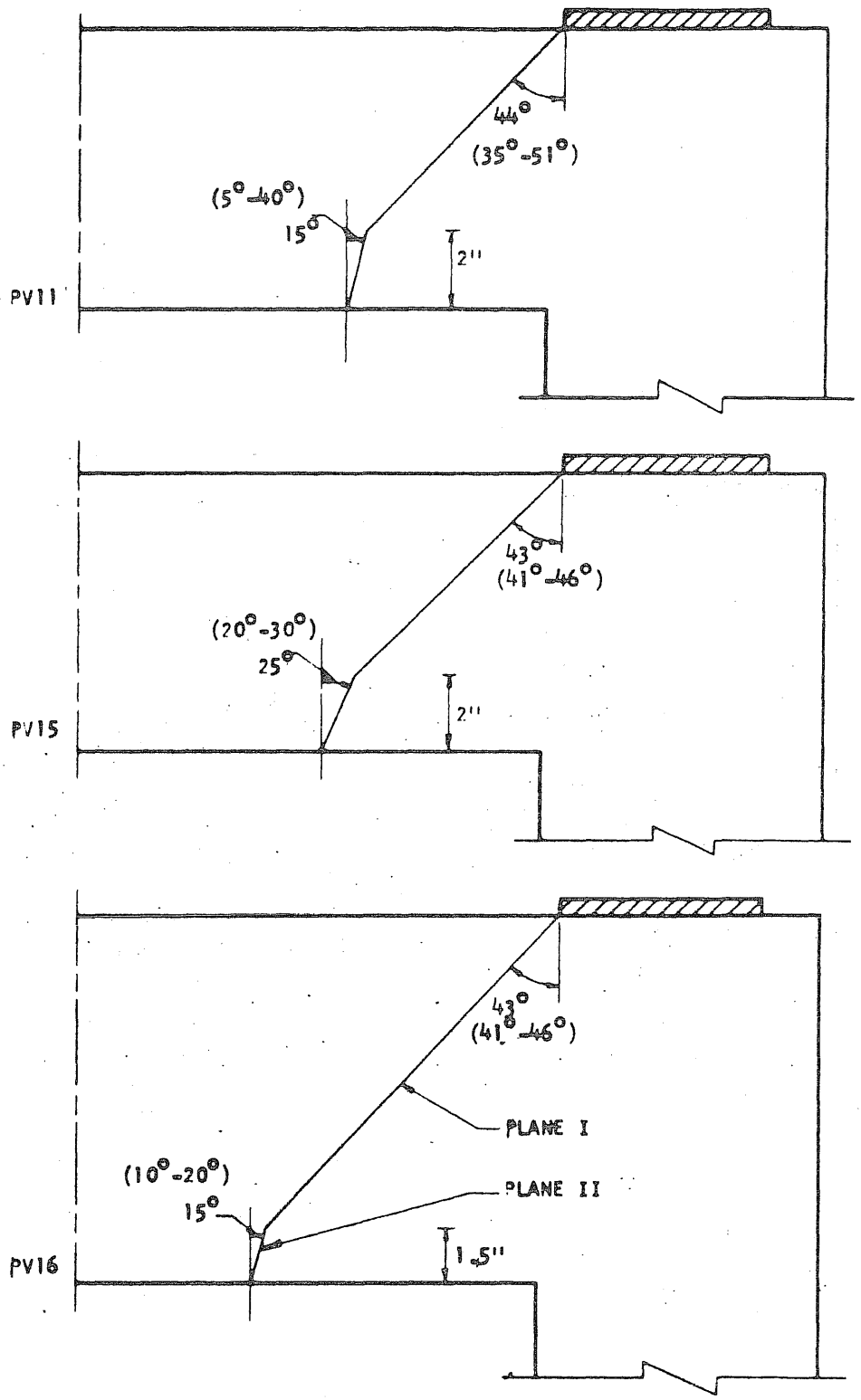

FIG. 3.29 SECTIONS OF THE INCLINED CRACKS AND FAILURE SURFACES FOR VESSELS FAILING IN SHEAR

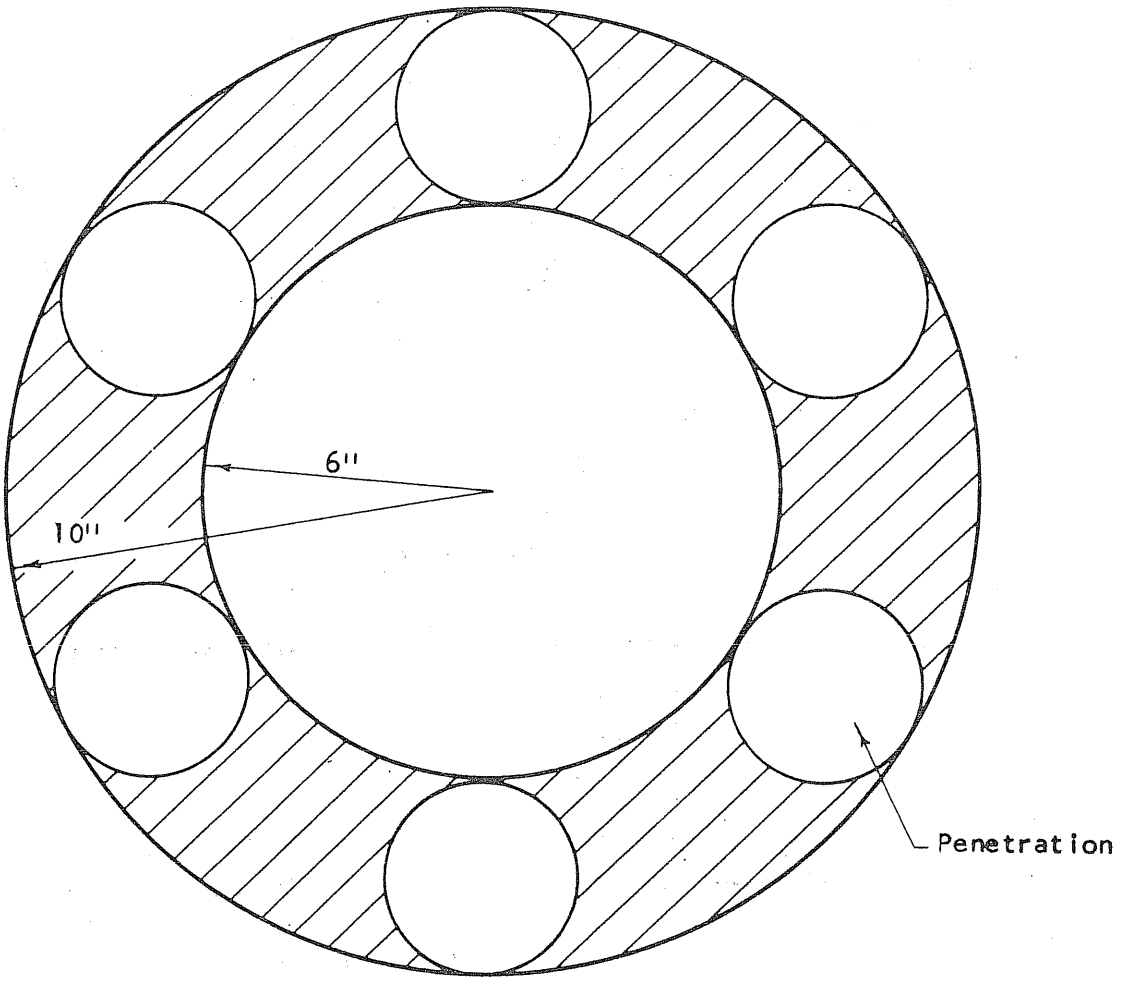

FIG. 4.1 TORUS BETWEEN 6 in. AND 10 in.
RADII WHERE PENETRATIONS ARE LOCATED

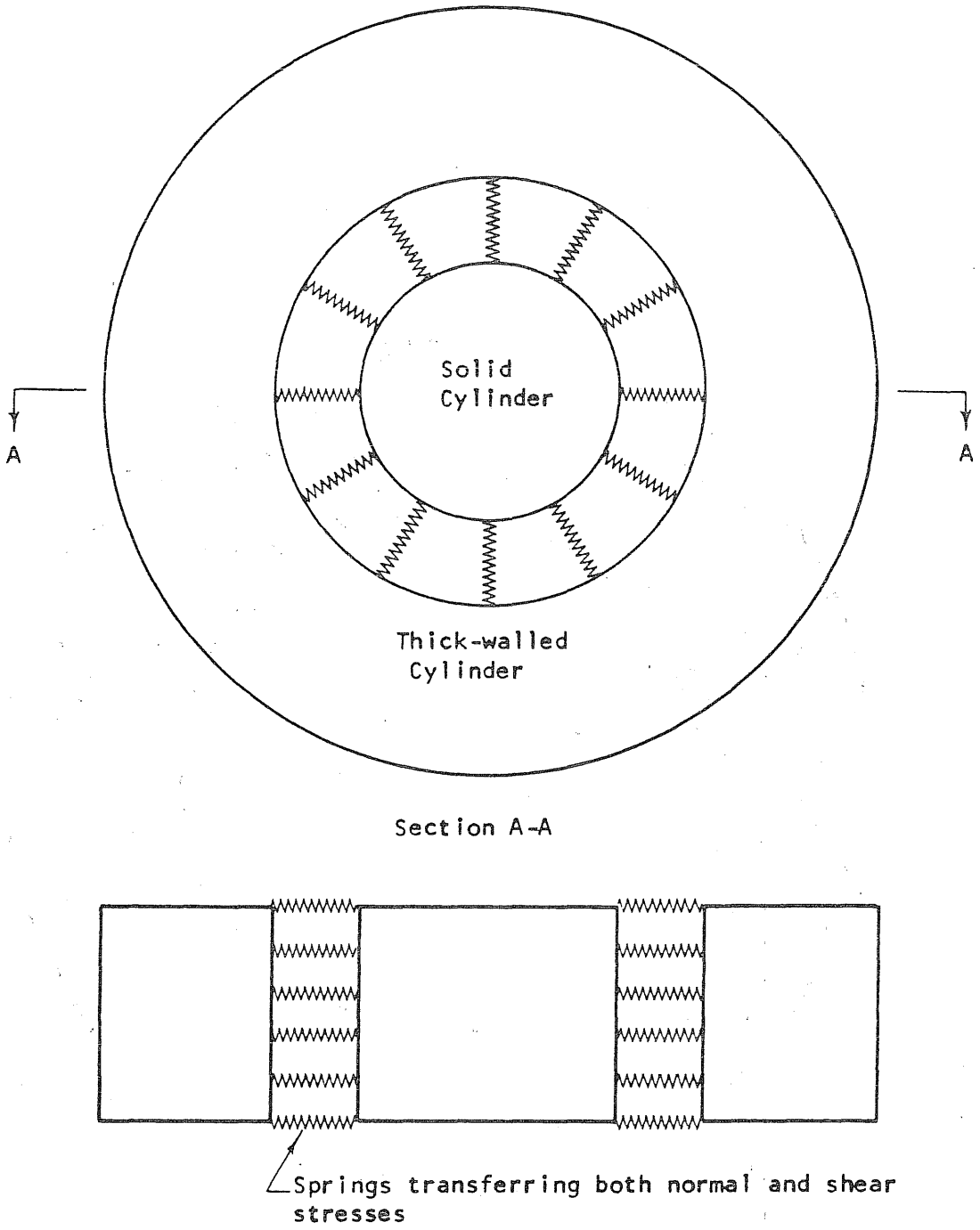

FIG. 4.2 METHOD USED TO SIMULATE PENETRATIONS IN AN AXISYMMETRIC MODEL

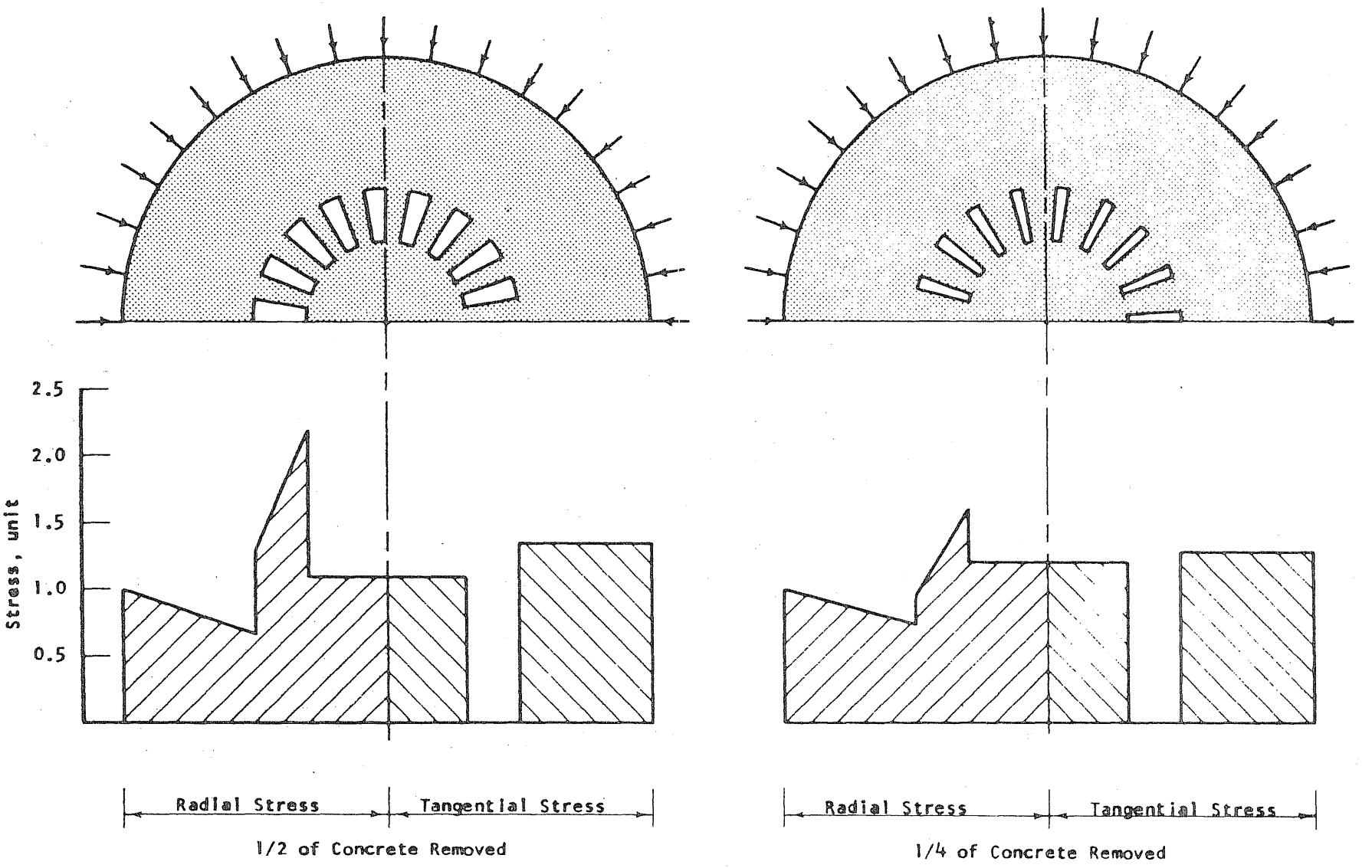

FIG. 4.3 IDEALIZED EFFECT OF PENETRATIONS IN SLABS SUBJECTED TO RADIAL PRESSURE

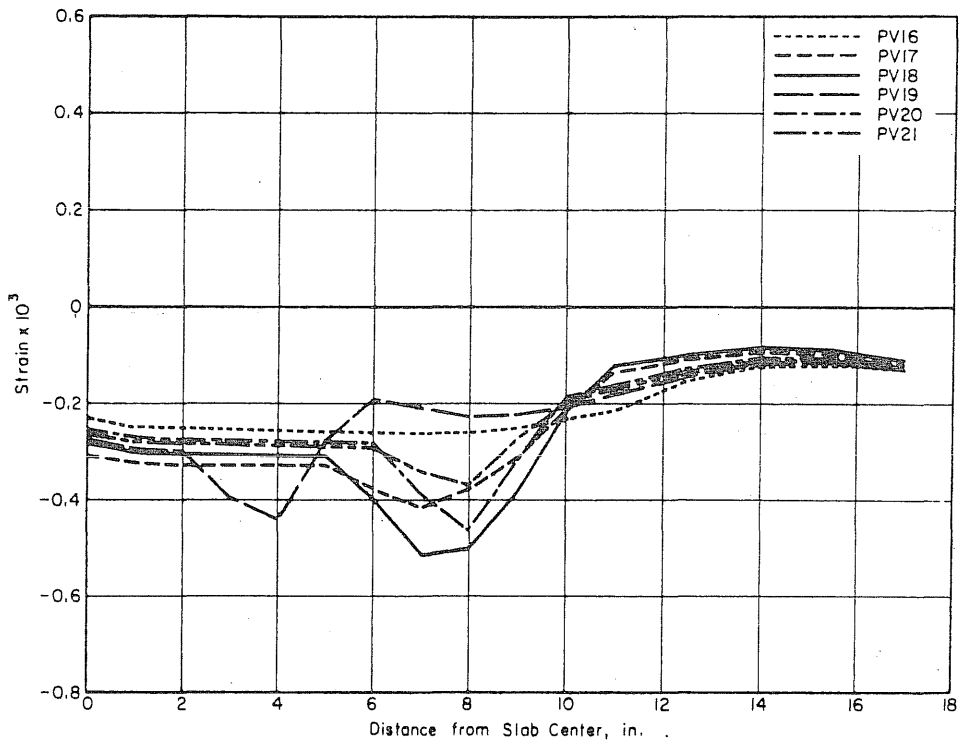

FIG. 4.4 CALCULATED RADIAL STRAINS AT MID-HEIGHT OF SLABS SUBJECTED TO PRESTRESSING FORCES

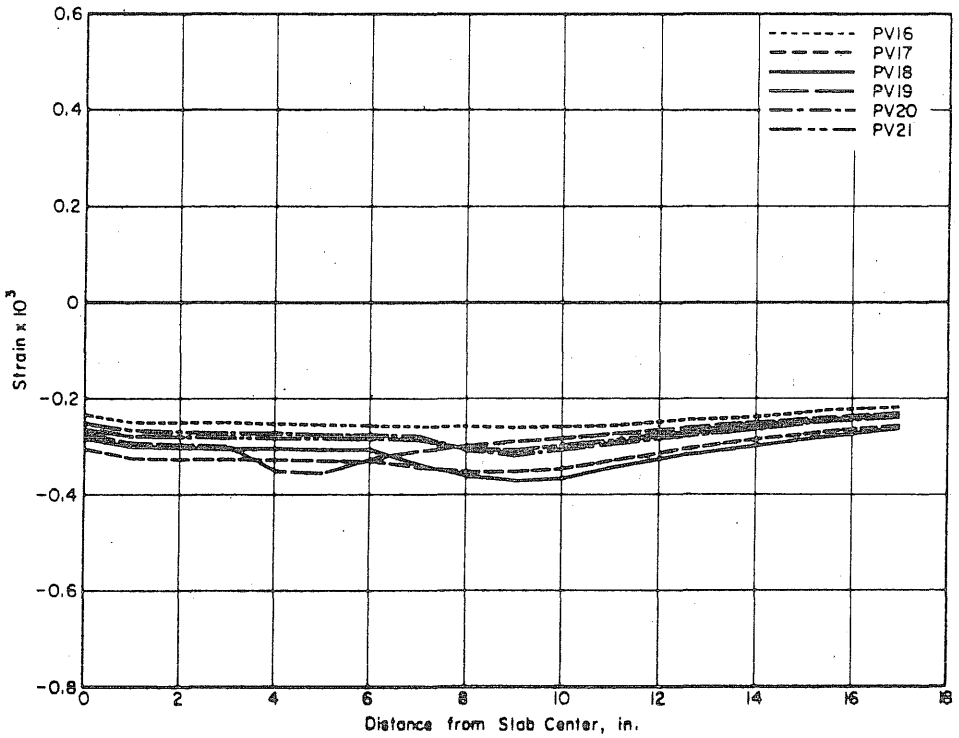

FIG. 4.5 CALCULATED TANGENTIAL STRAINS AT MID-HEIGHT OF SLABS SUBJECTED TO PRESTRESSING FORCES

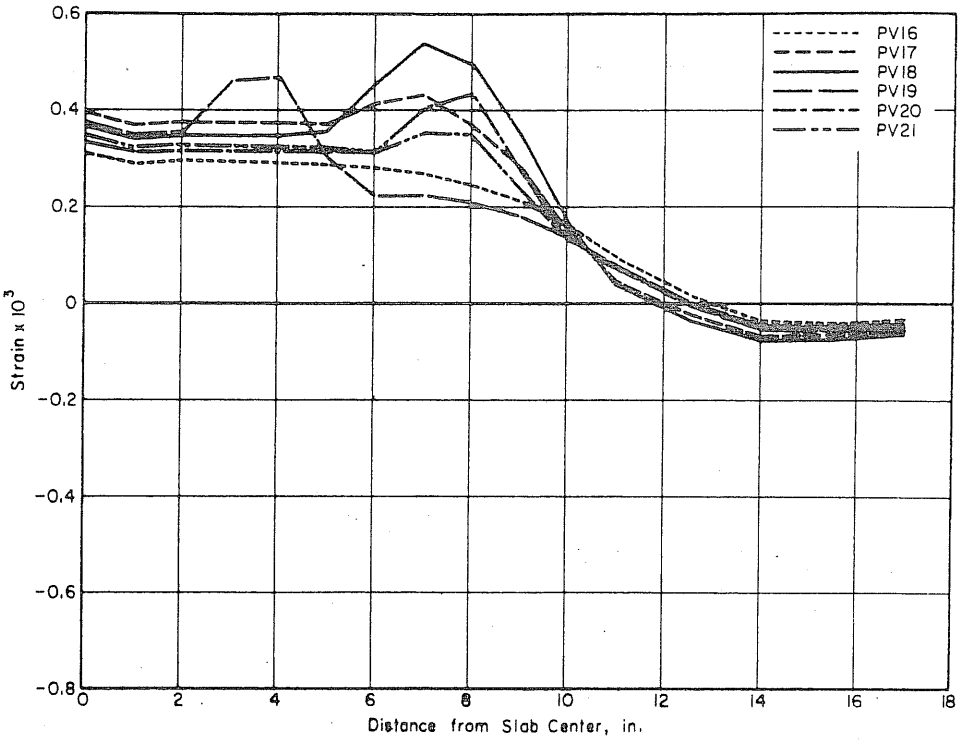

FIG. 4.6 CALCULATED RADIAL STRAINS AT MID-HEIGHT OF SLABS SUBJECTED TO 3200 psi INTERNAL PRESSURE ONLY

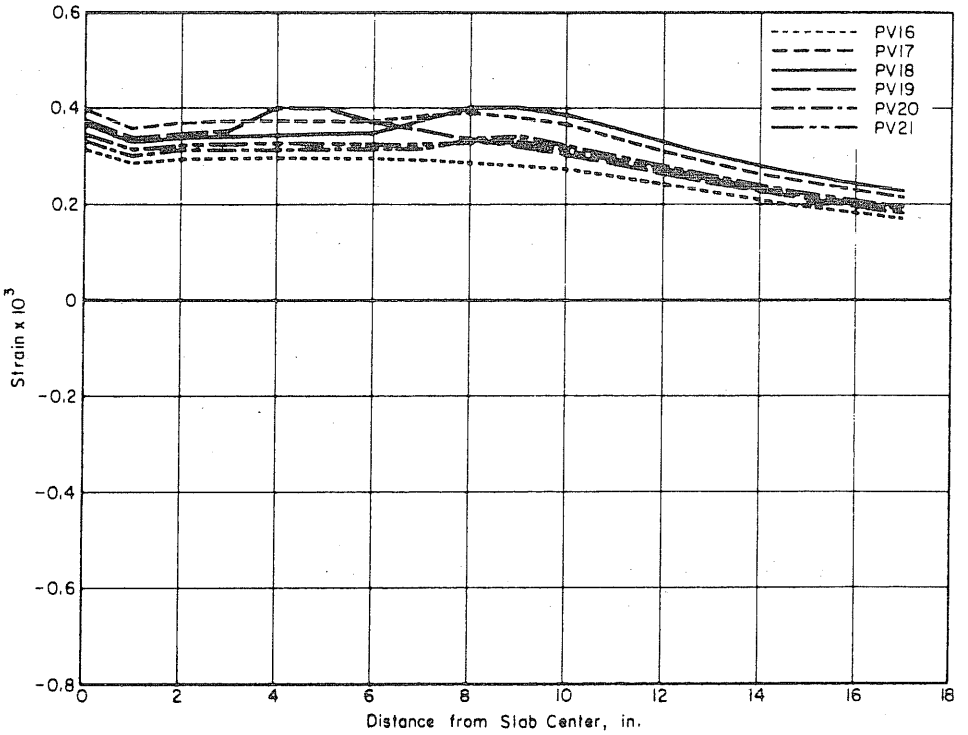

FIG. 4.7 CALCULATED TANGENTIAL STRAINS AT MID-HEIGHT OF SLABS SUBJECTED TO 3200 psi INTERNAL PRESSURE ONLY

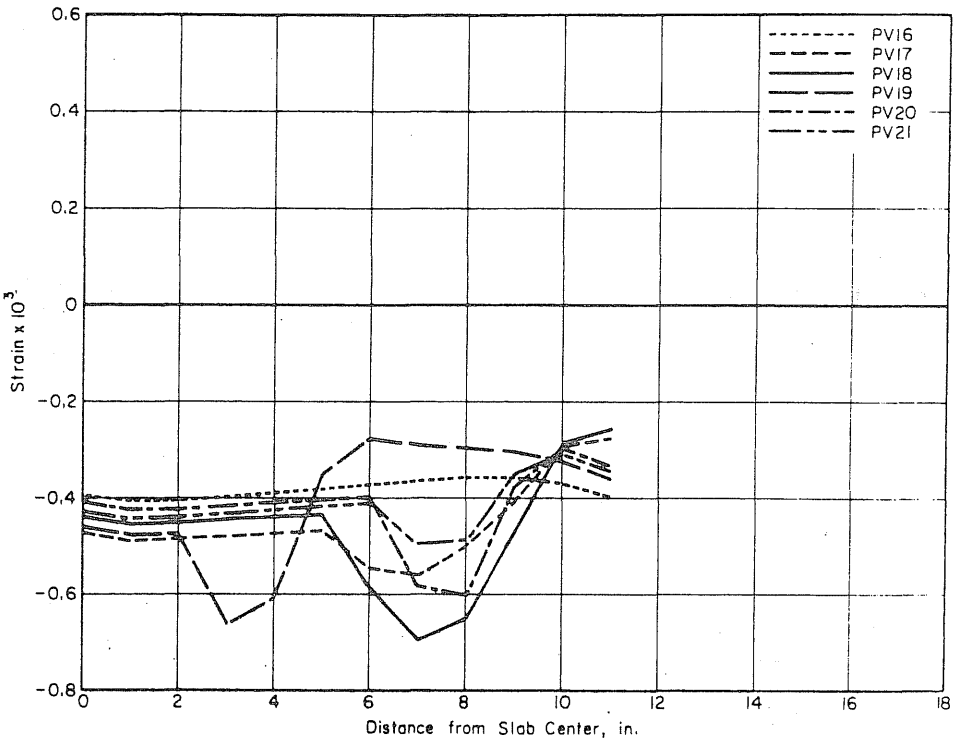

FIG. 4.8 CALCULATED RADIAL STRAINS AT INSIDE FACE OF SLABS SUBJECTED TO PRESTRESSING FORCES

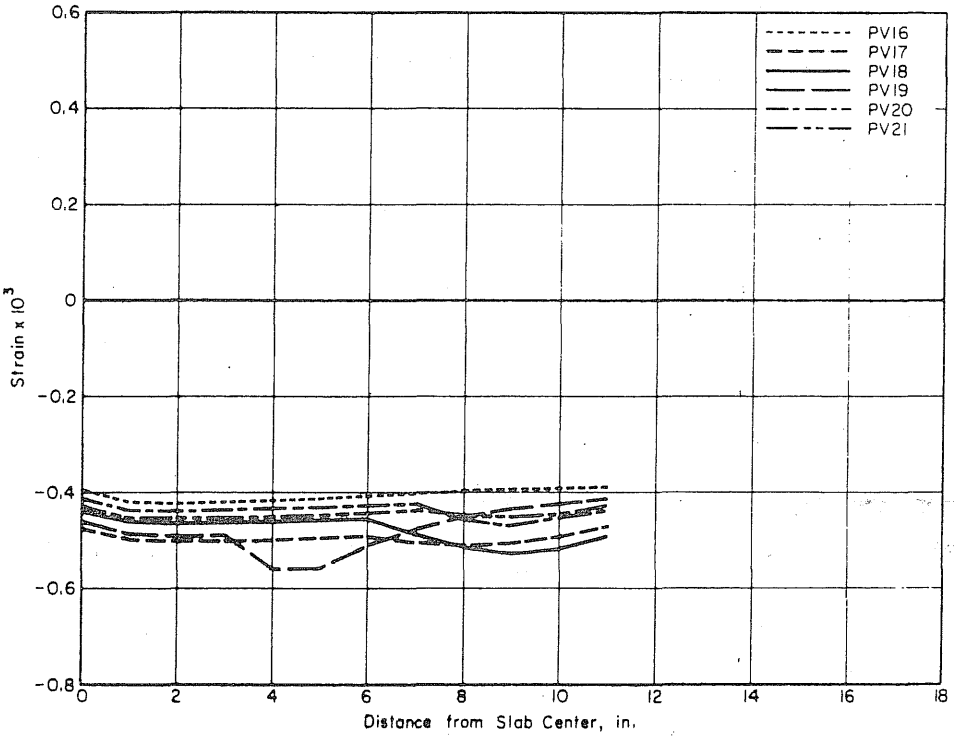

FIG. 4.9 CALCULATED TANGENTIAL STRAINS AT INSIDE FACE OF SLABS SUBJECTED TO PRESTRESSING FORCES

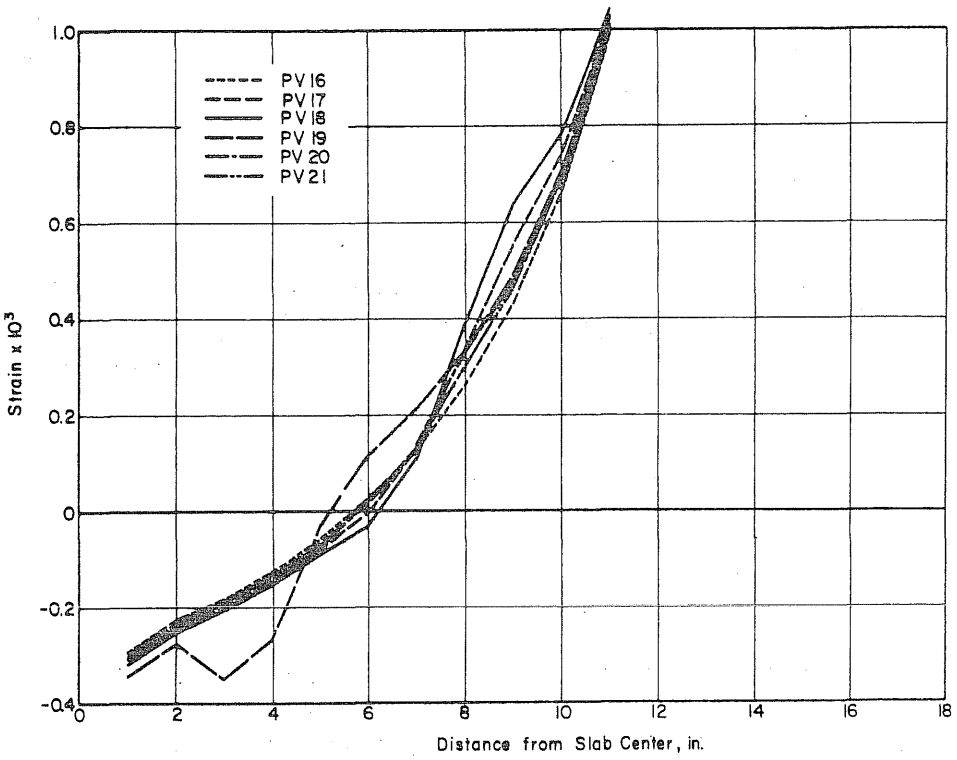

FIG. 4.10 CALCULATED RADIAL STRAINS AT INSIDE FACE OF SLABS SUBJECTED TO 3200 psi INTERNAL PRESSURE ONLY

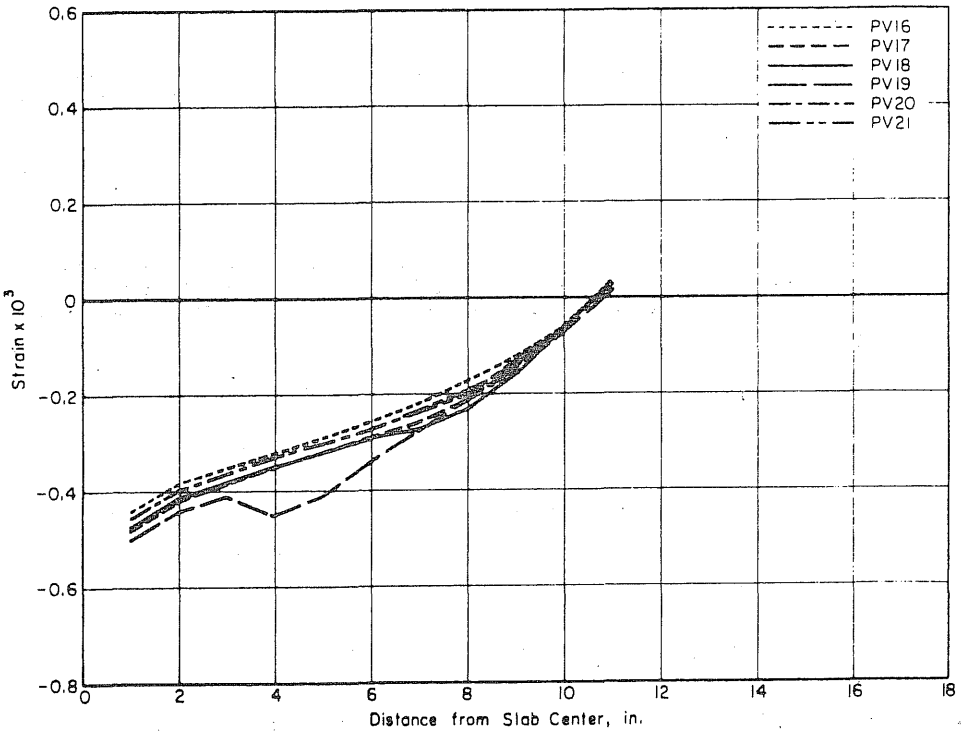

FIG. 4.11 CALCULATED TANGENTIAL STRAINS AT INSIDE FACE OF SLABS SUBJECTED TO 3200 psi INTERNAL PRESSURE ONLY

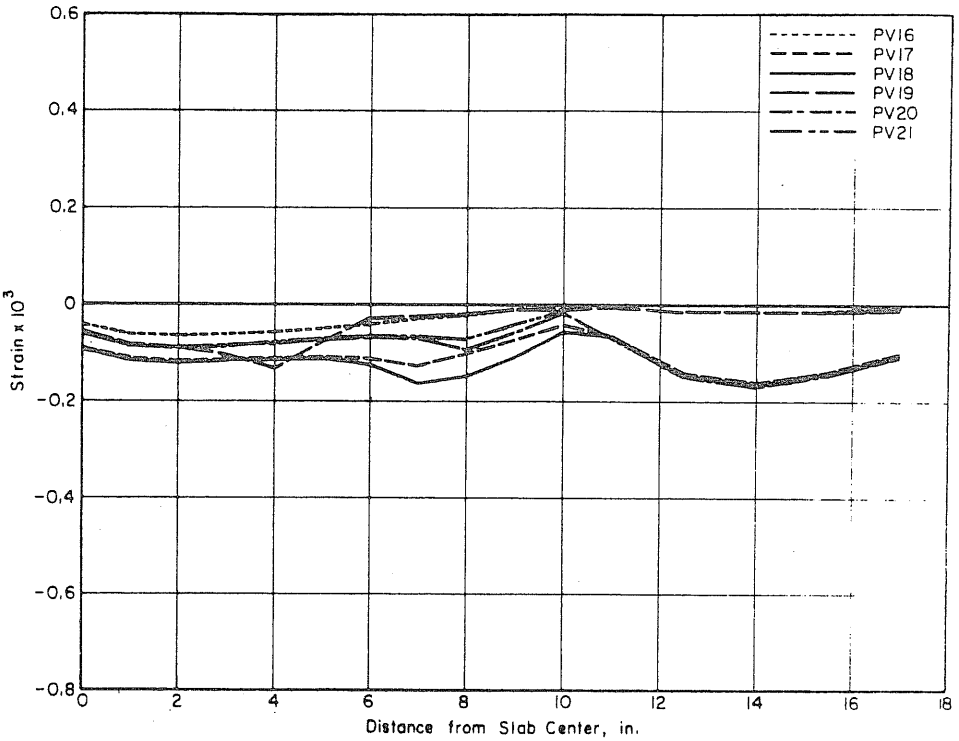

FIG. 4.12 CALCULATED RADIAL STRAINS AT OUTSIDE FACE OF SLABS SUBJECTED TO PRESTRESSING FORCES

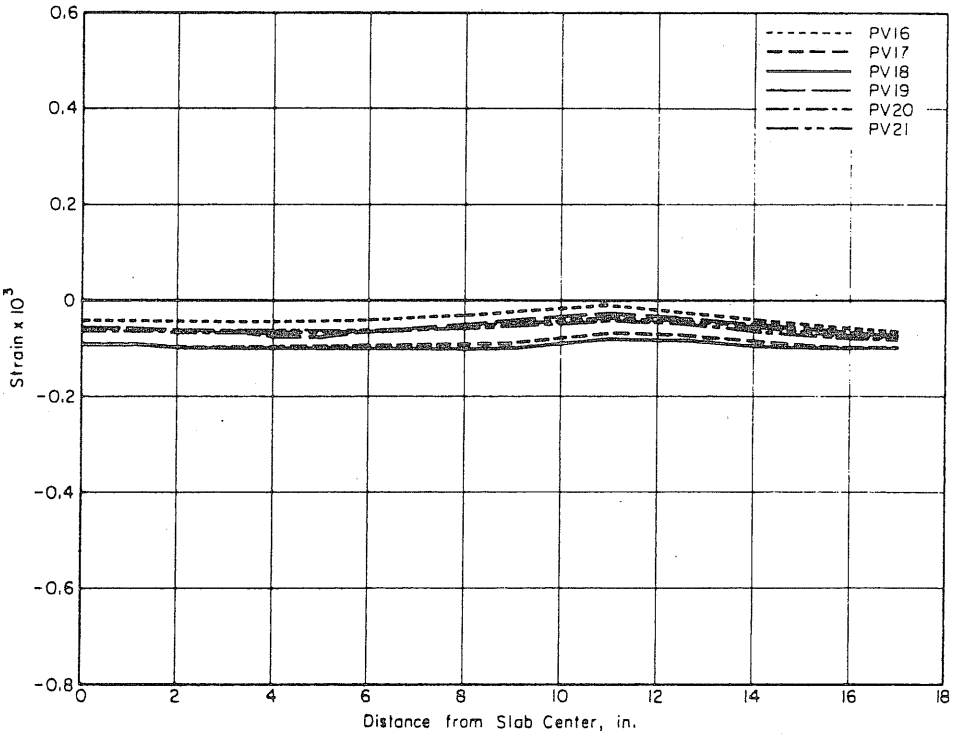

FIG. 4.13 CALCULATED TANGENTIAL STRAINS AT OUTSIDE FACE OF SLABS SUBJECTED TO PRESTRESSING FORCES

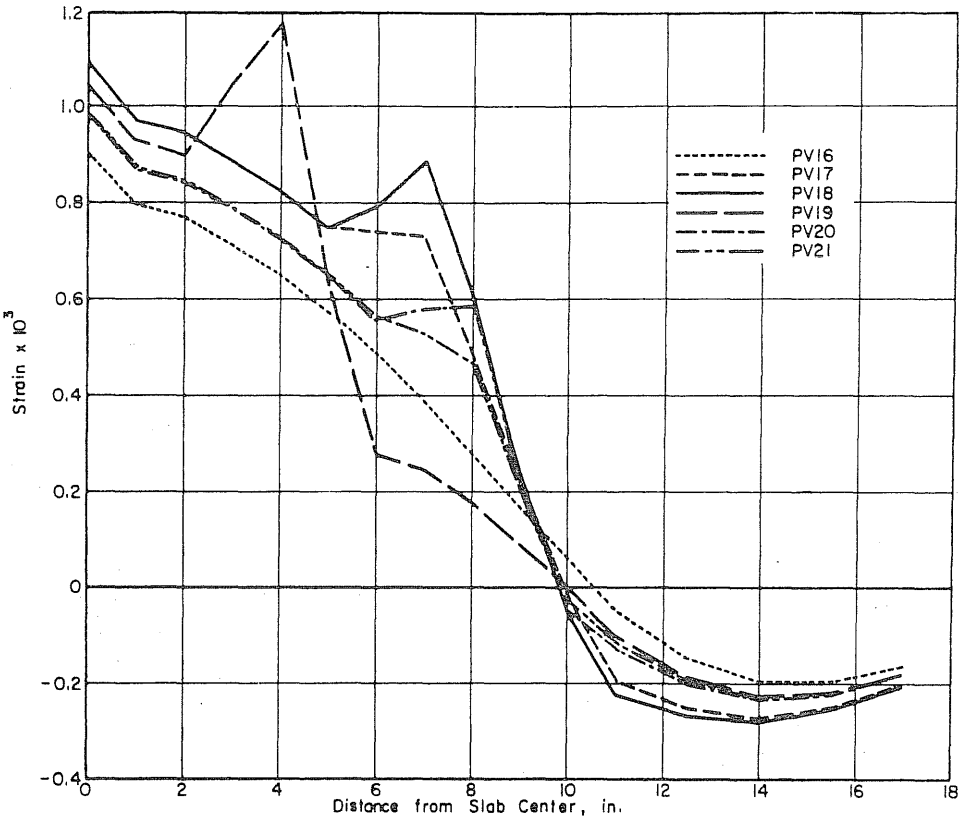

FIG. 4.14 CALCULATED RADIAL STRAINS AT OUTSIDE FACE OF SLABS SUBJECTED TO 3200 psi INTERNAL PRESSURE ONLY

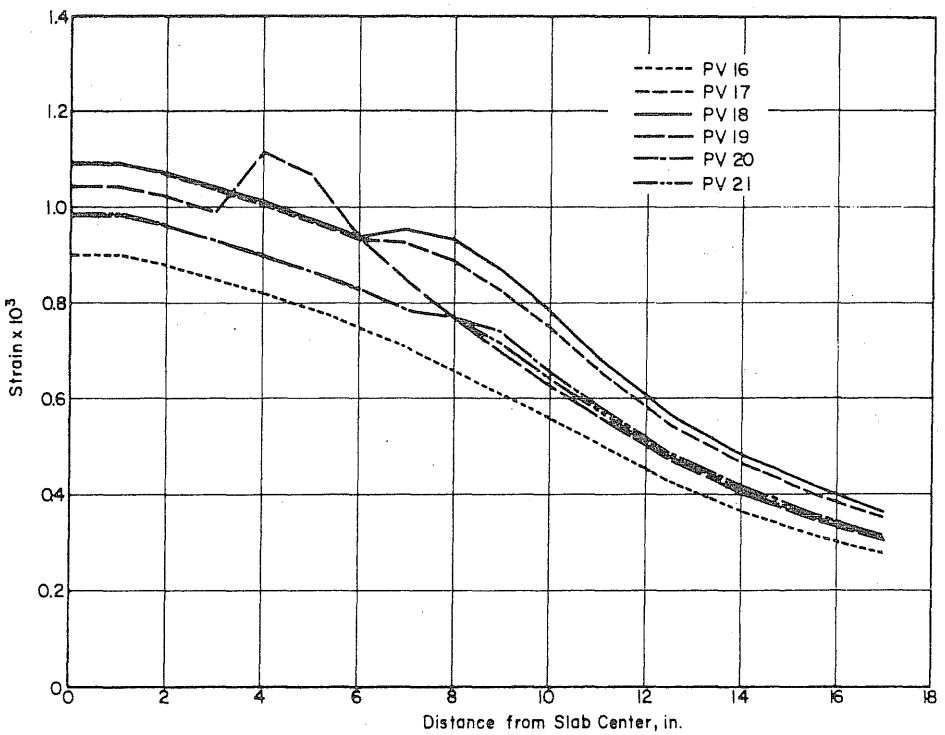

FIG. 4.15 CALCULATED TANGENTIAL STRAINS AT OUTSIDE FACE OF SLABS SUBJECTED TO 3200 psi INTERNAL PRESSURE ONLY

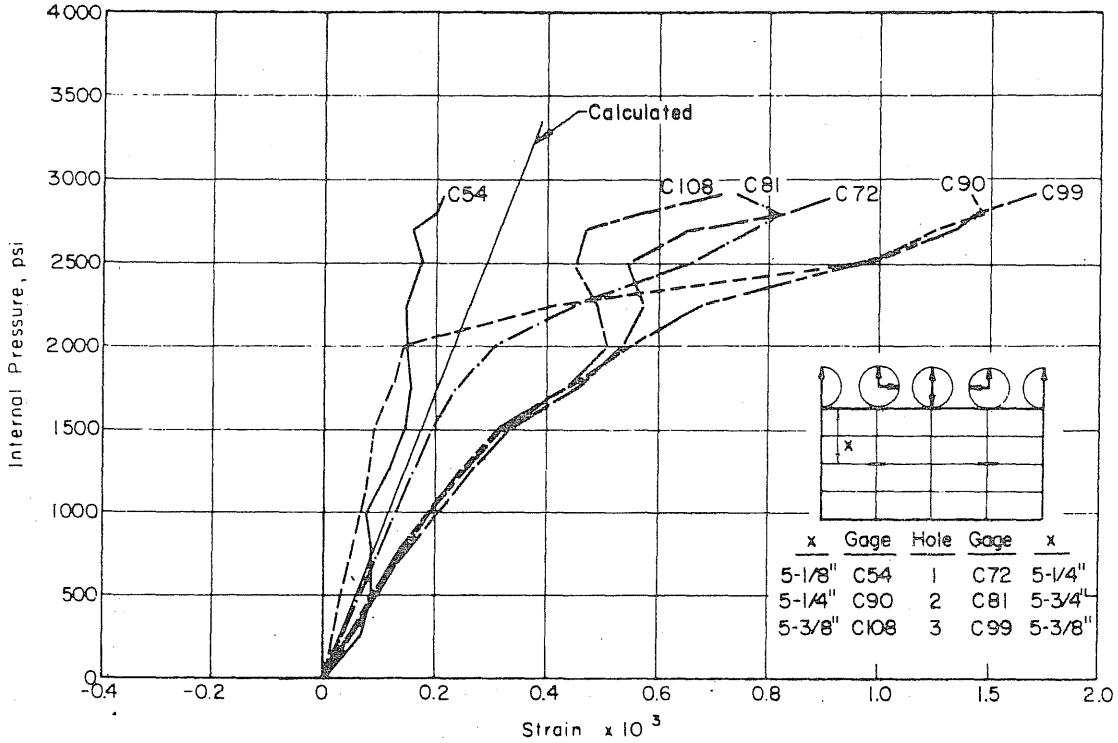

FIG. 4.16 MEASURED RADIAL STRAINS AT MID-HEIGHT OF PENETRATIONS AND 8 in. FROM THE CENTER OF THE SLAB OF VESSEL PV17

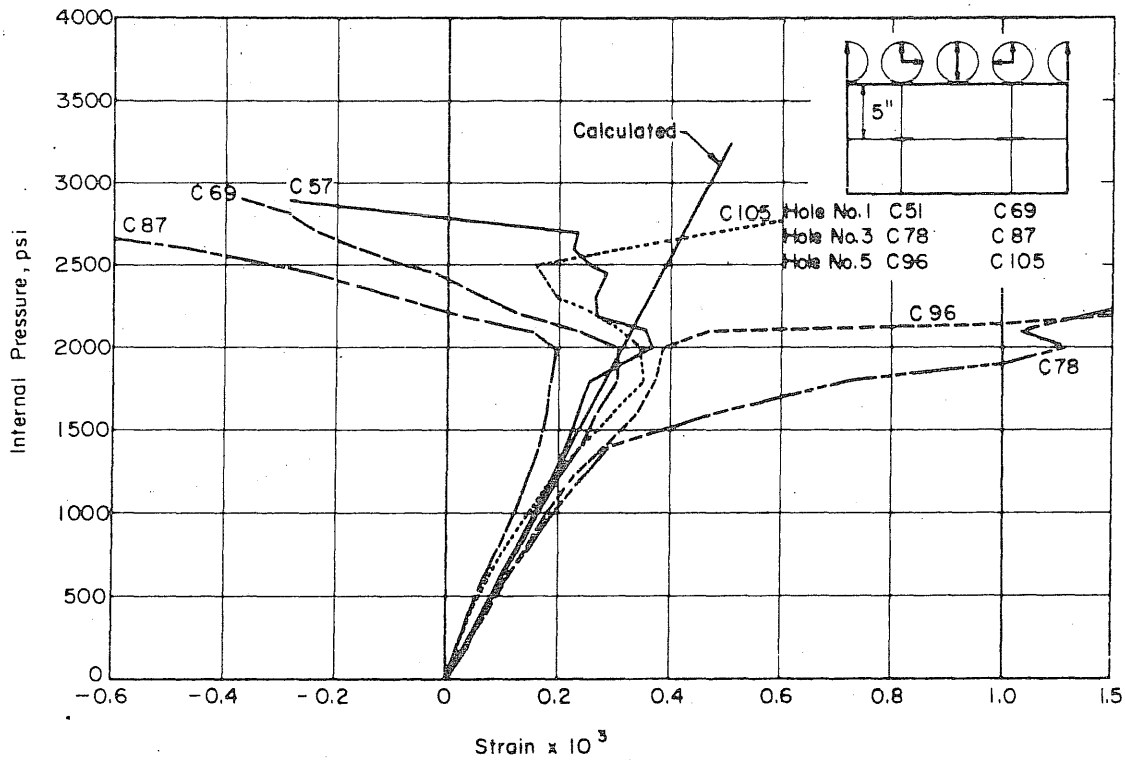

FIG. 4.17 MEASURED RADIAL STRAINS AT MID-HEIGHT OF PENETRATIONS AND 8 in. FROM THE CENTER OF THE SLAB OF VESSEL PV18

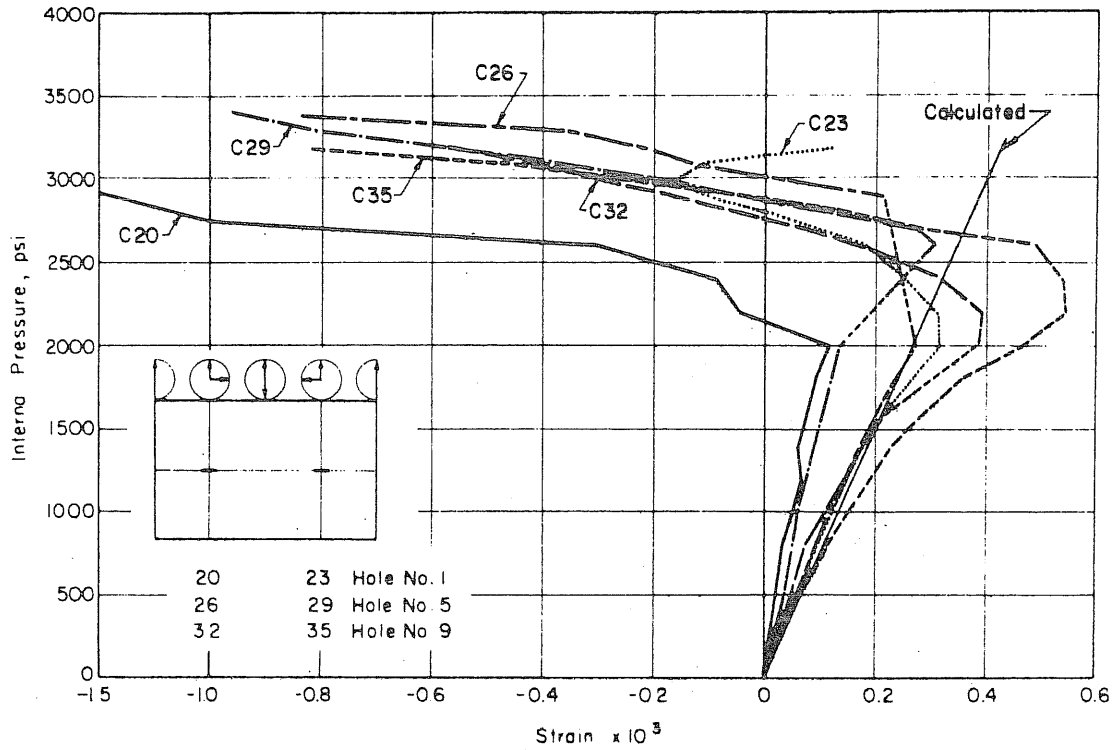

FIG. 4.18 MEASURED RADIAL STRAINS AT MID-HEIGHT OF PENETRATIONS AND 8 In. FROM THE CENTER OF THE SLAB OF VESSEL PV 20

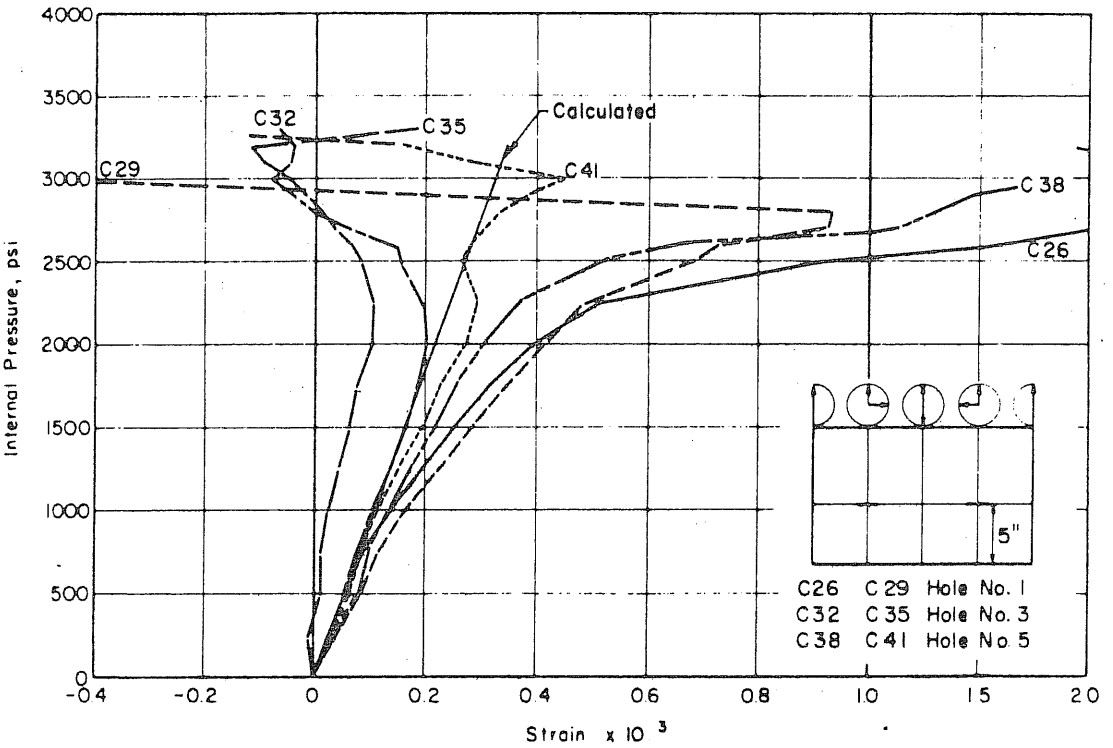

FIG. 4.19 MEASURED RADIAL STRAINS AT MID-HEIGHT OF PENETRATIONS AND 8 In. FROM THE CENTER OF THE SLAB OF VESSEL PV21

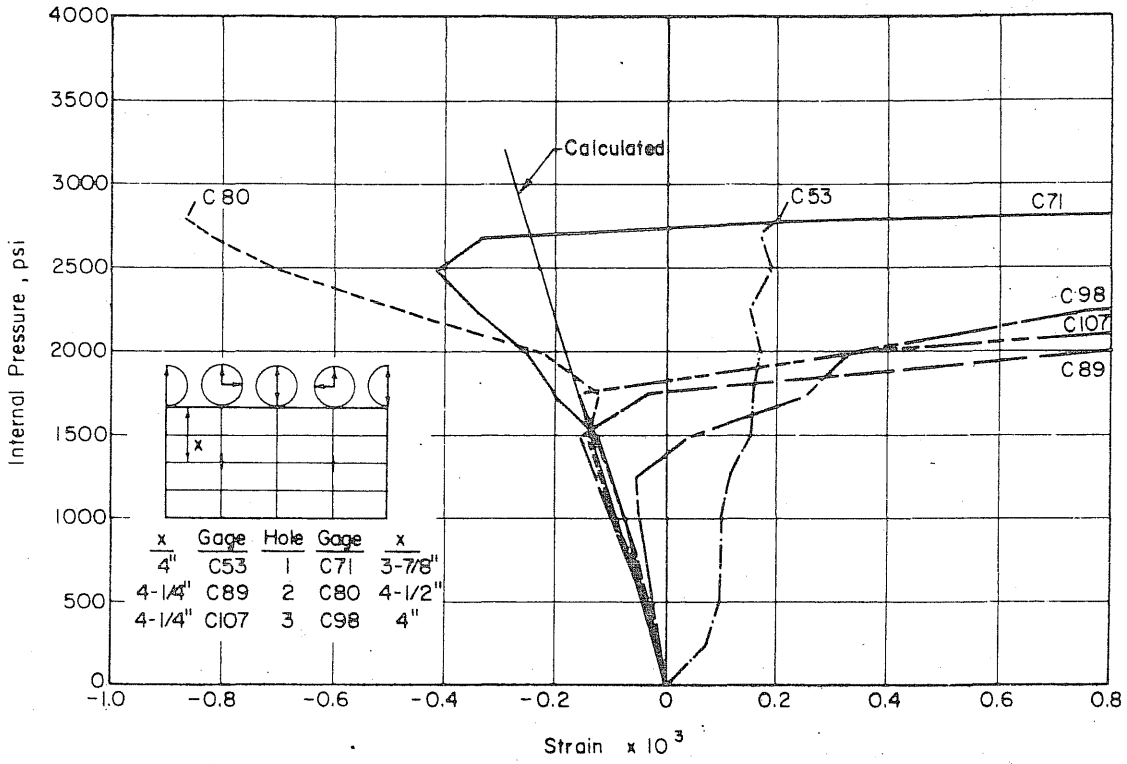

FIG. 4.20 MEASURED VERTICAL STRAINS AT MID-HEIGHT OF PENETRATIONS AND 8 in. FROM THE CENTER OF THE SLAB OF VESSEL PV17

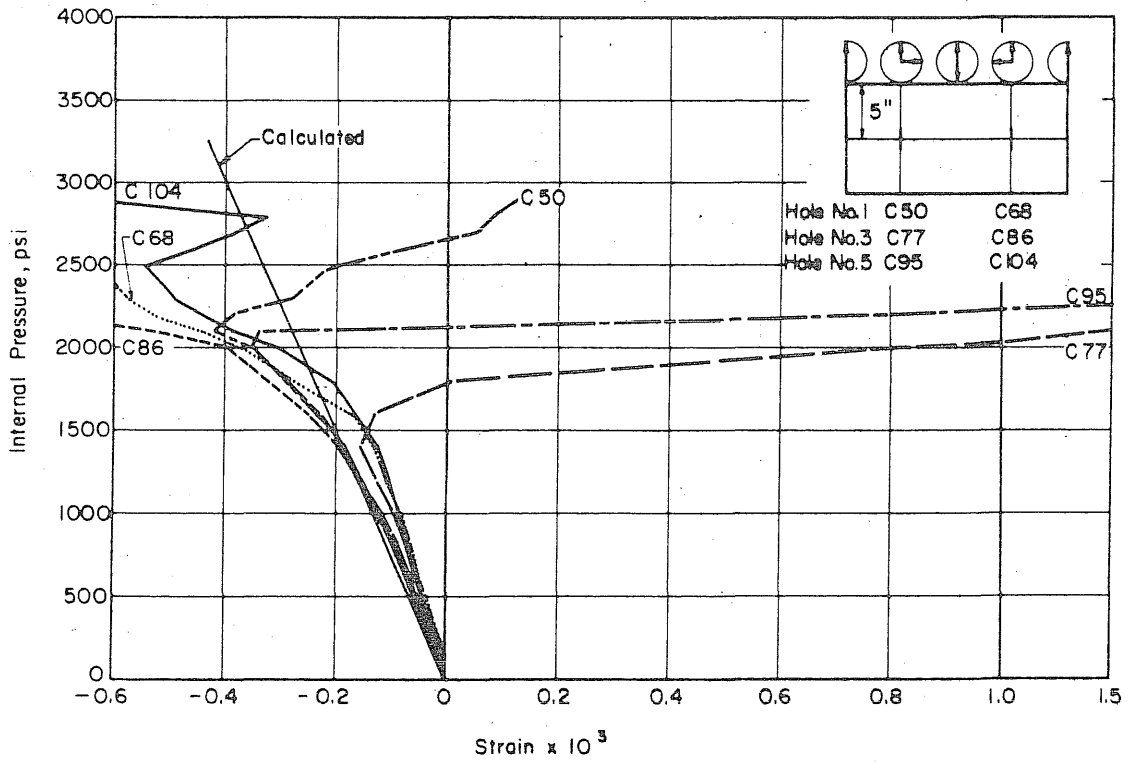

FIG. 4.21 MEASURED VERTICAL STRAINS AT MID-HEIGHT OF PENETRATIONS AND 8 in. FROM THE CENTER OF THE SLAB OF VESSEL PV18

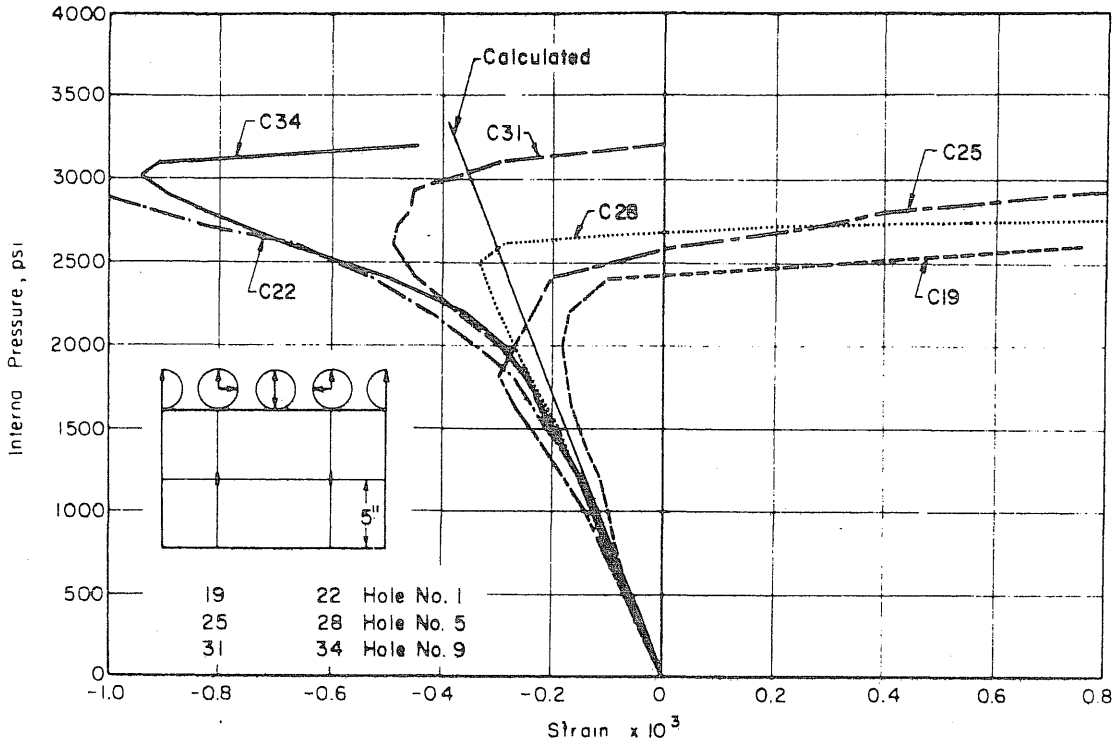

FIG. 4.22 MEASURED VERTICAL STRAINS AT MID-HEIGHT OF PENETRATIONS AND 8 in. FROM THE CENTER OF THE SLAB OF VESSEL PV20

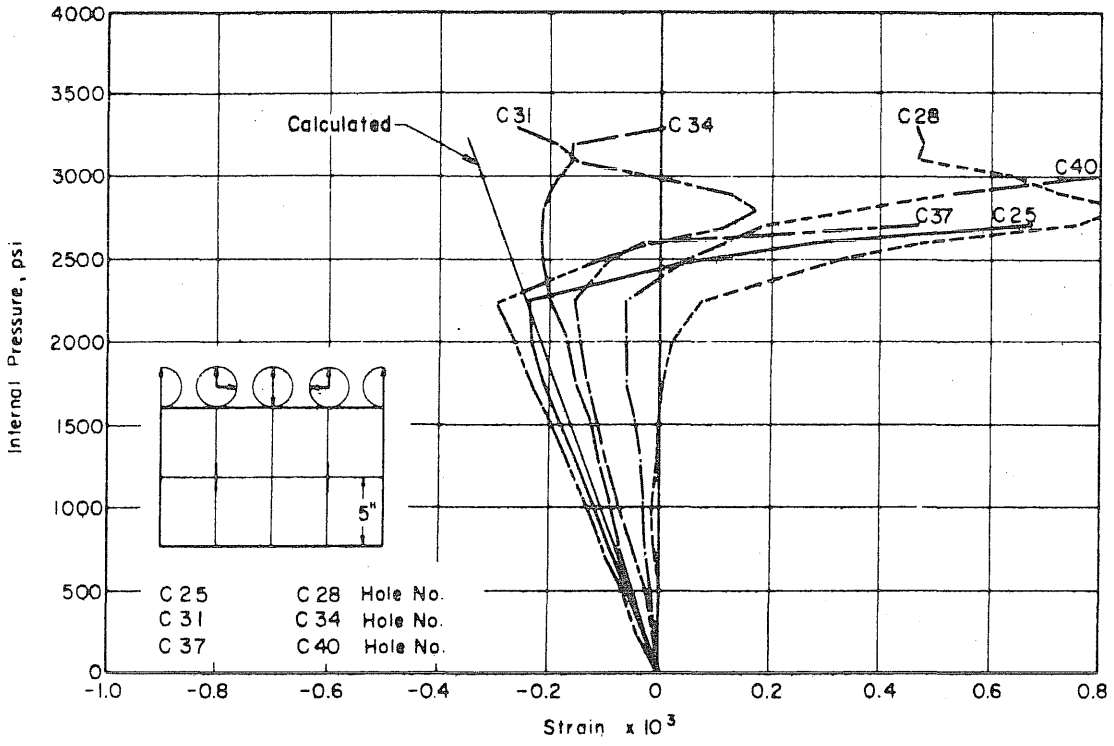

FIG. 4.23 MEASURED VERTICAL STRAINS AT MID-HEIGHT OF PENETRATIONS AND 8 in. FROM THE CENTER OF THE SLAB OF VESSEL PV21

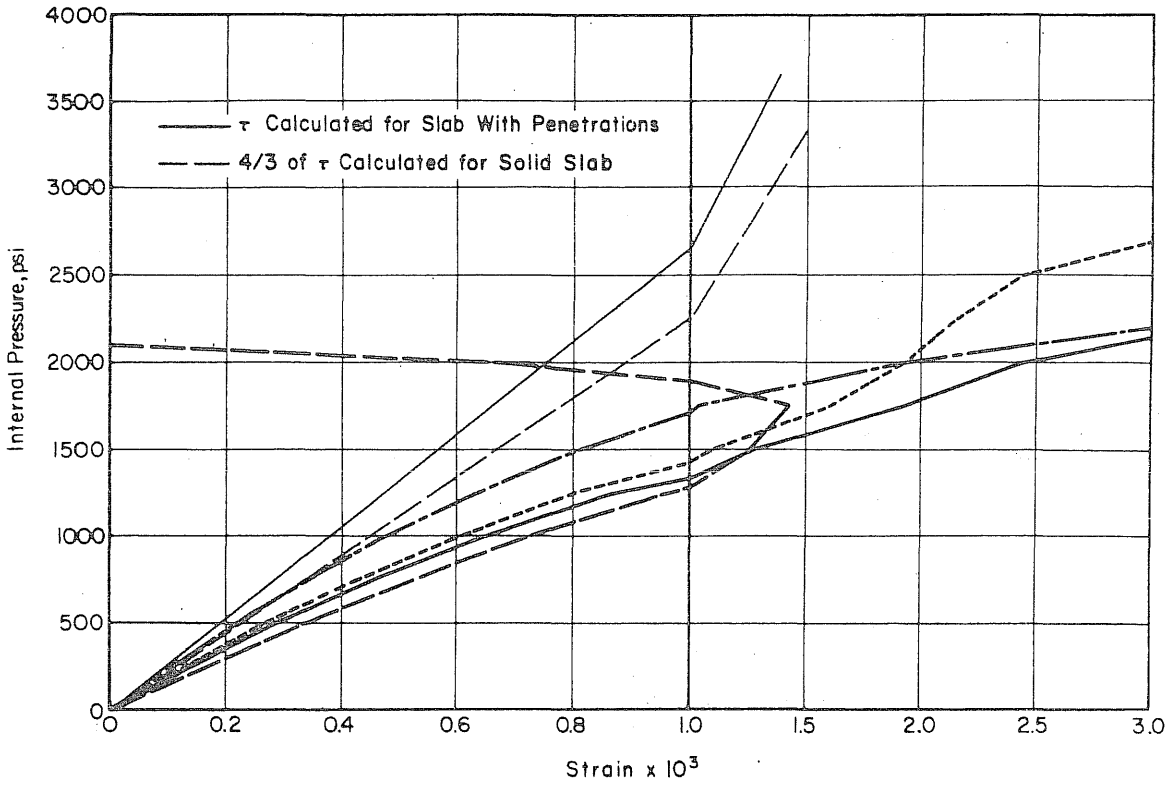

FIG. 4.24 MEASURED SHEAR STRAINS AT MID-HEIGHT OF PENETRATIONS AND 8 in. FROM THE CENTER OF THE SLAB OF VESSEL PV17

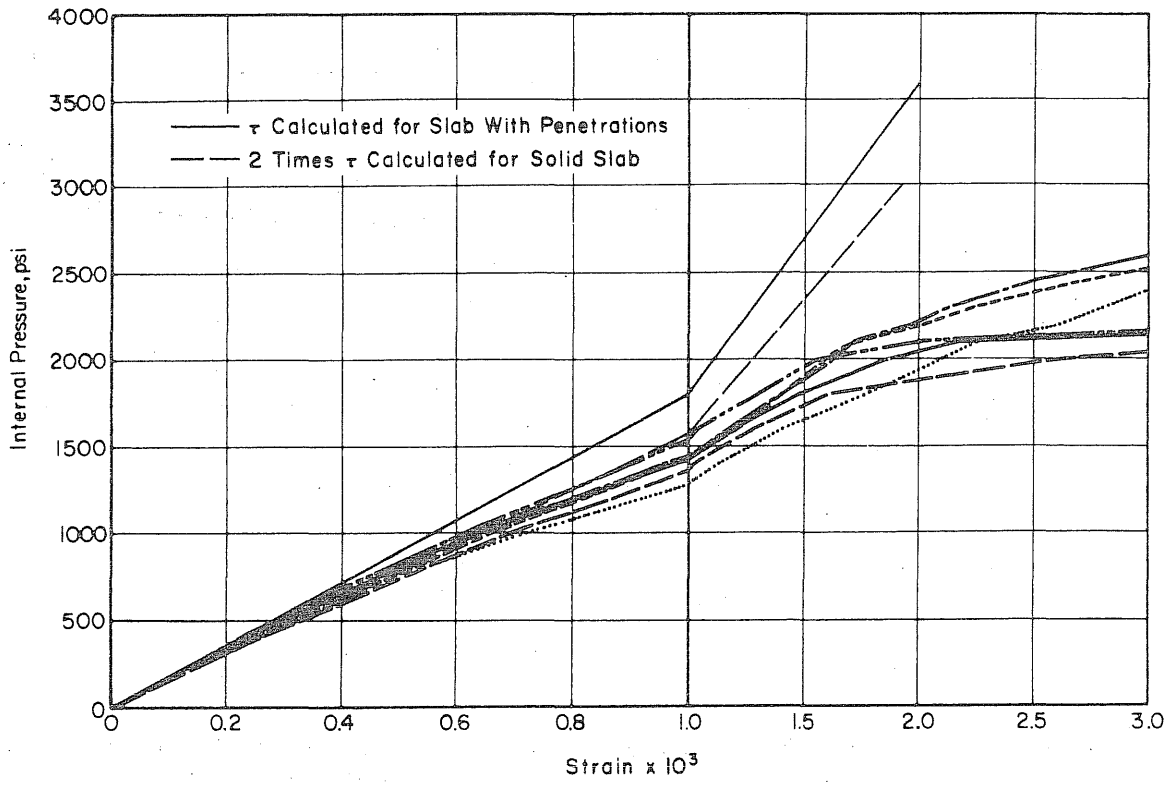

FIG. 4.25 MEASURED SHEAR STRAINS AT MID-HEIGHT OF PENETRATIONS AND 8 in. FROM THE CENTER OF THE SLAB OF VESSEL PV18

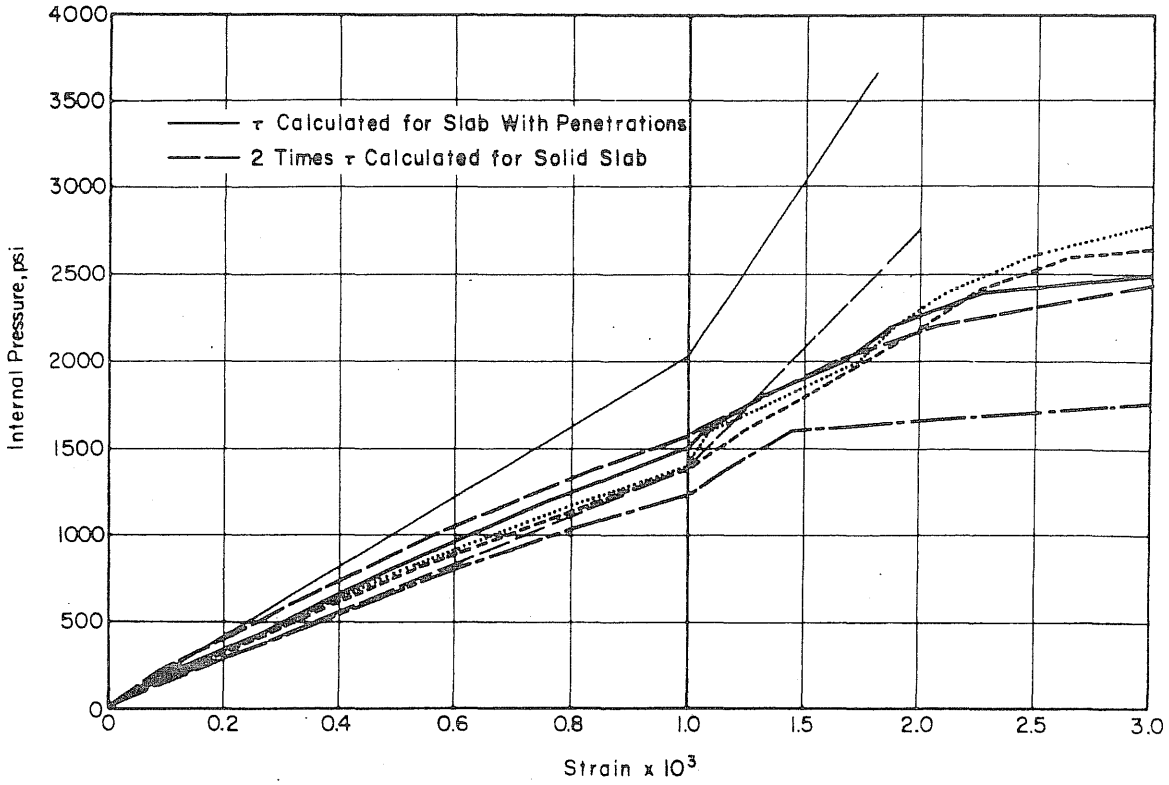

FIG. 4.26 MEASURED SHEAR STRAINS AT MID-HEIGHT OF PENETRATIONS AND 8 in. FROM THE CENTER OF THE SLAB OF VESSEL PV20

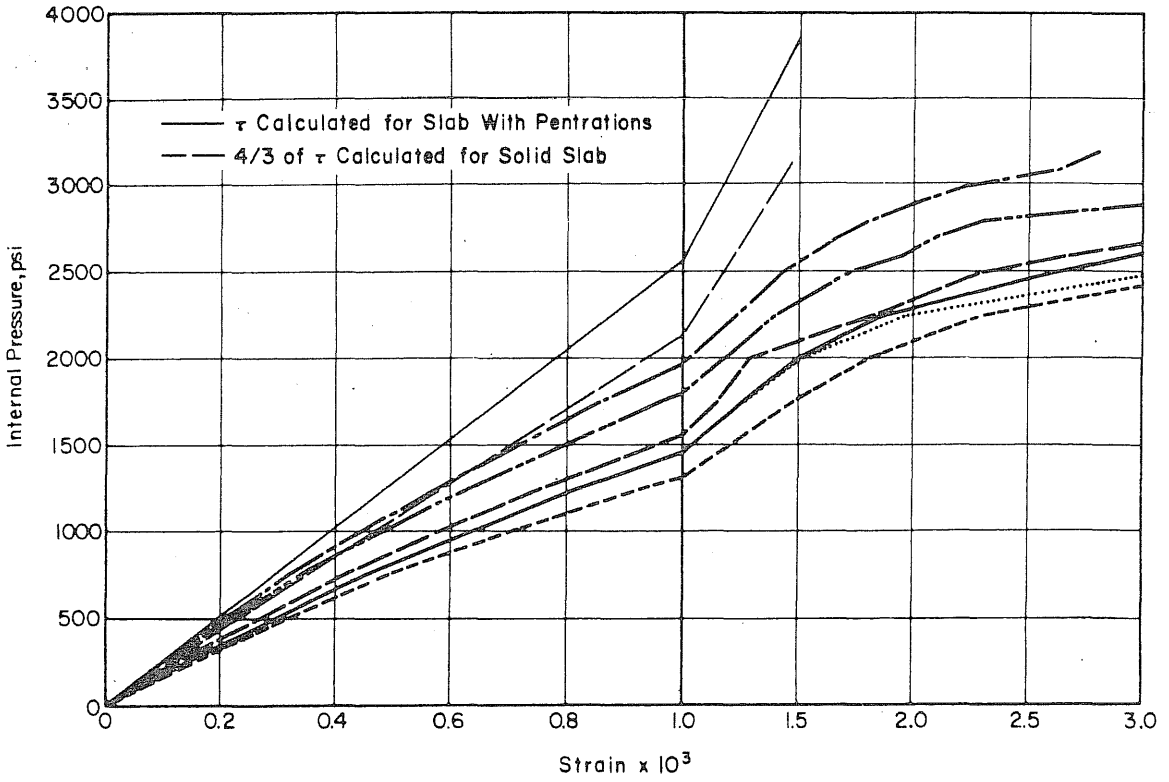

FIG. 4.27 MEASURED SHEAR STRAINS AT MID-HEIGHT OF PENETRATIONS AND 8 in. FROM THE CENTER OF THE SLAB OF VESSEL PV21

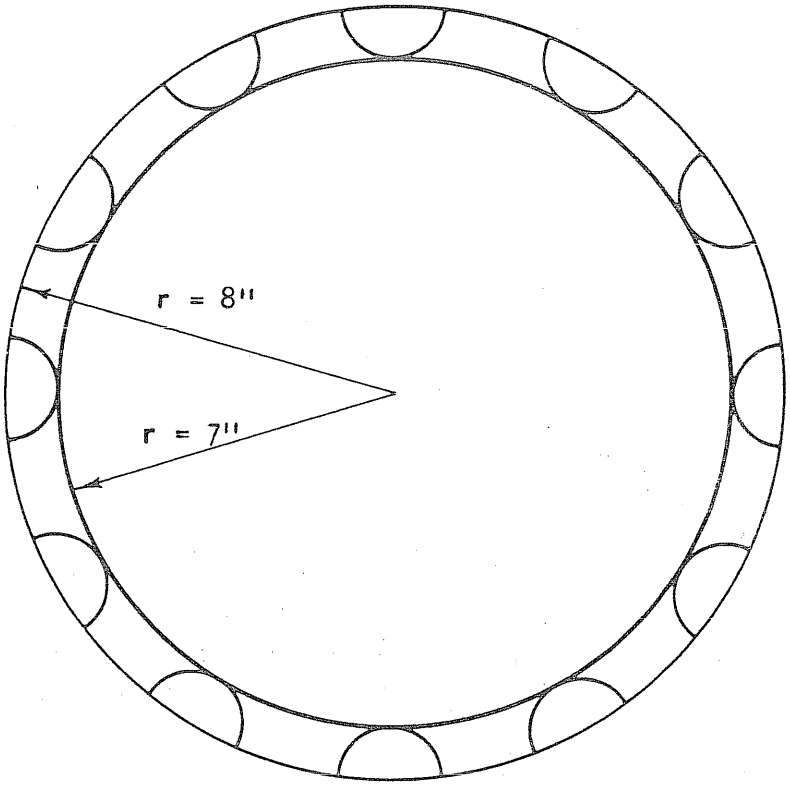

Percentage of concrete removed along a circle with the radius equal to 8 in. = 50

Percentage of concrete removed in the section limited by circles with radii 7 and 8 in. = 40

FIG. 4.28 CALCULATION OF THE SHEAR STRAIN BETWEEN THE PENETRATIONS

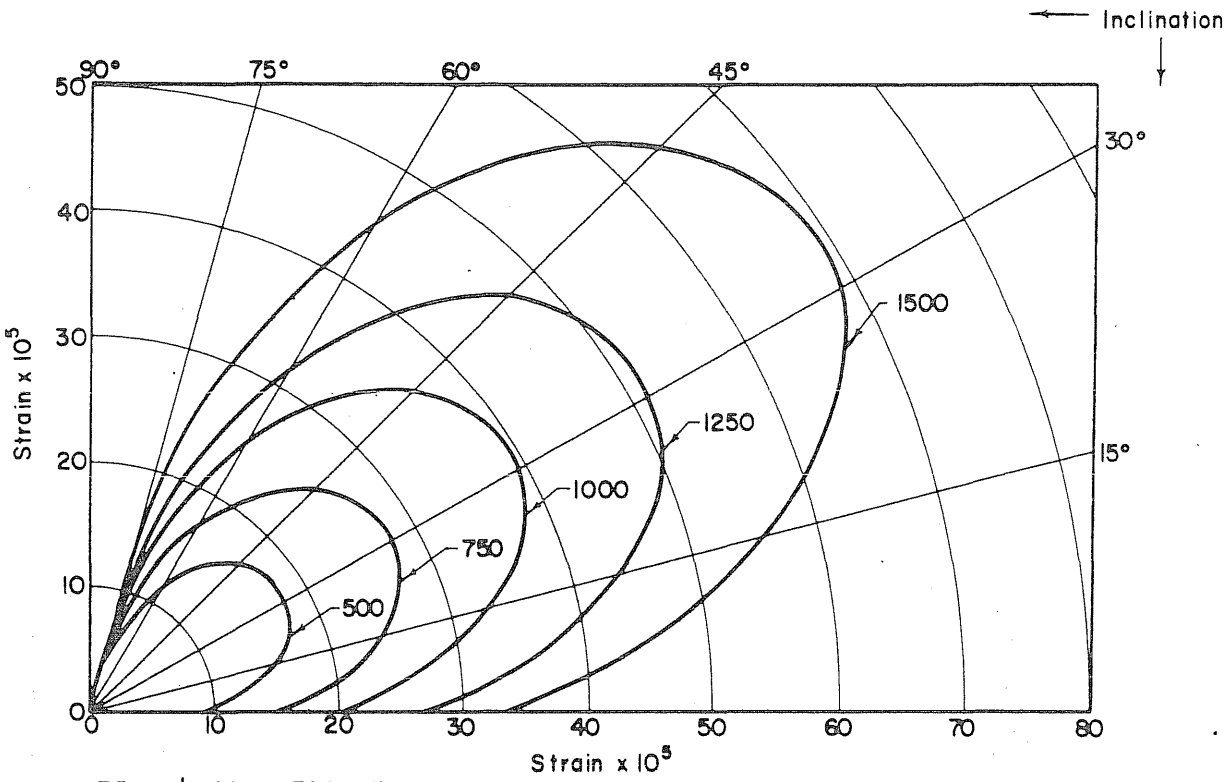

FIG. 4.29 MEASURED STRAINS IN POLAR COORDINATES AT DIFFERENT INTERNAL PRESSURES AT MID-HEIGHT OF PENETRATIONS IN THE SLAB OF PV17

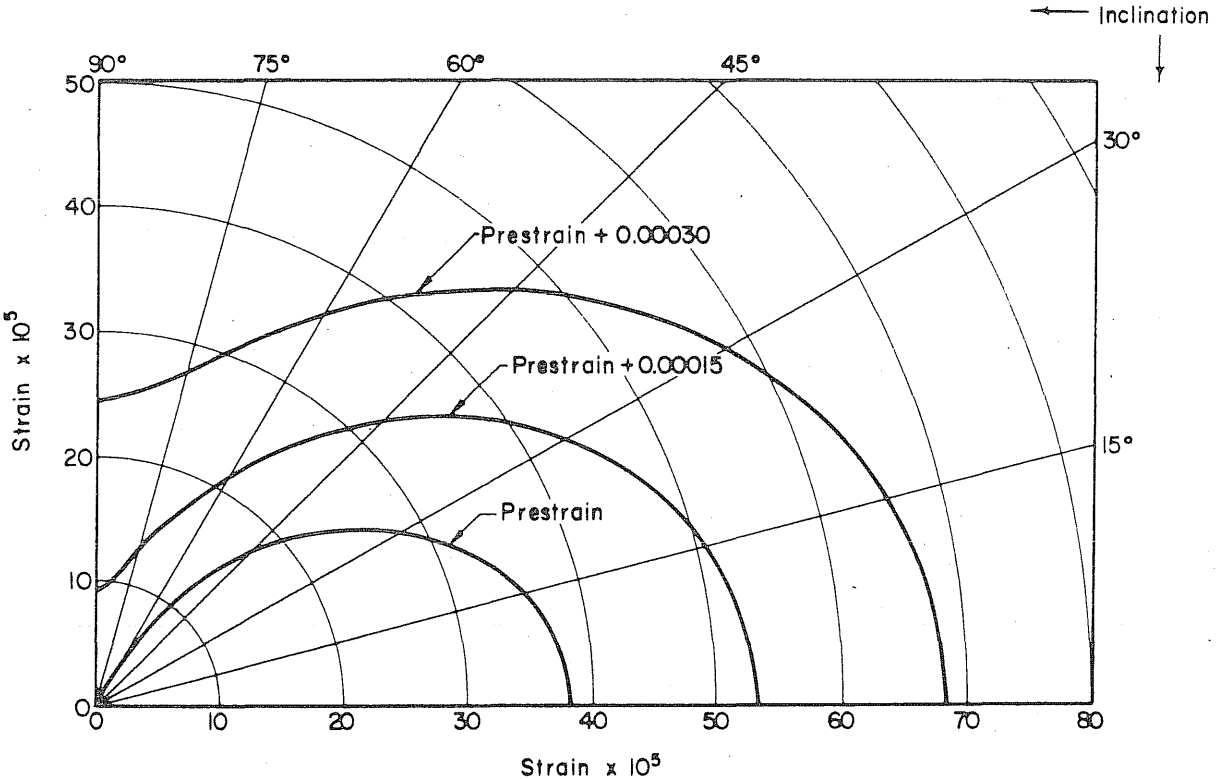

FIG. 4.30 CALCULATED PRESTRAIN IN POLAR COORDINATES AT MID-HEIGHT OF PENETRATIONS IN THE SLAB OF PV17

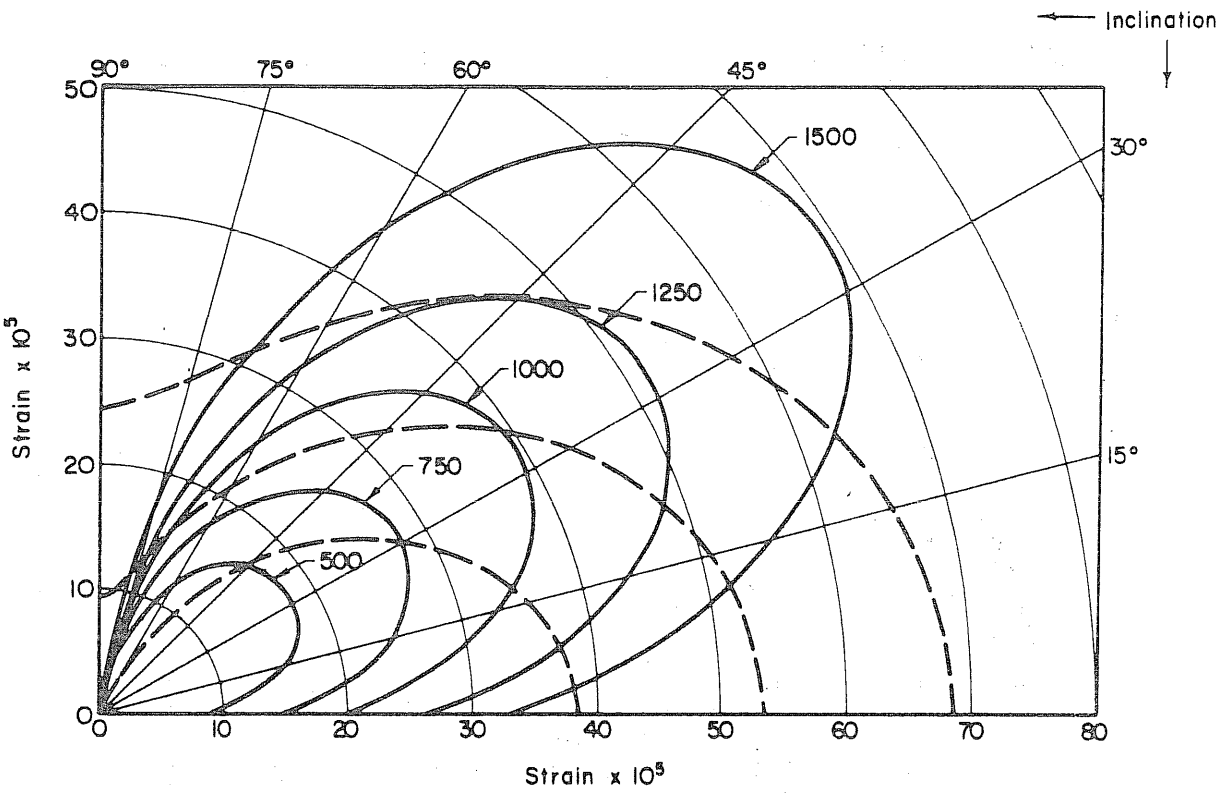

FIG. 4.31 CALCULATED PRESTRAIN AND MEASURED STRAINS AT MID-HEIGHT OF PENETRATIONS IN THE SLAB OF PV17

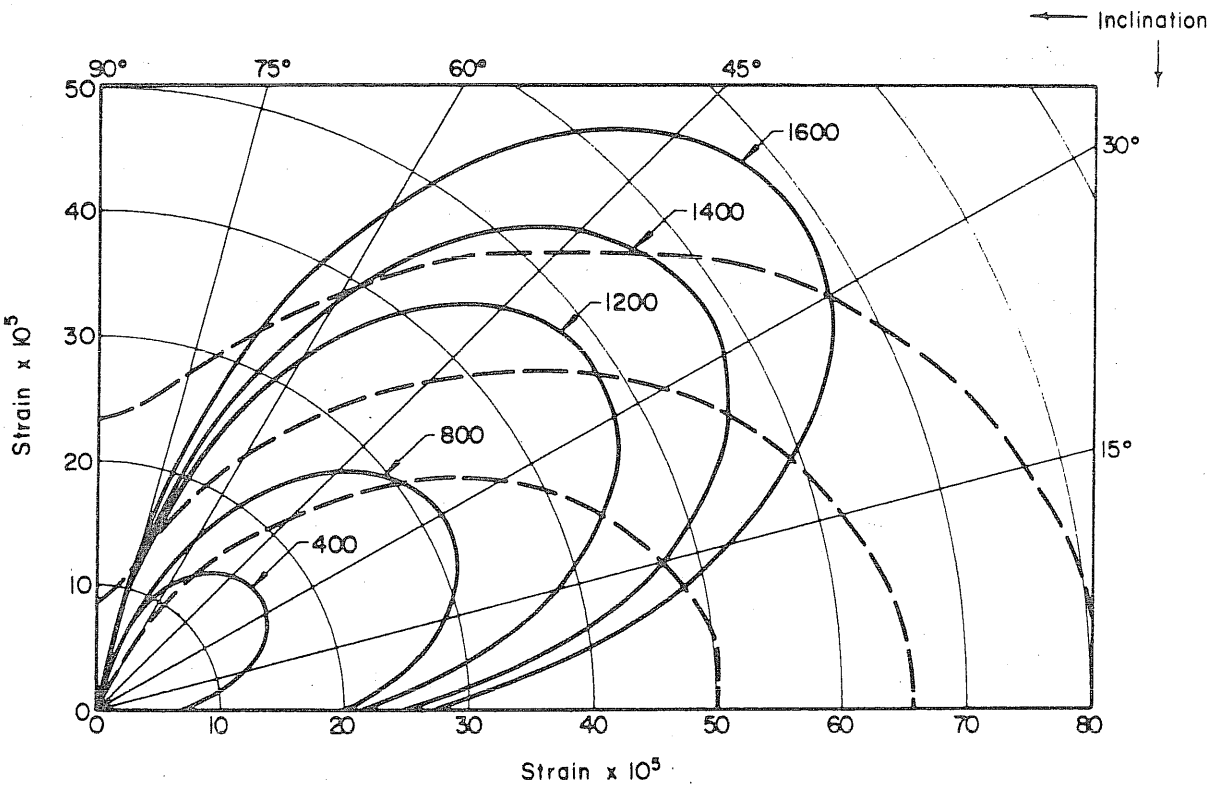

FIG. 4.32 CALCULATED PRESTRAIN AND MEASURED STRAINS AT MID-HEIGHT OF PENETRATIONS IN THE SLAB OF PV18

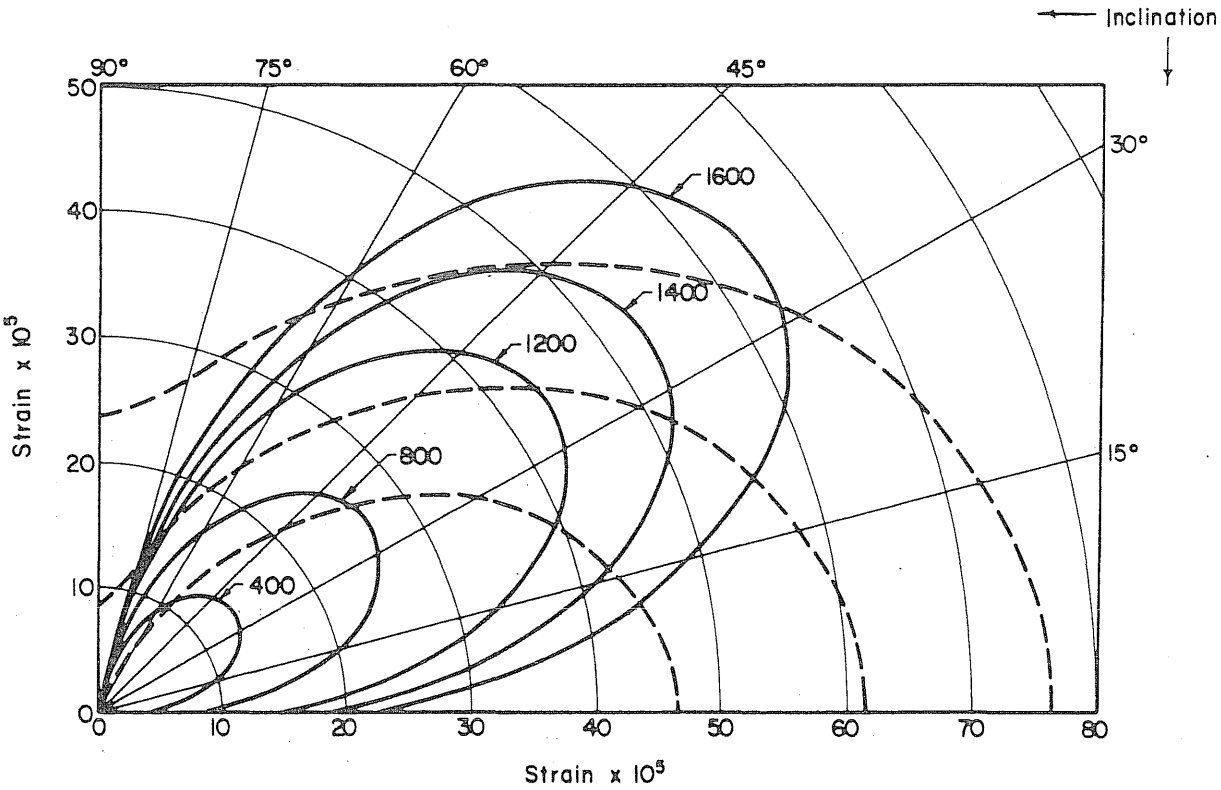

FIG. 4.33 CALCULATED PRESTRAIN AND MEASURED STRAINS AT MID-HEIGHT OF PENETRATIONS IN THE SLAB OF PV20

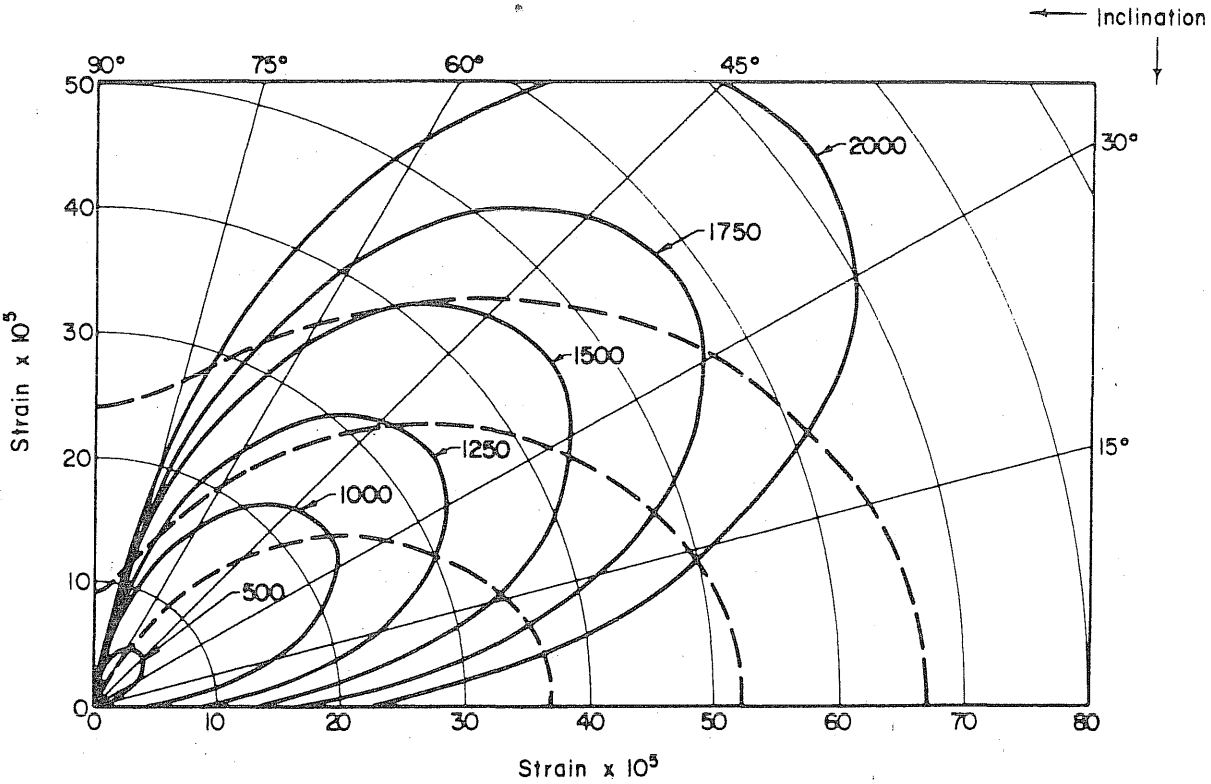

FIG. 4.34 CALCULATED PRESTRAIN AND MEASURED STRAINS AT MID-HEIGHT OF PENETRATIONS IN THE SLAB OF PV21

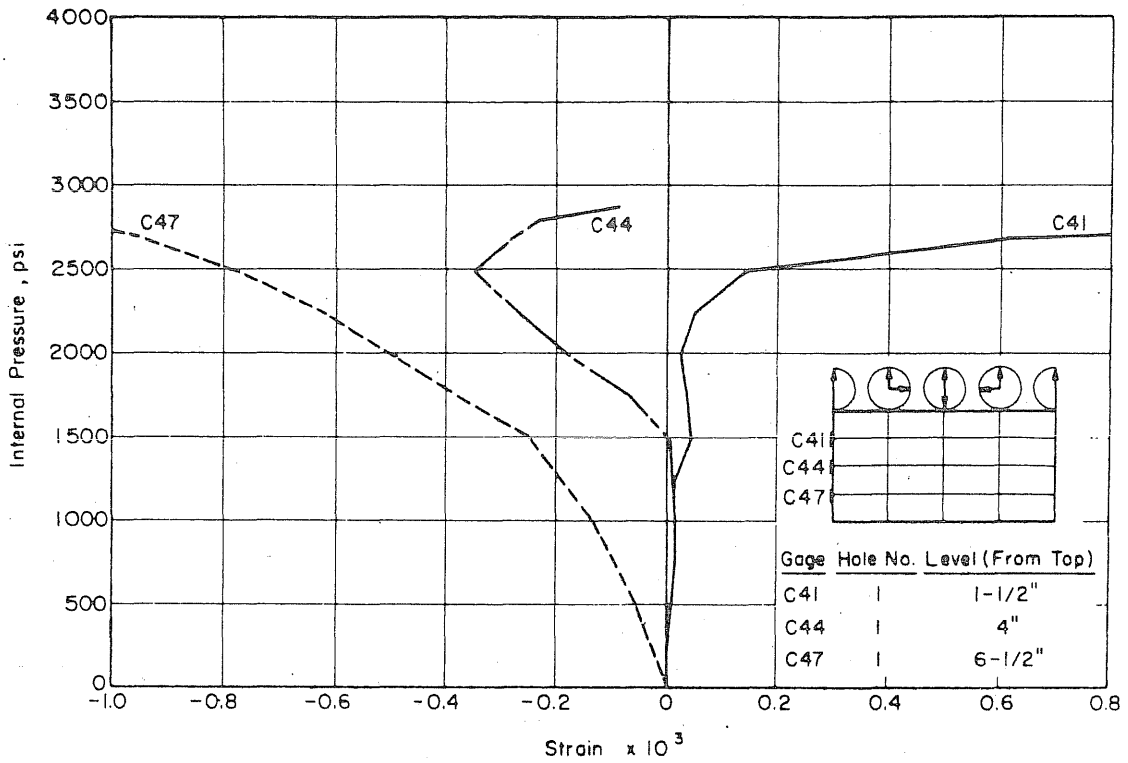

FIG. 4.35 MEASURED VERTICAL STRAINS IN ONE OF THE PENETRATIONS AND 10 in. FROM THE CENTER OF THE SLAB OF VESSEL PV17

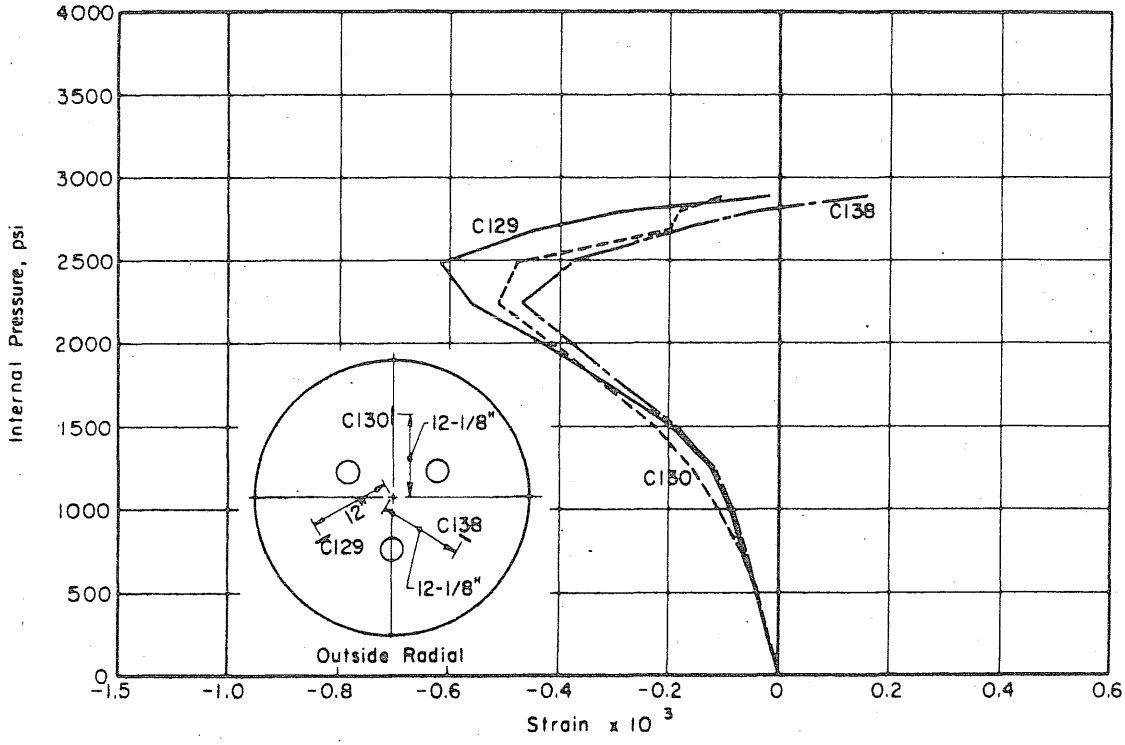

FIG. 4.36 MEASURED RADIAL STRAINS ON THE OUTSIDE FACE AND 12 In. FROM THE CENTER OF THE SLAB OF VESSEL PV17

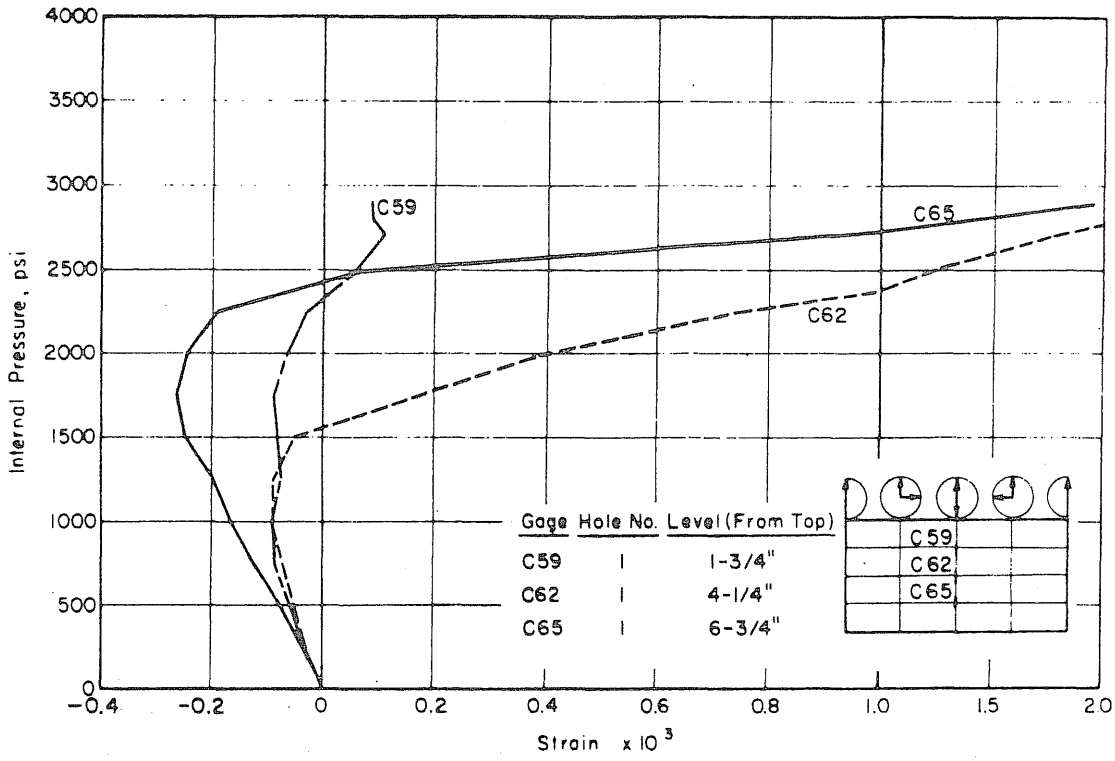

FIG. 4.37 MEASURED VERTICAL STRAINS IN ONE OF THE PENETRATIONS AND 6 in. FROM THE CENTER OF THE SLAB OF VESSEL PV17

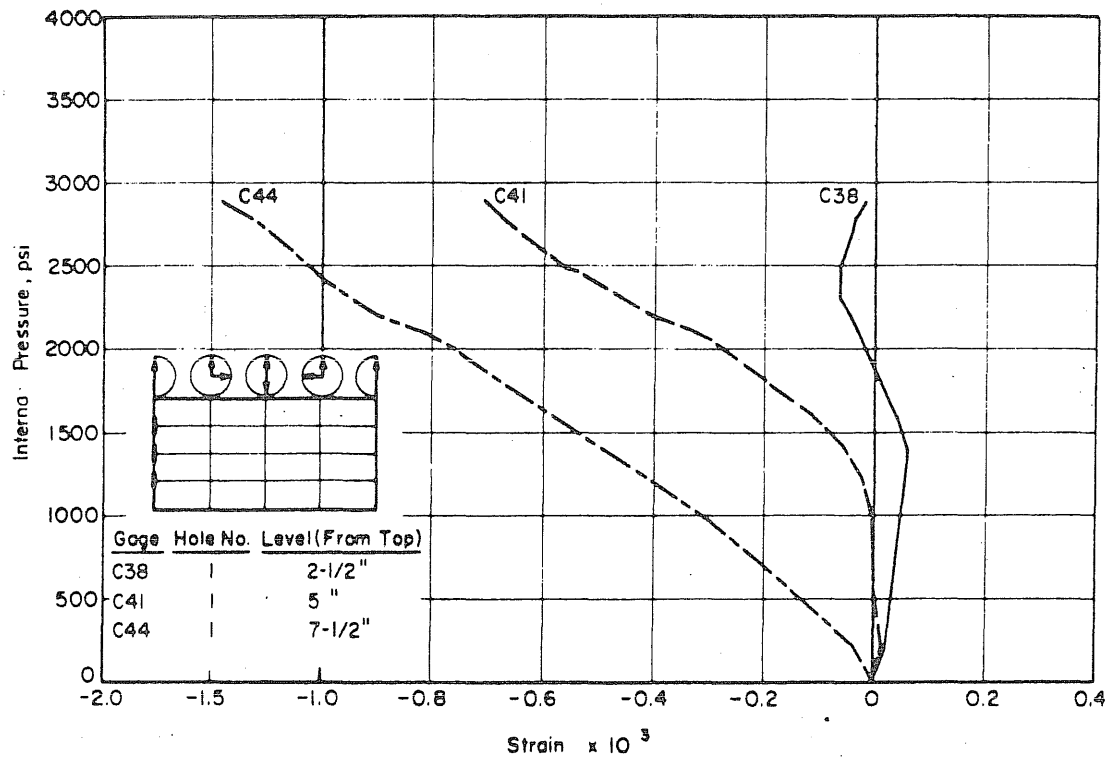

FIG. 4.38 MEASURED VERTICAL STRAINS IN ONE OF THE PENETRATIONS AND 10 in. FROM THE CENTER OF THE SLAB OF VESSEL PV18

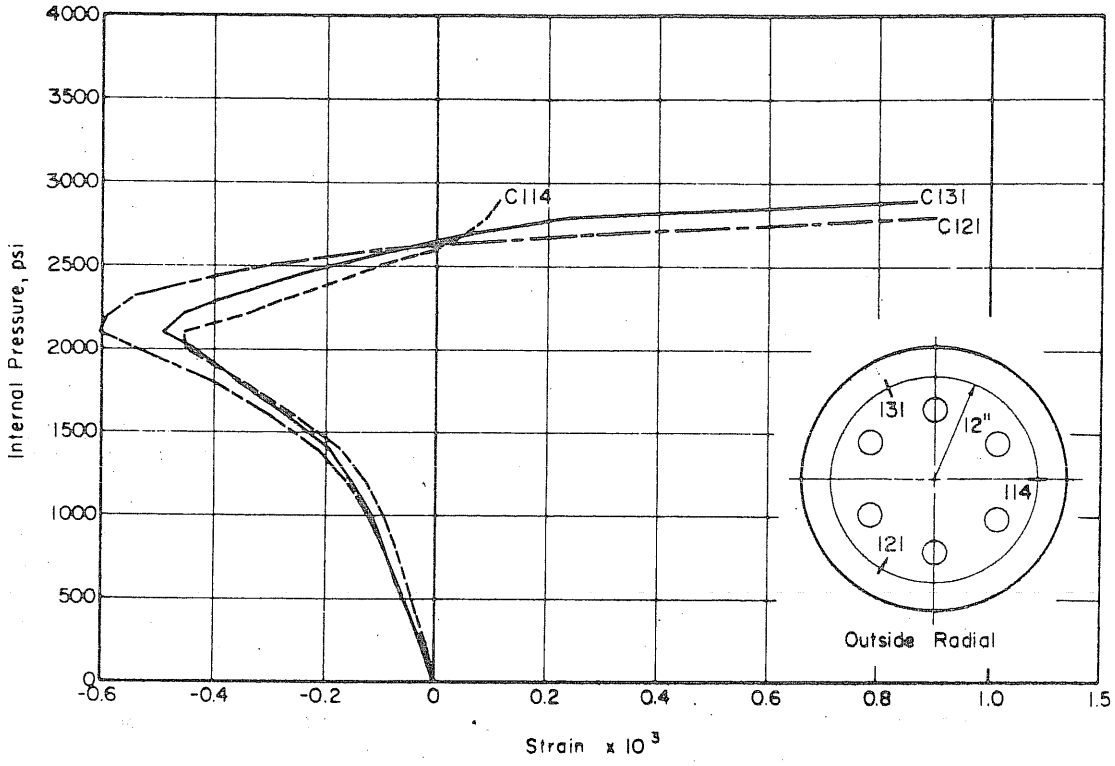

FIG. 4.39 MEASURED RADIAL STRAINS ON THE OUTSIDE FACE AND 12 In. FROM THE CENTER OF THE SLAB OF VESSEL PV18

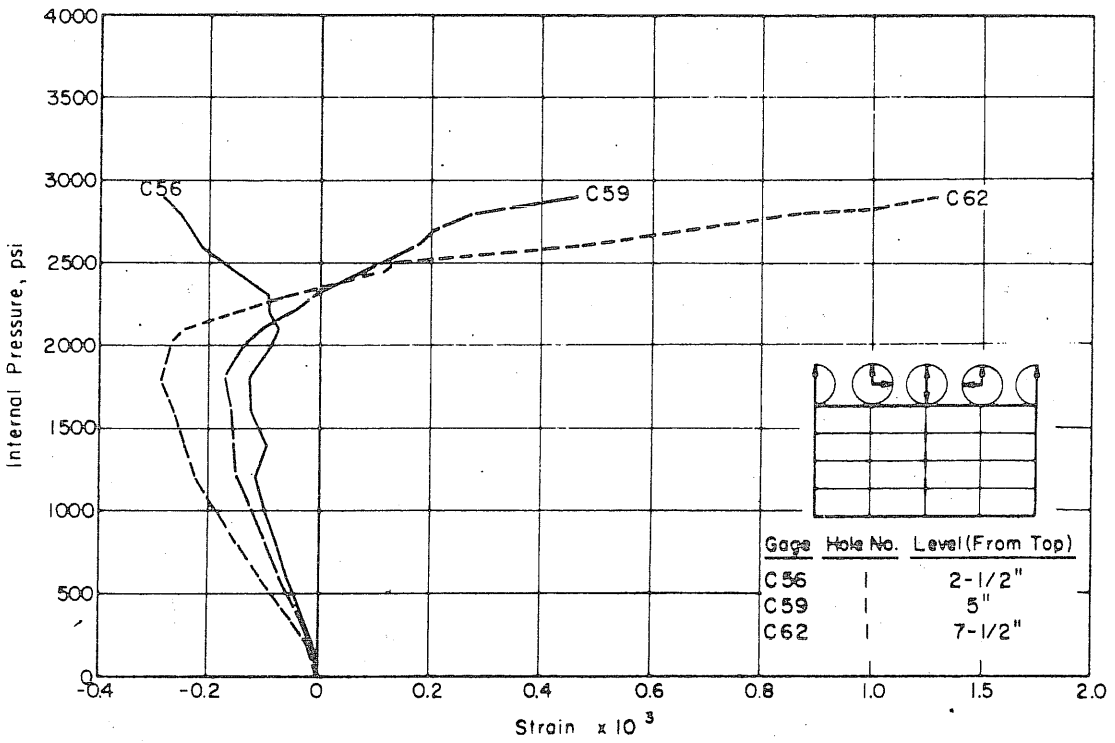

BIG. 4.40 MEASURED VERTICAL STRAINS IN ONE OF THE PENETRATIONS AND 6 in. FROM THE CENTER OF THE SLAB OF VESSEL PV18

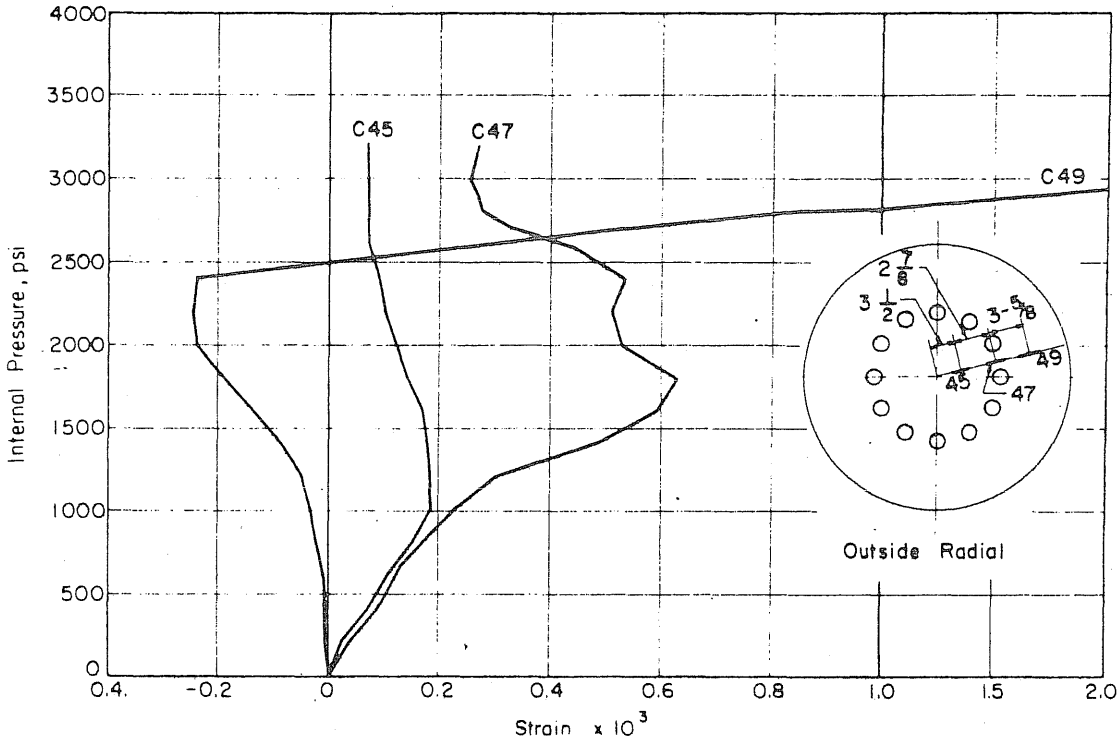

FIG. 4.41 MEASURED RADIAL STRAINS ON THE OUTSIDE FACE OF THE SLAB OF VESSEL PV20

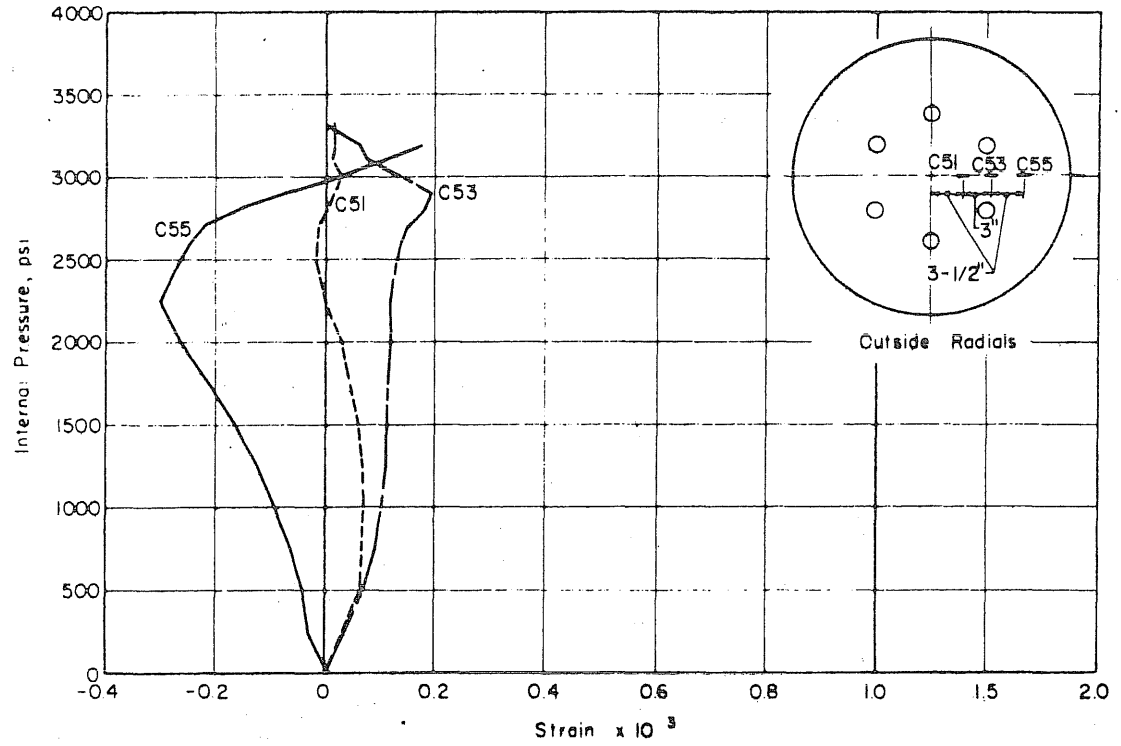

FIG. 4.42 MEASURED RADIAL STRAINS ON THE OUTSIDE FACE OF THE SLAB OF VESSEL PV21

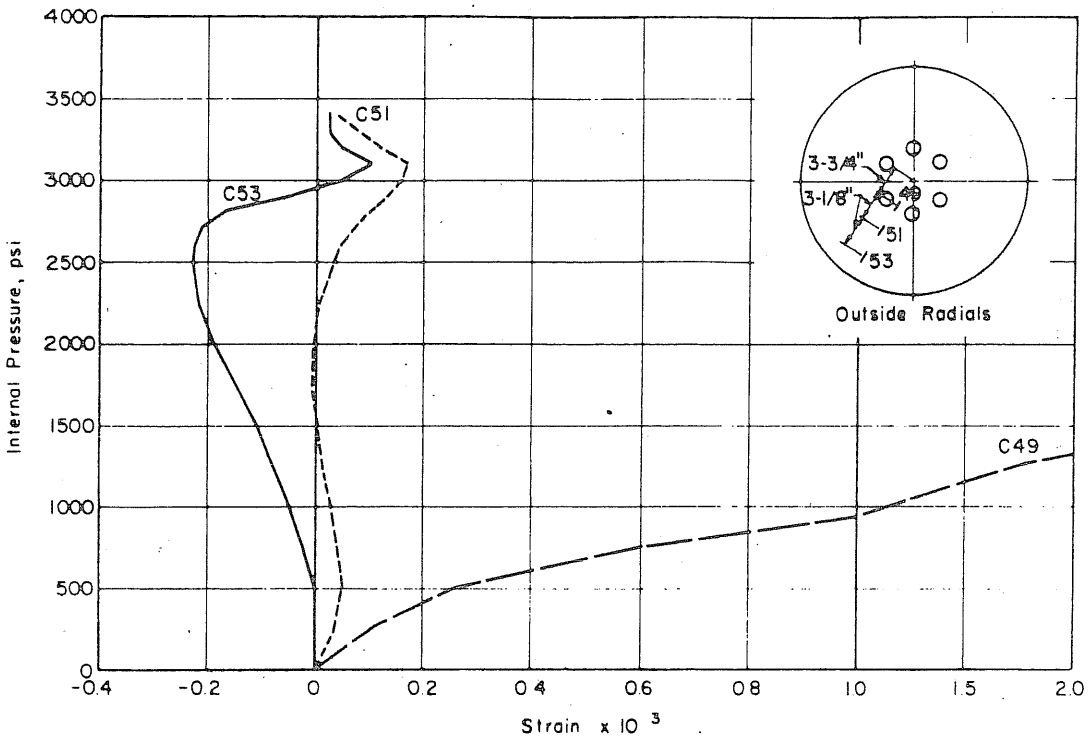

FIG. 4.43 MEASURED RADIAL STRAINS ON THE OUTSIDE FACE OF THE SLAB OF VESSEL PV19

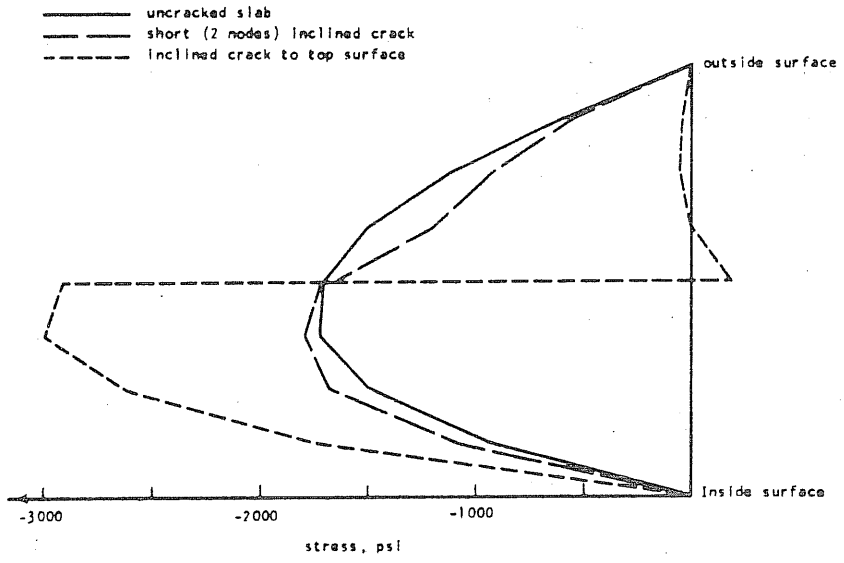

FIG. 4.44 DISTRIBUTION OF SHEAR STRESSES THROUGH A SOLID END SLAB FOR DIFFERENT CRACK CONFIGURATIONS ACCORDING TO THE FINITE-ELEMENT SOLUTIONS

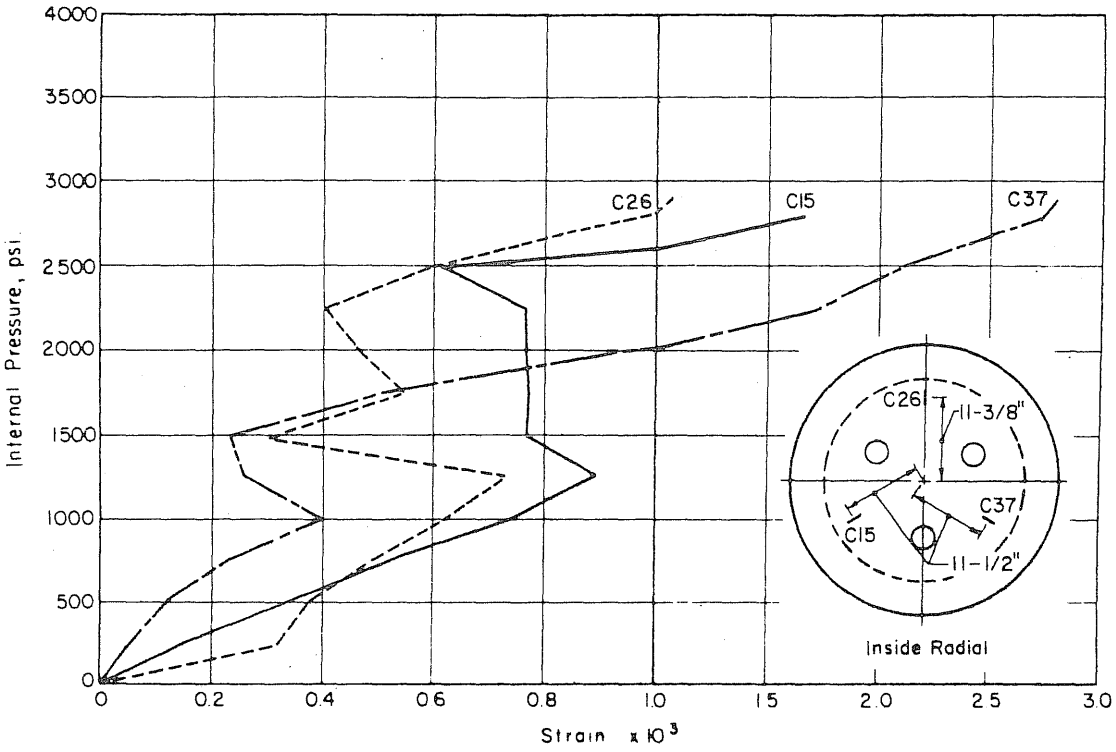

FIG. 4.45 MEASURED RADIAL STRAINS ON THE INSIDE FACE AND 11-1/2 in. FROM THE CENTER OF THE SLAB OF VESSEL PV17

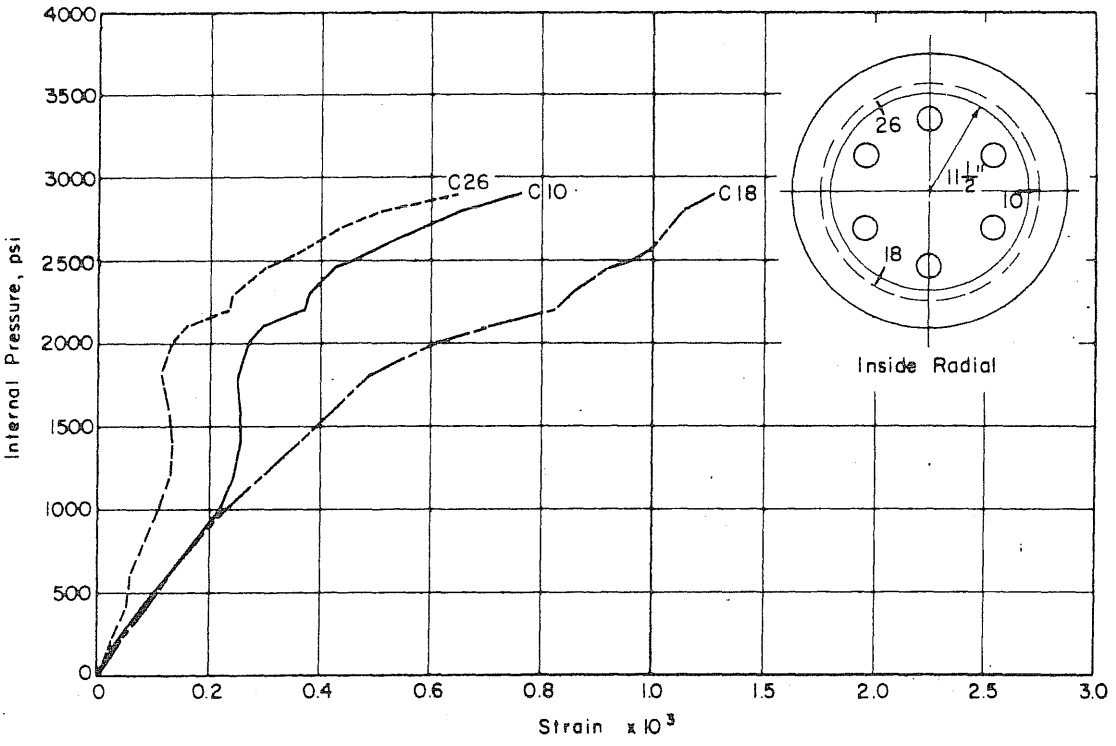

FIG. 4.46 MEASURED RADIAL STRAINS ON THE INSIDE FACE AND 11-1/2 in. FROM THE CENTER OF THE SLAB OF VESSEL PV18

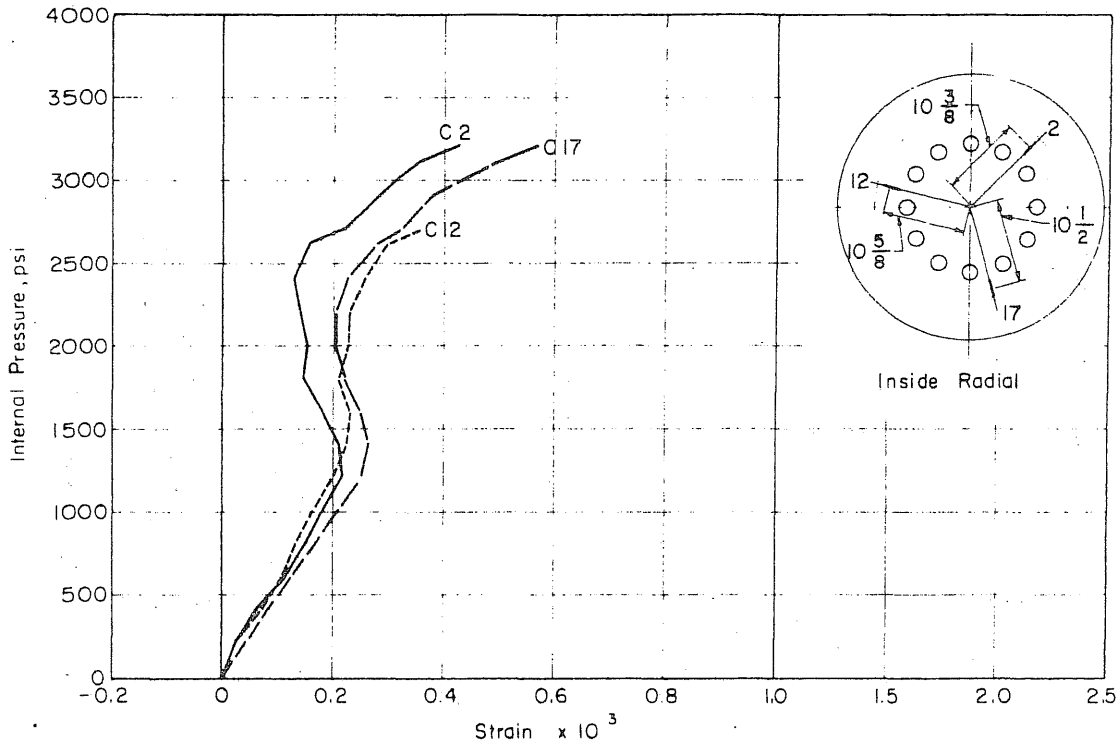

FIG. 4.47 MEASURED RADIAL STRAINS ON THE INSIDE FACE AND 10-1/2 in. FROM THE CENTER OF THE SLAB OF VESSEL PV20

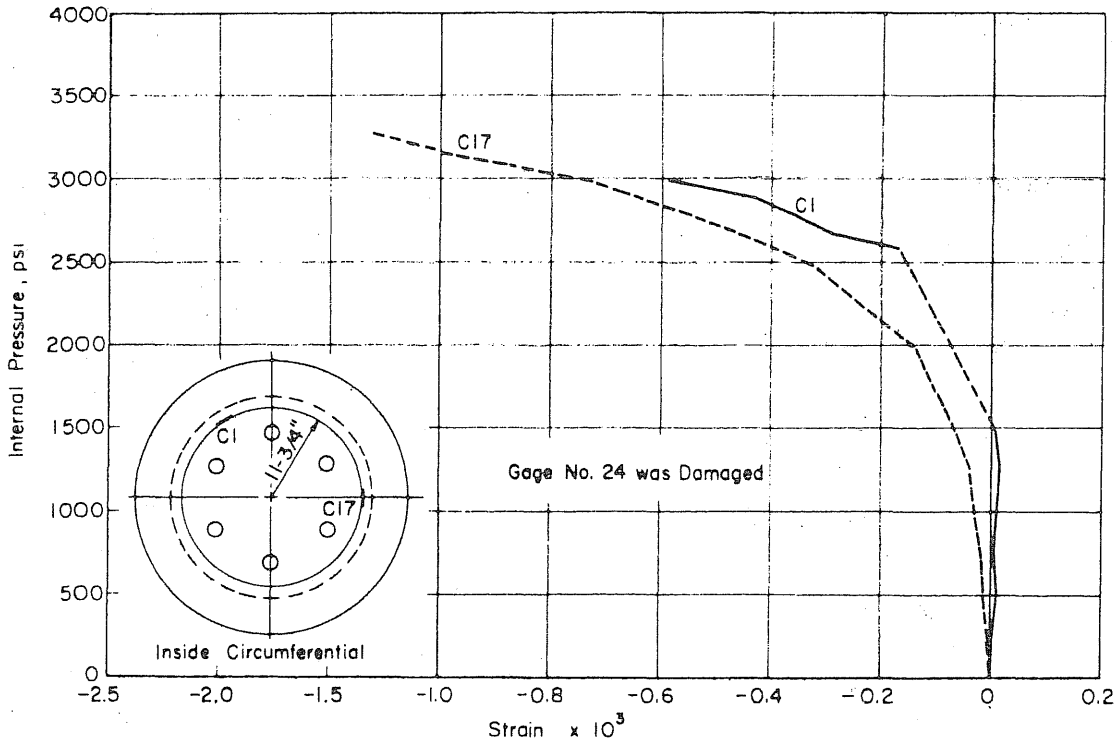

FIG. 4.48 MEASURED TANGENTIAL STRAINS ON THE INSIDE FACE AND 11-3/4 in. FROM THE CENTER OF THE SLAB OF VESSEL PV21

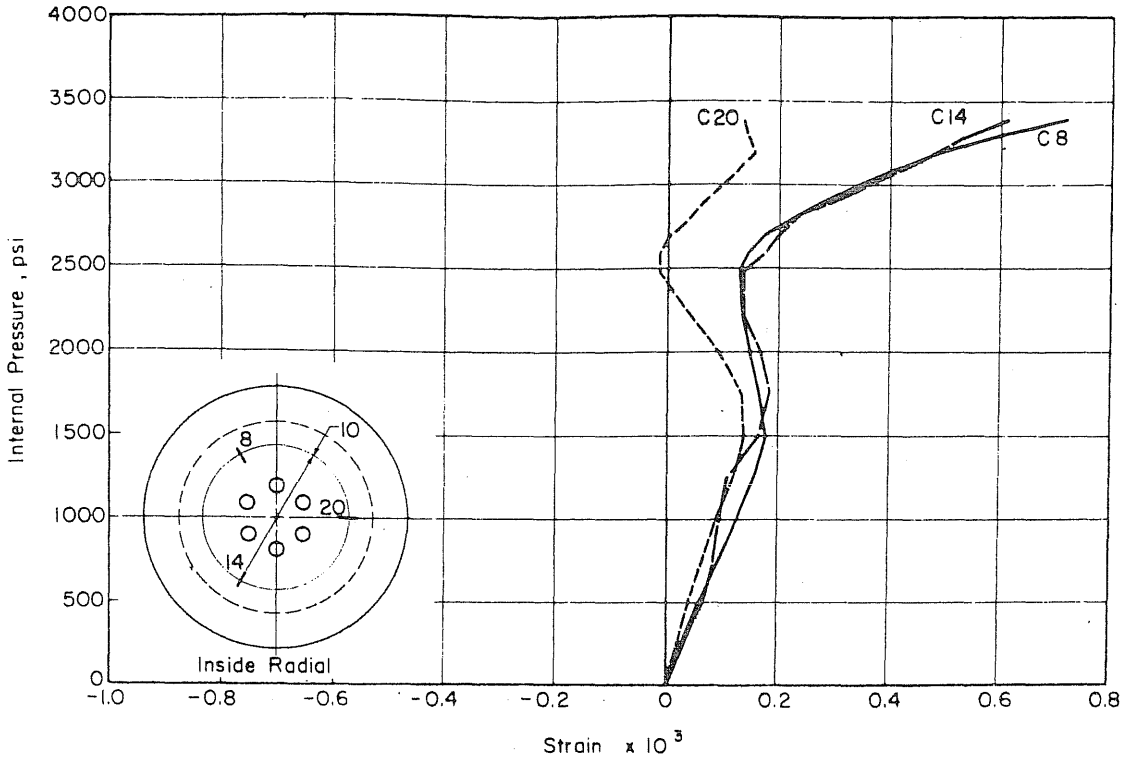

FIG. 4.49 MEASURED RADIAL STRAINS ON THE INSIDE FACE AND 10 in. FROM THE CENTER OF THE SLAB OF VESSEL PV19

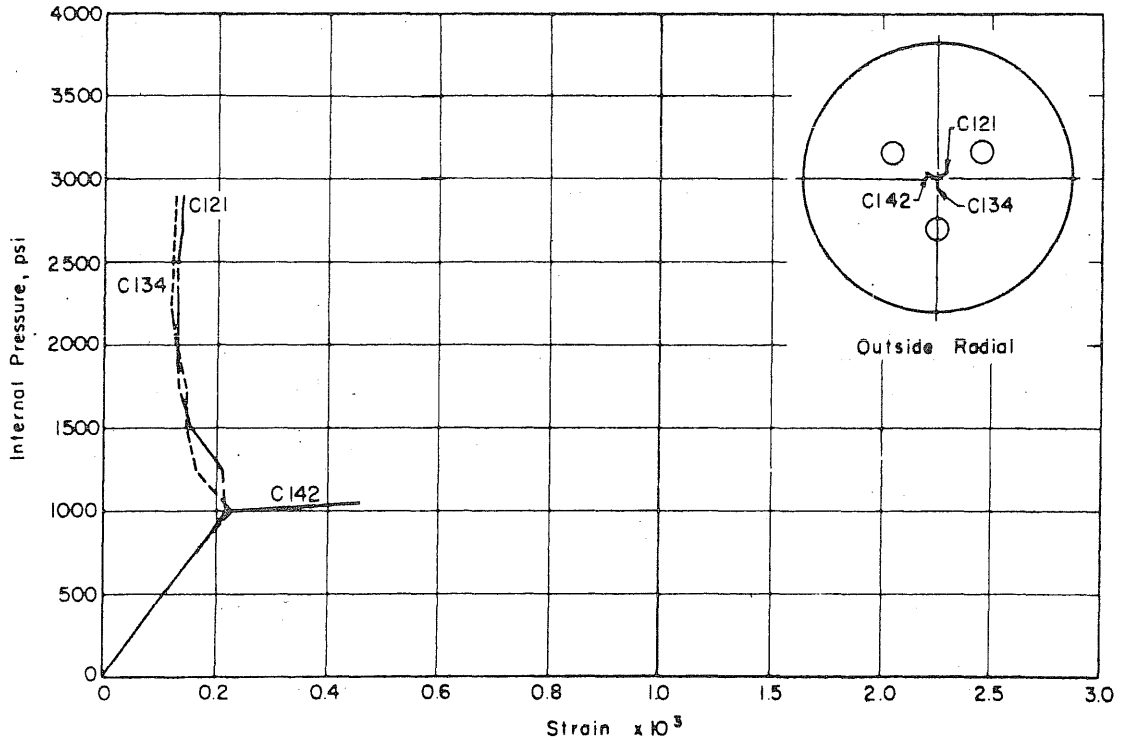

FIG. 4.50 MEASURED STRAINS ON THE OUTSIDE FACE AND AT THE CENTER OF THE SLAB OF VESSEL PV17

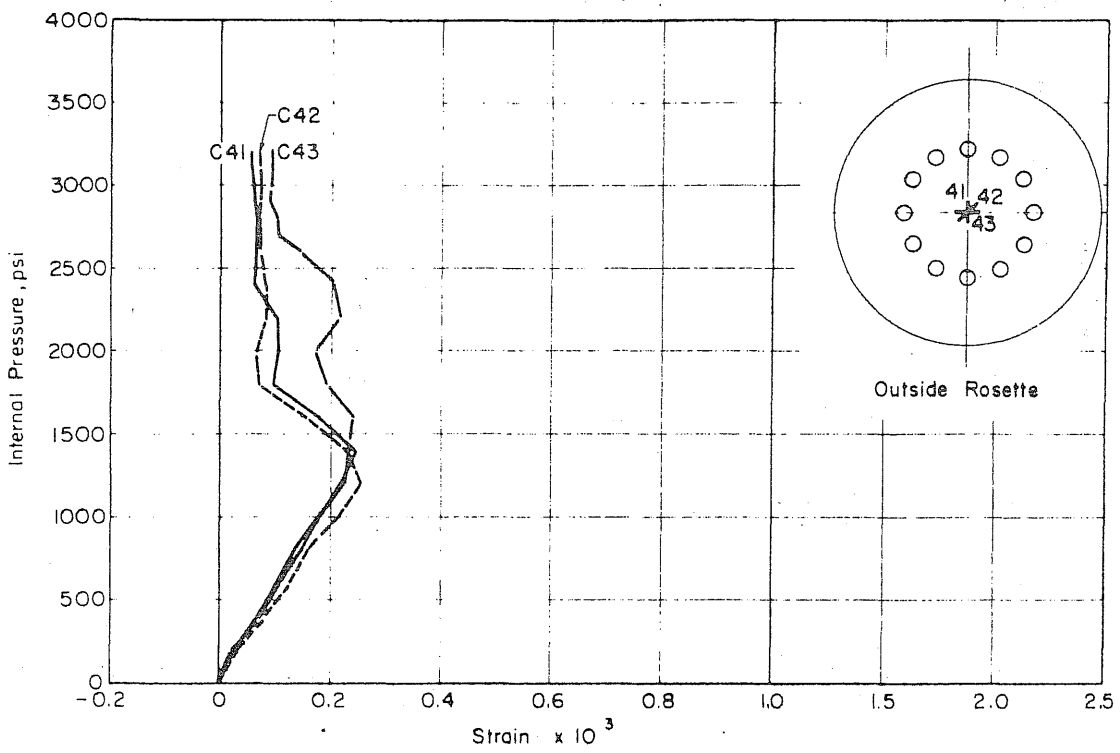

FIG. 4.51 MEASURED STRAINS ON THE OUTSIDE FACE AND AT THE CENTER OF THE SLAB OF VESSEL PV20

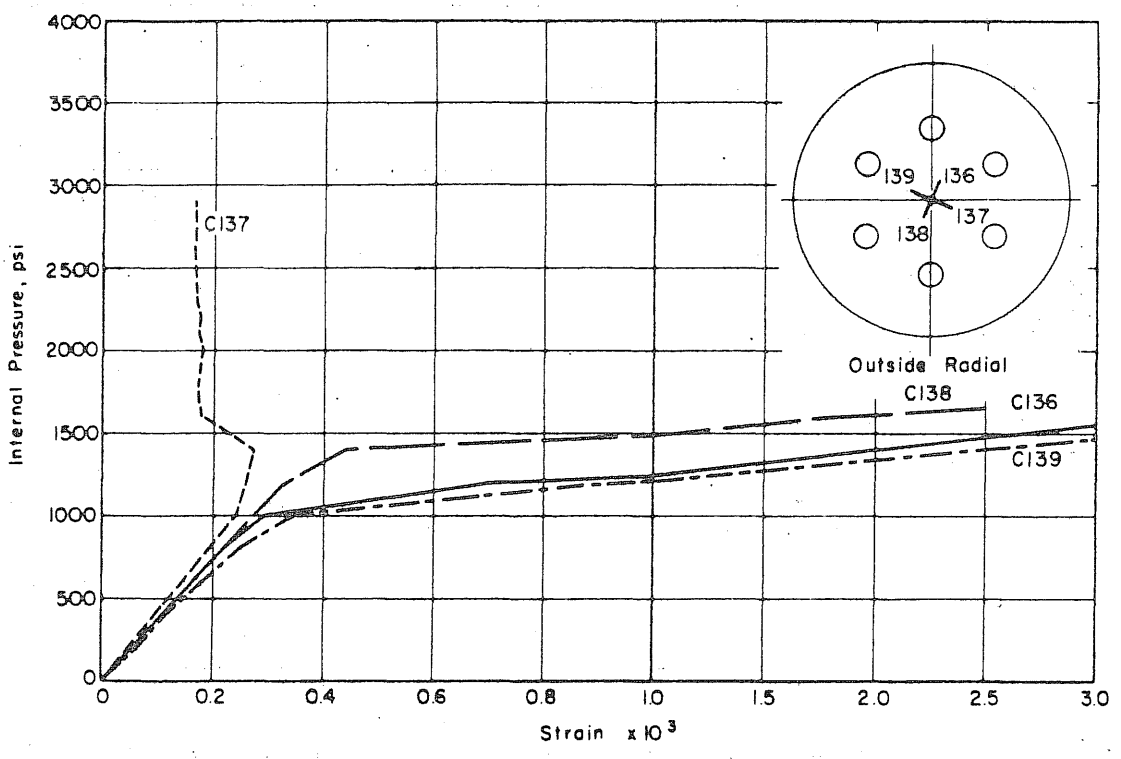

FIG. 4.52 MEASURED STRAINS ON THE OUTSIDE FACE AND AT THE CENTER OF THE SLAB OF VESSEL PV18

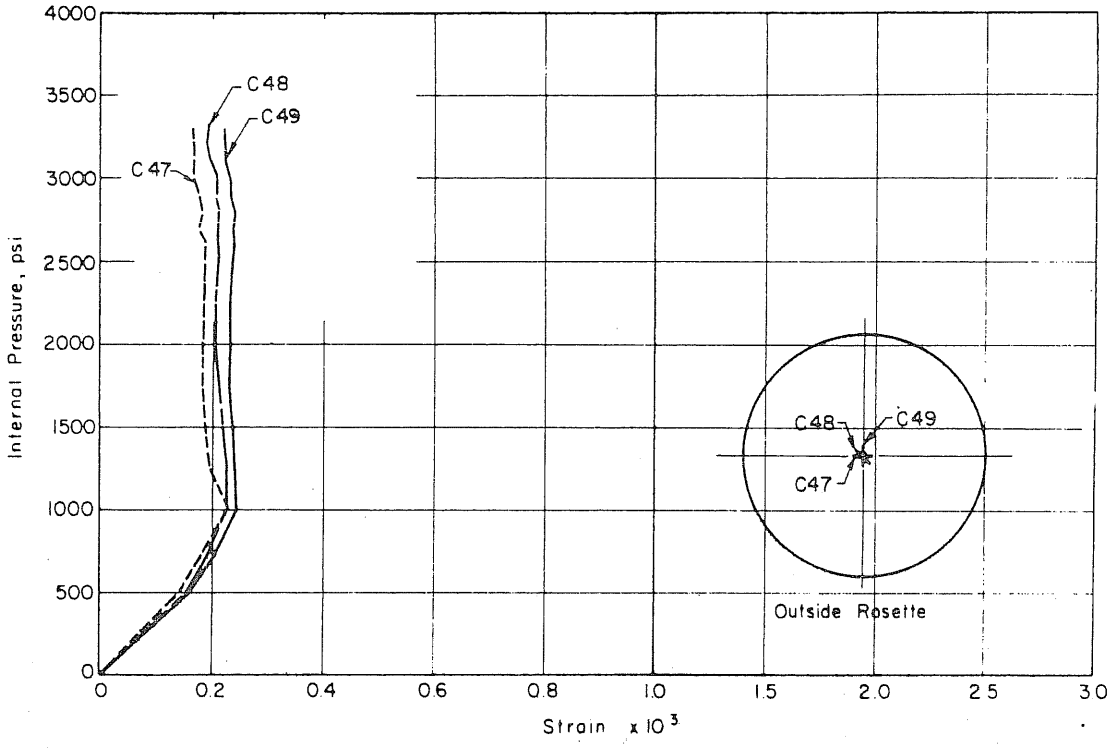

FIG. 4.53 MEASURED STRAINS ON THE OUTSIDE FACE AND AT THE CENTER OF THE SLAB OF VESSEL PV21

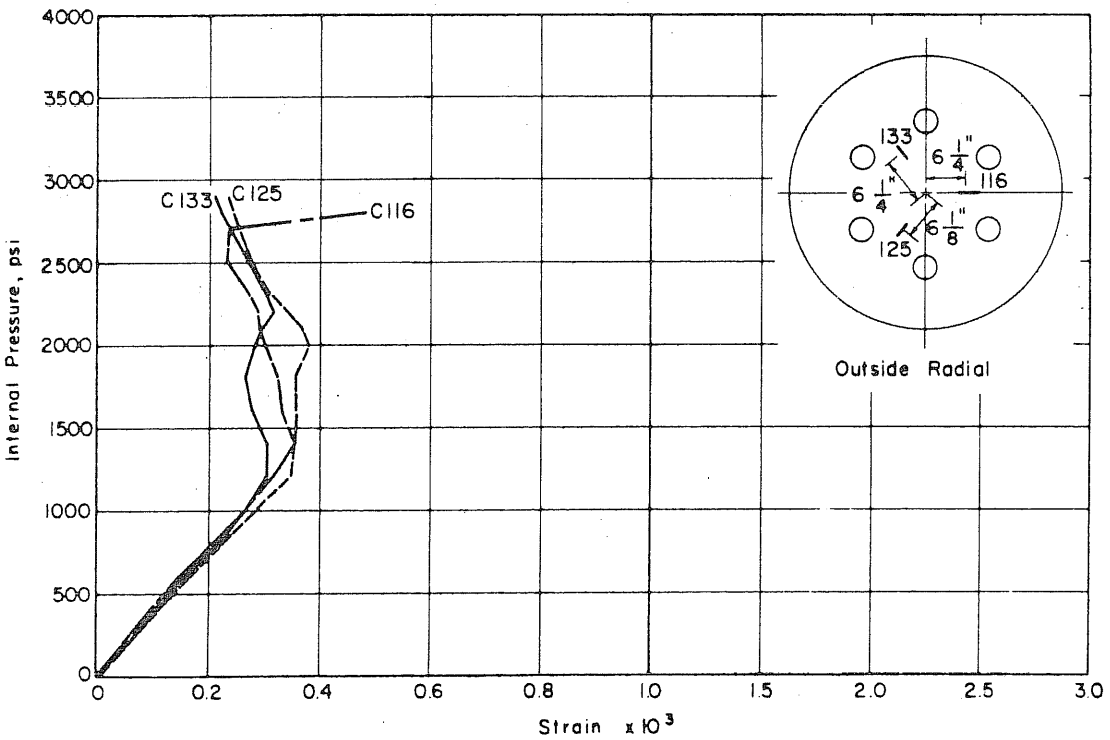

FIG. 4.54 MEASURED RADIAL STRAINS ON THE OUTSIDE FACE AND 6-1/4 in. FROM THE CENTER OF THE SLAB OF VESSEL PV18

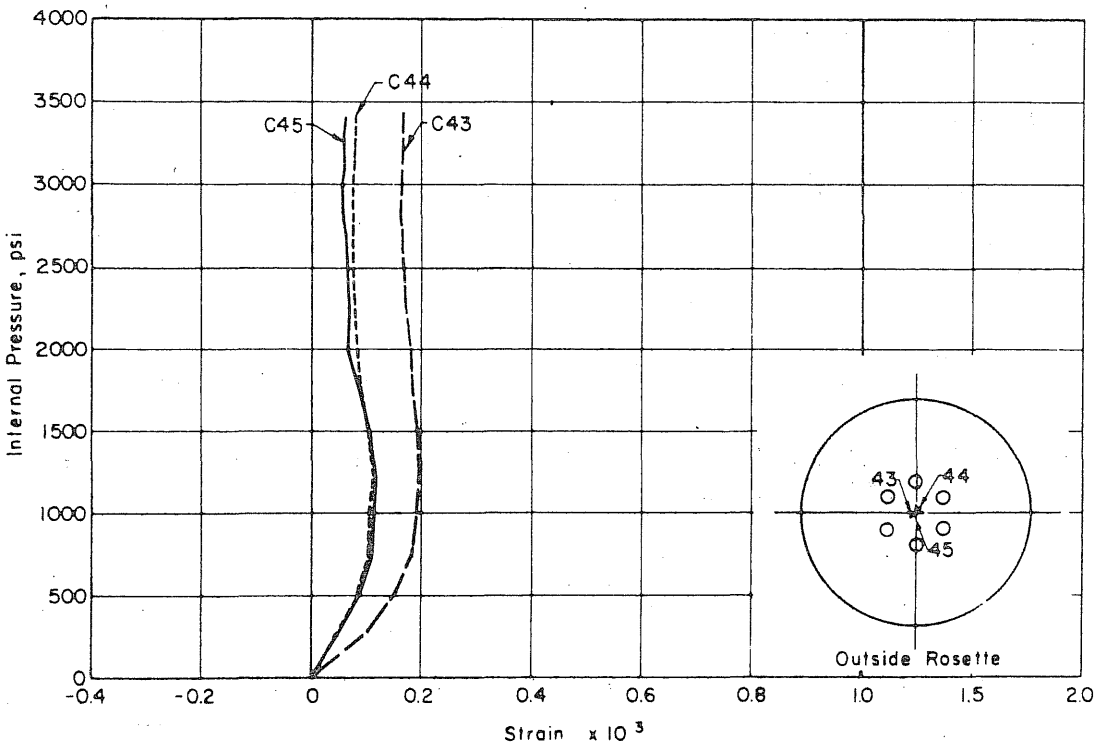

FIG. 4.55 MEASURED STRAINS ON THE OUTSIDE FACE AND AT THE CENTER OF THE SLAB OF VESSEL PV19

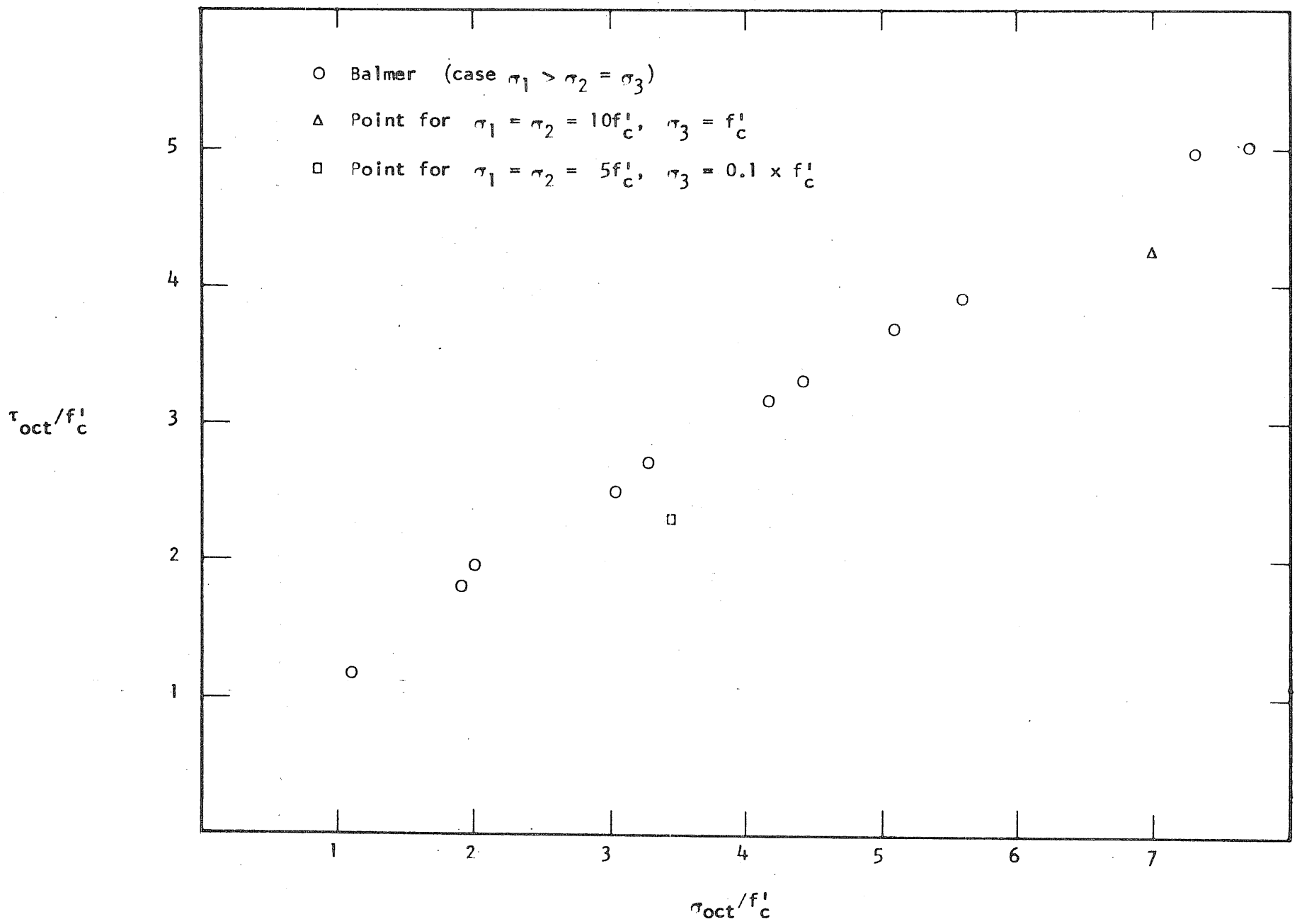

FIG. 5.1 OCTAHEDRAL SHEARING STRESS VS OCTAHEDRAL NORMAL STRESS CALCULATED FROM TEST DATA OBTAINED BY BALMER (1949). COMPARISON WITH TWO HYPOTHETICAL POINTS.

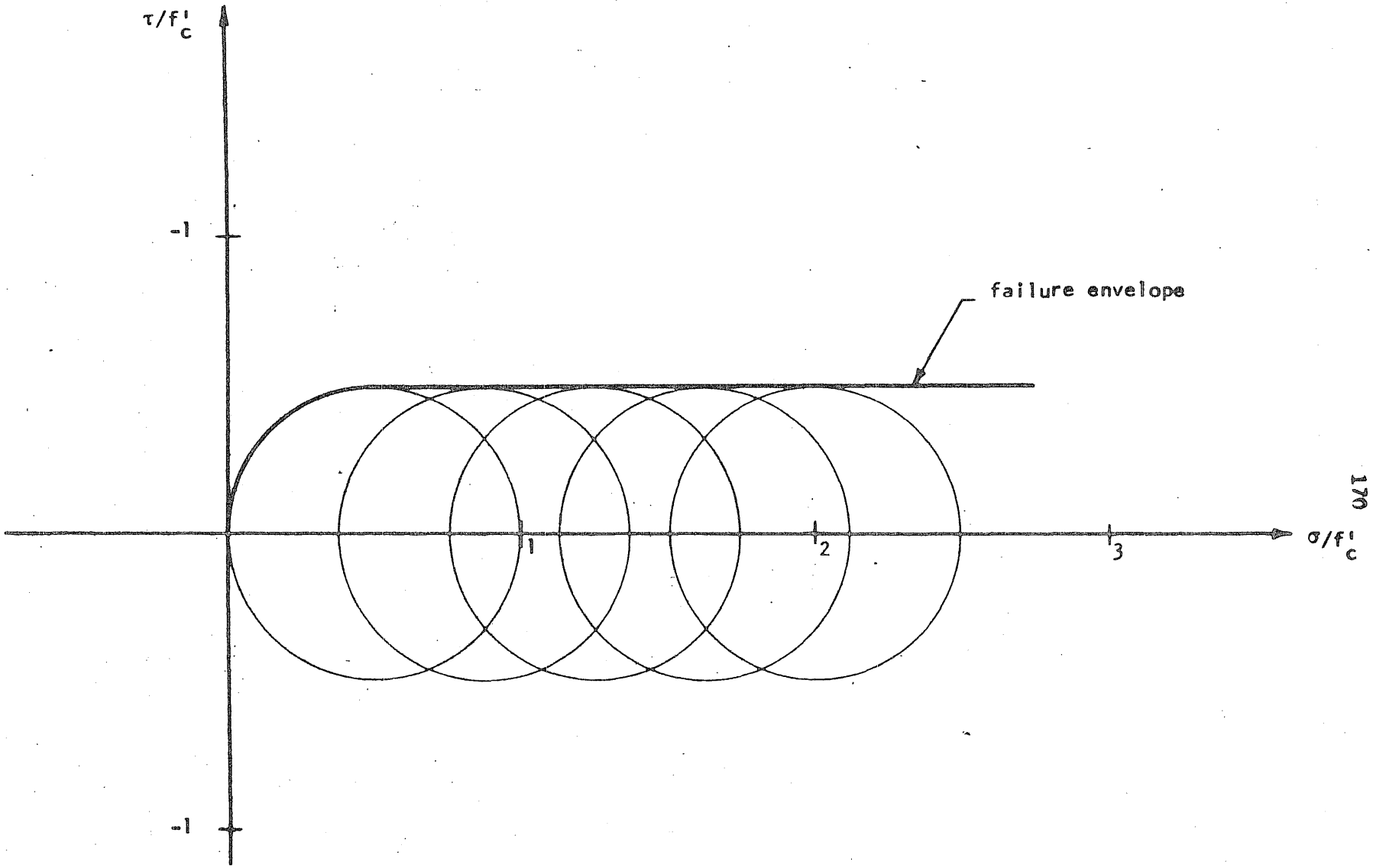

FIG. 5.2 FAILURE ENVELOPE USING THE MAXIMUM DISTORSION ENERGY THEORY

FIG. 5.3 FAILURE SURFACE ACCORDING TO HANNANT AND FREDERICK

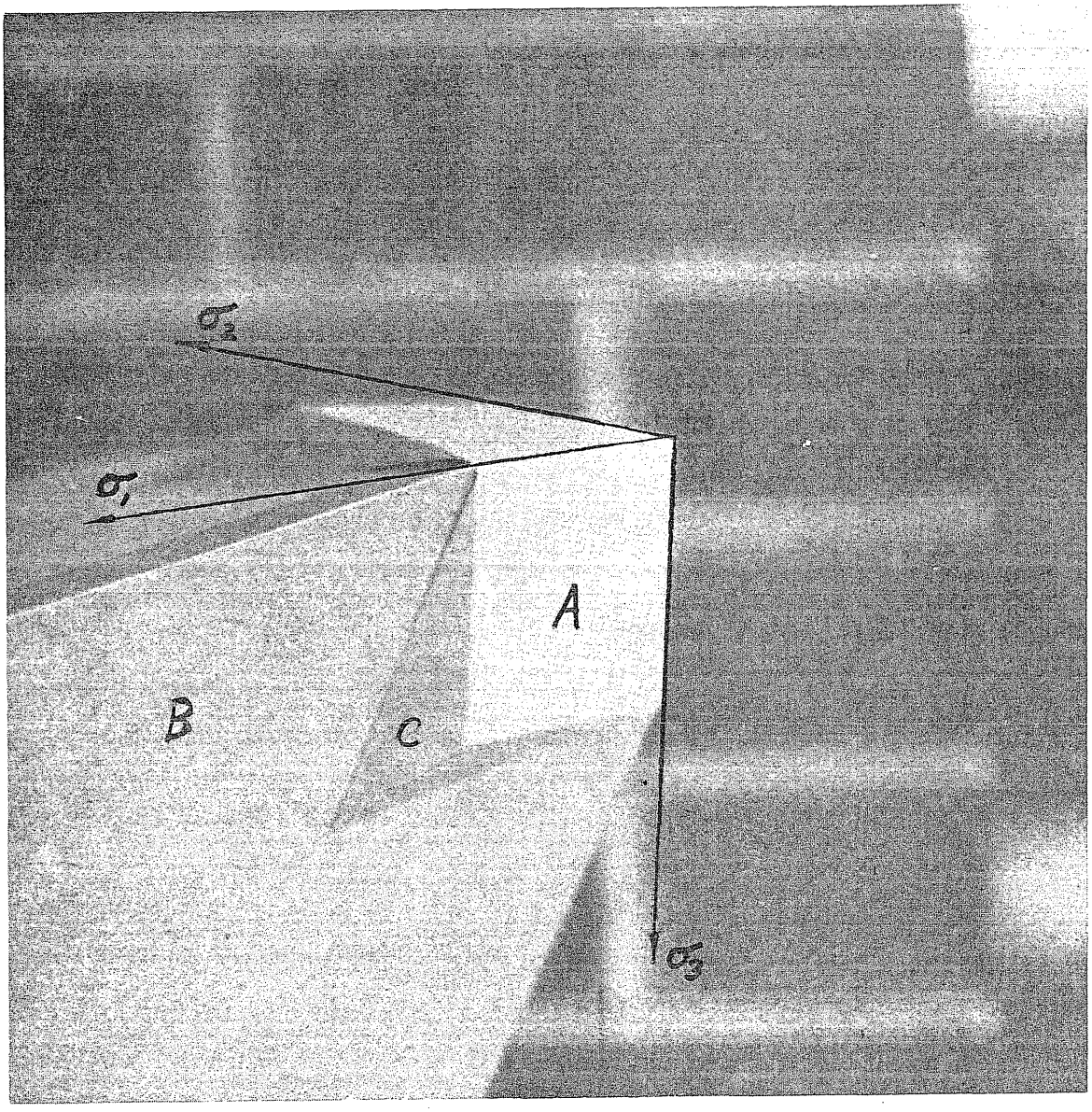

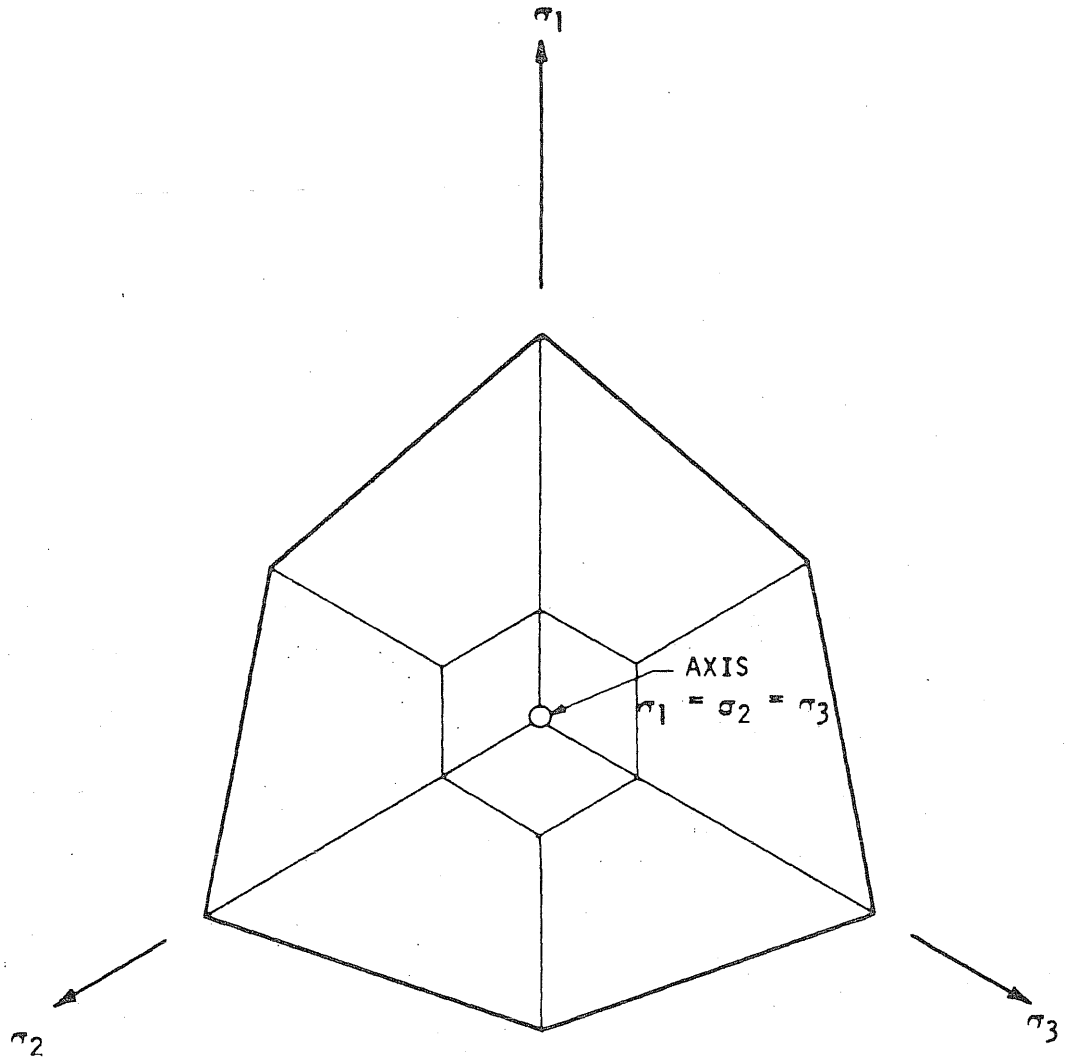

FIG. 5.4 SECTION THROUGH FAILURE SURFACE

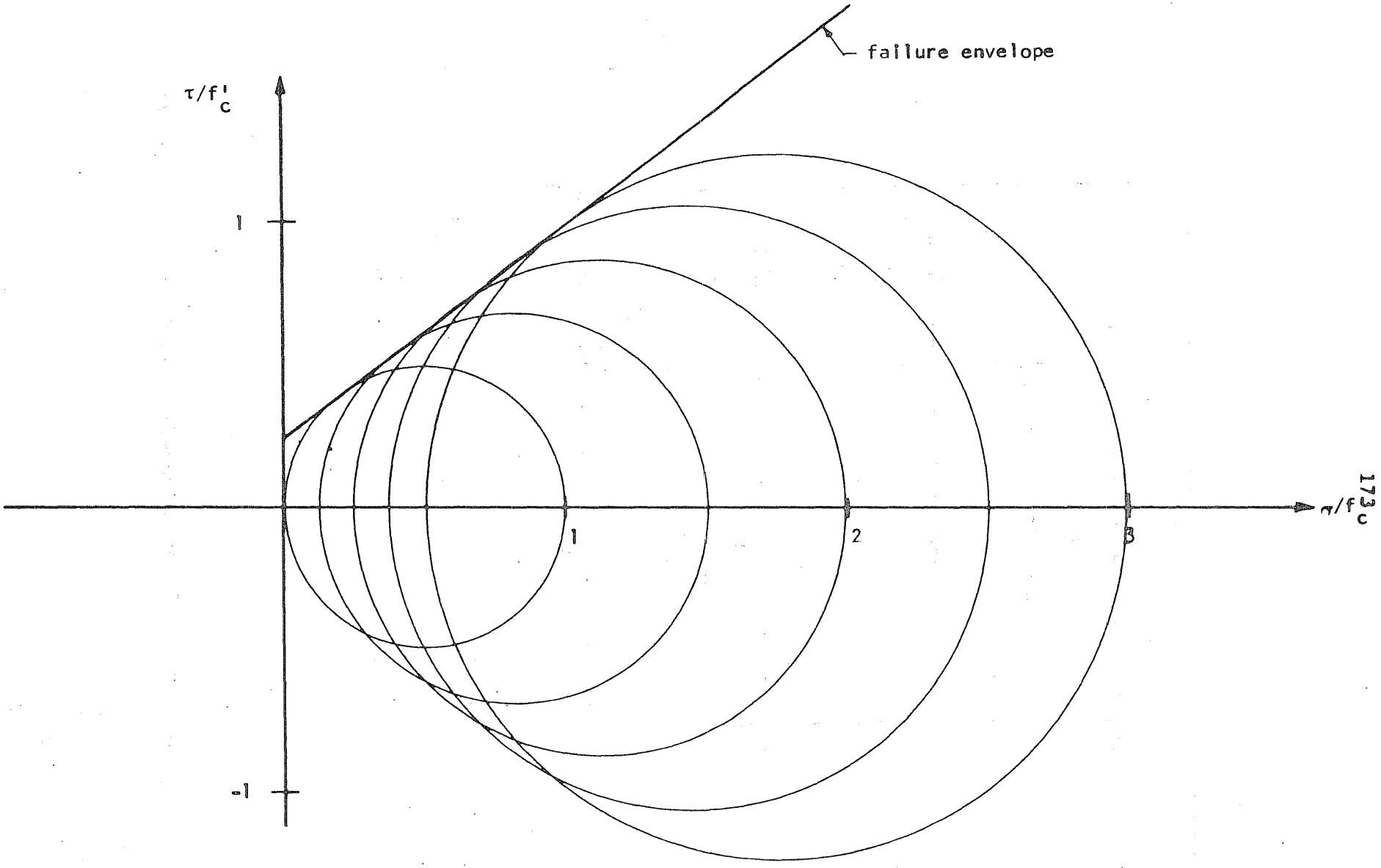

FIG. 5.5 FAILURE ENVELOPE BASED ON MOHR'S STRESS CIRCLES

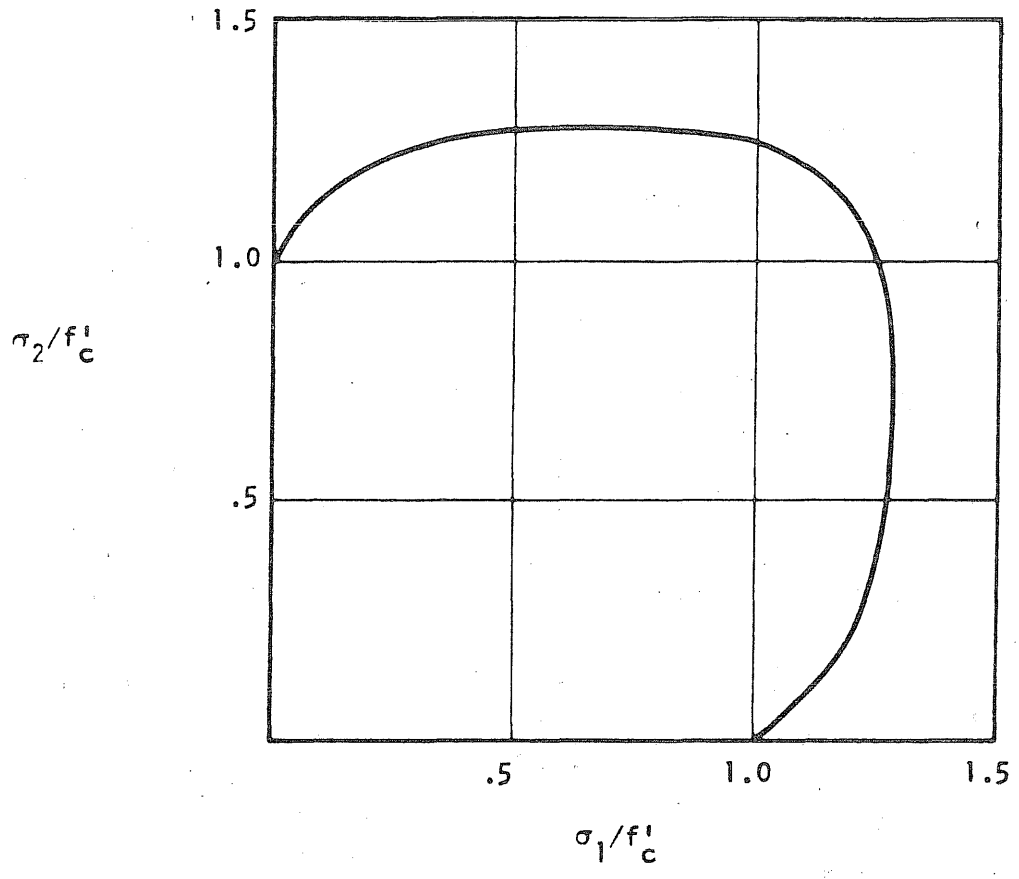

FIG. 5.6 STRENGTH OF CONCRETE UNDER BIAXIAL COMPRESSION

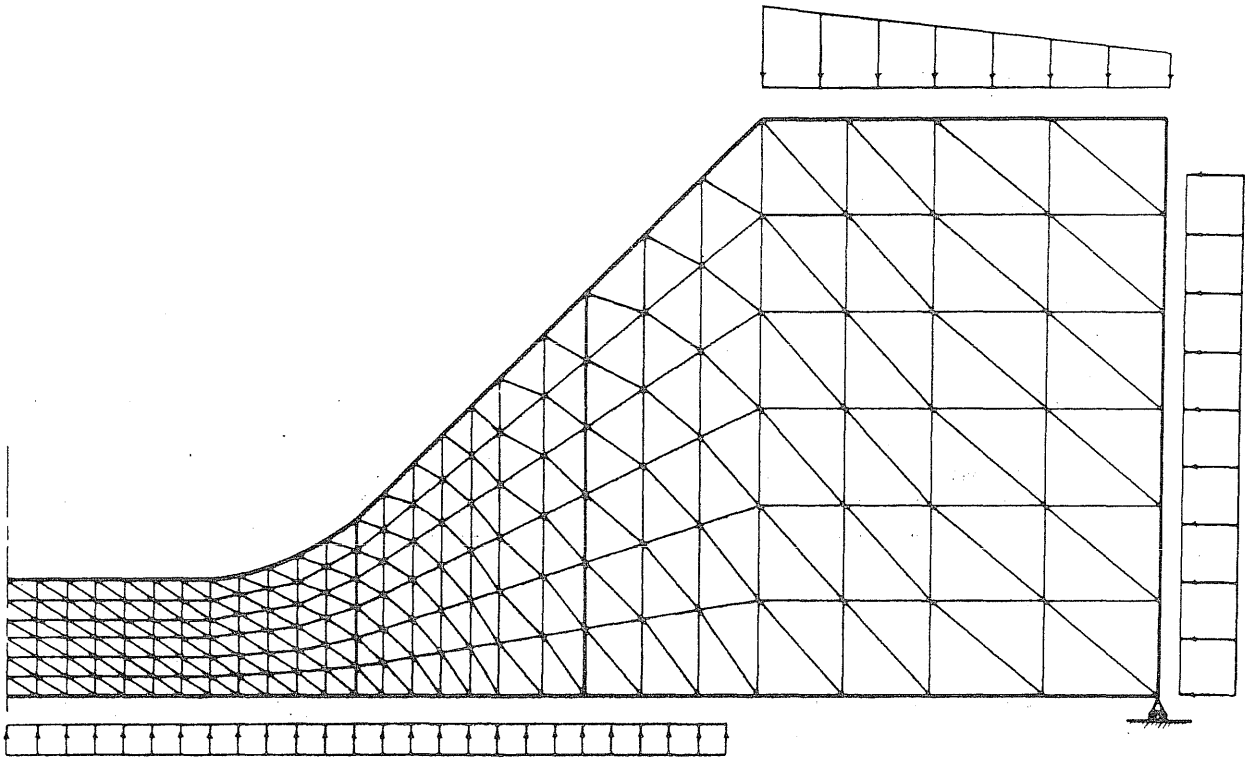

FIG. 6.1 FINITE-ELEMENT MODEL USED IN ANALYZING THE STRESS CONDITIONS IN THE CRYPTODOME

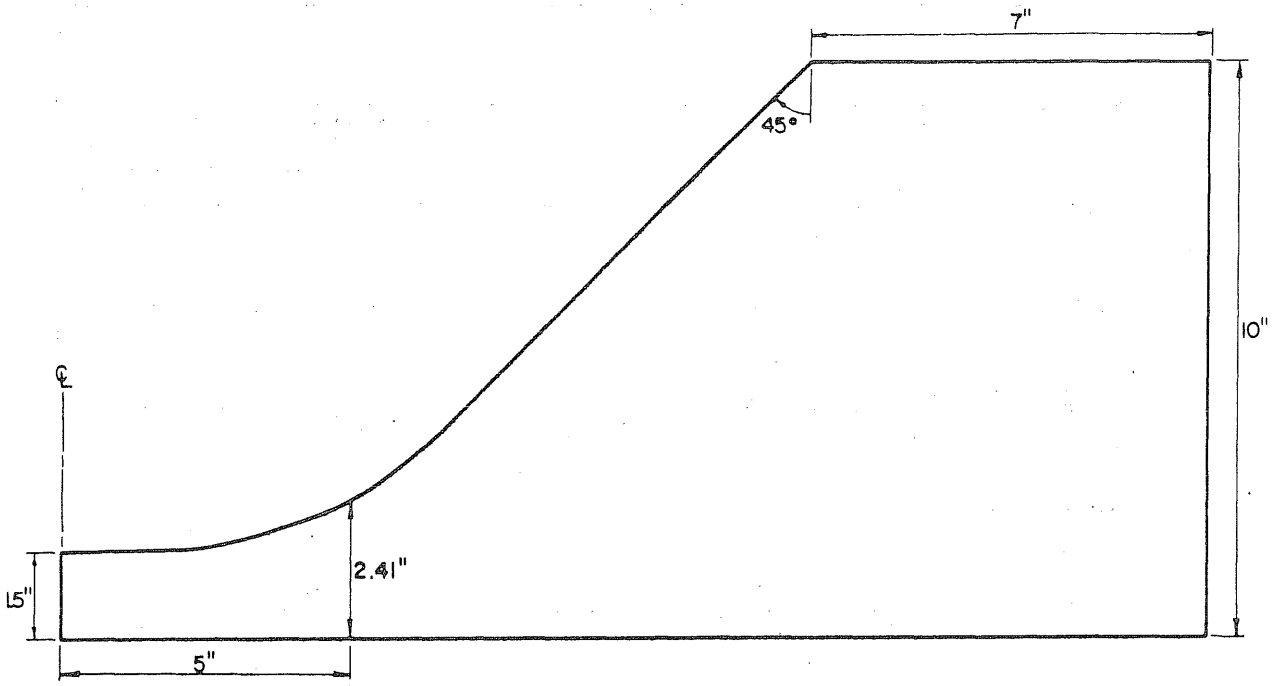

FIG. 6.2 A PLAUSIBLE SHAPE OF THE CRYPTODOME IN VESSEL PV16

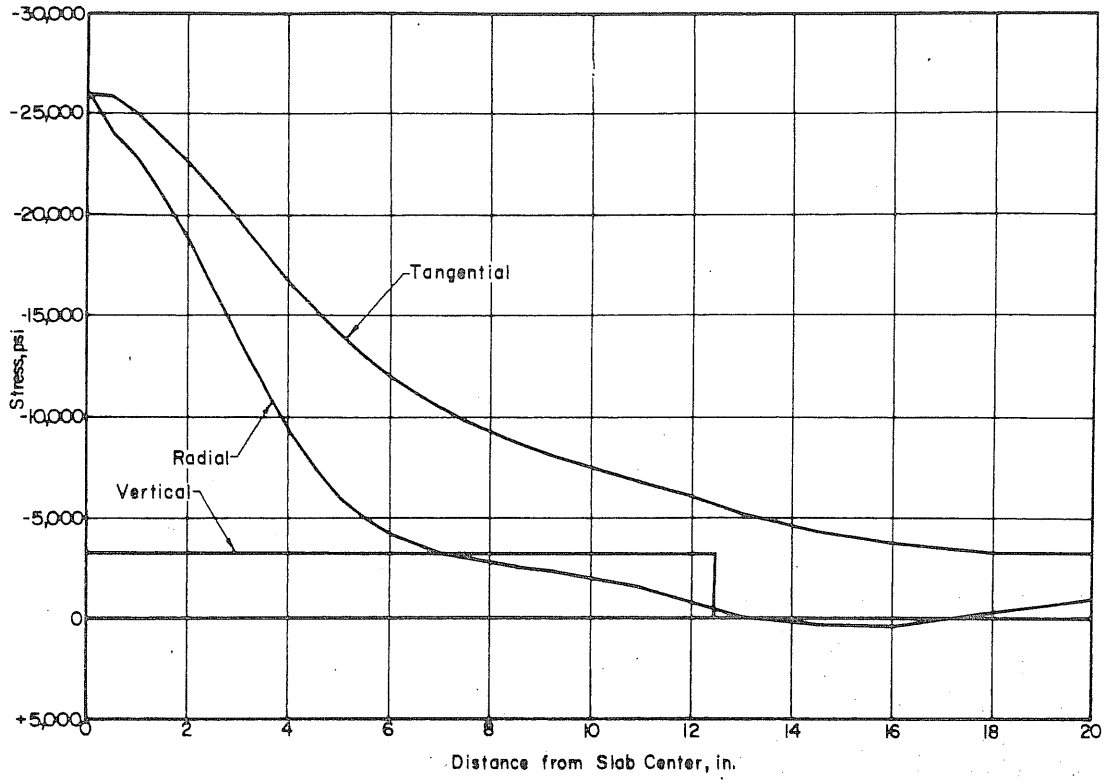

FIG. 6.3 CALCULATED STRESSES ALONG THE INSIDE SURFACE OF THE DOME IN FIG. 6.2 AT 3200 psi INTERNAL PRESSURE

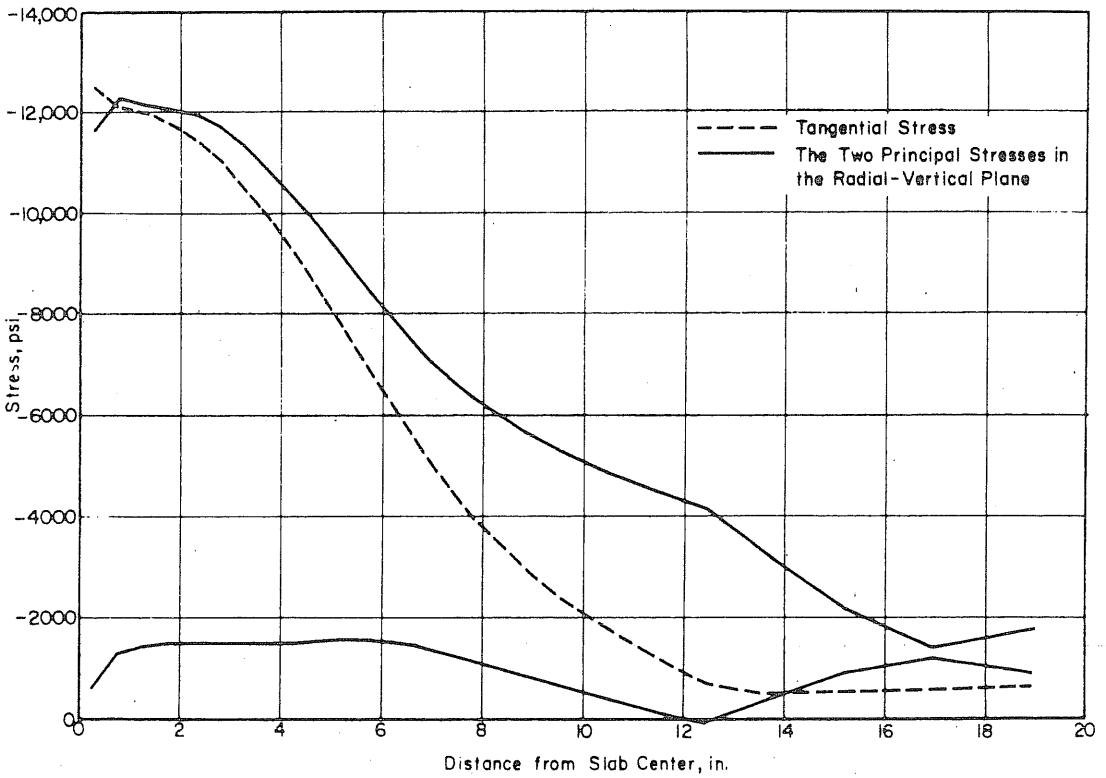

FIG. 6.4 PRINCIPAL STRESSES BASED ON AVERAGE STRESSES AT EACH VERTICAL SECTION OF THE DOME IN FIG. 6.2

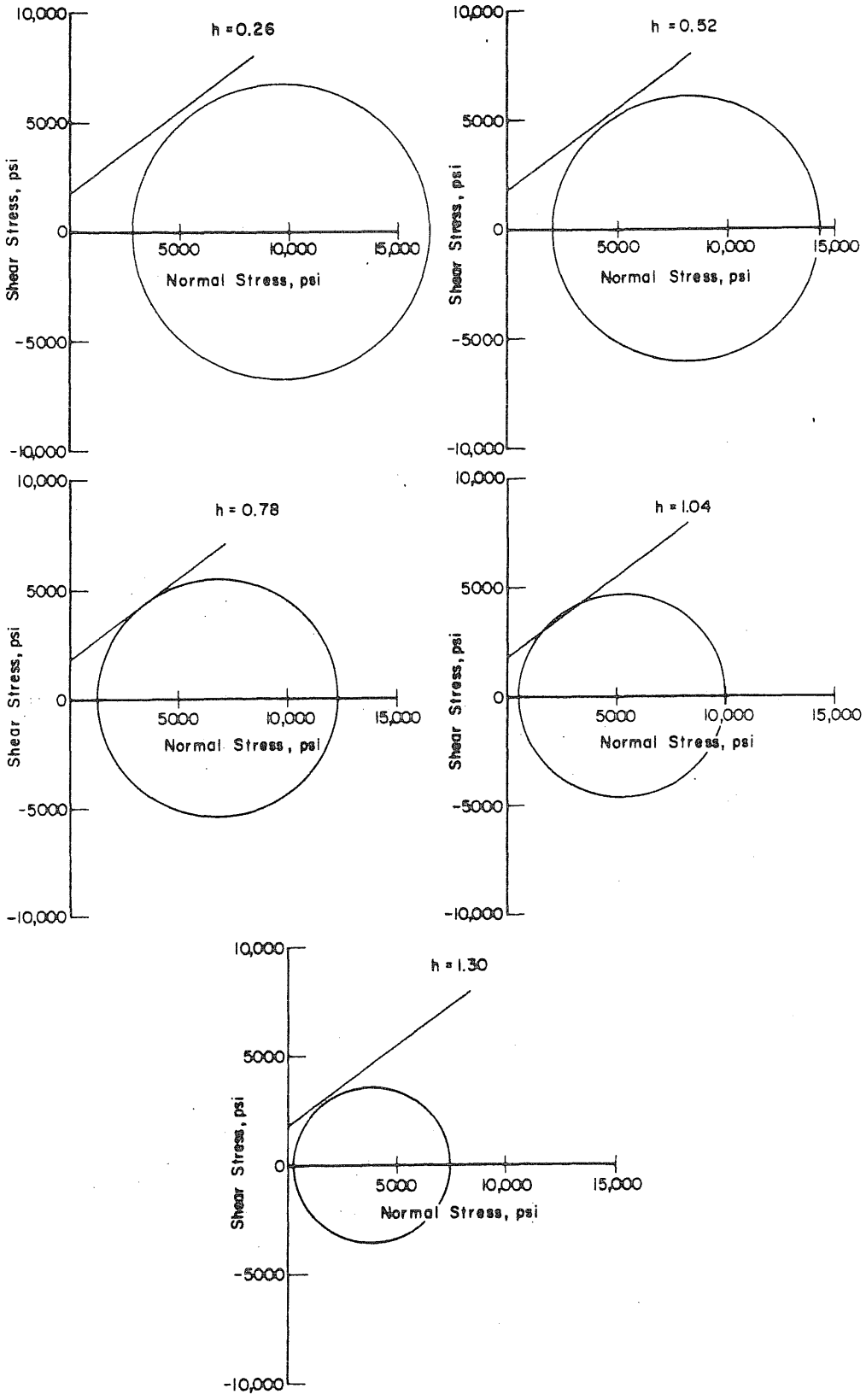

FIG. 6.5 CALCULATED PRINCIPAL STRESSES AT DIFFERENT HEIGHTS, 2 in. FROM THE CENTER OF THE CRYPTODOME IN FIG. 6.2

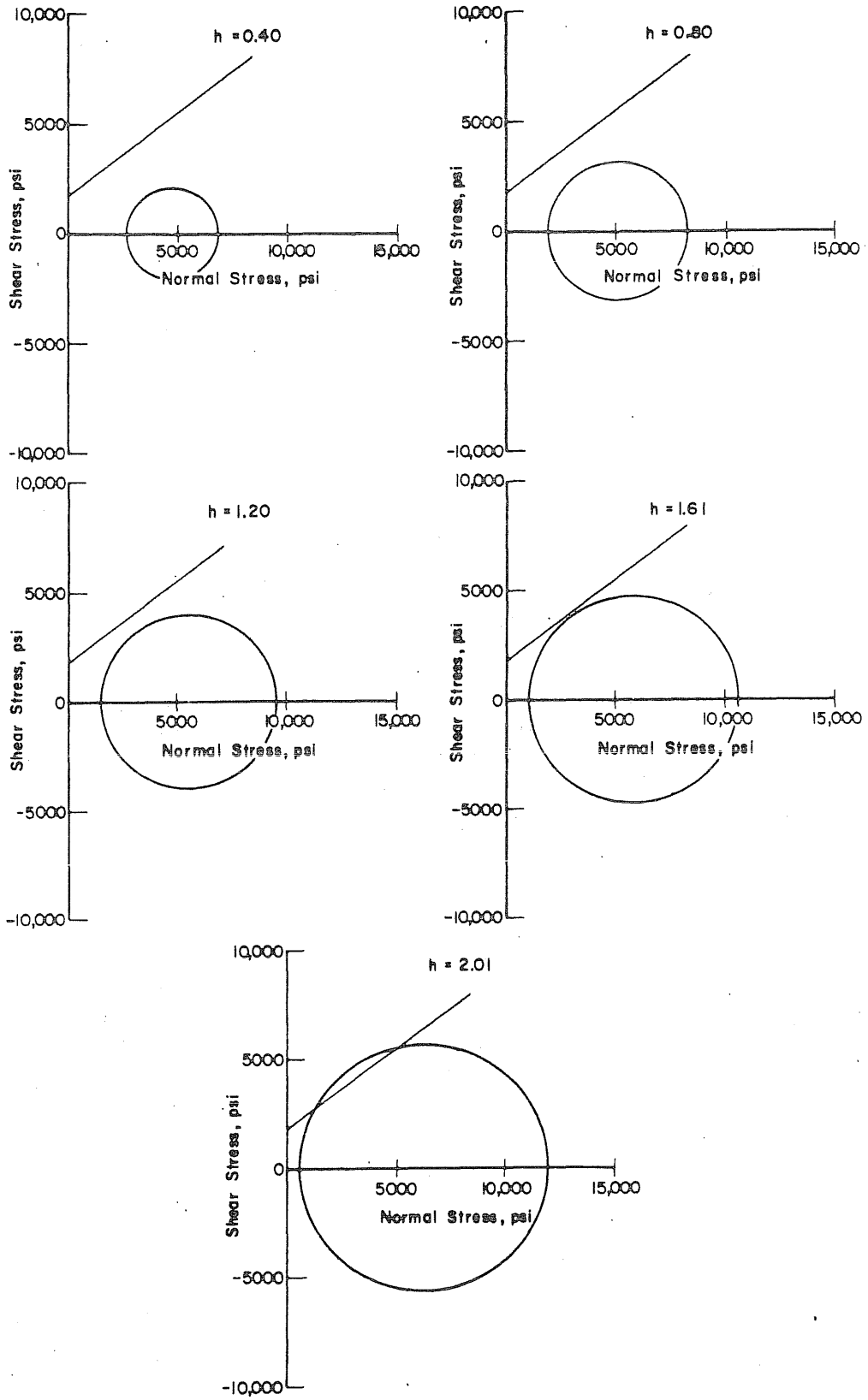

FIG. 6.6 CALCULATED PRINCIPAL STRESSES AT DIFFERENT HEIGHTS, 5 In. FROM THE CENTER OF THE CRYPTODOME IN FIG. 6.2

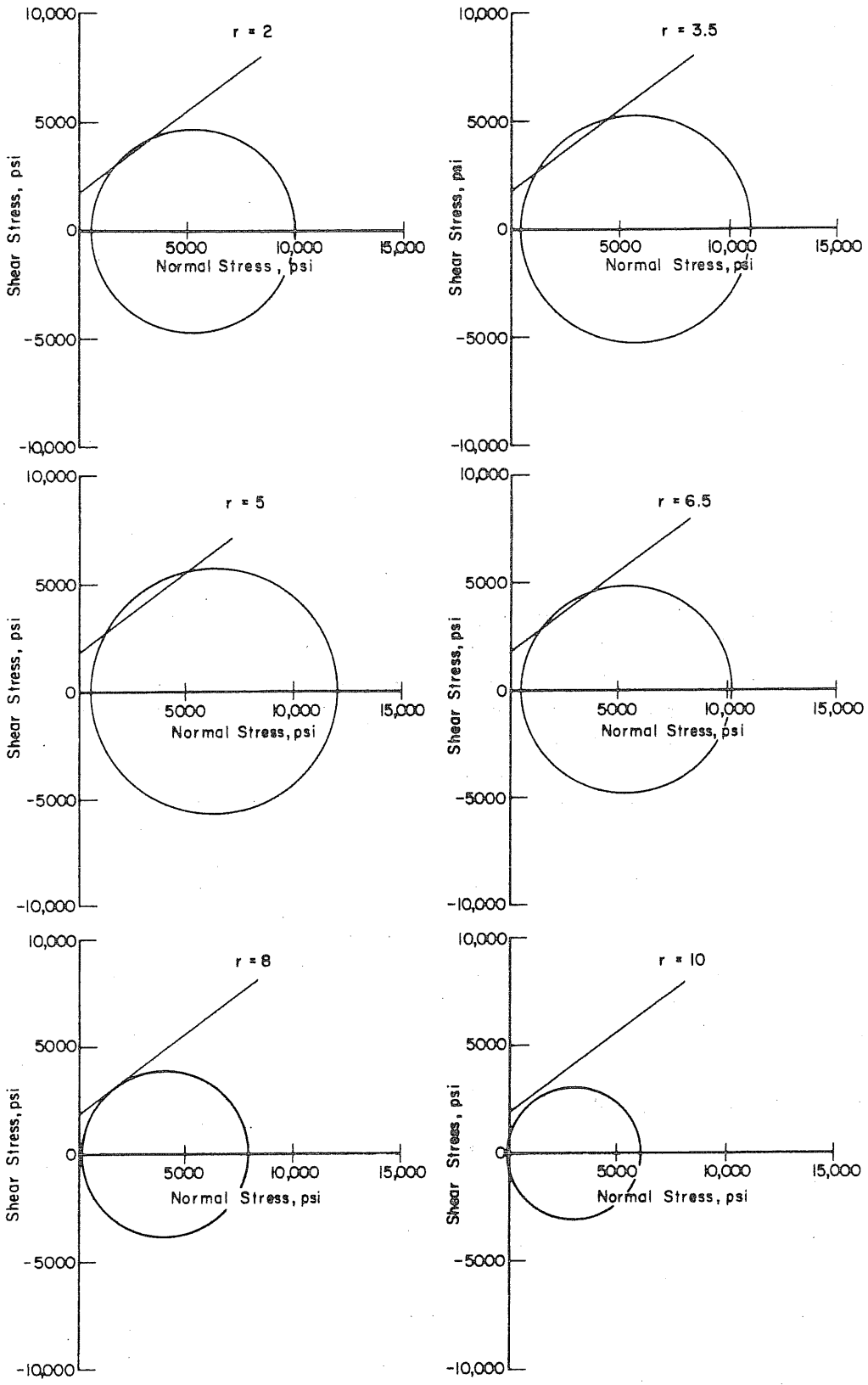

FIG. 6.7 THE WORST STRESS CONDITIONS AT DIFFERENT DISTANCES FROM THE CENTER OF THE CRYPTODOME IN FIG. 6.2

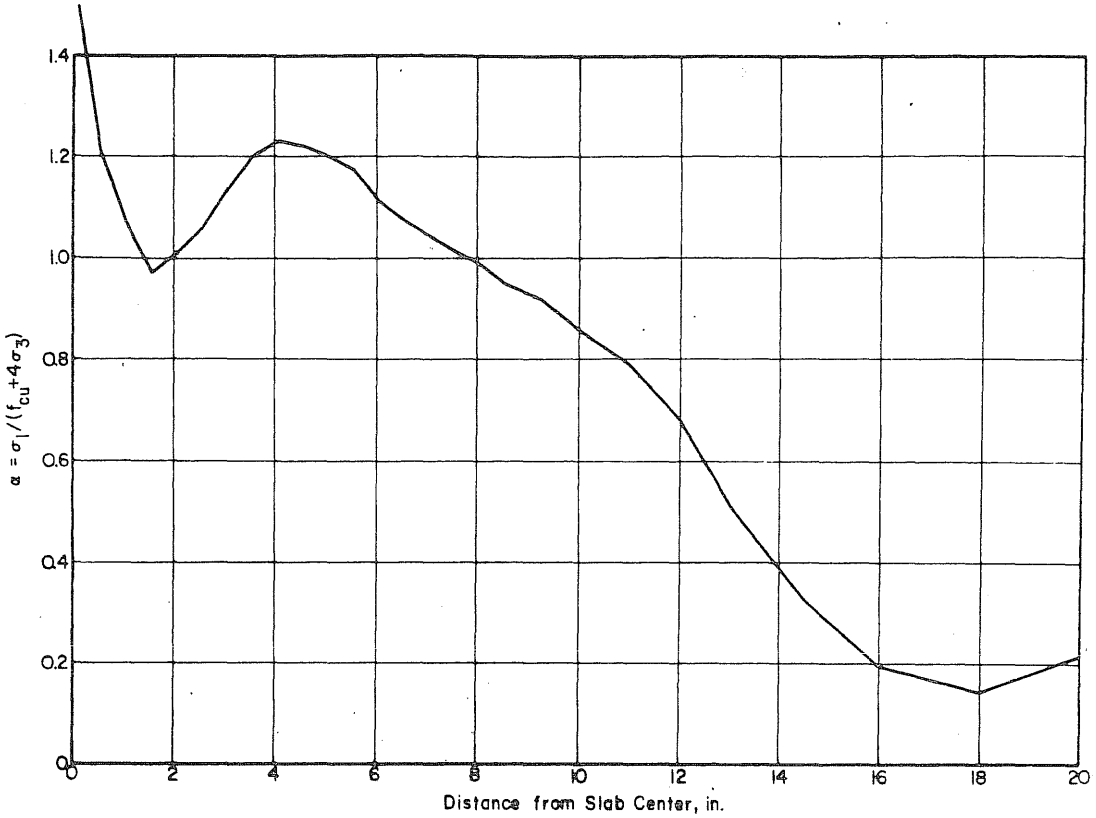

FIG. 6.8 THE VALUES OF THE FAILURE INDEX FOR THE WORST STRESS CONDITION AT EACH VERTICAL SECTION IN THE CRYPTODOME SHOWN IN FIG. 6.2

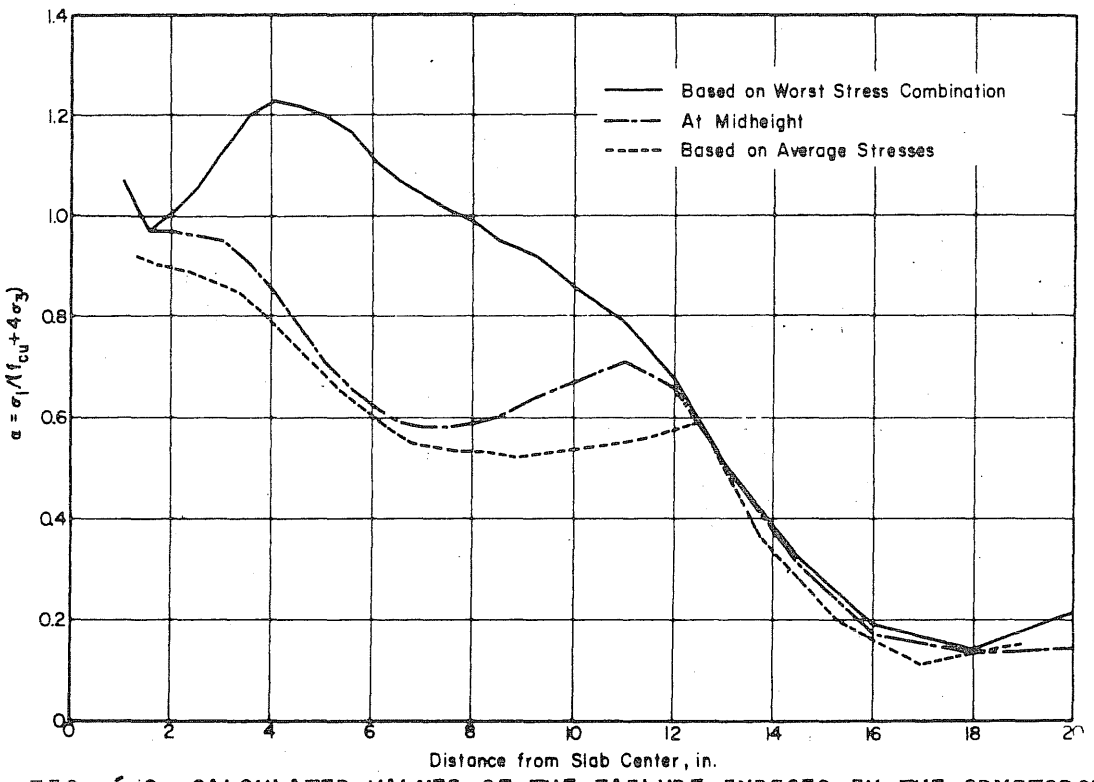

FIG. 6.9 CALCULATED VALUES OF THE FAILURE INDICES IN THE CRYPTODOME SHOWN IN FIG. 6.2

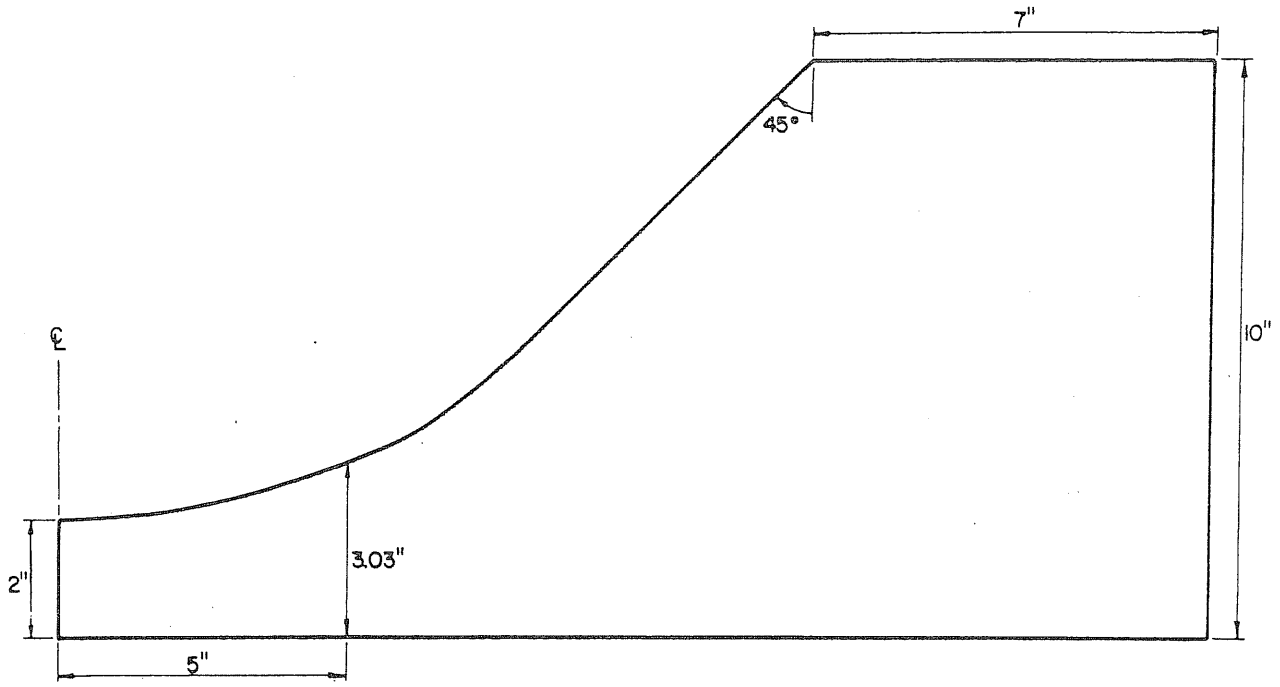

FIG. 6.10 A COMPARATIVELY THICK CRYPTODOME

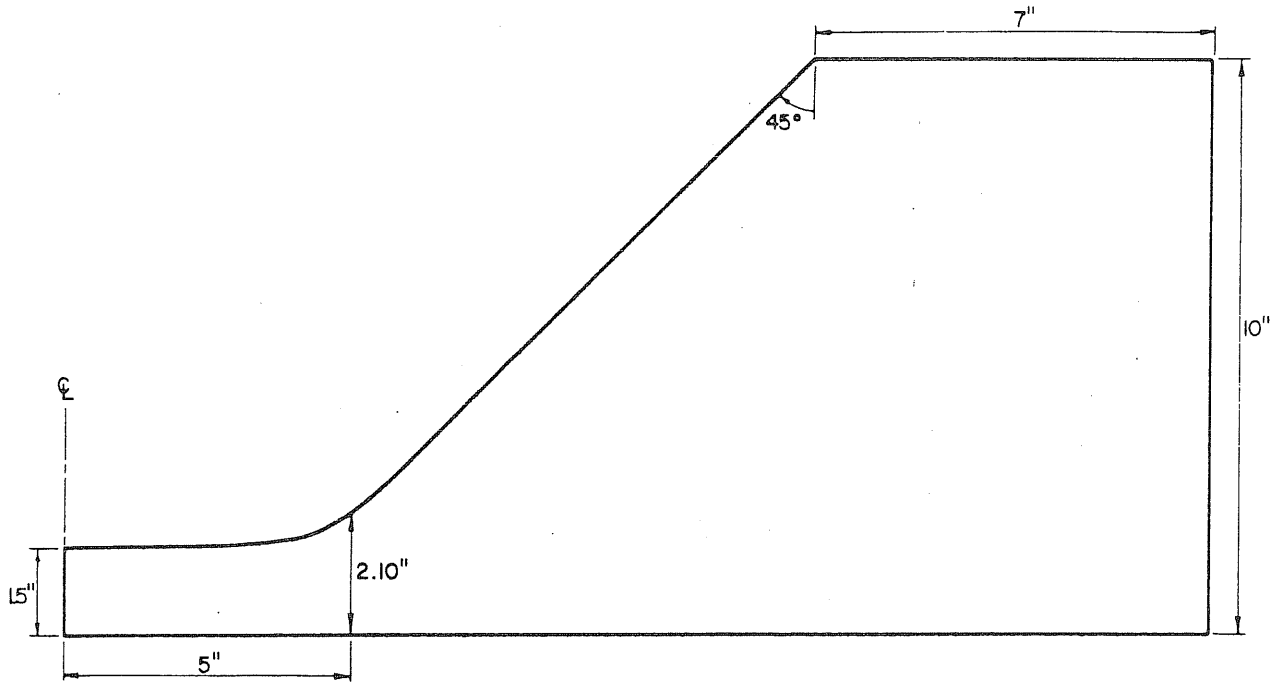

FIG. 6.11 A COMPARATIVELY THIN CRYPTODOME

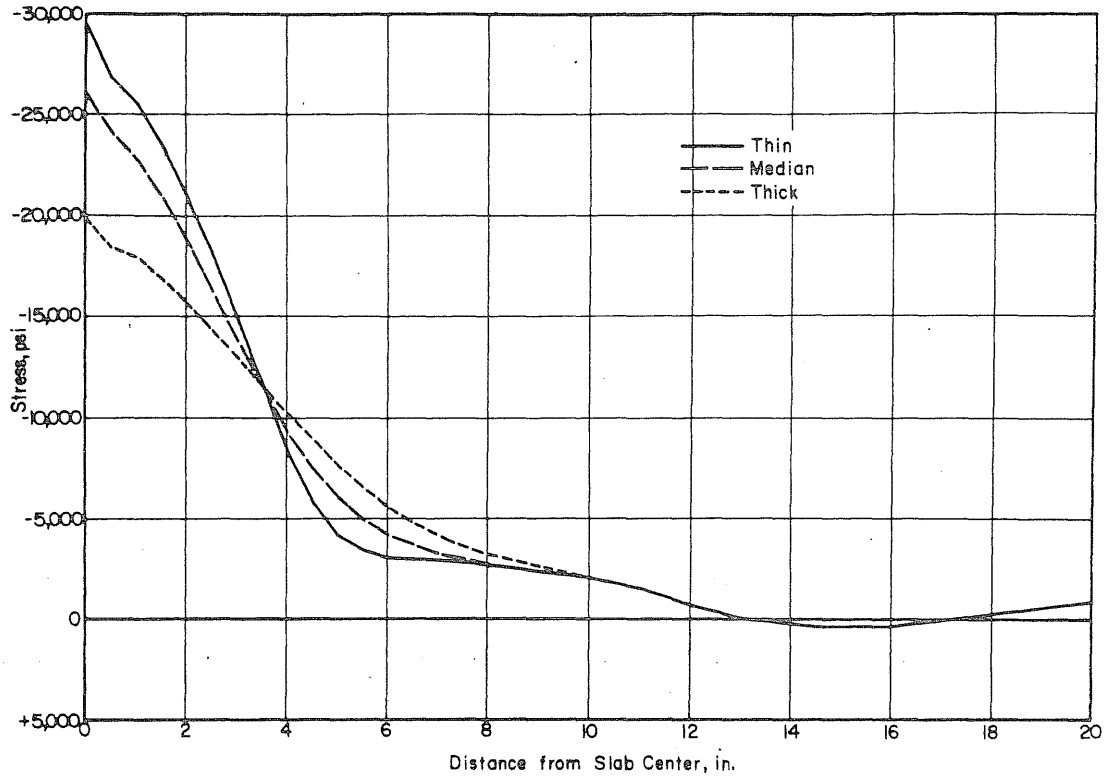

FIG. 6.12 RADIAL STRESSES ALONG THE INSIDE FACE OF THE SLAB ASSUMING THREE DIFFERENTLY SHAPED CRYPTODOMES

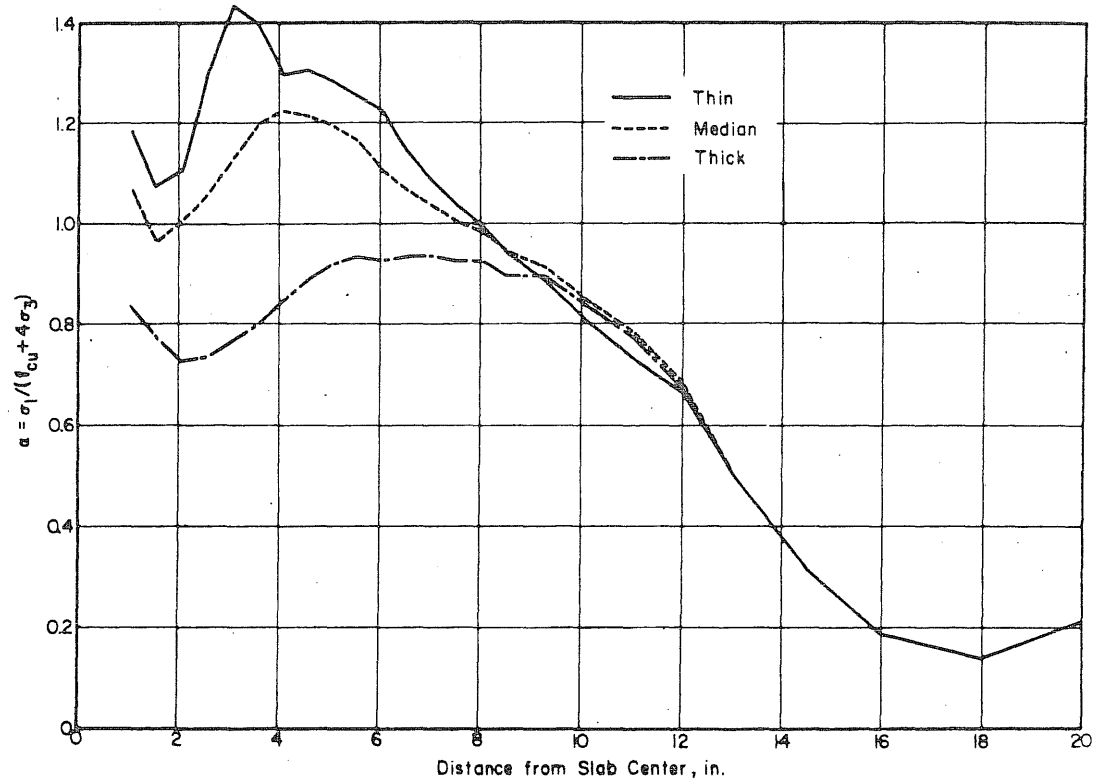

FIG. 6.13 FAILURE INDICES BASED ON THE WORST STRESS COMBINATIONS FOR THREE DIFFERENTLY SHAPED CRYPTODOMES

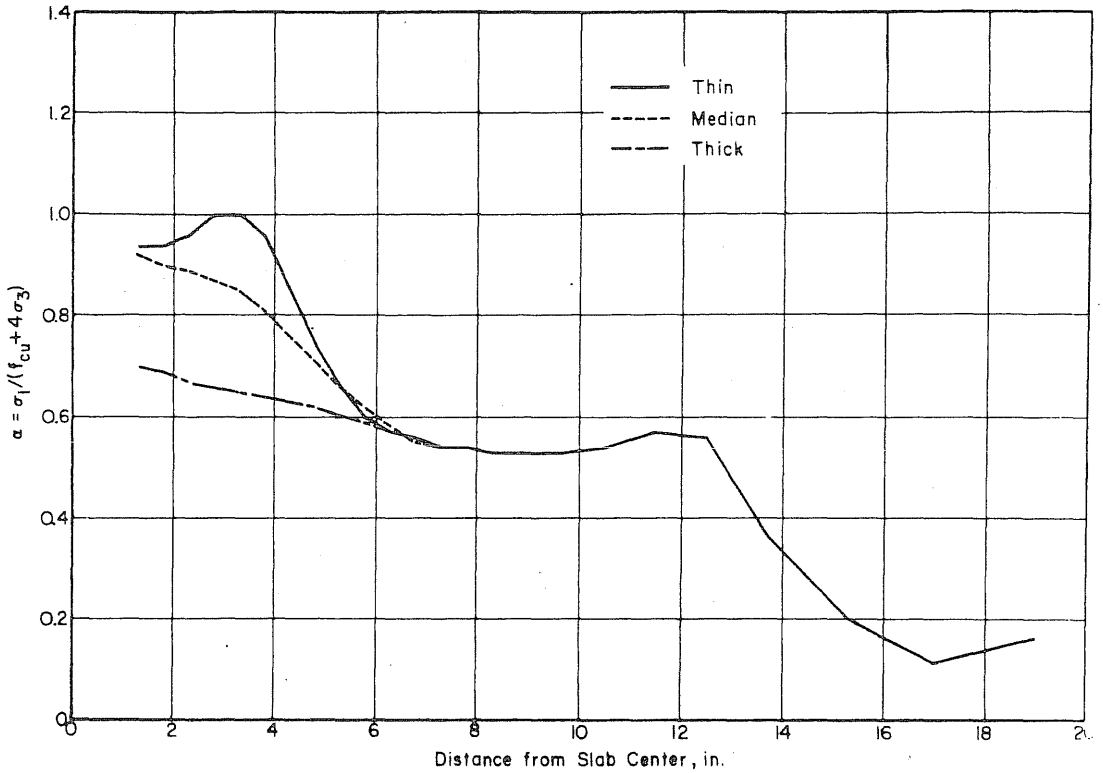

FIG. 6.14 FAILURE INDICES BASED ON AVERAGE STRESSES FOR THREE DIFFERENTLY SHAPED CRYPTODOMES

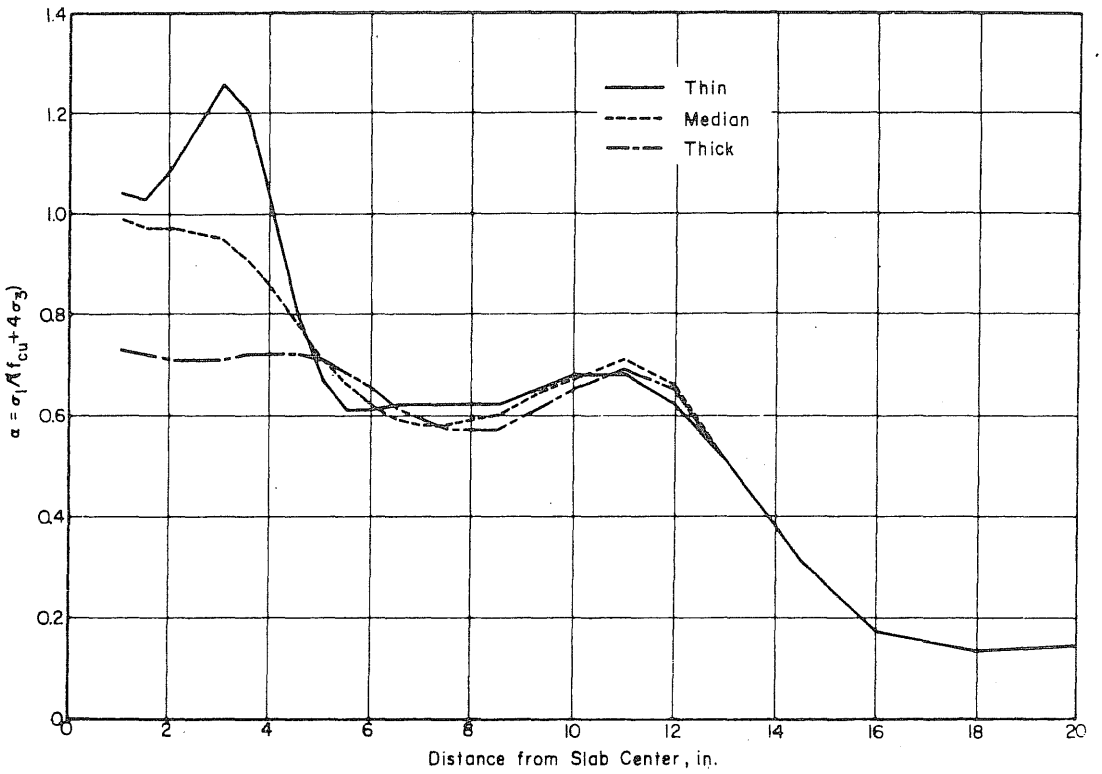

FIG. 6.15 FAILURE INDICES FOR STRESSES AT MID-HEIGHT OF THREE DIFFERENTLY SHAPED CRYPTODOMES

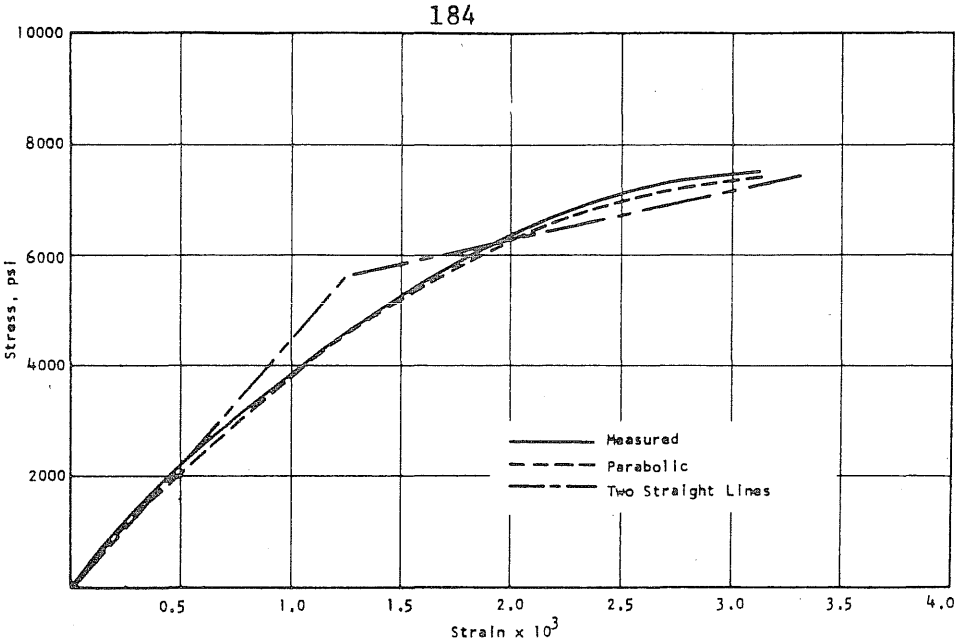

FIG. 6.16 STRESS-STRAIN CURVE FOR CONCRETE AND SUGGESTED IDEALIZATIONS

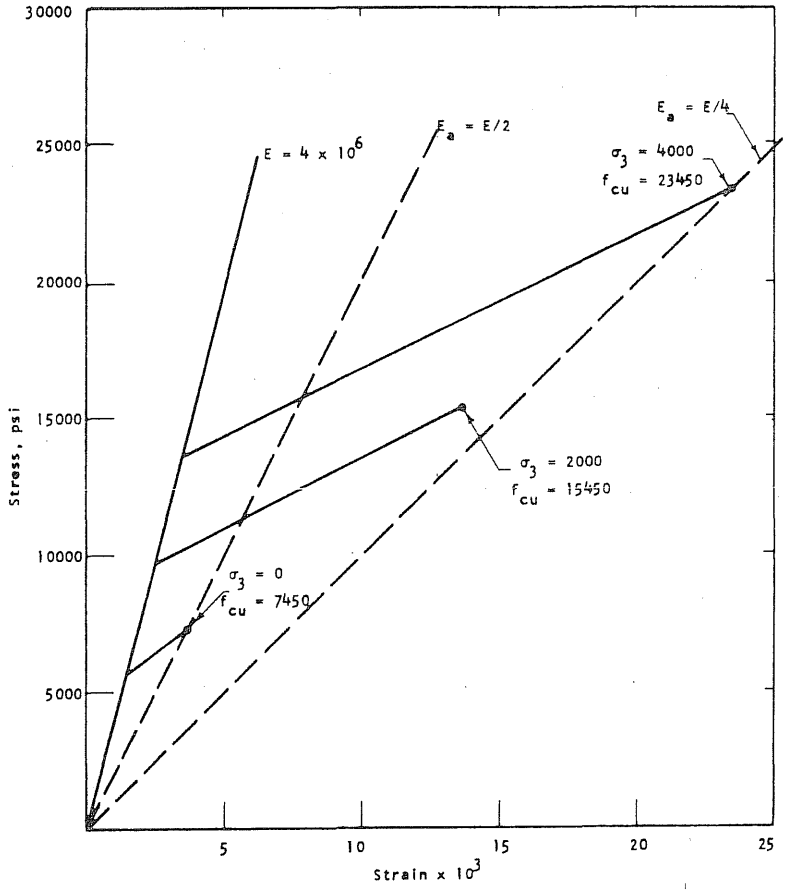

FIG. 6.17 ASSUMED STRESS-STRAIN RELATIONSHIP FOR DIFFERENT VALUES OF THE CONFINING PRESSURE

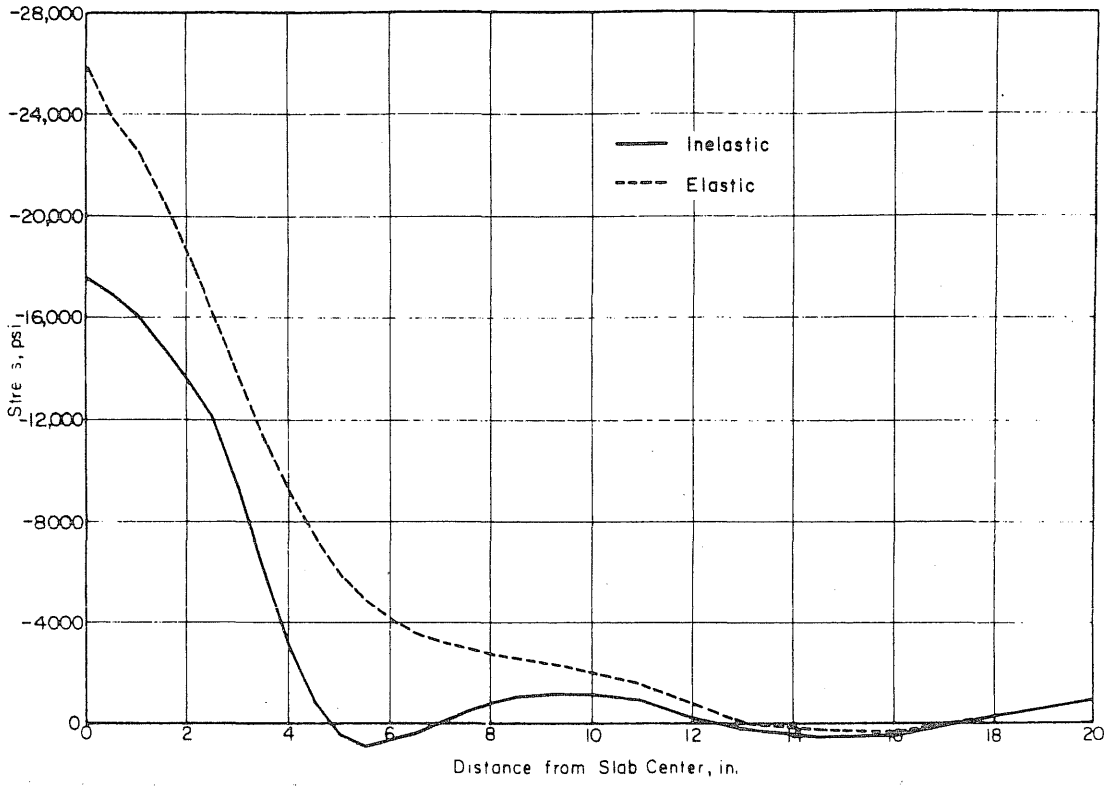

FIG. 6.18 RADIAL STRESSES ALONG THE INSIDE FACE OF THE DOME IN FIG. 6.2 FOR ELASTIC AND INELASTIC MATERIAL PROPERTIES

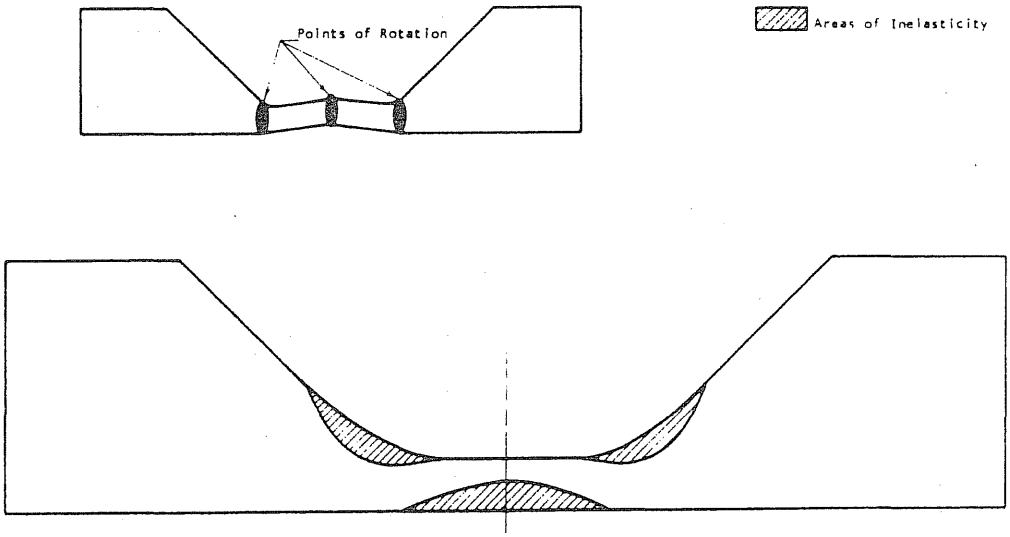

FIG. 6.19 AREAS OF INELASTICITY BECAUSE OF HIGH COMPRESSIVE STRESSES AND ITS EFFECT

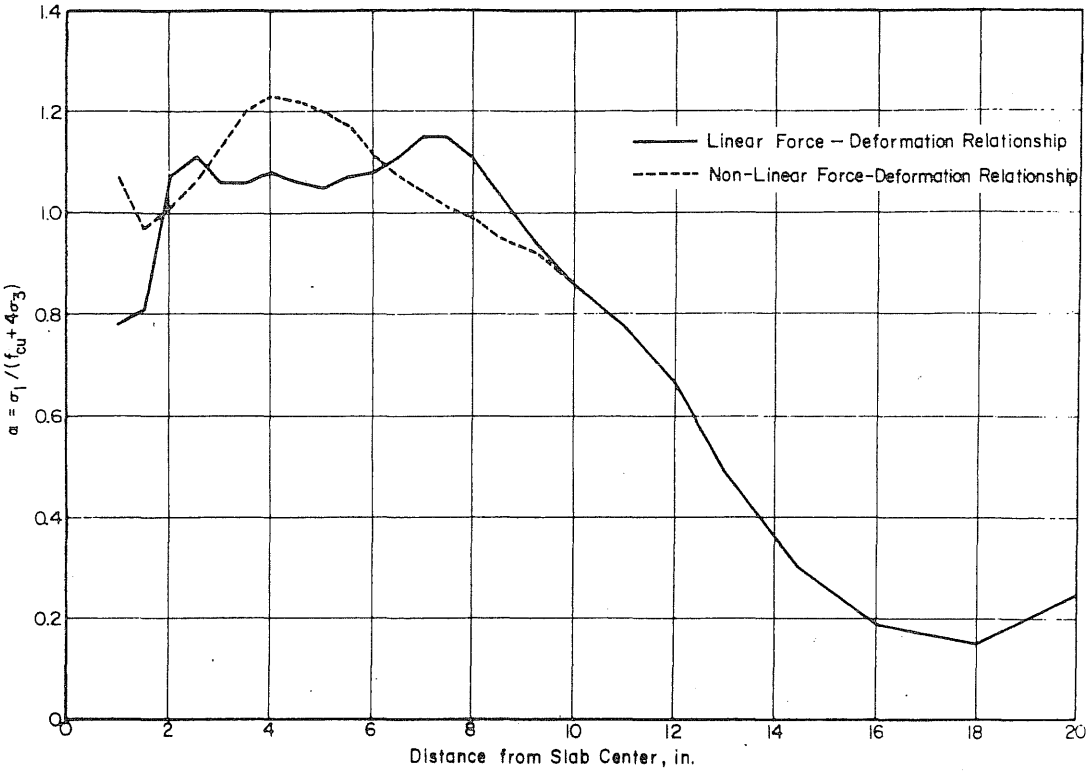

FIG. 6.20 FAILURE INDICES BASED ON WORST STRESS COMBINATIONS IN THE CRYPTODOME SHOWN IN FIG. 6.2

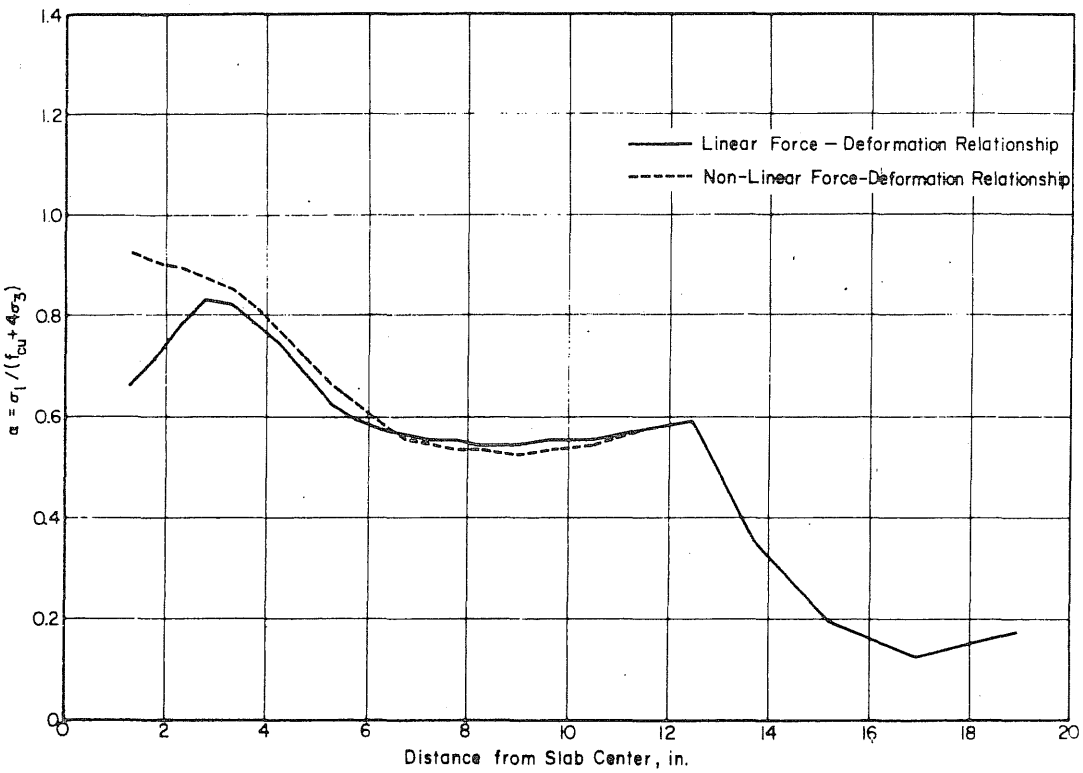

FIG. 6.21 FAILURE INDICES BASED ON AVERAGE STRESSES IN THE CRYPTODOME SHOWN IN FIG. 6.2

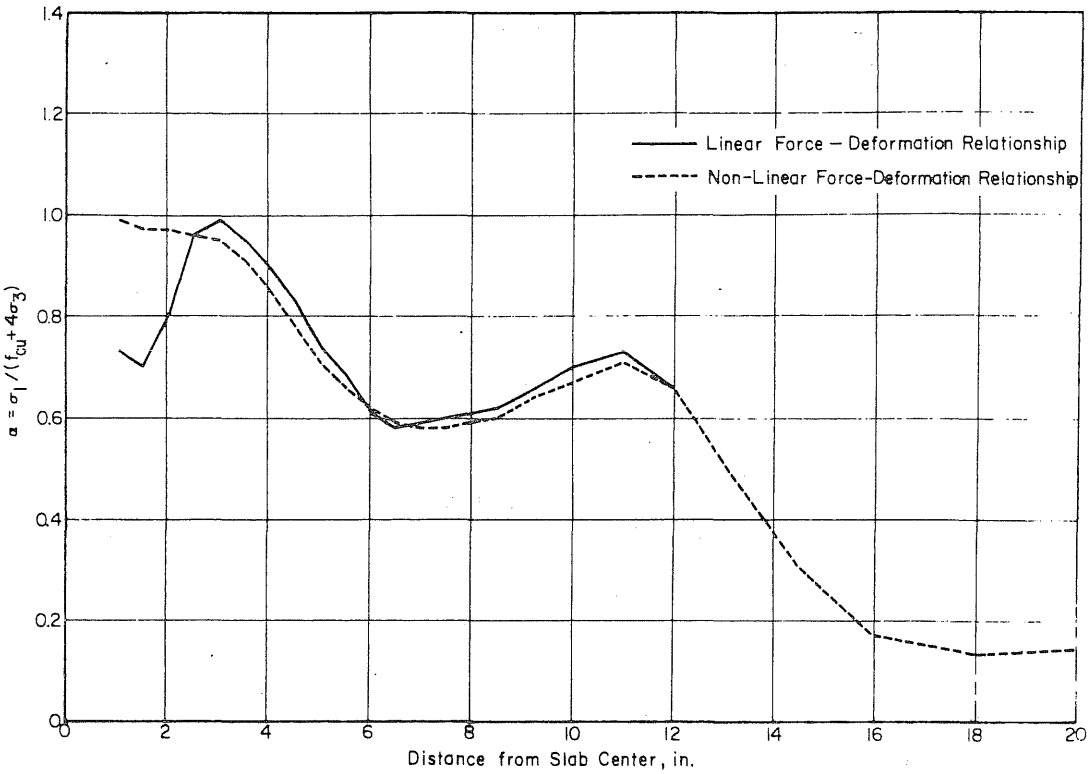

FIG. 6.22 FAILURE INDICES BASED ON STRESSES AT MID-HEIGHT IN THE CRYPTODOME SHOWN IN FIG. 6.2

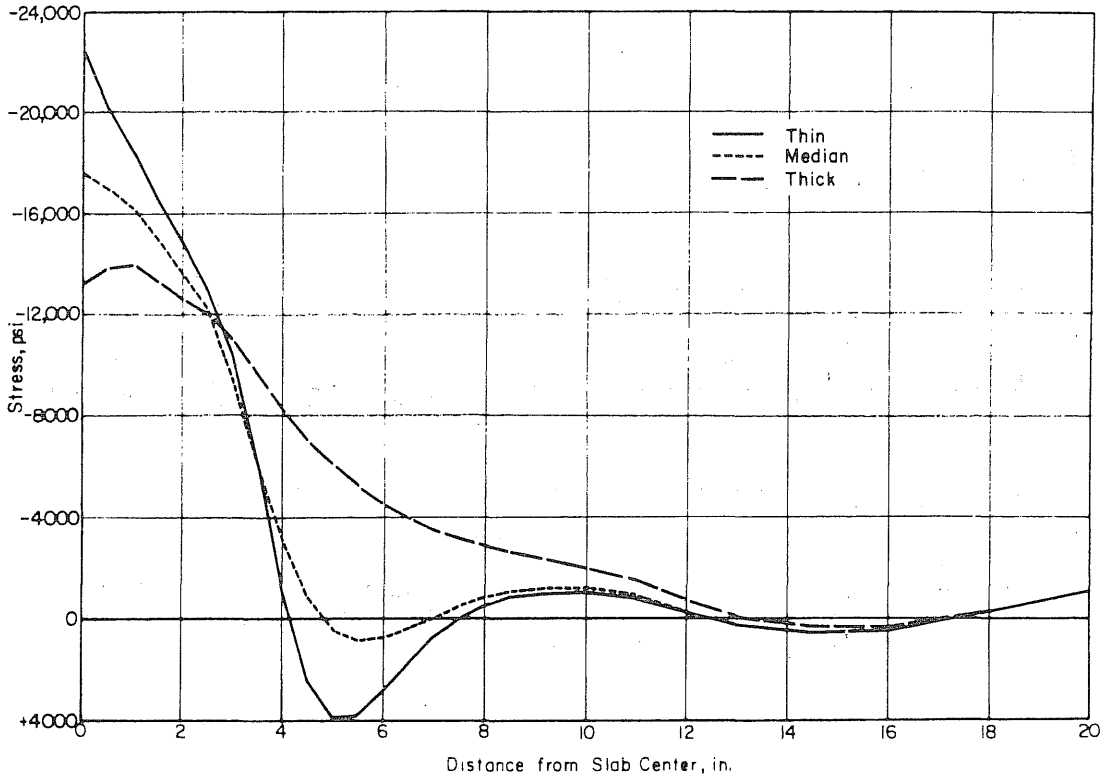

FIG. 6.23 RADIAL STRESSES ALONG THE INSIDE FACE OF THE SLAB FOR THREE DIFFERENT CRYPTODOMES ASSUMING INELASTIC MATERIAL PROPERTIES

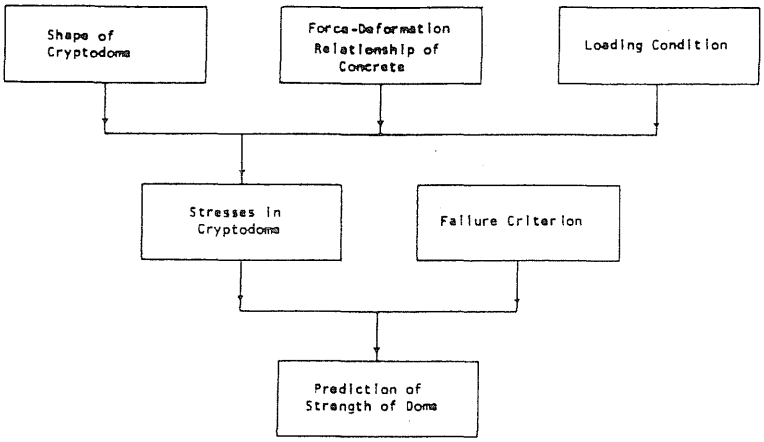

FIG. 6.24 FLOW-DIAGRAM FOR ANALYSIS OF THE SHEAR STRENGTH OF A THICK SLAB

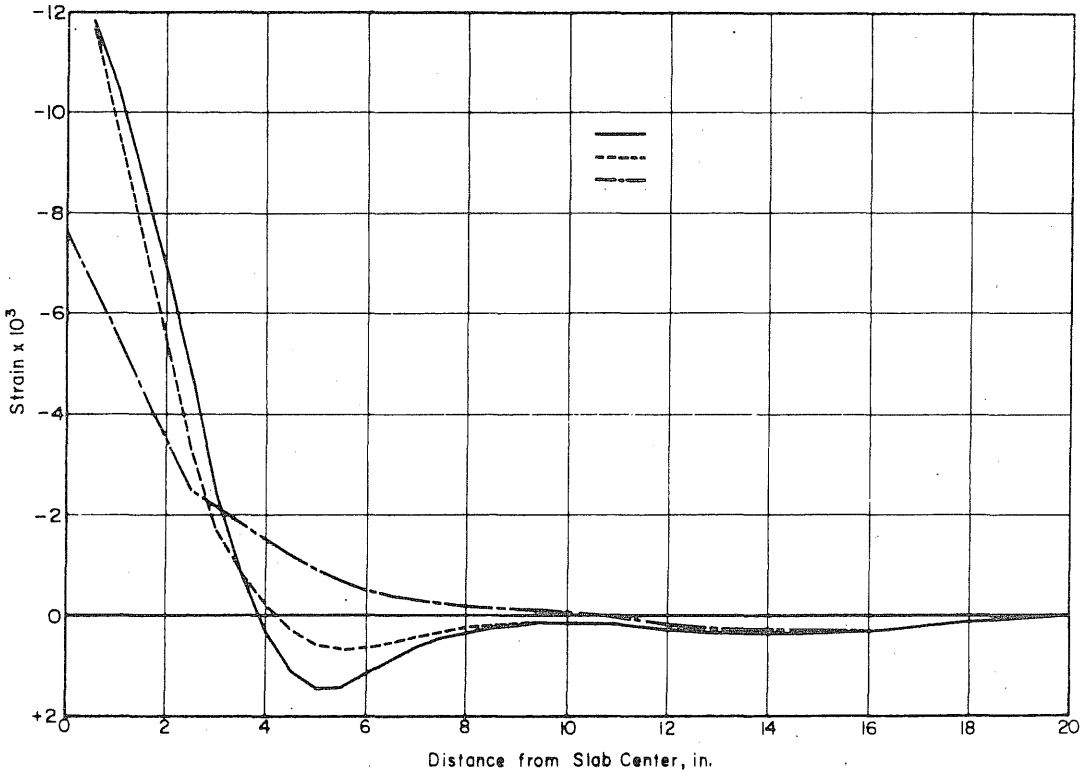

FIG. 6.25 RADIAL STRAINS ALONG THE INSIDE FACE OF THE SLAB ASSUMING THREE DIFFERENTLY SHAPED CRYPTODOMES AND INELASTIC MATERIAL PROPERTIES

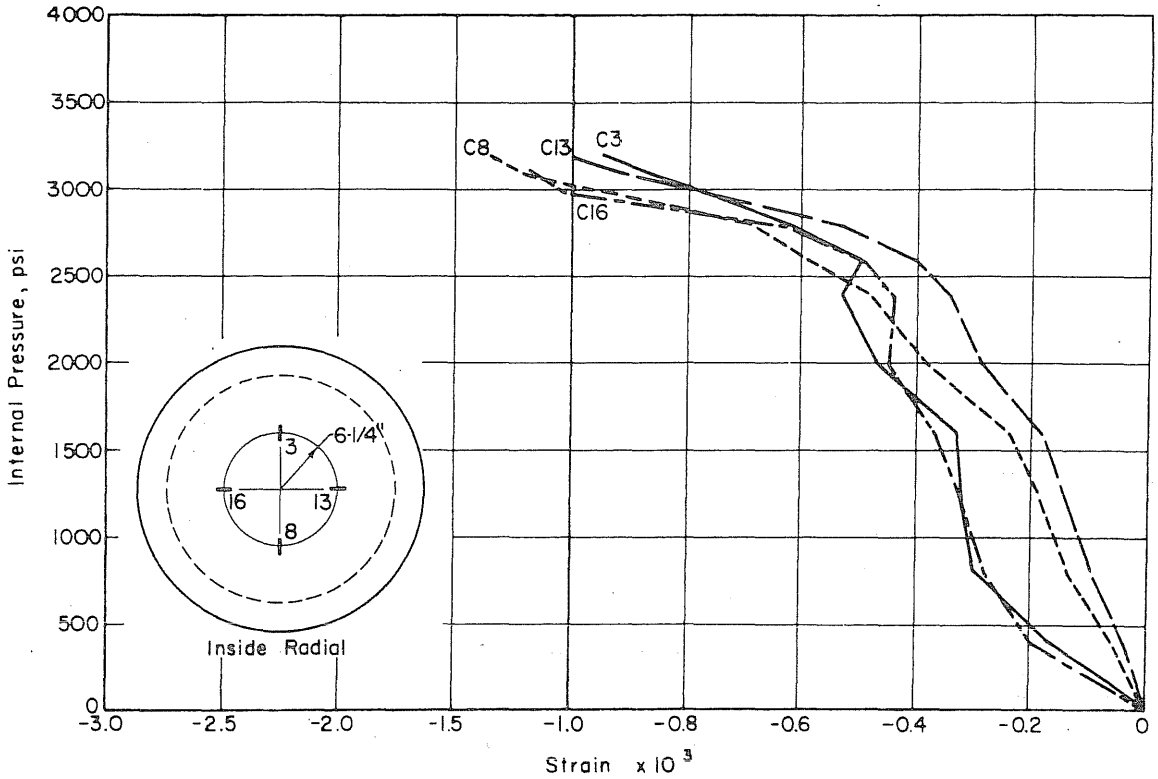

FIG. 6.26 MEASURED RADIAL STRAIN ON THE INSIDE FACE OF THE SLAB OF PV16, 6-1/4 in. FROM THE CENTER

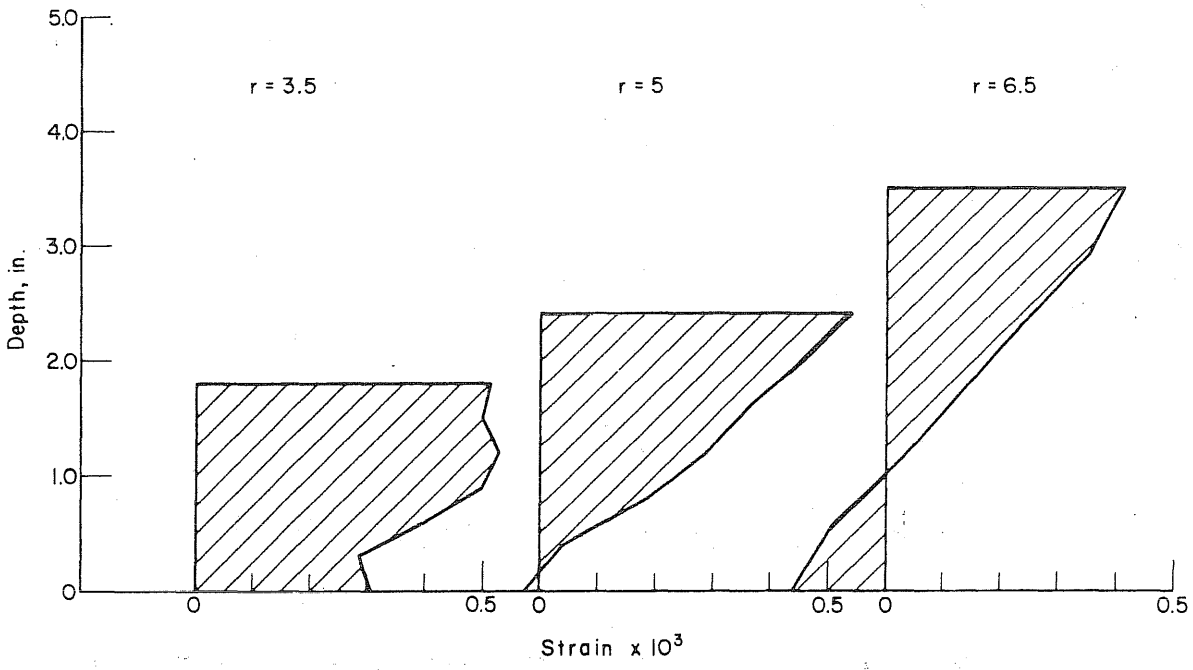

FIG. 6.27 MAXIMUM PRINCIPAL STRAINS AT DIFFERENT RADII OF THE DOME DEFINED IN FIG. 6.2

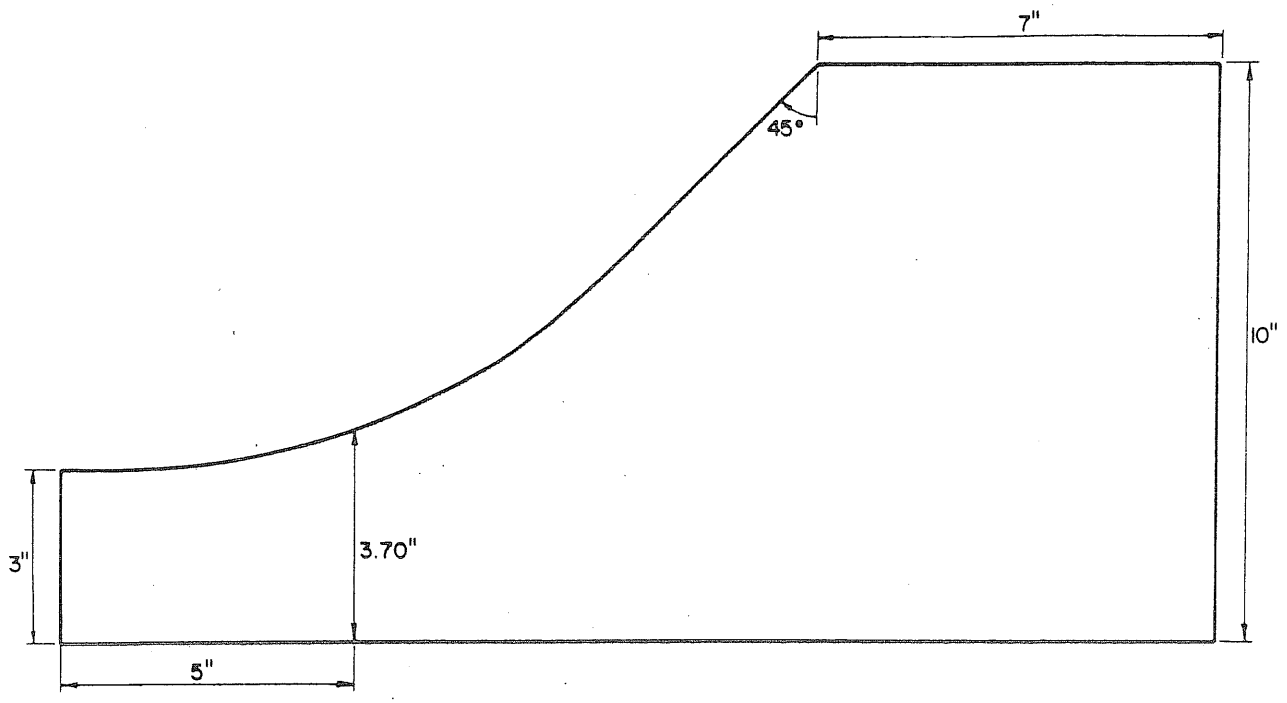

FIG. 6.28 A VERY THICK CRYPTODOME

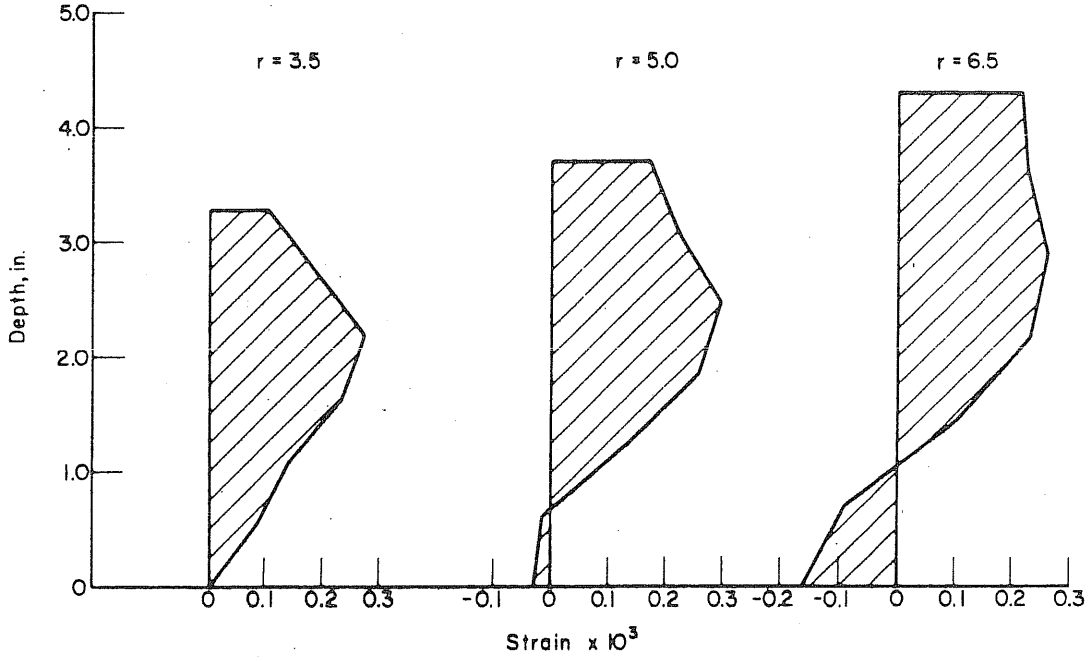

FIG. 6.29 MAXIMUM PRINCIPAL STRAINS AT DIFFERENT RADII OF THE DOME DEFINED IN FIG. 6.28

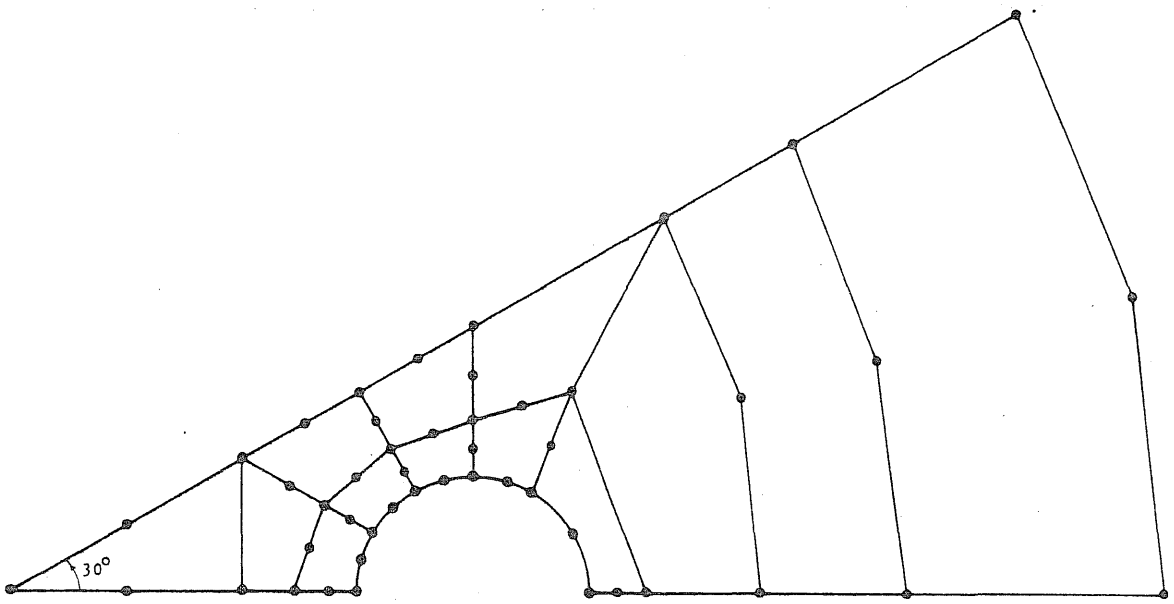

FIG. 7.1 HORIZONTAL SECTION OF THE THREE-DIMENSIONAL FINITE-ELEMENT GRID

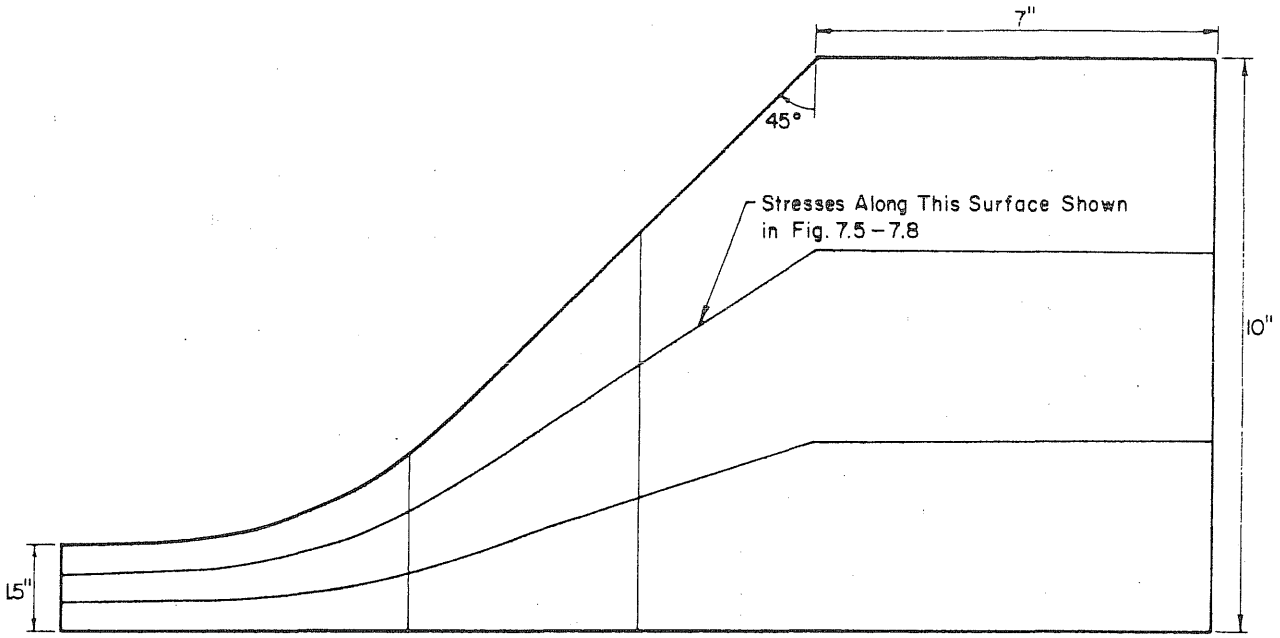

FIG. 7.2 SHAPE OF THE CRYPTODOME USED IN THE THREE-DIMENSIONAL FINITE-ELEMENT MODEL

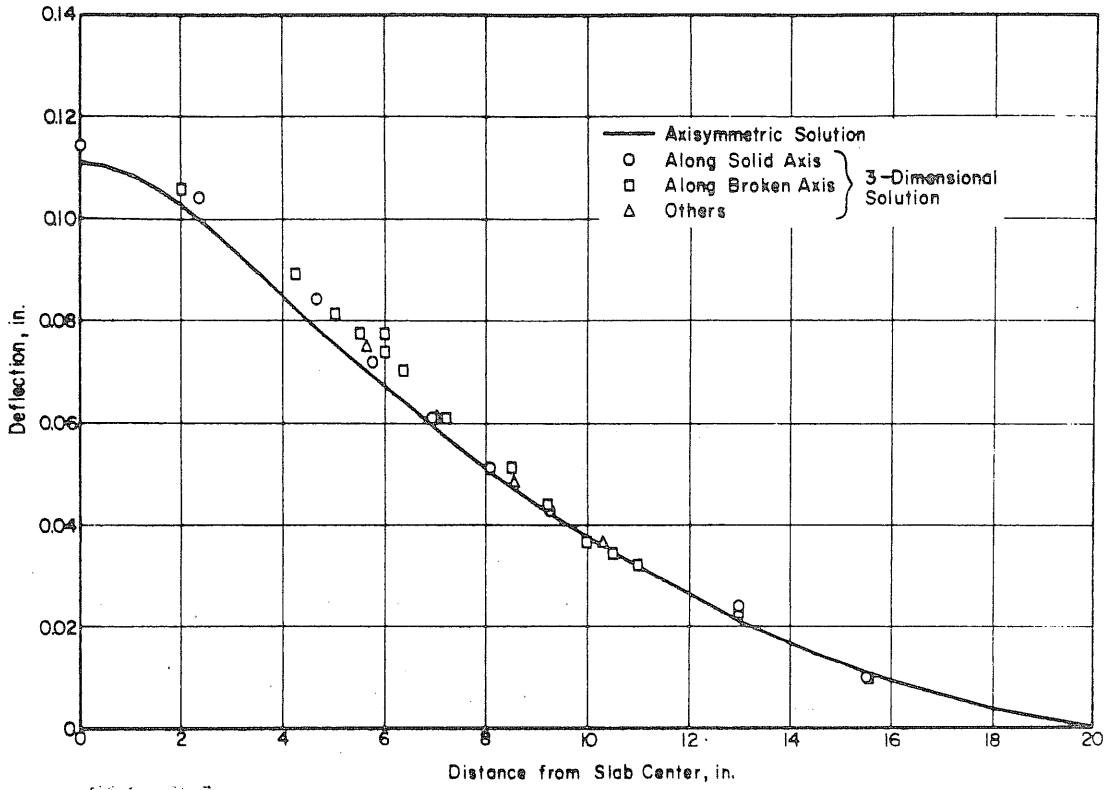

FIG. 7.3 CALCULATED VERTICAL DEFLECTIONS ALONG THE INSIDE FACE OF THE SLAB

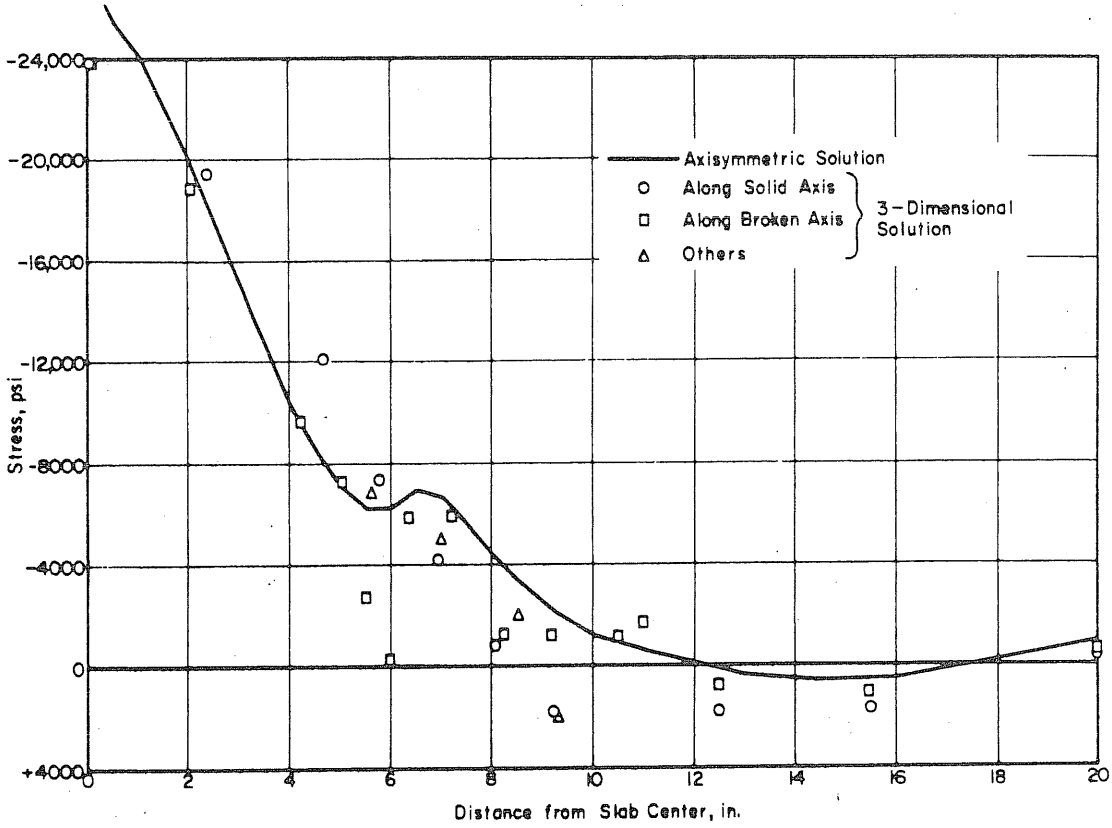

FIG. 7.4 CALCULATED RADIAL STRAINS ALONG THE INSIDE FACE OF THE SLAB

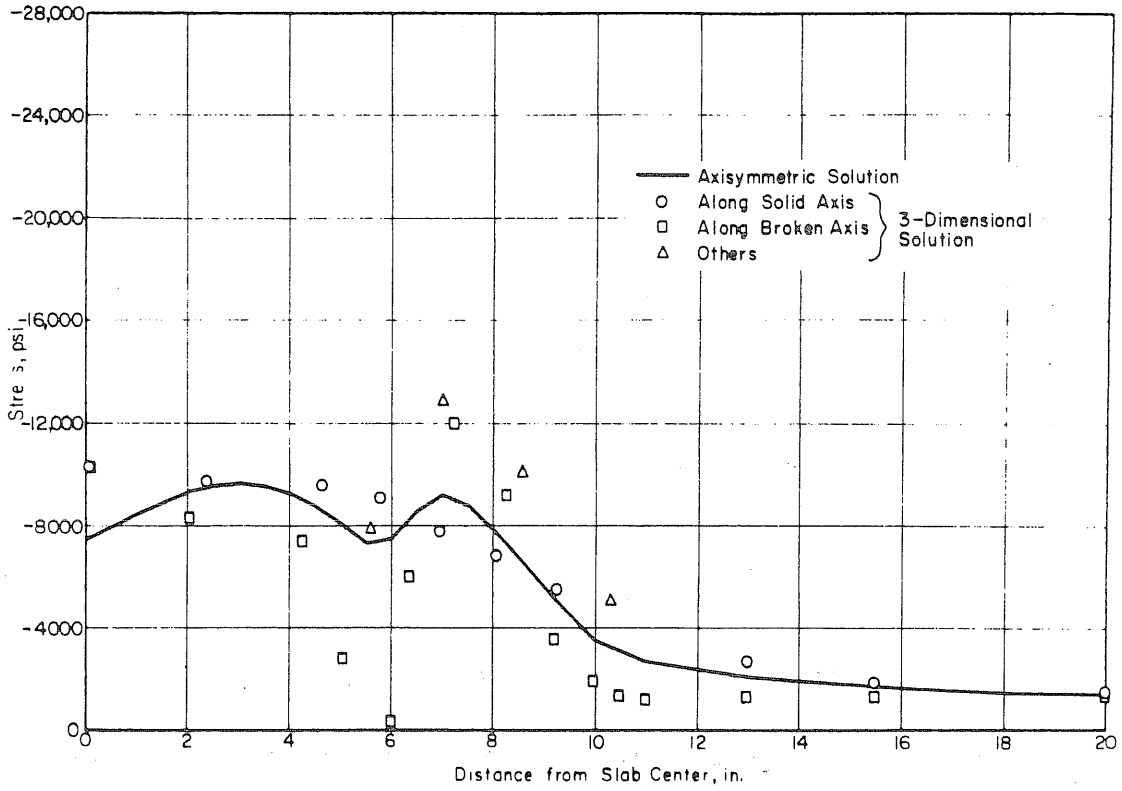

FIG. 7.5 CALCULATED RADIAL STRESSES ALONG THE SURFACE SHOWN IN FIG. 7.2

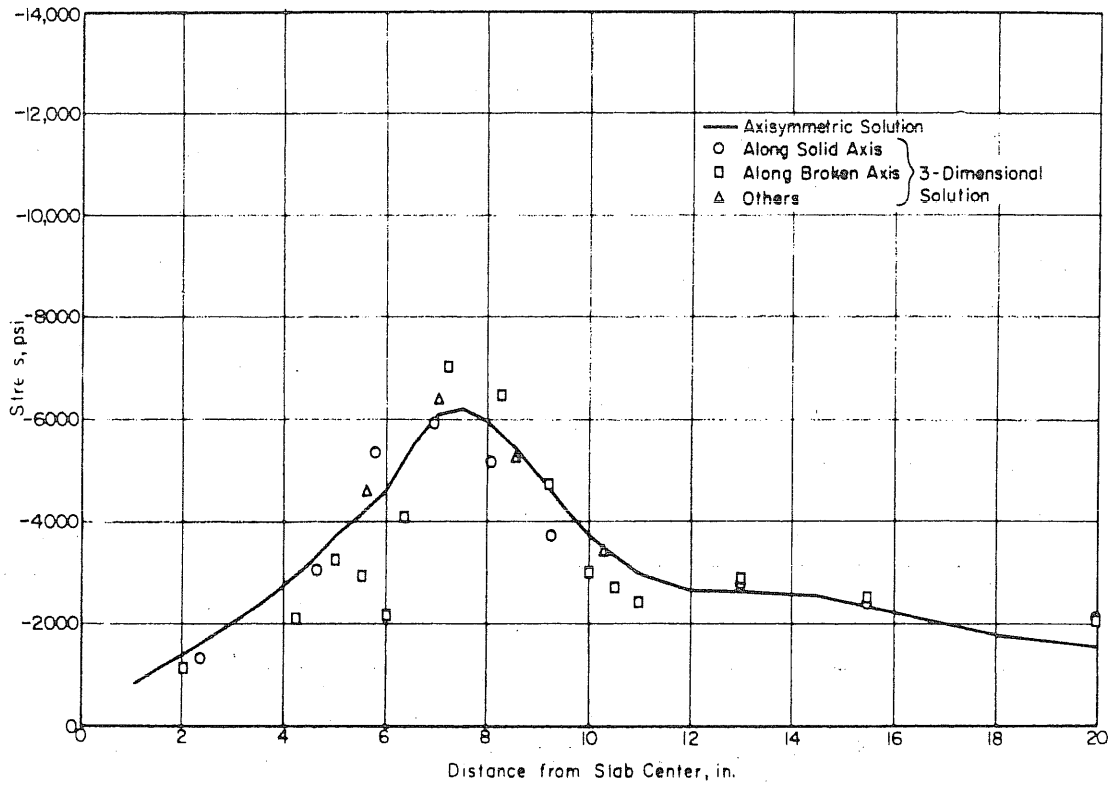

FIG. 7.6 CALCULATED VERTICAL STRESSES ALONG THE SURFACE SHOWN IN FIG. 7.2

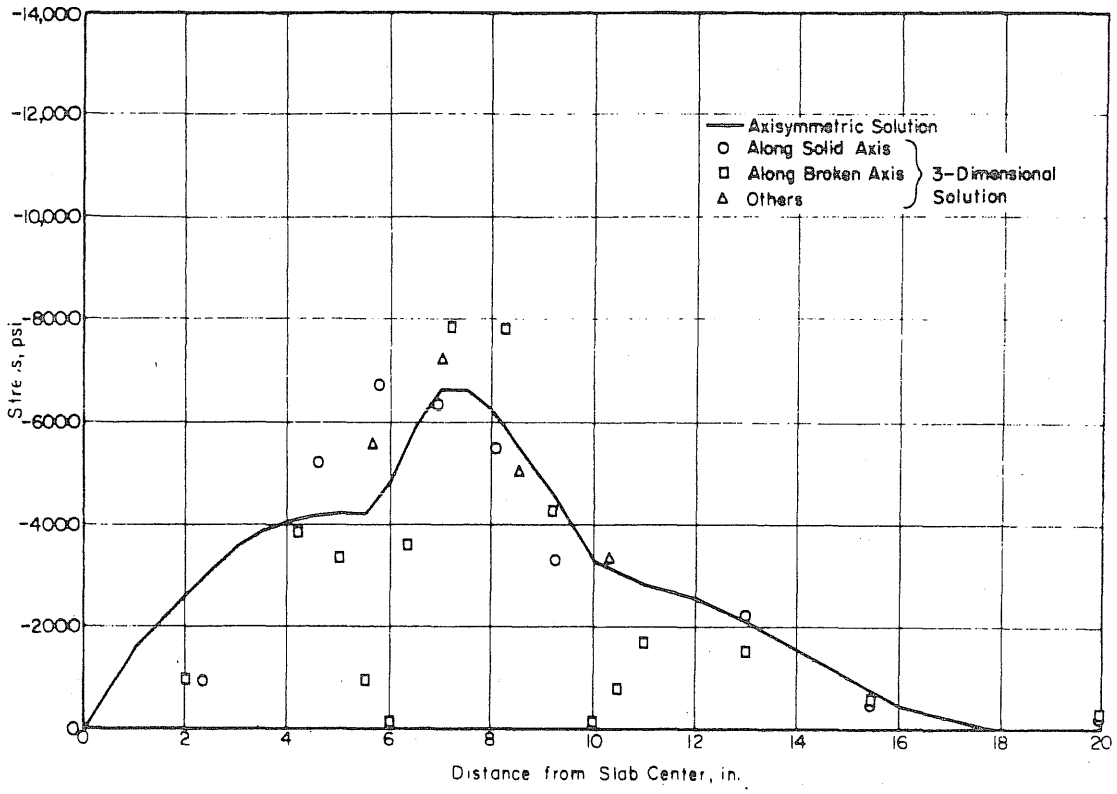

FIG. 7.7 CALCULATED SHEAR STRESSES ALONG THE SURFACE SHOWN IN FIG. 7.2

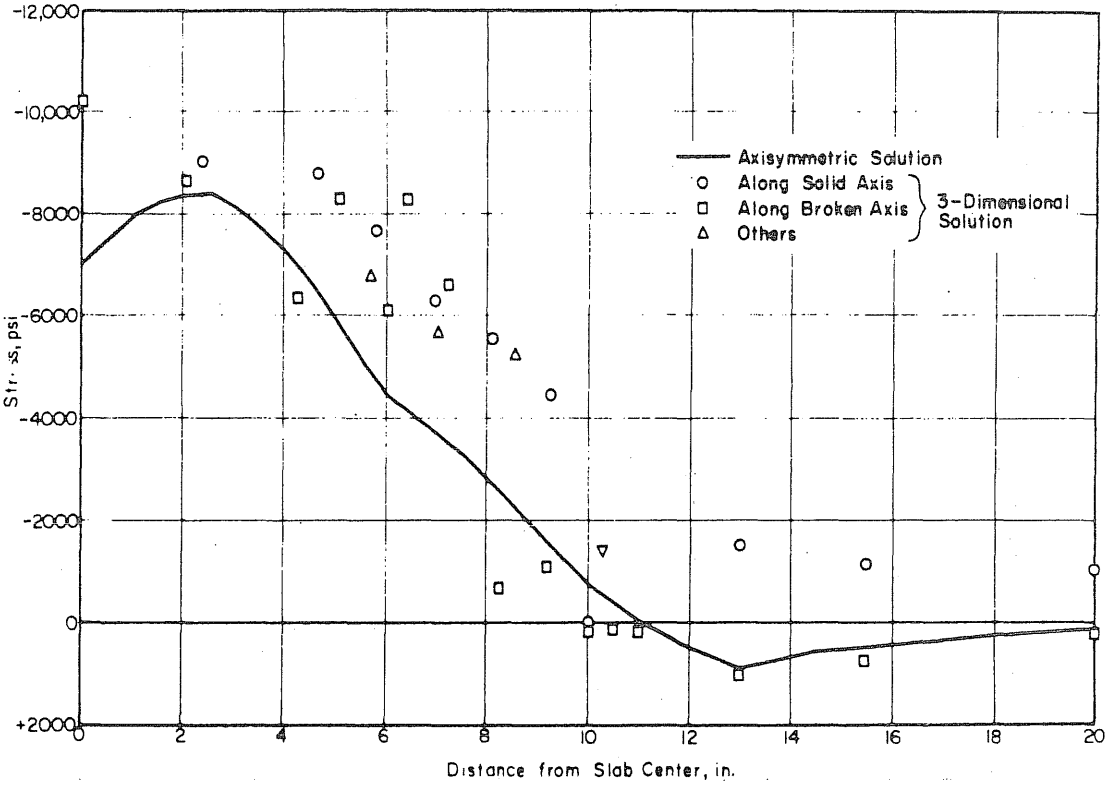

FIG. 7.8 CALCULATED TANGENTIAL STRESSES ALONG THE SURFACE SHOWN IN FIG. 7.2

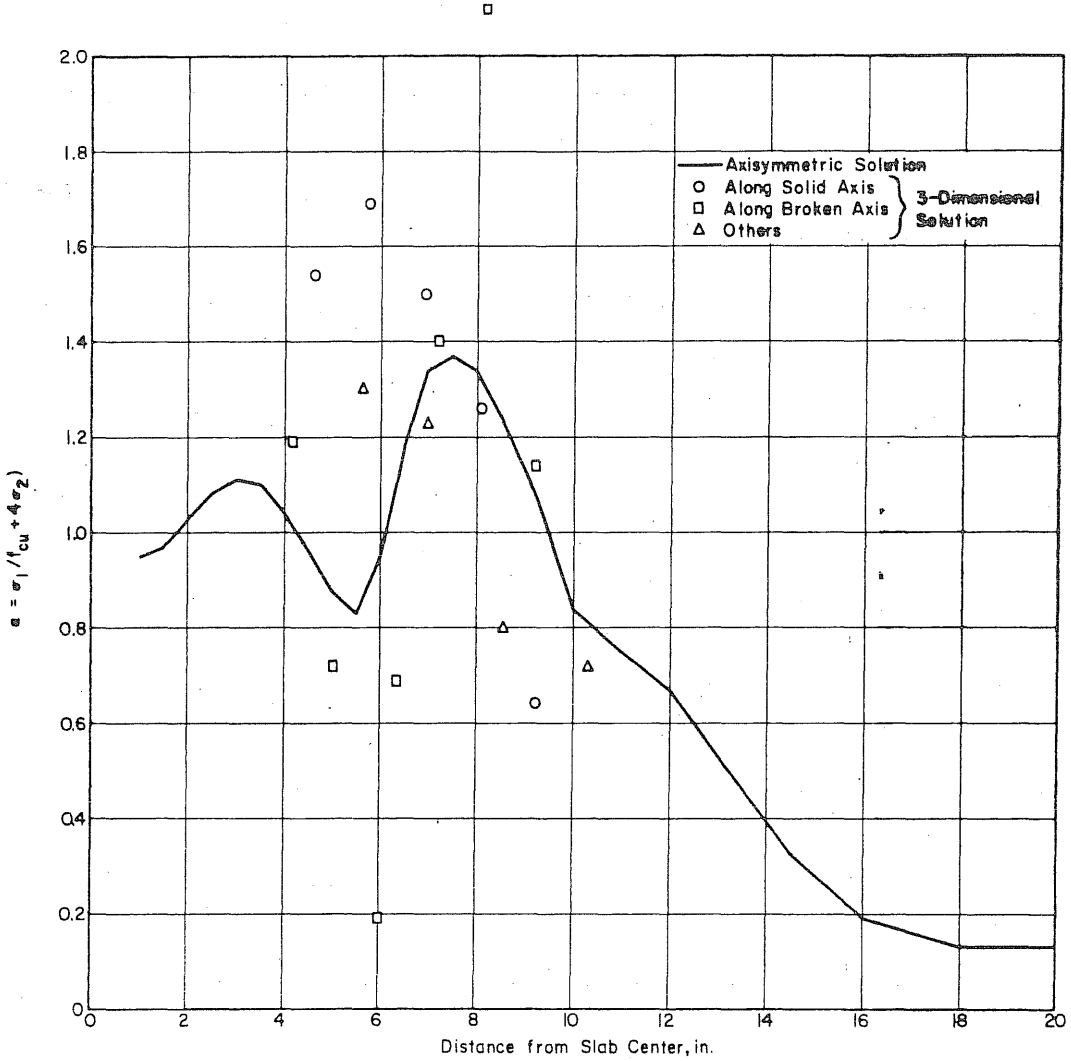

FIG. 7.9 CALCULATED VALUES OF THE FAILURE INDEX ALONG THE SURFACE SHOWN IN FIG. 7.2

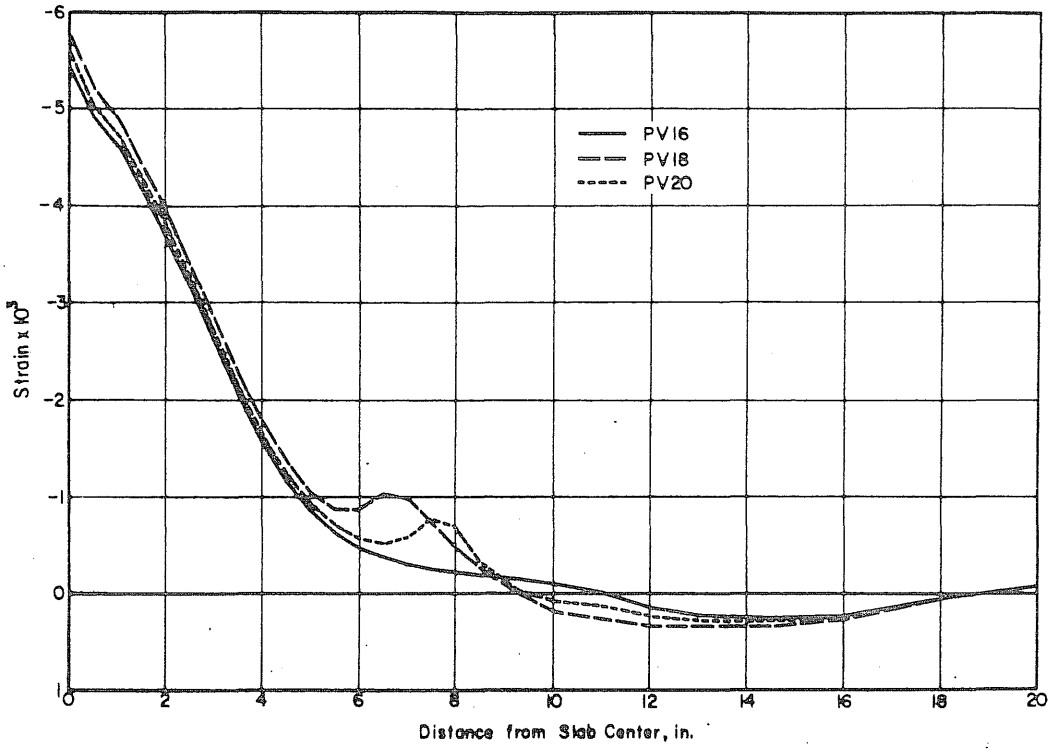

FIG. 7.10 CALCULATED RADIAL STRAINS ALONG THE INSIDE FACES OF THE SLABS OF THREE VESSELS

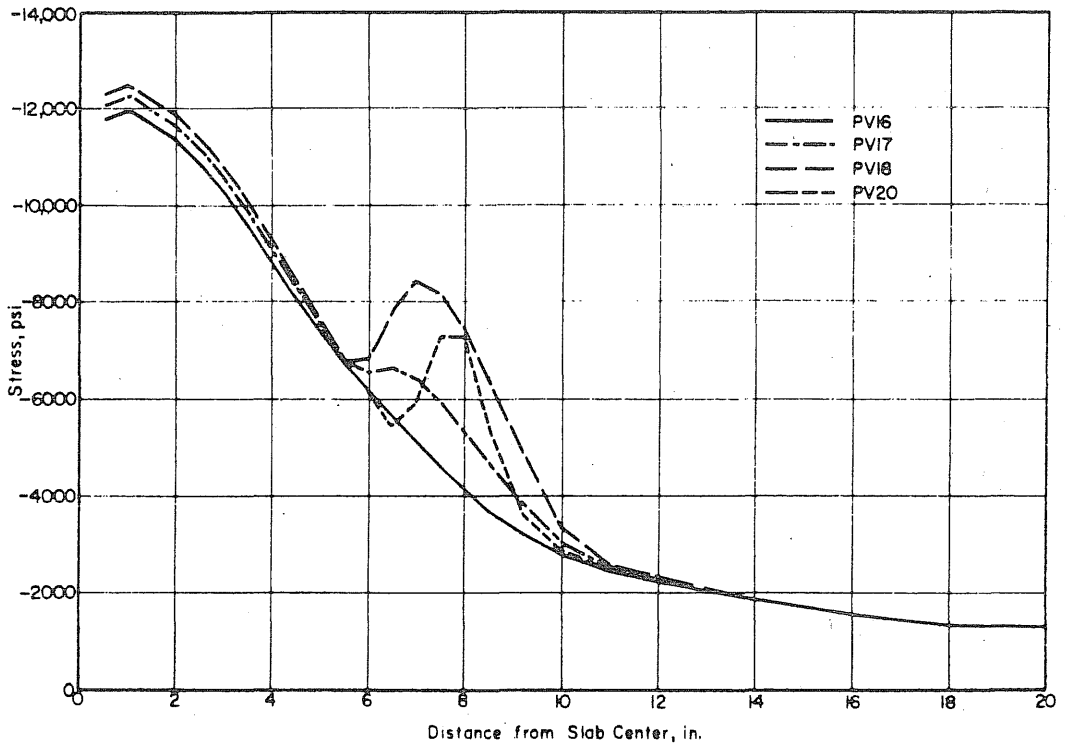

FIG. 7.11 CALCULATED RADIAL STRESSES AT MID-HEIGHT OF CRYPTODOMES

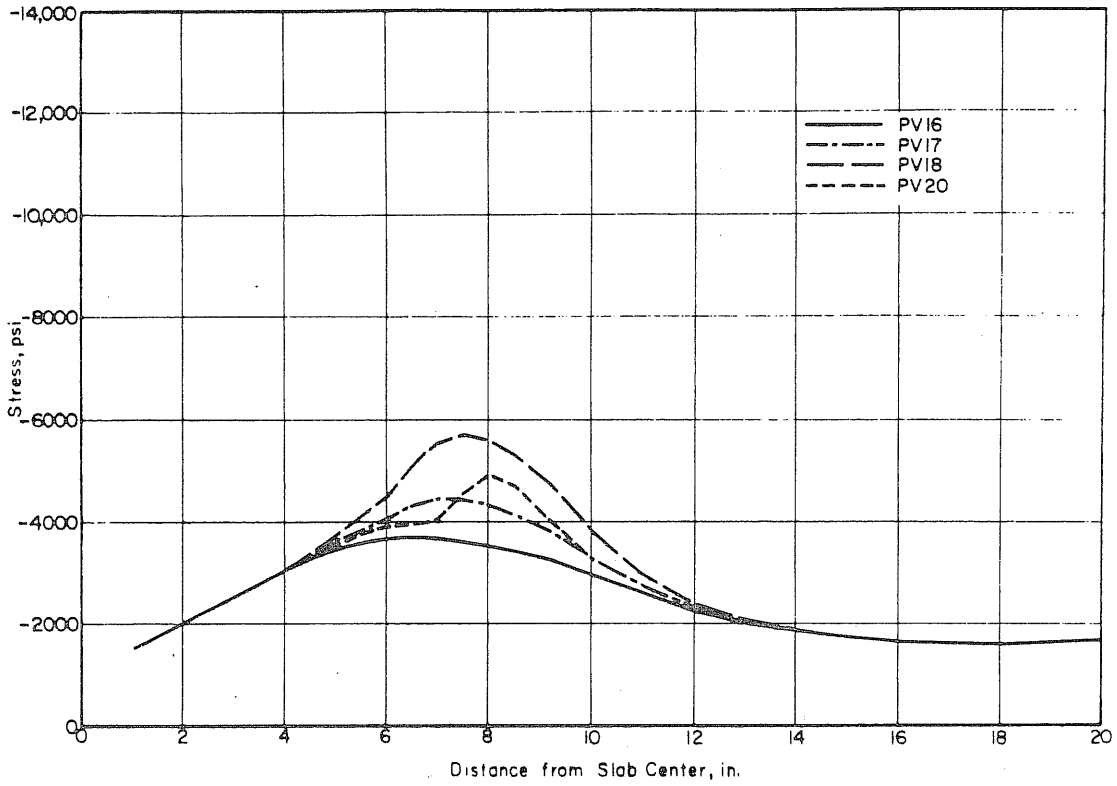

FIG. 7.12 CALCULATED VERTICAL STRESSES AT MID-HEIGHT OF CRYPTODOMES

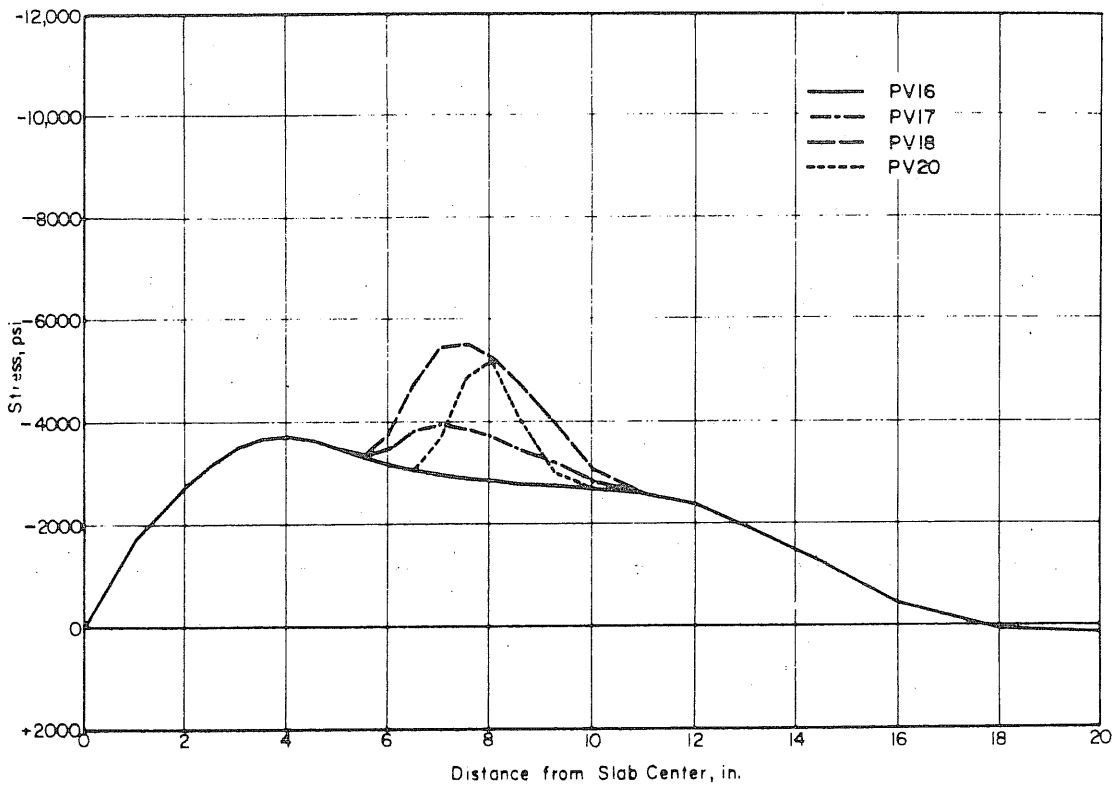

FIG. 7.13 CALCULATED SHEAR STRESSES AT MID-HEIGHT OF CRYPTODOMES

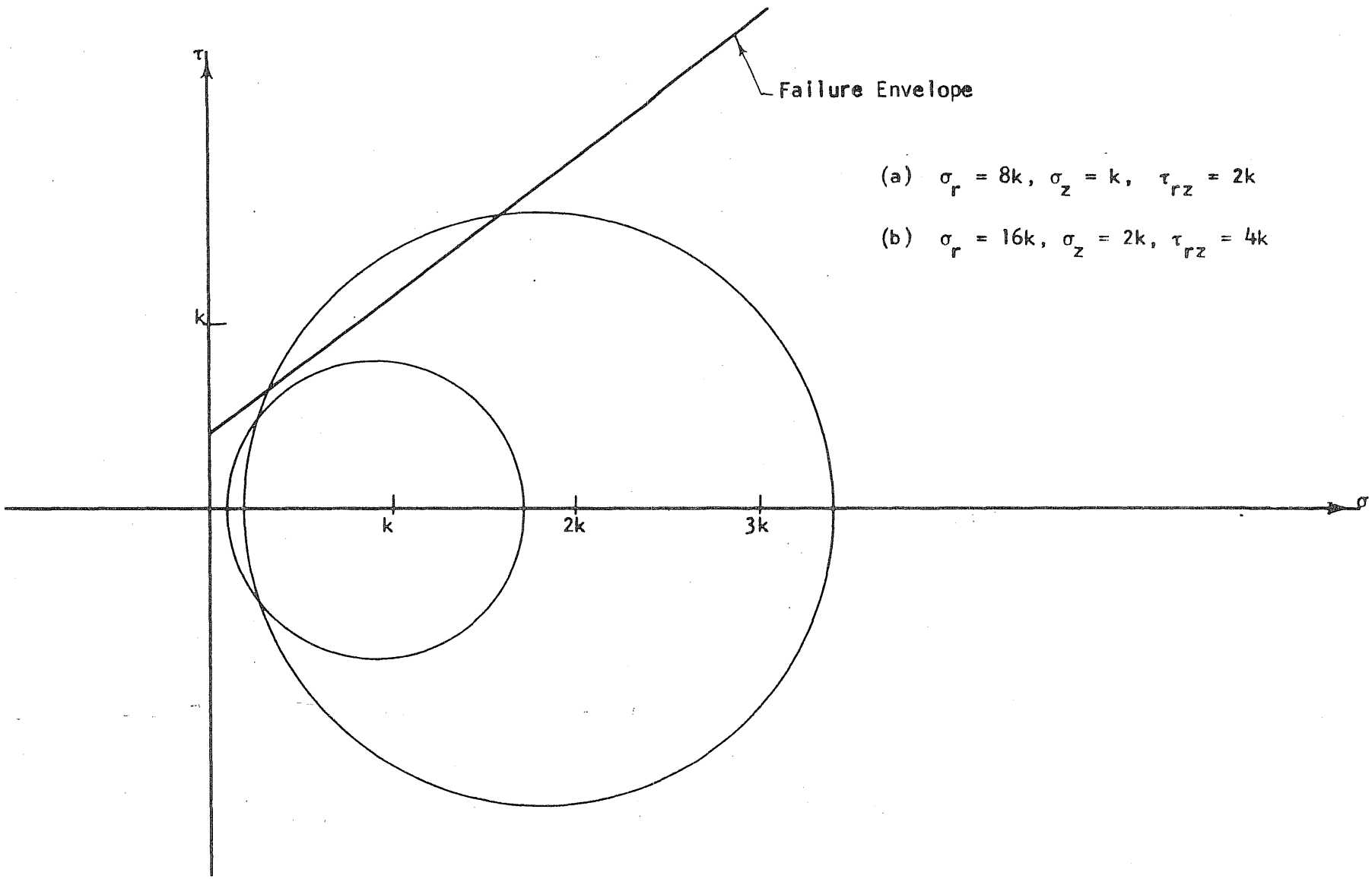

FIG. 7.14 STRESS CIRCLES FOR TWO STRESS COMBINATIONS

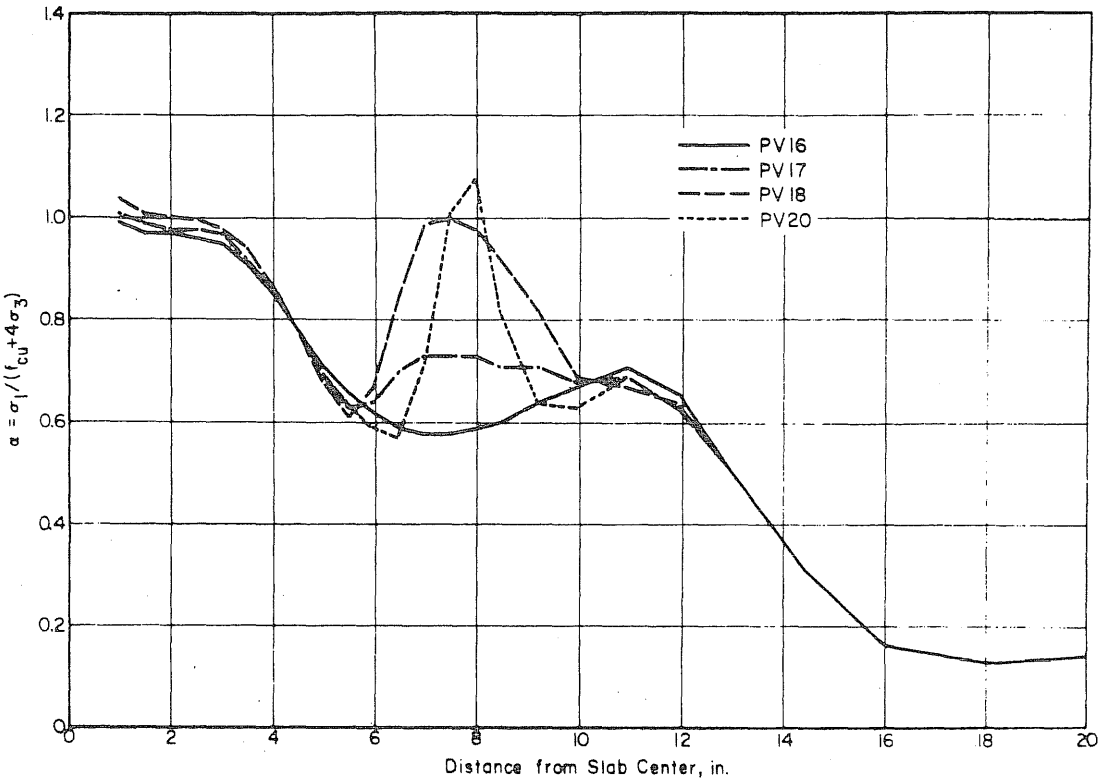

FIG. 7.15 FAILURE INDICES BASED ON STRESSES AT MID-HEIGHT OF CRYPTODOMES

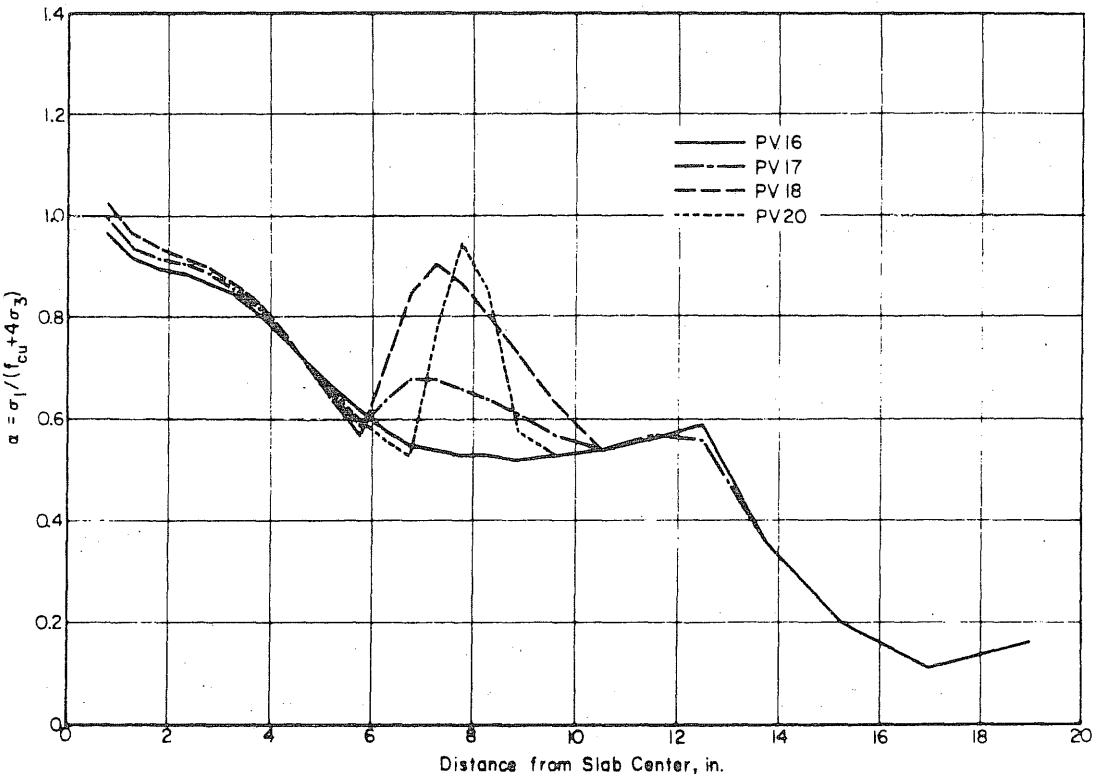

FIG. 7.16 FAILURE INDICES BASED ON AVERAGE STRESSES AT VERTICAL SECTIONS OF CRYPTODOMES

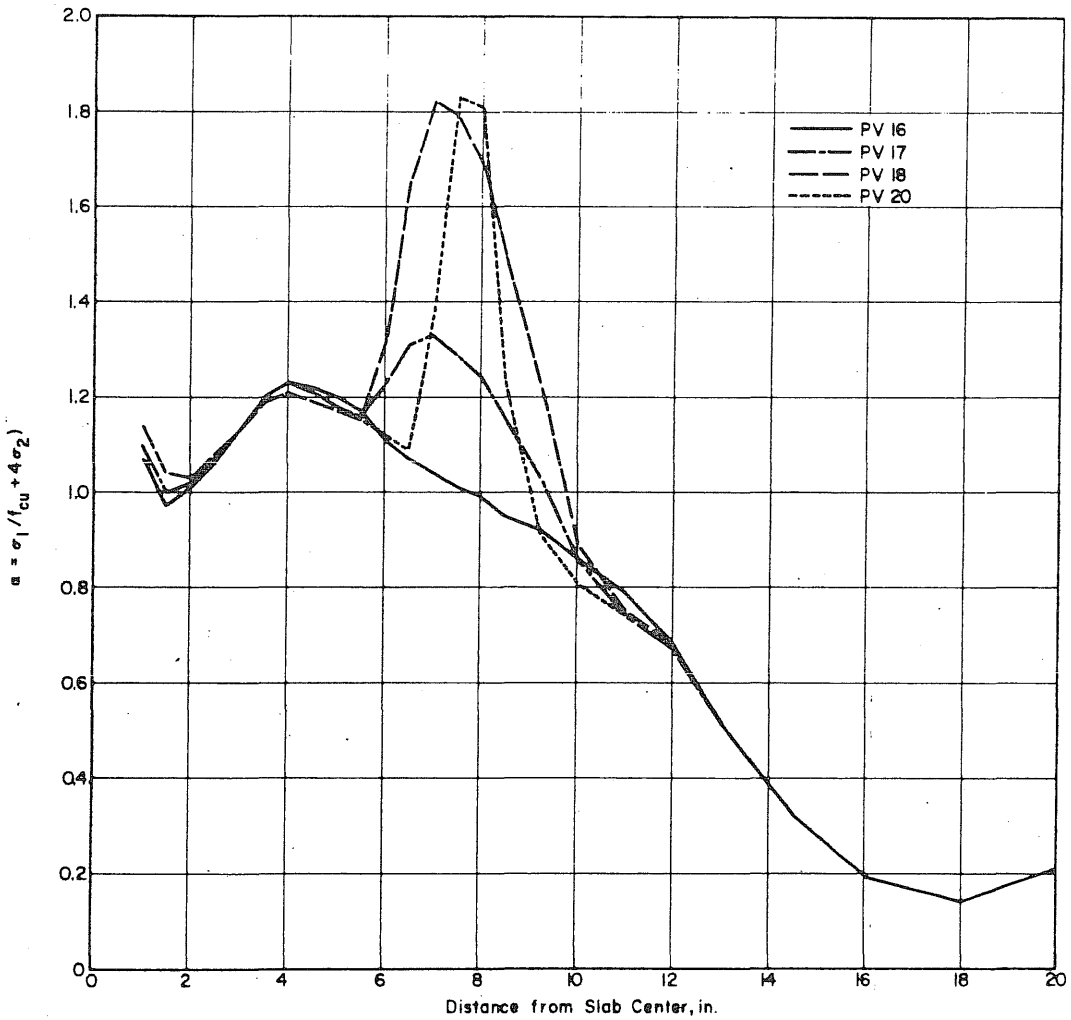

FIG. 7.17 FAILURE INDICES BASED ON THE WORST STRESS COMBINATIONS AT VERTICAL SECTIONS OF CRYPTODOMES

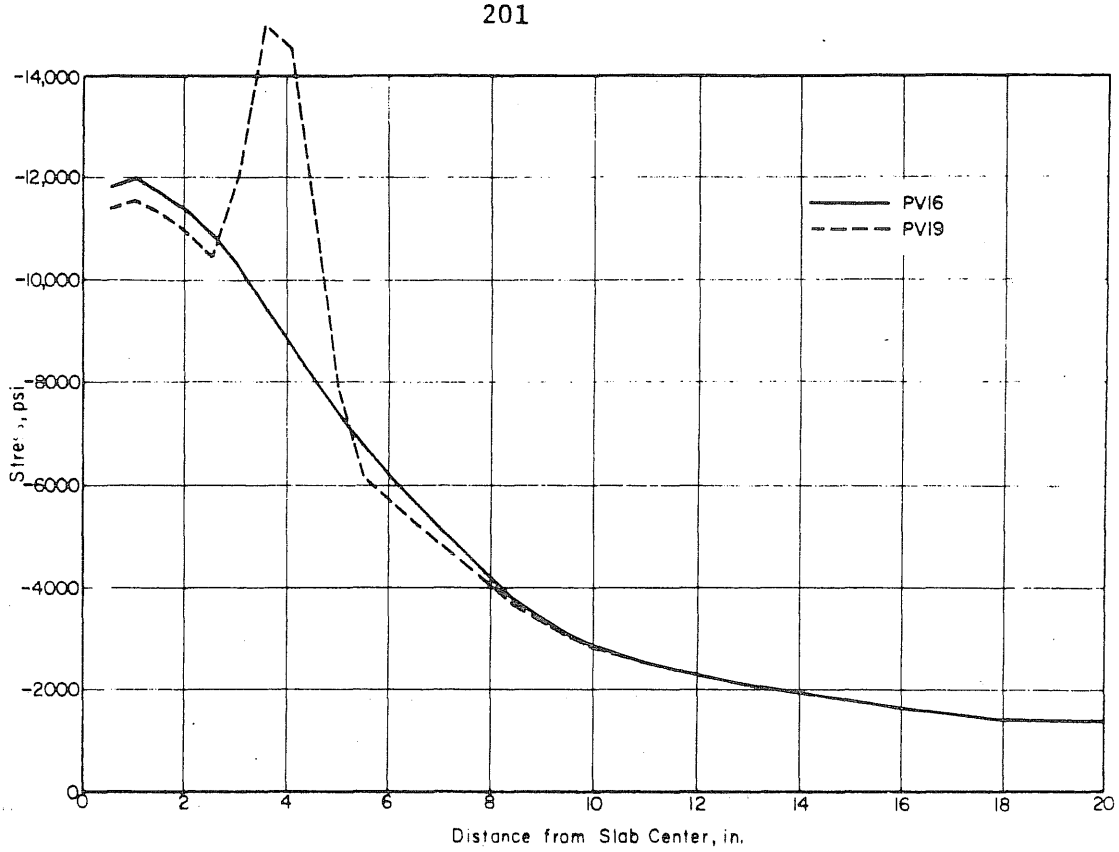

FIG. 7.18 CALCULATED RADIAL STRESSES AT MID-HEIGHT OF CRYPTODOMES

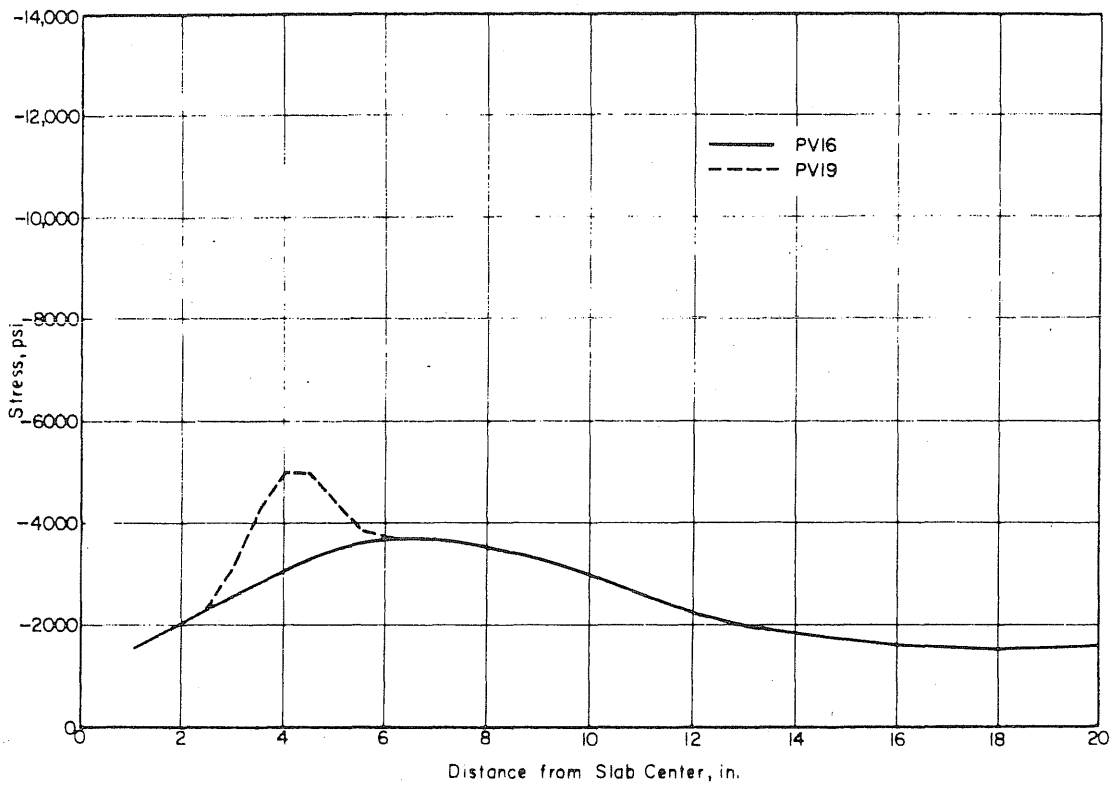

FIG. 7.19 CALCULATED VERTICAL STRESSES AT MID-HEIGHT OF CRYPTODOMES

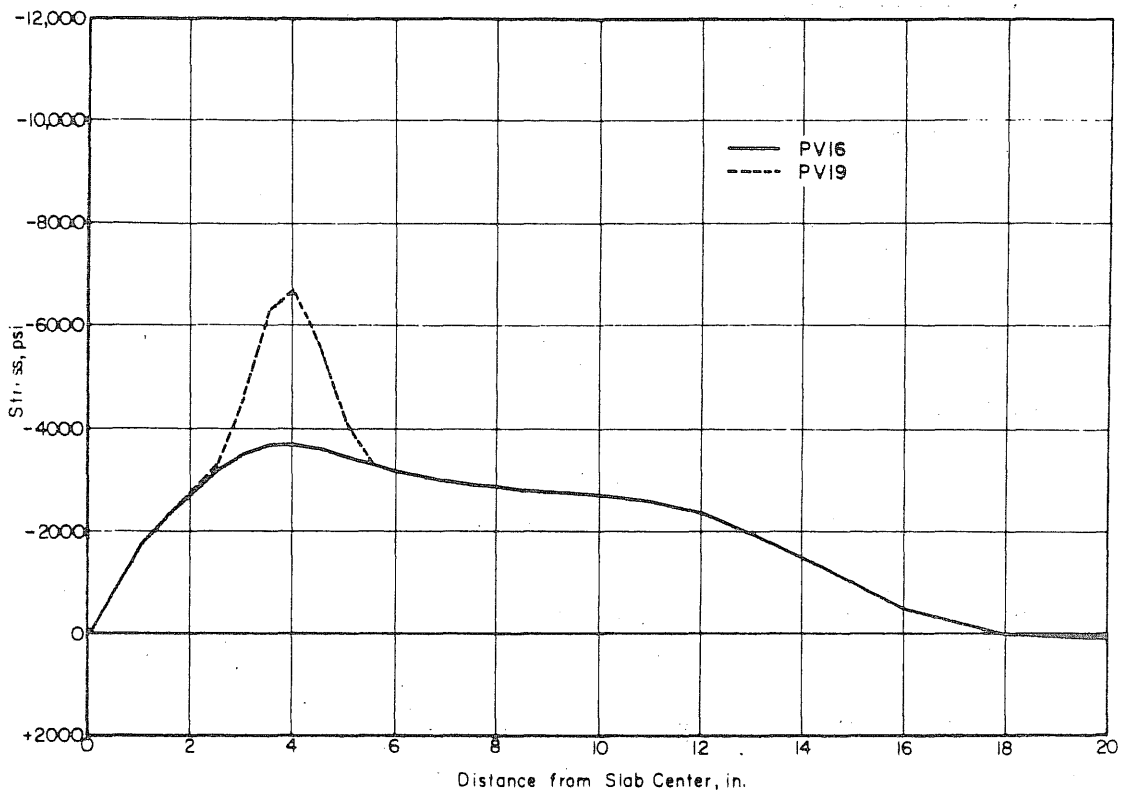

FIG. 7.20 CALCULATED SHEAR STRESSES AT MID-HEIGHT OF CRYPTODOMES

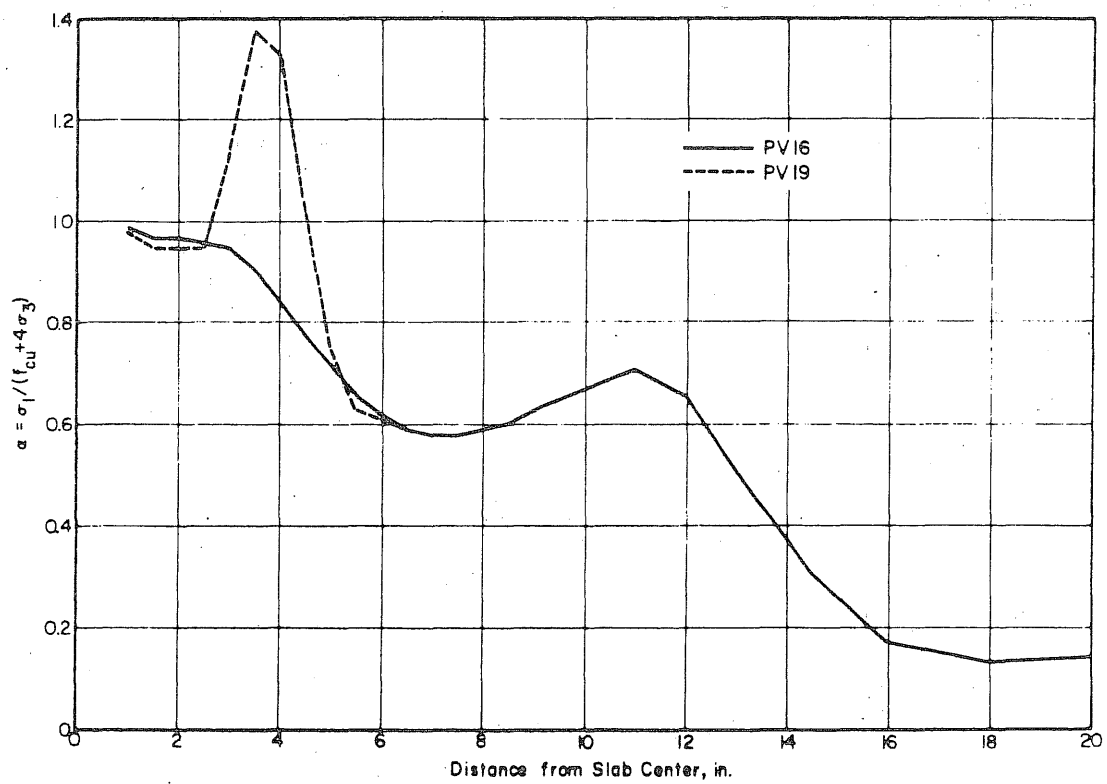

FIG. 7.21 FAILURE INDICES BASED ON STRESSES AT MID-HEIGHT OF CRYPTODOMES

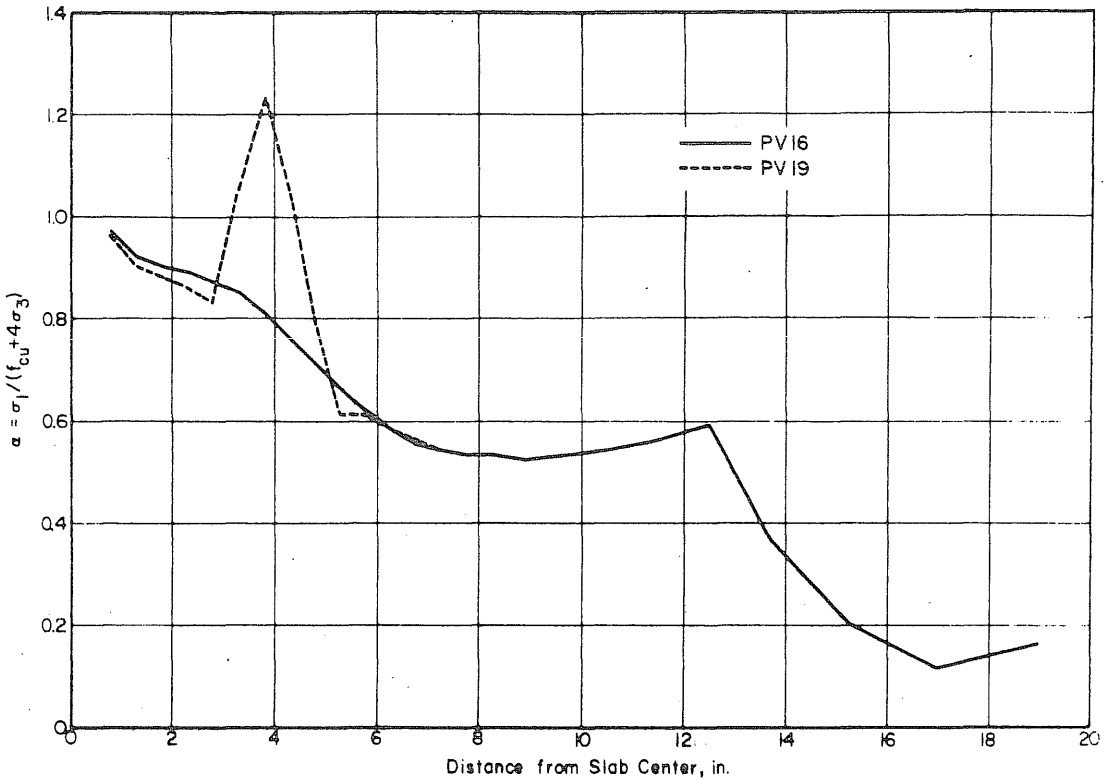

FIG. 7.22 FAILURE INDICES BASED ON AVERAGE STRESSES AT VERTICAL SECTIONS OF CRYPTODOMES

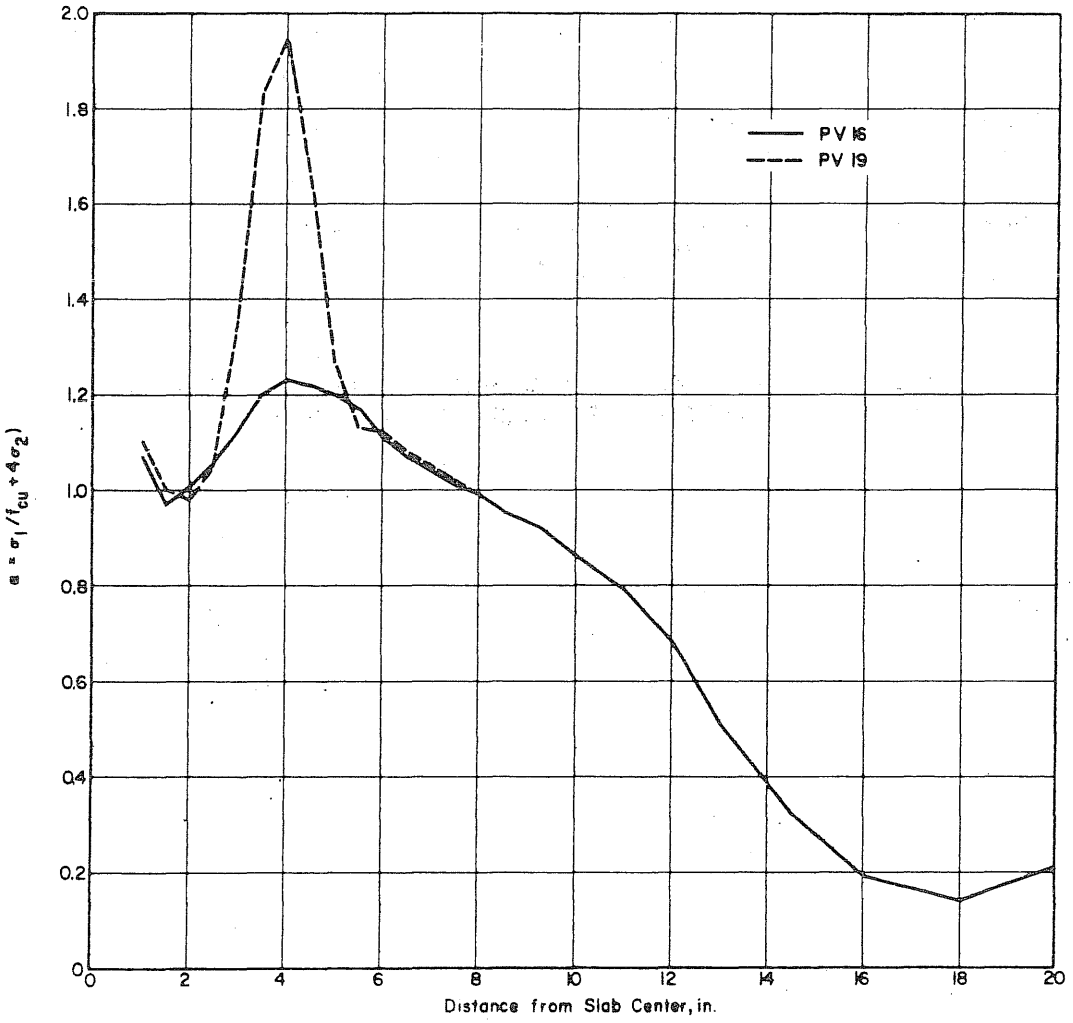

FIG. 7.23 FAILURE INDICES BASED ON THE WORST STRESS COMBINATIONS AT VERTICAL SECTIONS OF CRYPTODOMES

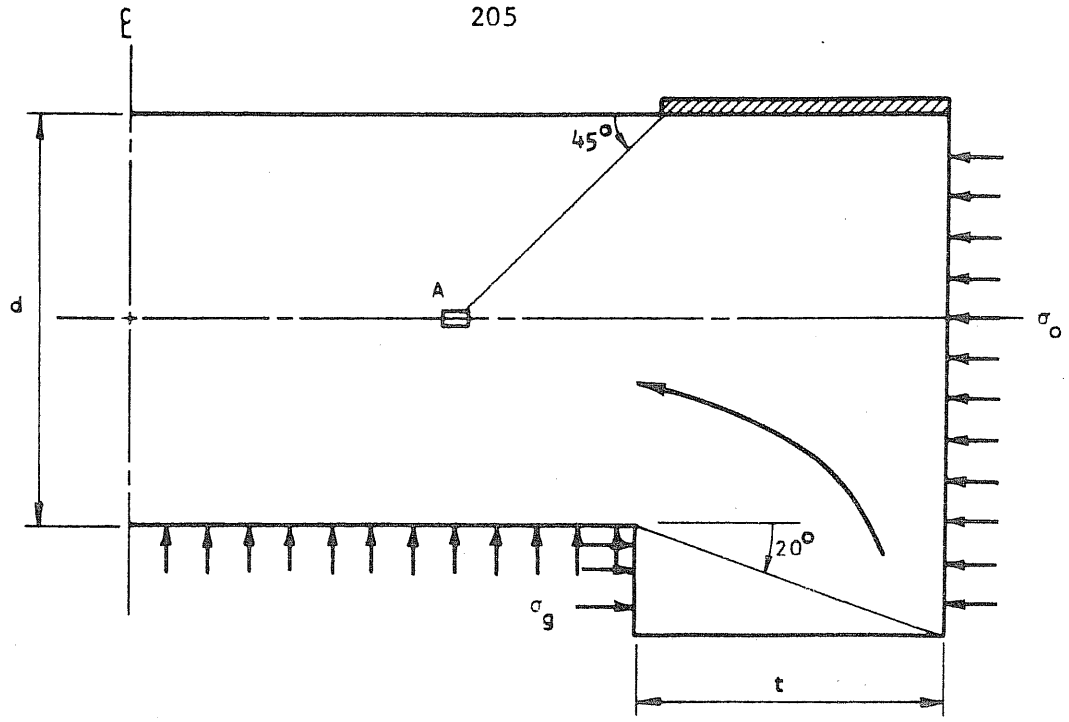

FIG. 8.1 CALCULATION OF THE RADIAL STRESS AT POINT A

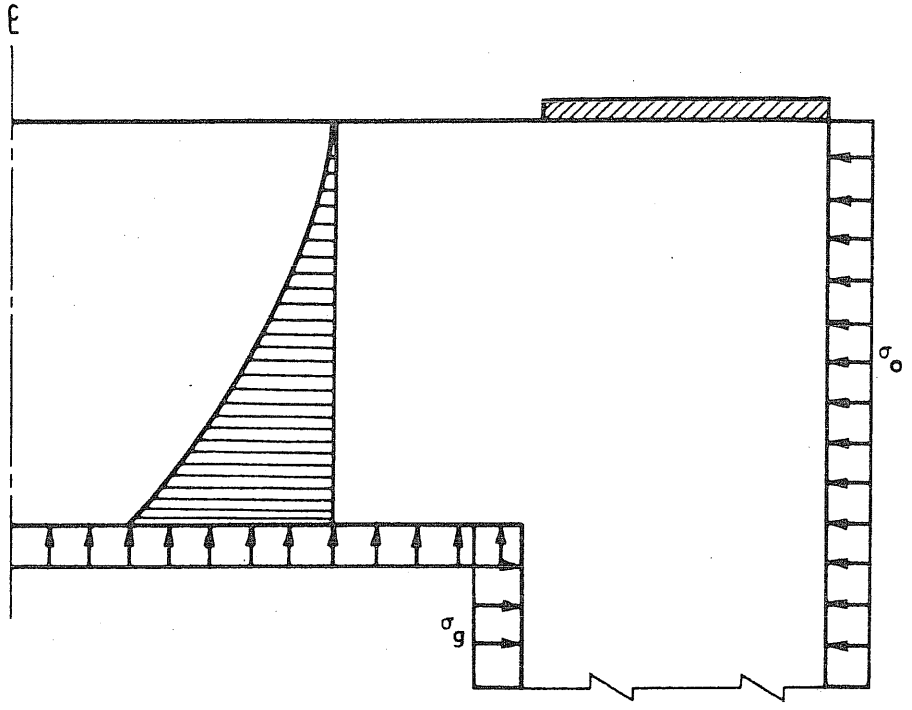

FIG. 8.2 CALCULATION OF THE VERTICAL STRESS AT POINT A

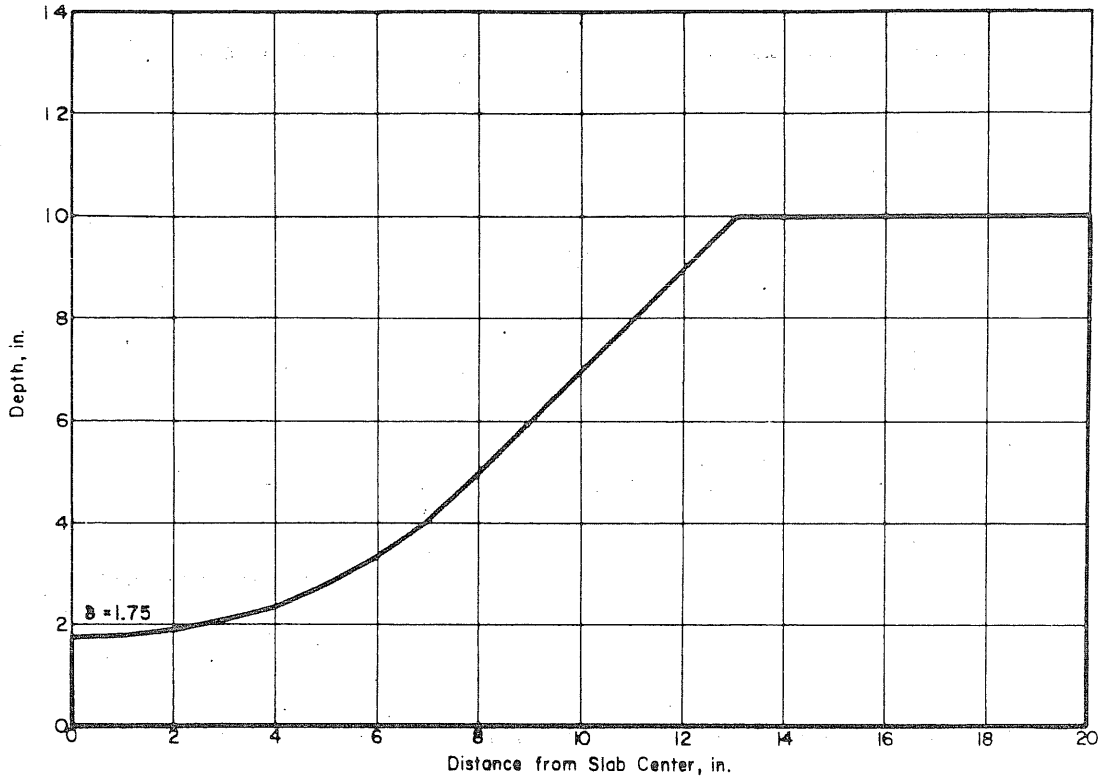

FIG. 9.1 HYPOTHETICAL SHAPE OF THE CRYPTODOME IN END SLAB OF VESSEL PV16

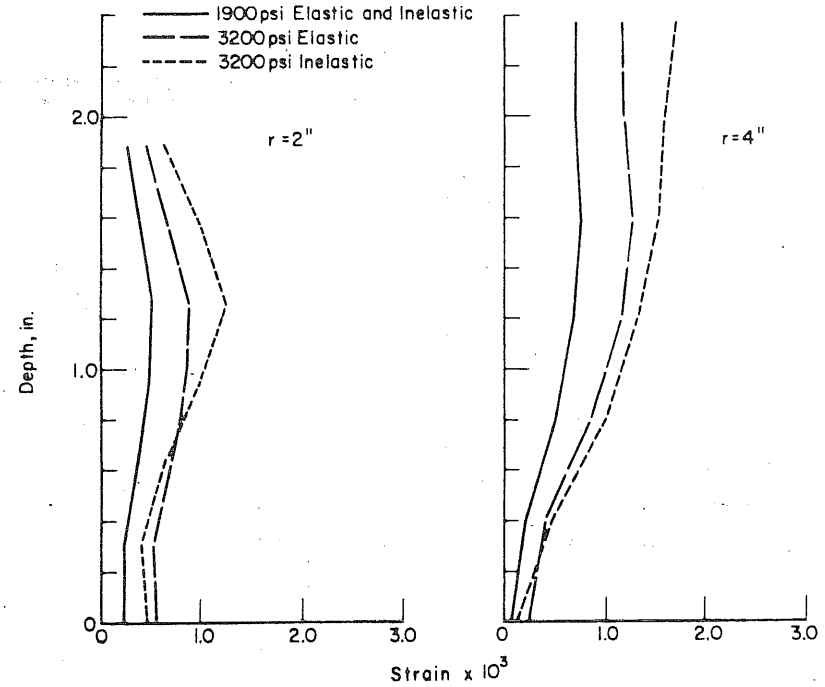

FIG. 9.2 CALCULATED STRAINS IN THE CRYPTODOME SHOWN IN FIG. 9.1 AT TWO INTERNAL PRESSURES AND ASSUMING ELASTIC AND INELASTIC MATERIAL PROPERTIES

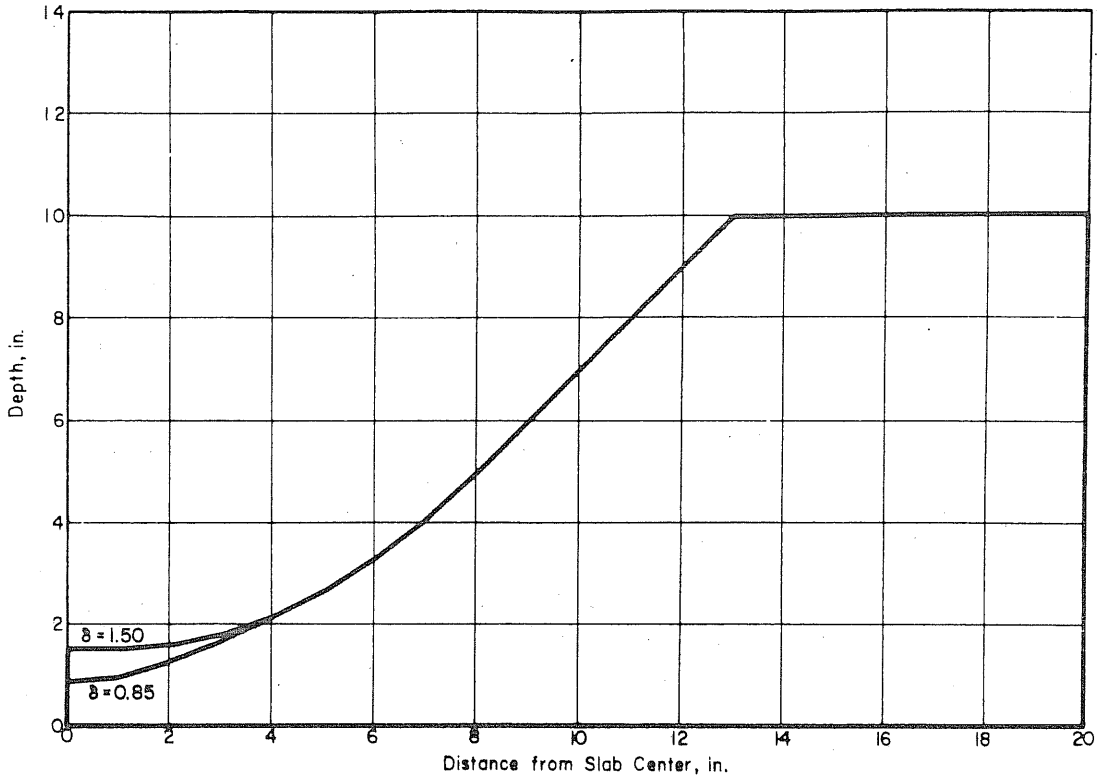

FIG. 9.3 TWO CRYPTODOMES THAT HAVE IDENTICAL SHAPES AT RADII LARGER THAN 4 in.

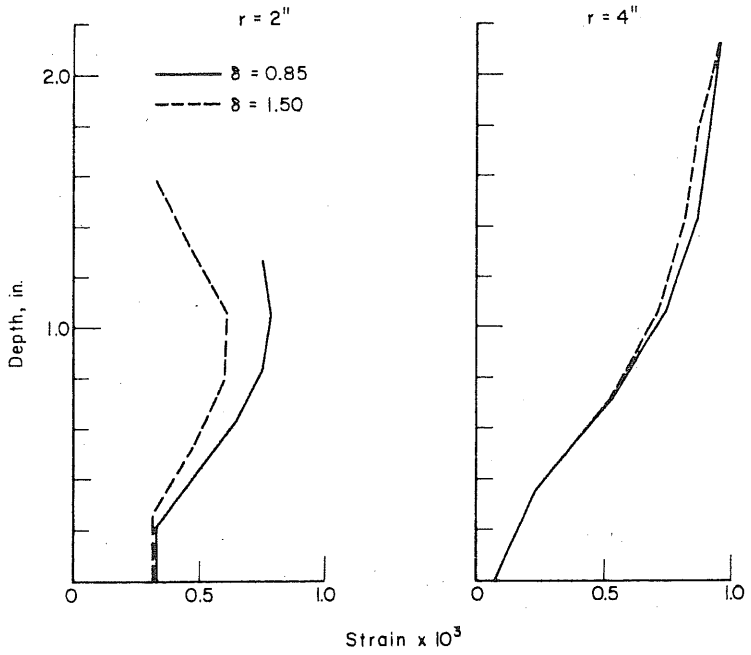

FIG. 9.4 CALCULATED MAXIMUM TENSILE STRAINS IN THE CRYPTODOMES SHOWN IN FIG. 9.3

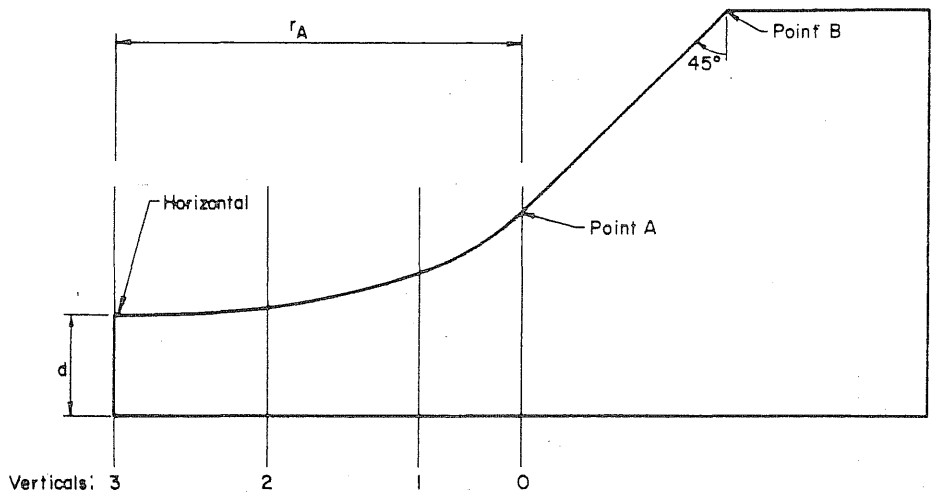

FIG. 9.5 GEOMETRICAL CONDITIONS THAT HAVE TO BE SATISFIED BY THE INCLINED CRACK

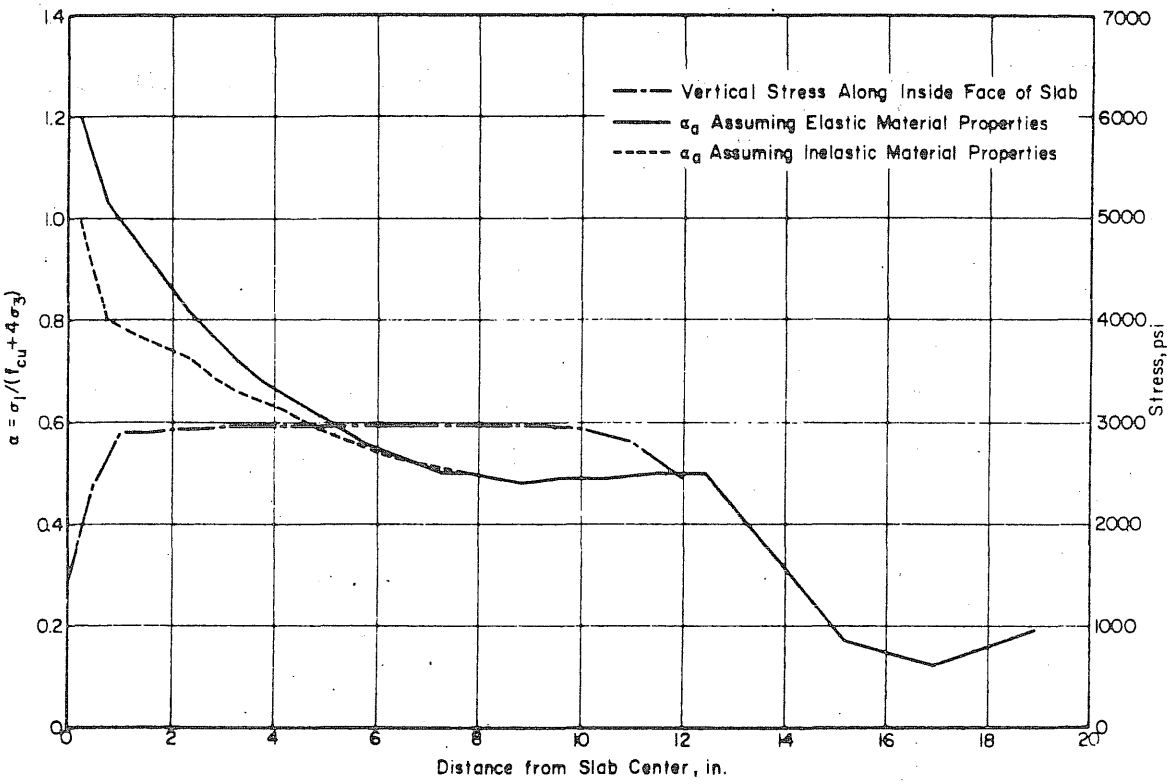

FIG. 9.6 FAILURE INDICES BASED ON AVERAGE STRESSES AND THE VERTICAL STRESS ALONG THE INSIDE FACE OF THE SLAB FOR AN ARBITRARY DOME AT 2850 psi INTERNAL PRESSURE

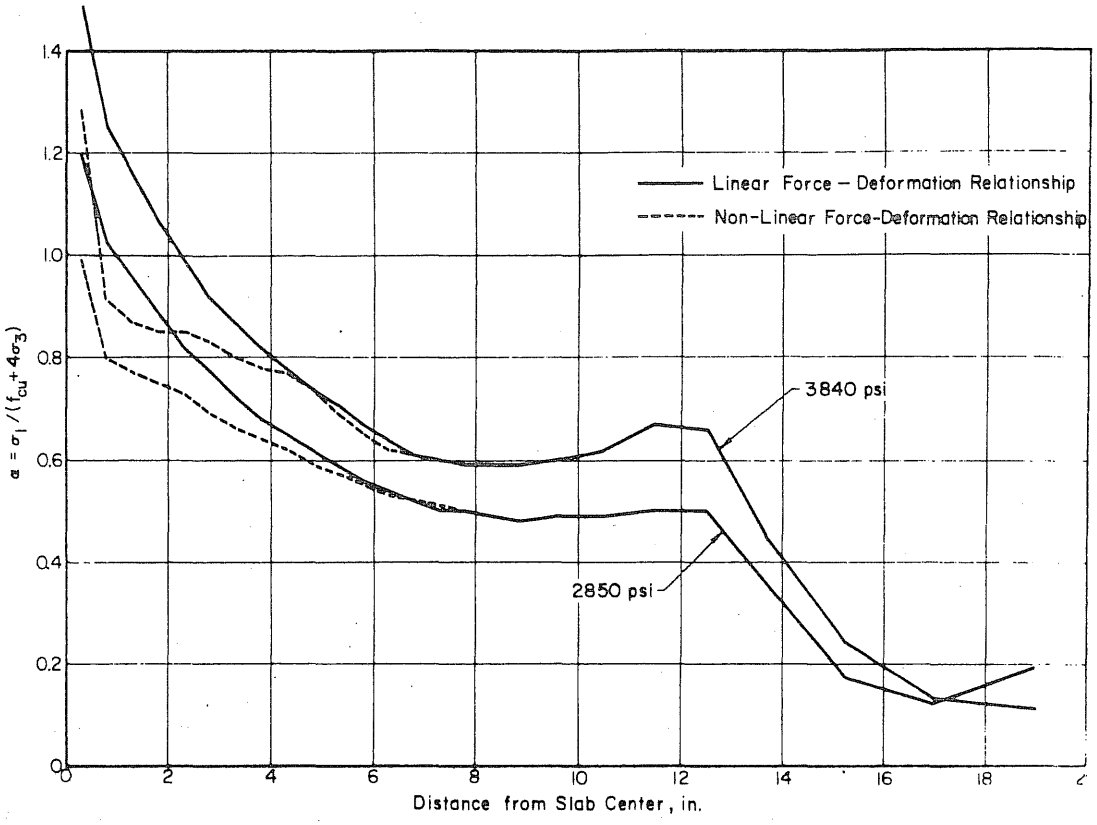

FIG. 9.7 FAILURE INDICES BASED ON AVERAGE STRESSES FOR AN ARBITRARY DOME AT TWO DIFFERENT INTERNAL PRESSURES

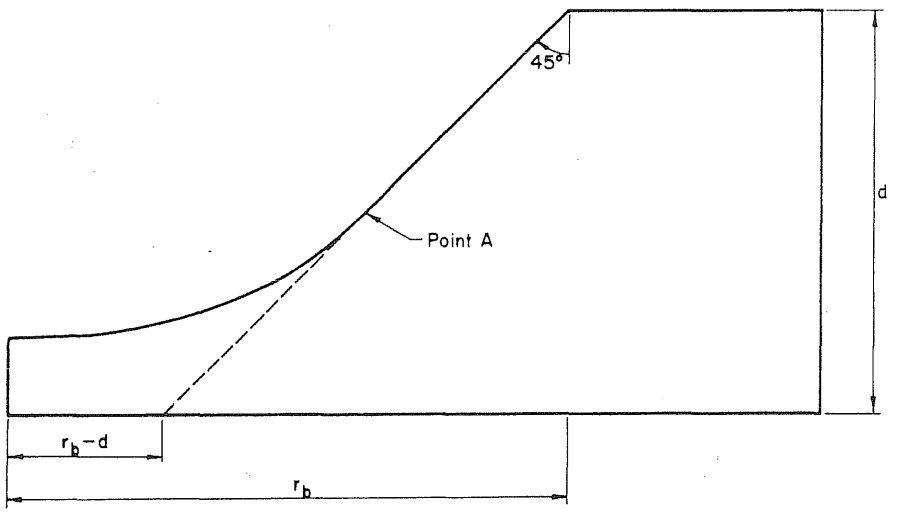

FIG. 9.8 THE EXTENT OF THE DOME THAT HAS TO SATISFY THE TWO FAILURE CRITERIA

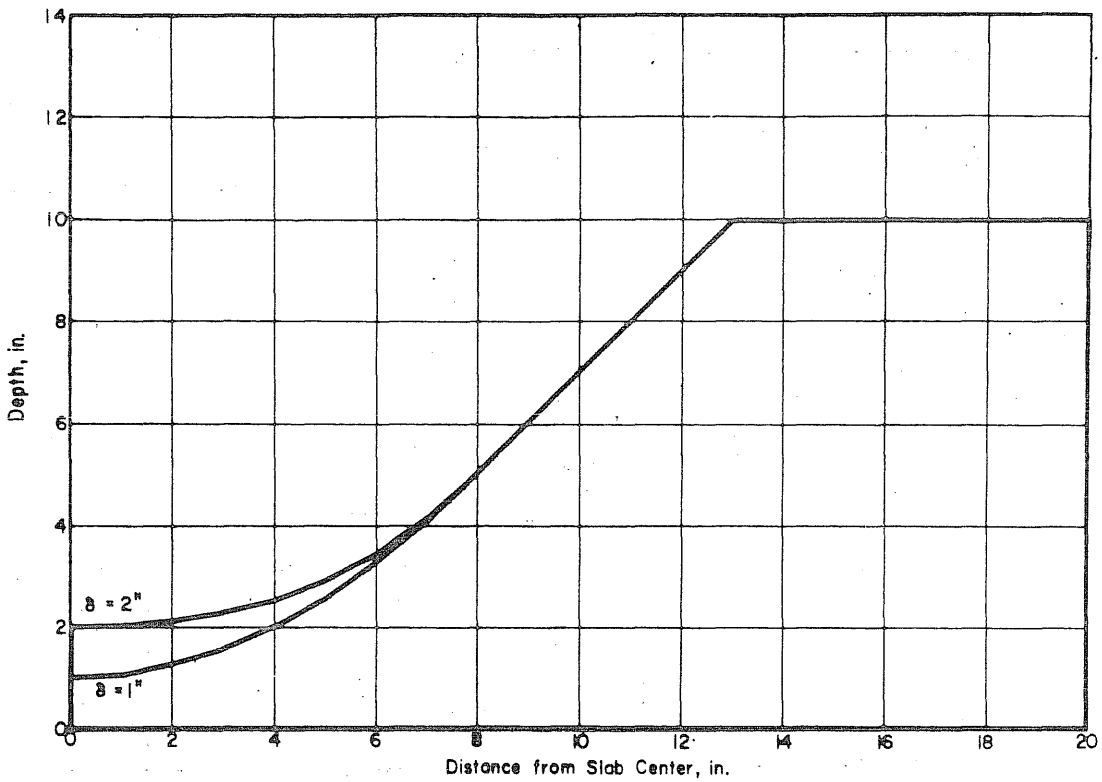

FIG. 9.9 POSSIBLE SHAPES OF THE CRYPTODOME IN THE END SLAB OF VESSEL PV16 AS DETERMINED BY EQ. 9.4

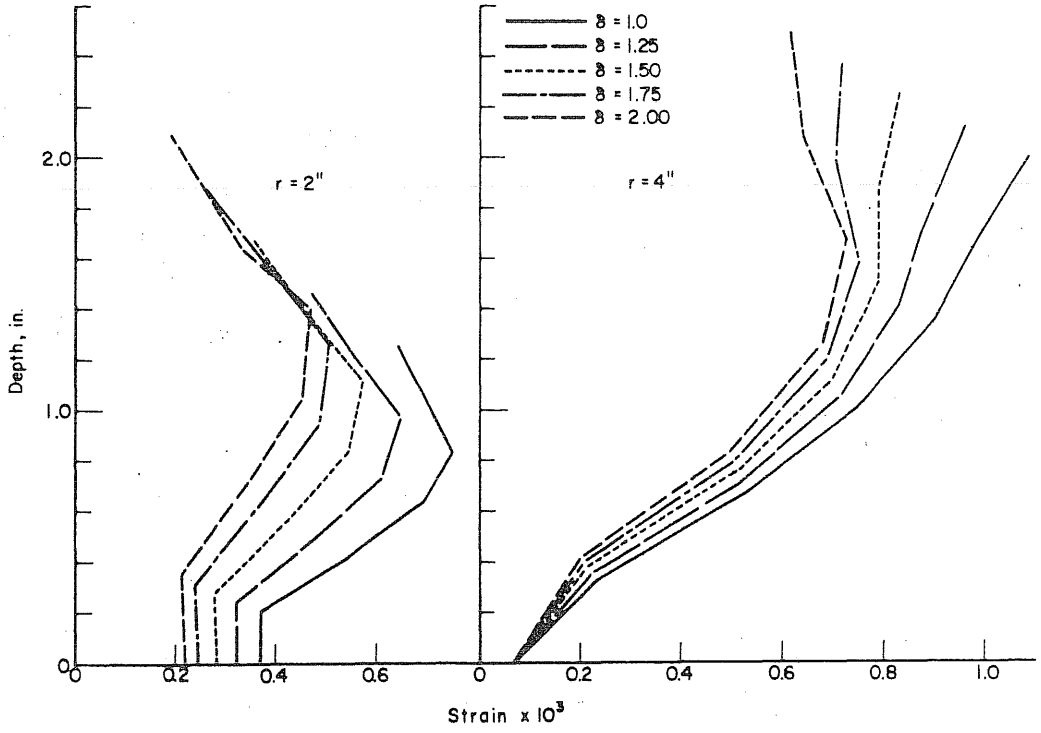

FIG. 9.10 CALCULATED MAXIMUM TENSILE STRAINS IN THE DOMES SHOWN IN FIG. 9.9

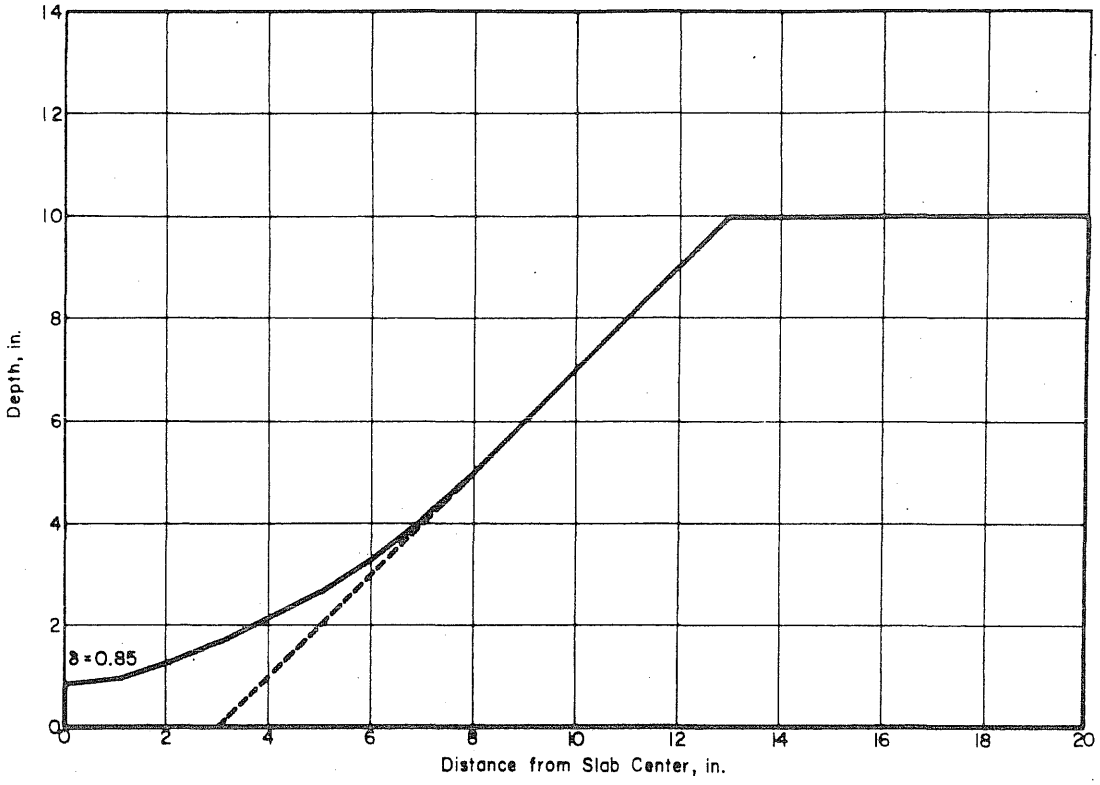

FIG. 9.11 CALCULATED SHAPE OF THE DOME IN THE END SLAB OF VESSEL PV16 AND THE DEFINED EXTENT OF THE STACK OF THE DOME

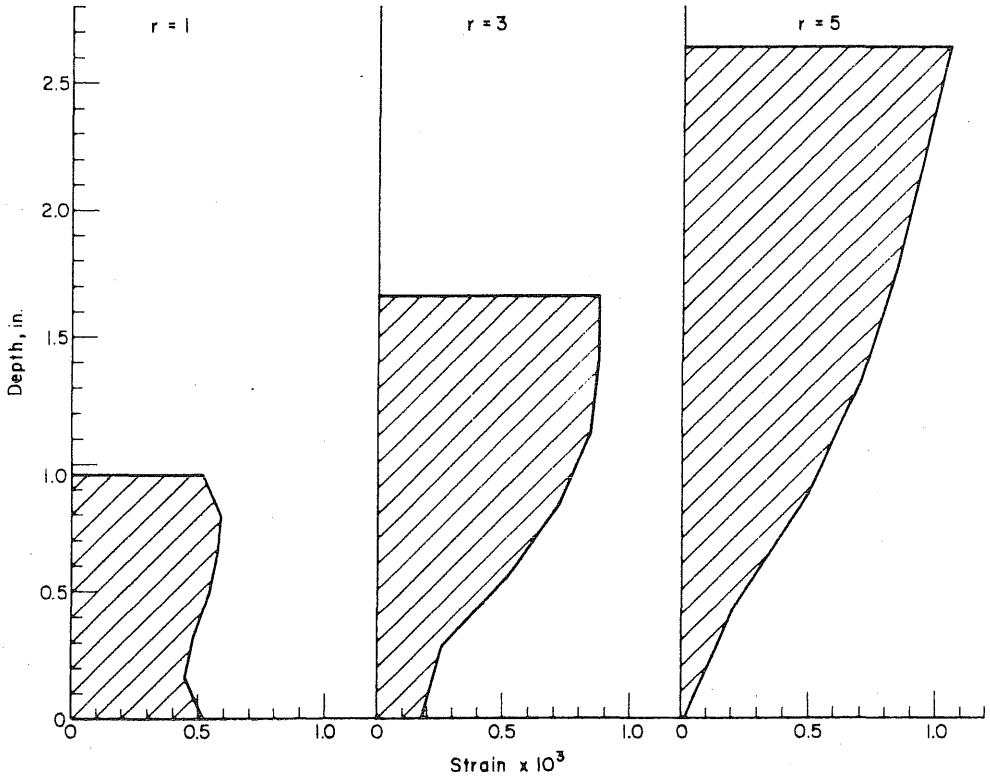

FIG. 9.12 CALCULATED MAXIMUM PRINCIPAL STRAINS IN THE DOME SHOWN IN FIG. 9.11 AT AN INTERNAL PRESSURE OF 1900 psi

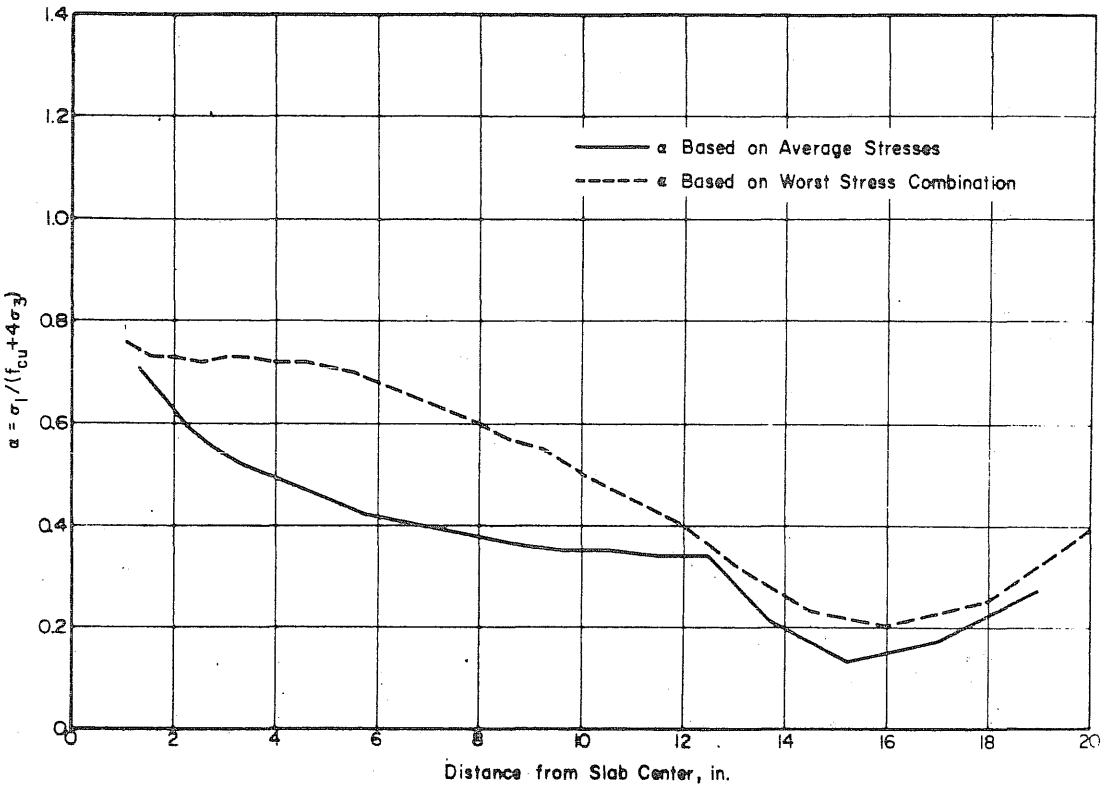

FIG. 9.13 CALCULATED FAILURE INDICES IN THE DOME SHOWN IN FIG. 9.11 AT AN INTERNAL PRESSURE OF 1900 psi

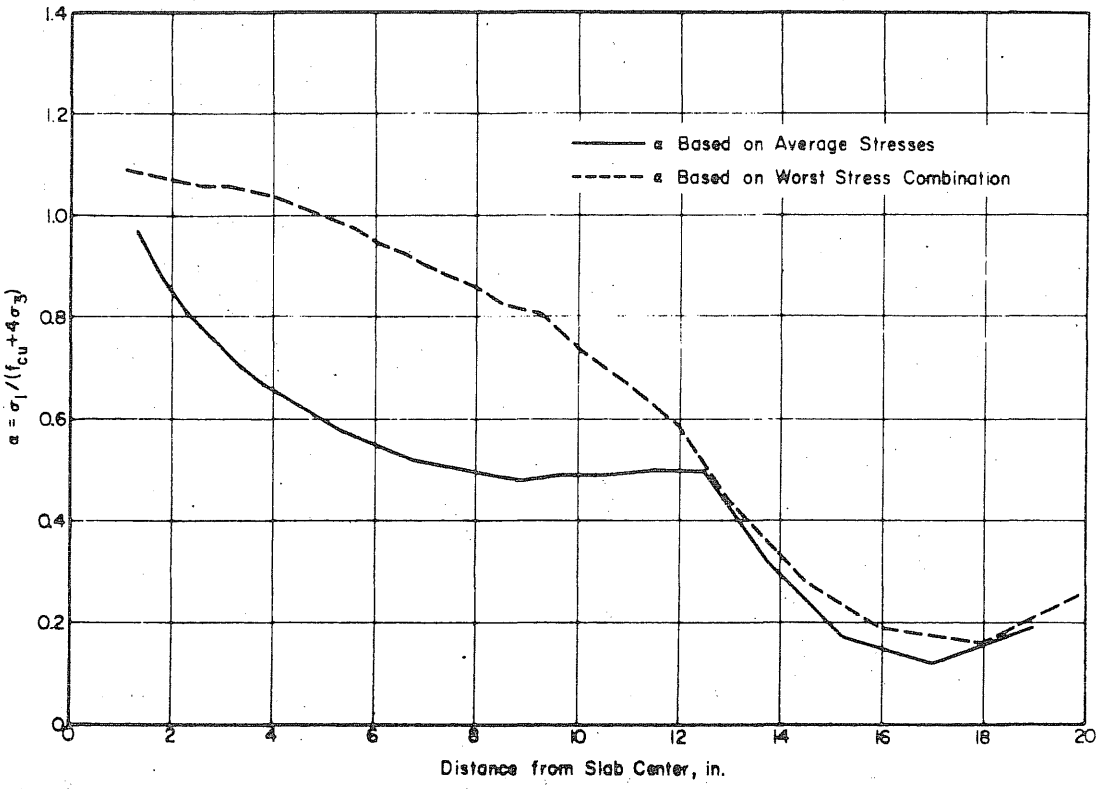

FIG. 9.14 CALCULATED FAILURE INDICES IN THE DOME SHOWN IN FIG. 9.11 AT AN INTERNAL PRESSURE OF 2850 psi

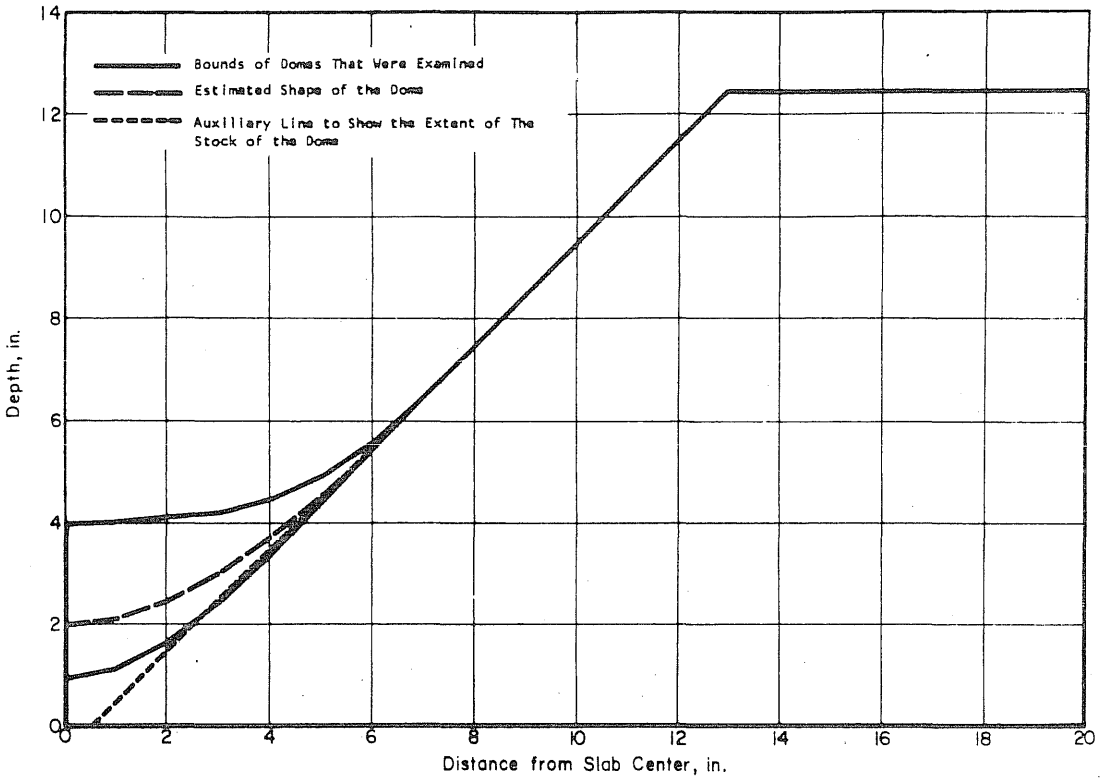

FIG. 9.15 POSSIBLE SHAPES OF THE CRYPTODOME IN THE END SLAB OF VESSEL PV13 AS DETERMINED BY A CUBIC EQUATION

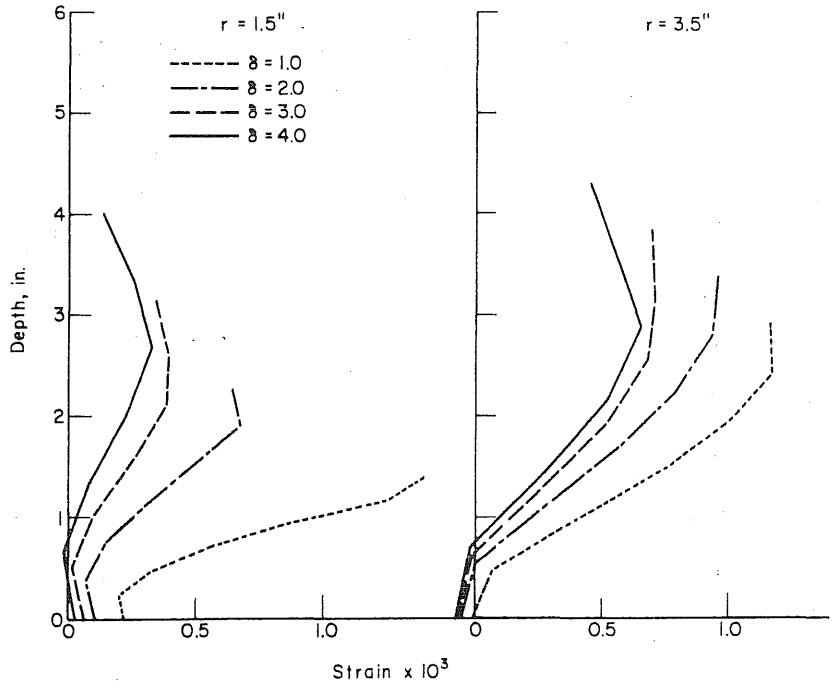

FIG. 9.16 CALCULATED MAXIMUM TENSILE STRAINS IN THE DOMES SHOWN IN FIG. 9.15

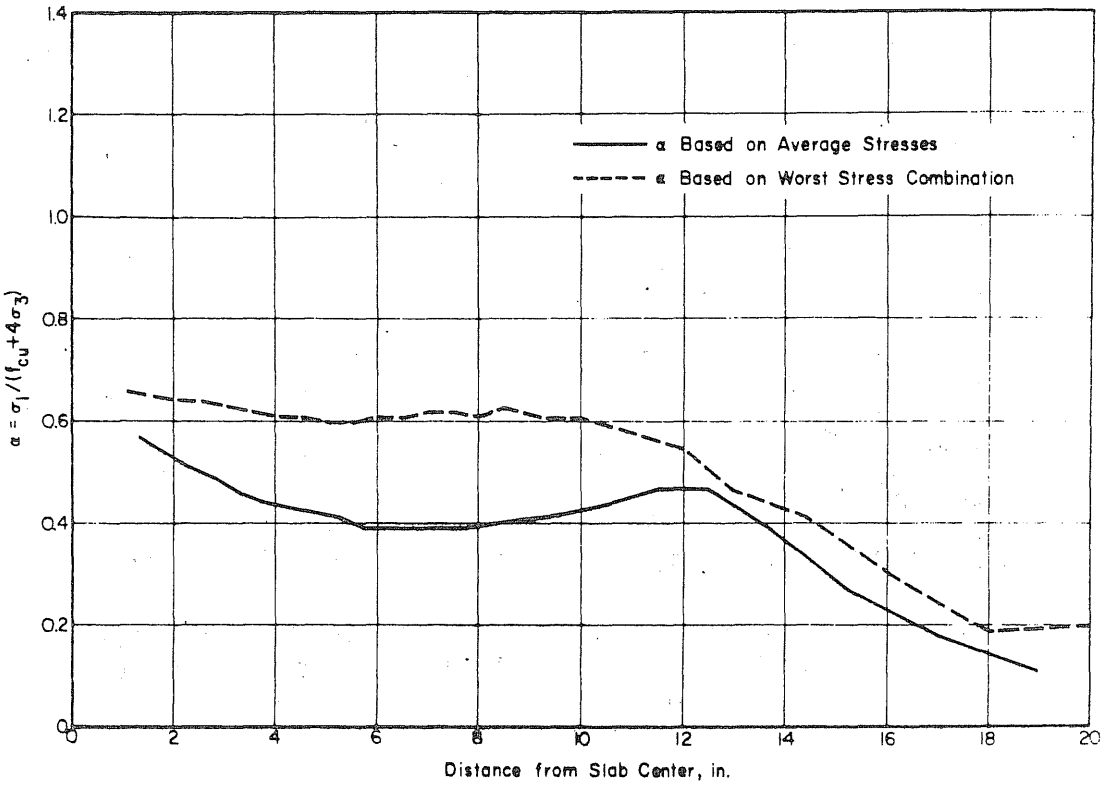

FIG. 9.17 CALCULATED FAILURE INDICES IN THE DOME SHOWN IN FIG. 9.15 THAT HAD A DEPTH AT VERTEX OF 2 in. AT AN INTERNAL PRESSURE OF 3500 psi

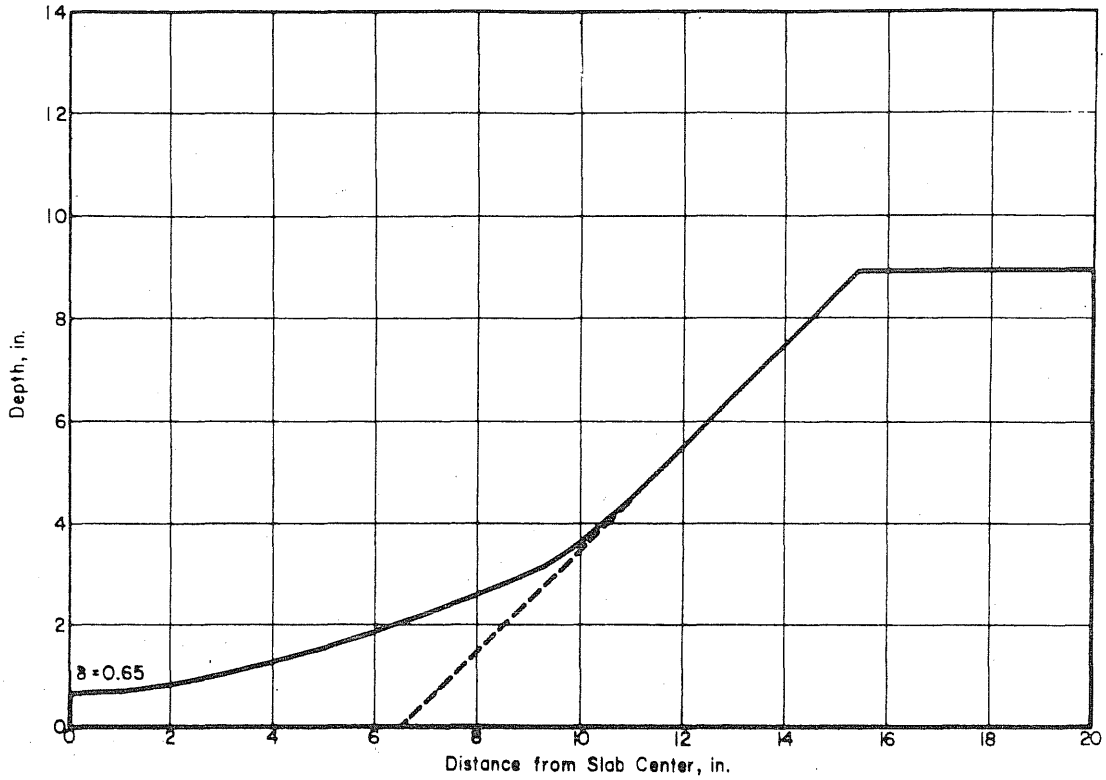

FIG. 9.18 THE SHAPE OF THE CRYPTODOME IN THE END SLAB OF VESSEL PV9 THAT WAS USED IN CALCULATING THE FAILURE INDICES

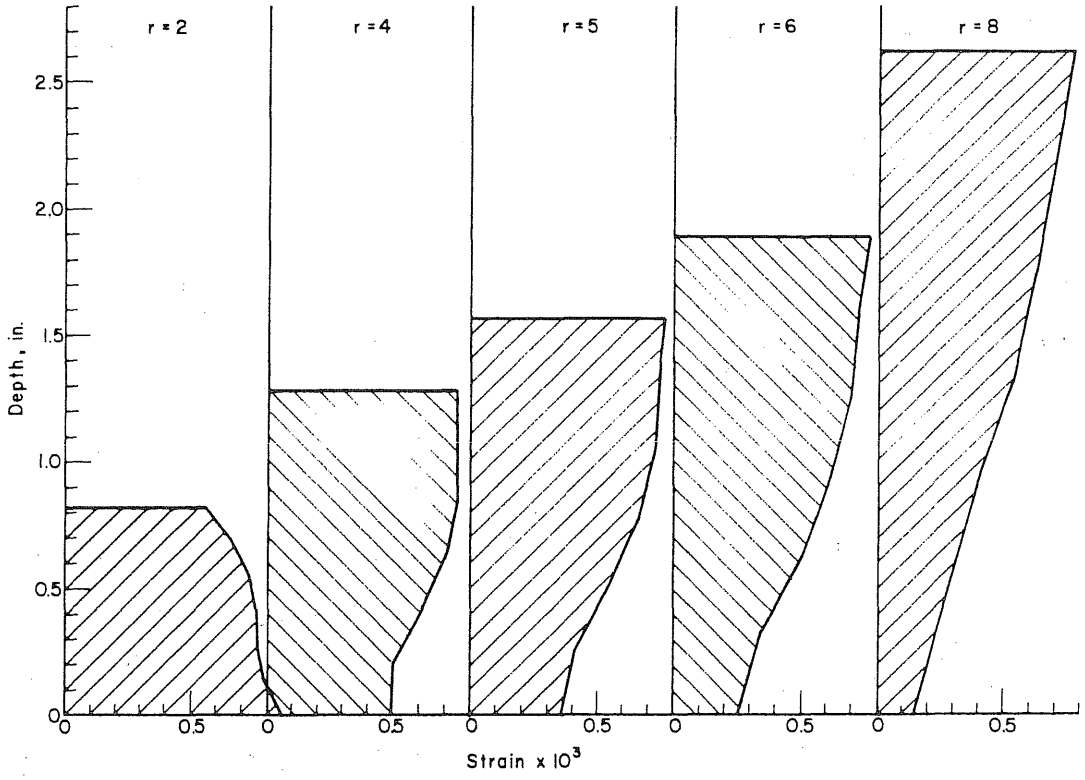

FIG. 9.19 THE DISTRIBUTION OF MAXIMUM TENSILE STRAINS IN THE DOME SHOWN IN FIG. 9.18 AT AN INTERNAL PRESSURE OF 810 psi

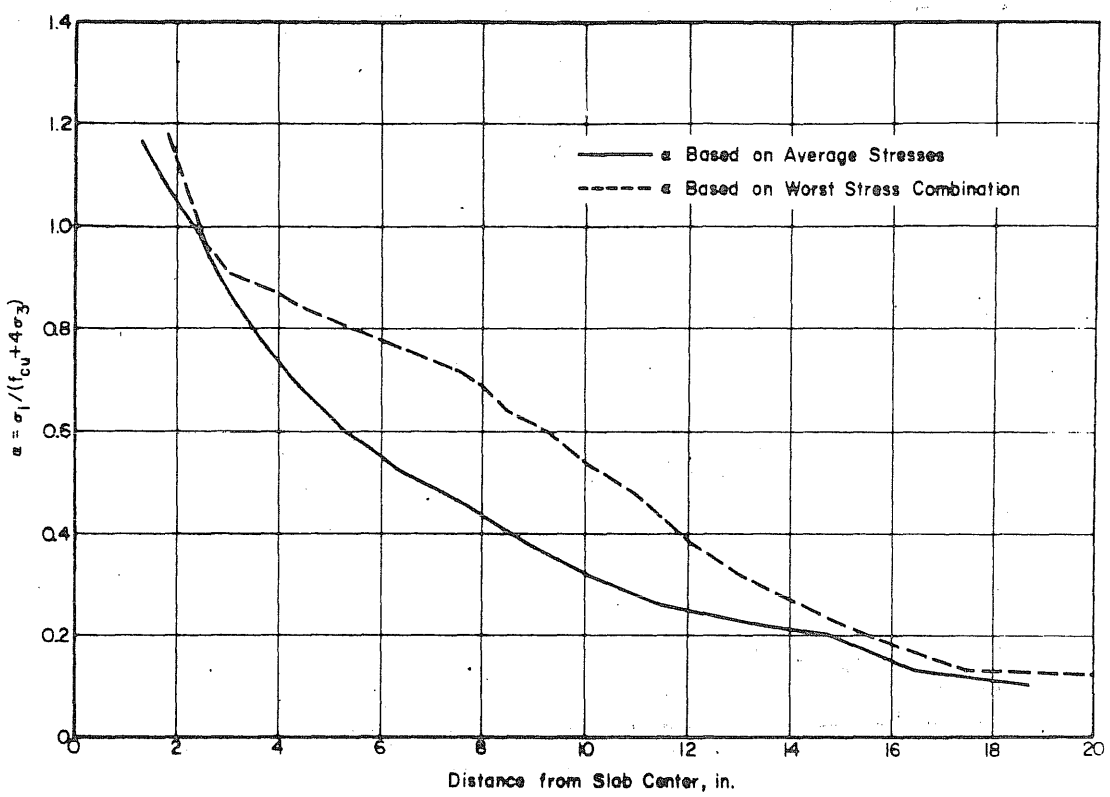

FIG. 9.20 CALCULATED FAILURE INDICES IN THE DOME SHOWN IN FIG. 9.18 AT AN INTERNAL PRESSURE OF 810 psi

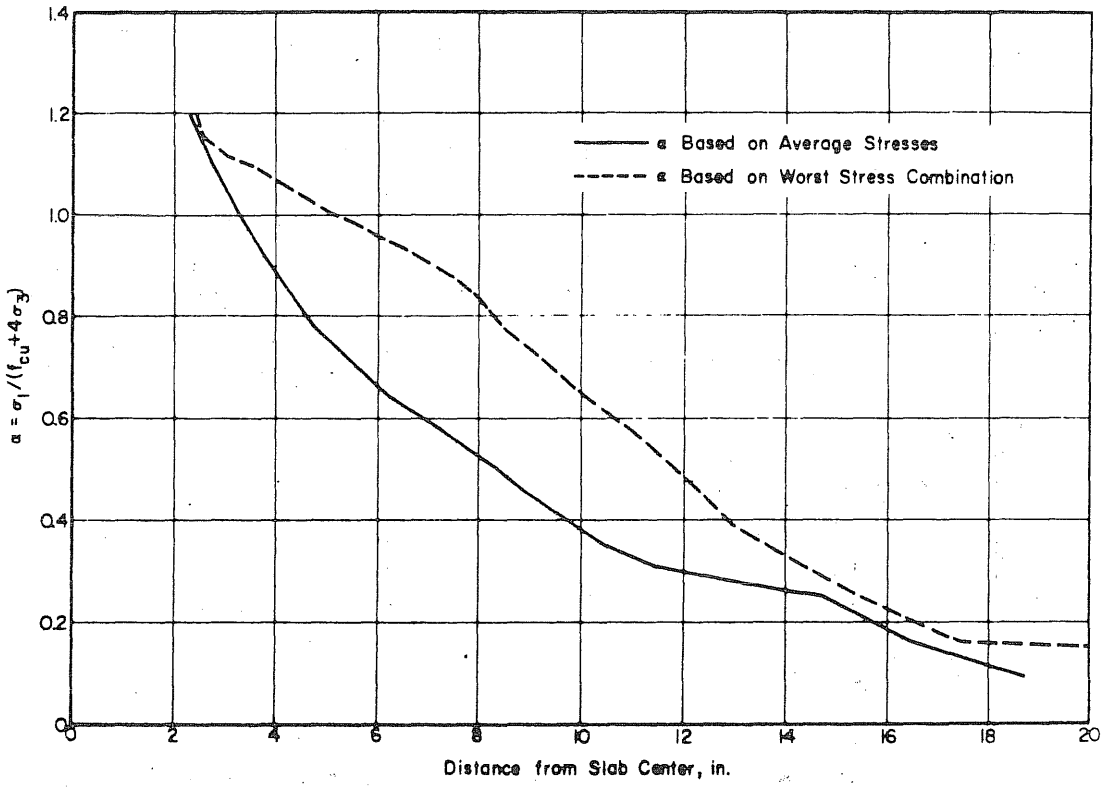

FIG. 9.21 CALCULATED FAILURE INDICES IN THE DOME SHOWN IN FIG. 9.18 AT AN INTERNAL PRESSURE OF 1000 psi

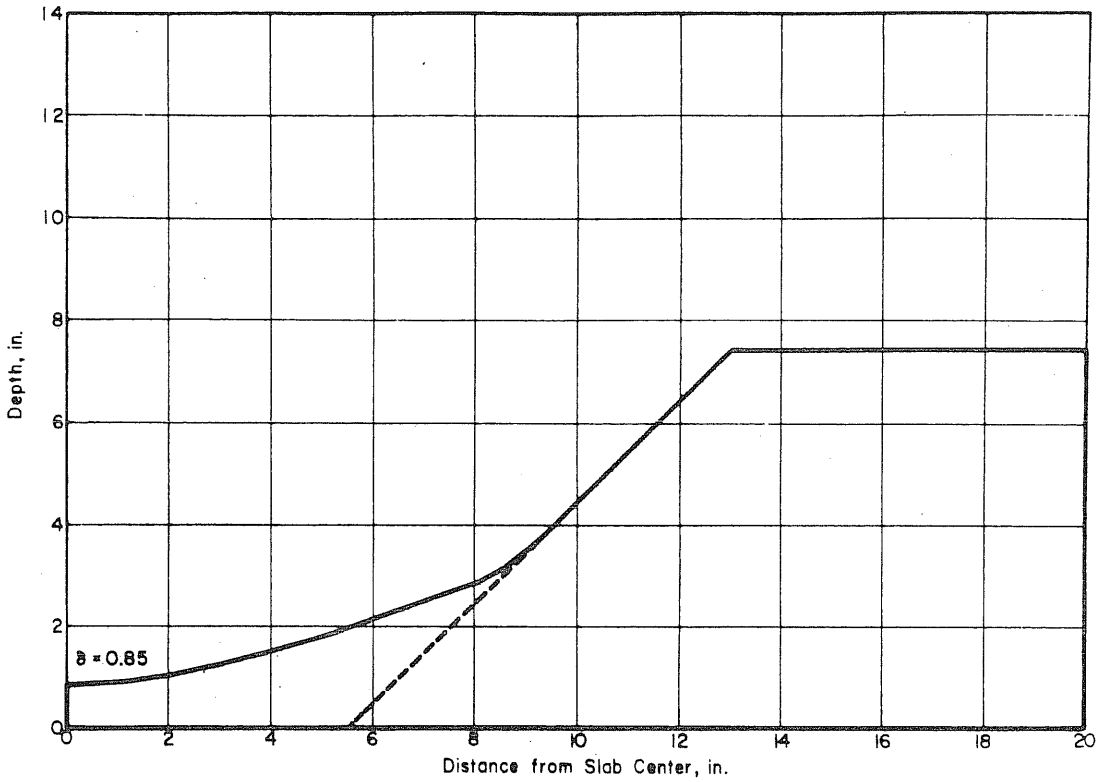

FIG. 9.22 THE SHAPE OF THE CRYPTODOME IN THE END SLAB OF VESSEL PV15 THAT WAS USED IN CALCULATING THE FAILURE INDICES

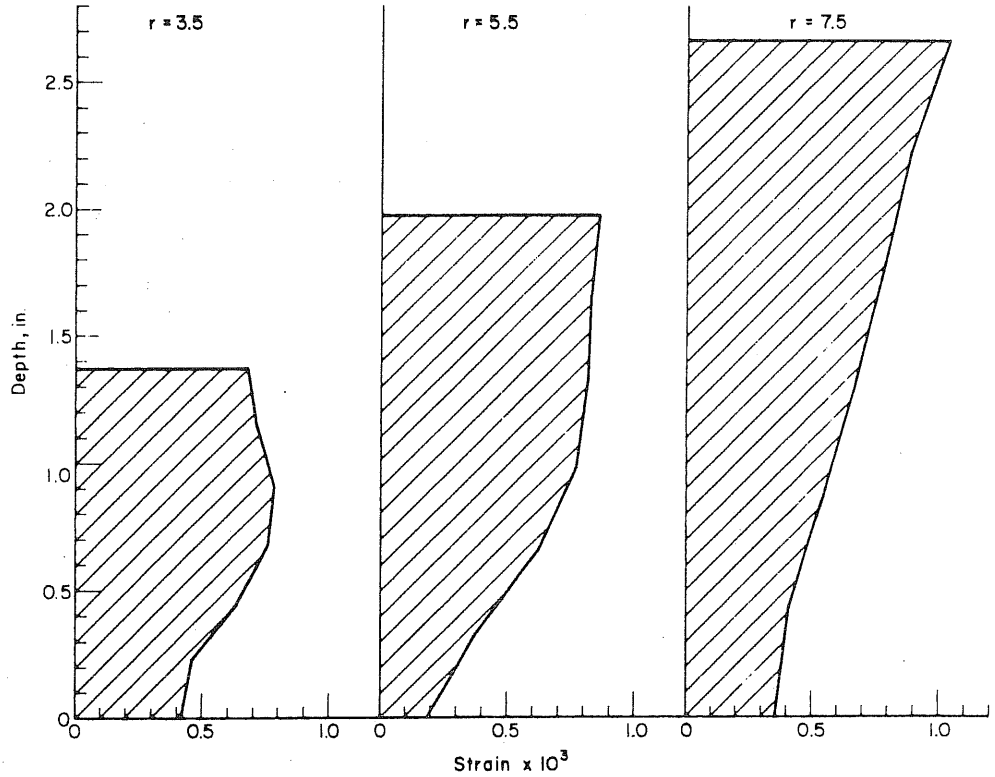

FIG. 9.23 THE DISTRIBUTION OF MAXIMUM TENSILE STRAINS IN THE DOME SHOWN IN FIG. 9.22 AT AN INTERNAL PRESSURE OF 1200 psi

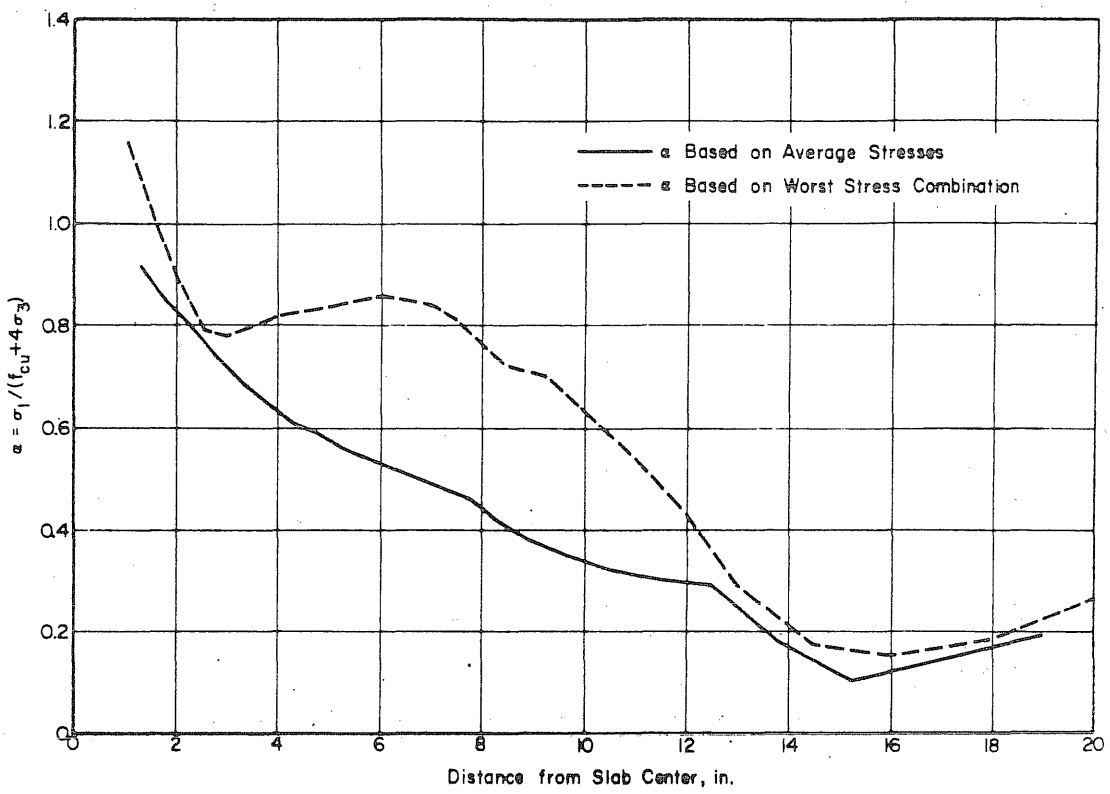

FIG. 9.24 CALCULATED FAILURE INDICES IN THE DOME SHOWN IN FIG. 9.22 AT AN INTERNAL PRESSURE OF 1200 psi

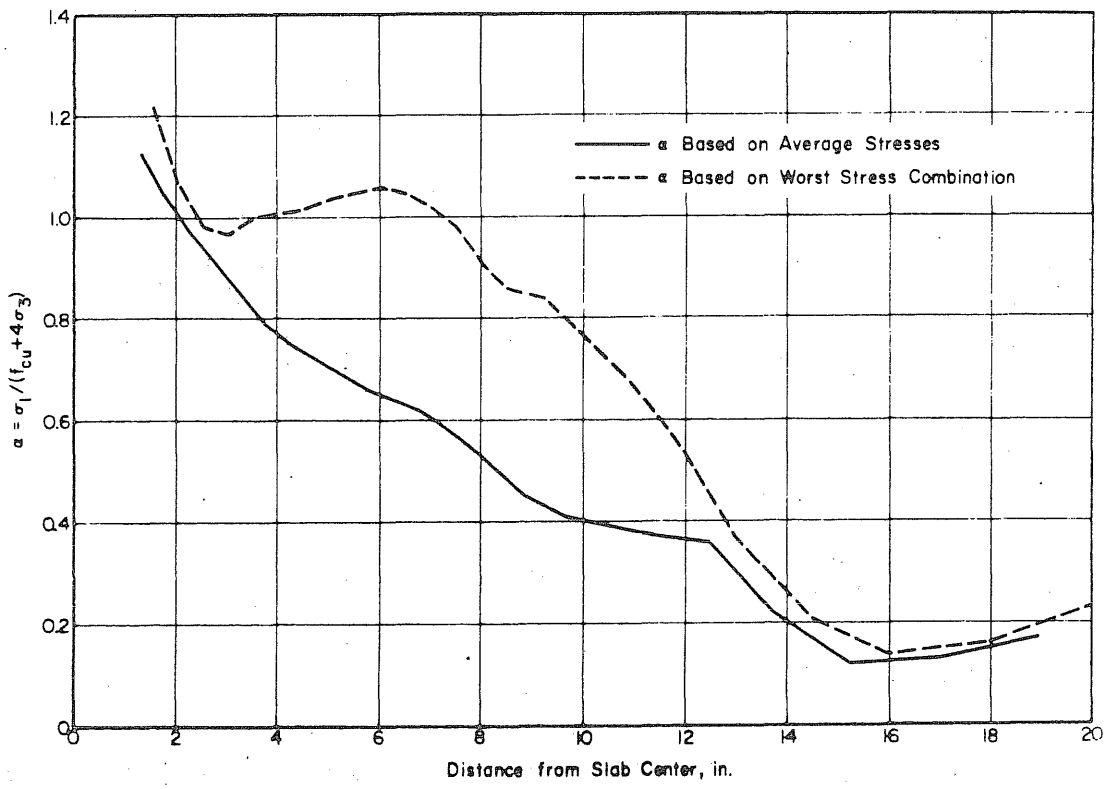

FIG. 9.25 CALCULATED FAILURE INDICES IN THE DOME SHOWN IN FIG. 9.22 AT AN INTERNAL PRESSURE OF 1600 psi

APPENDIX A: DESCRIPTION OF TESTS

A.1 Materials

(a) Concrete

The vessels were cast from concrete mixed in the laboratory. Two different mixes were used, one for the cylindrical skirt and one for the end slab.

The first mix was used for the skirt up to a level of 2 in. below the reentrant corner. Two batches of concrete were required to cast the skirt. The concrete contained pea gravel aggregate and Wabash river sand with type III cement. The proportions by weight of cement:sand:gravel were 1.00:2.77:3.07 and the water cement ratio was 0.56.

The second mix was used for the slab and the top 2 in. of the skirt and was made in one batch. The concrete contained crushed limestone aggregate with a maximum particle size of one inch and Wabash river sand with type III cement. The proportions by weight of cement:sand:gravel were 1.00:3.51:3.40. Type III cement was used with a water cement ratio of 0.74.

Five 6x12-in. cylinders were cast from each batch for compression tests. Five 6x6-in. cylinders were also cast from the batch used in the end slab for split cylinder tests. The properties of the batches used in the end slabs of the vessels are shown in Table A.1.

(b) Longitudinal Reinforcement

The vessels were prestressed with 0.775-in. diameter Stressteel rods.

The result of a tensile test of a 30-in. Stressteel rod is plotted in Fig. A.1. The strain was measured using an 8-in. extensometer.

The ultimate stress in the rod, which had a measured cross-sectional area of 0.471 sq. in. was 140 ksi.

(c) Circumferential Reinforcement

The wire that was used to prestress the vessels circumferentially was obtained from Interpace. Tests conducted on samples cut from the unstressed coil before prestressing and cut from the wire on the vessels after pressure testing showed no significant difference in stress-strain response.

The wire had a diameter of 0.250-in. and an area of 0.0491 sq. in. The wire was tested on a Baldwin testing machine. Tests were made using a 2-in. electrical extensometer to measure deformations. Another set of tests was made using a portable strain indicator to read strains from two BLH HE121 strain gages. The two strain gages were mounted on opposite sides of the wire and wired in series in order to average the strain readings. A typical stress-strain curve is shown in Fig. A.2.

(d) Liner Materials

The neoprene used to seal the pressure vessels was purchased in 200-lb rolls. The sheets were 72-in. wide and 1/16-in. thick. It was specified as "60 Durometer Shore A Black neoprene Sheeting, Type #260".

The O-ring material was obtained in 200-ft lengths. The diameters of the 3/16-in. and 3/4-in. O-ring stock were (0.210 ± 0.010) in. and (0.750 ± 0.010) in. respectively. The material was specified as "70 Durometer Shore A Extruded Buna N O-ring cord stock".

The caulking used to complete the seal at the end slab was General Electric Silicone Caulking.

Sheets of aluminum with a thickness of 0.017-in. and of 16-oz. soft copper were used on the sides and end slabs of the vessels.

A.2 Fabrication

(a) Casting and Curing

The pressure vessels were cast in the steel form shown in Fig. A.3. The outer form was rolled from 5/16-in. steel plate and reinforced with rolled 2x2x1/4 in. angles. The inner form was rolled from 3/16-in. plate. It was divided into four major pieces so that it could be dismantled after casting. Holes were drilled into the base plate for the 7/8-in. diameter rods which formed ducts for the longitudinal prestressing. The tops of the rods were secured by a template of 1/2-in. steel plate which was supported by sections of 4-in. wide channel attached to the sides of the form. The center of the template plate was cut out to permit access to the form for pouring the concrete.

The penetrations were obtained by attaching pipes to the top surface of the inner form (Fig. A.4). The pipes were 10-in. long. Around the pipes and next to the top surface of the inner form, 1x1-in. tori of cork were attached to form indentations for the steel plates which were used to seal the penetrations. No indentations were formed around the penetrations of vessel PV19.

The specimens were cast in three batches as noted previously. The batches were proportioned so that the end slab and at least 2-in. of the skirt were cast from the third batch. The concrete was vibrated internally with an electric vibrator during casting. Five 6x12-in. cylinders were cast from each batch. Five 6x6-in. cylinders were also

cast from the end slab batch for use in the splitting test. The side walls of the vessels were reinforced with No. 4 bars to have a reinforcement ratio of one percent. The bars were placed longitudinally about 1/2-in. from the outside surface of the concrete.

When the concrete had begun to set, usually about two hours after casting, the greased rods and the greased pipes forming the penetrations were manually extracted and the top of the vessel was trowelled to a smooth finish. The vessels were then covered with polyethylene film until the form was struck on the second day after casting. The vessels were cured under wet burlap for one week in the laboratory, which had environmental control set at 70°F and 50 percent relative humidity.

(b) Circumferential Prestressing

The INTERPACE plant at South Beloit, Illinois, made their facilities available for applying the circumferential prestressing wire. A mandrel and end fittings as shown in Fig. A.5 were designed to adapt the vessels to the equipment at INTERPACE, which is normally used to wrap concrete pipes. The vessels were transported to and from South Beloit by truck.

Anchors for the prestressing wire were cast into the vessels. An anchor is shown bolted to the form in Fig. A.6a. Figure A.6b shows a closeup of the anchor. A steel block about 3/4 x 3/4 x 1-1/4 in. was grooved and stamped, forming a toothed channel to grasp the wire. The block was then welded to a 3/8-in. diameter rod that had been bent into a U-shape to provide anchorage. The block and rod were hardened as a unit. The anchors were provided by INTERPACE and performed well throughout the test series.

The prestressing operation was started by securing the wire in the anchor at the closed end. This was done by driving the wire into the toothed channel with a hammer. The first wrap of prestress was applied at a slightly reduced load. Subsequent wraps of the 0.250-in. diameter wire were applied at a tension of 7,800 lb.

A schematic diagram of the machine at INTERPACE is shown in Fig. A.7. When the mandrel and vessels were in place, an axial load of about 20,000 lb was applied to create a friction force between the end fittings and the rubber bearing surfaces on the turning heads. The turning heads were rotated by a motor mounted at one end of the frame. The prestressing wire passed through a straight duct about 50 ft long from an uncoiling area to a friction wheel. The wire then passed through a load cell above the friction wheel and travelled overhead to the spacing apparatus which ran on a track above the mandrel and vessels. The spacing apparatus could advance automatically at a rate proportional to rotation of the turning heads or be adjusted by an operator. Tension was developed in the wire at the friction wheel by a D. C. motor which supplied a resisting torque. The load cell, which was located above the friction wheel, gave an account of the tension in the wire. Deviation from the desired load could be compensated by adjusting the torque transmitted by the D. C. motor. The load cell was calibrated to indicate the tension in the wire at the turning heads. Approximately five minutes were required to prestress a vessel.

The force in the wire as it was being wrapped around the specimen was known. To obtain the effective prestress at the time of the test, the

following procedure was used. All calculations refer to the prestress around the end slab. The initial prestress was assumed to be the force in the wire less the calculated effect of the reduction in diameter of the vessel due to elastic deformation of the concrete. The time-dependent losses were estimated using the creep and shrinkage data given in Fig. A.8, which had been obtained in an earlier phase of the project (Paul et al., 1969). Relaxation of the prestress wire, estimated to be less than four percent in most cases, was ignored because of lack of directly relevant data and because the scatter in the time-dependent properties of the concrete was expected to be much larger. The increase in circumferential prestress caused by longitudinal prestressing was calculated by assuming that the Poisson's ratio for concrete was 0.15.

(c) Sealing of Vessels

The penetrations were sealed with steel plates on the inside of the slab. The steel plates for the vessels with penetrations 8 in. from the center of the slab were 1-in. thick and were flush with the inside face of the slab when they were placed in the indentations. For the vessel with penetrations 4 in. from the center of the slab indentations were not formed around the penetrations. The sealing plates, which had a thickness of 0.25 in. close to the edge and 1 in. at the center were supported directly on the inside face of the slab.

After the sealing plates were placed, a 0.25-in. thick layer of hydrocal was applied on the inside face of the slab to protect the strain gages.

The seal consisted of lining the wall and the end slab with a sheet of 0.017-in. thick aluminum bonded to the concrete with rubber cement (Fig. A.9). Next, a liner of 16-oz. soft copper was placed over the aluminum. The copper-aluminum interface was greased so that the copper would not develop large stress concentrations during deformation. The copper sheet used on the end slab had a 1-in. lip which was soldered to the copper sheet on the wall. The lap in the copper wall sheet was also soldered as was the copper-steel joint at the 1-in. steel base ring. The vessels were placed on a 4-in. steel plate and then lightly prestressed longitudinally and pressurized to 50 psi gas pressure to deform the metal liners to the contours of the concrete and to check for any major leaks in the liner. The steel plate was then removed and a layer of 1/16-in. thick neoprene was placed over the copper and secured with rubber cement. A 3/4-in. neoprene O-ring was also installed at the junction of the end slab and the side wall.

(d) Longitudinal Reinforcement

The vessels were prestressed longitudinally with sixty 0.775-in. diameter Stressteel bolts. Strain gages were placed on twenty-eight of the bolts, and these bolts were calibrated in the laboratory. Loading of the bolts was accomplished with a 30-ton Simplex jack with the scheme shown in Fig. A.10. The jack chair permitted a nut to be tightened against a continuous steel plate that was 1-1/2 in. thick. The plate had an inner diameter of 26 in. and an outer diameter of 40 in. The plate was cut radially between each rod to reduce any reinforcing effect (Fig. A.11). The load in the bolts after the jack was released varied from 40 to 45 kips

but was reduced when the surrounding bolts were stressed. The forces in the bolts were measured immediately after the prestressing was finished and again before the test.

A.3 Instrumentation and Test Procedure

In general the instrumentation consisted of deflection measurements across one diameter of the head and down the side on a line at one end of this diameter, strain measurements on the concrete on the inside and on the outside faces of the slab and on the concrete inside the penetrations, strain measurements on the circumferential prestressing steel, and on some of the longitudinal prestressing bolts. The strain gages on the concrete and on the circumferential steel reinforcement were placed after the steel was wrapped so that only the change in strain during the test was measured. The strain gages on the longitudinal prestressing bolts were monitored during the prestressing operation and during the test so that the total load could be calculated. The actual number of measurements of each type and their locations are shown in Appendix B for each test.

The strain gages used on the concrete were BLH type A12 which have a 1-in. gage length and are flat wound wire gages with paper backing. These gages were applied with Eastman 910 cement. There was some concern that the strain gages located on the inside of the head would be affected by the normal pressure on the gage grid. This problem is discussed in Appendix C. On the inside of the head the gages were applied by first sanding the concrete to a smooth finish and then placing a layer of cement on the concrete and allowing it to set. The gages were then cemented to this prepared surface with Eastman 910 cement and a soft rubbery protective coating placed over the

The test shed was located about 100 ft from the Structural Dynamics Laboratory. Approximately 135 ft of cable was required to reach the area where readings were taken in the main laboratory. A 4-conductor cable with heavy rubber coating passing through an overhead metal cable tray was used between the two buildings. This cable is Belden 8424 and contains 20 gage conductors. Several of the tests were performed during the winter so a heater was placed in the test shed to keep it warm enough for men to work. It was not possible to maintain room temperature at all times with this heater but temperature compensating strain gages were placed in the test chamber with the test specimen. The specimen was then left in the test shed for sufficient time to allow the temperature to stabilize.

Strains were read with an automatic reader, VIDAR. Switching between the different gages was done manually.

Deflections across the head of the specimen and down the outside wall were measured with 0.001 in. Ames dial gages located within the test shed but outside the test specimen enclosure. The dial gages were connected to piano wires which were strung over ball bearing pulleys and attached to metal tabs glued to the specimen. Tension springs, connected to the back end of the dial gage plunger, kept the piano wire taut. The pulleys over the top of the specimen were attached to an arm which was broken off by the flying debris each time a specimen failed. The dial gages were read with a closed circuit television hookup with the receiver in the main laboratory. The television camera, which was located inside the test shed but outside the test specimen enclosure, had a telephoto lens so that the dial gage face almost

gage. The sealing plates for the penetrations were set in place in their indentations. After the protective coating had set, a 1/16-in. sheet of neoprene was glued over the gages to provide further protection and assure that the applied pressure was uniformly distributed over the gage. The entire inside surface of the end slab was then covered with a 1/4-in. thick layer of hydrocal. The gage wires were run down the inside of the vessel and out between the concrete and the 1-in. steel ring. Channels, 1-in. wide by 1/4-in. deep, were cast in the concrete to accommodate the gage wires. On the outer surface of the concrete the strain gages were applied in the same manner, but no protective coating was used on them. The strain gages used to measure the change in strain of the circumferential reinforcement were BLH type A19 which is a flat grid wire gage with a gage length of 1/16 in. and temperature compensation for steel. These gages were applied with Eastman 910 cement following standard procedures.

The test shed was erected on the grounds of the Structural Dynamics Laboratory which is situated in farmland about three miles south of the university campus. The shed is a wooden enclosure built on a 12-ft square slab-on-grade floor. It features a 5 x 5-ft steel test chamber in its center which extends from the floor through a hole in the roof. The test chamber was constructed of four 4 x 4 x 3/8 in. angles which extend vertically from the corners of the opening to the floor with 1/2-in. steel plate on the four sides. Figure A.12 shows vessel PV18 inside the test chamber after the test. A hatch was provided to cover the hole in the roof when the shed was not in use. During tests the hole was covered with three layers of wire mesh to impede concrete projectiles. The blast mats were anchored with 3/8-in. cable fastened to ground anchors at the sides of the shed.

filled the television receiver screen, and was mounted on a system of two television antenna rotors so that it could be adjusted in direction for each gage. This arrangement proved quite satisfactory for this purpose, though some of the gages were damaged by the sudden tension on the piano wire at failure of the specimen.

The vessels were filled with water to within approximately 1/2 in. of the end slab. They were initially pressurized with oil to further reduce the quantity of compressed gas that would be released when failure occured. When the maximum pressure was approached small leaks developed and it was not possible to hold the pressure with the oil pumps. Nitrogen gas was then used until the maximum pressure was reached. The pressure within the specimen was monitored with a pressure gage. For each load step about ten minutes were needed to take the readings. The size of pressure increments were reduced as the failure pressure was approached.

TABLE A.1

CONCRETE PROPERTIES

Vessel	Age at Test	Slump	Modulus of Elasticity	Splitting Strength 6 x 6-in. Cylinder	Compressive Strength 6 x 12-in. Cylinder
	days	in.	psi x 10^6	psi	psi
PV16	79	2	4.0	518	7450
PV17	52	3	3.8	534	7180
PV18	89	2	4.0	447	7590
PV19	105	2	3.9	406	7470
PV20	142	2 1/2	3.8	469	6890
PV21	183	2	3.7	496	7400

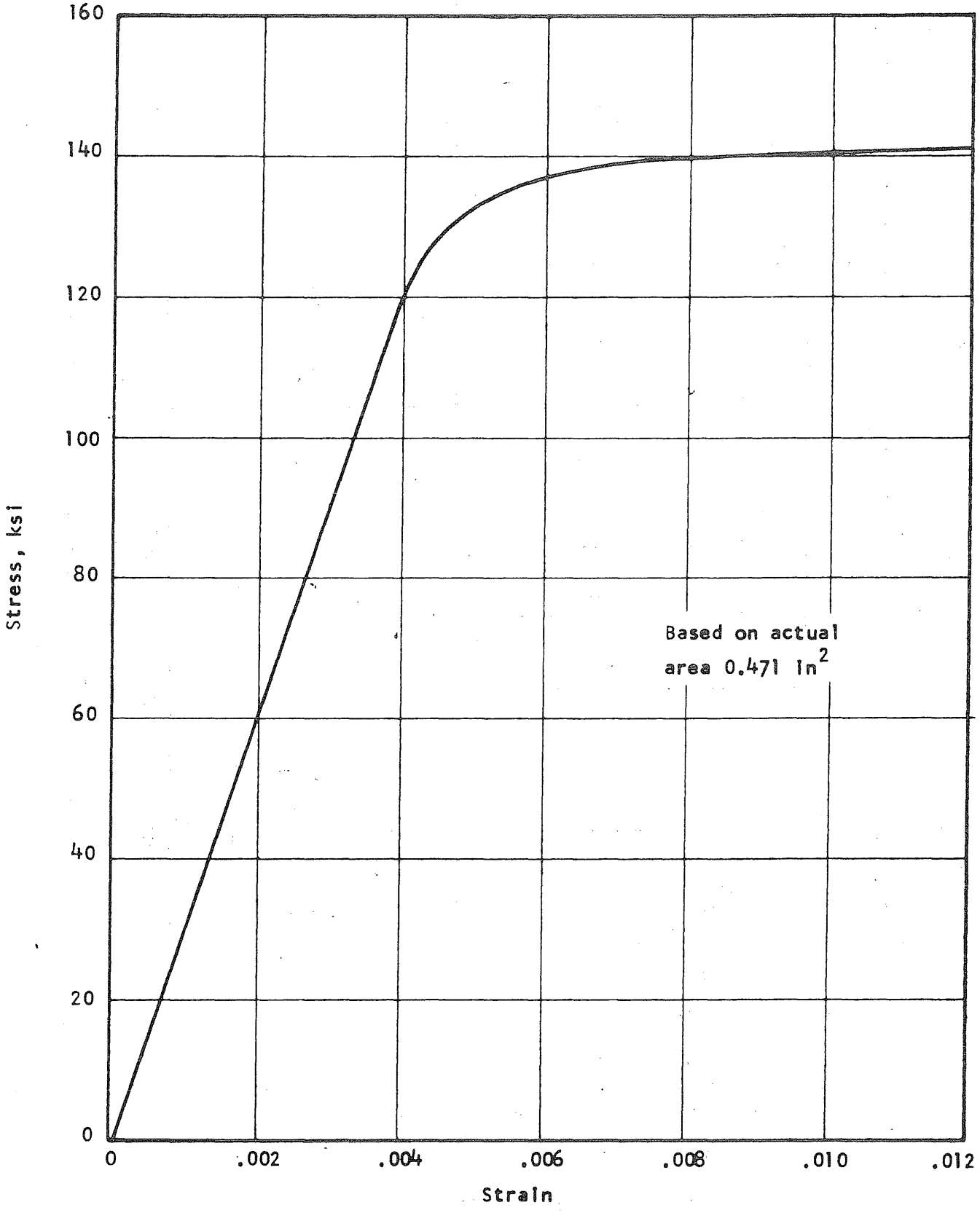

FIG. A.1 STRESS-STRAIN CURVE FOR STRESSTEEL RODS

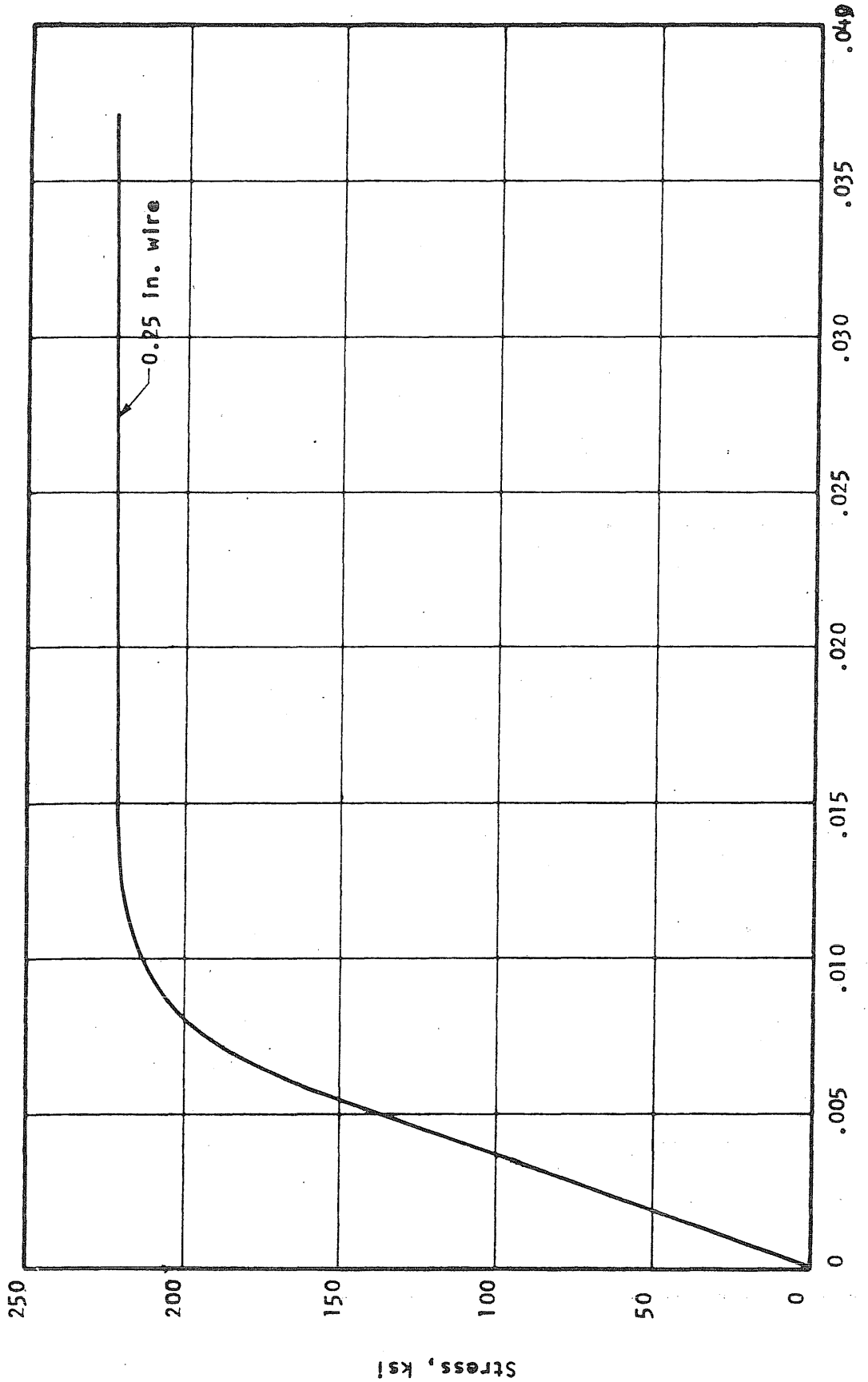

FIG. A.2 STRESS-STRAIN CURVE FOR PRESTRESSING WIRE

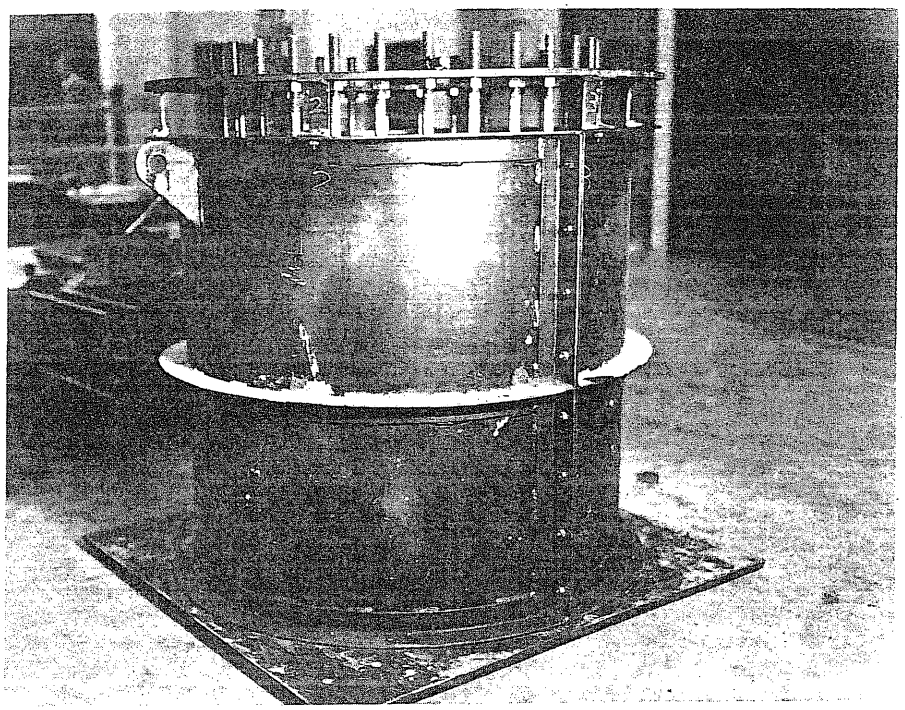

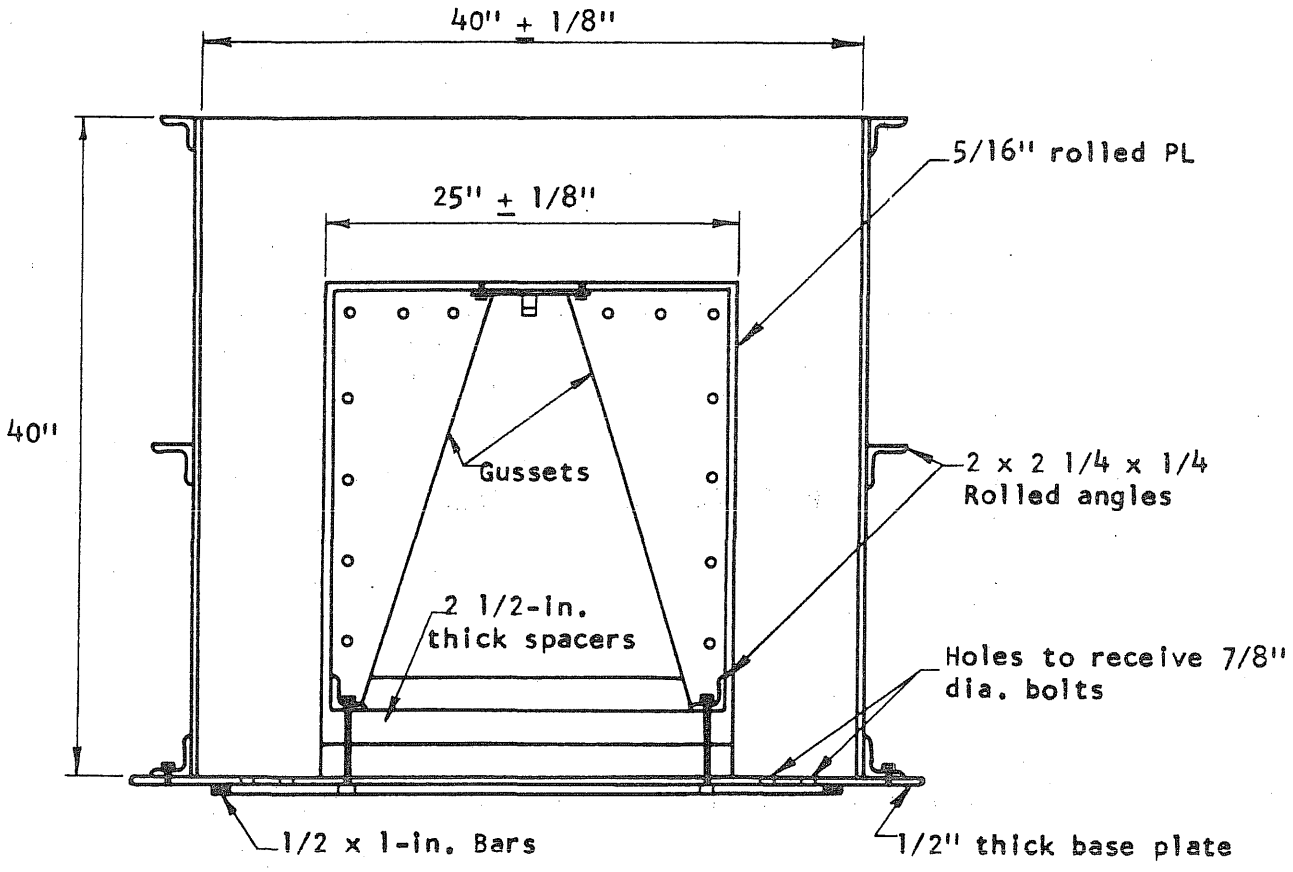

FIG. A.3 DETAILS OF THE STEEL FORM USED TO CAST PRESSURE VESSELS

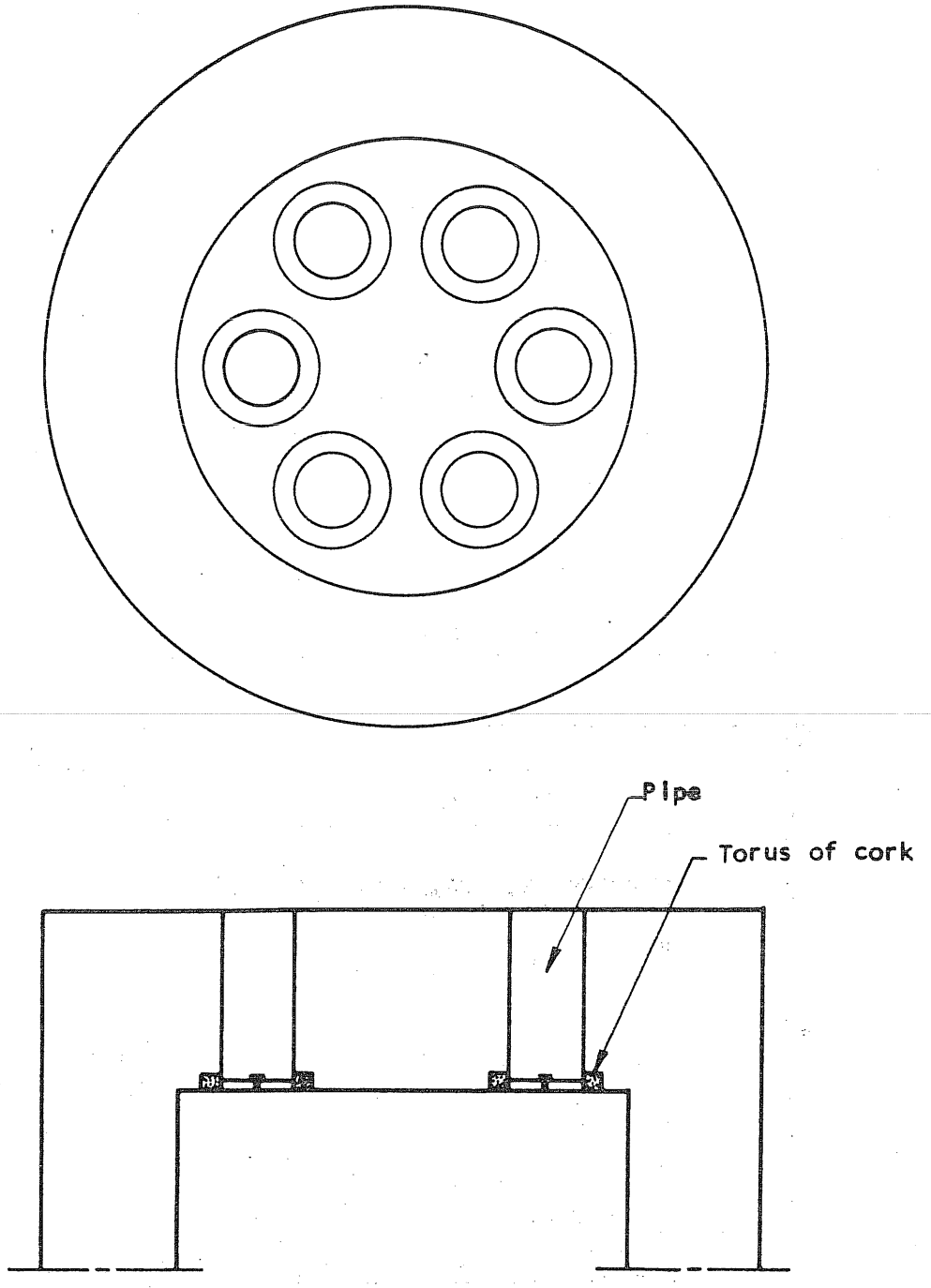

FIG. A.4 ATTACHMENT OF PIPES TO FORM THE PENETRATIONS

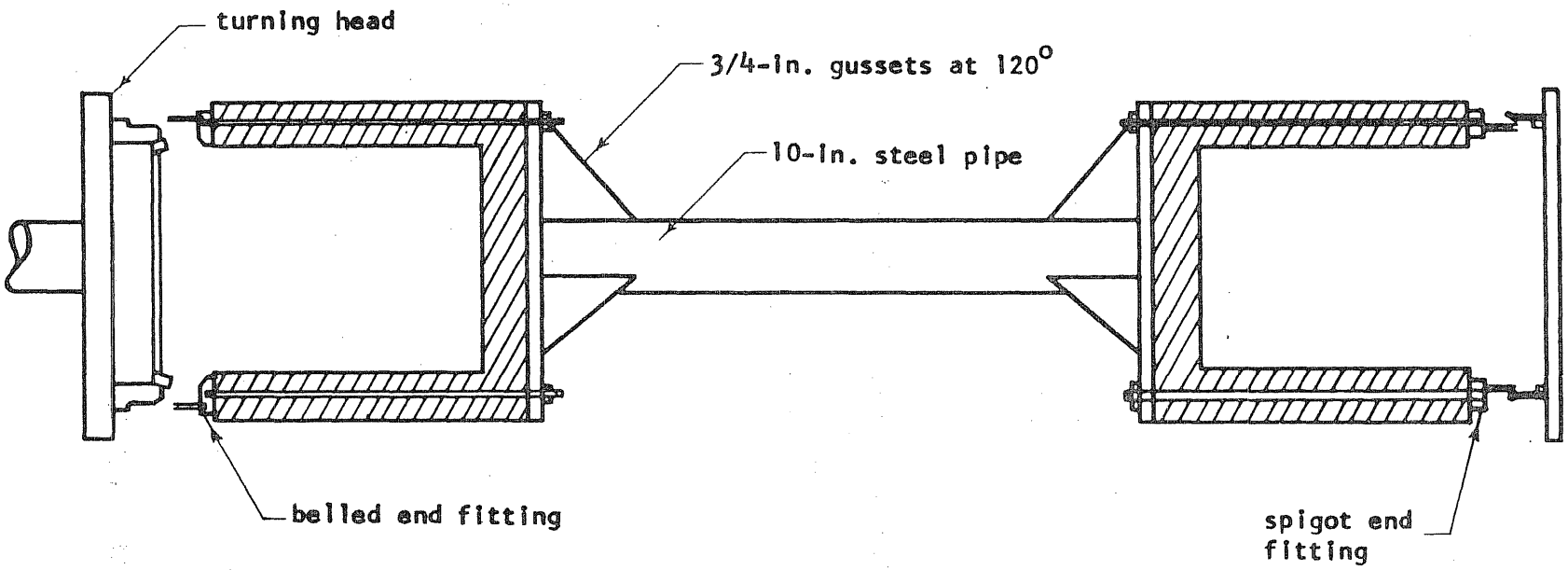

FIG. A.5 SETUP FOR CIRCUMFERENTIAL PRESTRESSING

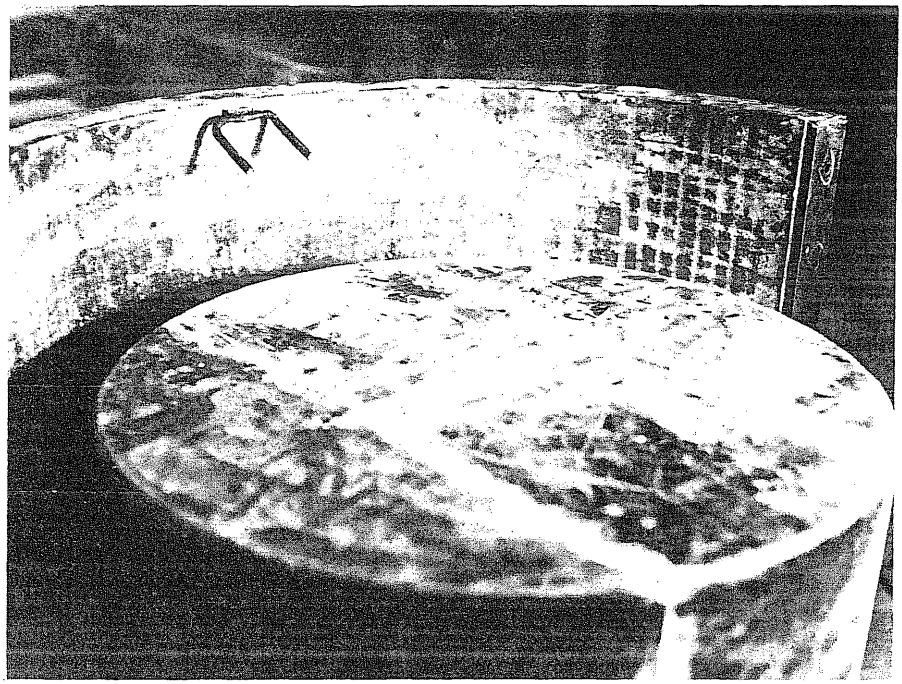

FIG. A.6a ANCHOR BOLTED TO FORM

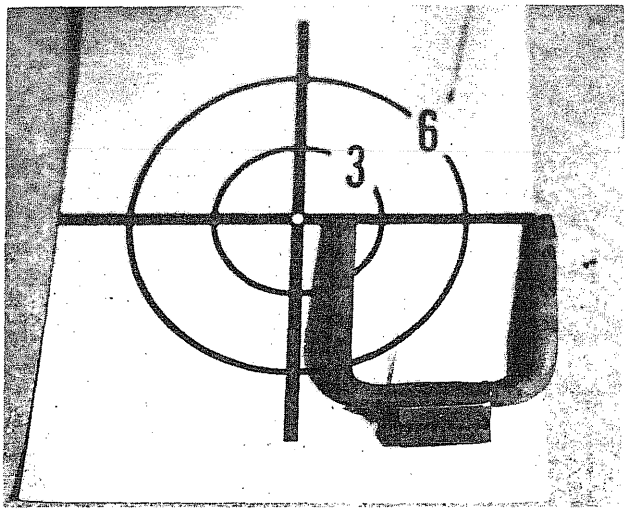

FIG. A.6b CLOSEUP OF A TYPICAL ANCHOR

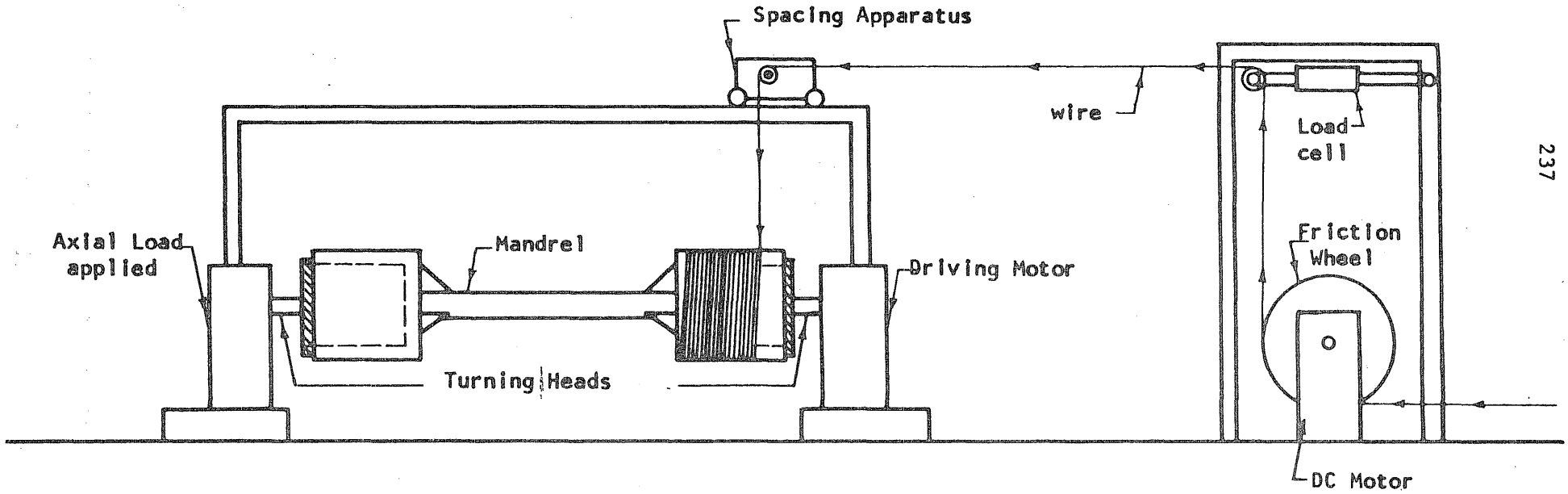

FIG. A.7 SCHEMATIC DIAGRAM OF THE EQUIPMENT AT INTERPACE USED TO PRESTRESS THE PRESSURE VESSELS

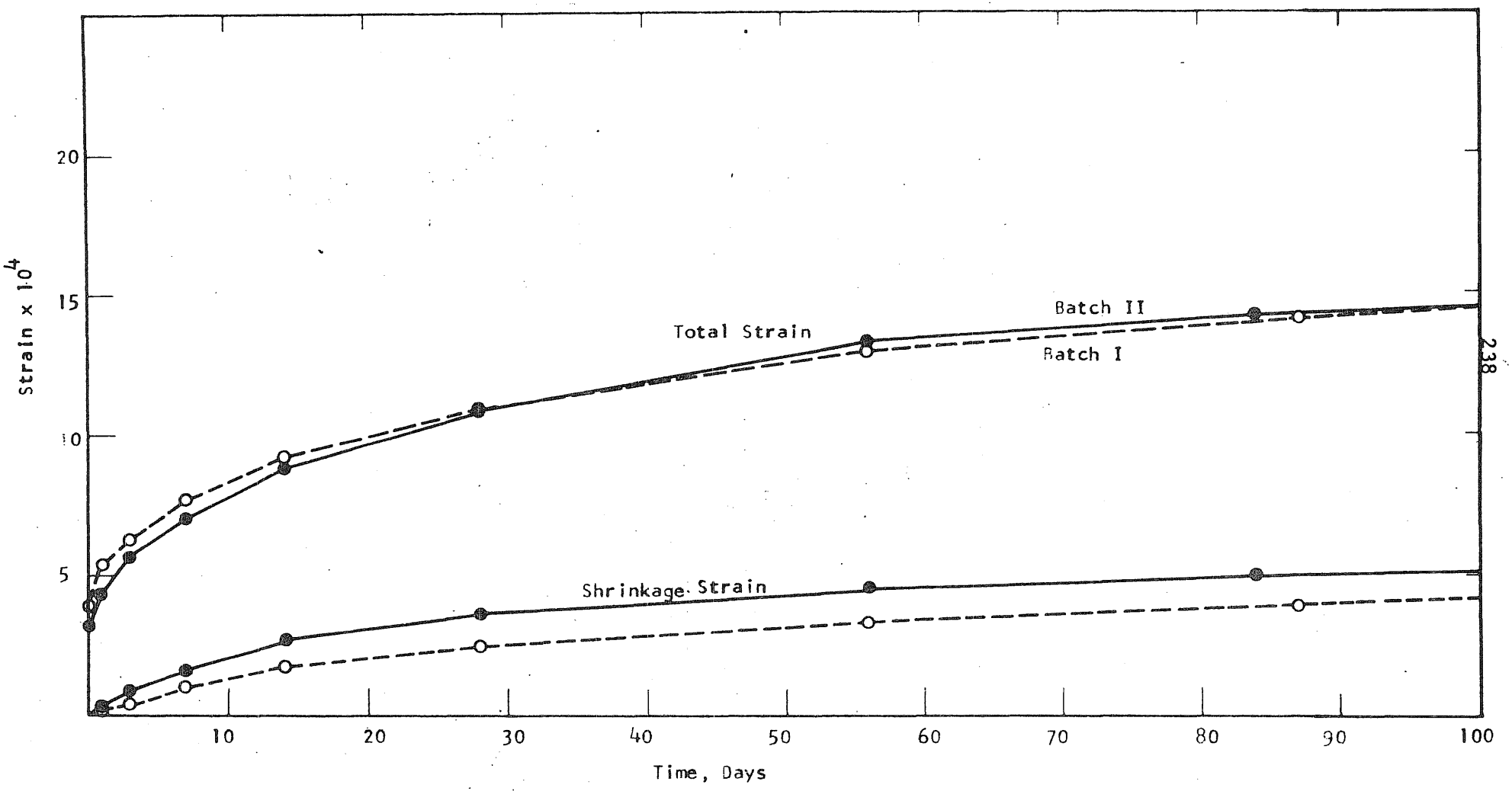

FIG. A.8 SHRINKAGE STRAIN AND TOTAL STRAIN FOR 6x12-in. CYLINDER UNDER 1000 psi COMPRESSION

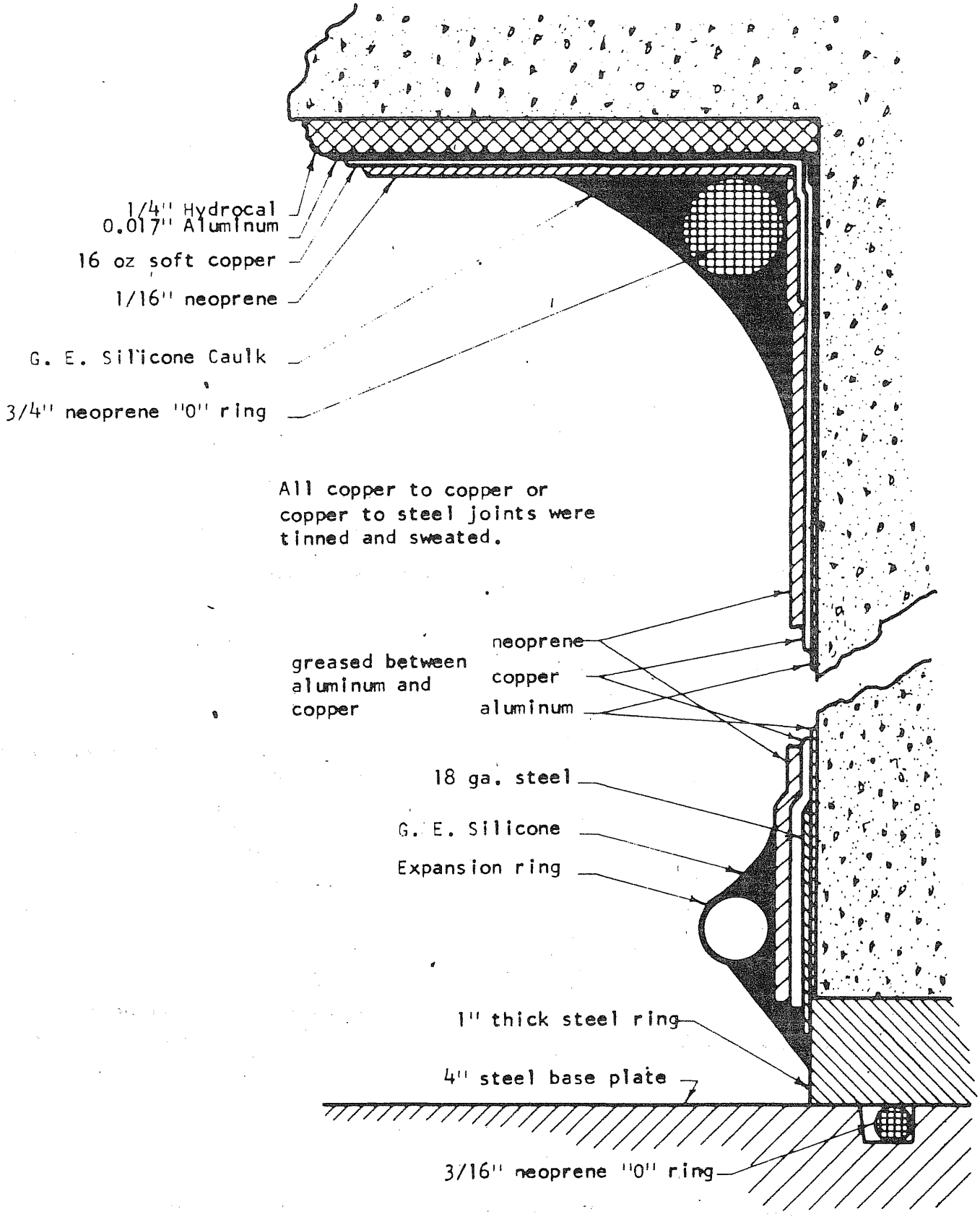

FIG. A.9 SEALING DETAIL

APPENDIX B: TEST DATA

B.1 Introduction

Test data for six pressure vessels, designated PV16 to PV21 are included in this appendix. The test data for vessel PV16 have been reported before (Paul et al., 1969). The dates of casting, prestressing and testing of each specimen are reported in Table B.1. The properties and strength of each vessel are reported in Table 2.1.

Each section consists of a description of the test and descriptive information concerning the vessel, followed by the data in graphic form resulting from the test. The observed path of the inclined cracks, the location of the failure plane and a photograph of the end slab after failure are shown in Fig. 2.8 - 2.13.

The data consist of deflection measurements and recorded strains in the concrete, the circumferential wire and the longitudinal rods. Deflections were measured along the outside face of the slab and the cylinder. The recorded deflections were often erratic for small deflections. This was especially the case for horizontal deflections along the outside face of the cylinder and these data are completely excluded. The measured strains in the circumferential wire provide an accurate picture of the horizontal deflection. For the vertical deflection along the outside face of the slab, only selected results are shown. For the recorded strains, some editing was done when it was obvious that the zero for strain shifted or that an error was made in a reading.

The measurements of deflections and strains started after prestressing was completed and reflect additional deflections and strains due to the internal pressure.

TABLE B.1

CHRONOLOGY

Vessel	Casting	Circumferential Prestressing	Longitudinal Prestressing	Testing
PV16	Nov. 12 68	Nov. 26 68	Jan. 3 69 Jan. 24 69	Jan. 28 69
PV17	June 24 69	July 8 69	Aug. 13 69 Aug. 14 69	Aug. 15 69
PV18	June 27 69	July 8 69	Sept. 22 69	Sept. 24 69
PV19	Aug. 1 69	Aug. 15 69	Nov. 24 69	Nov. 25 69
PV20	July 28 69	Aug. 15 69	Dec. 15 69	Dec. 17 69
PV21	July 22 69	Aug. 4 69	Jan. 19 70	Jan. 21 70

B.2 Test Vessel PV16

The vessel was filled with water to about 1/4-in. below the inside surface of the end slab. It was loaded with nitrogen gas and failed about 5 minutes after a pressure of 3200 psi had been obtained. The creep in the vertical deflection gages at 3200 psi was quite large and increasing in speed.

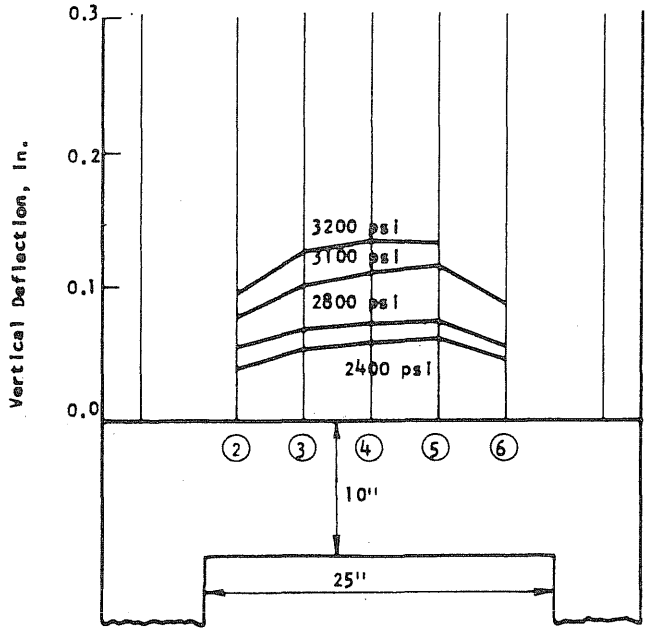

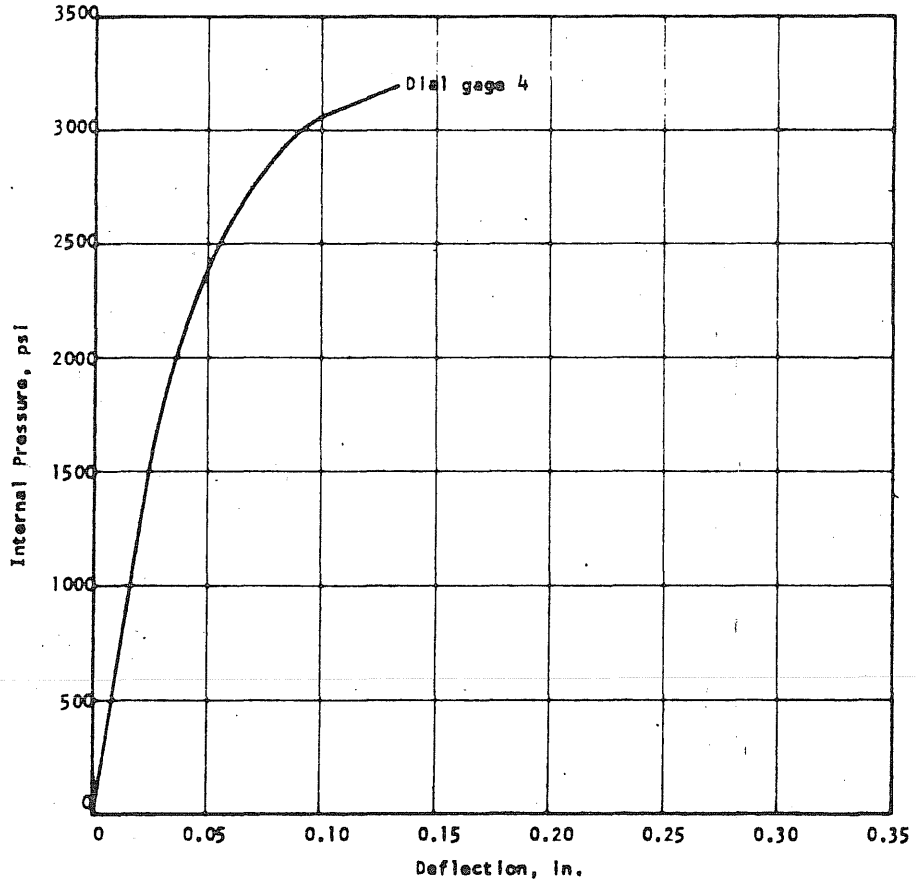

FIG. B.1 MEASURED DEFLECTION PROFILES AND DEFLECTION AT THE CENTER OF THE END SLAB OF PV16

Concrete Gages on the Inside of the End Slab

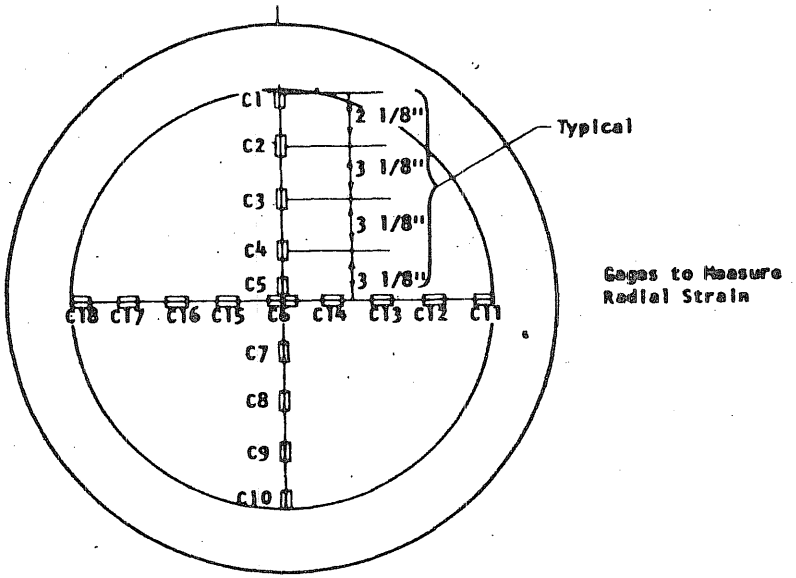

Gages to Measure Radial Strain

Concrete gages on the Outside of the End Slab

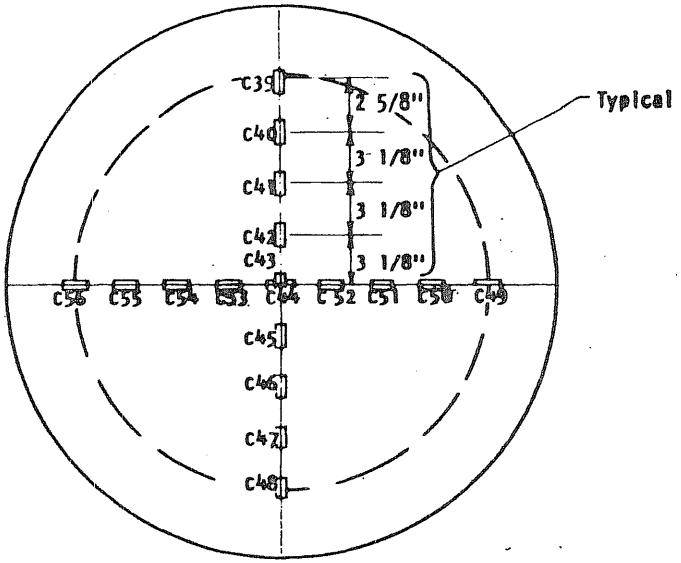

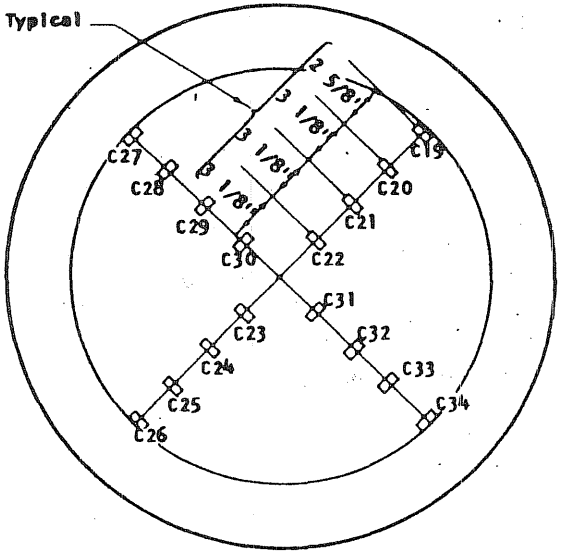

Gages to Measure Circumferential Strains

Steel Gages on Circumferential Prestress Wire

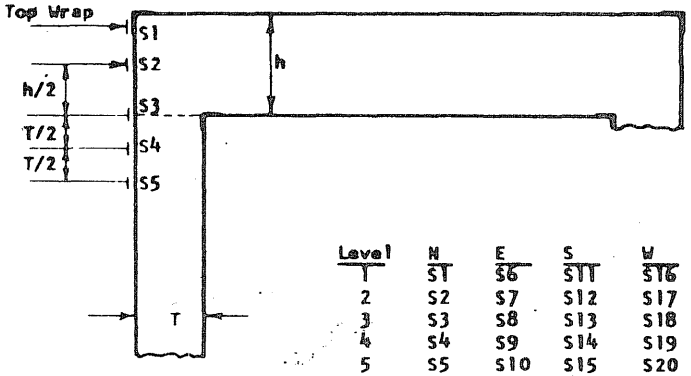

Level	N	E	S	W
T	S1	S6	S11	S16
2	S2	S7	S12	S17
3	S3	S8	S13	S18
4	S4	S9	S14	S19
5	S5	S10	S15	S20

FIG. B.2 STRAIN GAGE LOCATION ON PV16

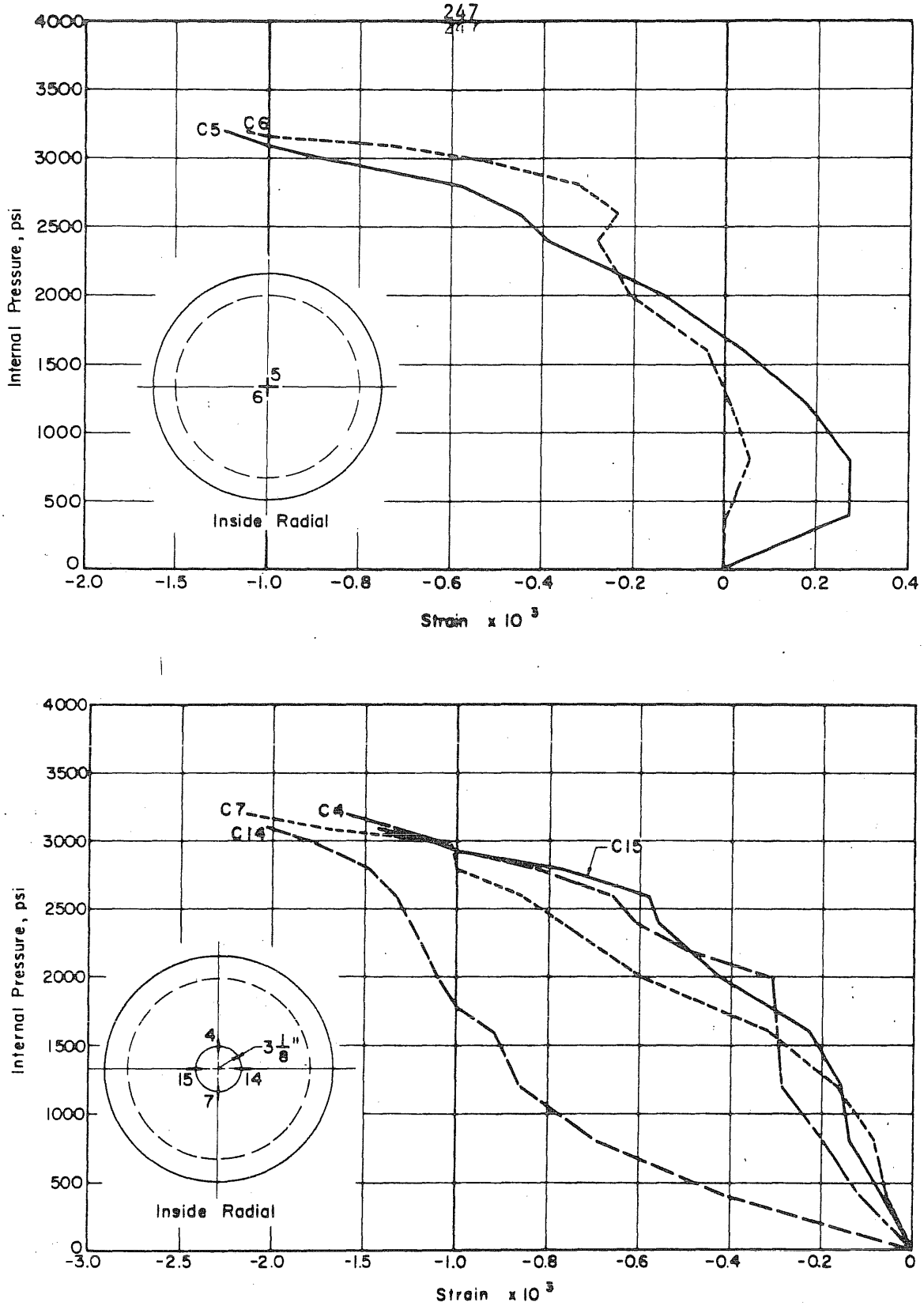

FIG. B.3 MEASURED STRAINS ON THE INSIDE FACE OF THE SLAB OF PV16

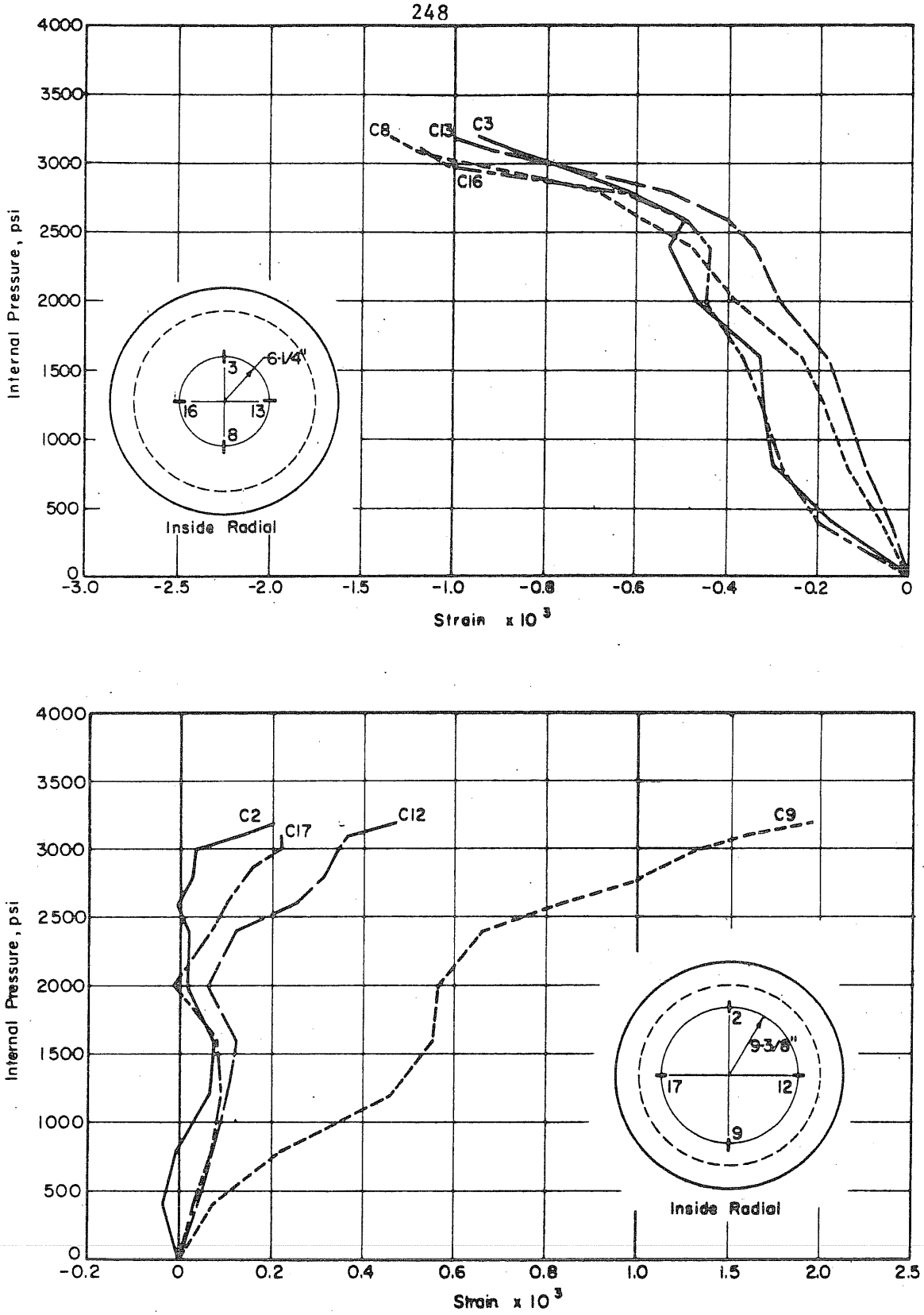

FIG. B.3 (Continued) MEASURED STRAINS ON THE INSIDE FACE OF THE SLAB OF PV16

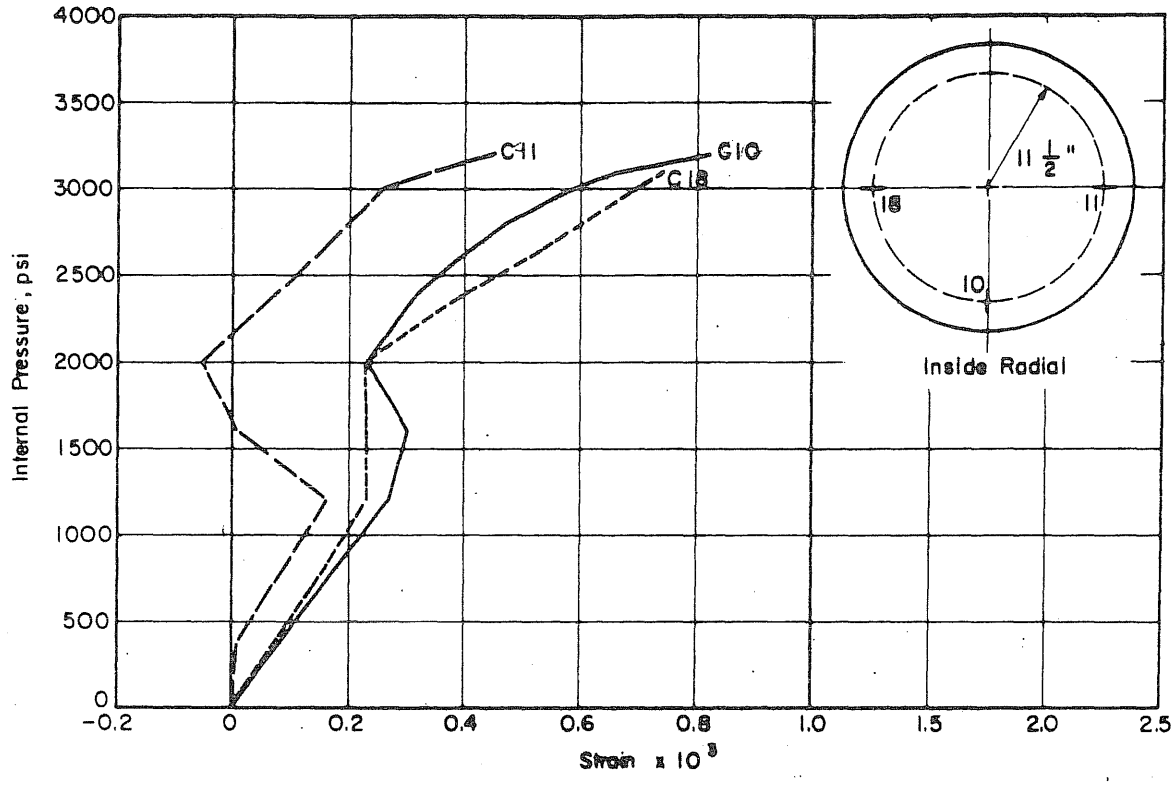

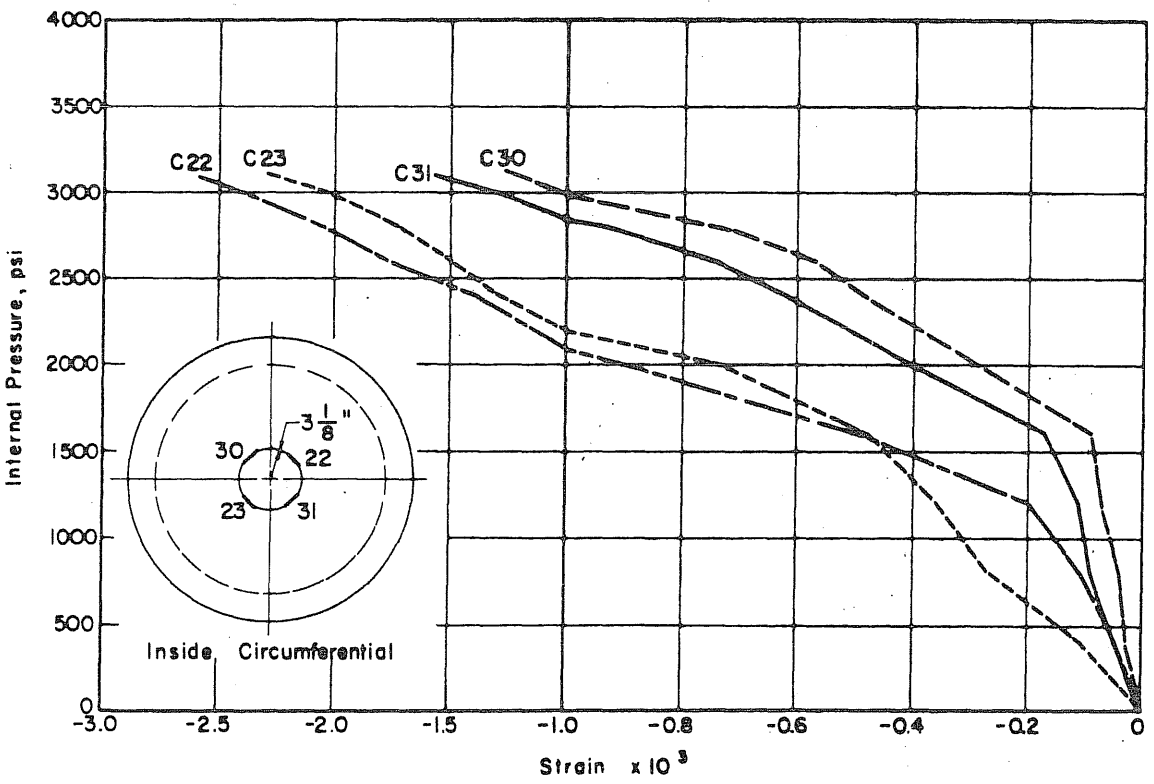

FIG. B.3 (Continued) MEASURED STRAINS ON THE INSIDE FACE OF THE SLAB OF PV16

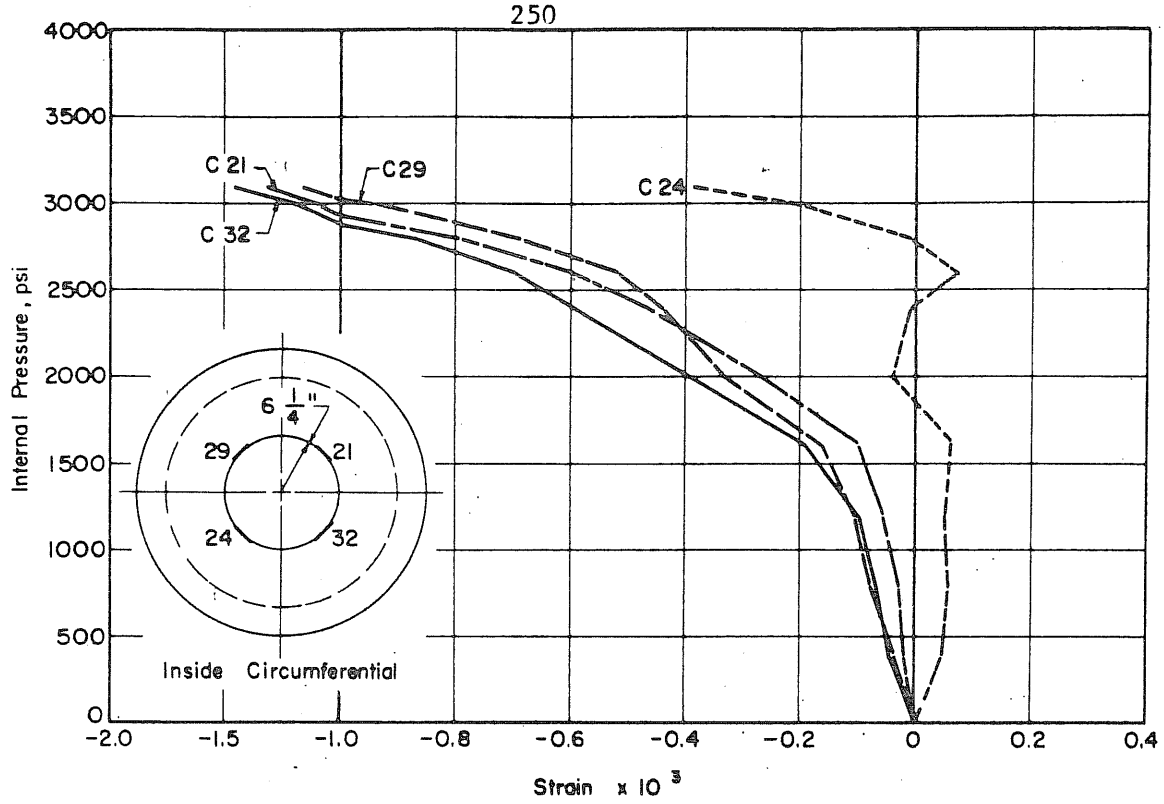

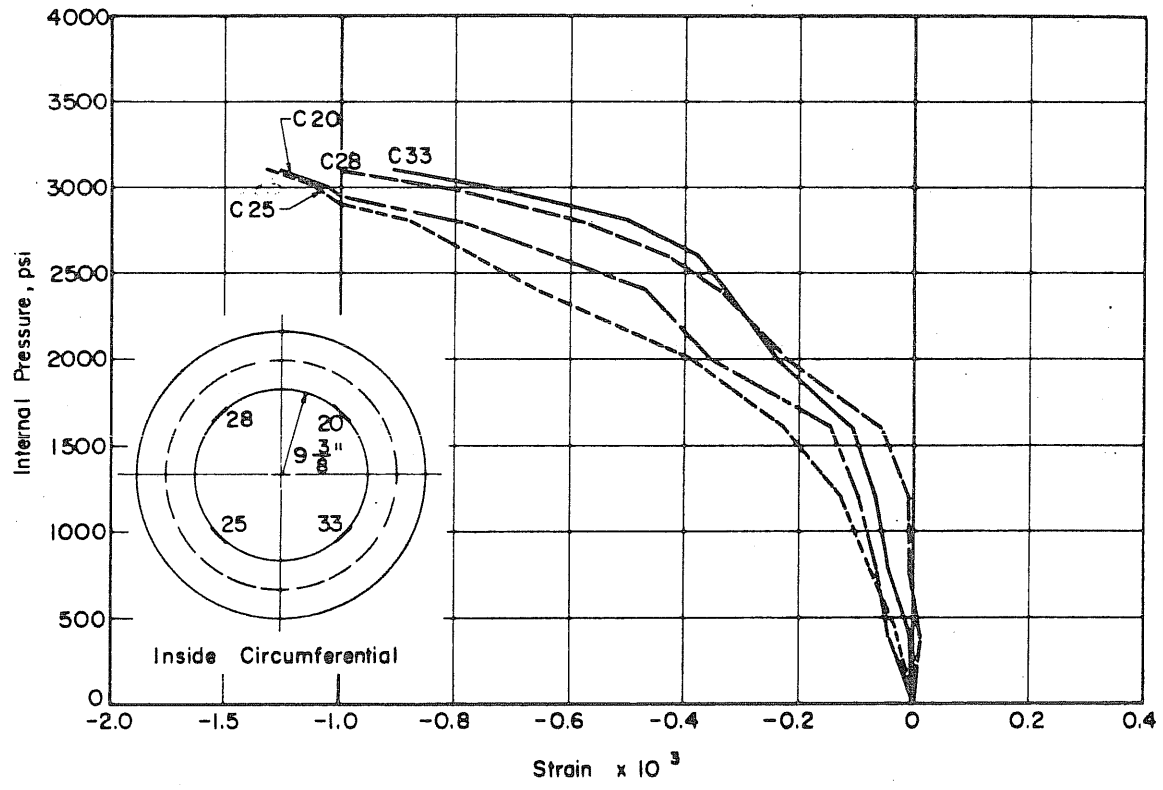

FIG. B.3 (Continued) MEASURED STRAINS ON THE INSIDE FACE OF THE SLAB OF PV16

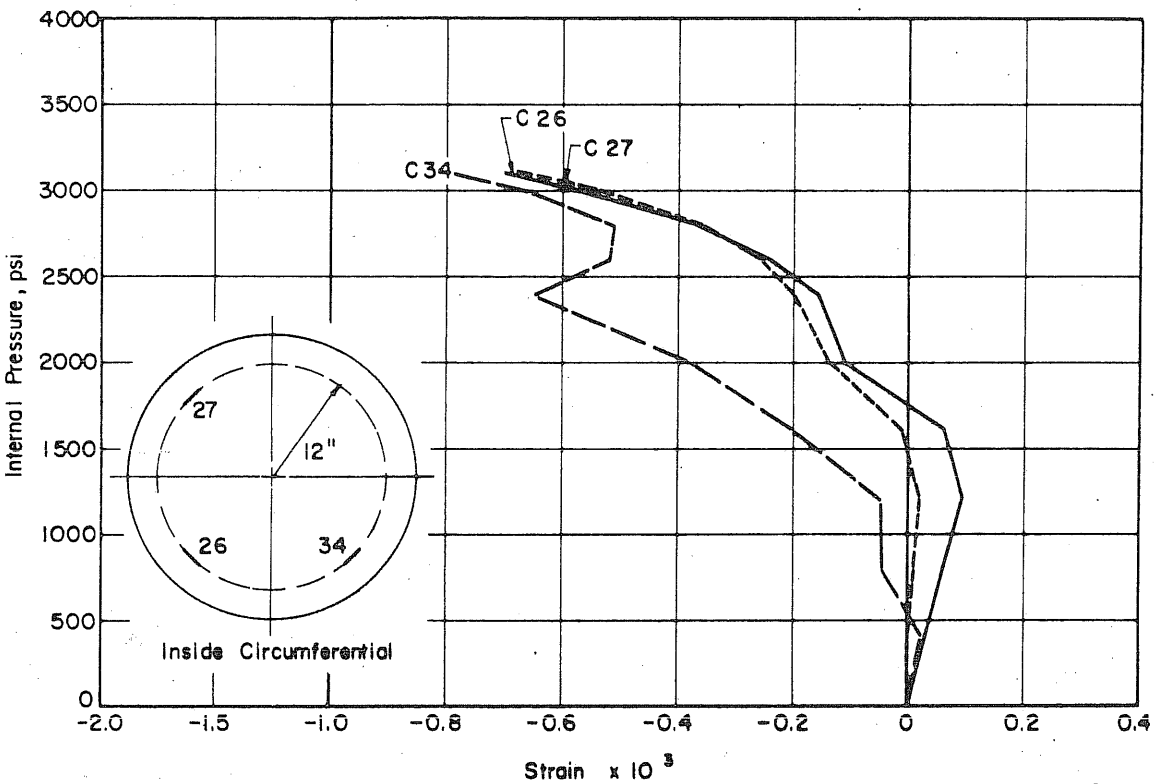

FIG. B.3 (Continued) MEASURED STRAINS ON THE INSIDE FACE OF THE SLAB OF PV16

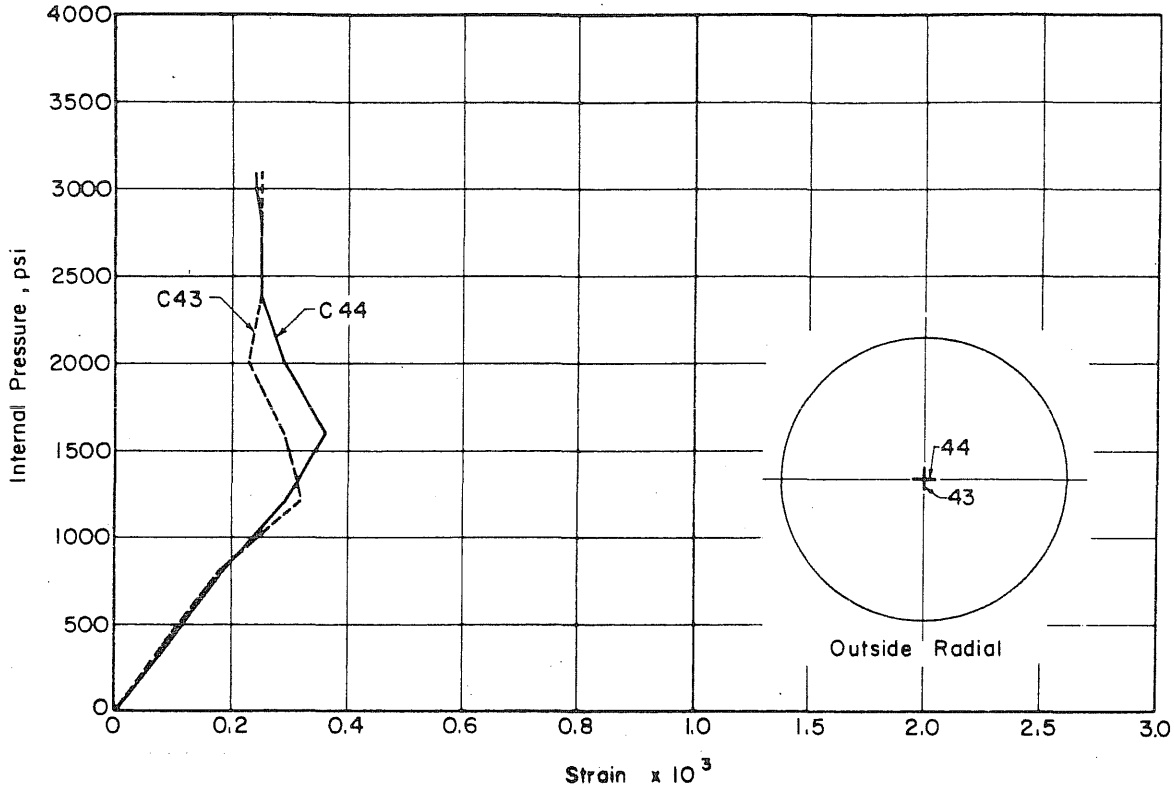

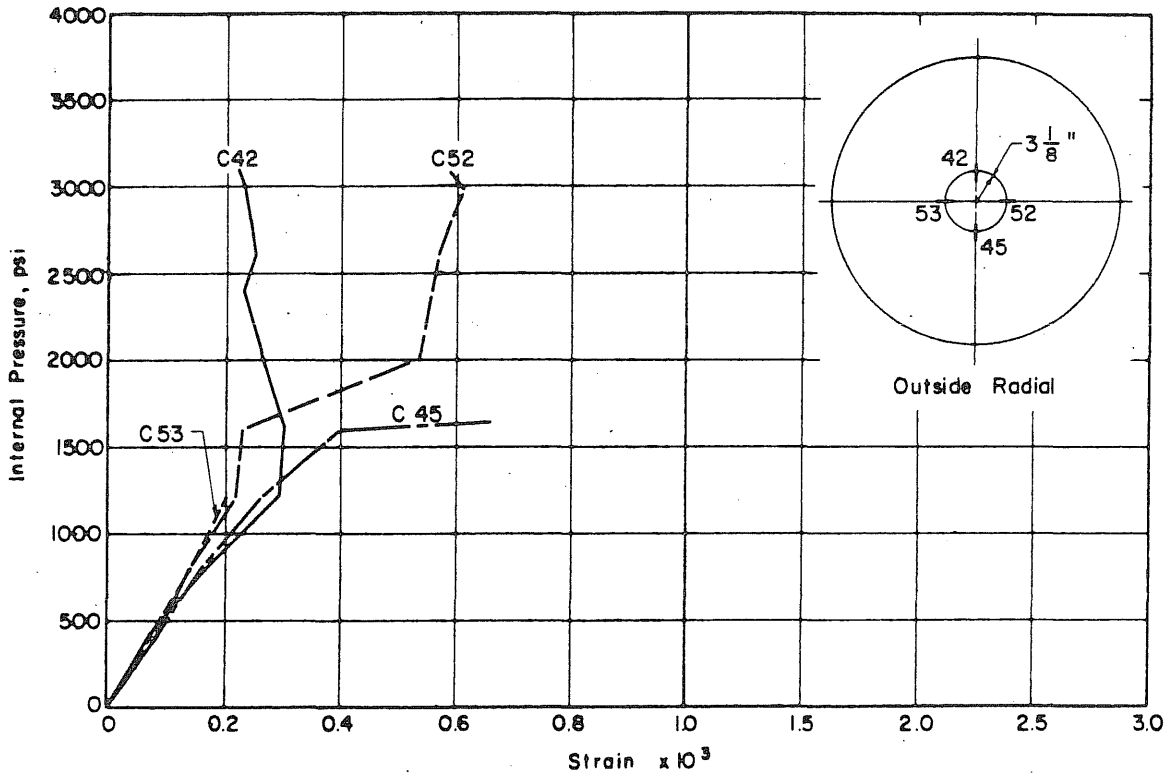

FIG. B.4 MEASURED STRAINS ON THE OUTSIDE FACE OF THE SLAB OF PV16

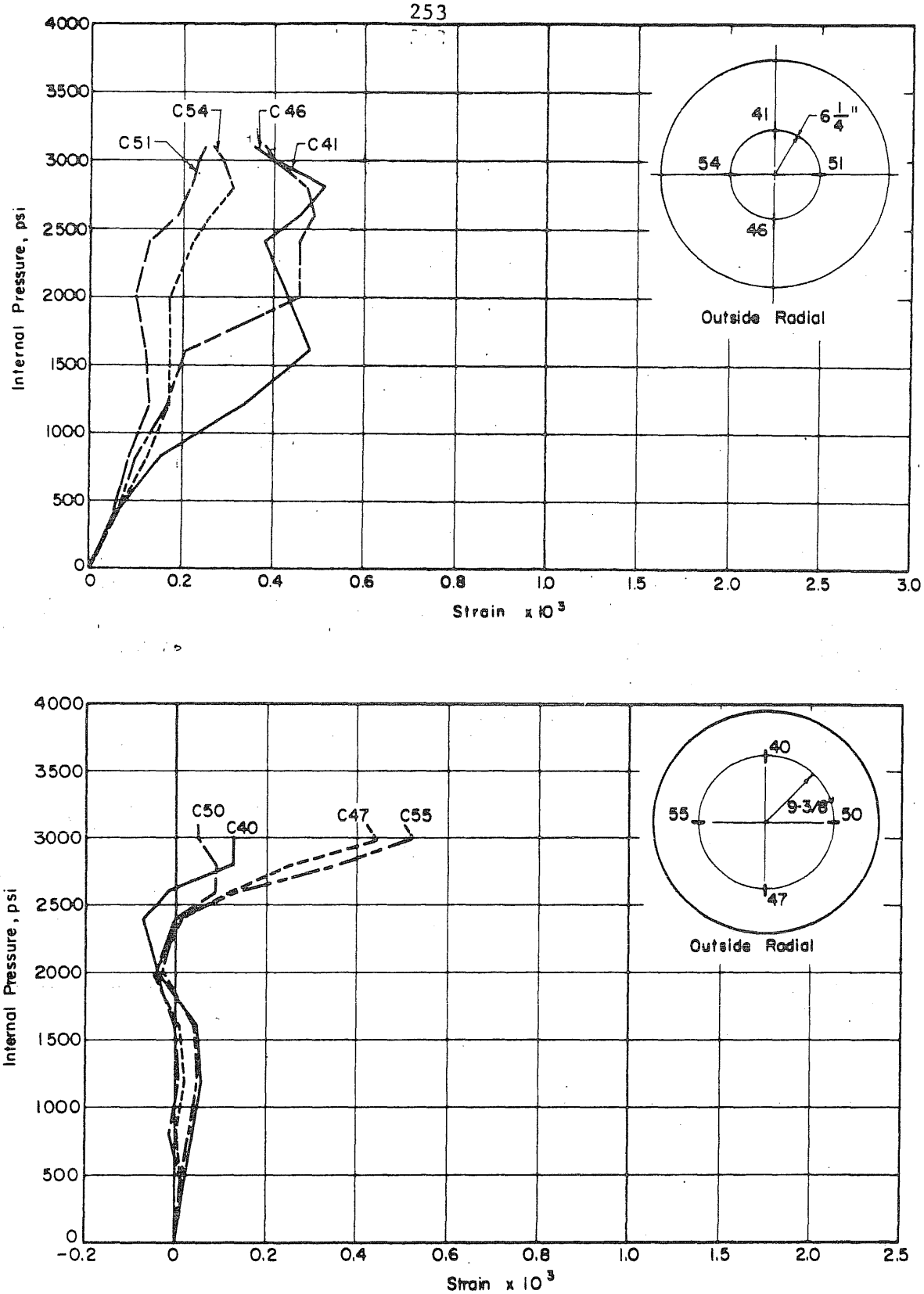

FIG. B.4 (Continued) MEASURED STRAINS ON THE OUTSIDE FACE OF THE SLAB OF PV16

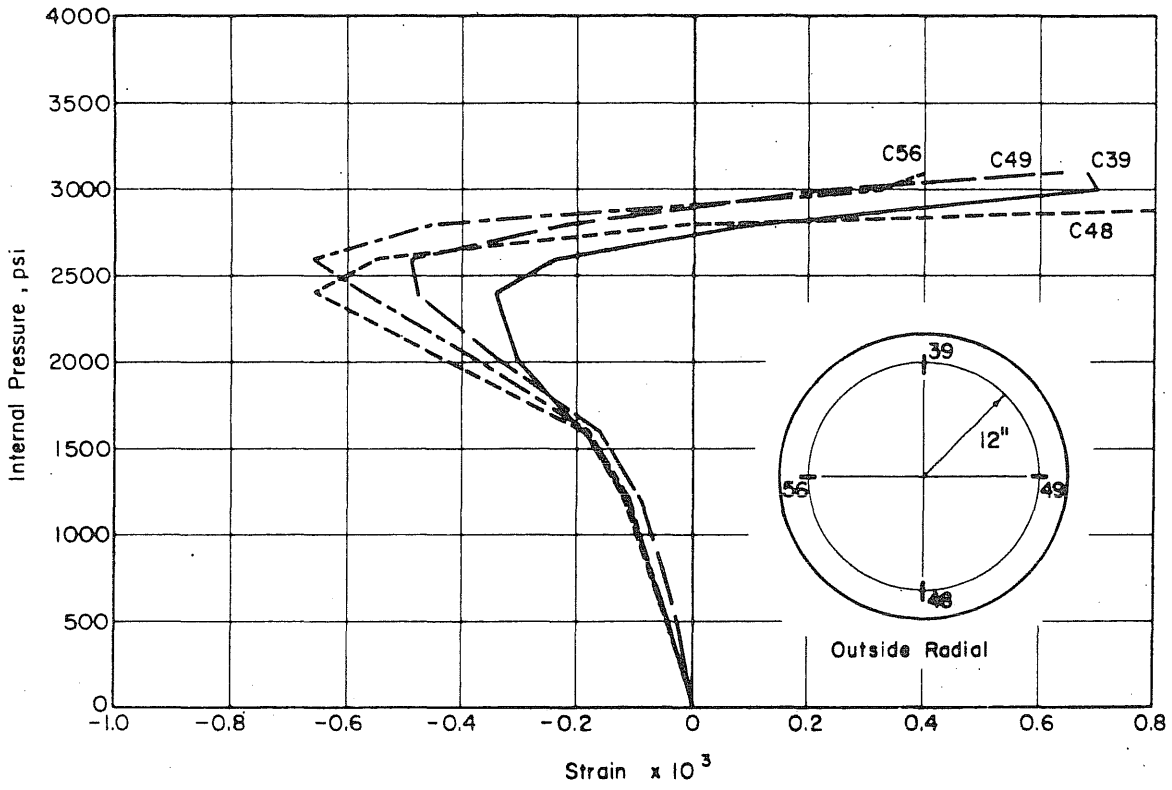

FIG. B.4 (Continued) MEASURED STRAINS ON THE OUTSIDE FACE OF THE SLAB OF PV16

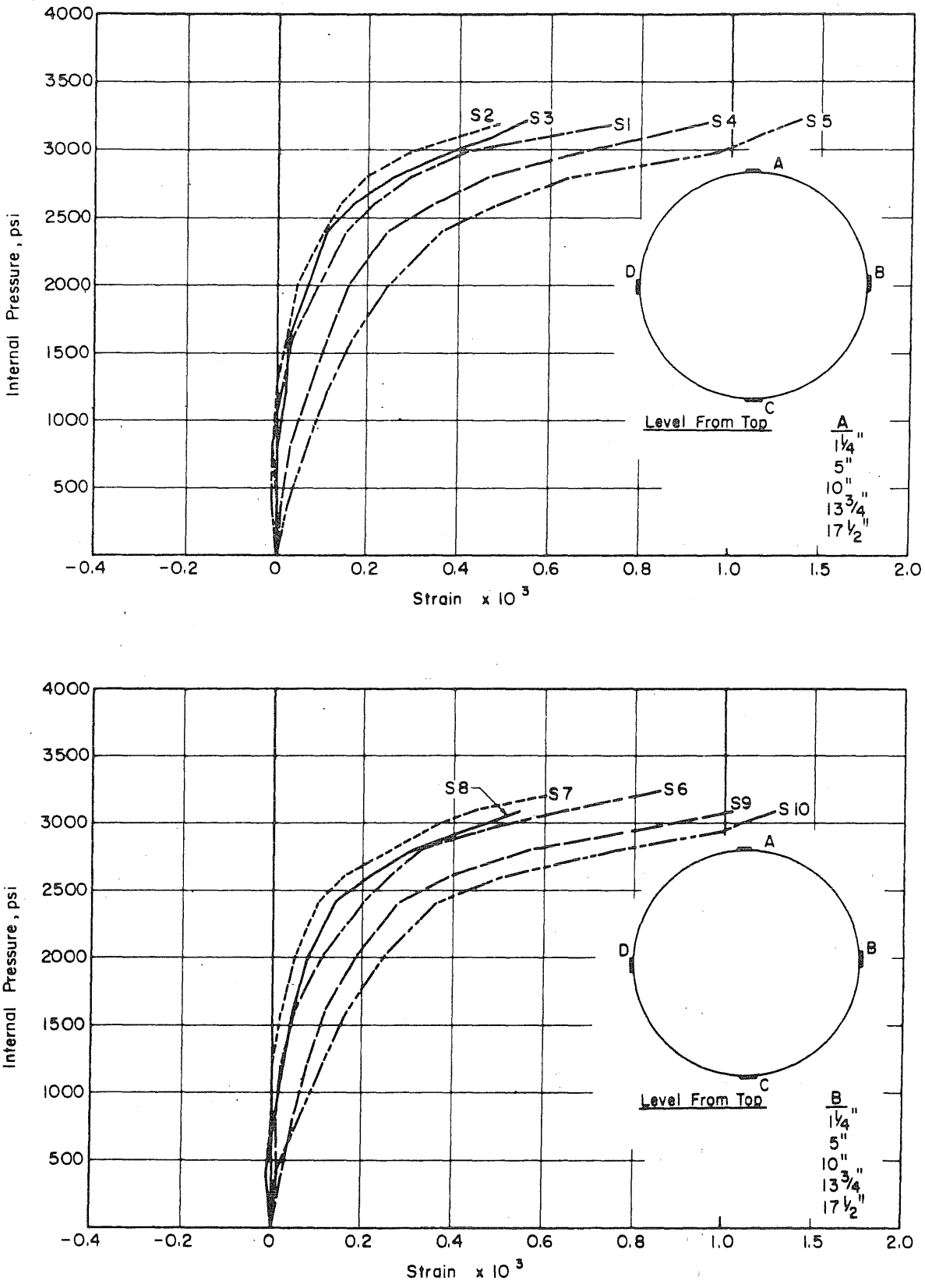

FIG. B.5 MEASURED STRAINS IN THE CIRCUMFERENTIAL PRESTRESSING WIRE OF PV16

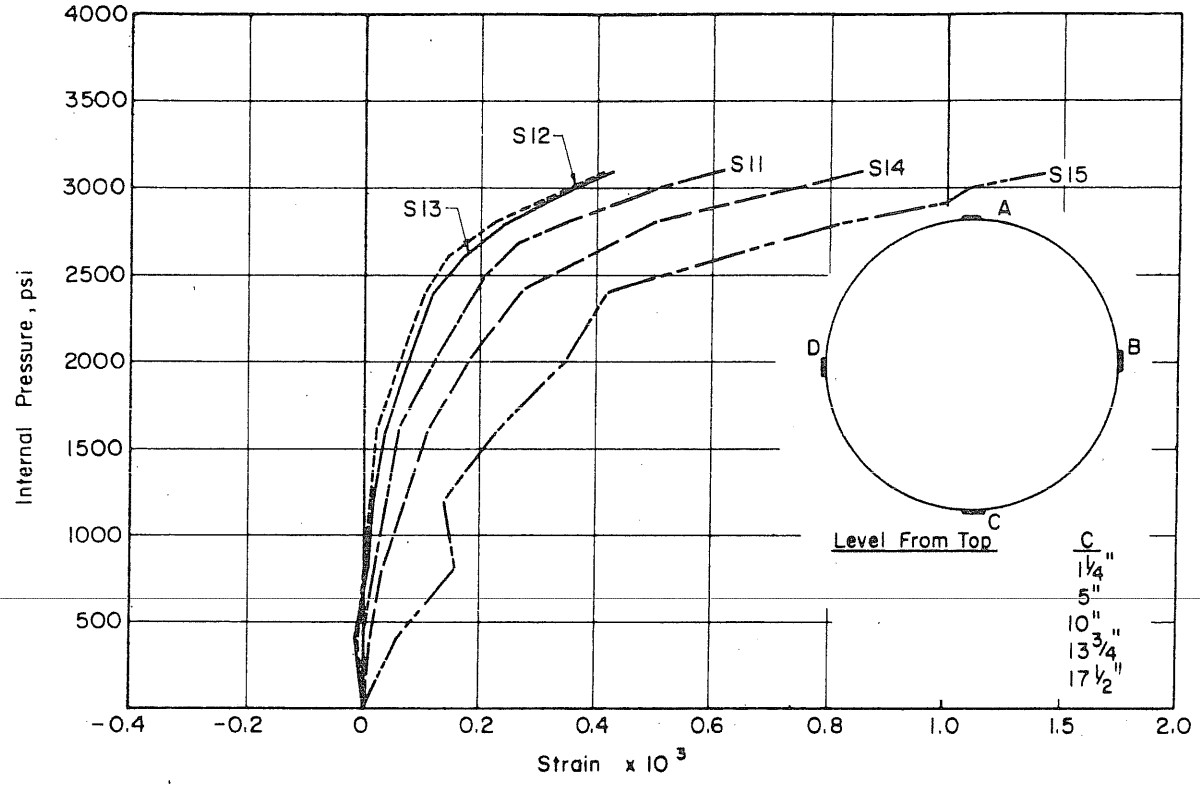

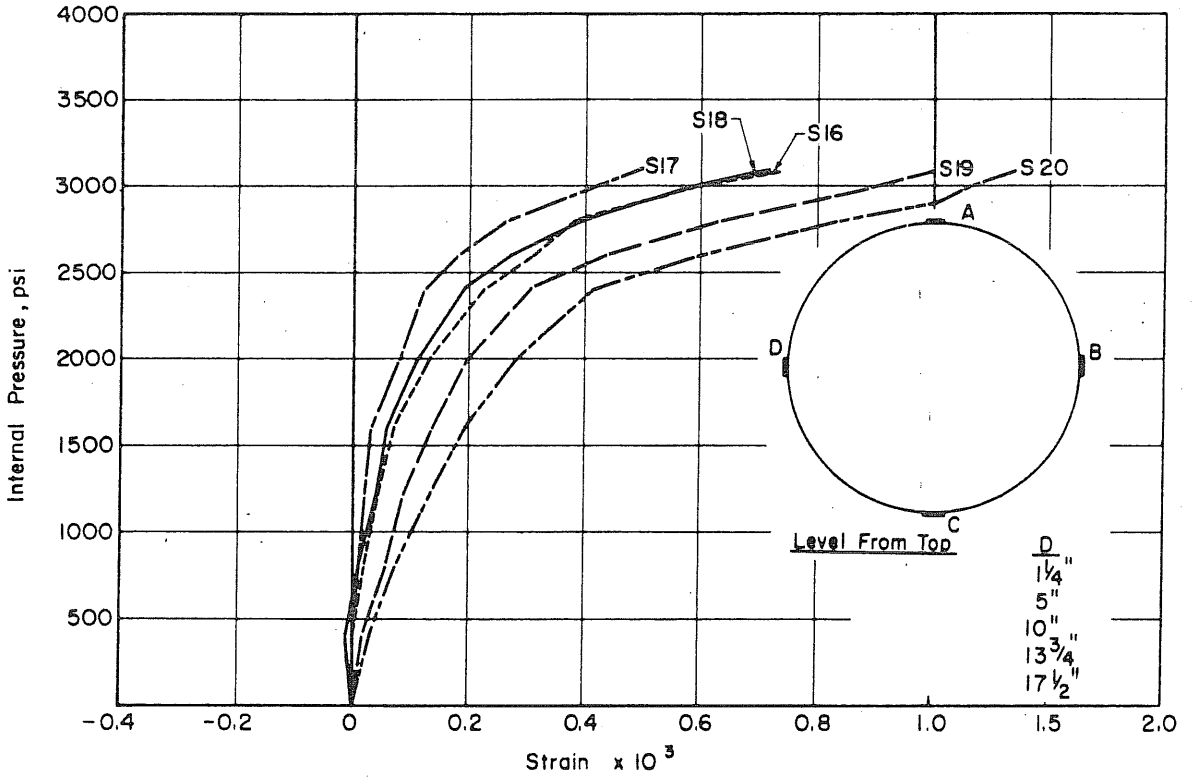

FIG. B.5 (Continued) MEASURED STRAINS IN THE CIRCUMFERENTIAL PRESTRESSING WIRE OF PV16

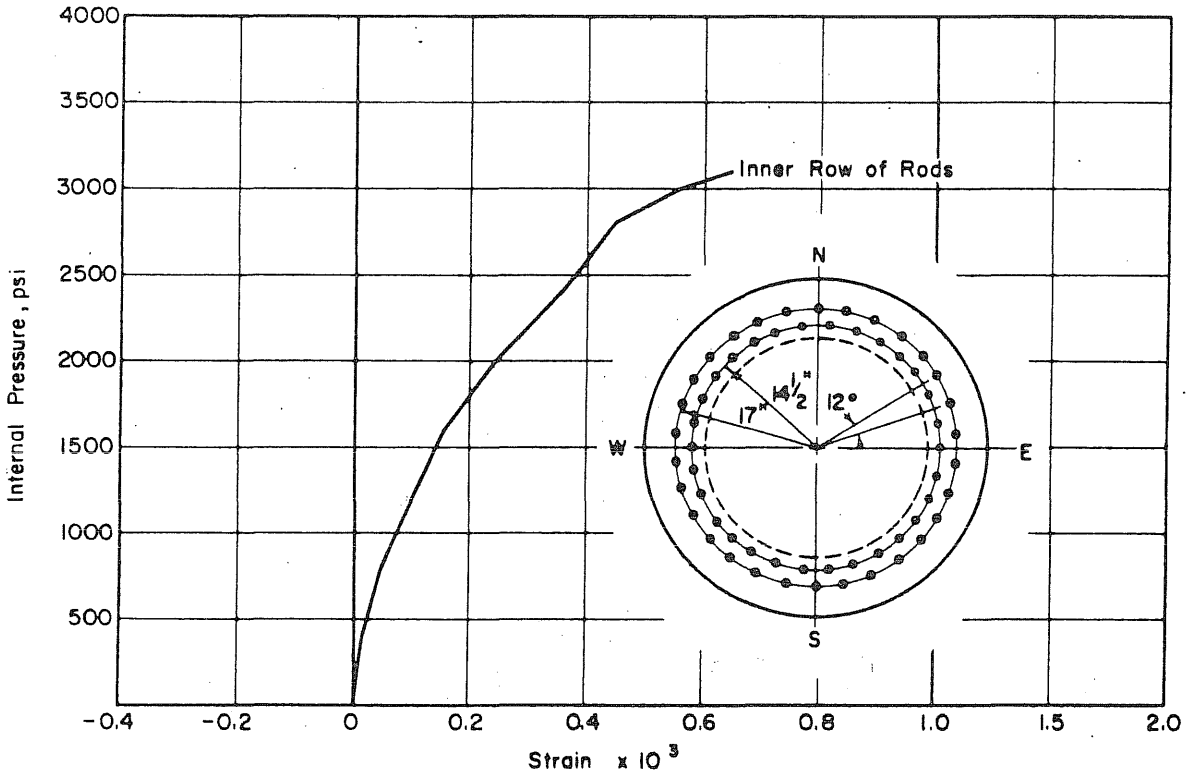

FIG. B.6 MEASURED STRAINS IN THE LONGITUDINAL PRESTRESSING RODS OF PV16

B.3 Test Vessel PV17

The vessel was filled with water to about 1/4-in. below the inside surface of the end slab. It was pressurized with nitrogen gas. The end slab failed explosively at a pressure of 3000 psi while strain and deflection readings were being made.

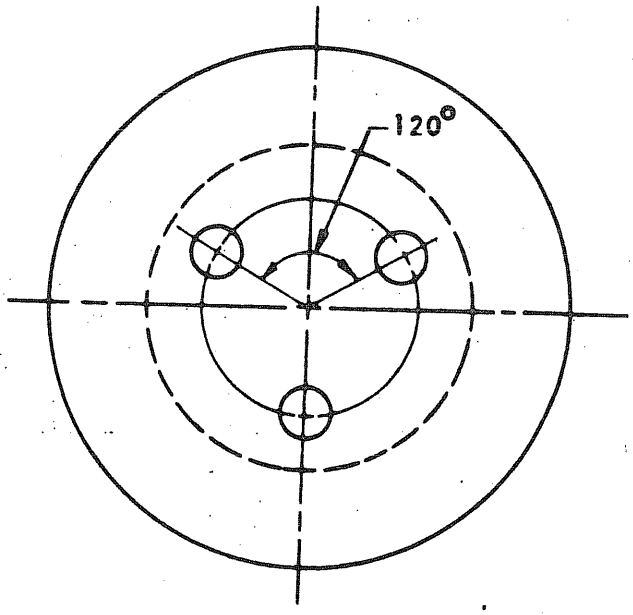

FIG. B.7 VESSEL PV17 WITH THREE 4-in. PENETRATIONS ON AN 8-in. RADIUS

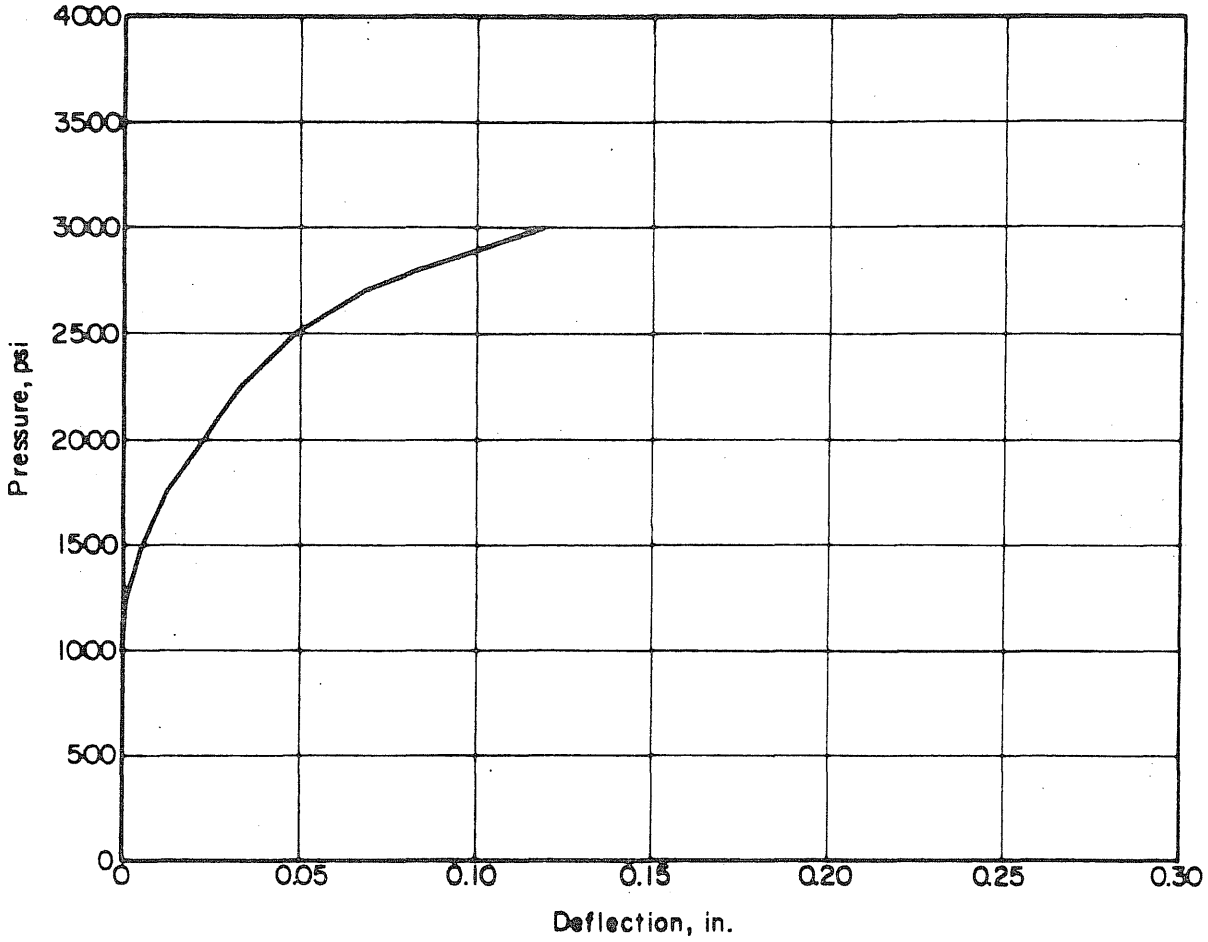

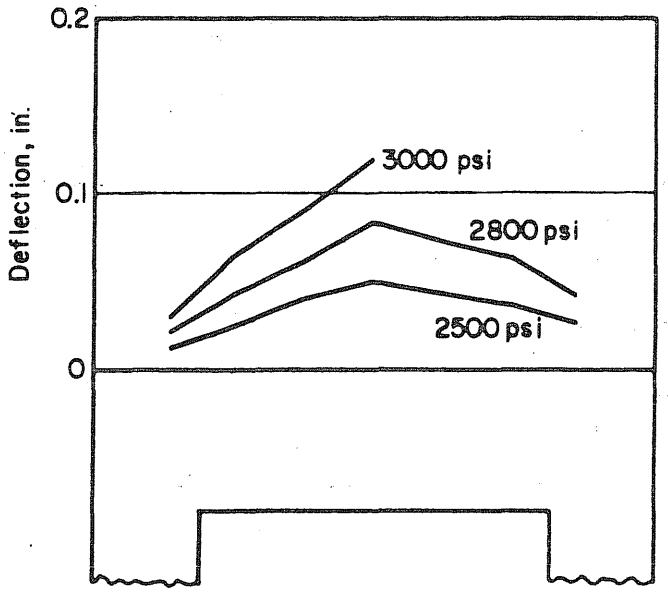

FIG. B.8 MEASURED DEFLECTION PROFILES AND DEFLECTION AT THE CENTER OF THE END SLAB OF PV17

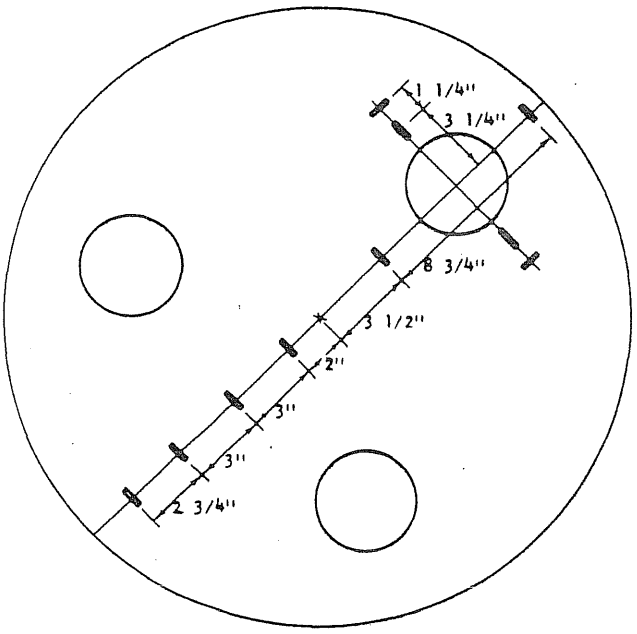

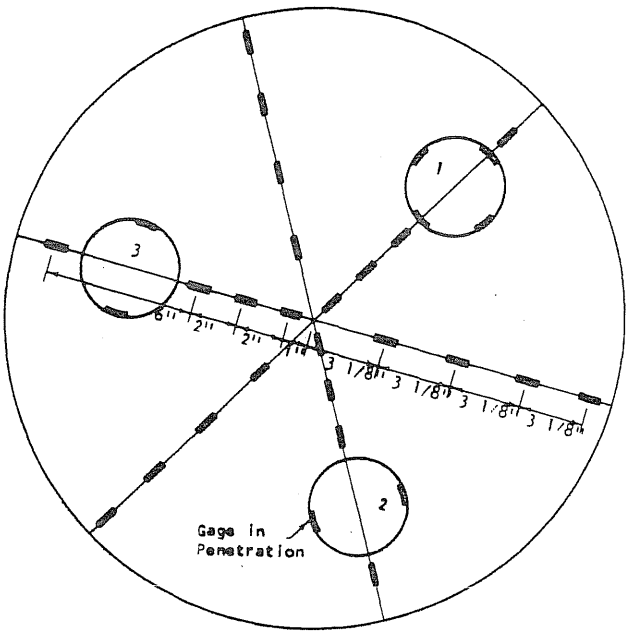

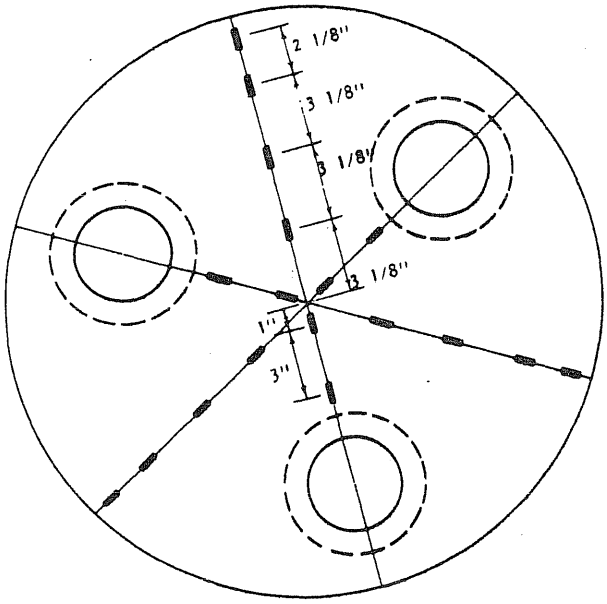

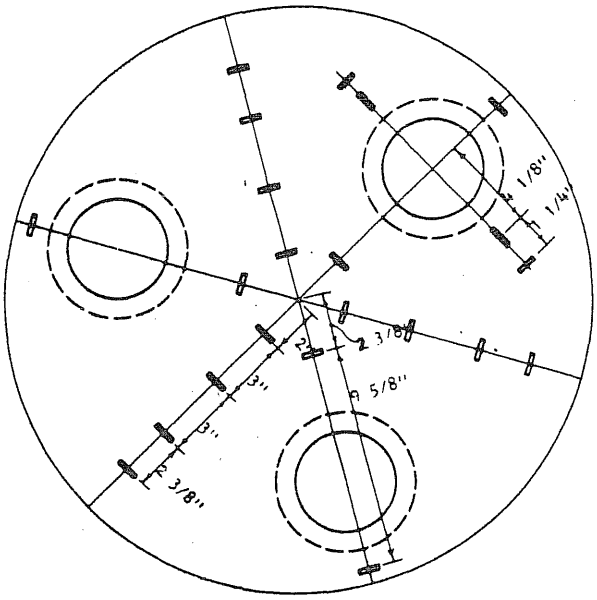

FIG. B.9 STRAIN GAGE LOCATION ON PV17

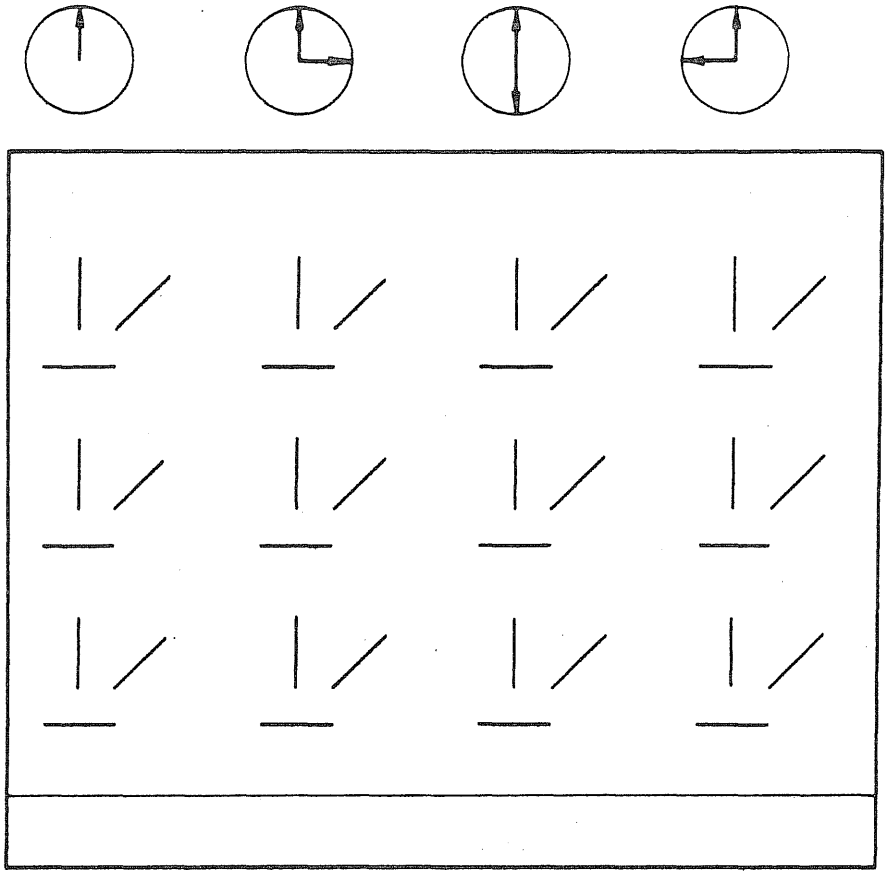

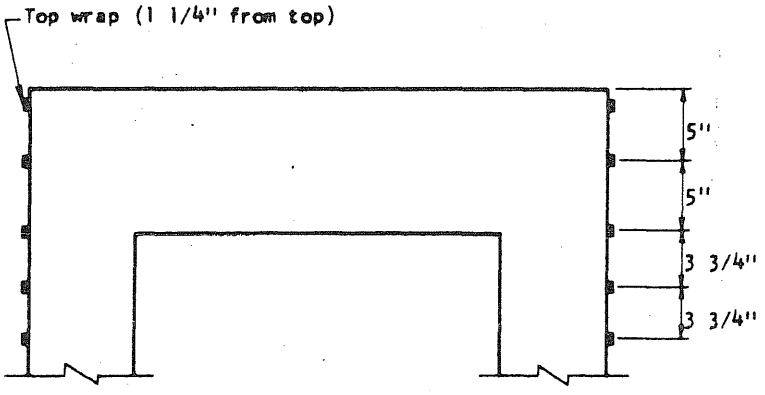

FIG. B.9 (Continued) STRAIN GAGE LOCATION ON PV17

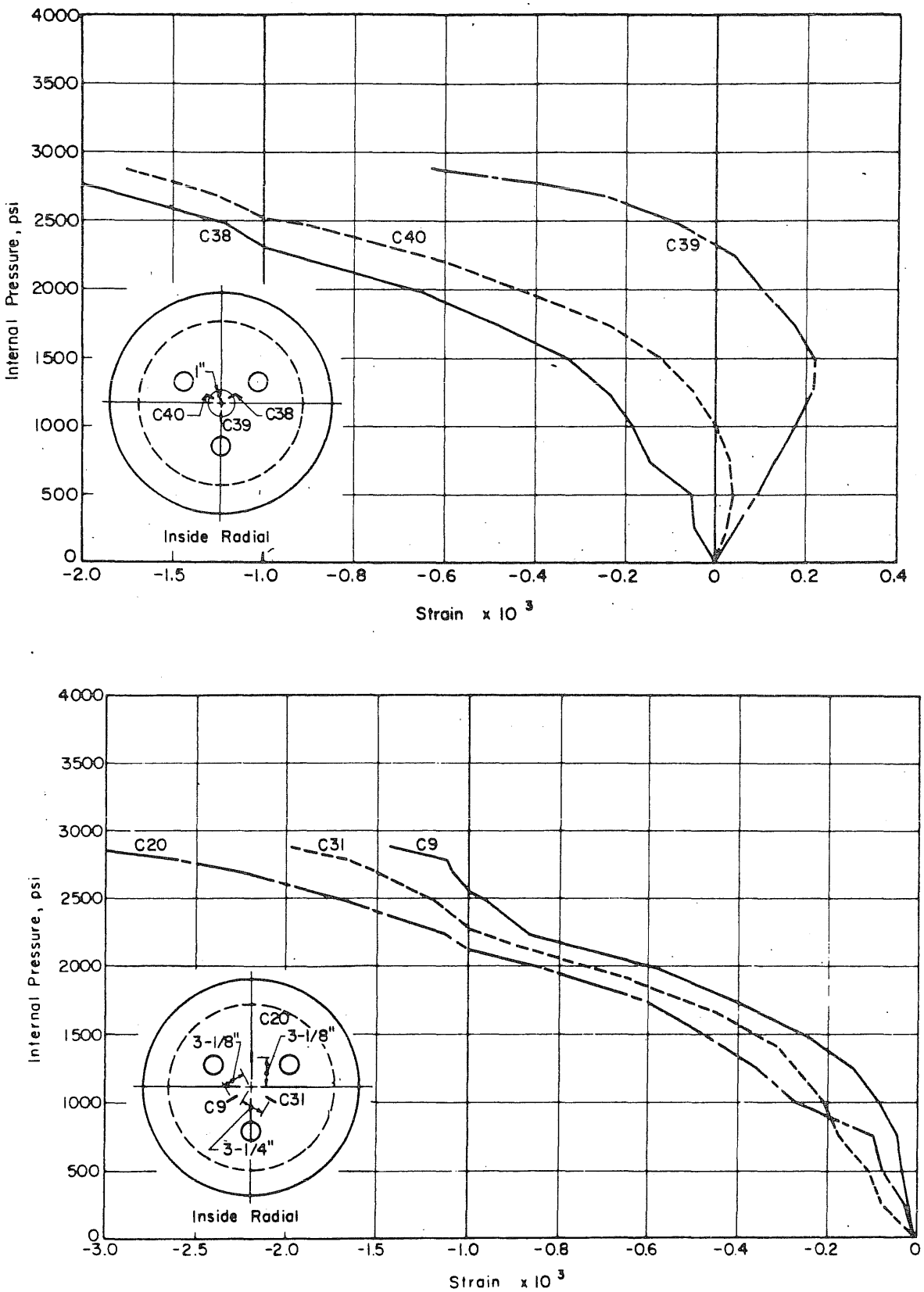

FIG. B.10 MEASURED STRAINS ON THE INSIDE FACE OF THE SLAB OF PV17

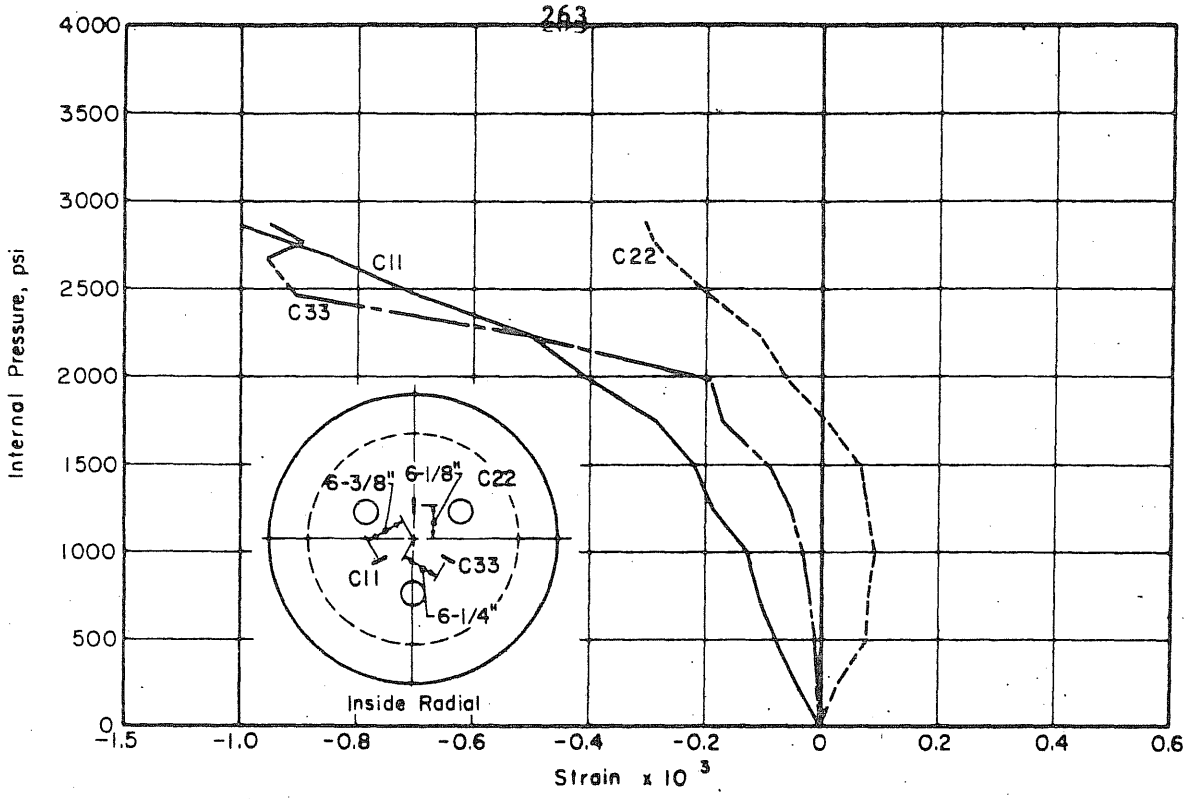

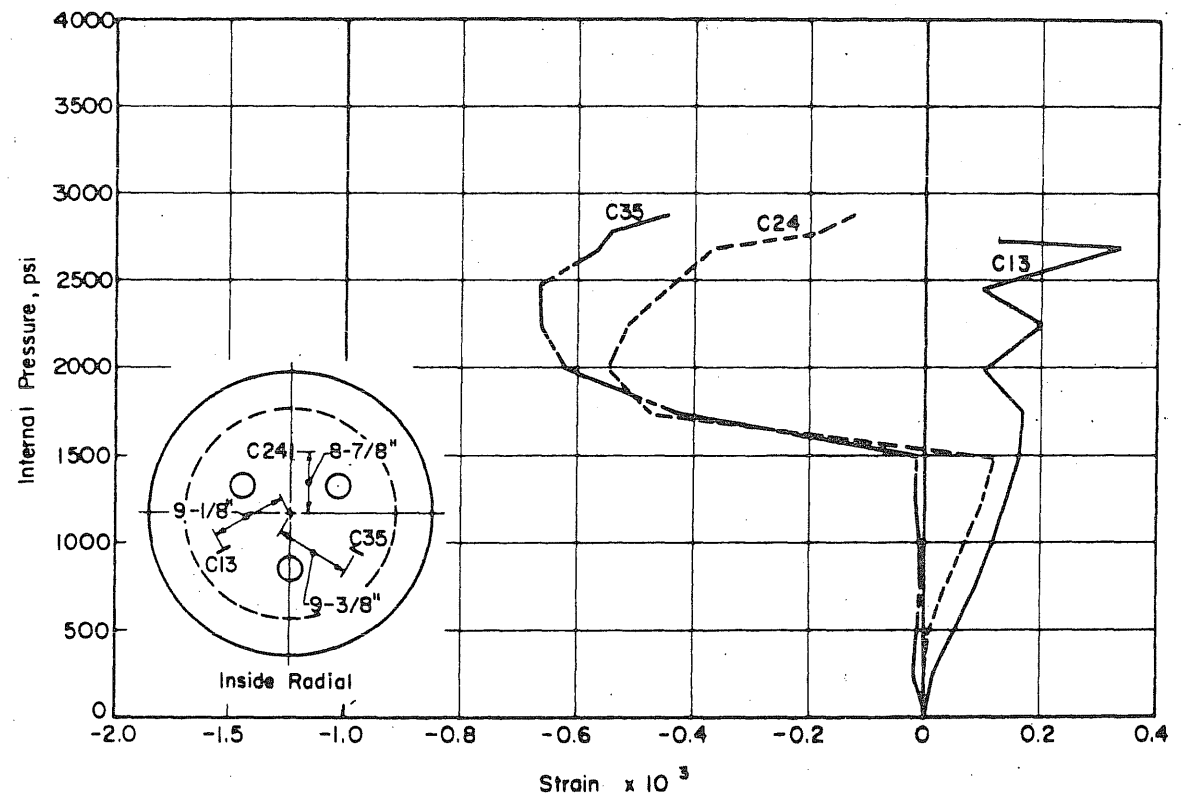

FIG. B.10 (Continued) MEASURED STRAINS ON THE INSIDE FACE OF THE SLAB OF PV17

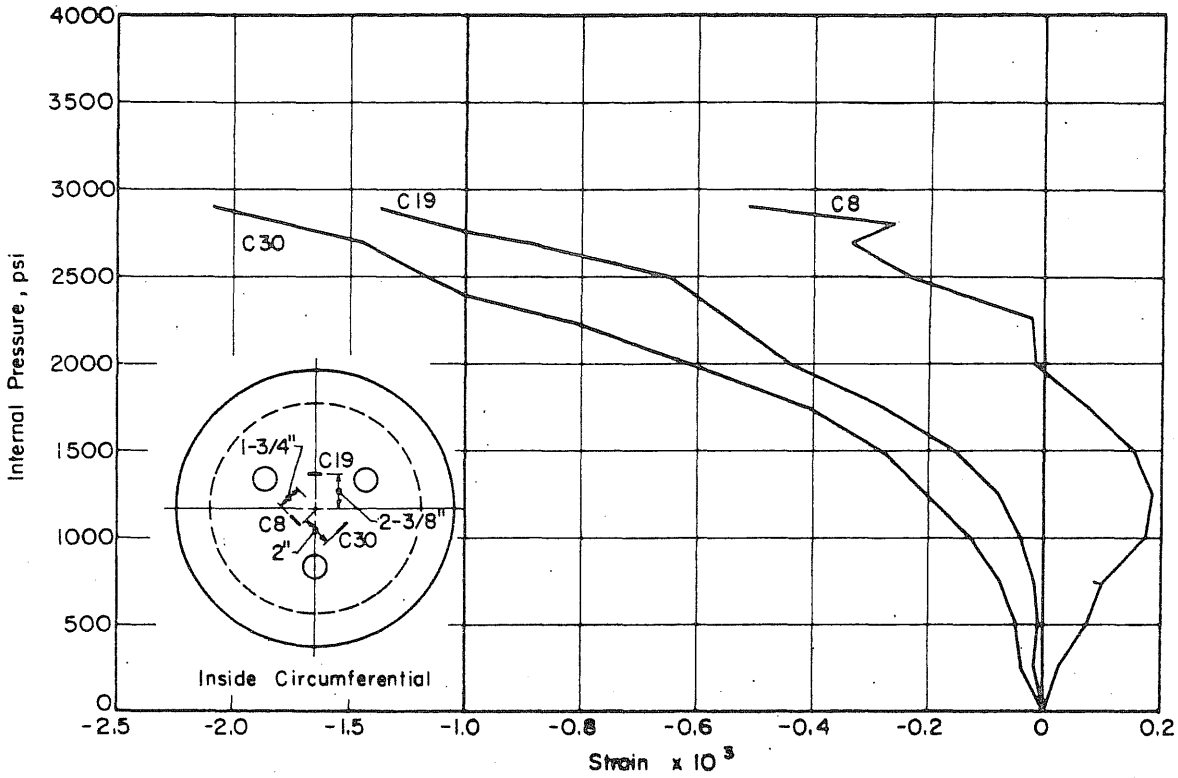

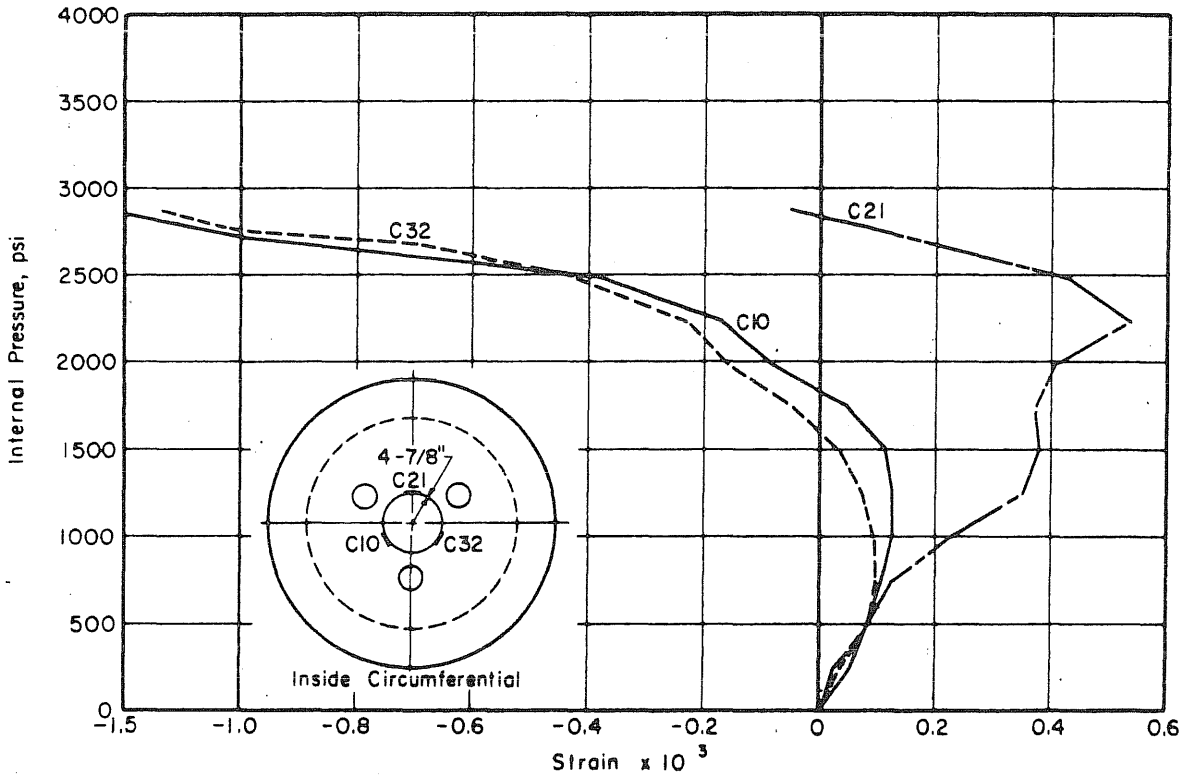

FIG. B.10 (Continued) MEASURED STRAINS ON THE INSIDE FACE OF THE SLAB OF PV17

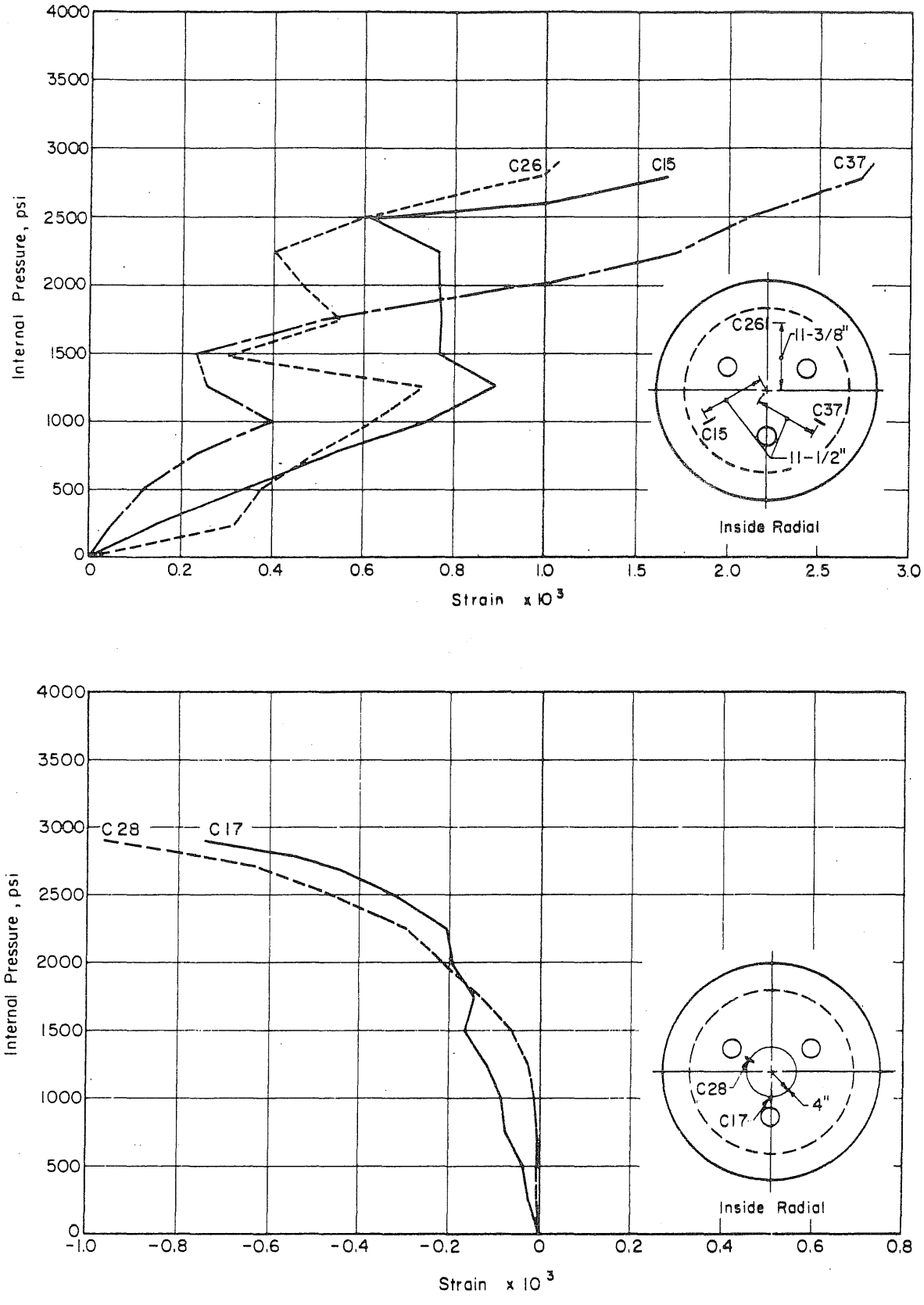

FIG. B.10 (Continued) MEASURED STRAINS ON THE INSIDE FACE OF THE SLAB OF PV17

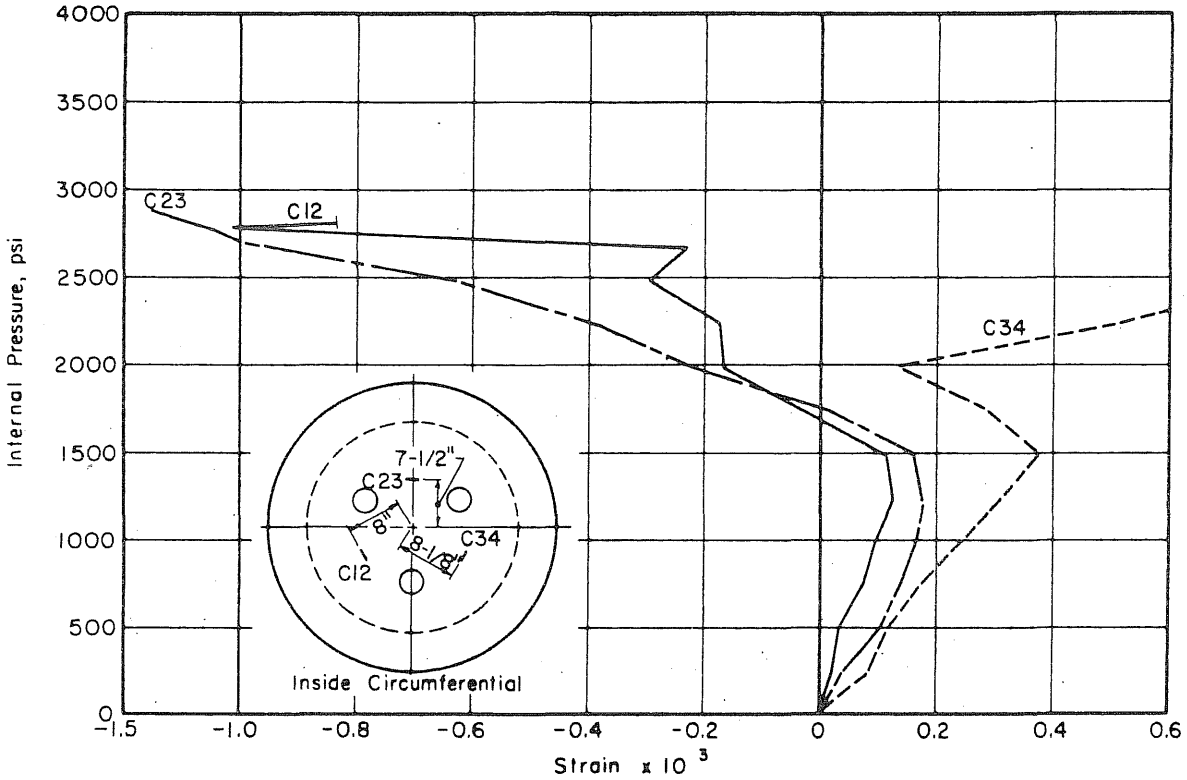

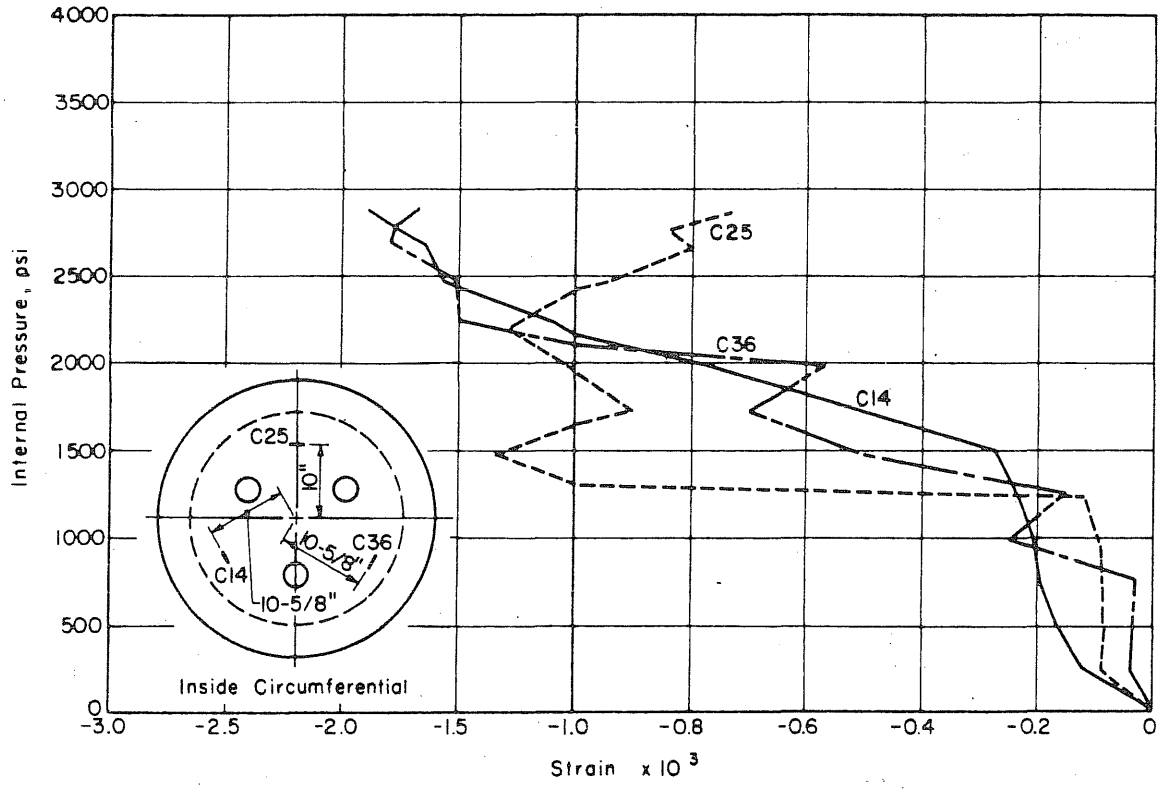

FIG. B.10 (Continued) MEASURED STRAINS ON THE INSIDE FACE OF THE SLAB OF PV17

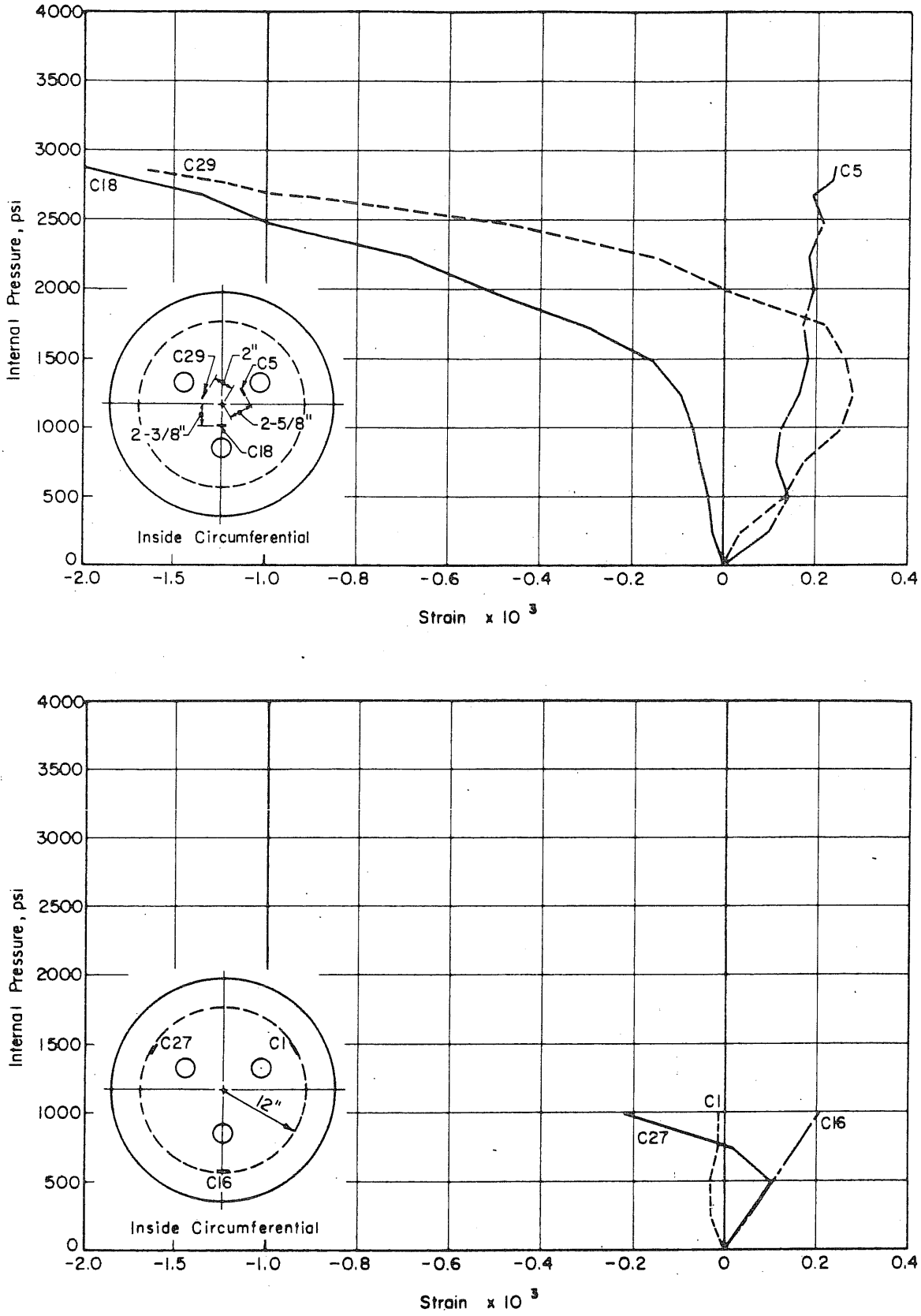

FIG. B.10 (Continued) MEASURED STRAINS ON THE INSIDE FACE OF THE SLAB OF PV17

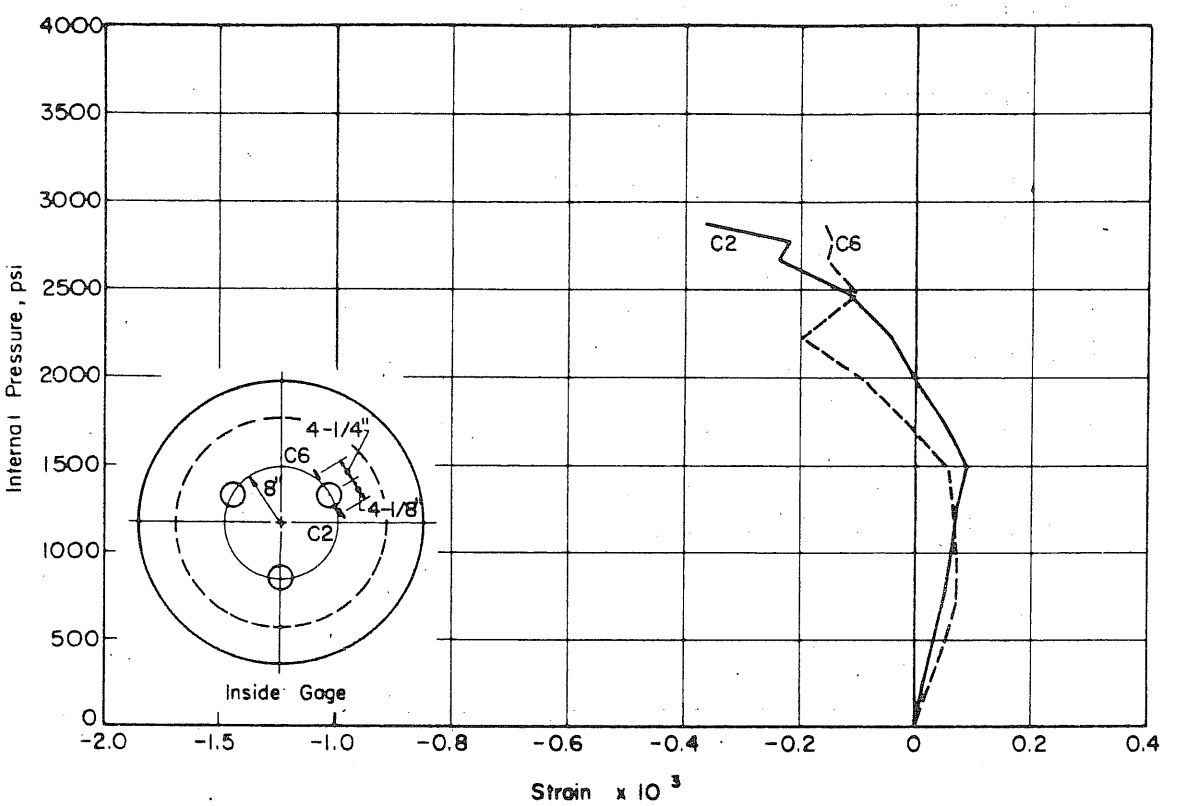

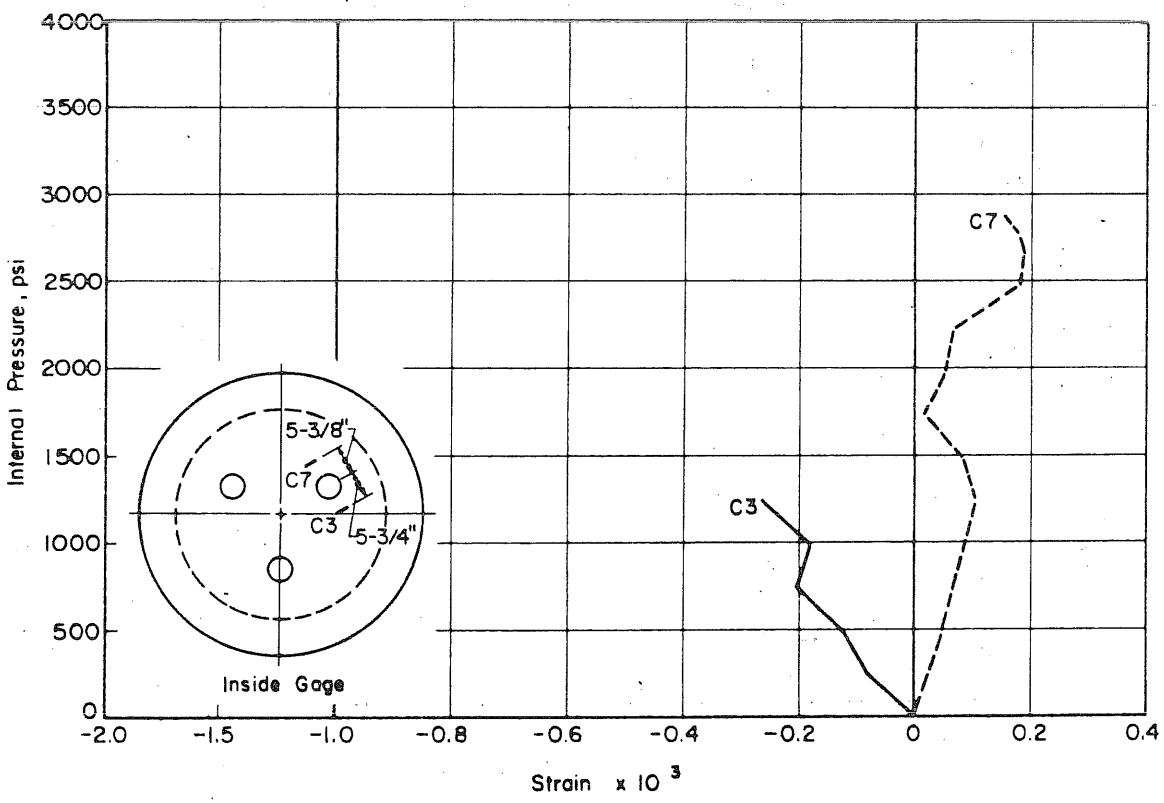

FIG. B.10 (Continued) MEASURED STRAINS ON THE INSIDE FACE OF THE SLAB OF PV17

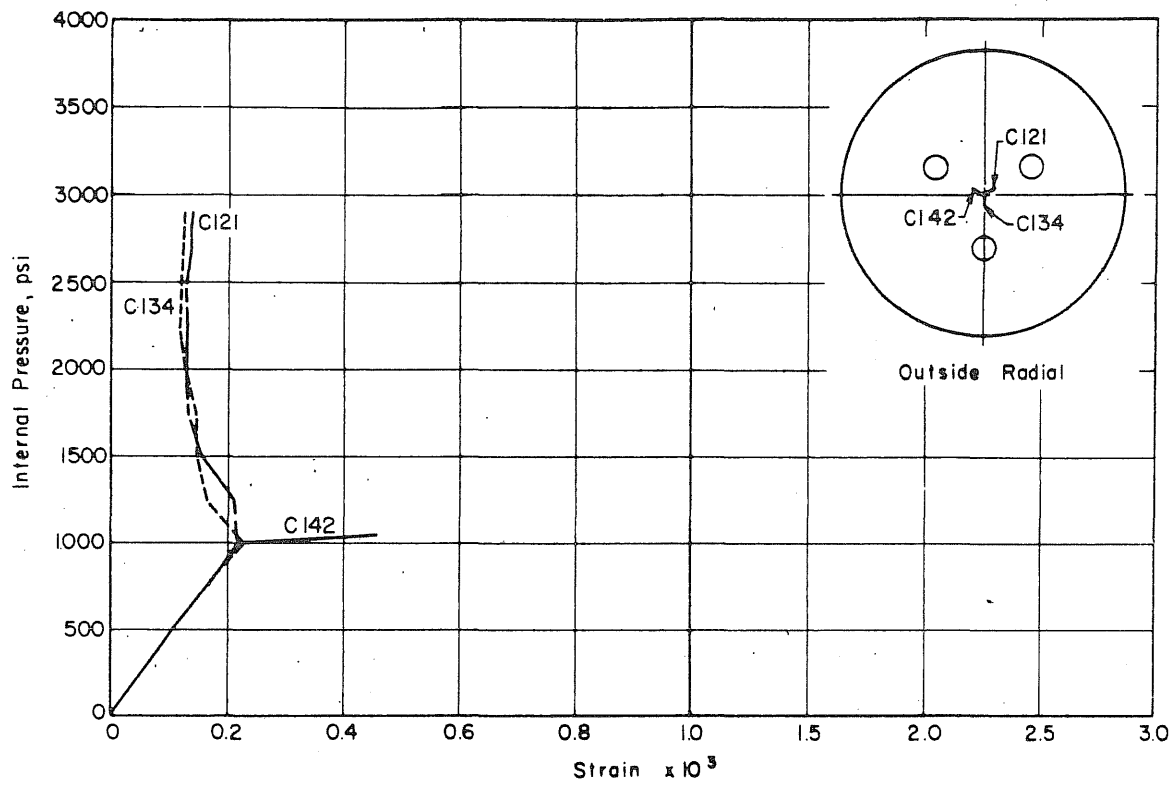

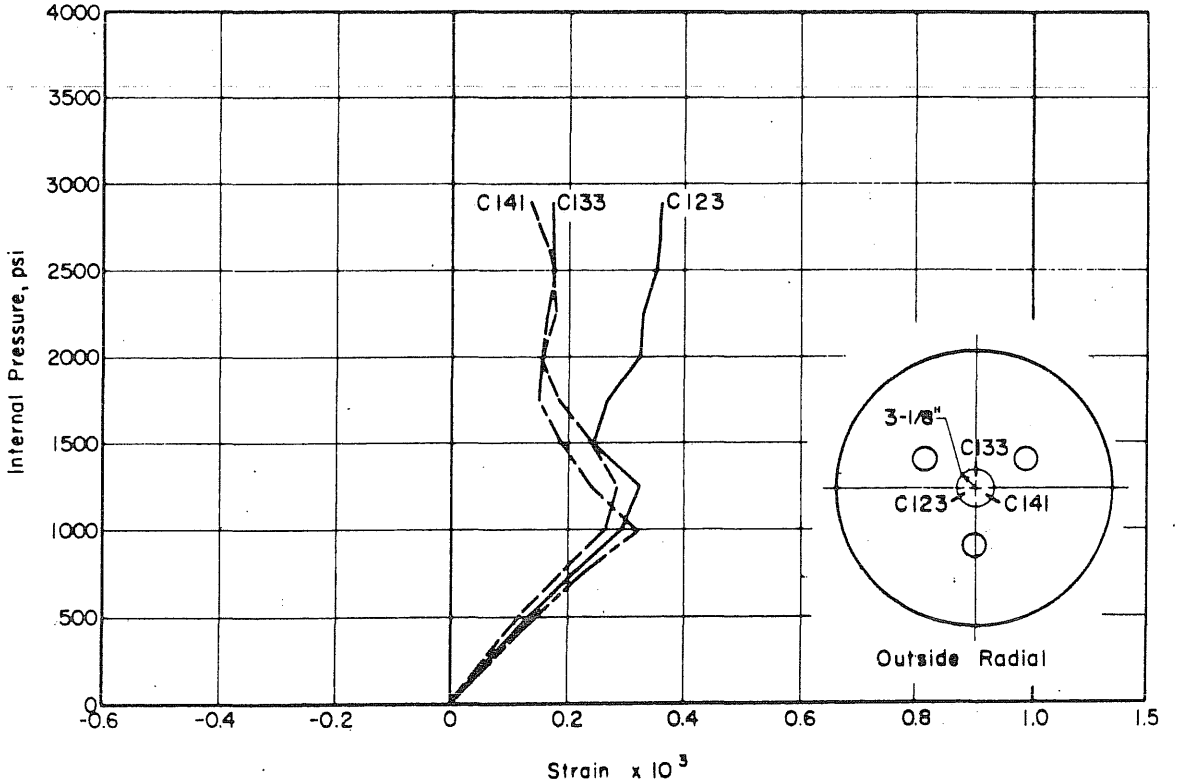

FIG. B.11 MEASURED STRAINS ON THE OUTSIDE FACE OF THE SLAB OF PV17

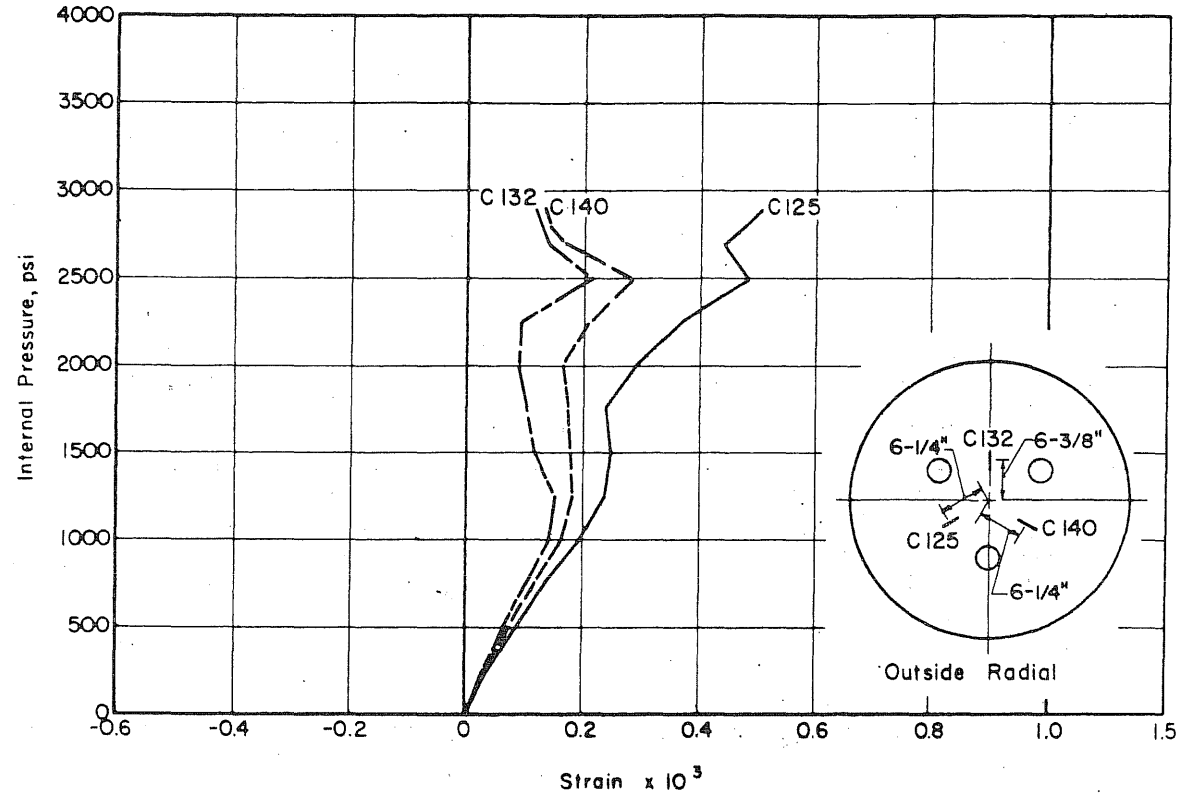

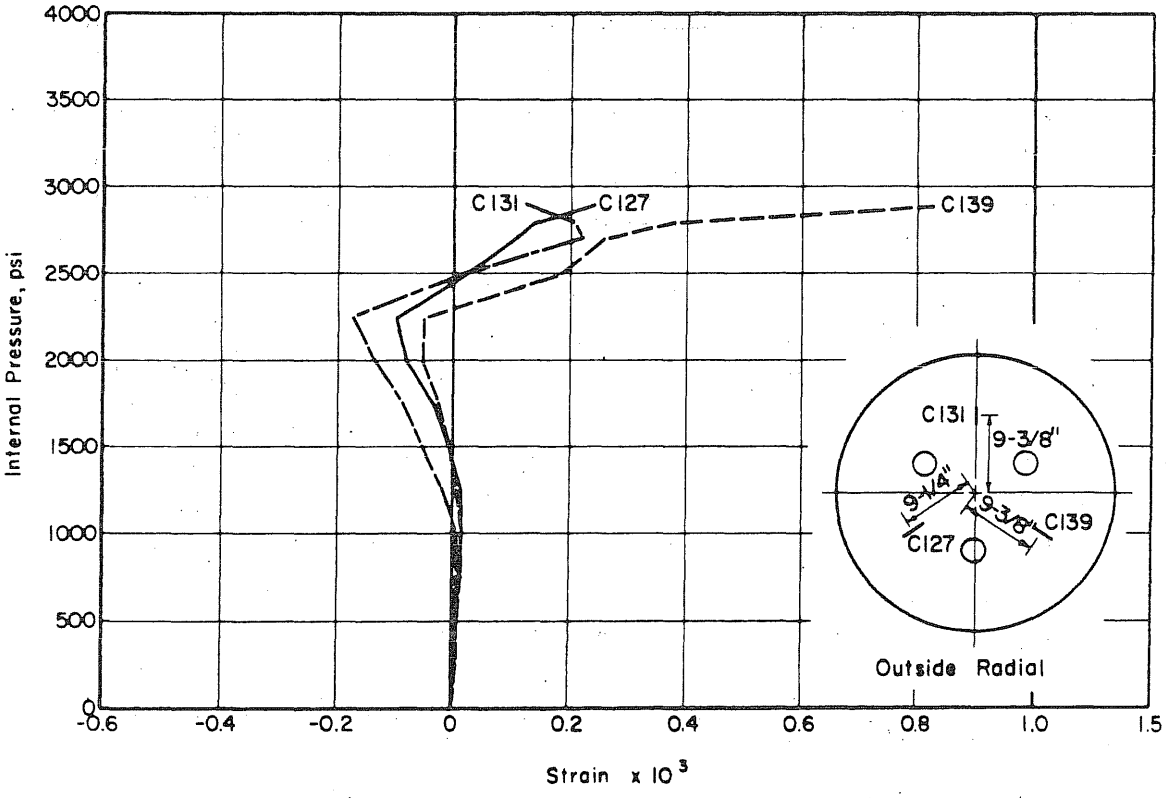

FIG. B.11 (Continued) MEASURED STRAINS ON THE OUTSIDE FACE OF THE SLAB OF PV17

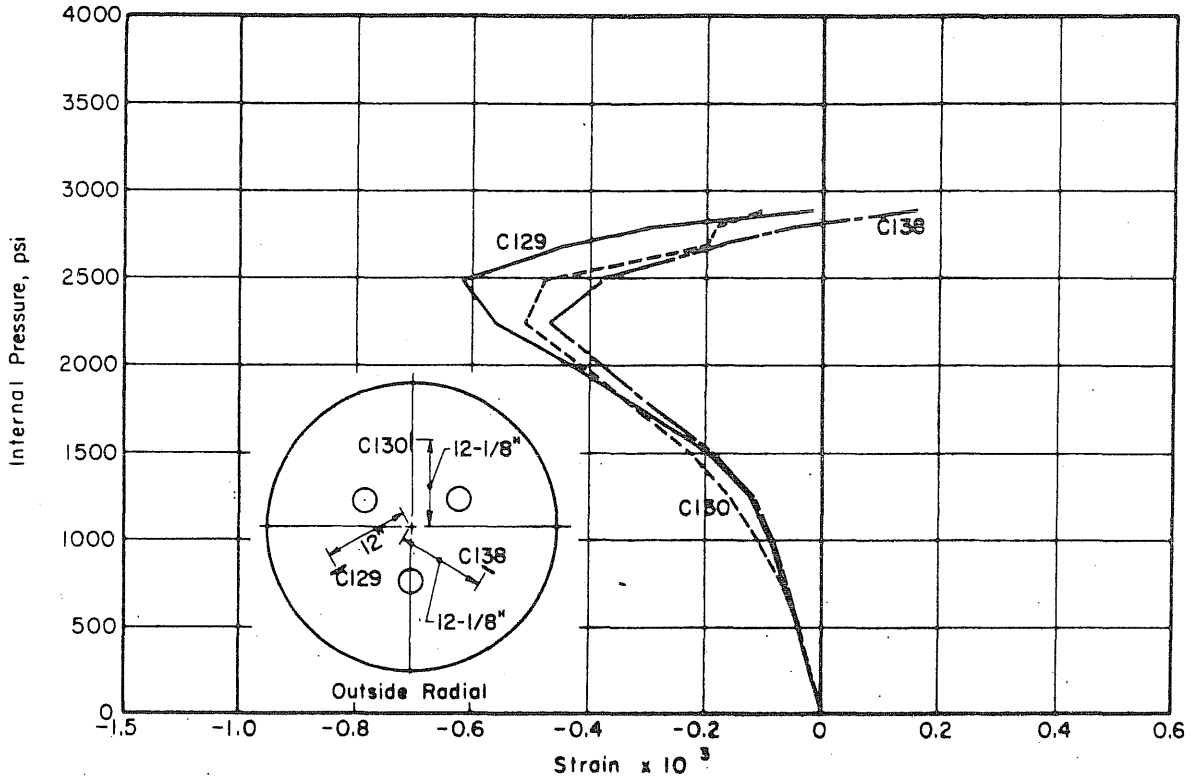

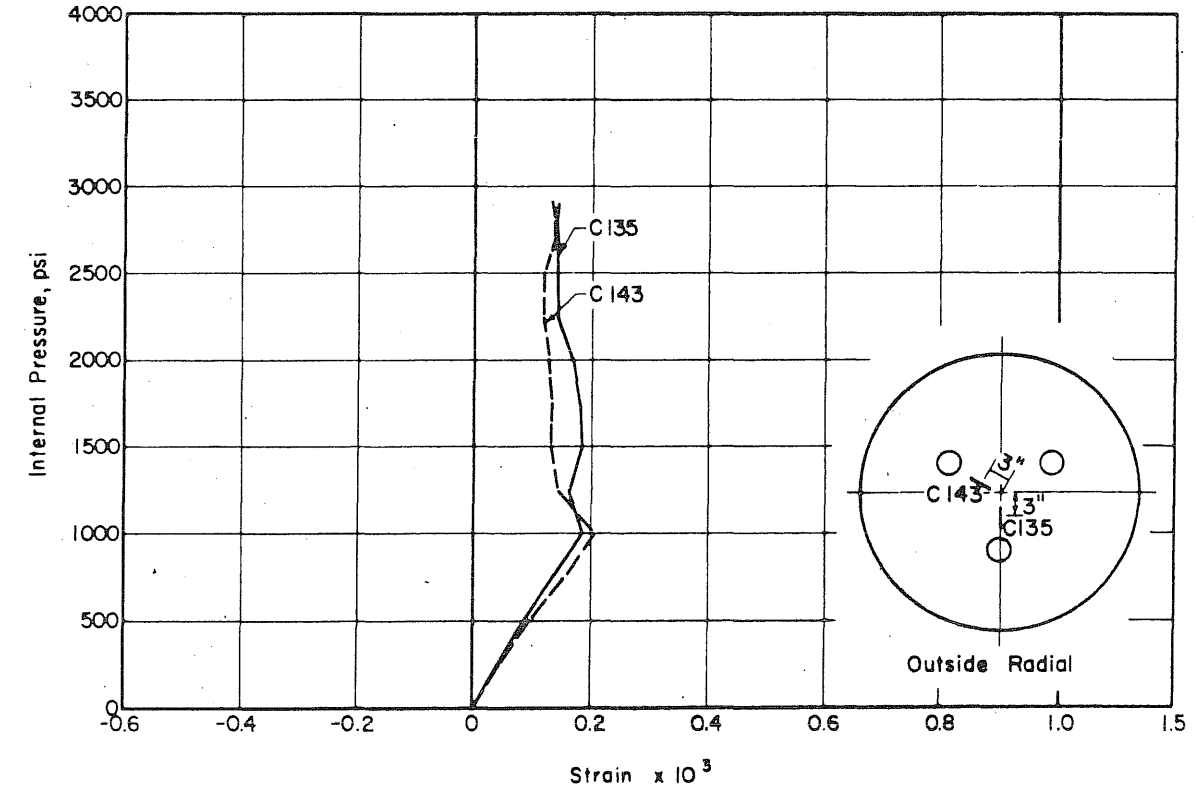

FIG. B.11 (Continued) MEASURED STRAINS ON THE OUTSIDE FACE OF THE SLAB OF PV17

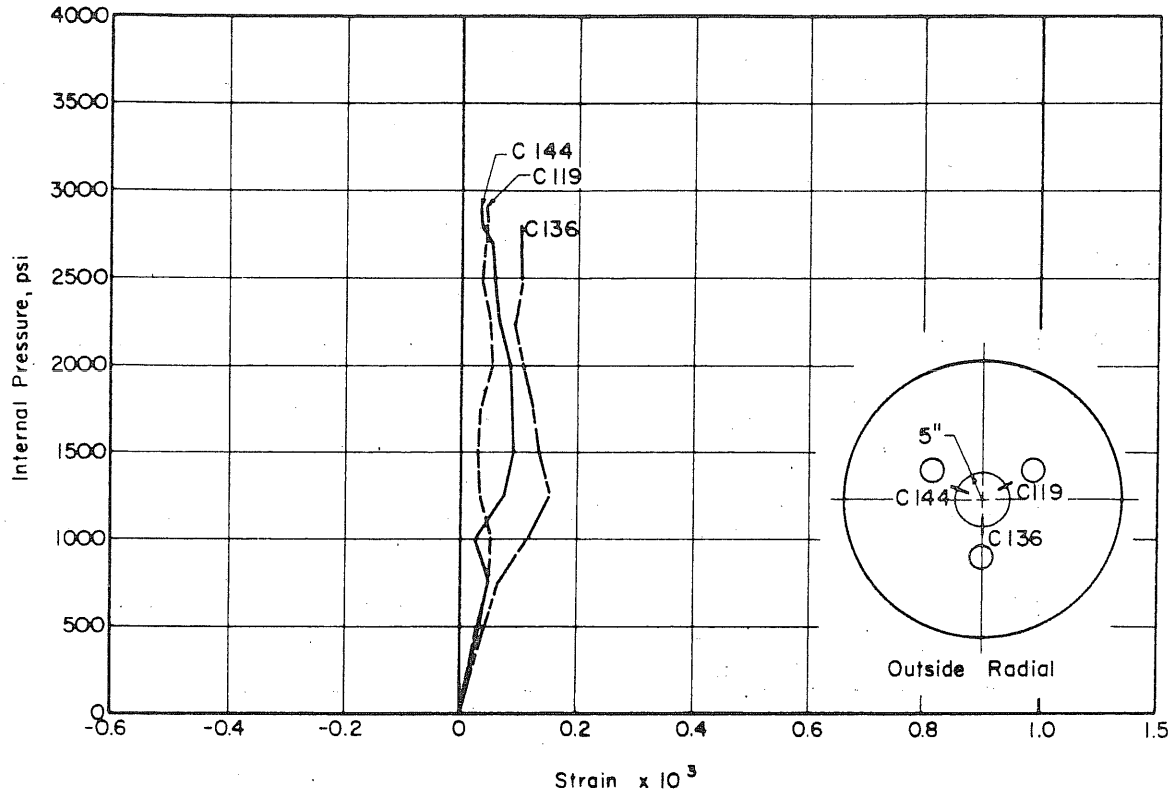

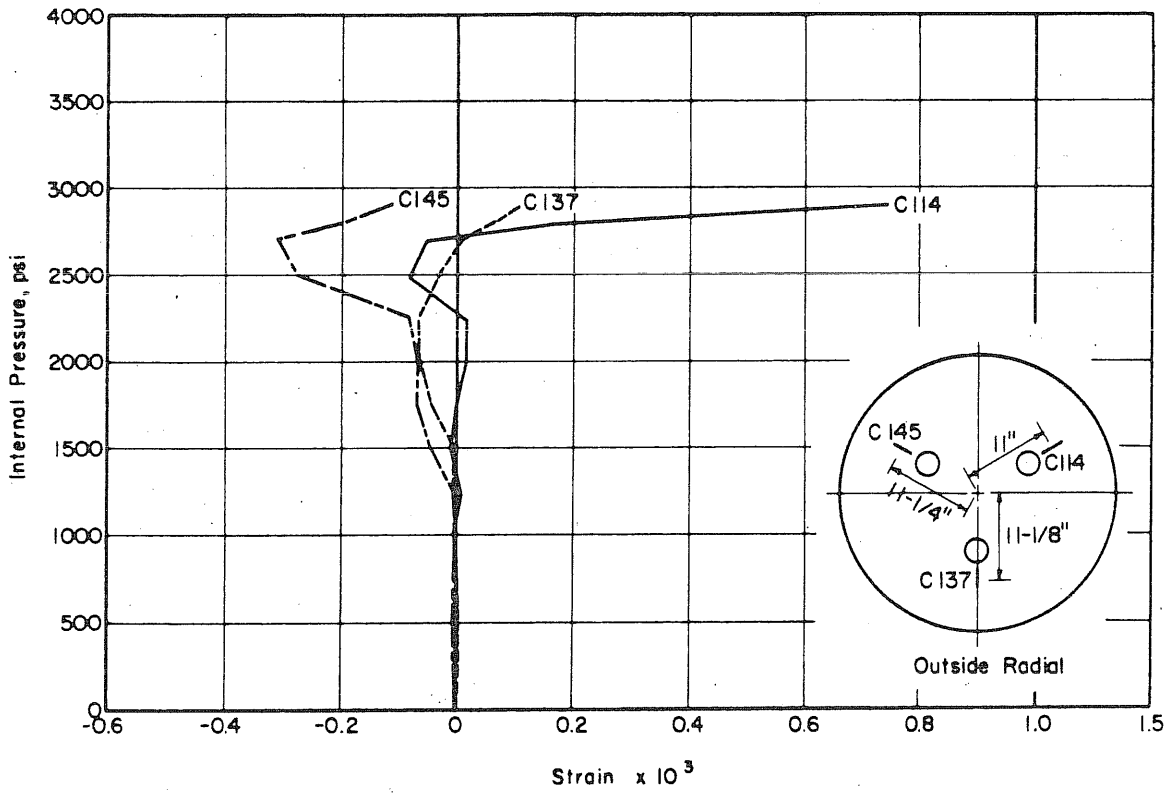

FIG. B.11 (Continued) MEASURED STRAINS ON THE OUTSIDE FACE OF THE SLAB OF PV17

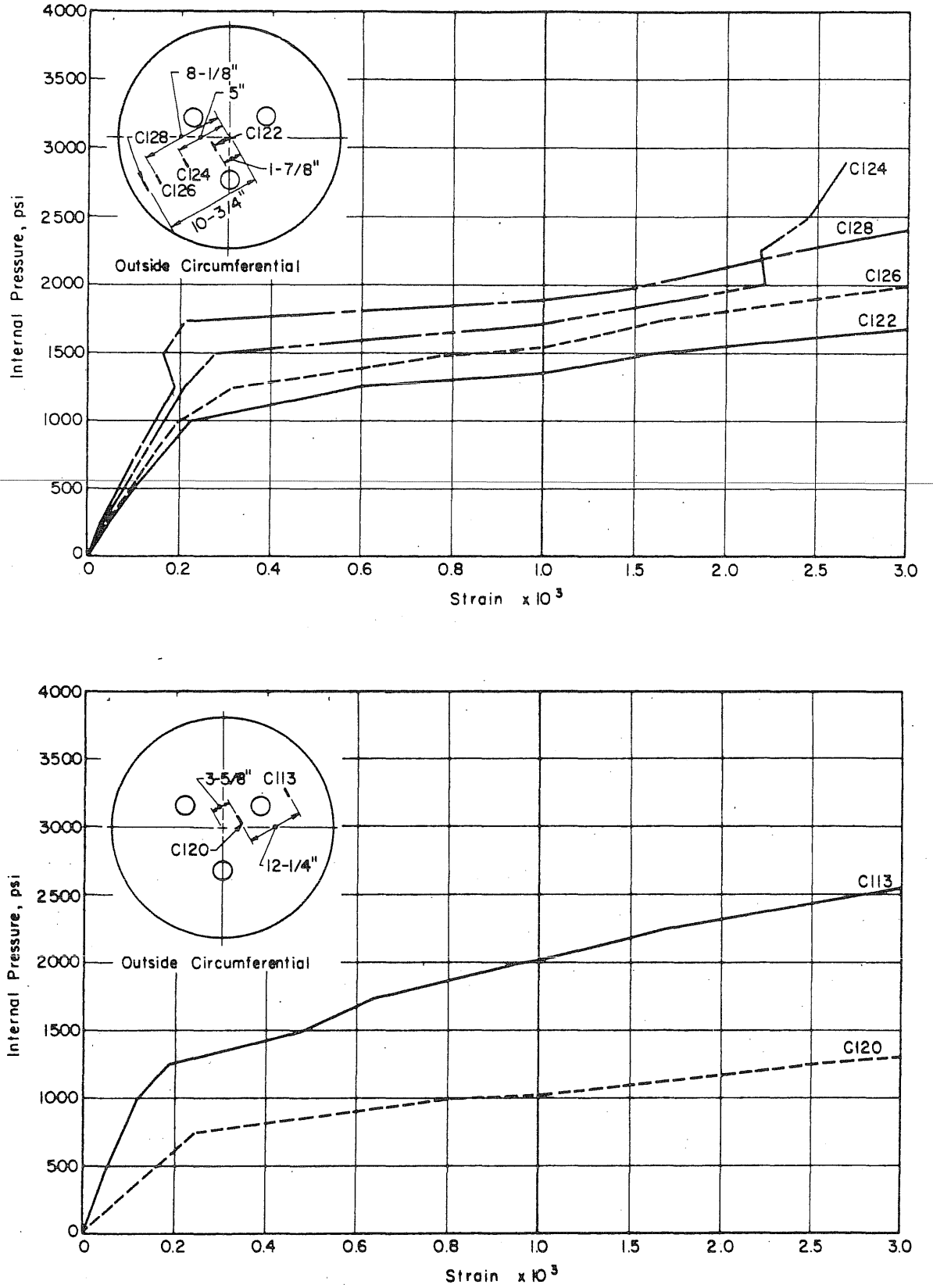

FIG. B.11 (Continued) MEASURED STRAINS ON THE OUTSIDE FACE OF THE SLAB OF PV17

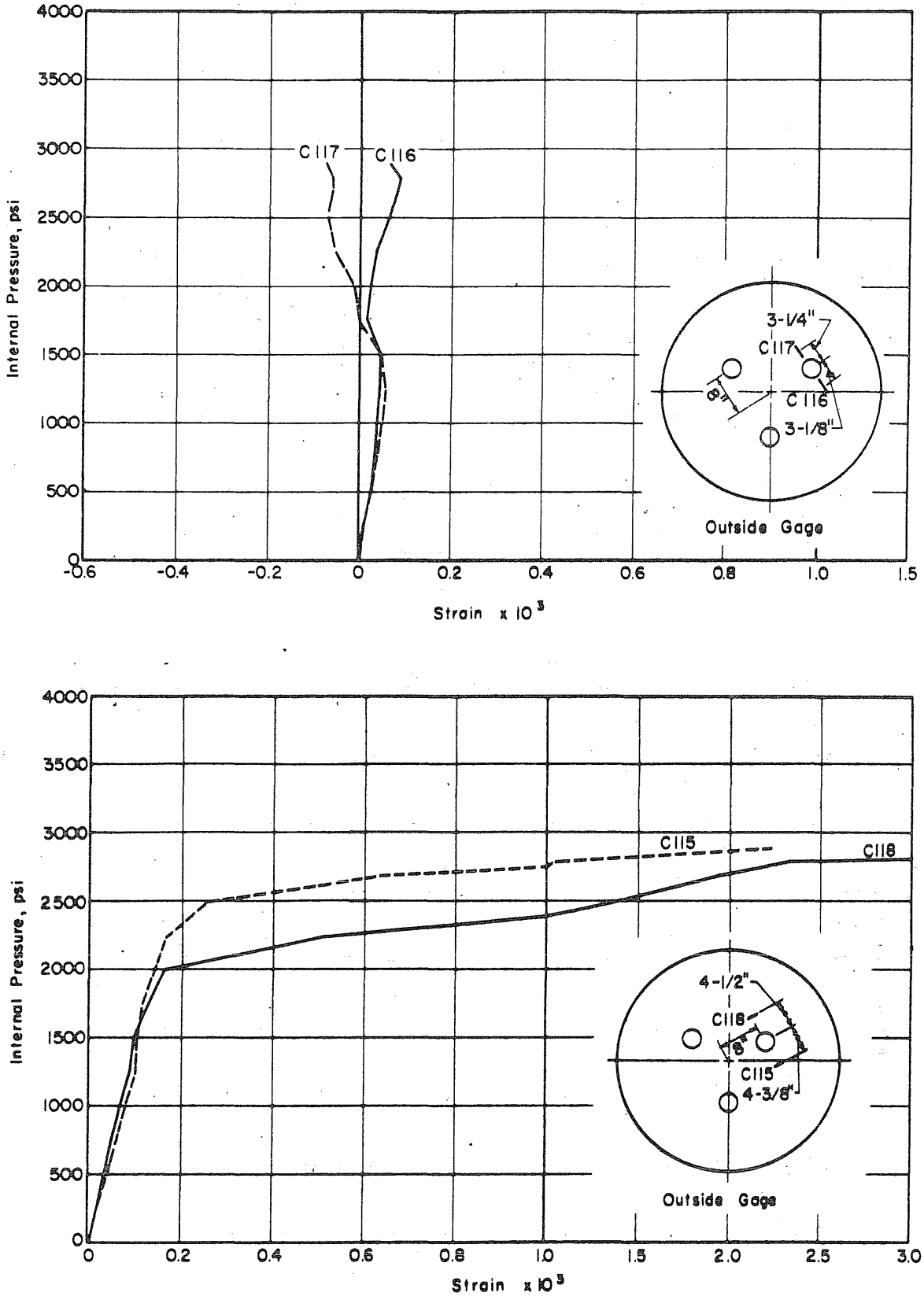

FIG. B.11 (Continued) MEASURED STRAINS ON THE OUTSIDE FACE OF THE SLAB OF PV17

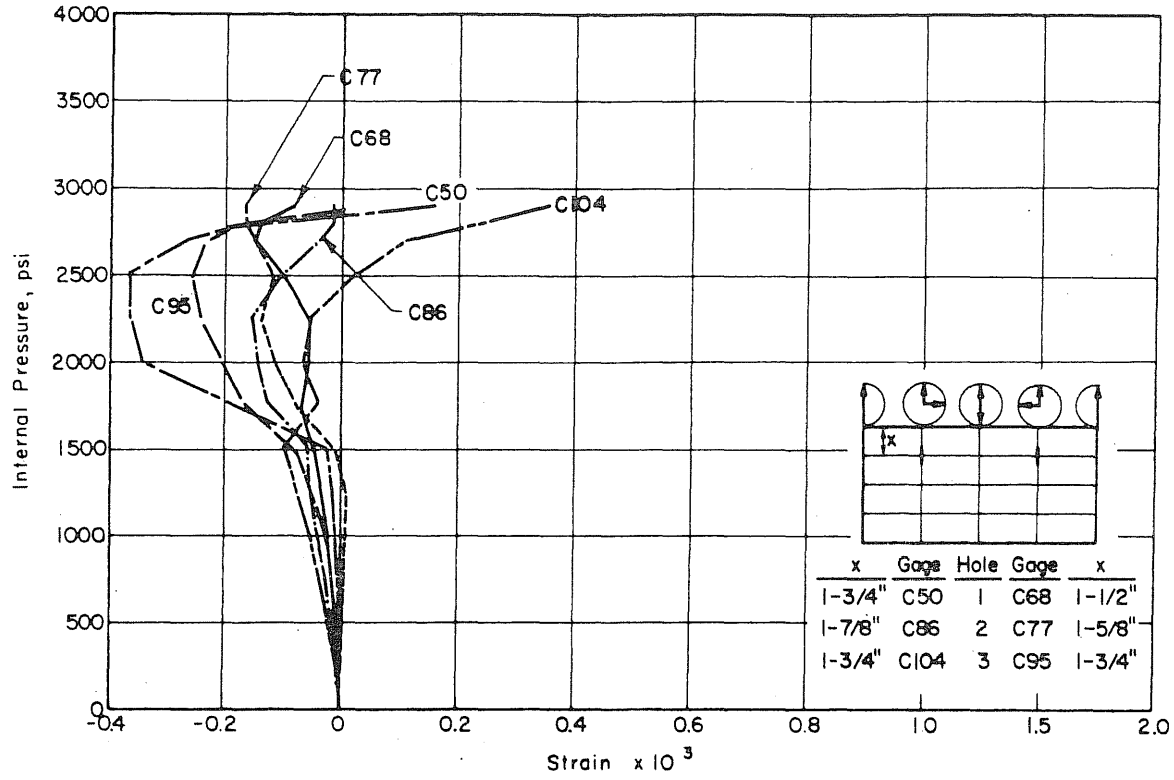

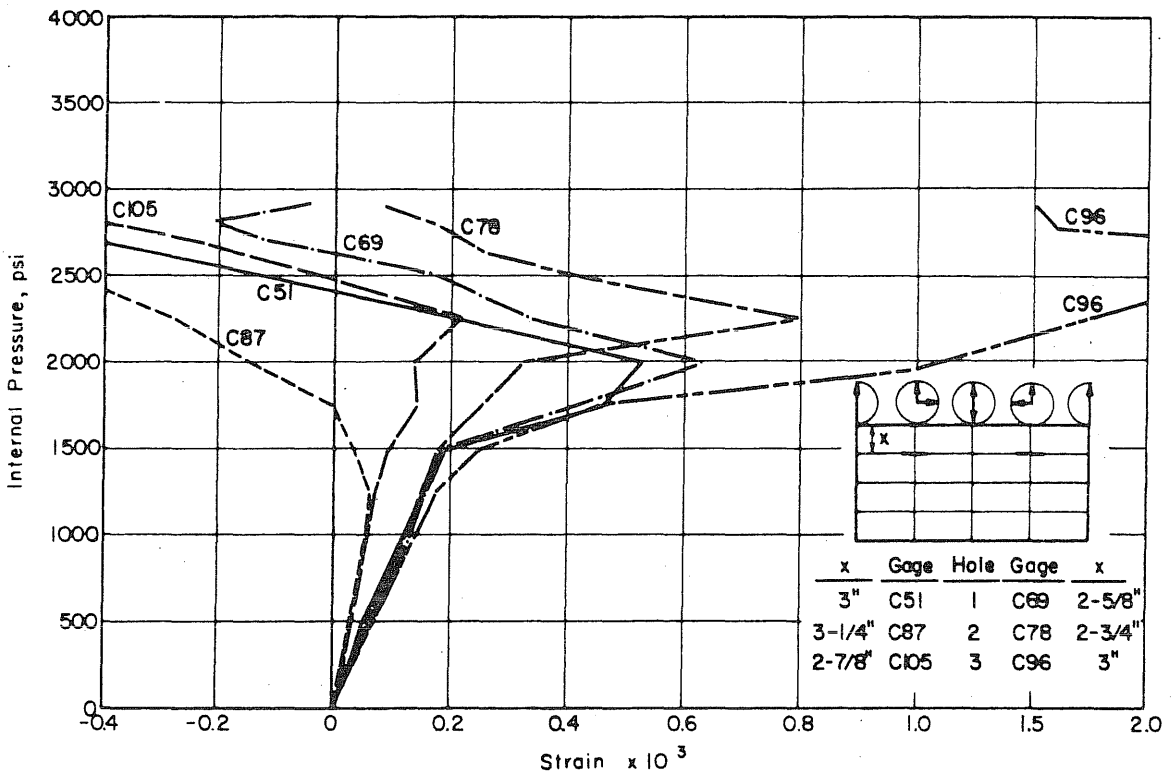

FIG. B.12 MEASURED STRAINS IN THE PENETRATIONS OF PV17

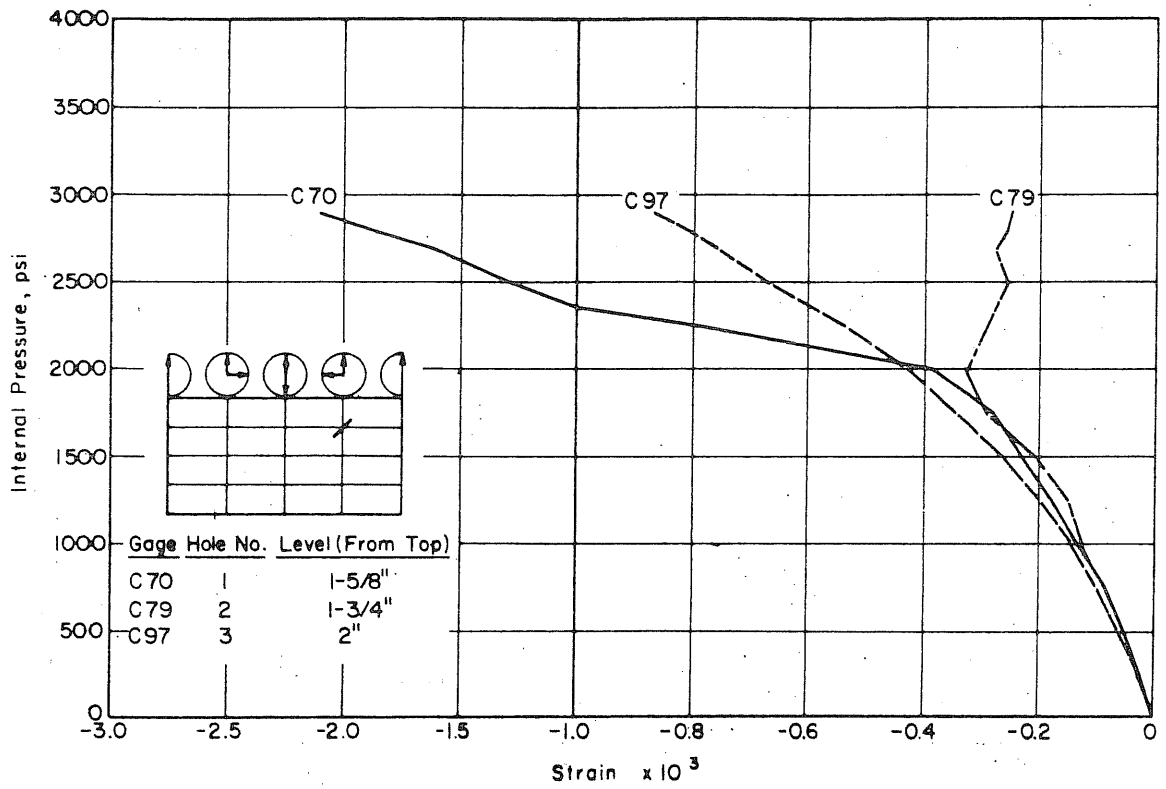

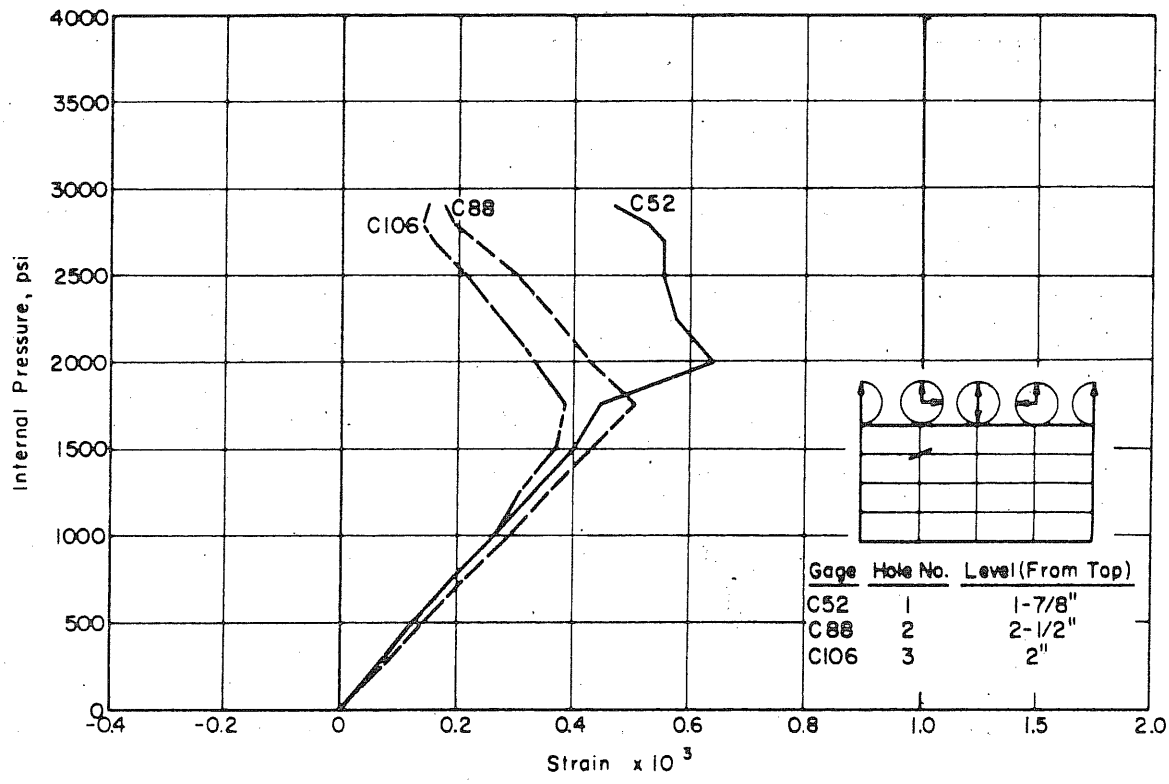

FIG. B.12 (Continued) MEASURED STRAINS IN THE PENETRATIONS OF PV17

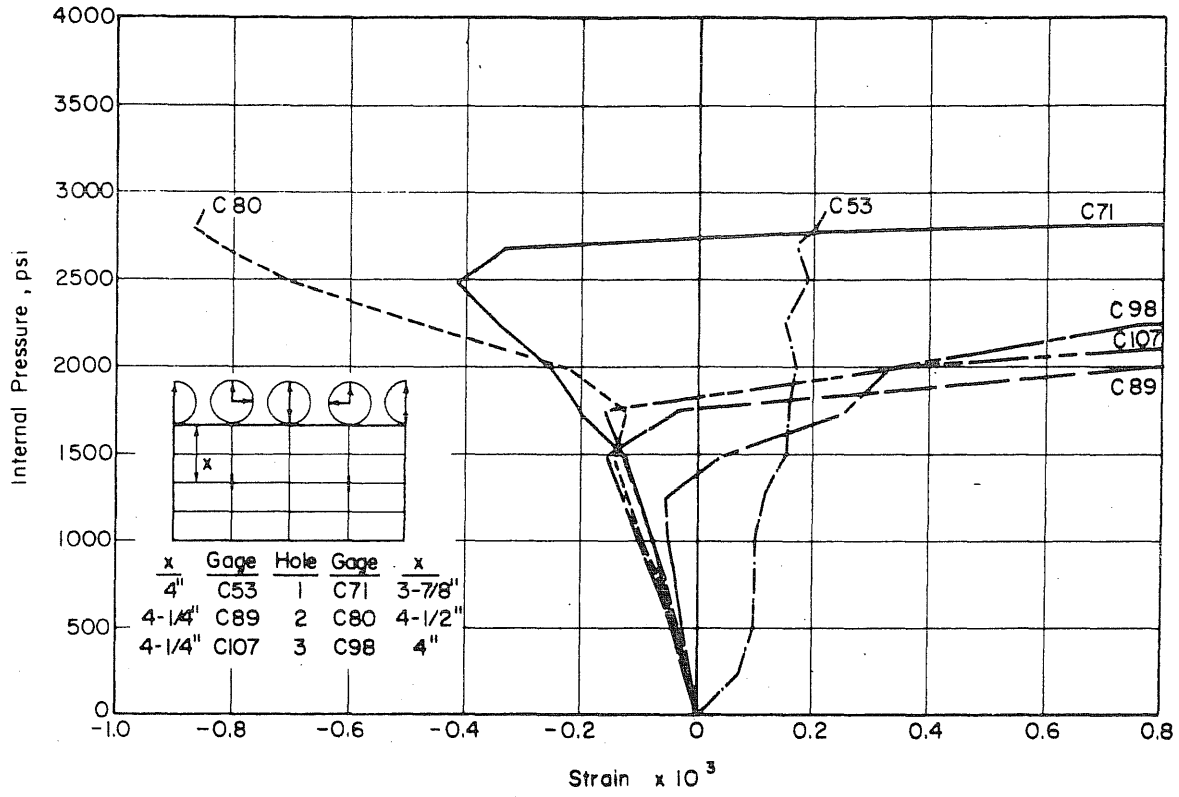

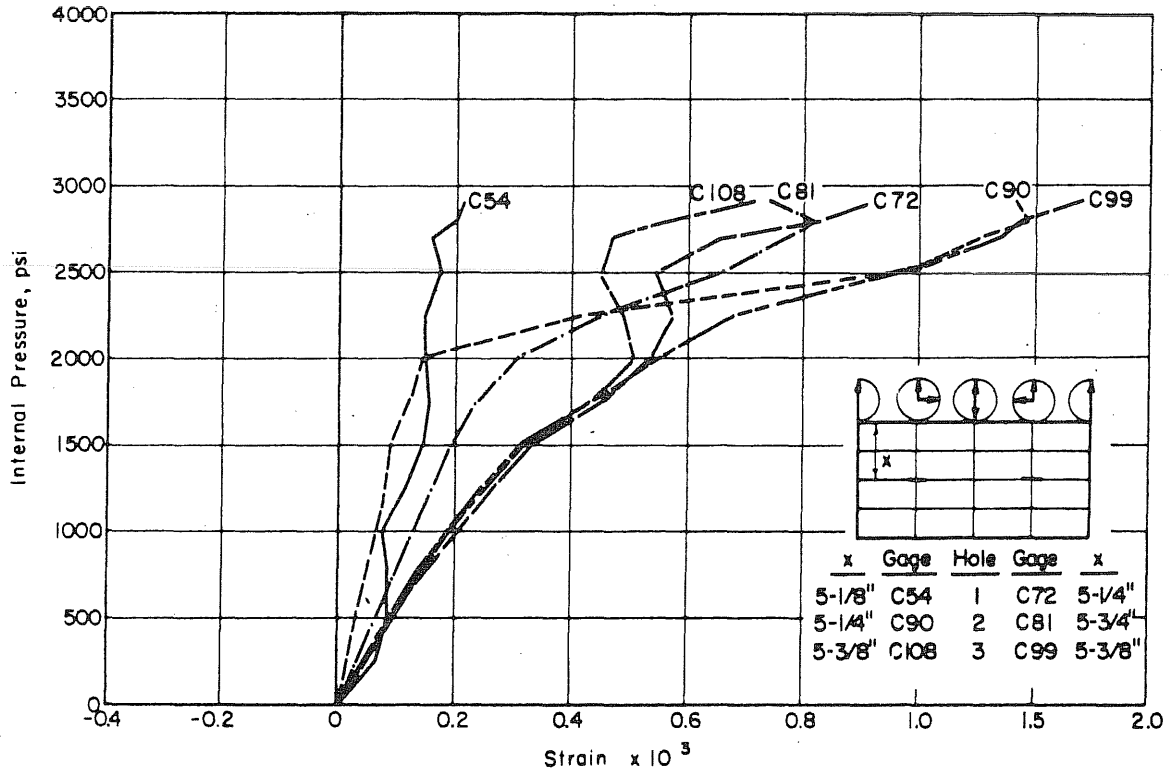

FIG. B.12 (Continued) MEASURED STRAINS IN THE PENETRATIONS OF PV17

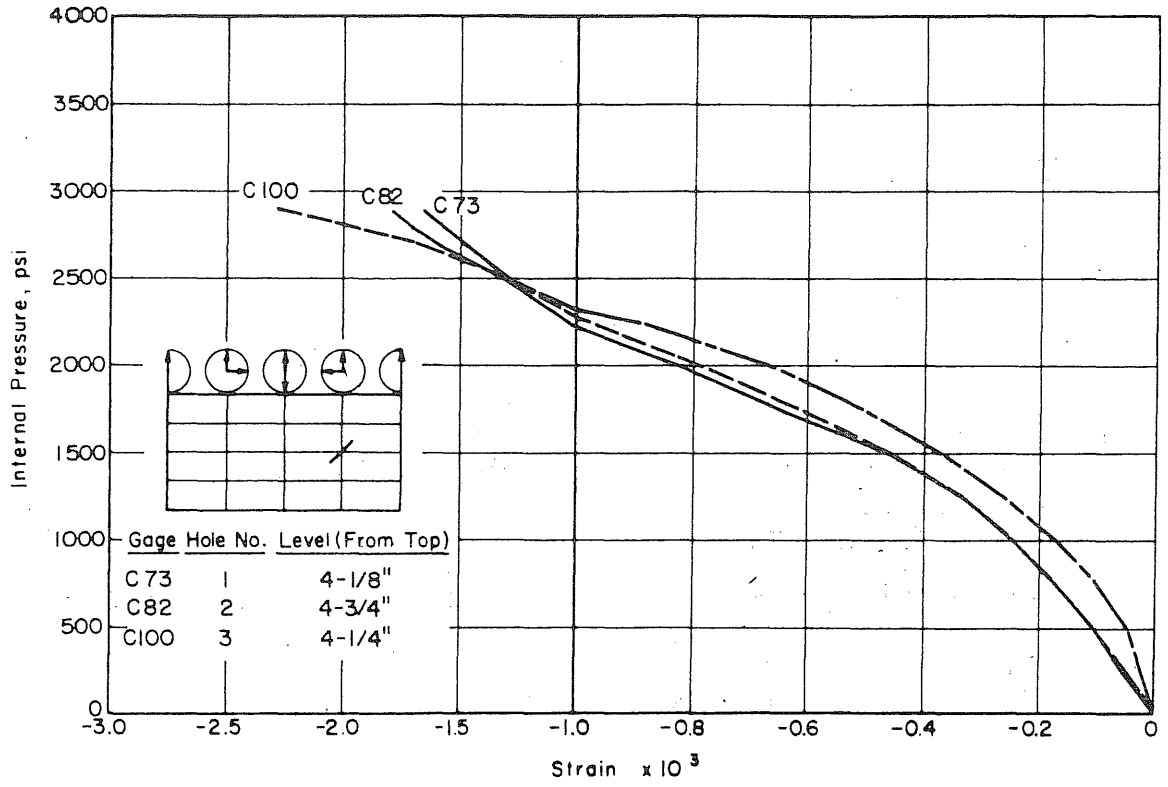

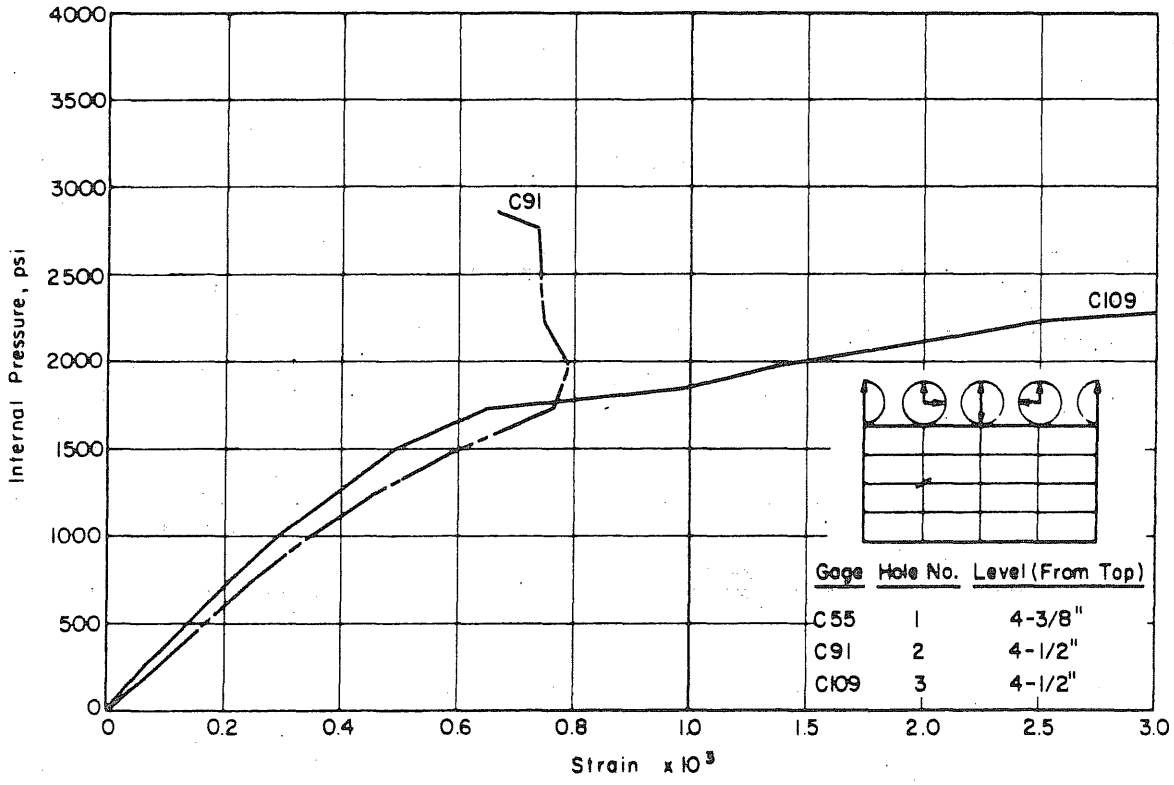

FIG. B.12 (Continued) MEASURED STRAINS IN THE PENETRATIONS OF PV17

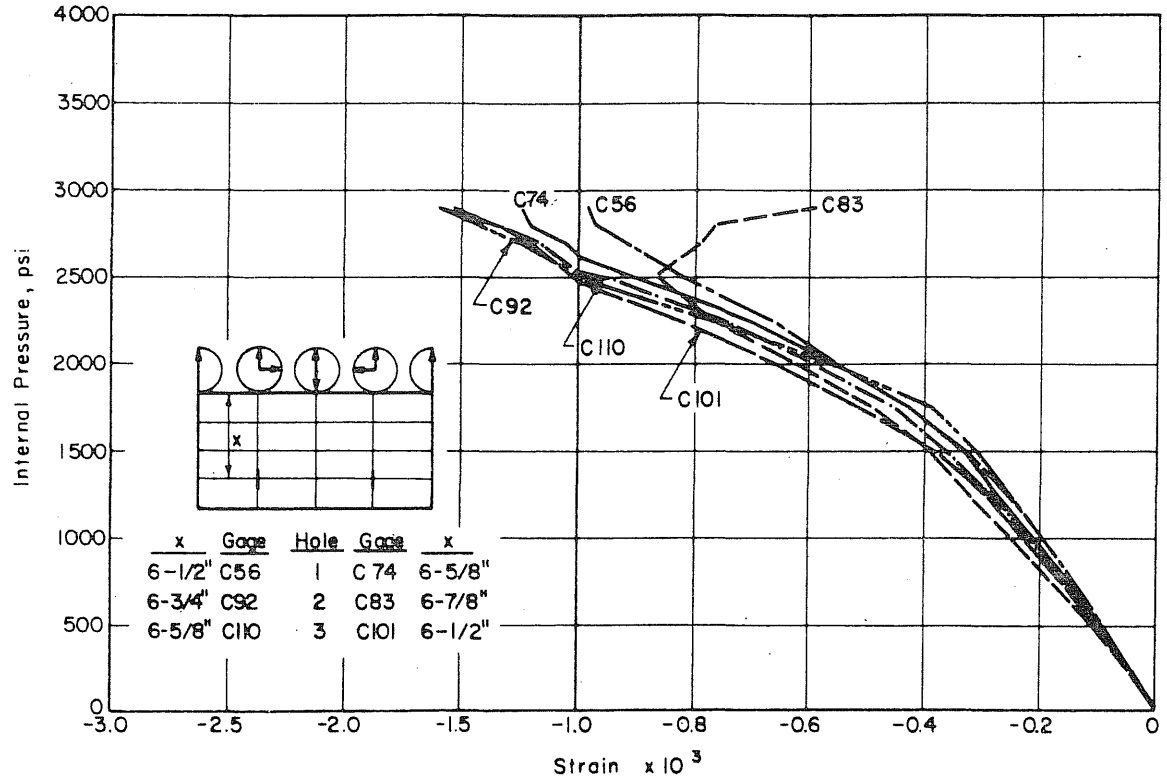

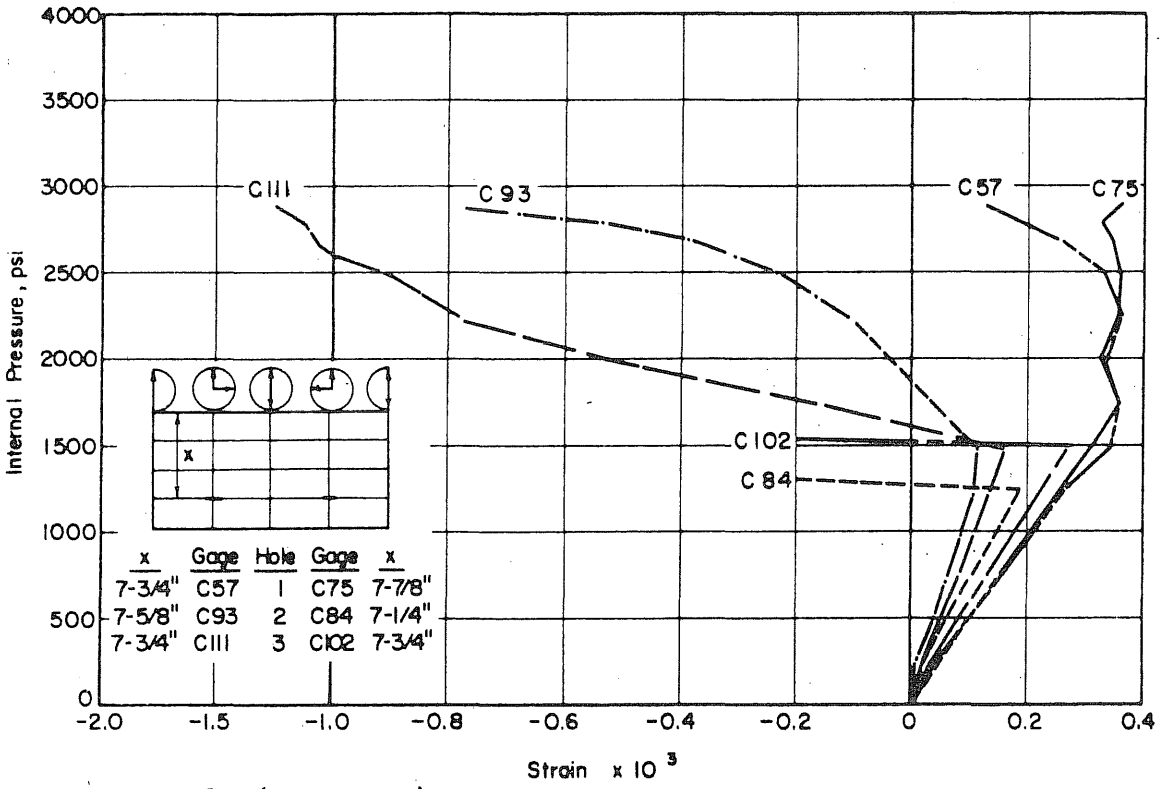

FIG. B.12 (Continued) MEASURED STRAINS IN THE PENETRATIONS OF PV17

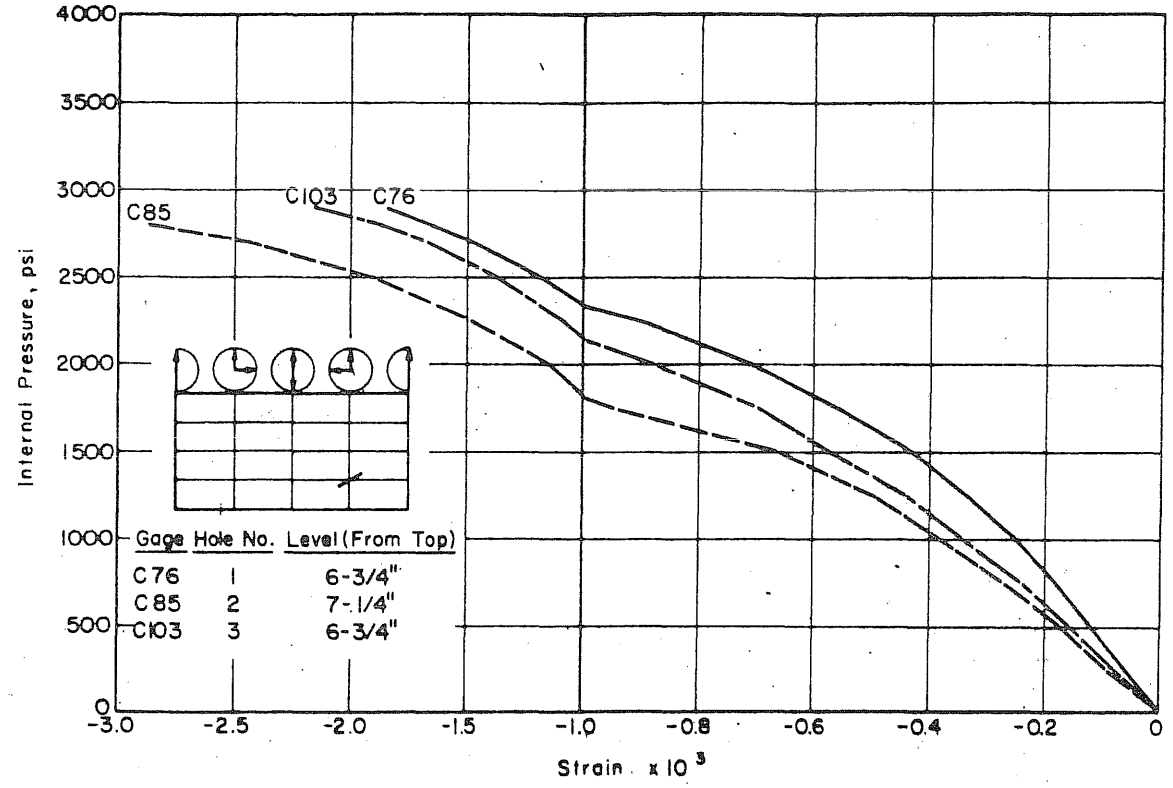

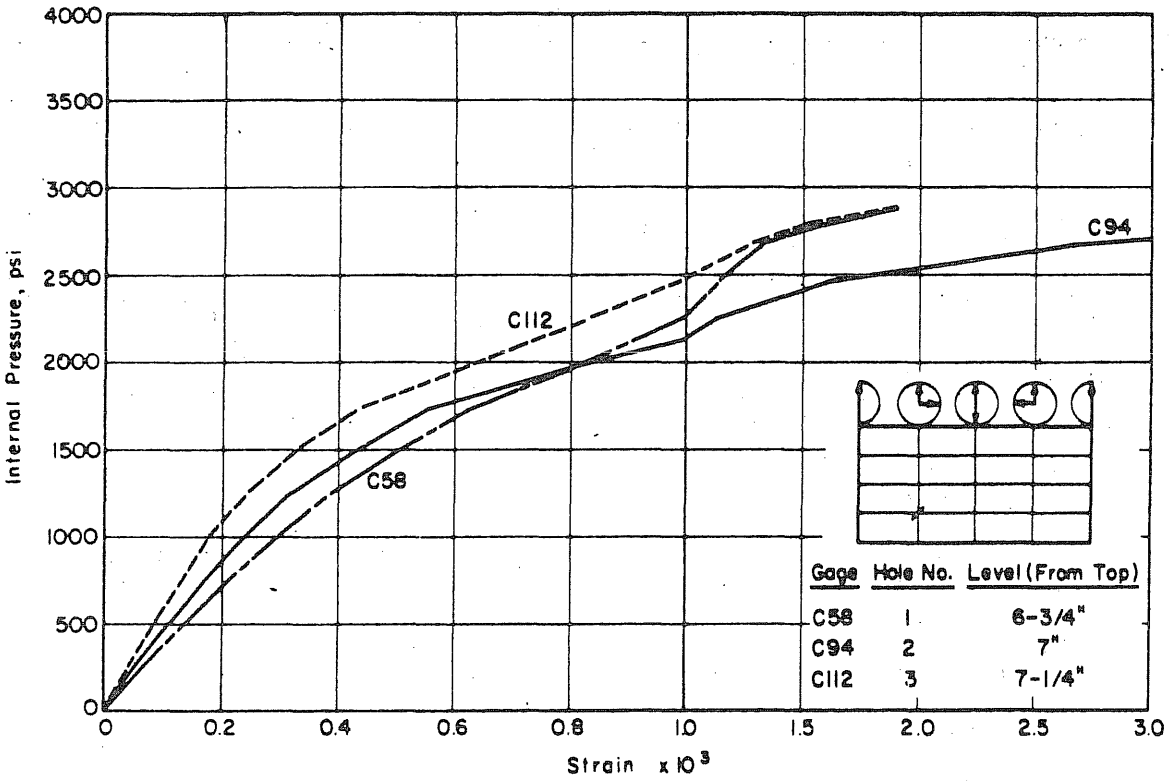

FIG. B.12 (Continued) MEASURED STRAINS IN THE PENETRATIONS OF PV17

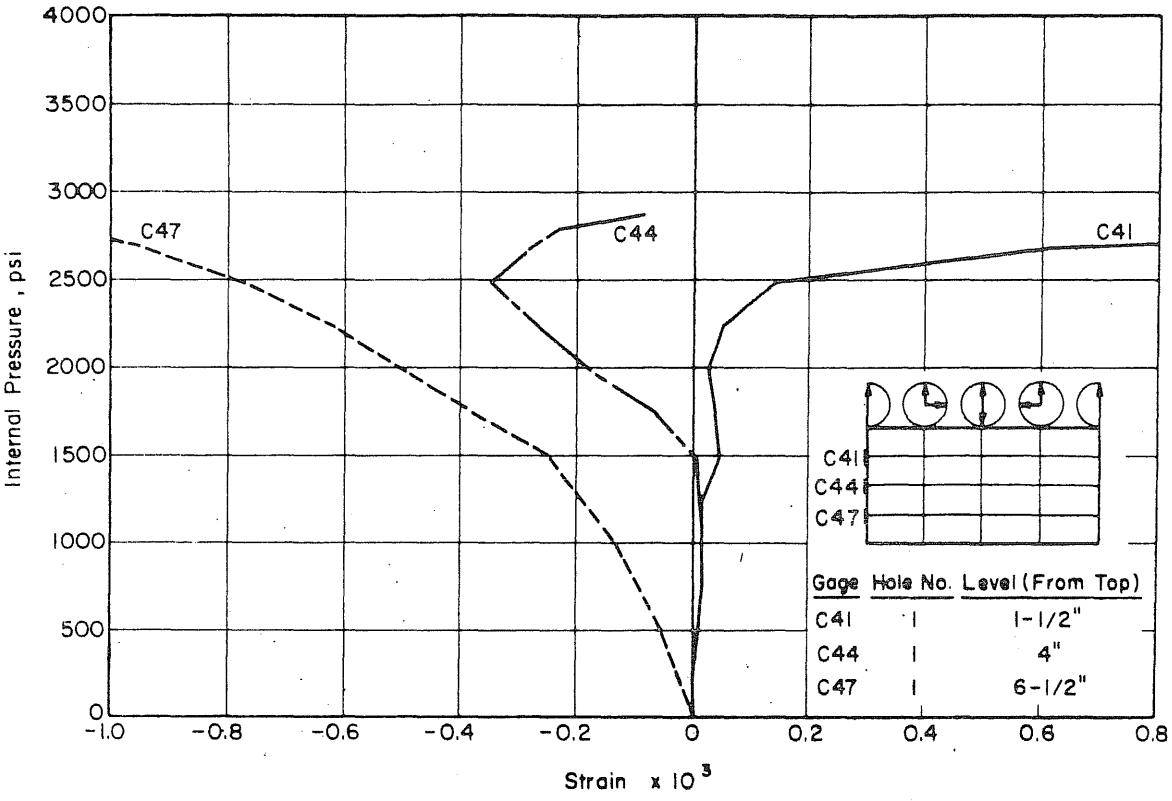

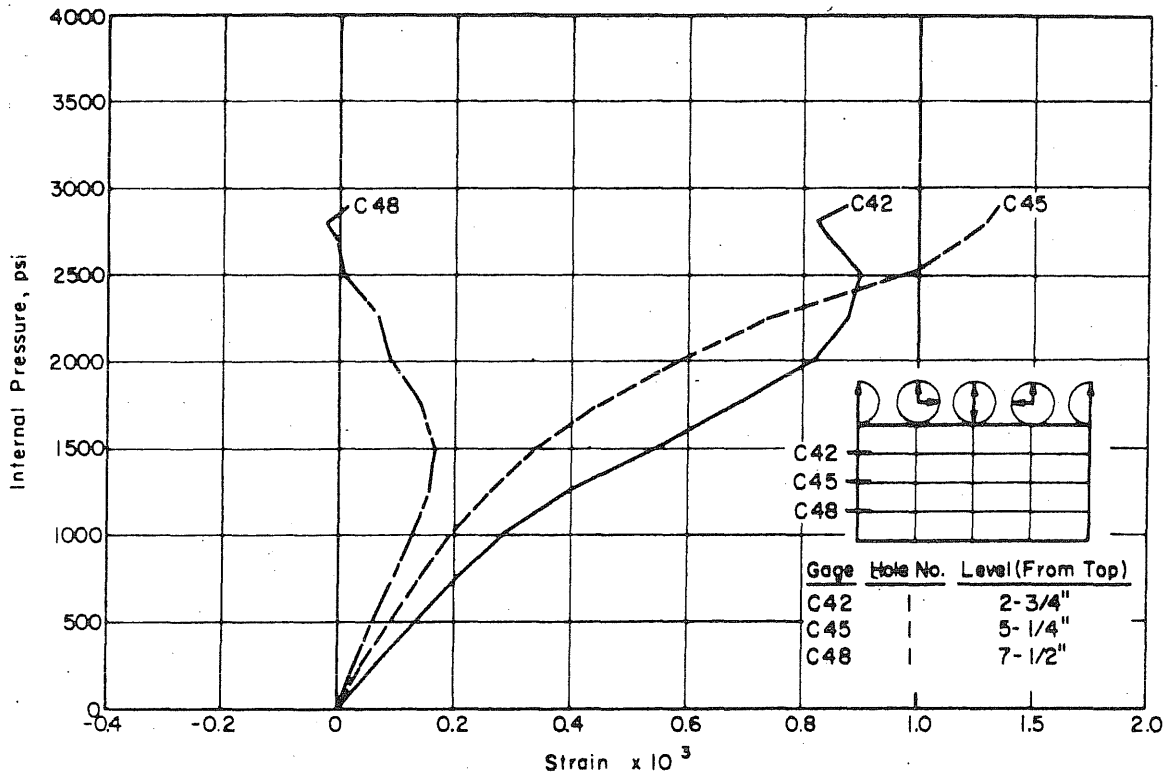

FIG. B.12 (Continued) MEASURED STRAINS IN THE PENETRATIONS OF PV17

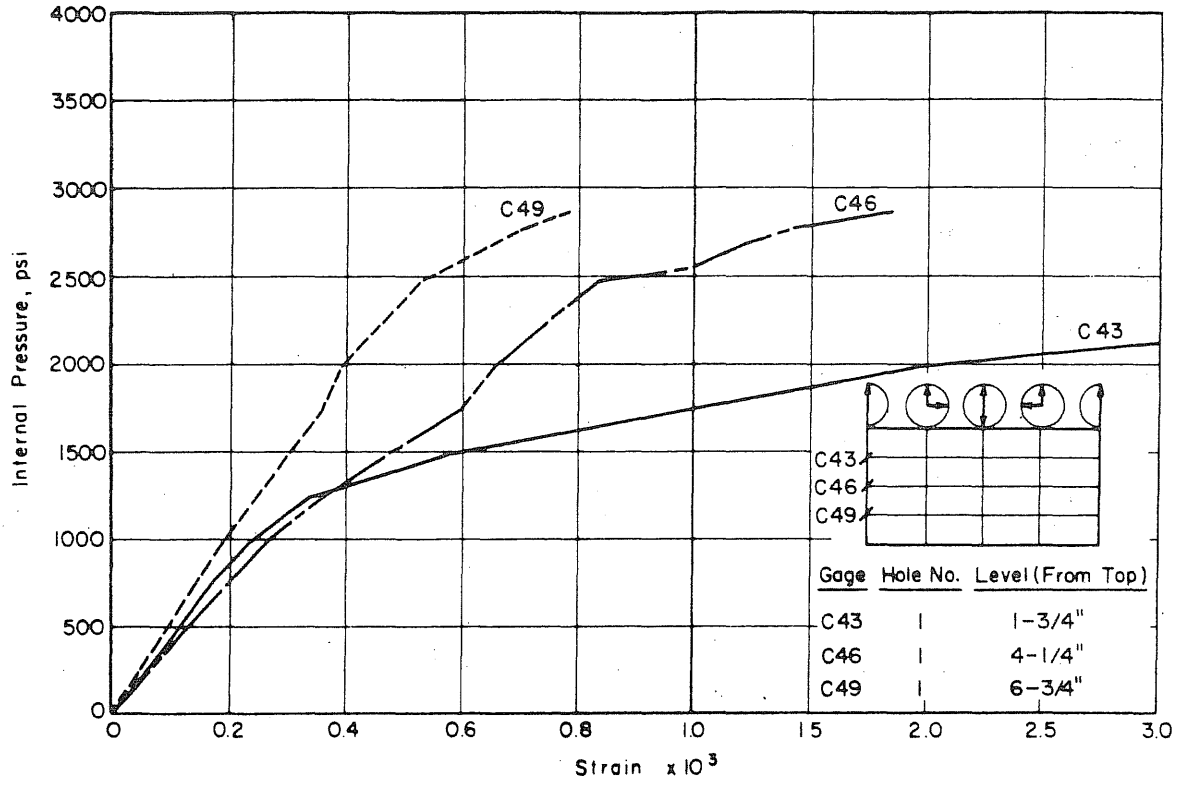

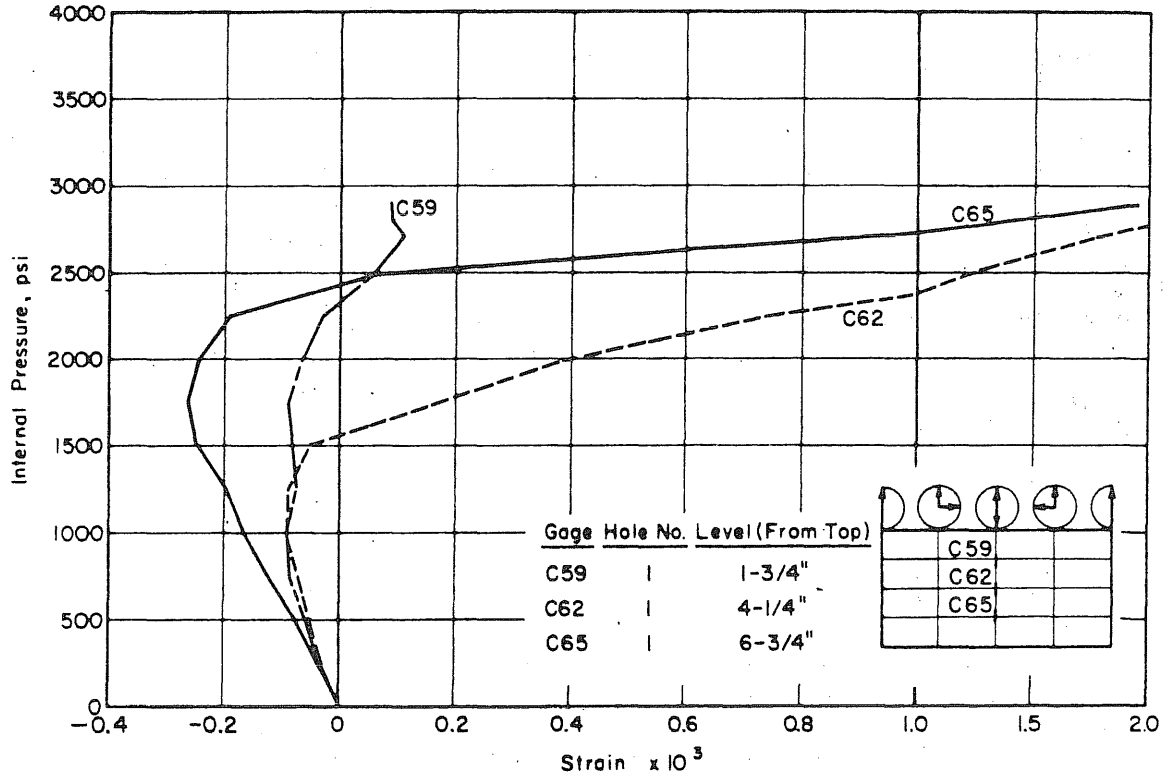

FIG. B.12 (Continued) MEASURED STRAINS IN THE PENETRATIONS OF PV17

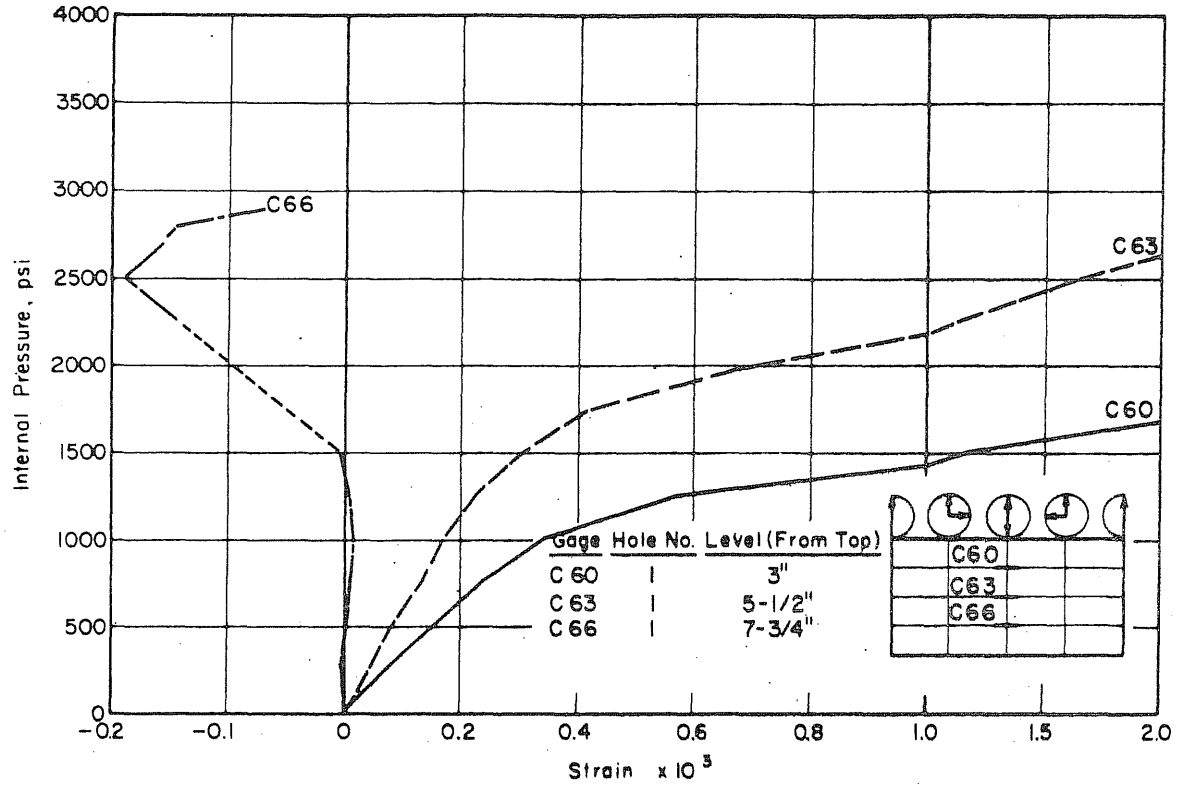

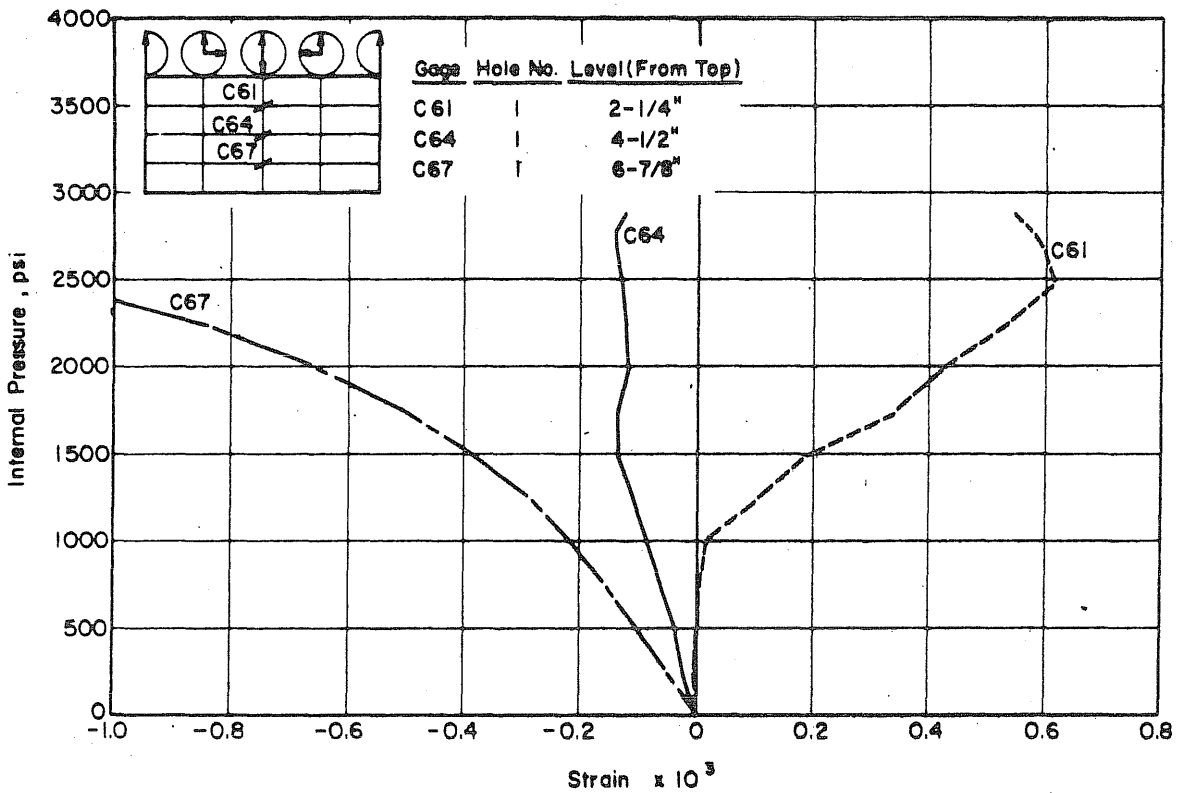

FIG. B.12 (Continued) MEASURED STRAINS IN THE PENETRATIONS OF PV17

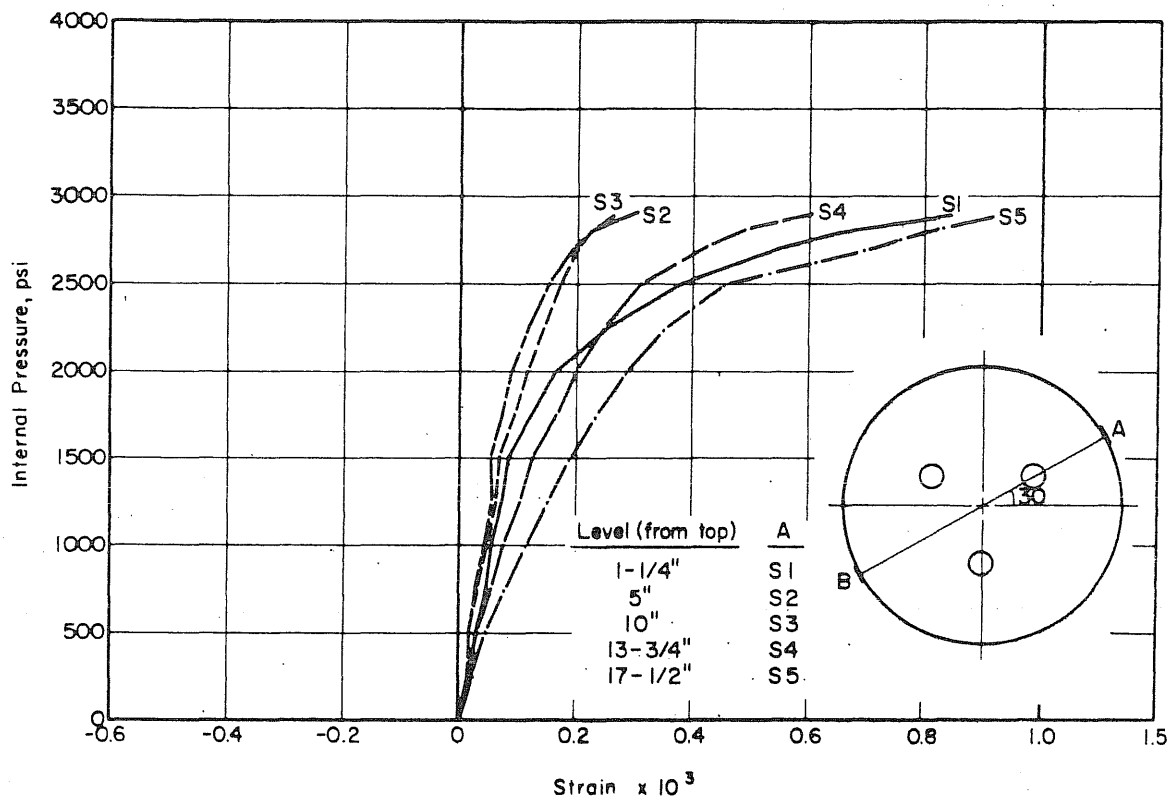

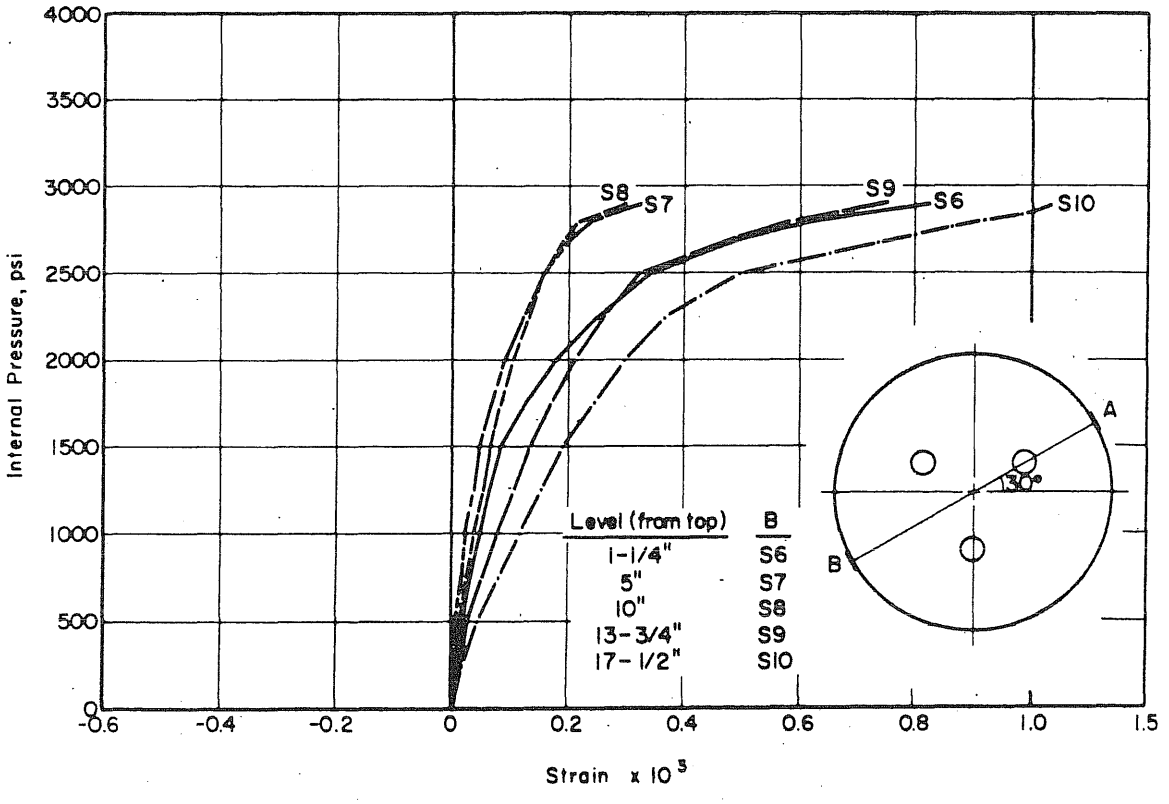

FIG. B.13 MEASURED STRAINS IN THE CIRCUMFERENTIAL PRESTRESSING WIRE OF PV17

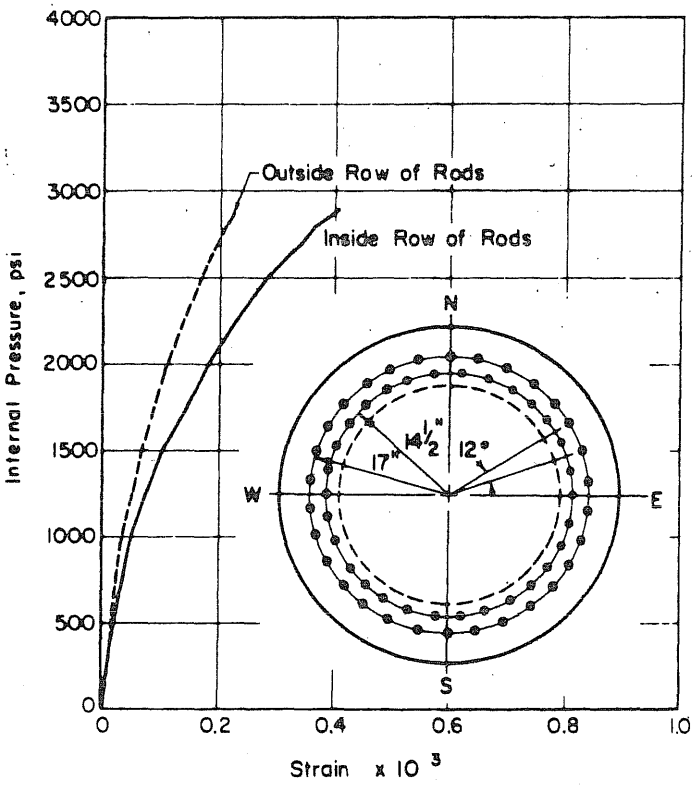

FIG. B.14 MEASURED STRAINS IN THE LONGITUDINAL PRESTRESSING RODS OF PV17

B.4 Test Vessel PV18

This vessel was tested hydraulically with the option to switch to pneumatic pressure if the leakage exceeded the capacity of the oil pump. At 3000 psi internal pressure the vessel started to leak. The deflection was then as large as the deflection for vessel PV17 when it failed and failure was probably imminent. Instead of using gas pressure to attempt to fail the vessel, the test was aborted. The end slab was later cut to reveal the geometry and extent of the inclined crack.

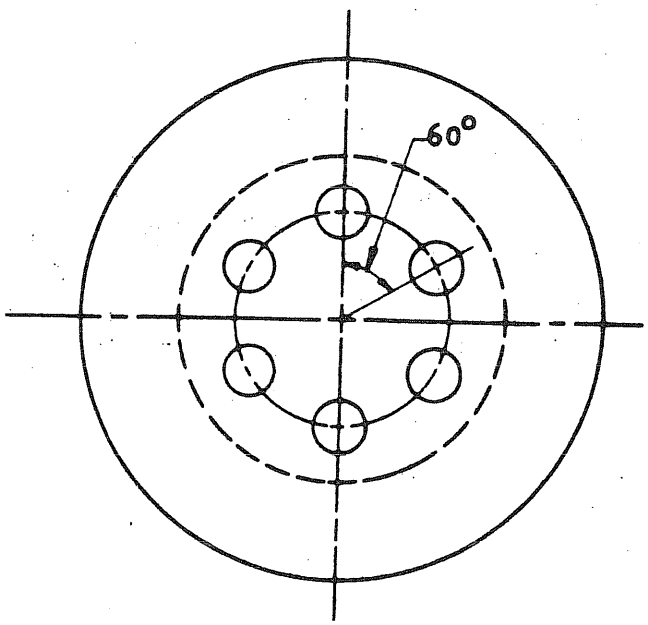

FIG. B.15 VESSEL PV18 WITH SIX 4-in. PENETRATIONS ON AN 8-in. RADIUS

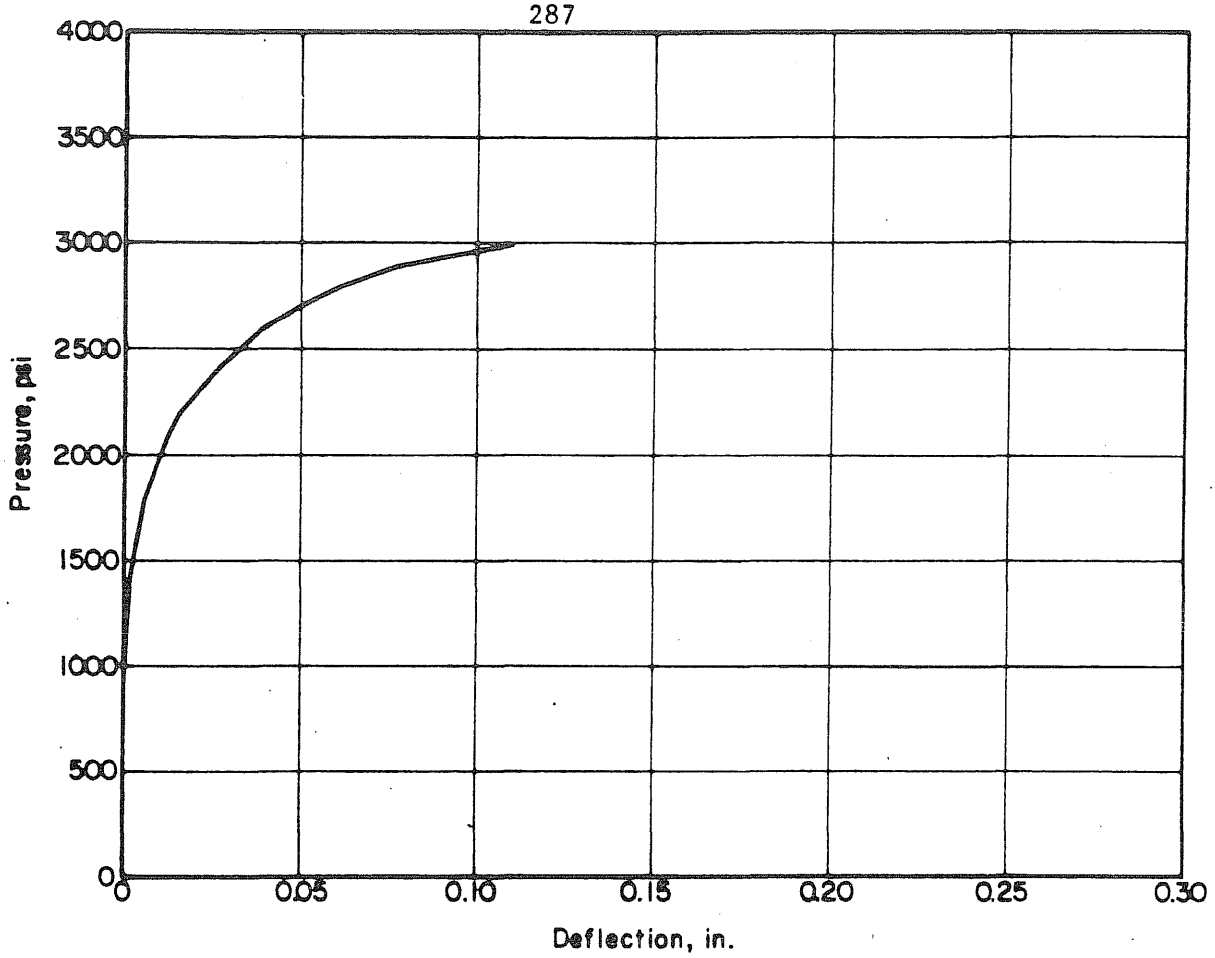

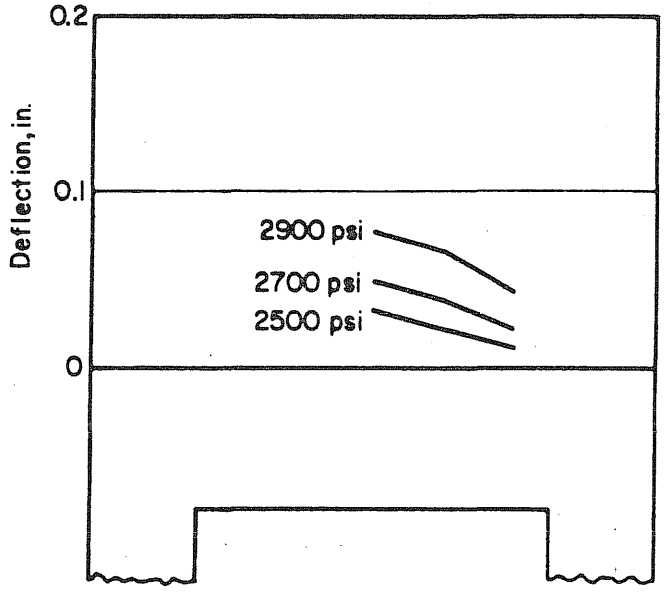

FIG. B.16 MEASURED DEFLECTION PROFILES AND DEFLECTION AT THE CENTER OF THE END SLAB OF PV18

Outside Face

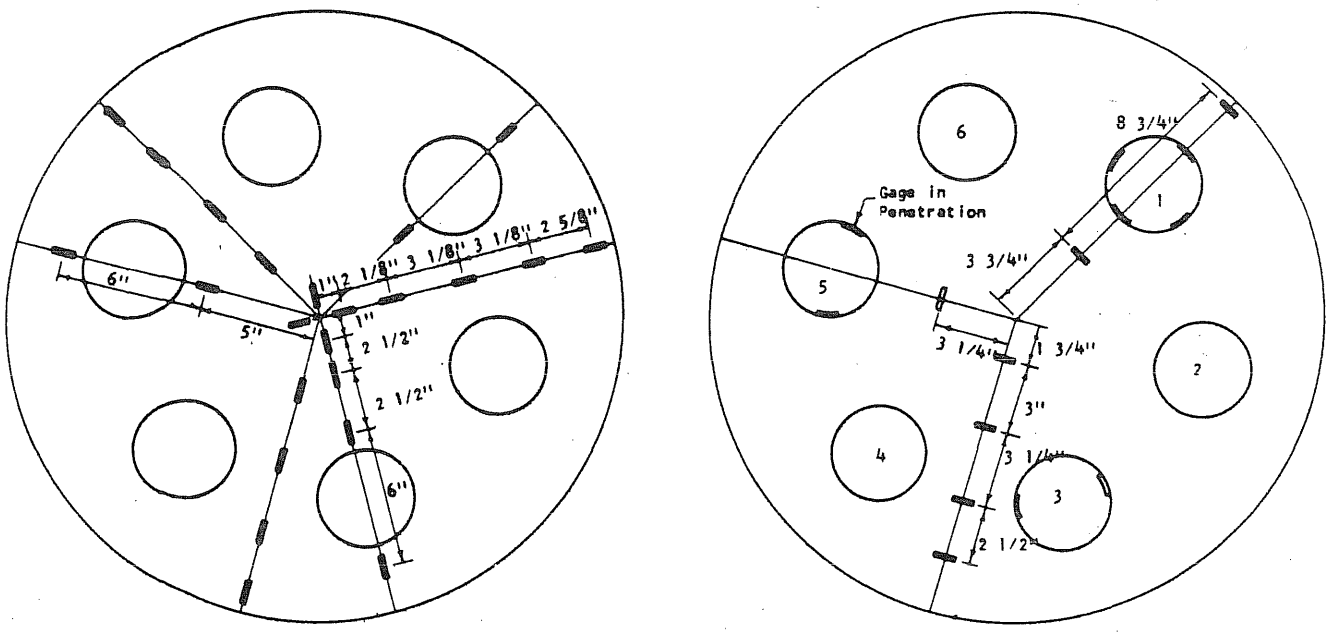

Inside Face

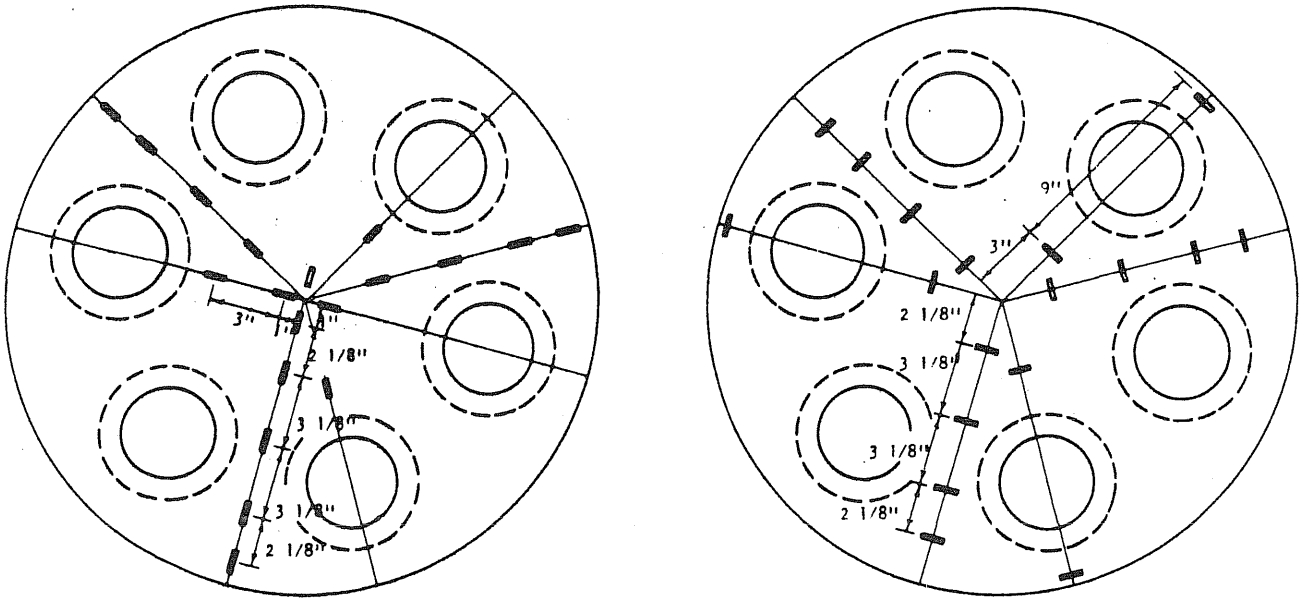

FIG. B.17 STRAIN GAGE LOCATION ON PV18

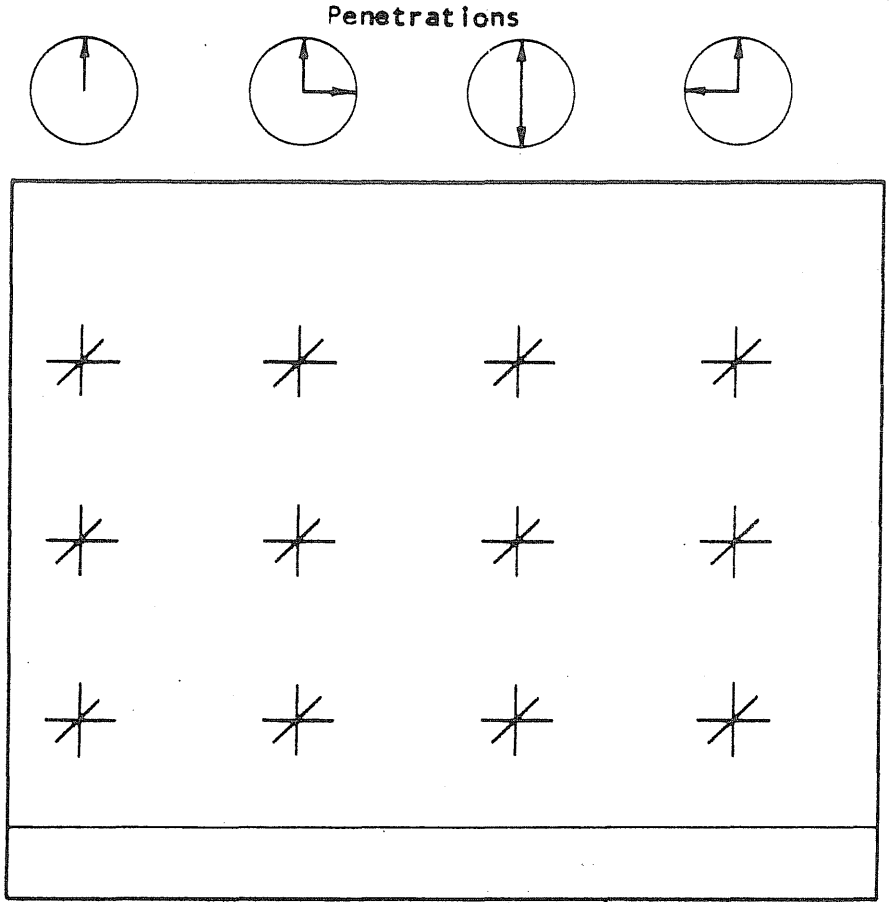

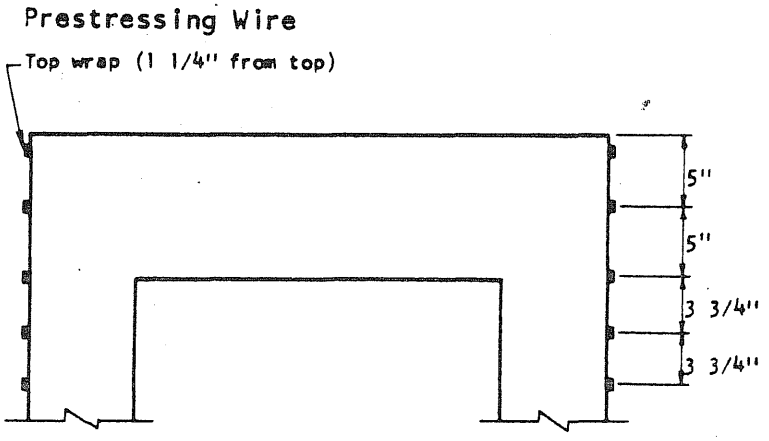

FIG. B.17 (Continued) STRAIN GAGE LOCATION ON PV18

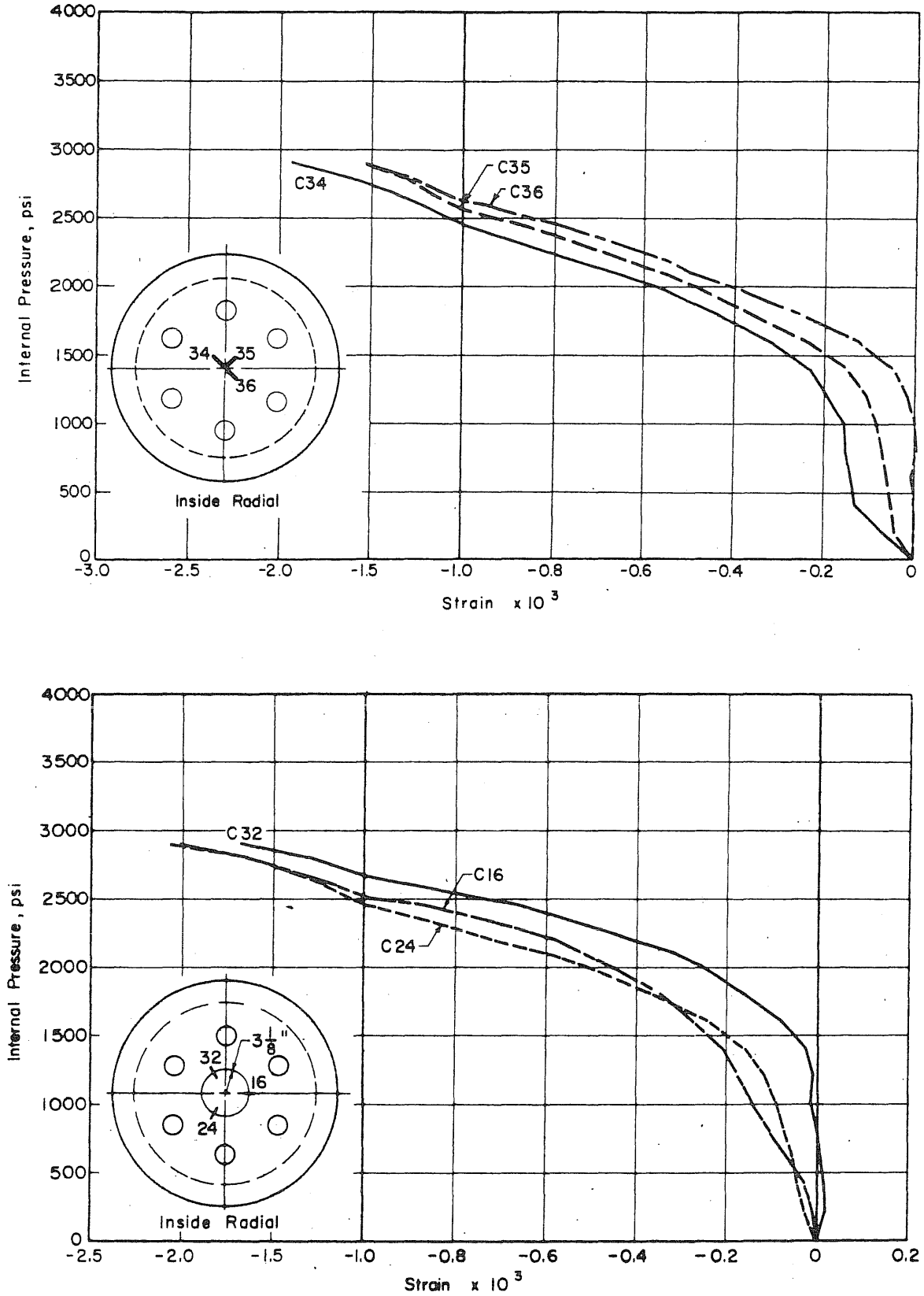

FIG. B.18 MEASURED STRAINS ON THE INSIDE FACE OF THE SLAB OF PV18

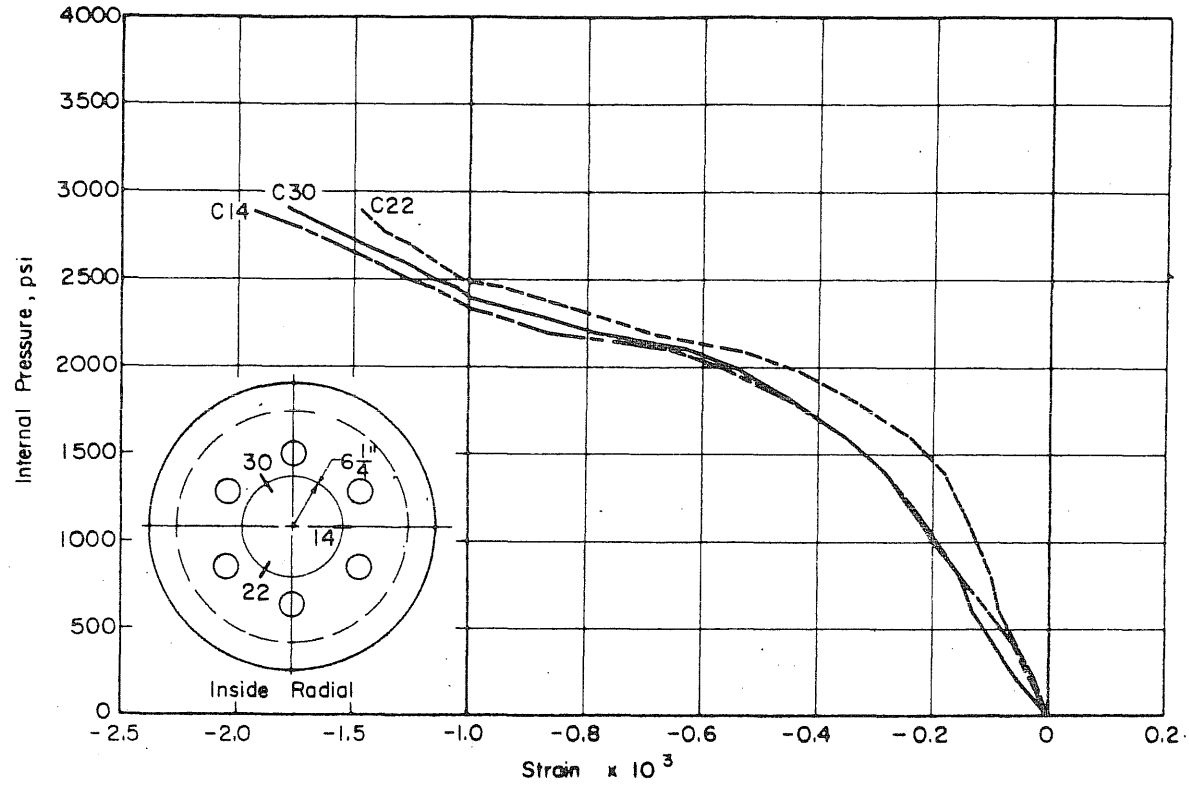

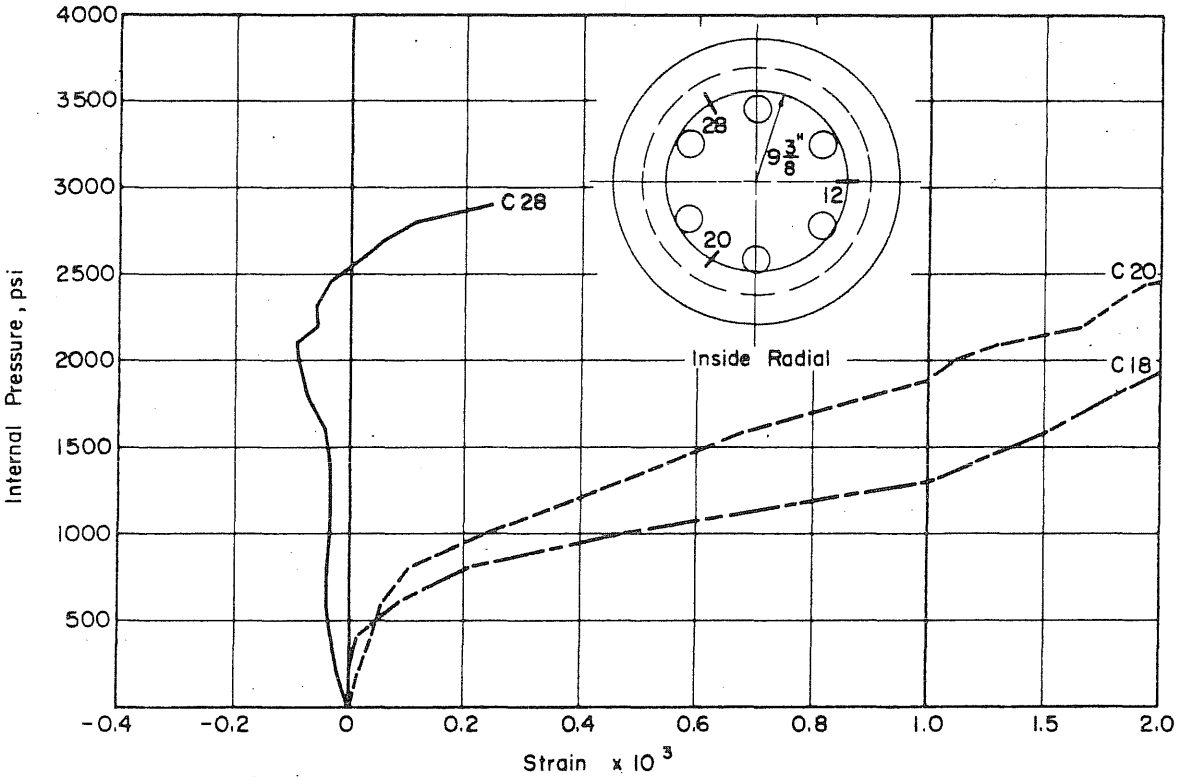

FIG. B.18 (Continued) MEASURED STRAINS ON THE INSIDE FACE OF THE SLAB OF PV18

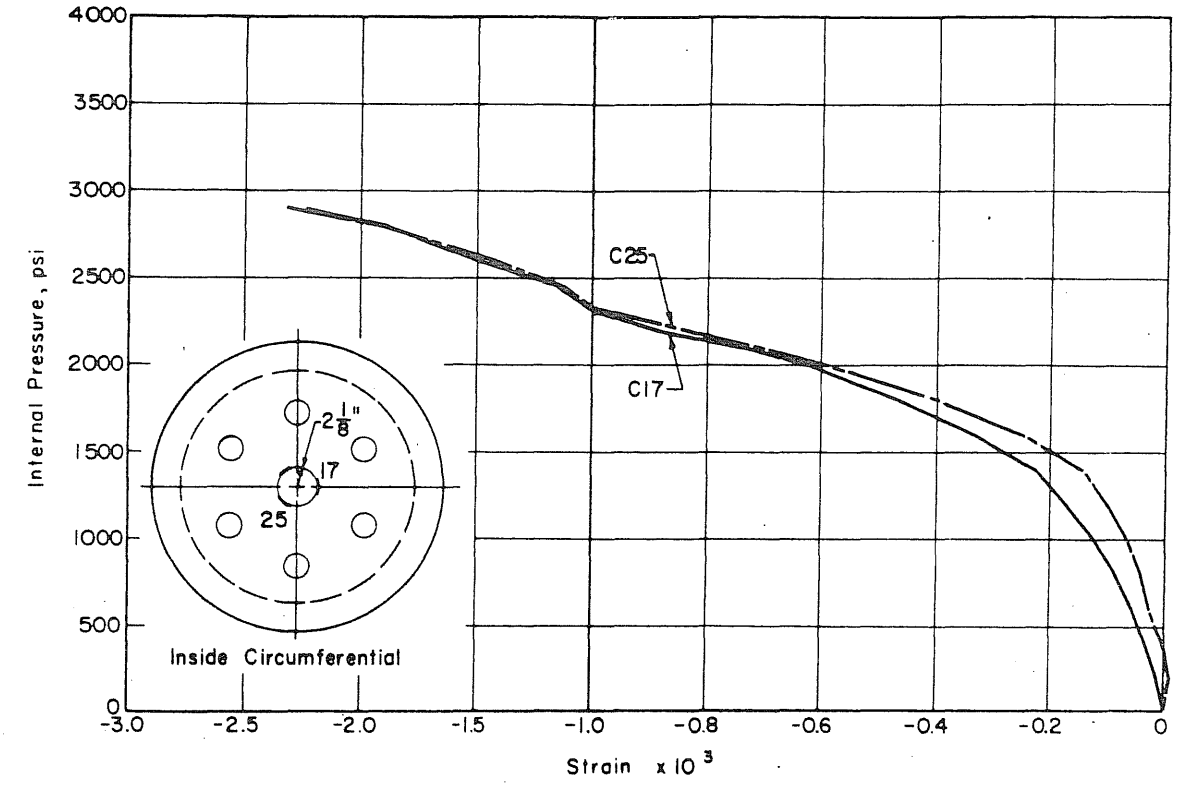

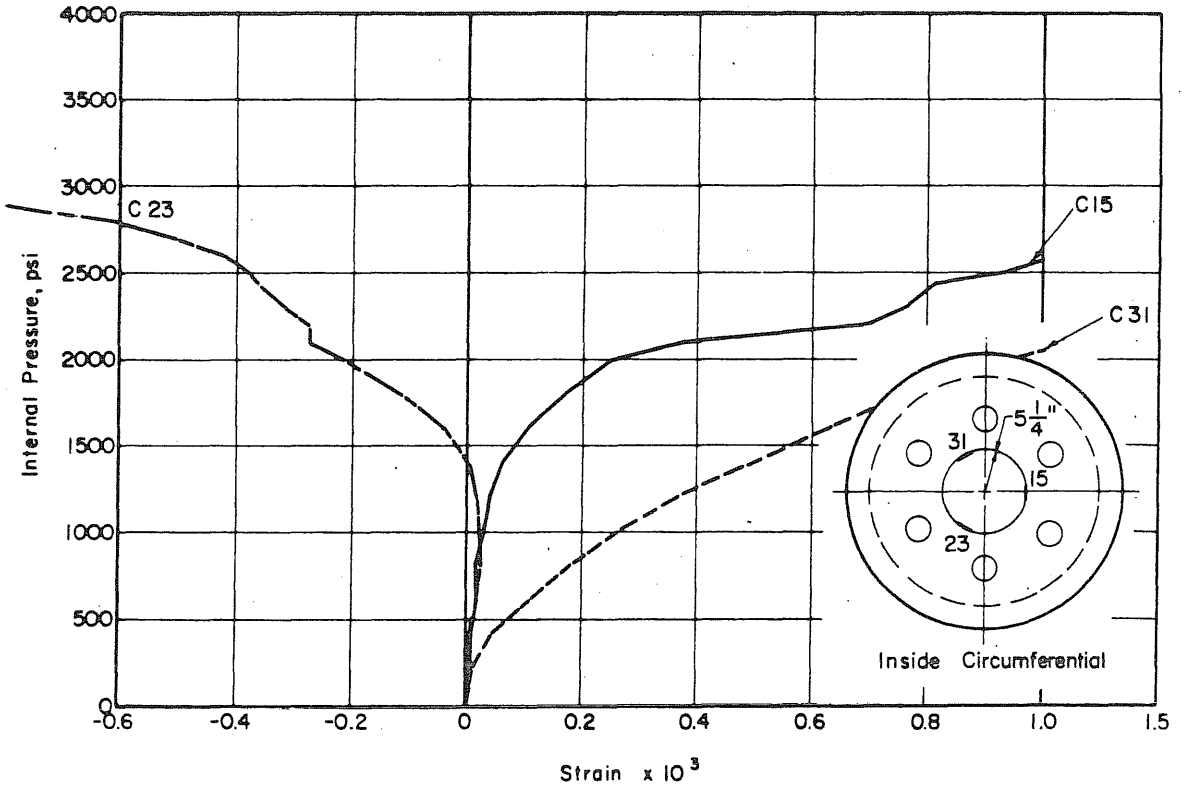

FIG. B.18 (Continued) MEASURED STRAINS ON THE INSIDE OF THE SLAB OF PV18

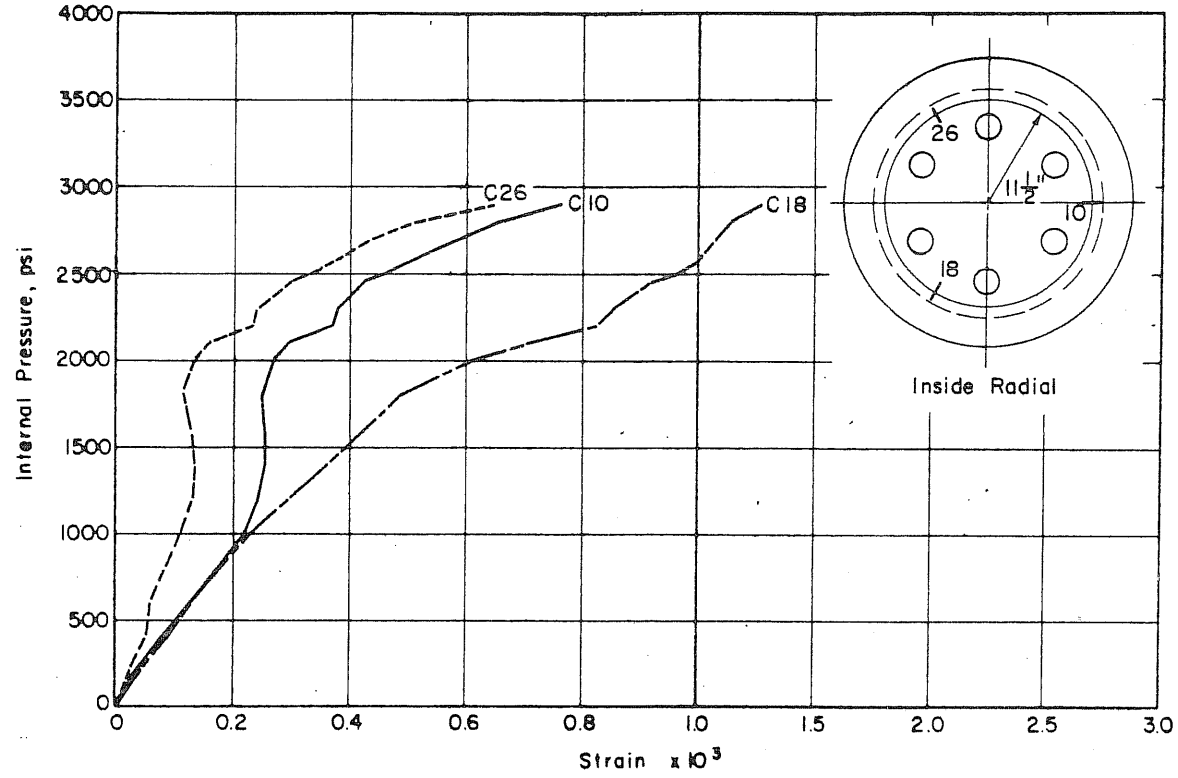

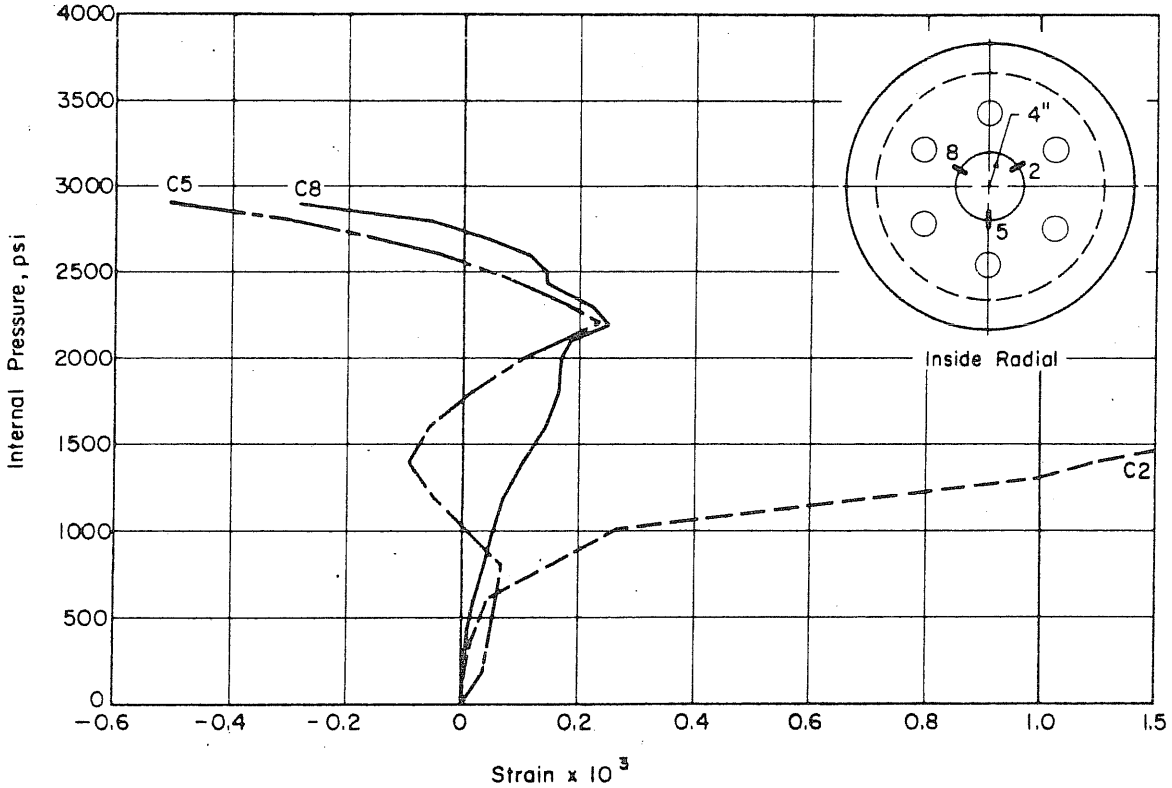

FIG. B.18 (Continued) MEASURED STRAINS ON THE INSIDE FACE OF THE SLAB OF PV18

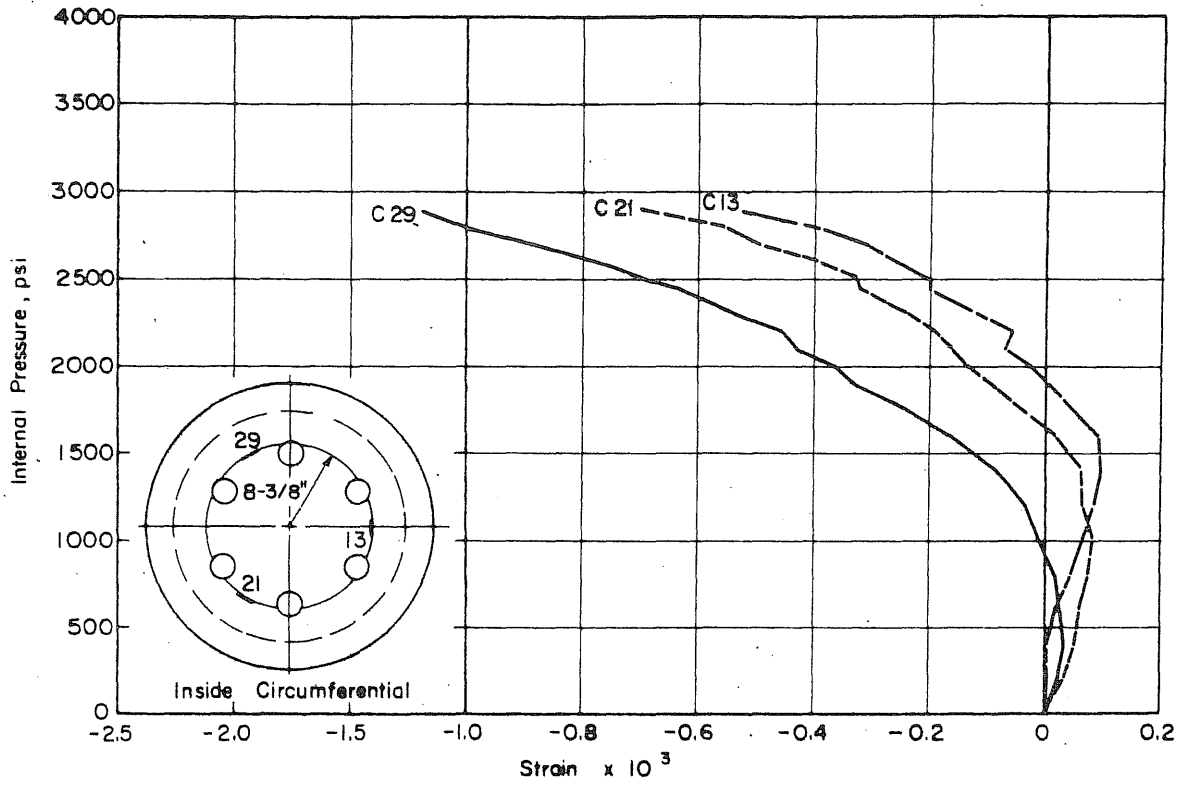

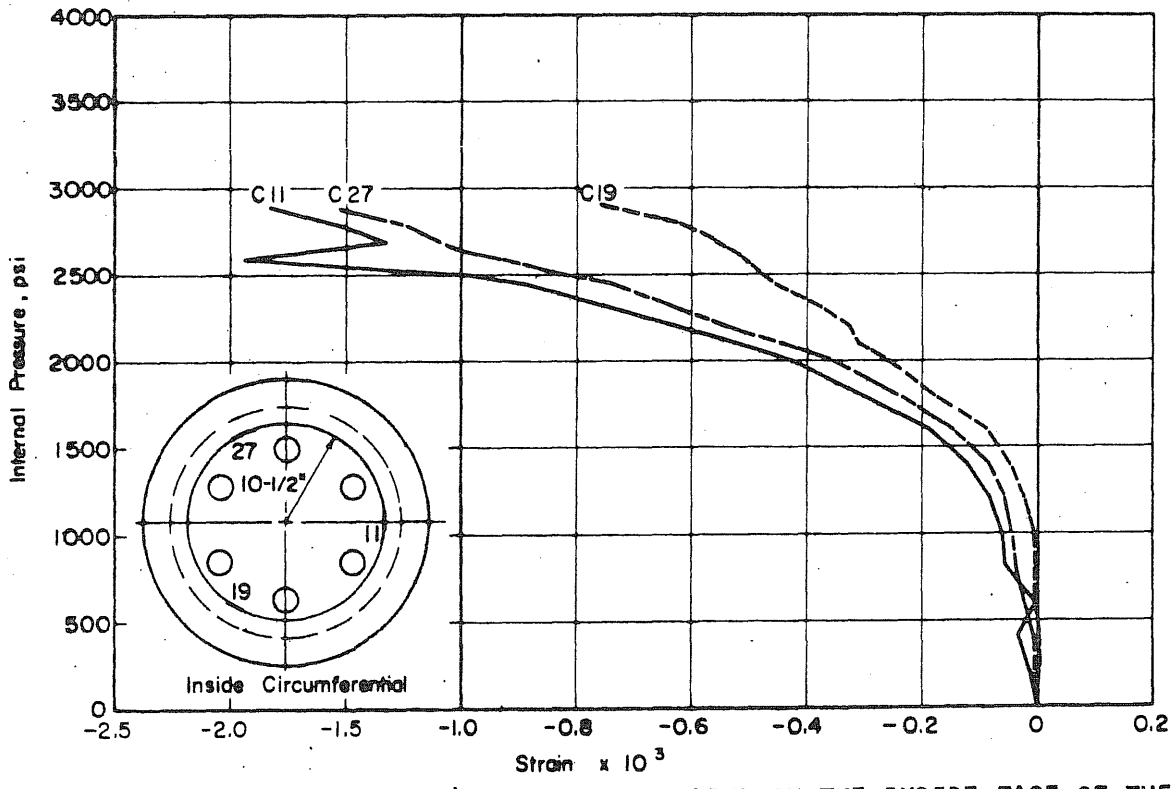

FIG. B.18 (Continued) MEASURED STRAINS ON THE INSIDE FACE OF THE SLAB OF PV18

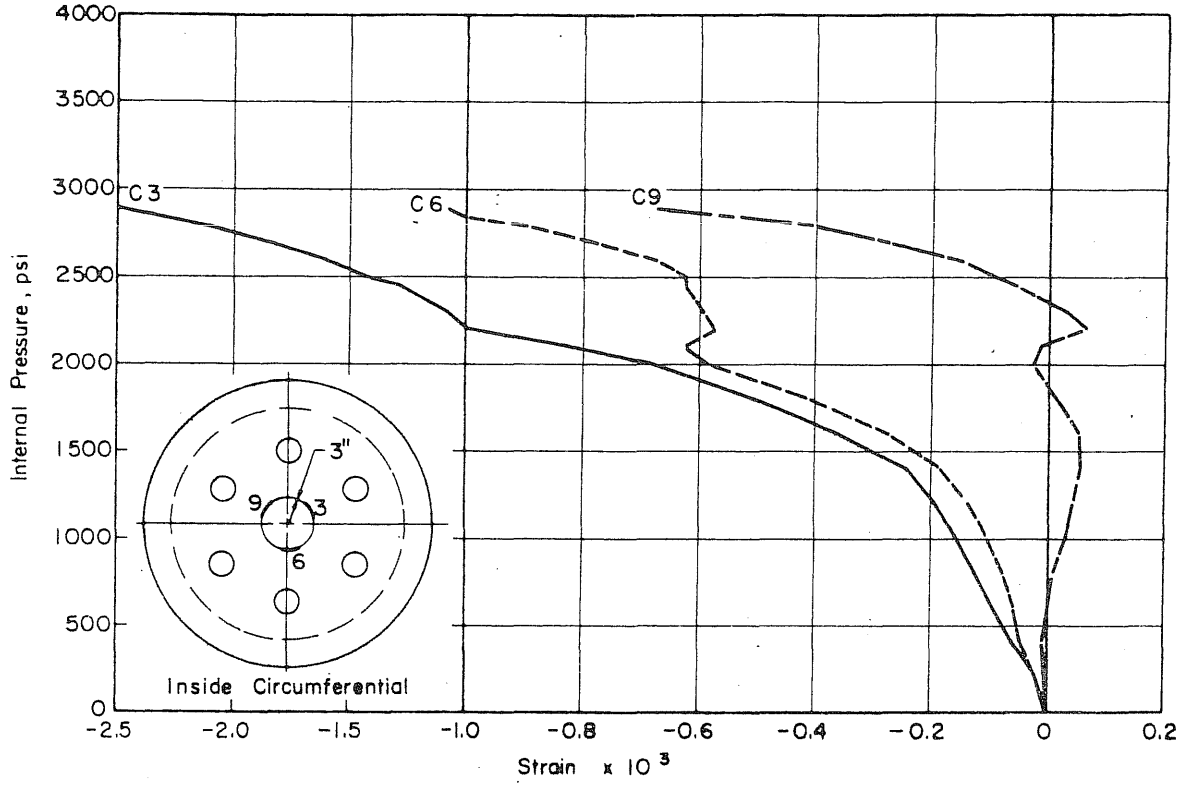

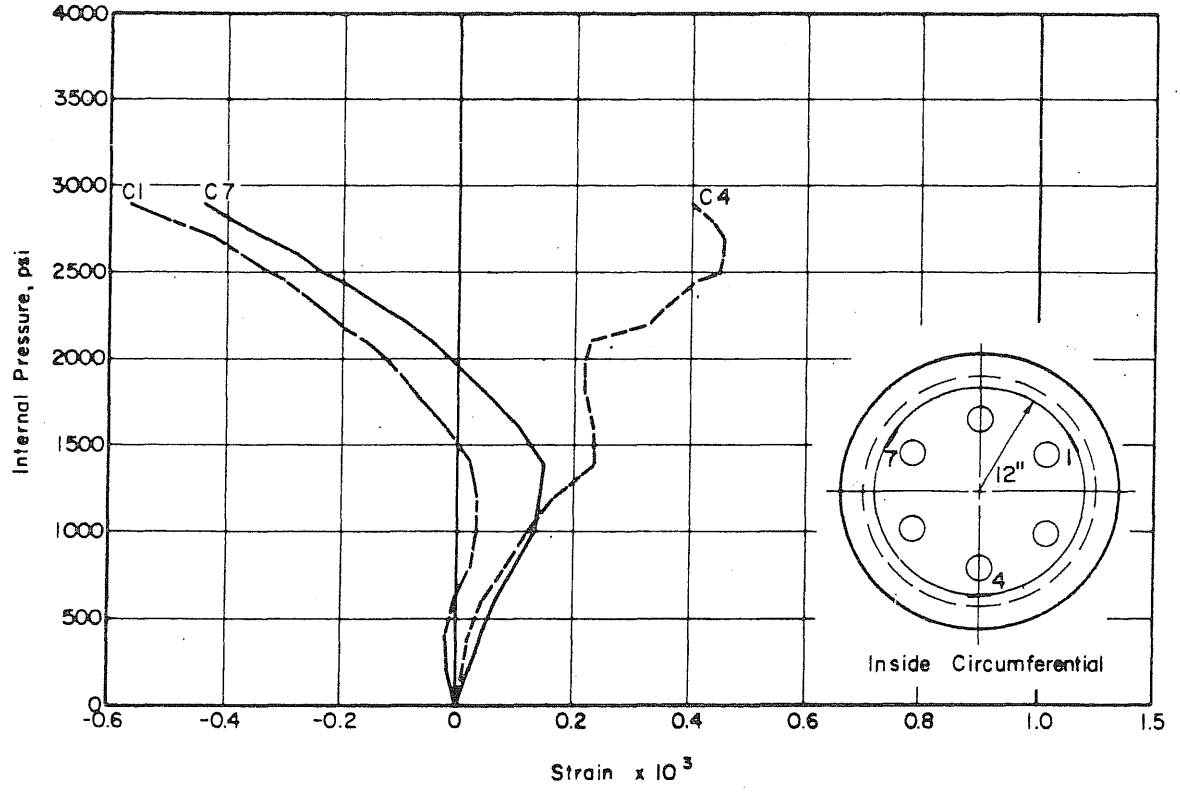

FIG. B.18 (Continued) MEASURED STRAINS ON THE INSIDE FACE OF THE SLAB OF PV18

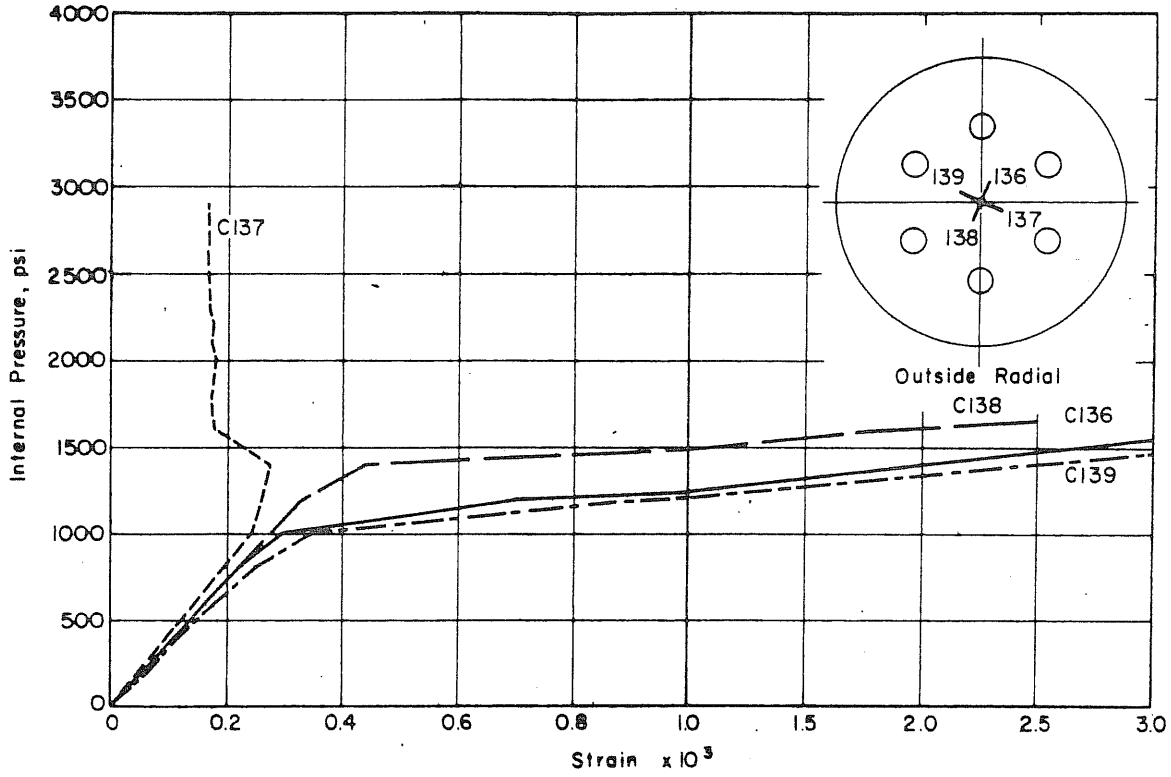

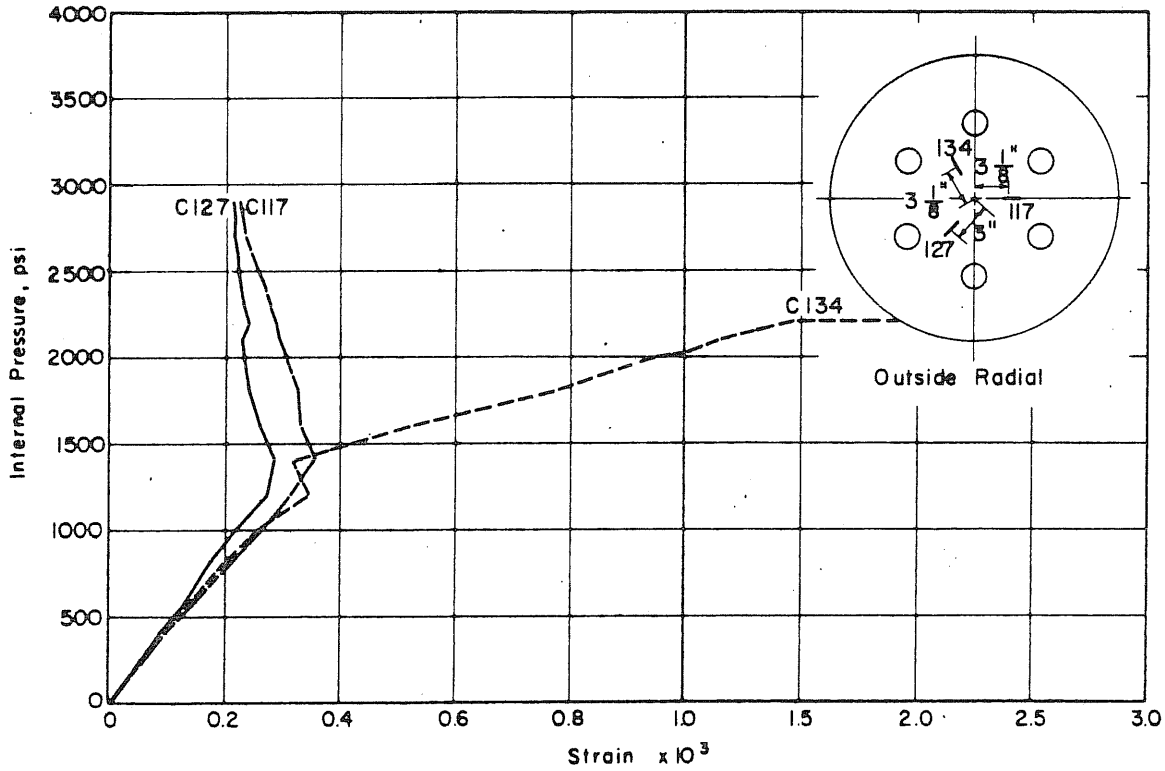

FIG. B.19 MEASURED STRAINS ON THE OUTSIDE FACE OF THE SLAB OF PV18

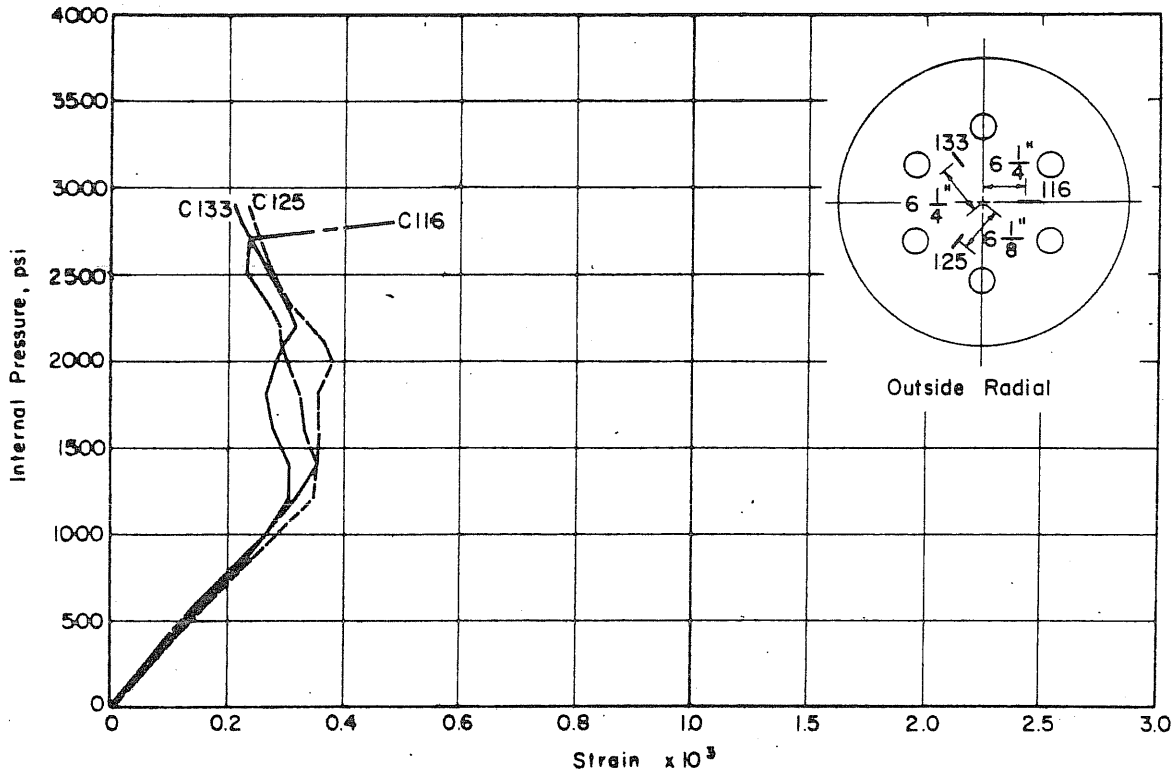

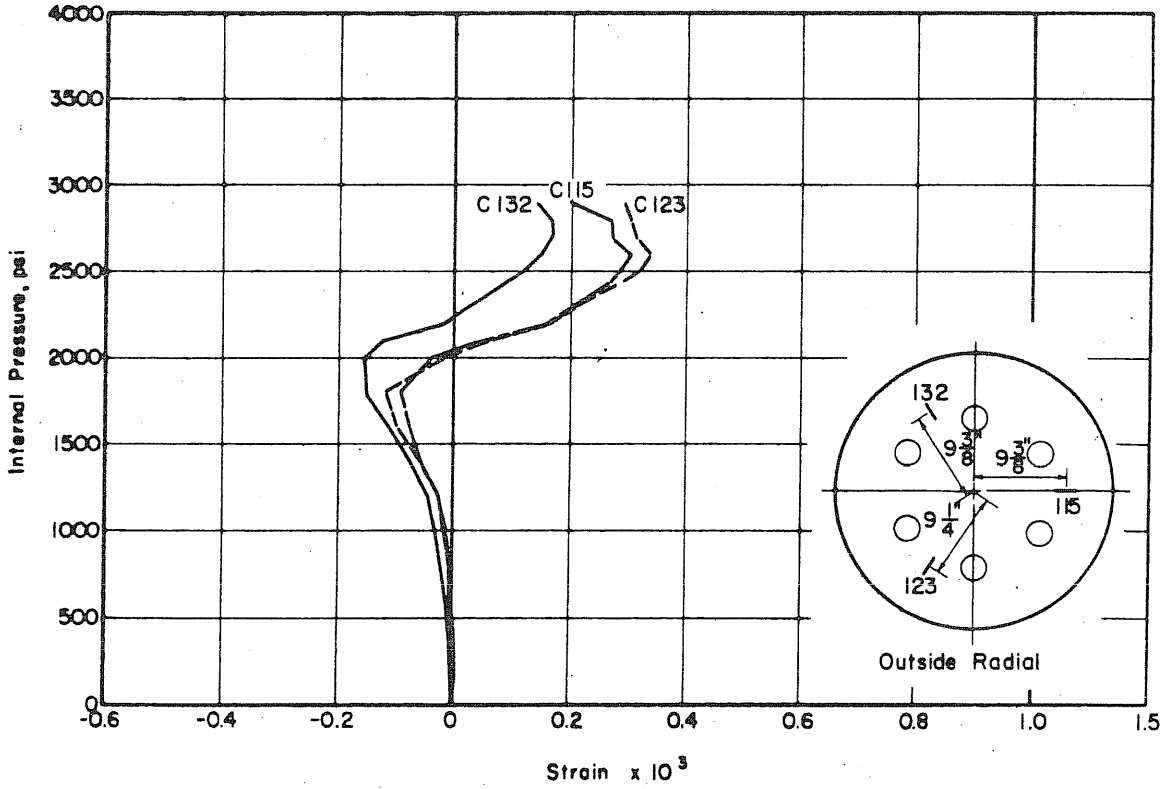

FIG. B.19 (Continued) MEASURED STRAINS ON THE OUTSIDE FACE OF THE SLAB OF PV18

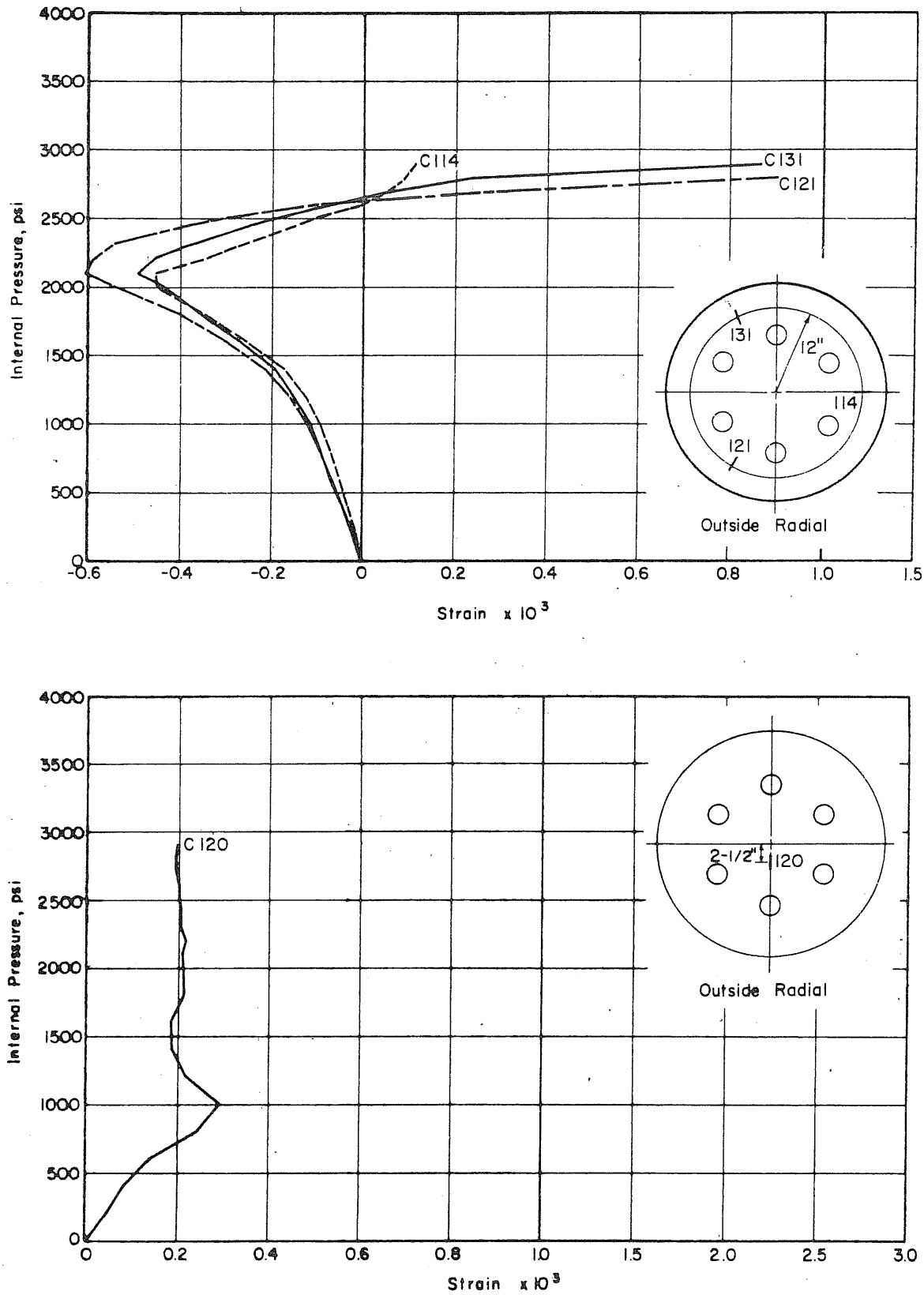

FIG. B.19 (Continued) MEASURED STRAINS ON THE OUTSIDE FACE OF THE SLAB OF PV18

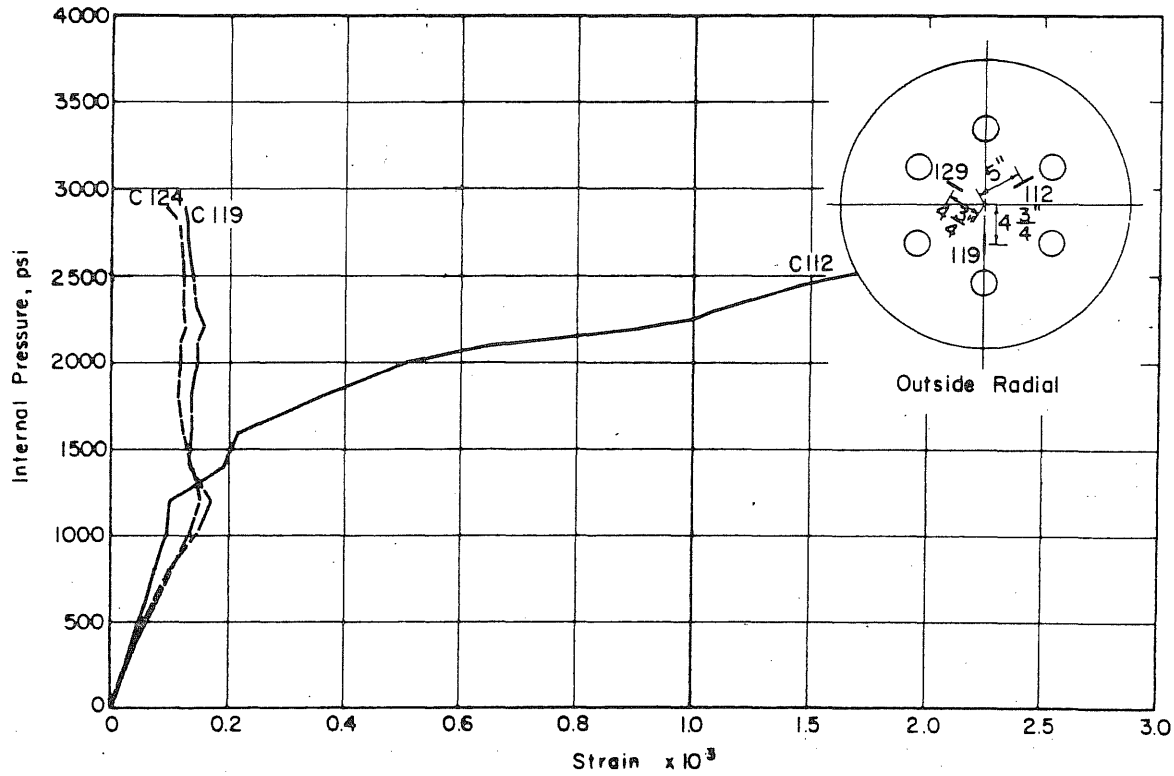

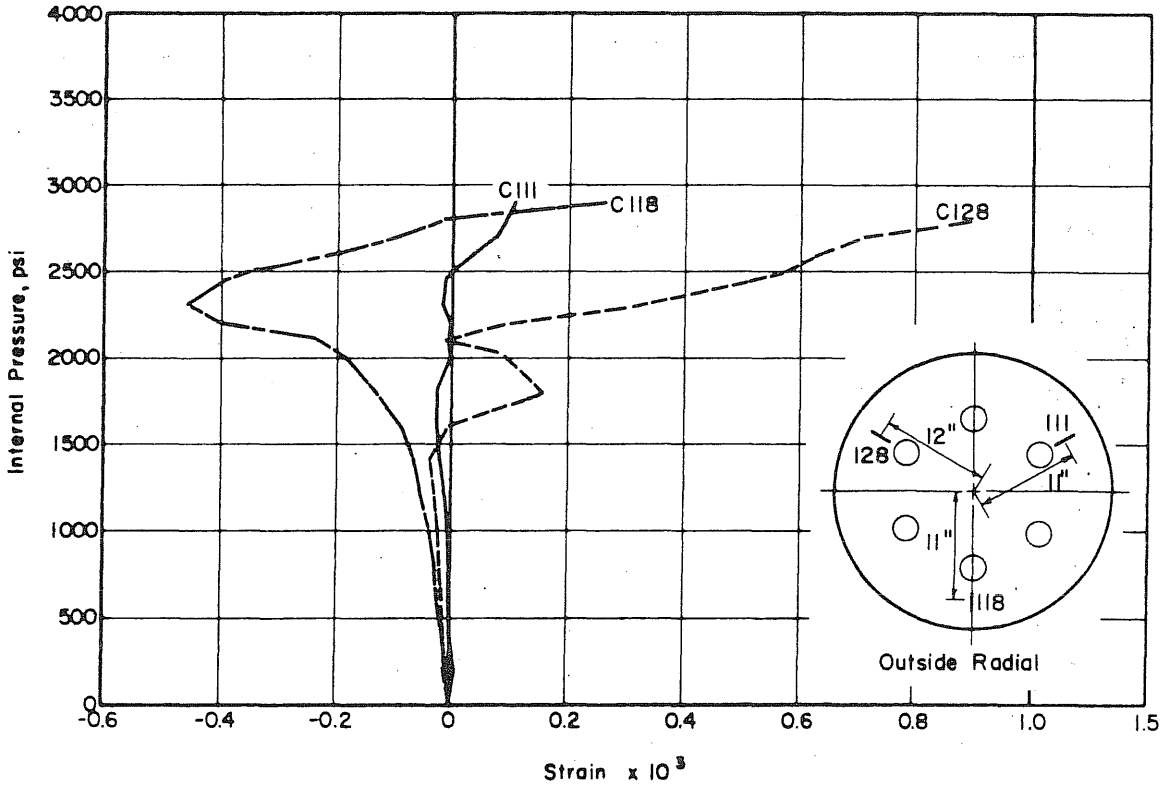

FIG. B.19 (Continued) MEASURED STRAINS ON THE OUTSIDE FACE OF THE SLAB OF PV18

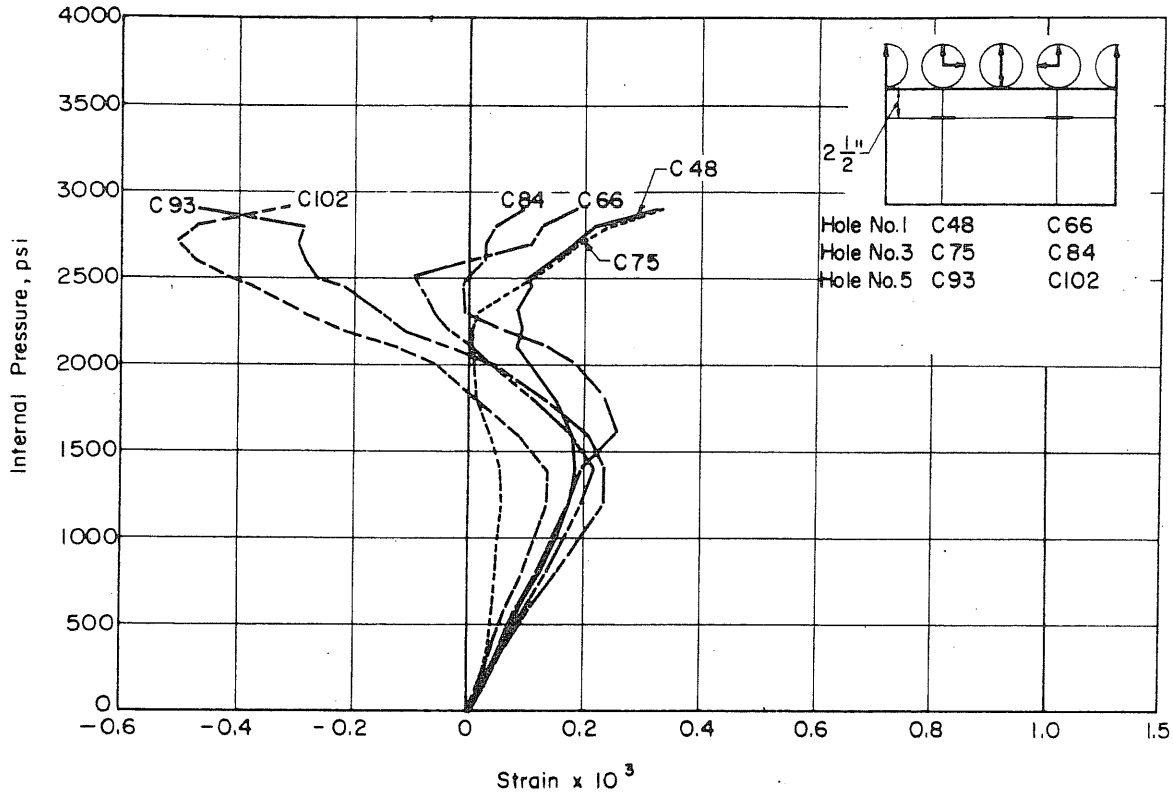

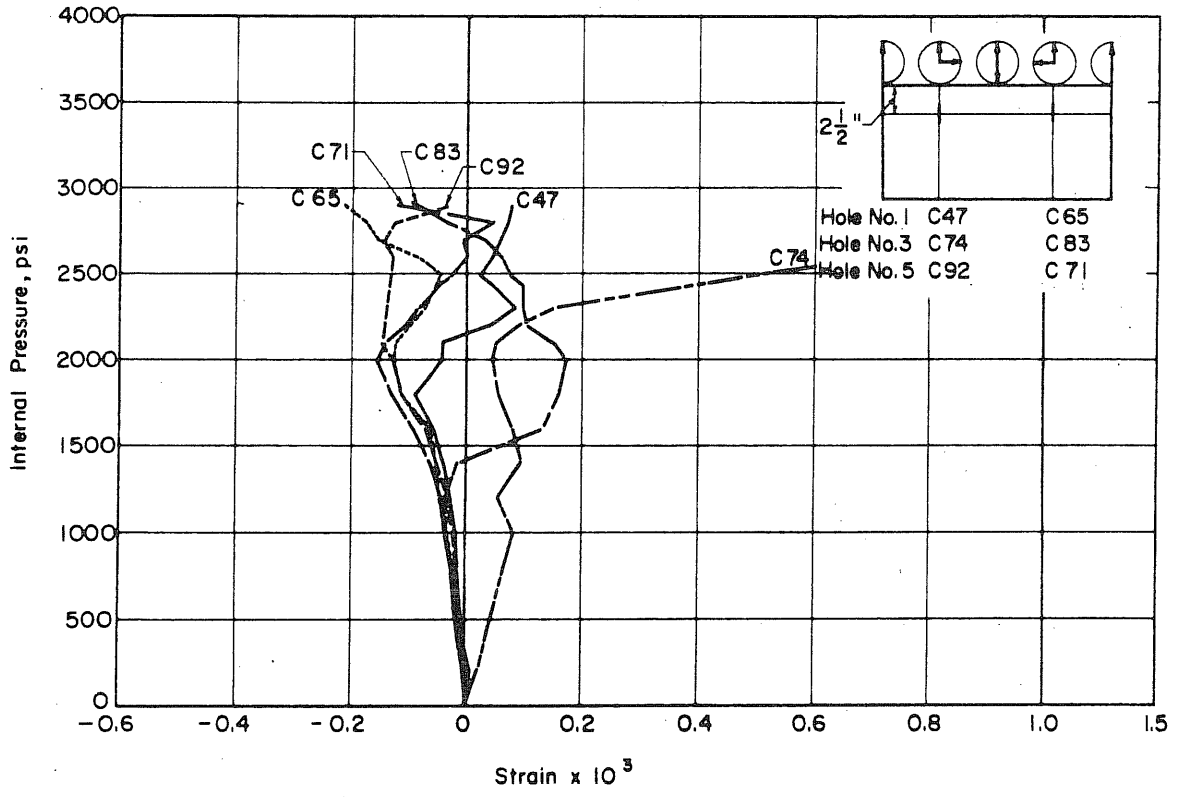

FIG. B.20 MEASURED STRAINS IN THE PENETRATIONS OF PV18

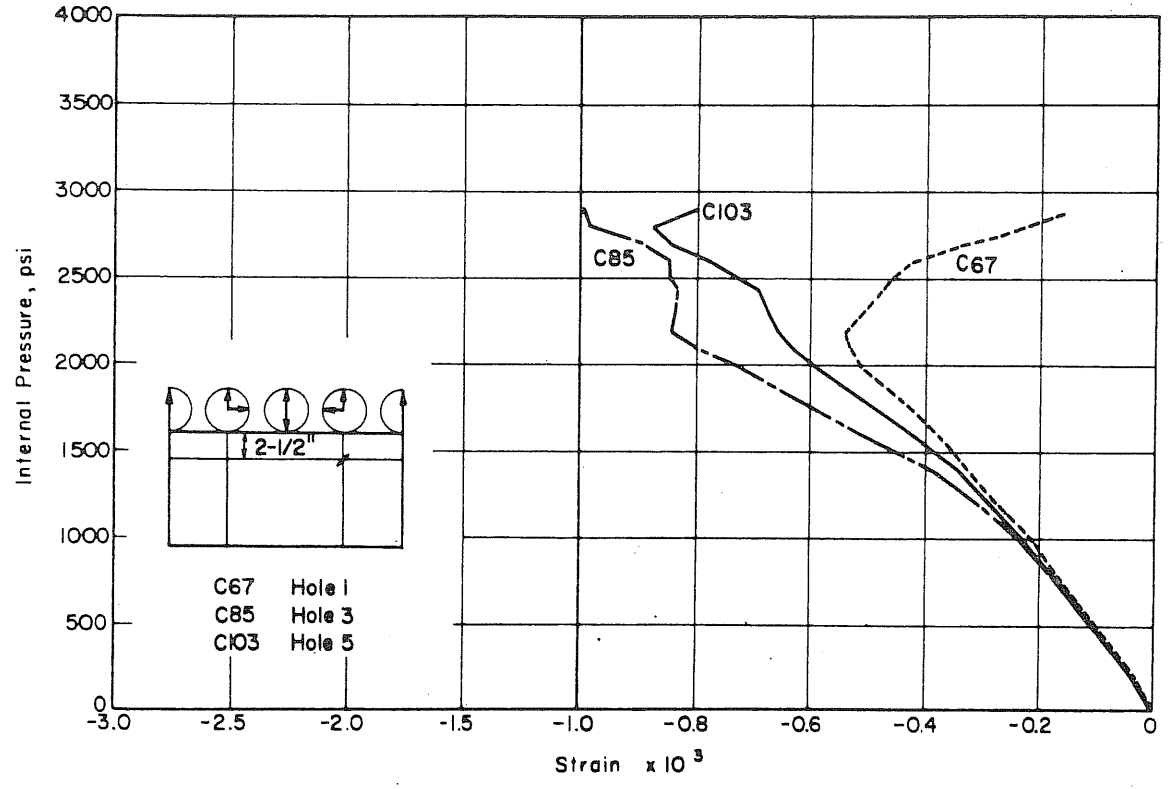

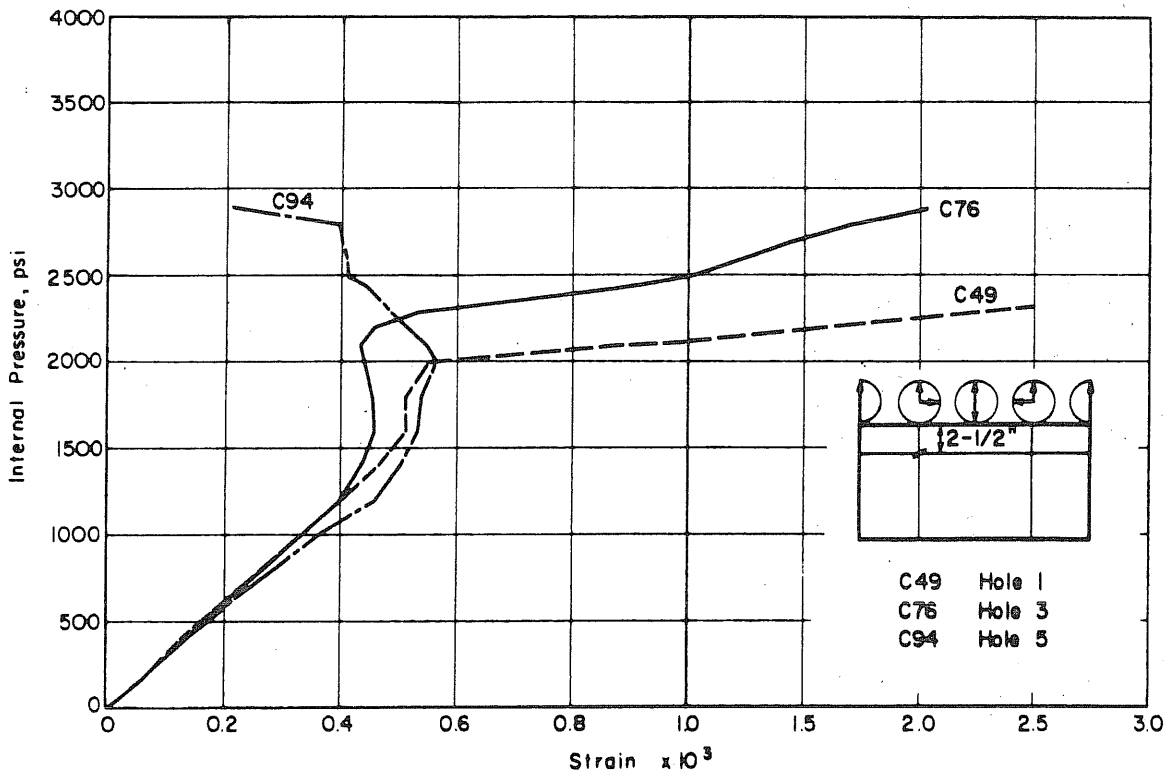

FIG. B.20 (Continued) MEASURED STRAINS IN THE PENETRATIONS OF PV18

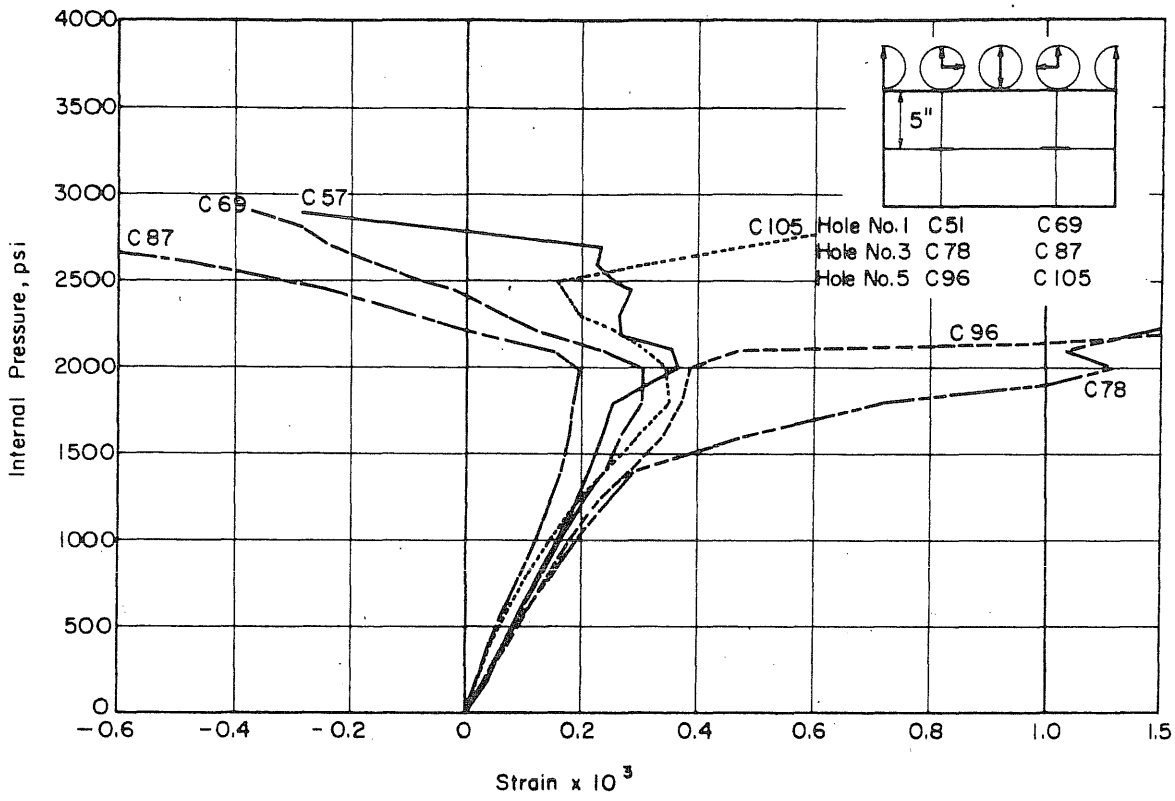

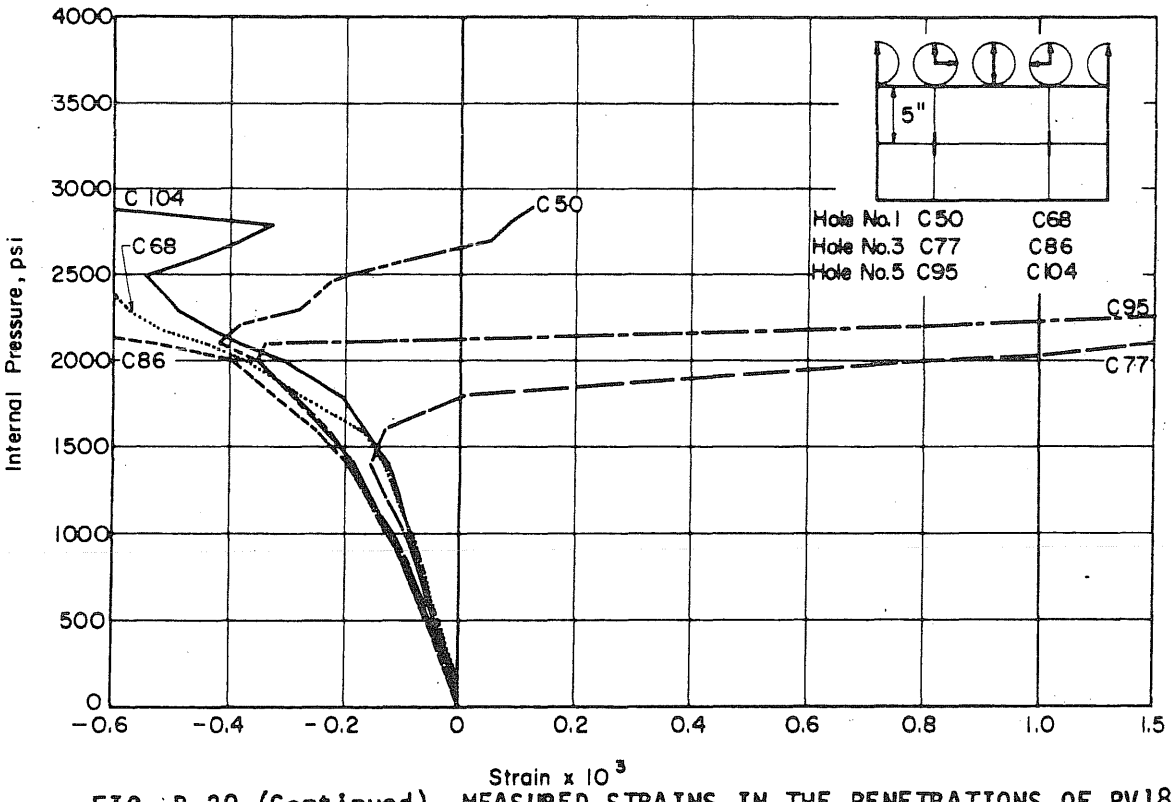

FIG. B.20 (Continued) MEASURED STRAINS IN THE PENETRATIONS OF PV18

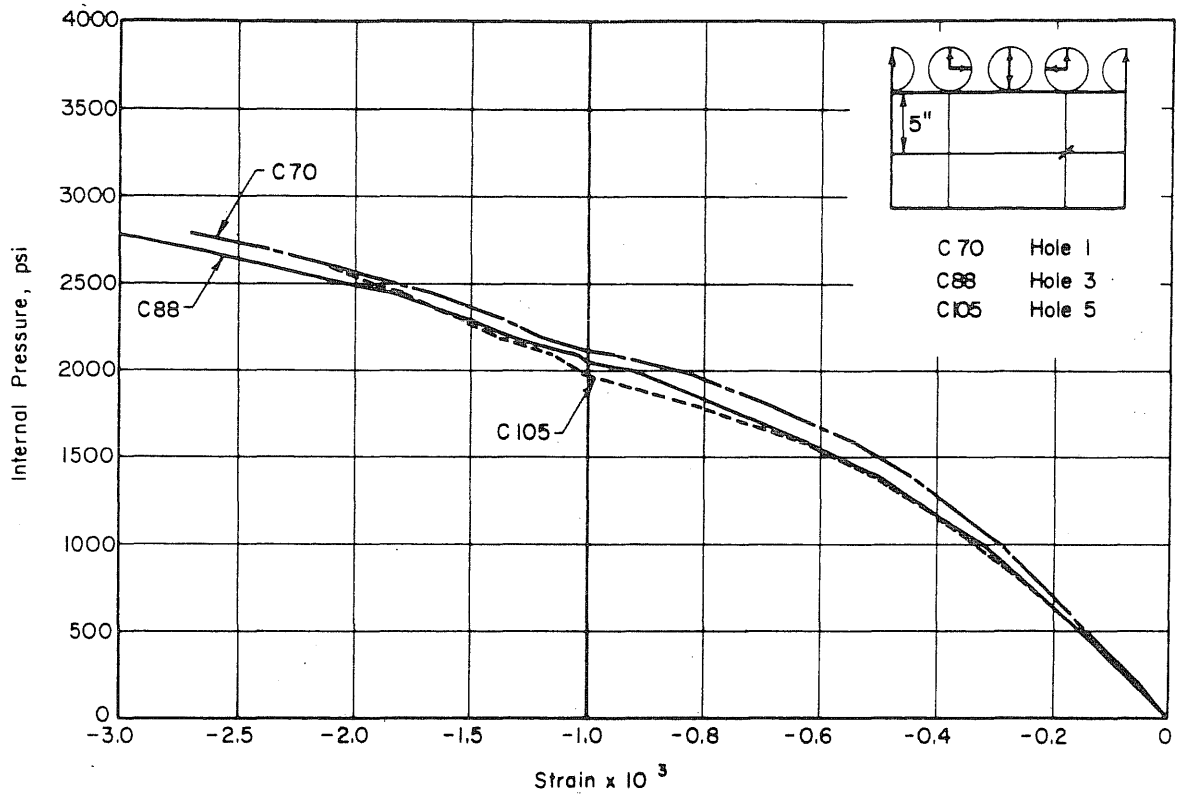

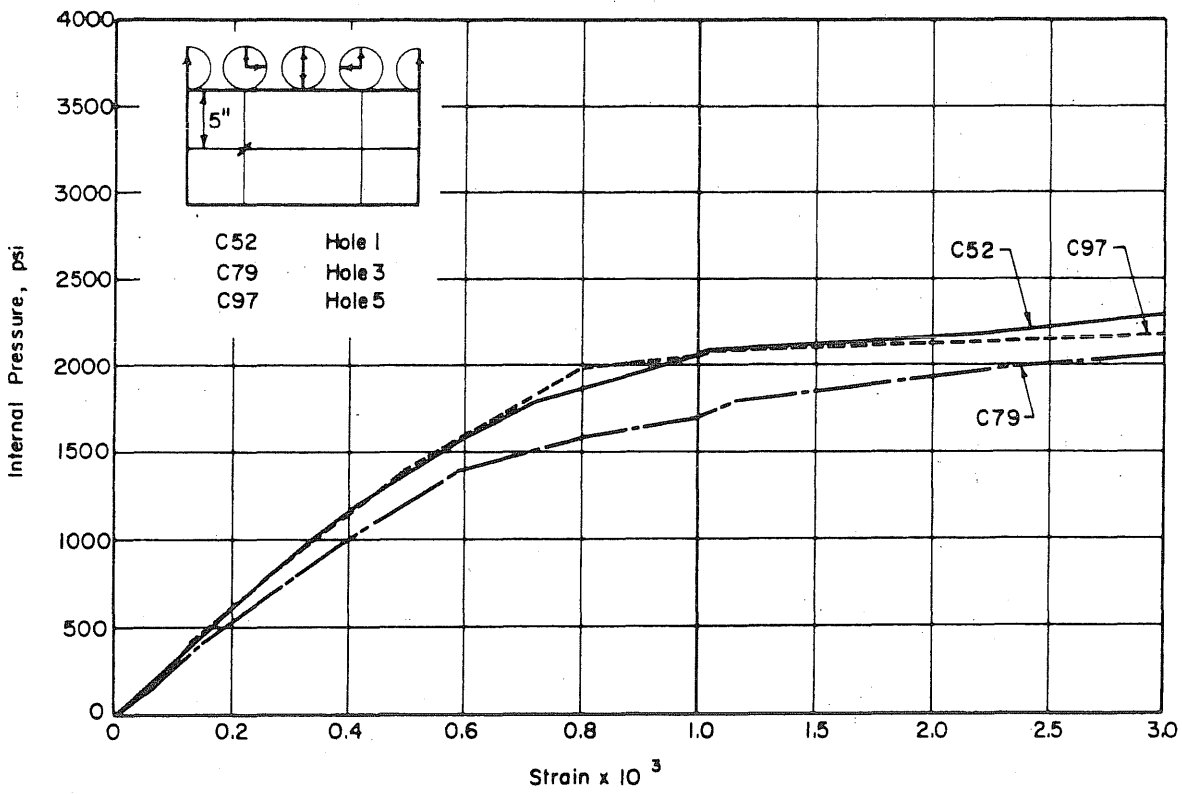

FIG. B.20 (Continued) MEASURED STRAINS IN THE PENETRATIONS OF PV18

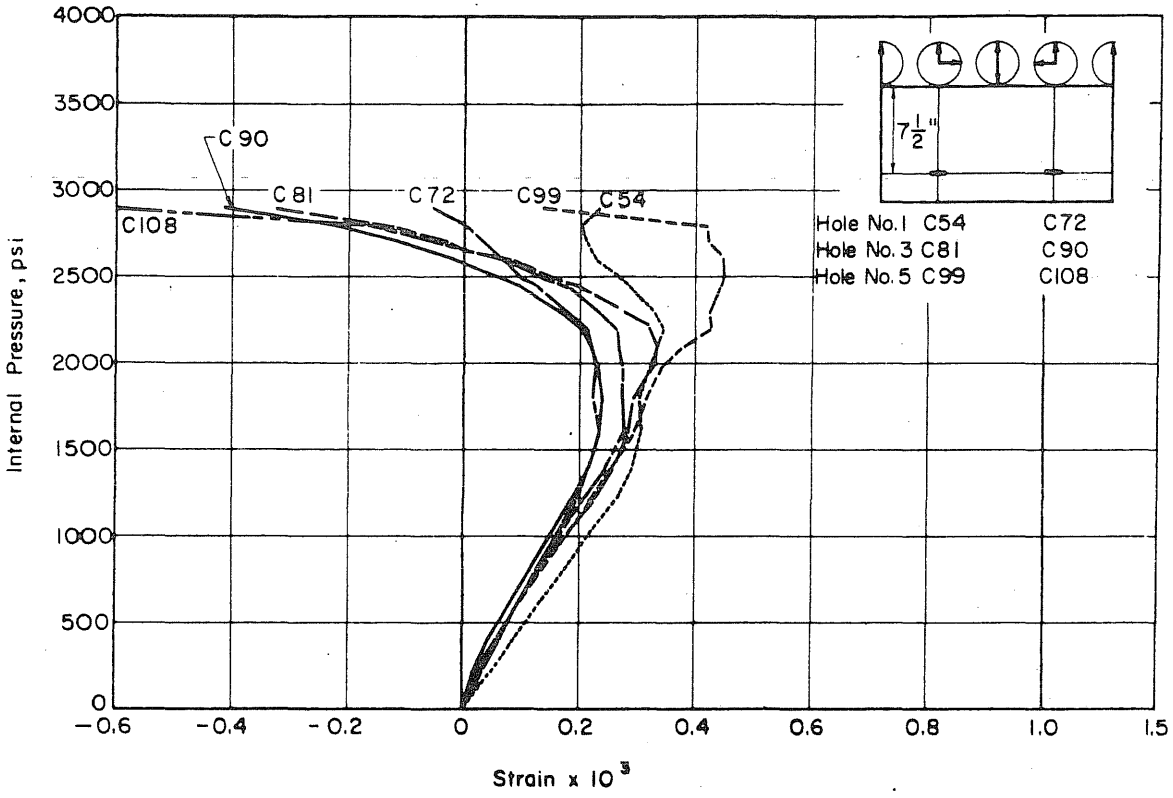

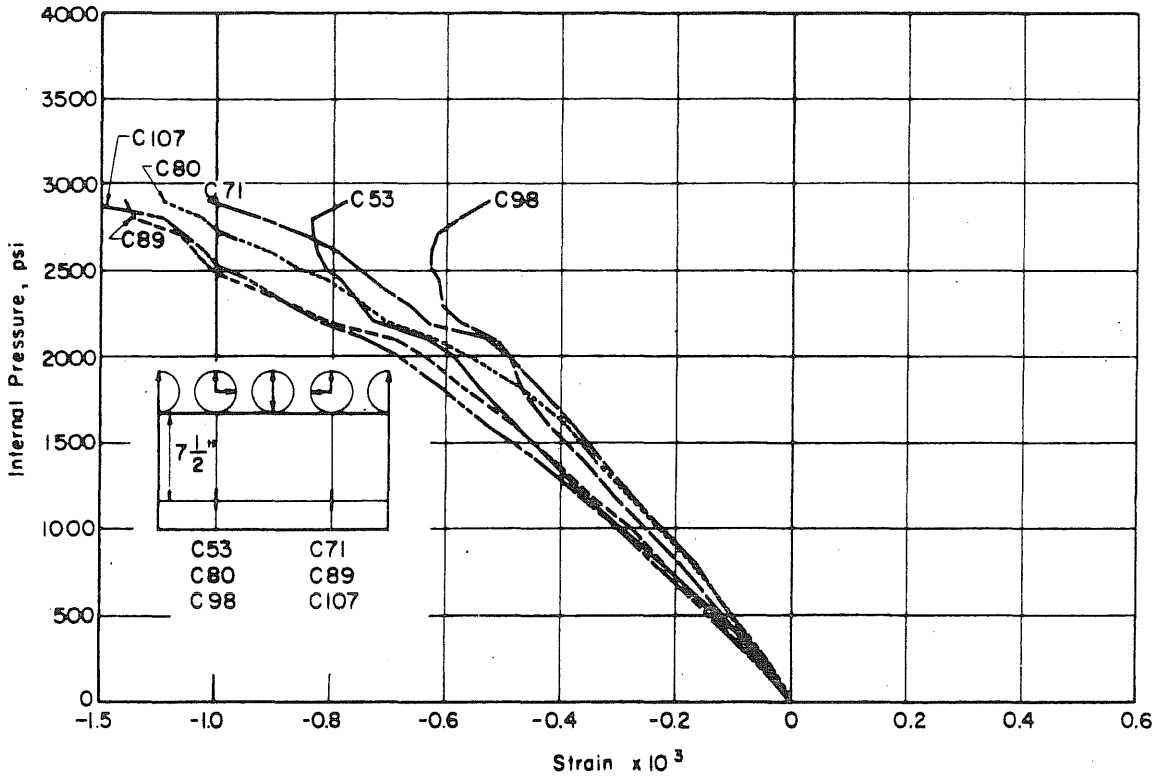

FIG. B.20 (Continued) MEASURED STRAINS IN THE PENETRATIONS OF PV18

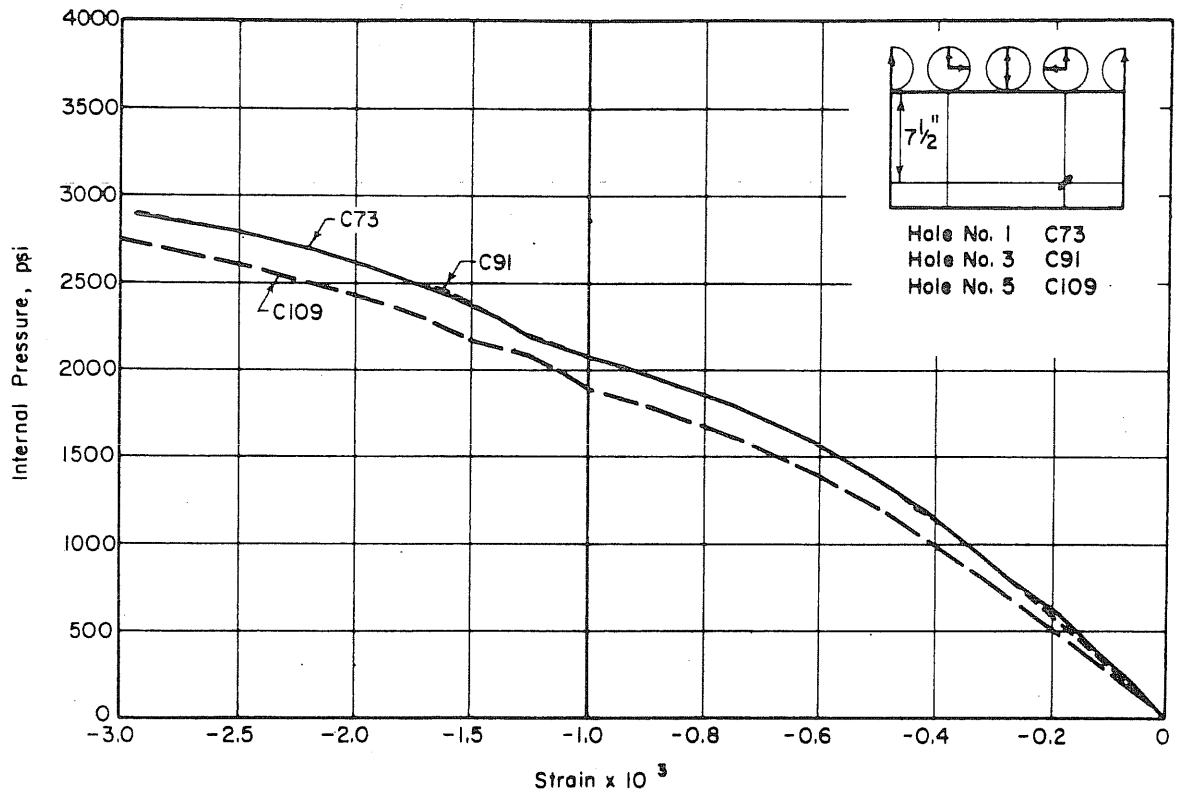

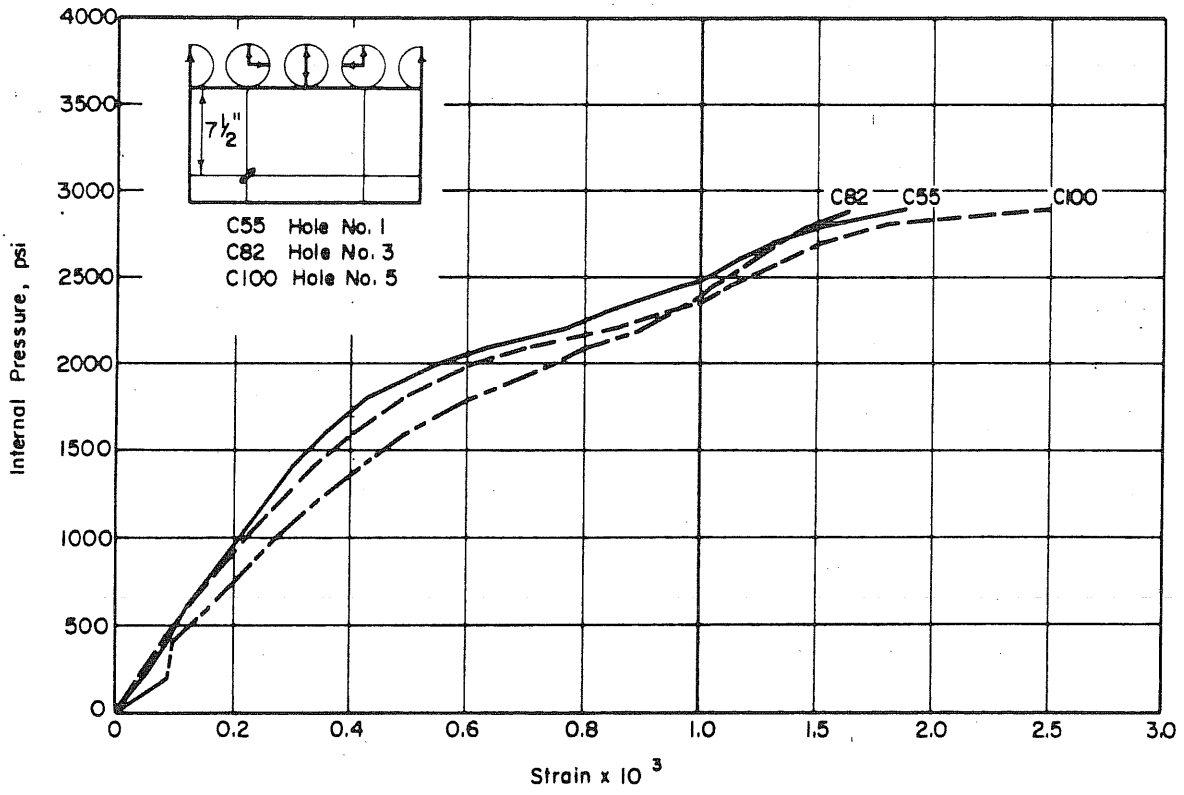

FIG. B.20 (Continued) MEASURED STRAINS IN THE PENETRATIONS OF PW18

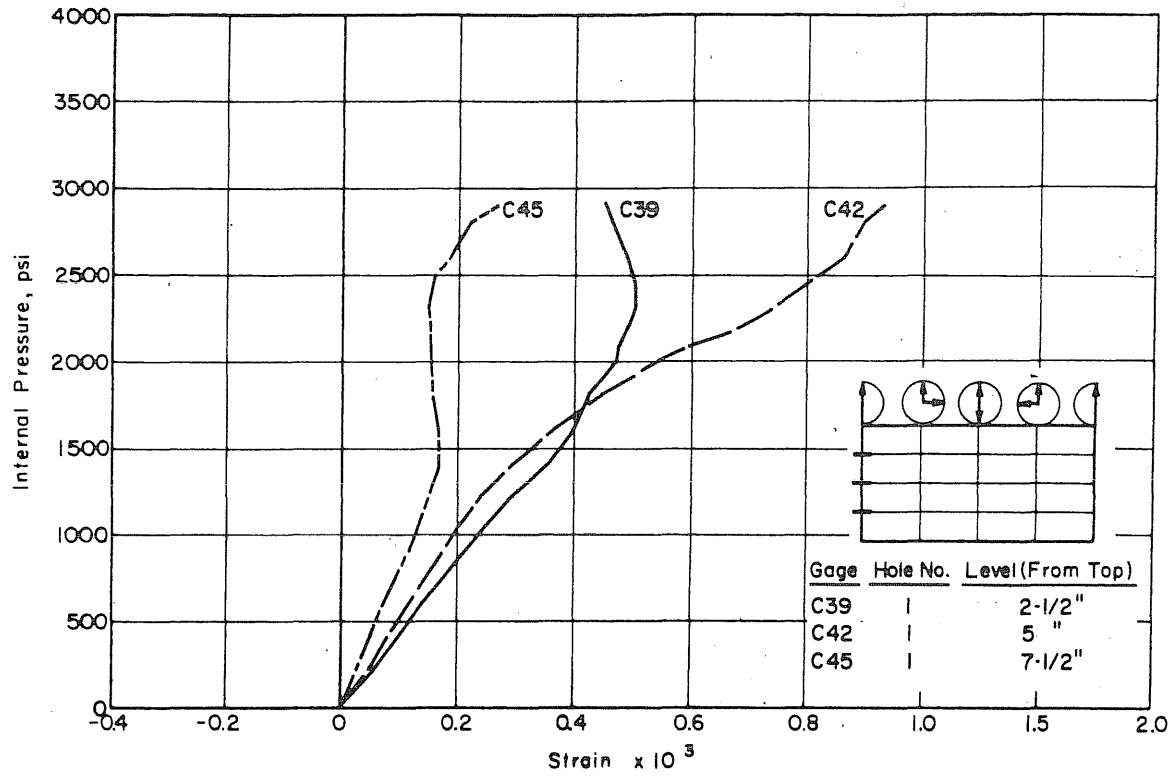

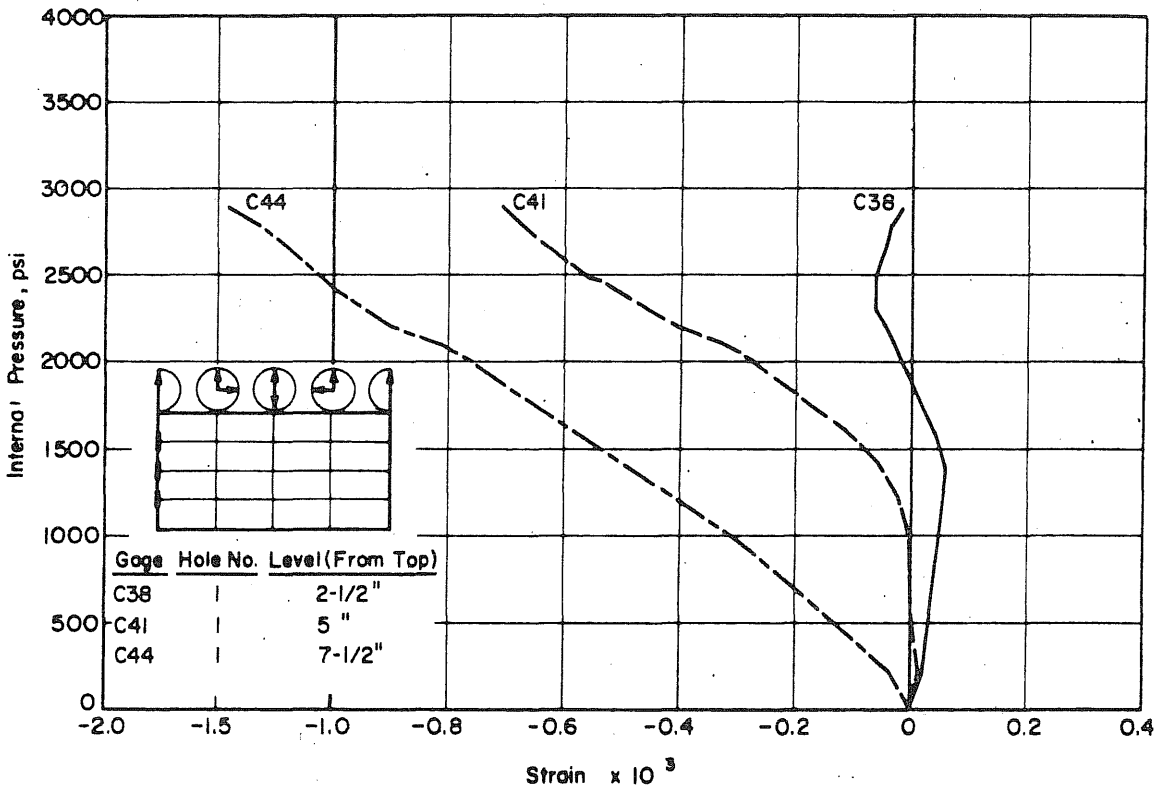

FIG. B.20 (Continued) MEASURED STRAINS IN THE PENETRATIONS OF PV18

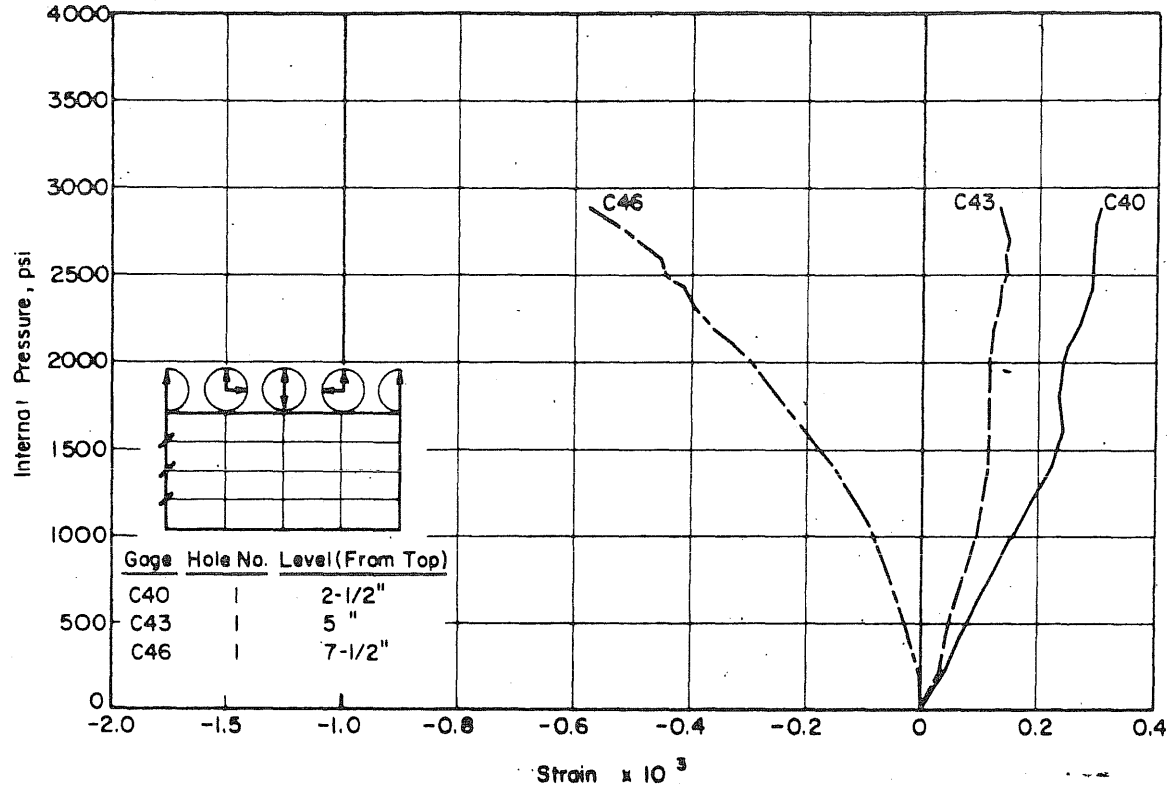

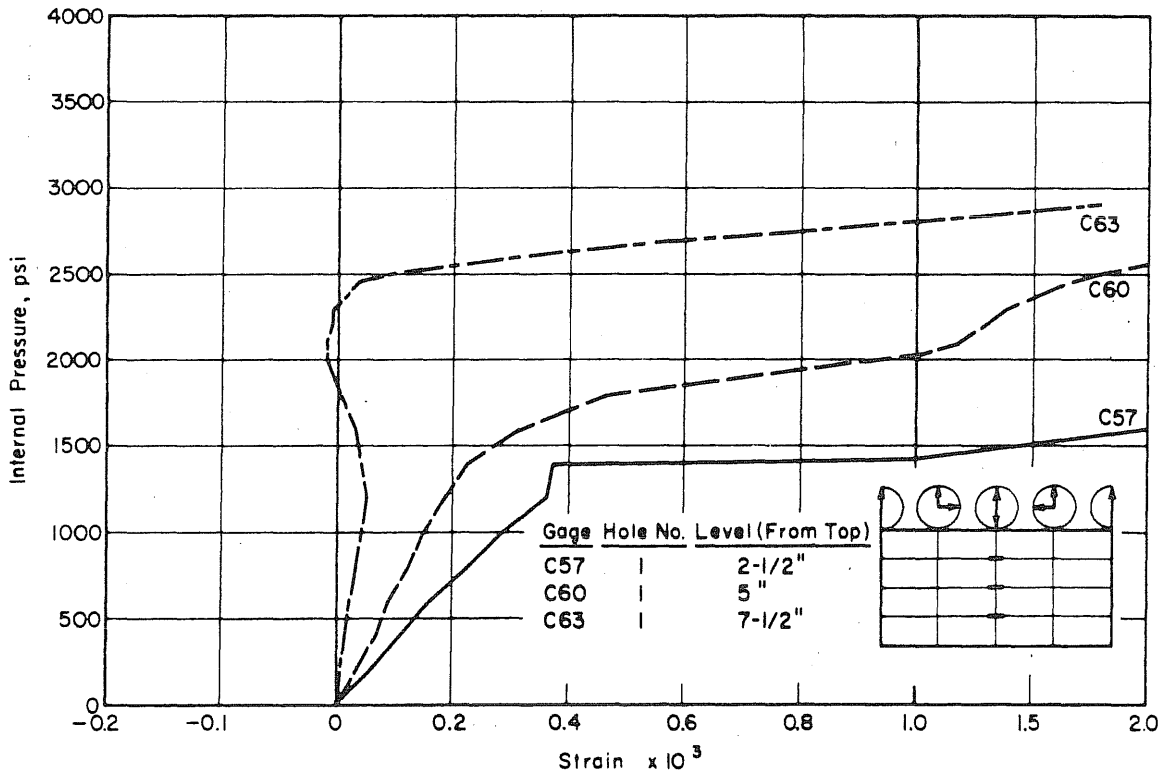

FIG. B.20 (Continued) MEASURED STRAINS IN THE PENETRATIONS OF PV18

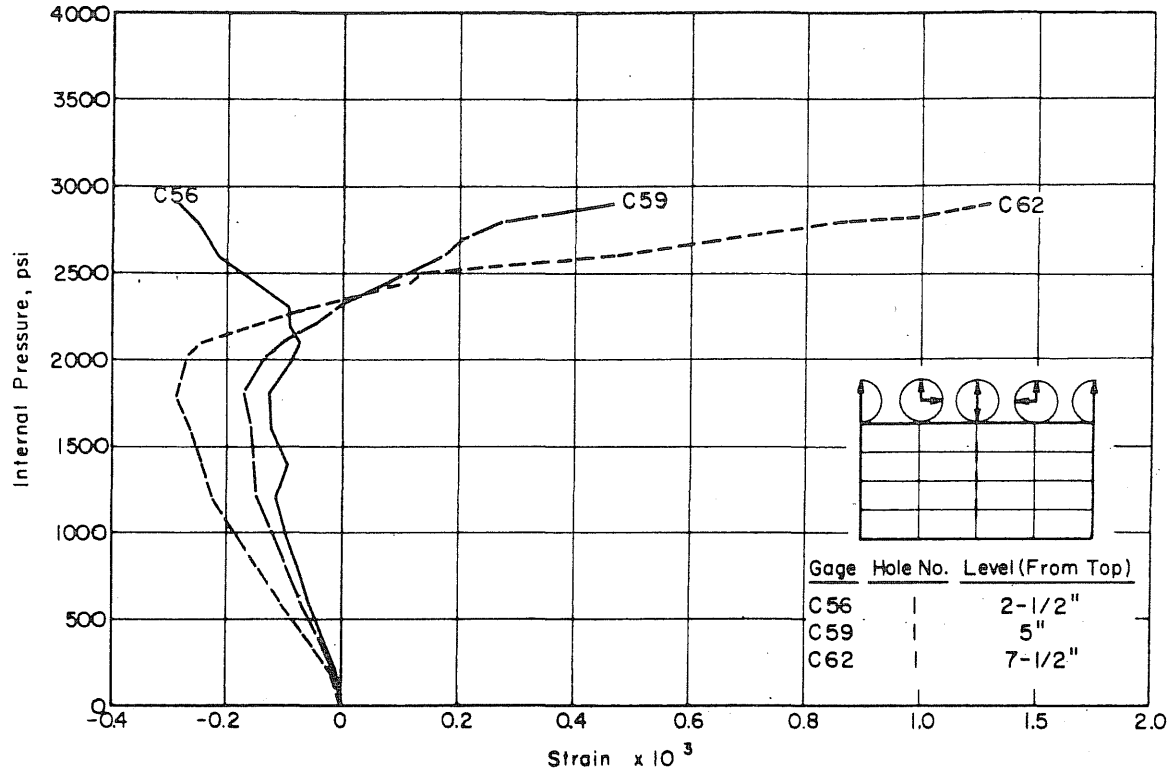

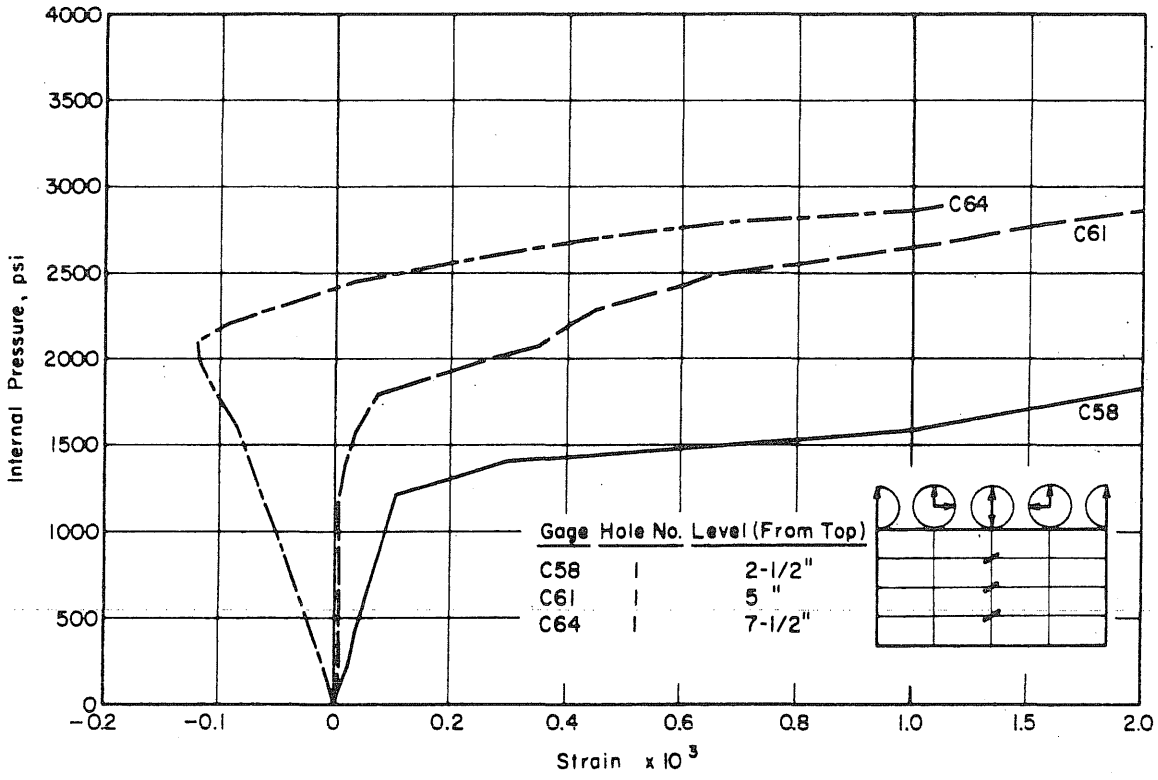

FIG. B.20 (Continued) MEASURED STRAINS IN THE PENETRATIONS OF PV18

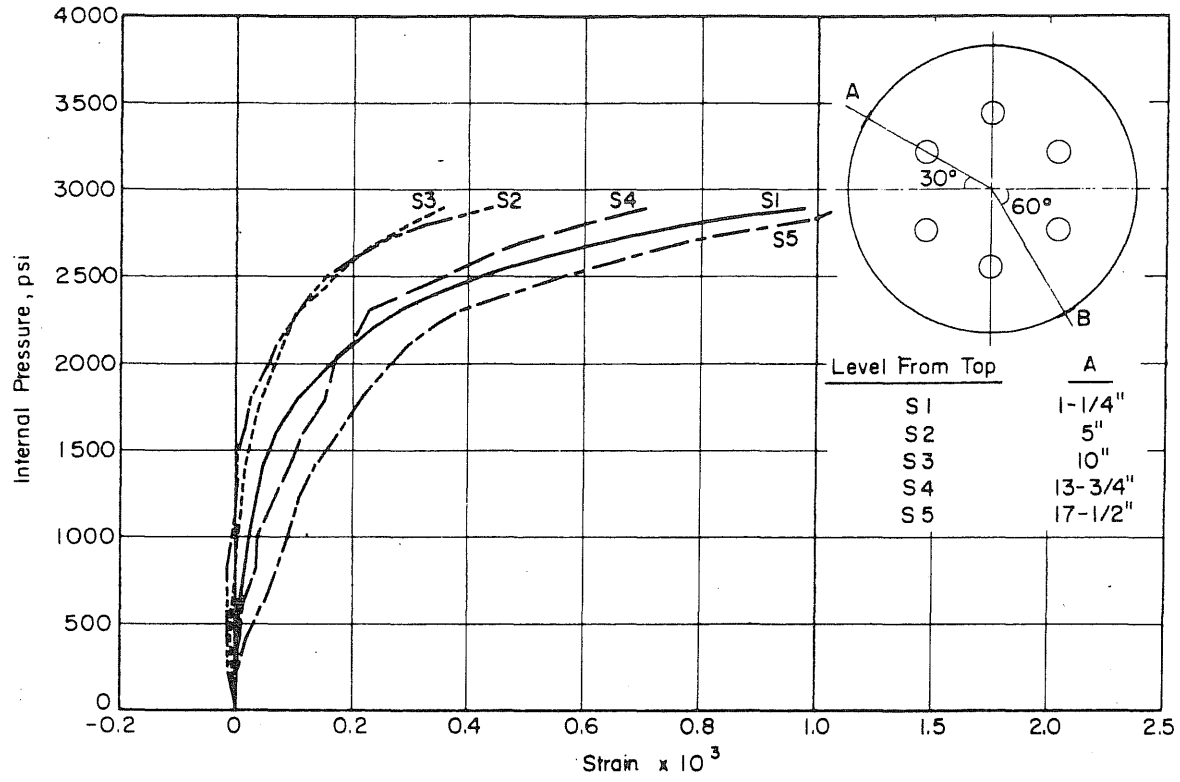

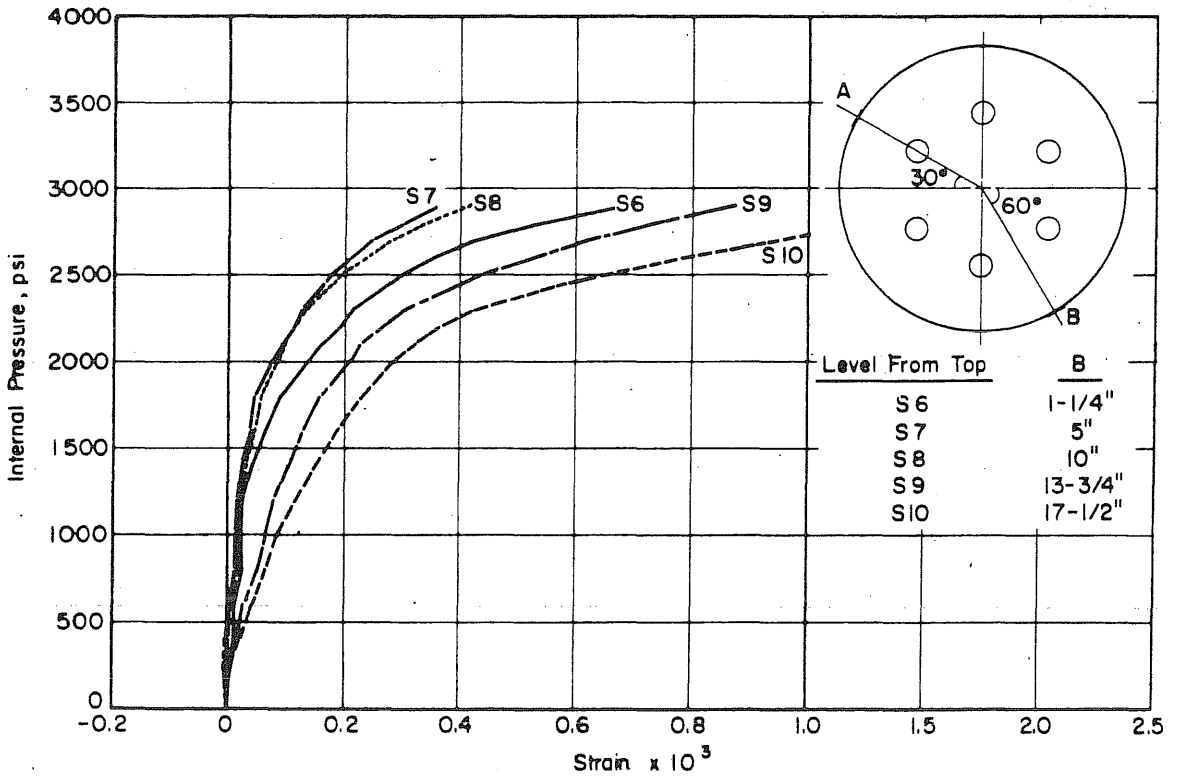

FIG. B.21 MEASURED STRAINS IN THE CIRCUMFERENTIAL PRESTRESSING WIRE OF PV18

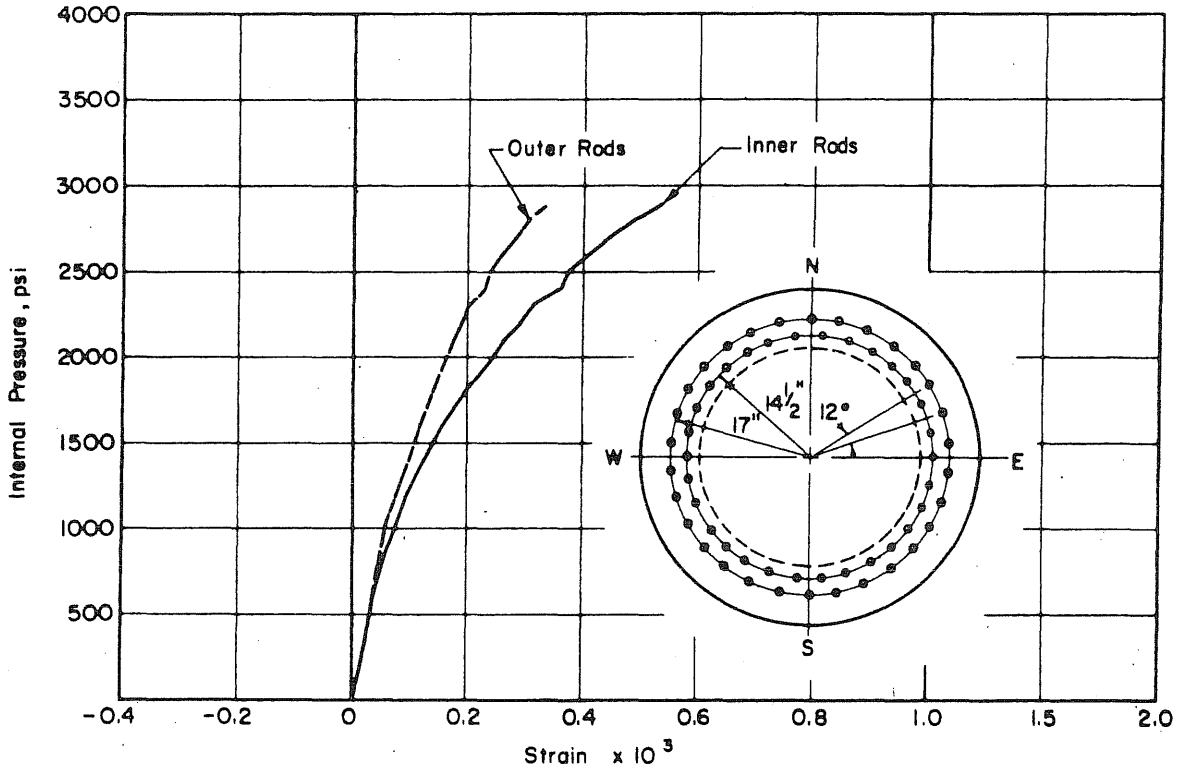

FIG. B.22 MEASURED STRAINS IN THE LONGITUDINAL PRESTRESSING RODS OF PV18

B.5 Test Vessel PV19

The vessel was tested hydraulically with the option to swtich to gas pressure. The pressure dropped suddenly after 3500 psi internal pressure had been reached. The pressure decreased to 2400 psi before the gas pressure could be turned on. The pressure was increased to 3000 psi but higher pressures could not be reached because of leakage. It is likely that the failure pressure had been reached, but the absence of compressed gas in the vessel prevented a violent failure or the development of a clearly recognized failure plane.

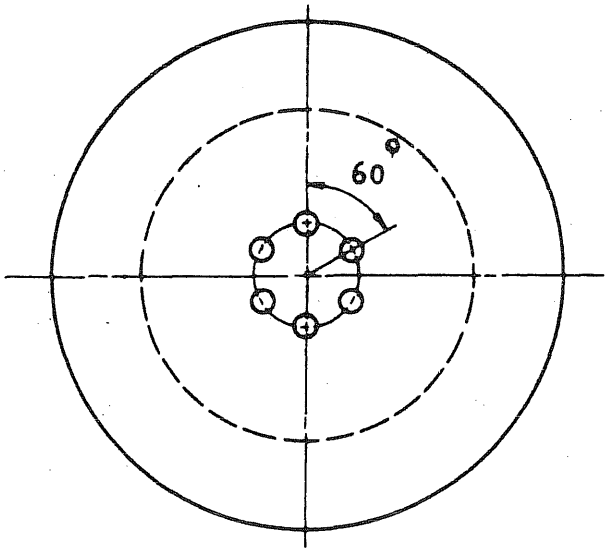

FIG. B.23 VESSEL PV19 WITH SIX 2-in. PENETRATIONS ON A 4-in. RADIUS

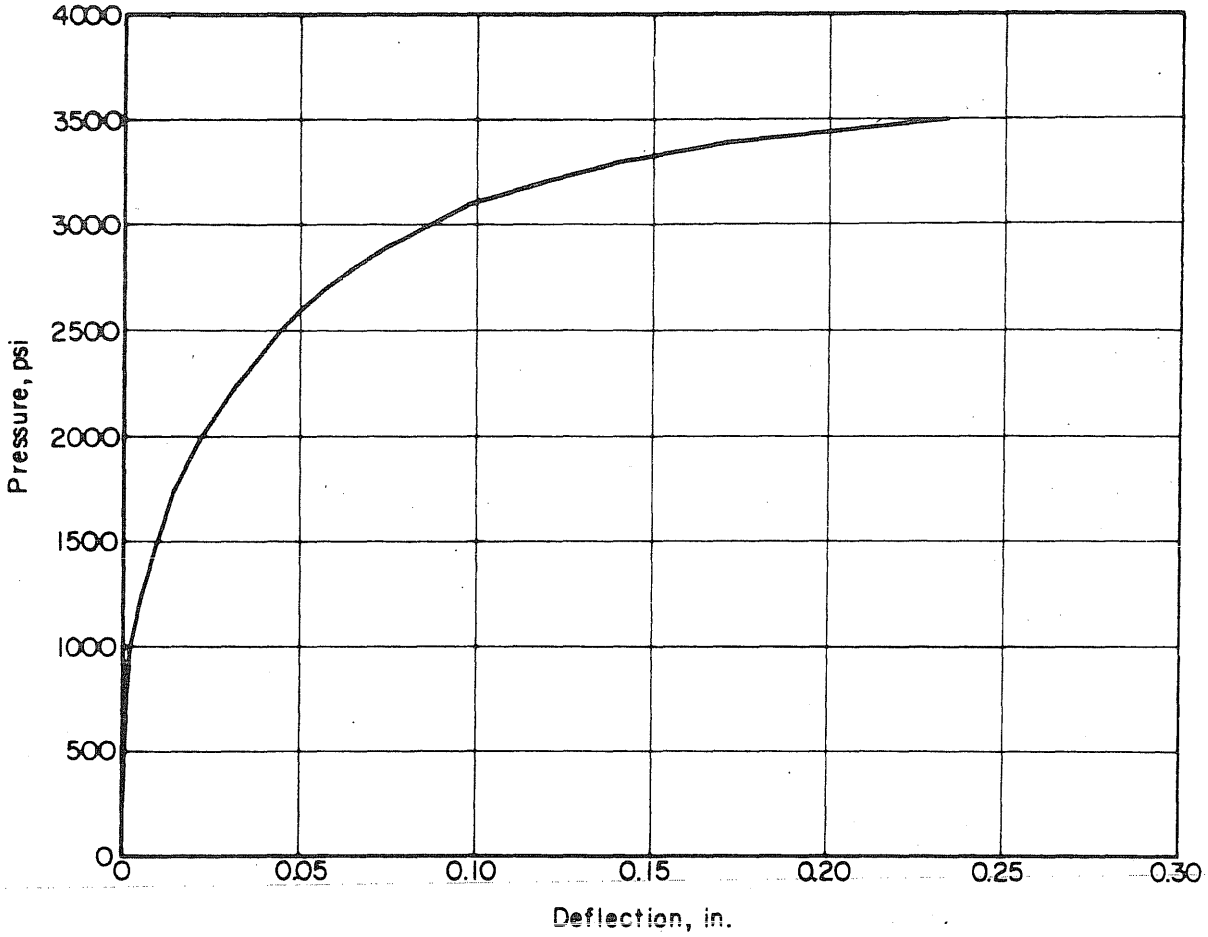

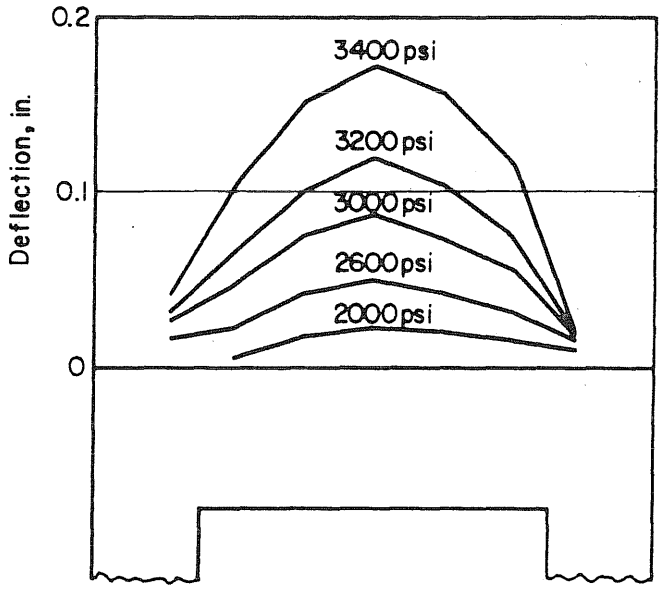

FIG. B.24 MEASURED DEFLECTION PROFILES AND DEFLECTION AT THE CENTER OF THE END SLAB OF PV19

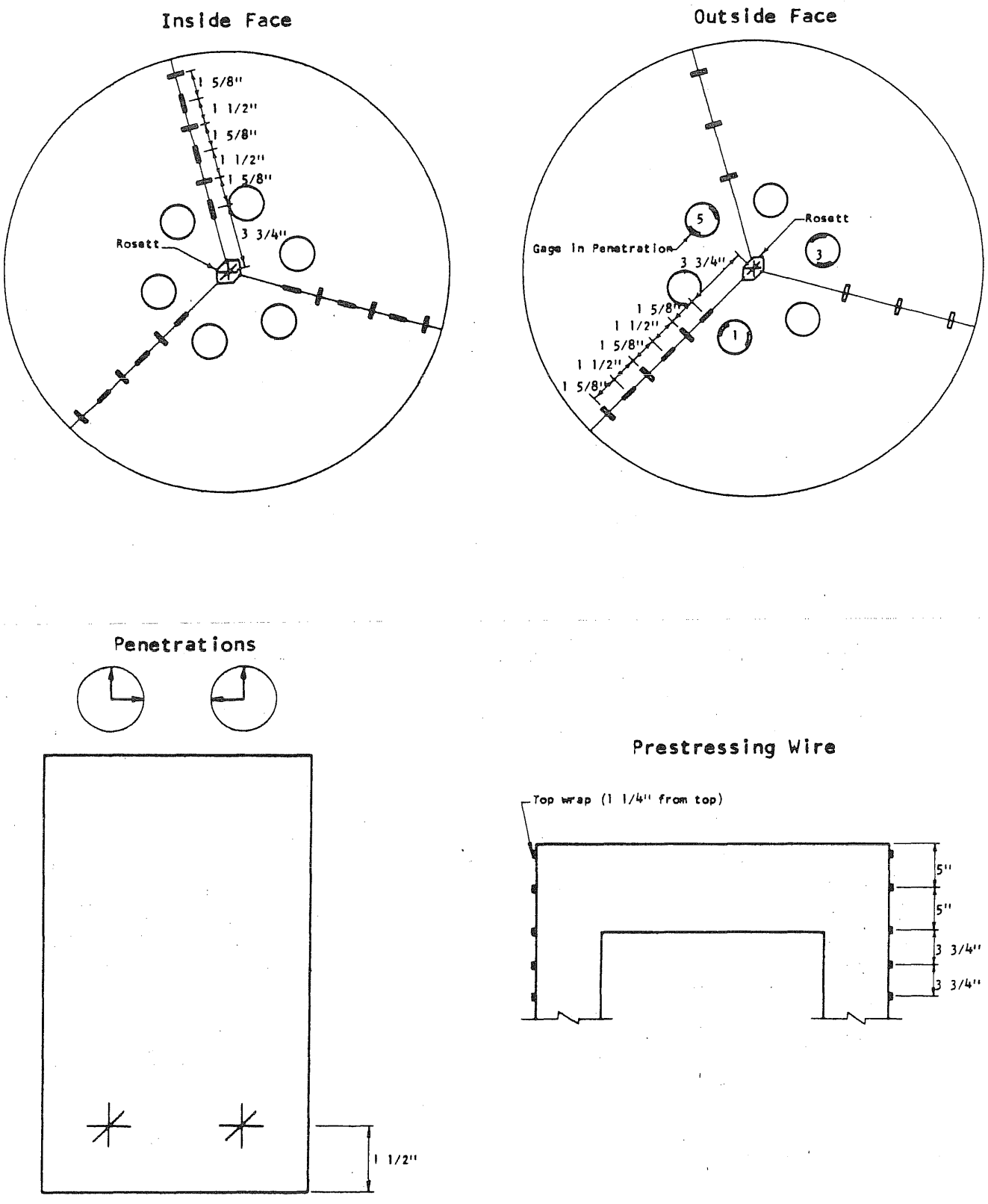

FIG. B.25 STRAIN GAGE LOCATION ON PV19

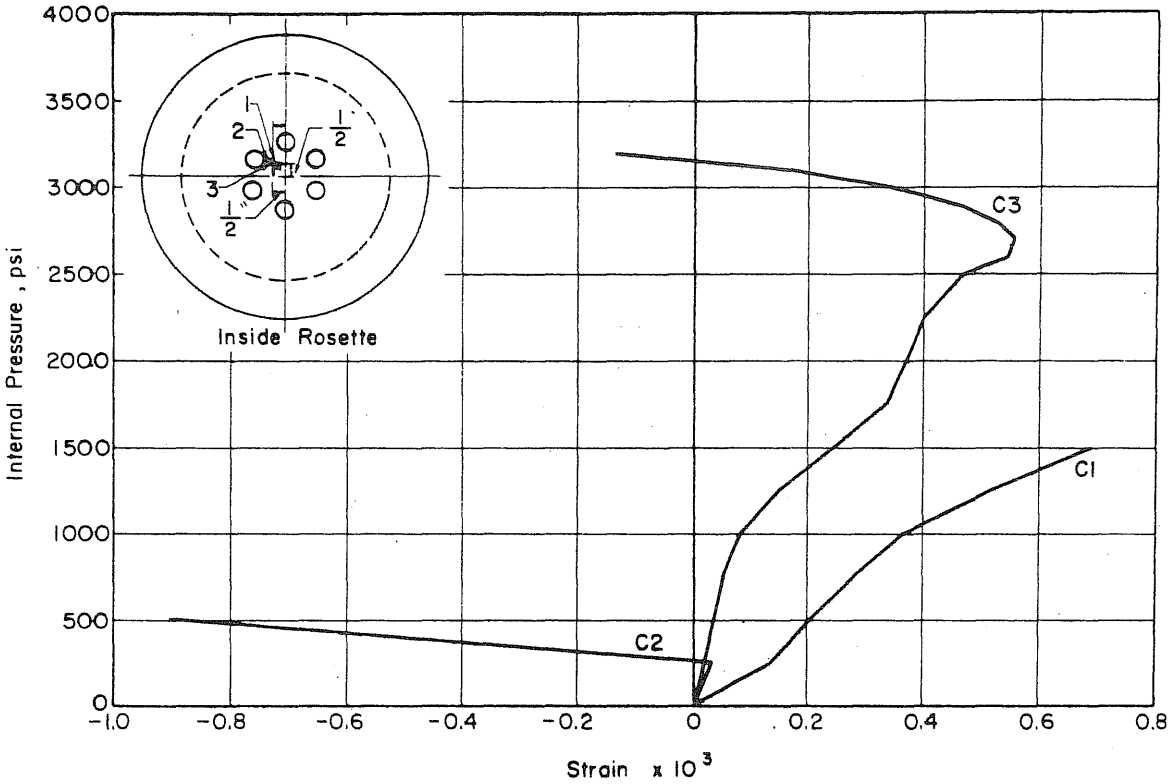

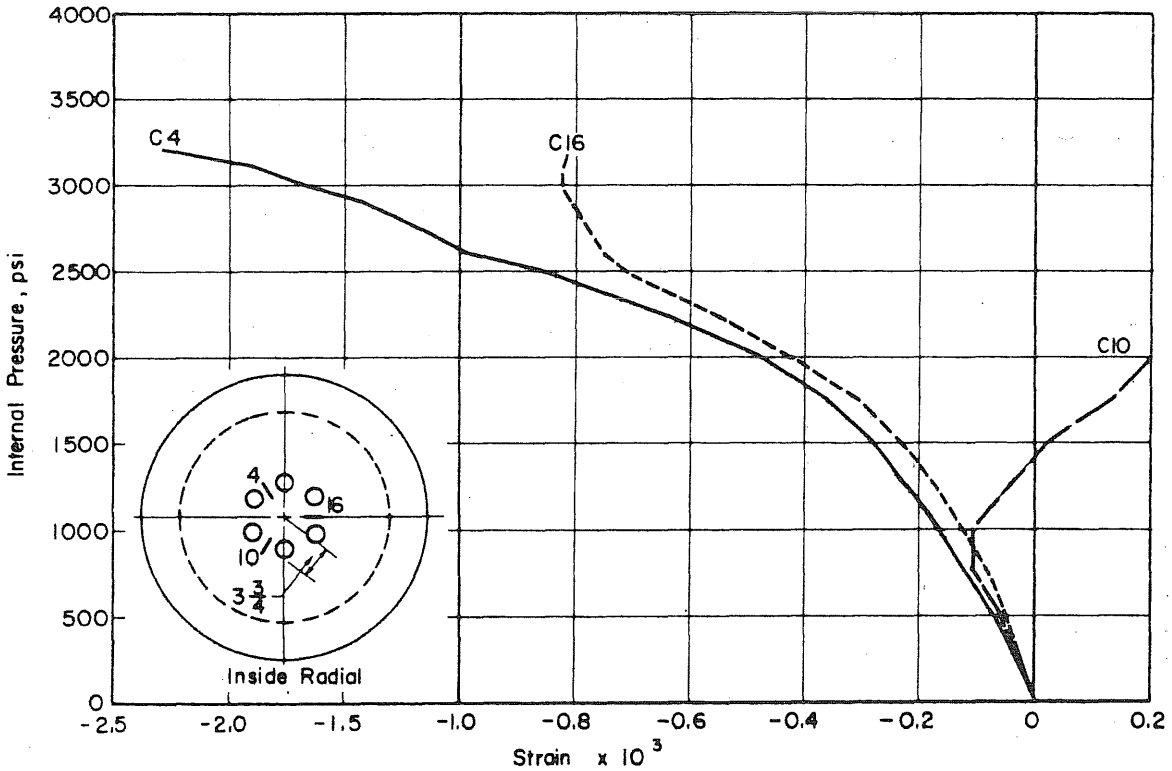

FIG. B.26 MEASURED STRAINS ON THE INSIDE FACE OF THE SLAB OF PV19

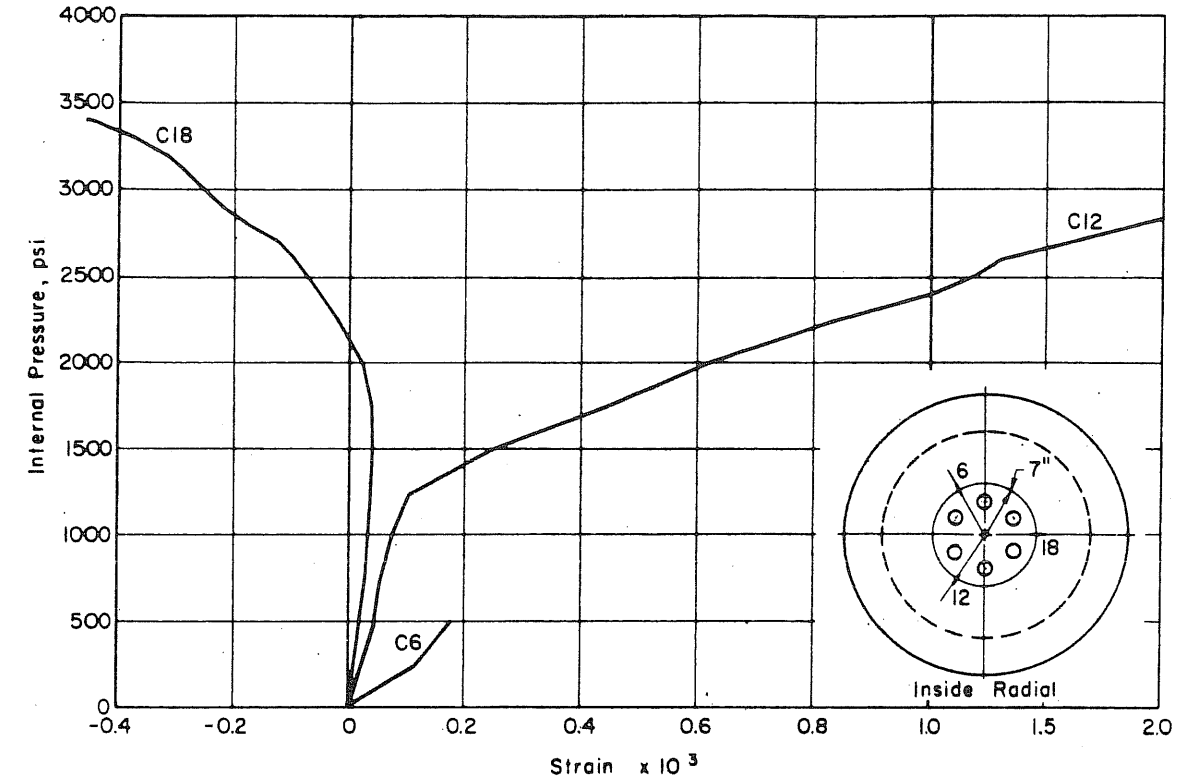

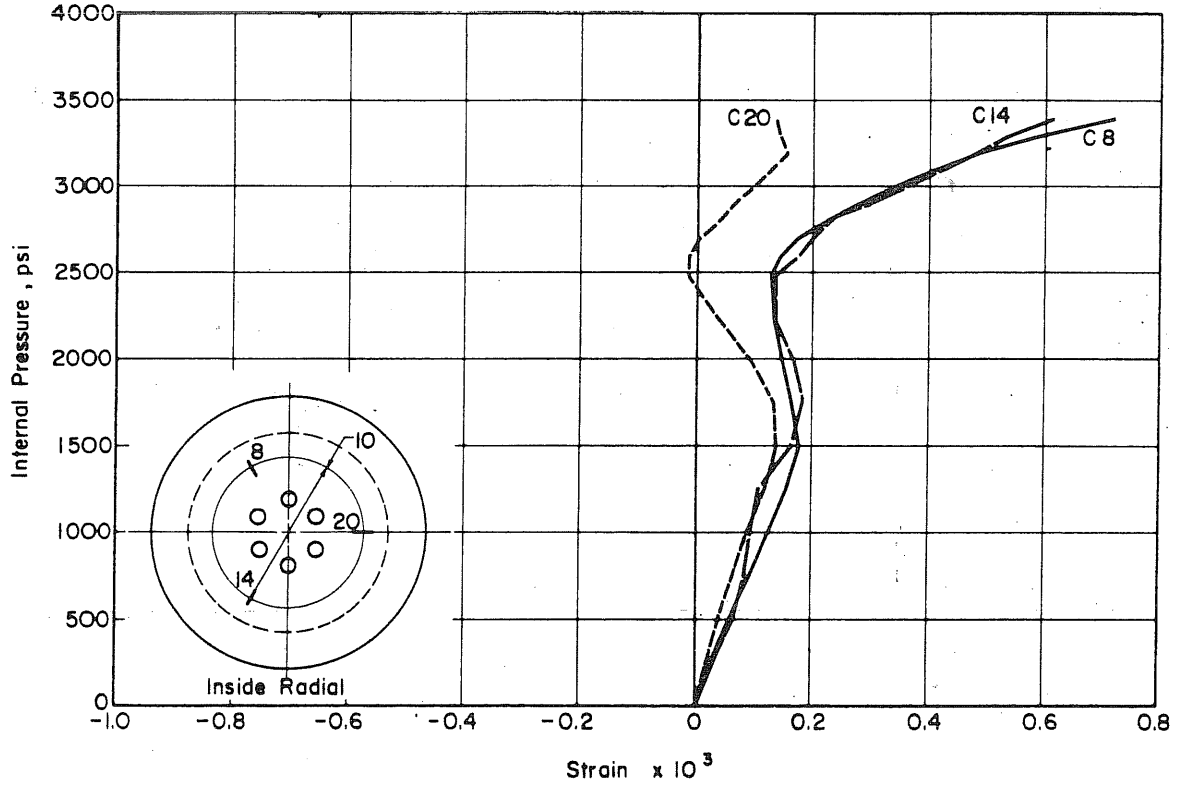

FIG. B.26 (Continued) MEASURED STRAINS ON THE INSIDE FACE OF THE SLAB OF PV19

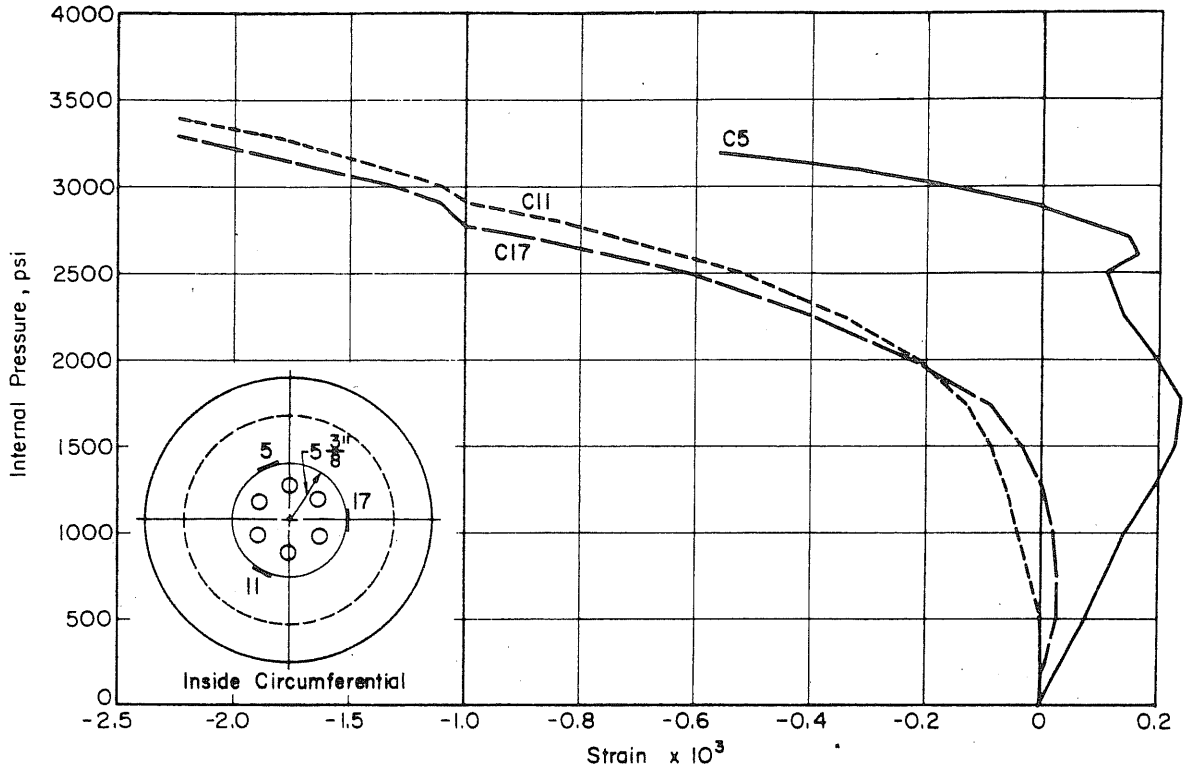

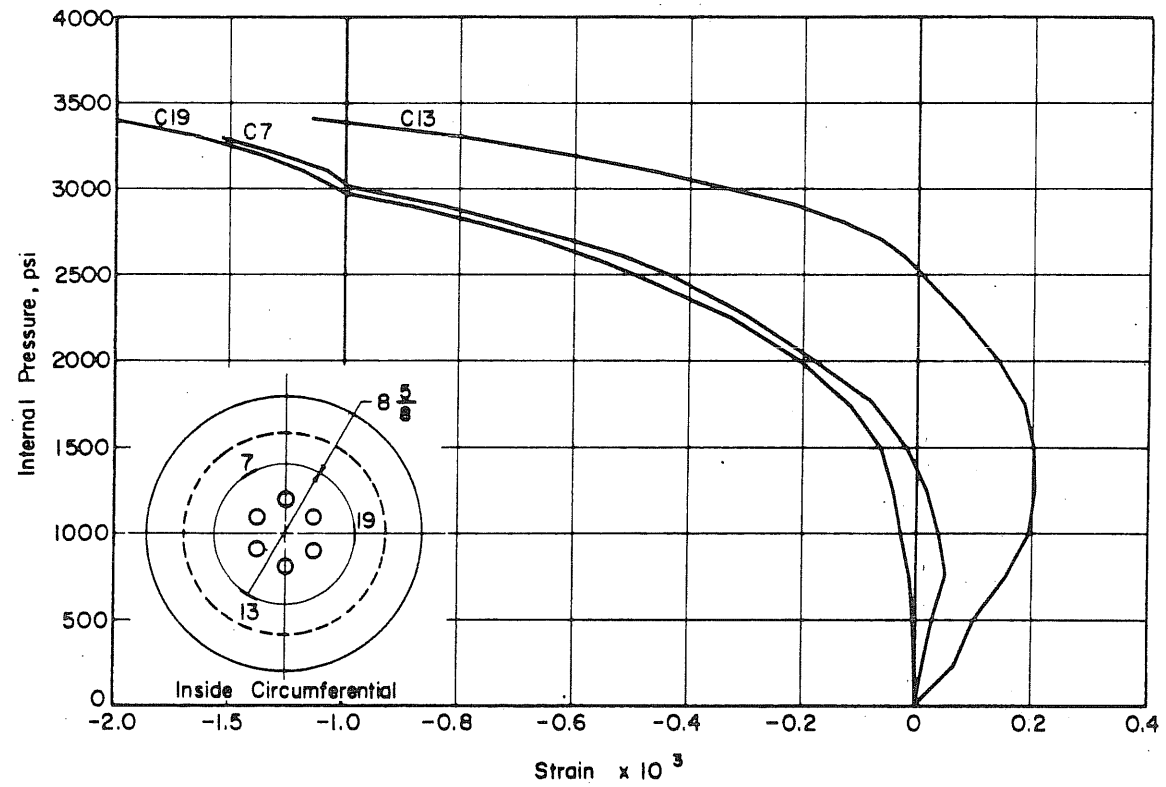

FIG. B.26 (Continued) MEASURED STRAINS ON THE INSIDE FACE OF THE SLAB OF PV19

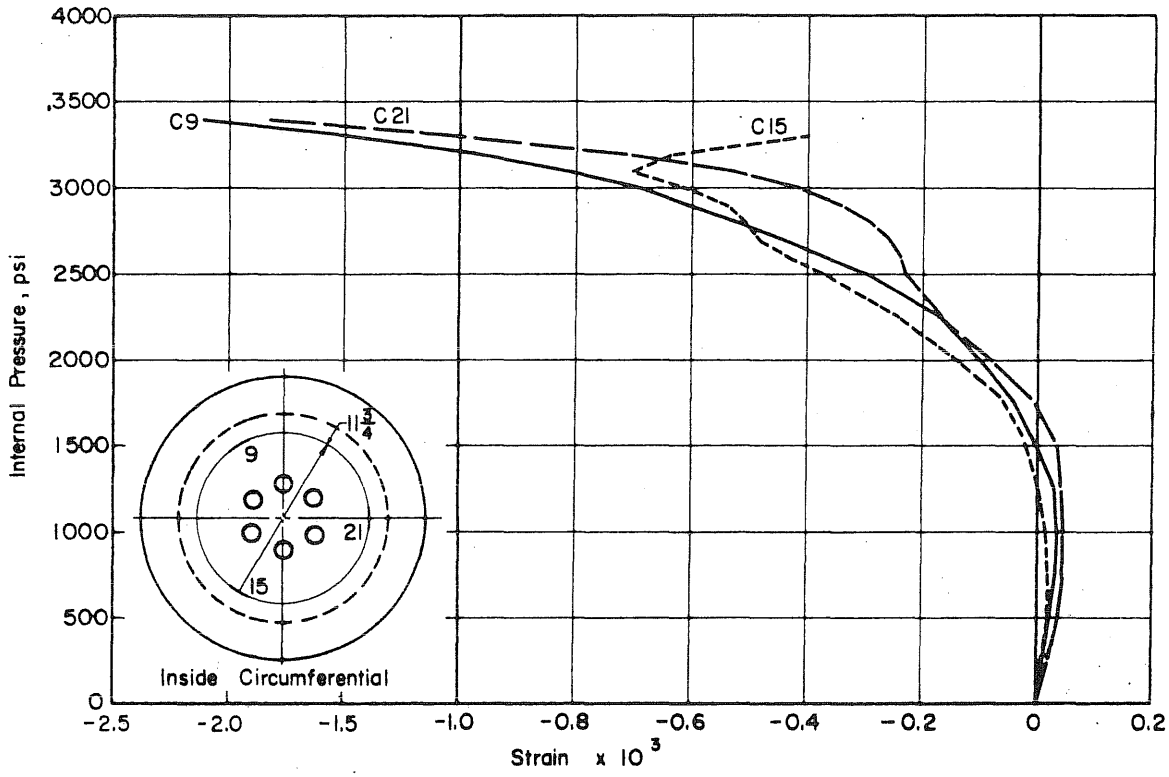

FIG. B.26 (Continued) MEASURED STRAINS ON THE INSIDE FACE OF THE SLAB OF PV19

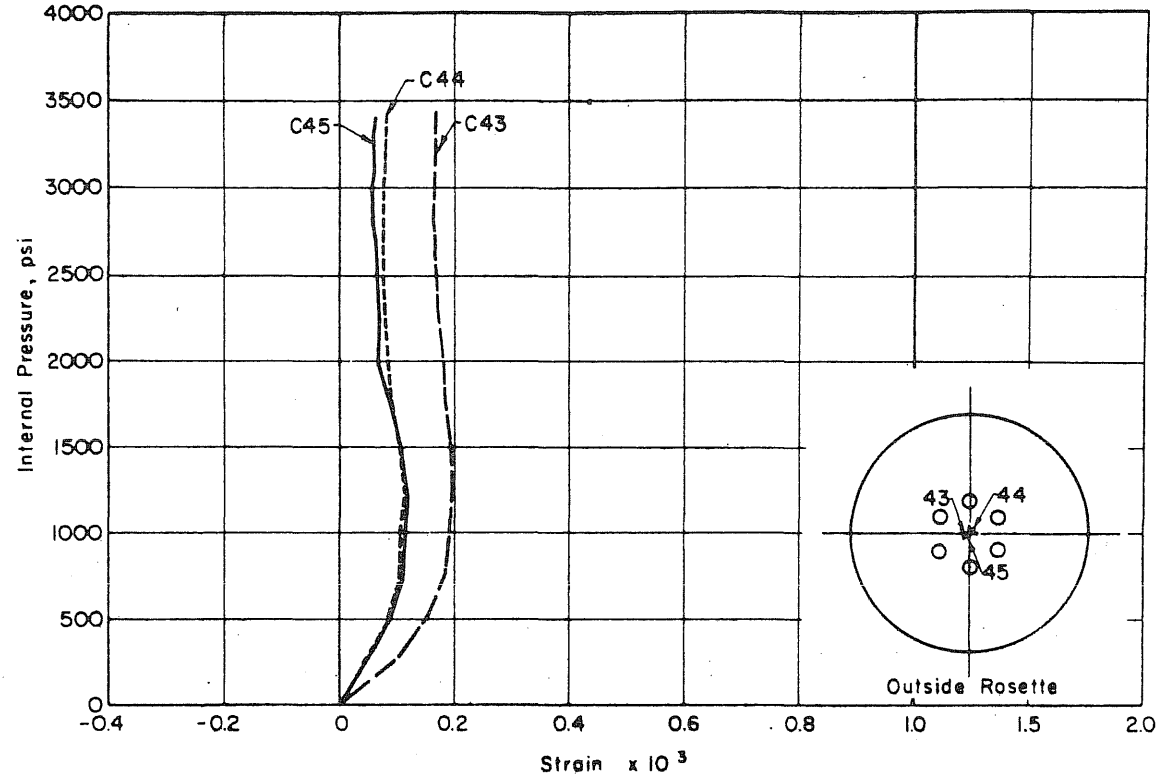

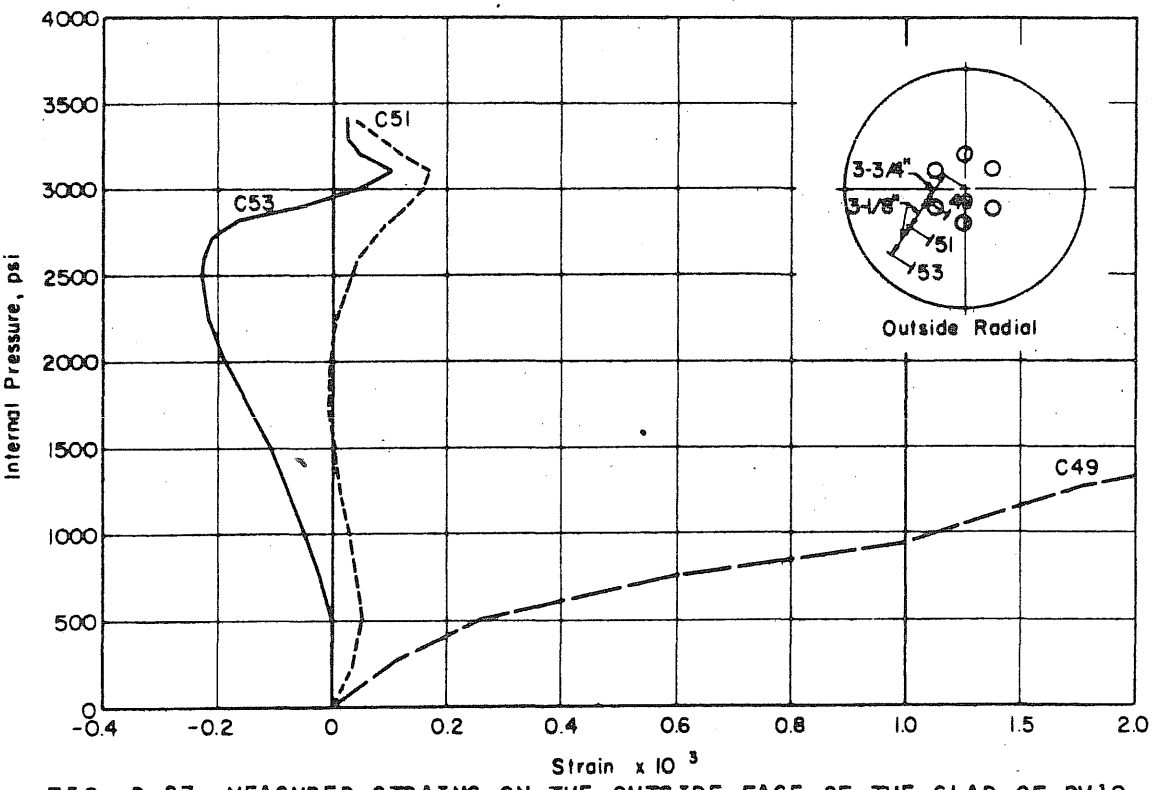

FIG. B.27 MEASURED STRAINS ON THE OUTSIDE FACE OF THE SLAB OF PV19

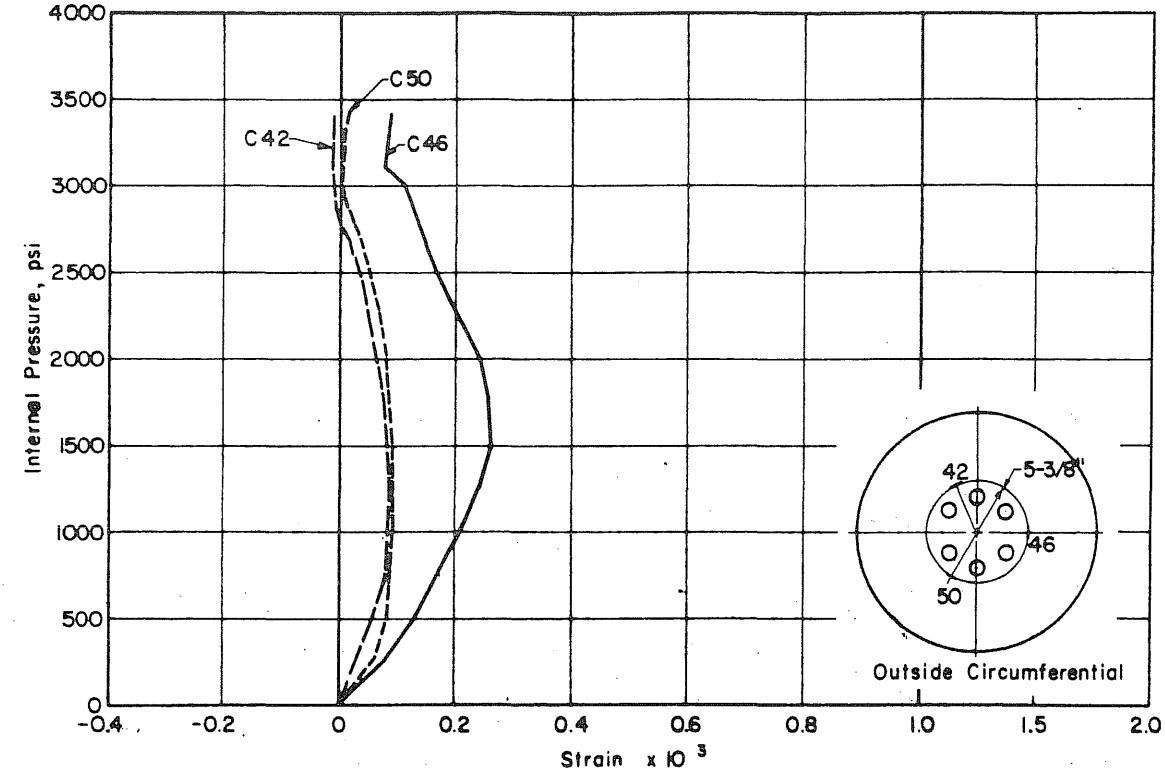

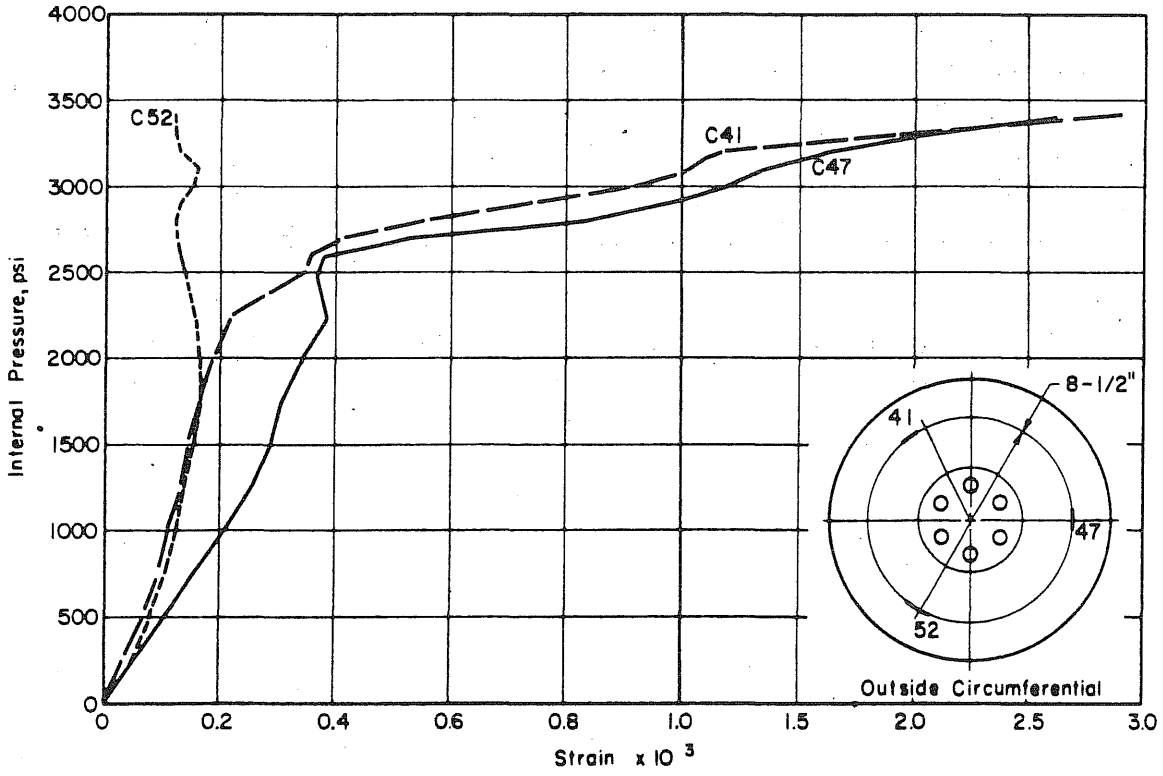

FIG. B.27 (Continued) MEASURED STRAINS ON THE OUTSIDE FACE OF THE SLAB OF PV19

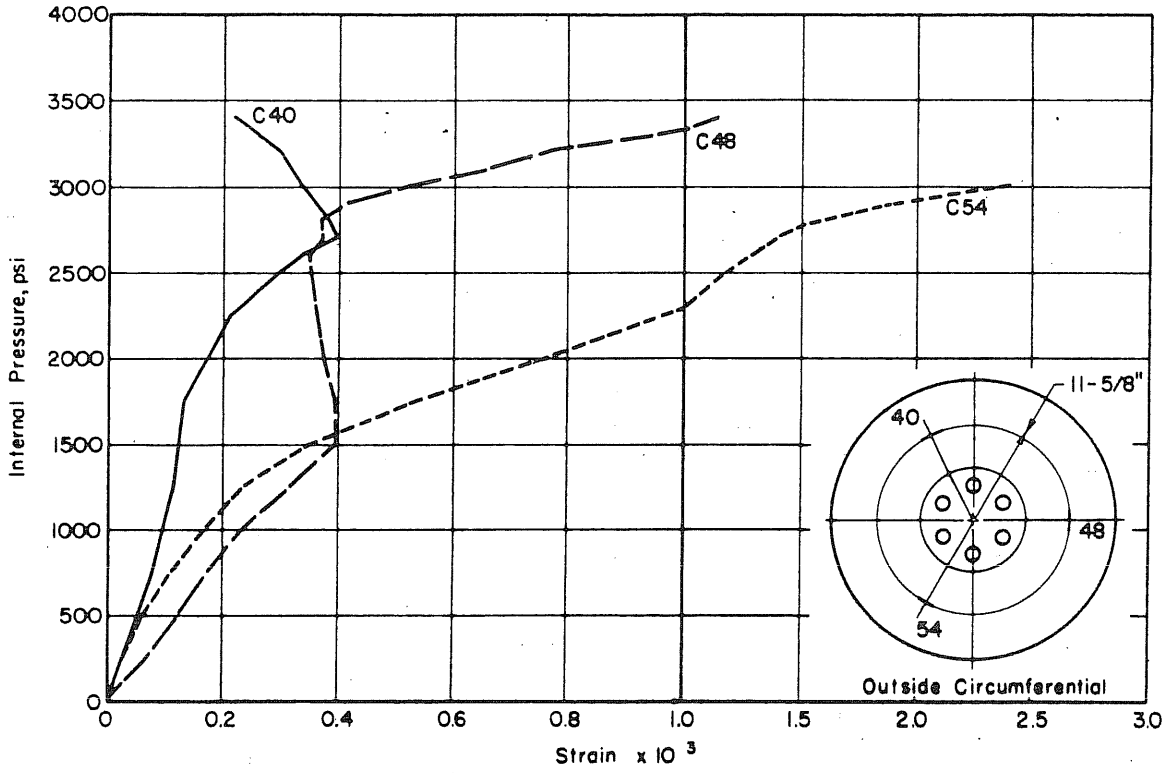

FIG. B.27 (Continued) MEASURED STRAINS ON THE OUTSIDE FACE OF THE SLAB OF PV19

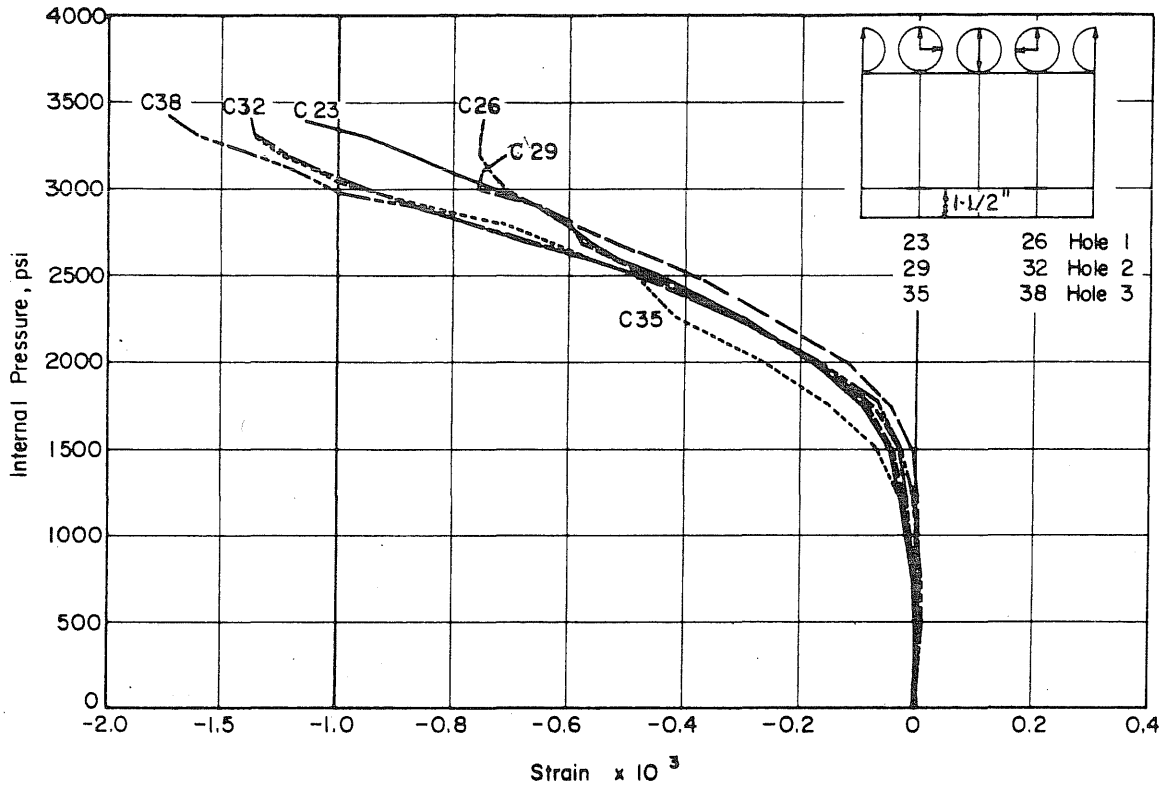

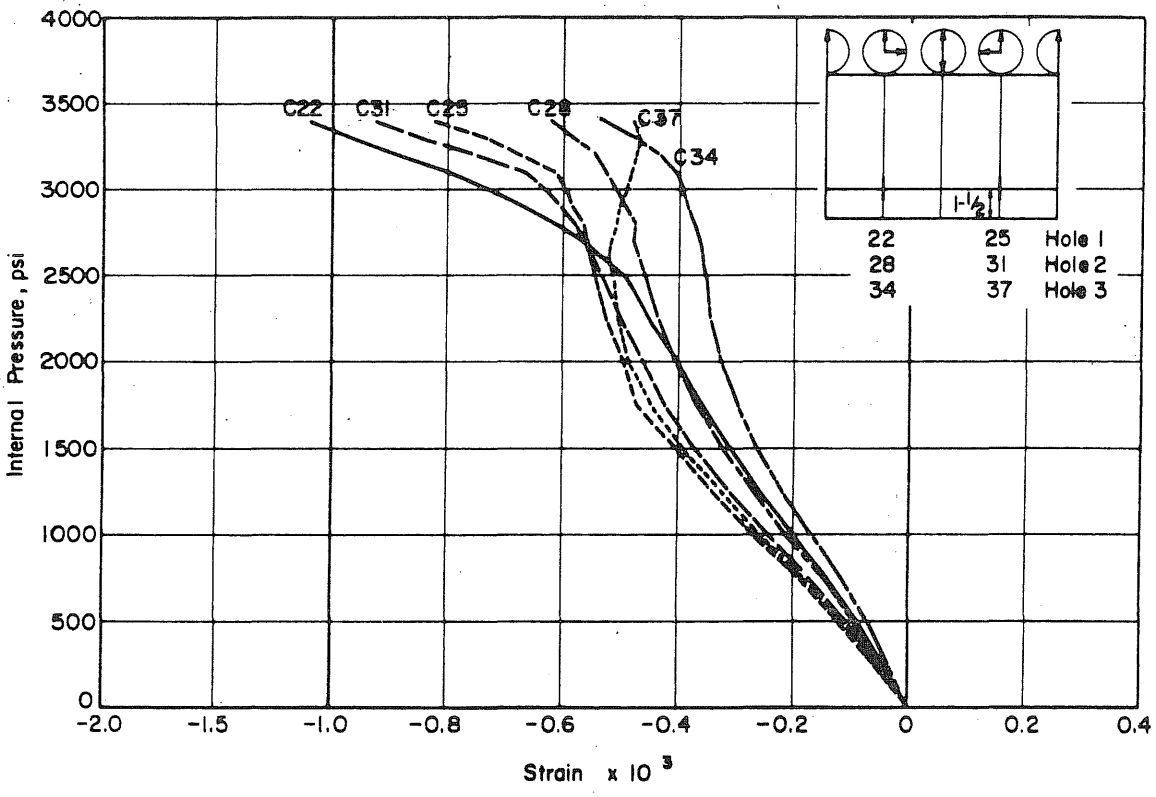

FIG. B.28 MEASURED STRAINS IN THE PENETRATIONS OF PV19

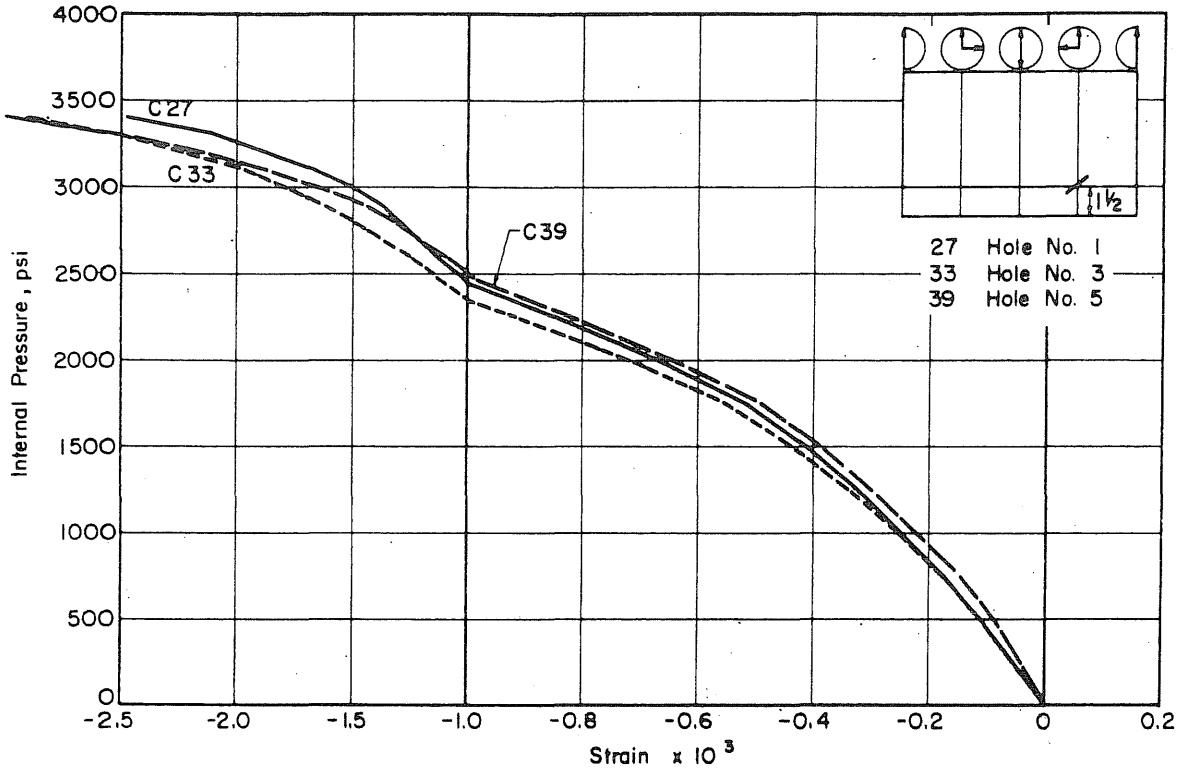

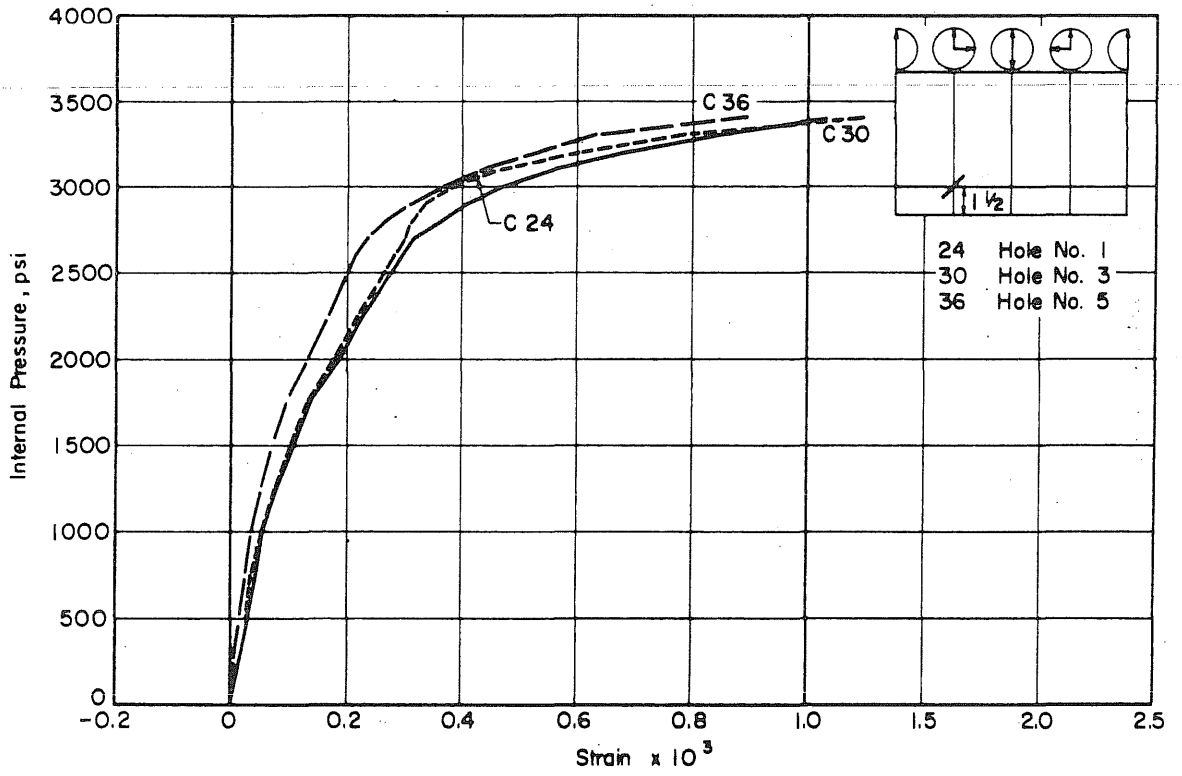

FIG. B.28 (Continued) MEASURED STRAINS IN THE PENETRATIONS OF PV19

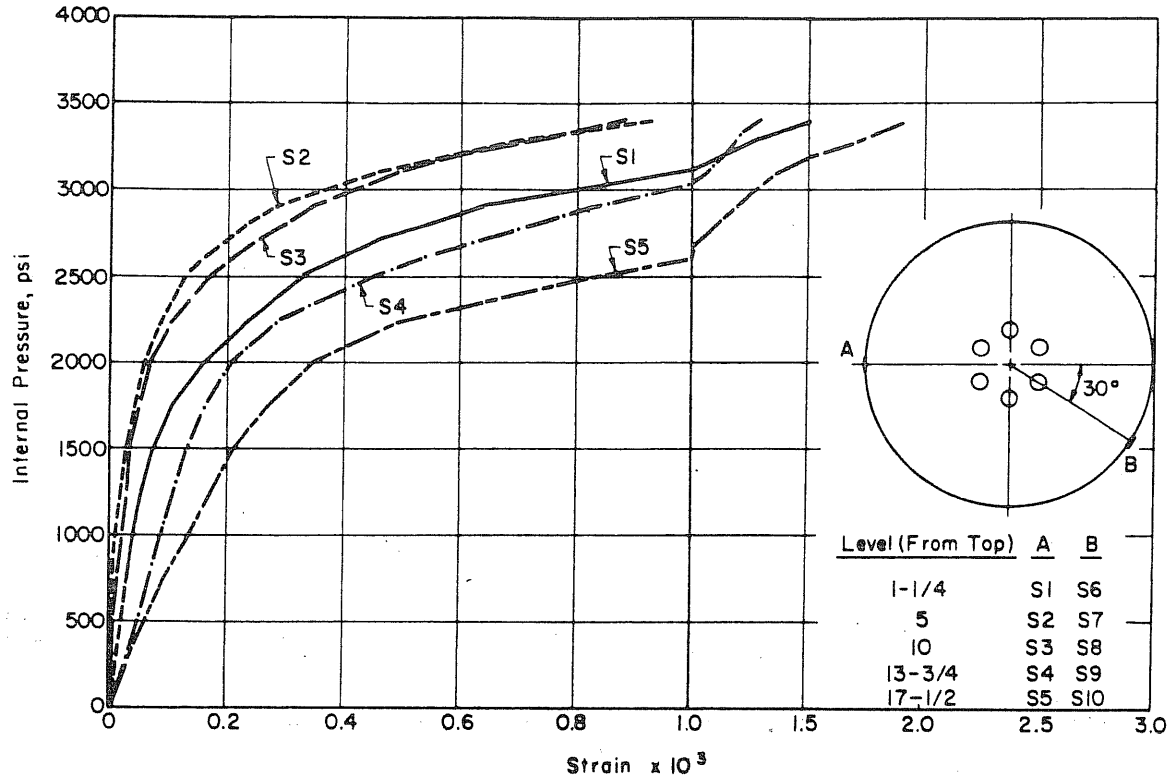

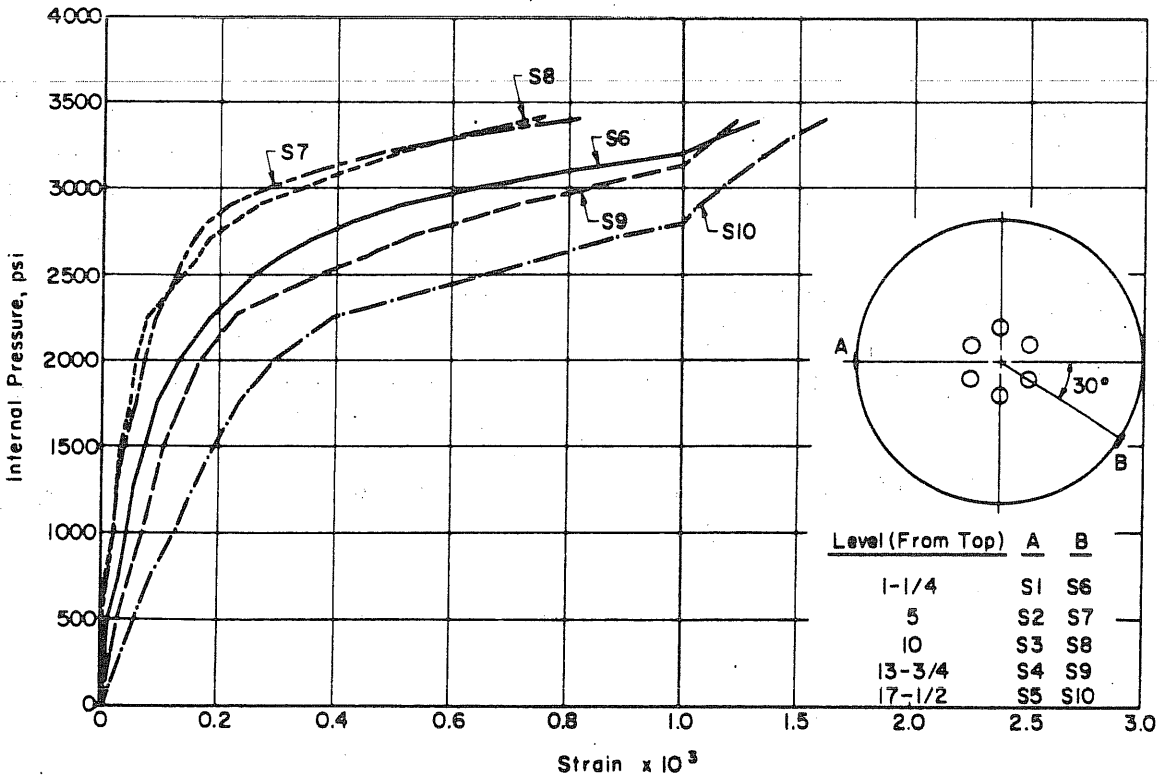

FIG. B.29 MEASURED STRAINS IN THE CIRCUMFERENTIAL PRESTRESSING WIRE OF PV19

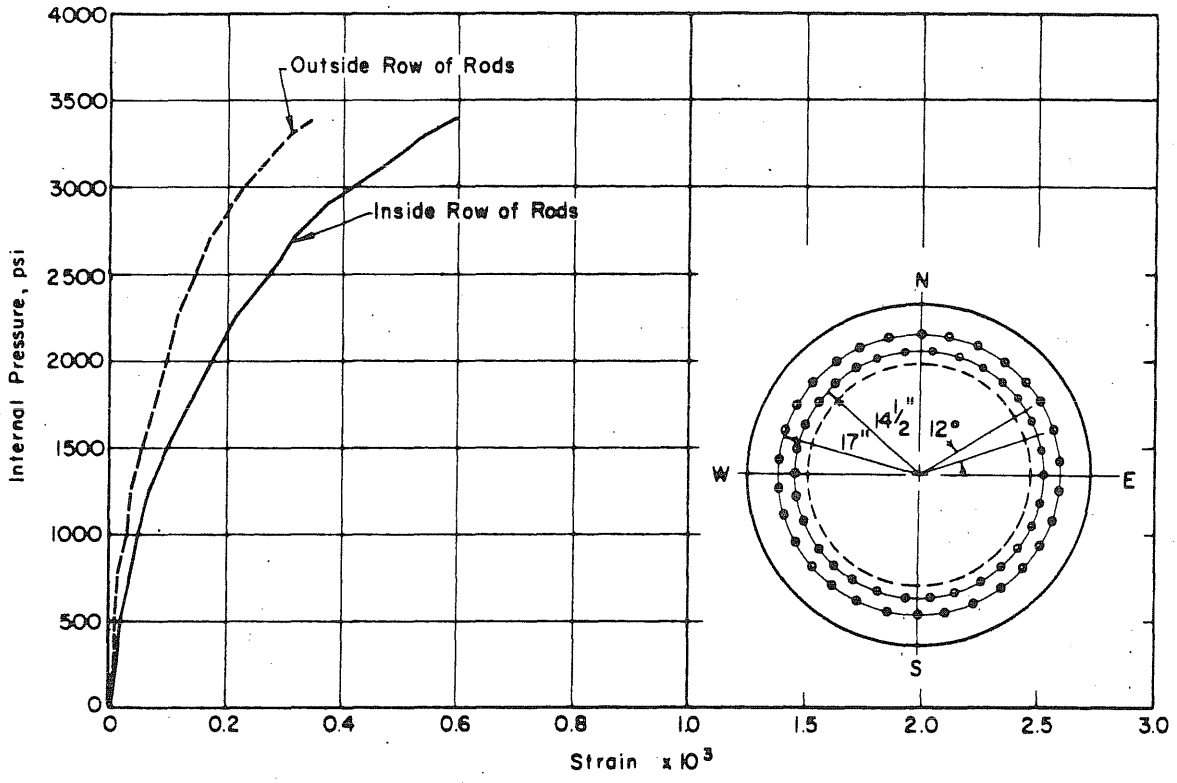

FIG. B.30 MEASURED STRAINS IN THE LONGITUDINAL PRESTRESSING RODS OF PV19

B.6 Test Vessel PV20

The vessel was initially pressurized hydraulically to reduce the amount of compressed gas in the vessel and thus reducing the amount of energy that is released at failure. At 2000 psi internal pressure a change to pneumatic pressure was made, thus reducing the risk of a sudden drop in internal pressure before the failure pressure was reached. Failure occurred at 3300 psi internal pressure while readings were taken.

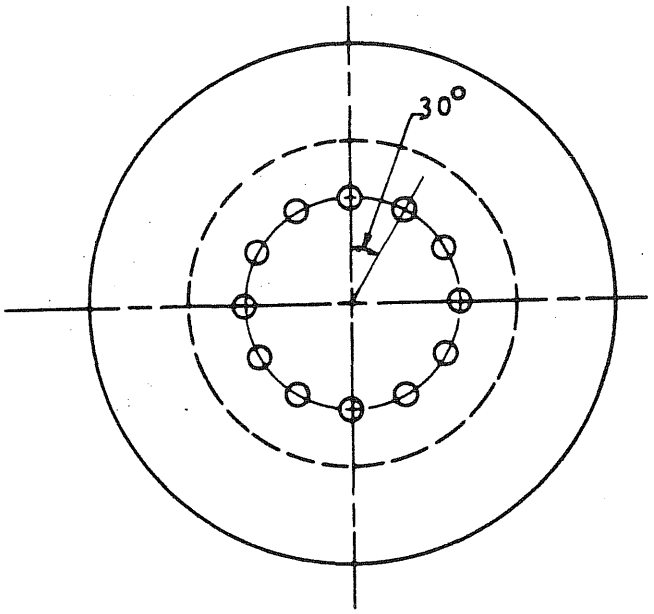

FIG. B.31 VESSEL PV20 WITH TWELVE 2-in. PENETRATIONS ON AN 8-in. RADIUS

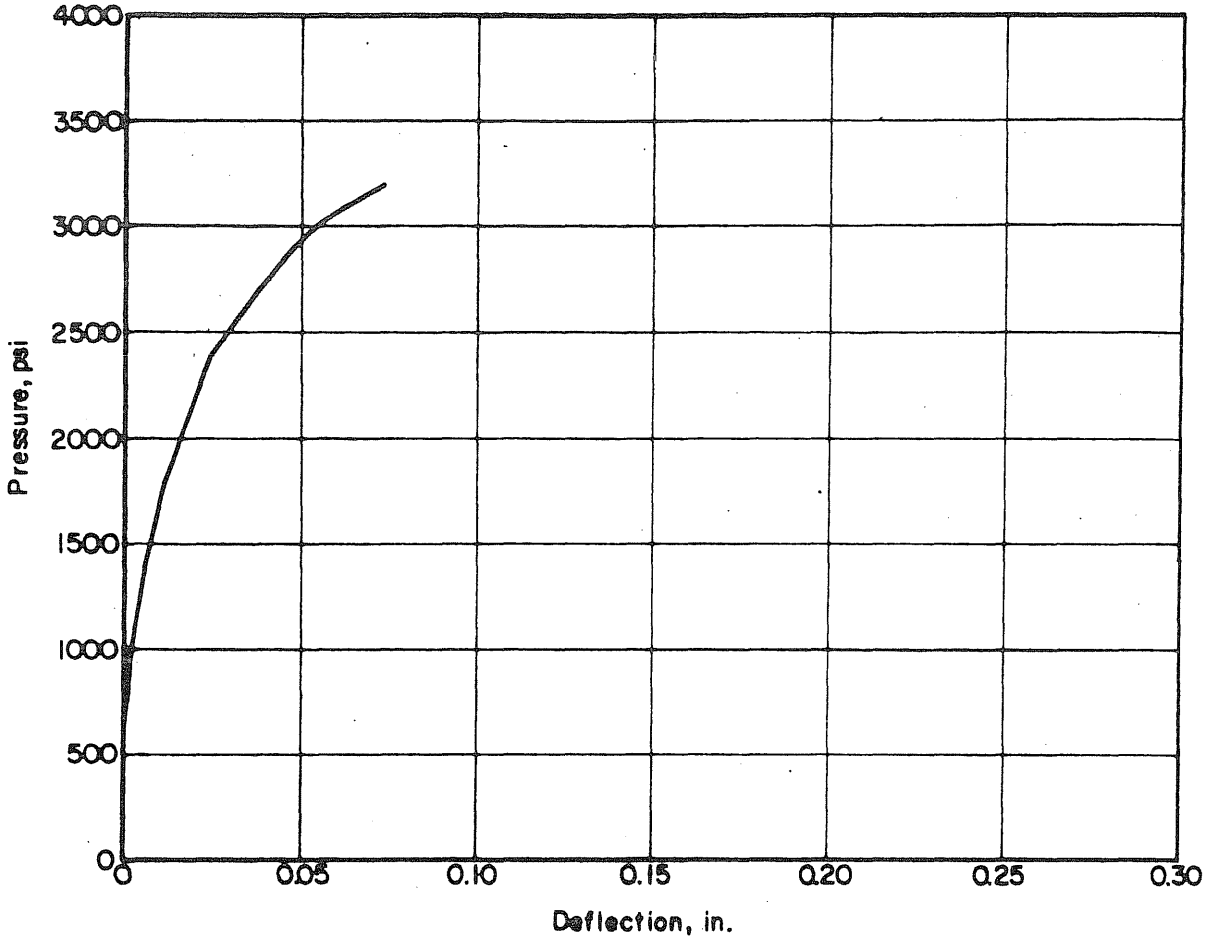

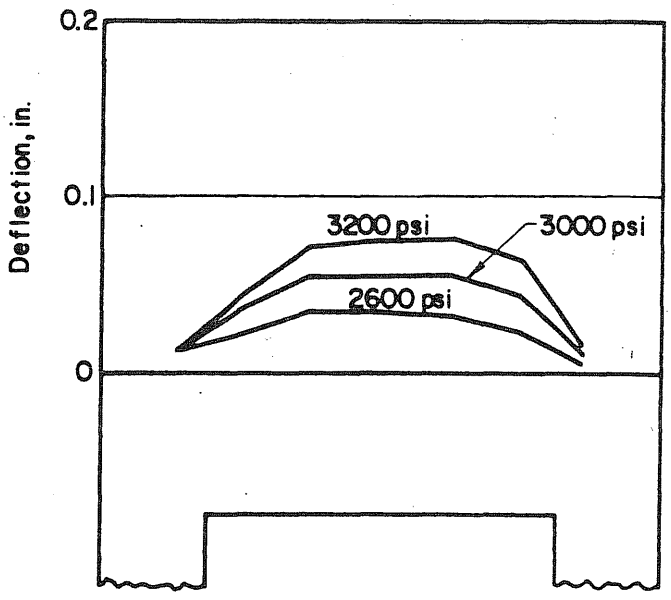

FIG. B.32 MEASURED DEFLECTION PROFILES AND DEFLECTION AT THE CENTER OF THE END SLAB OF PV20

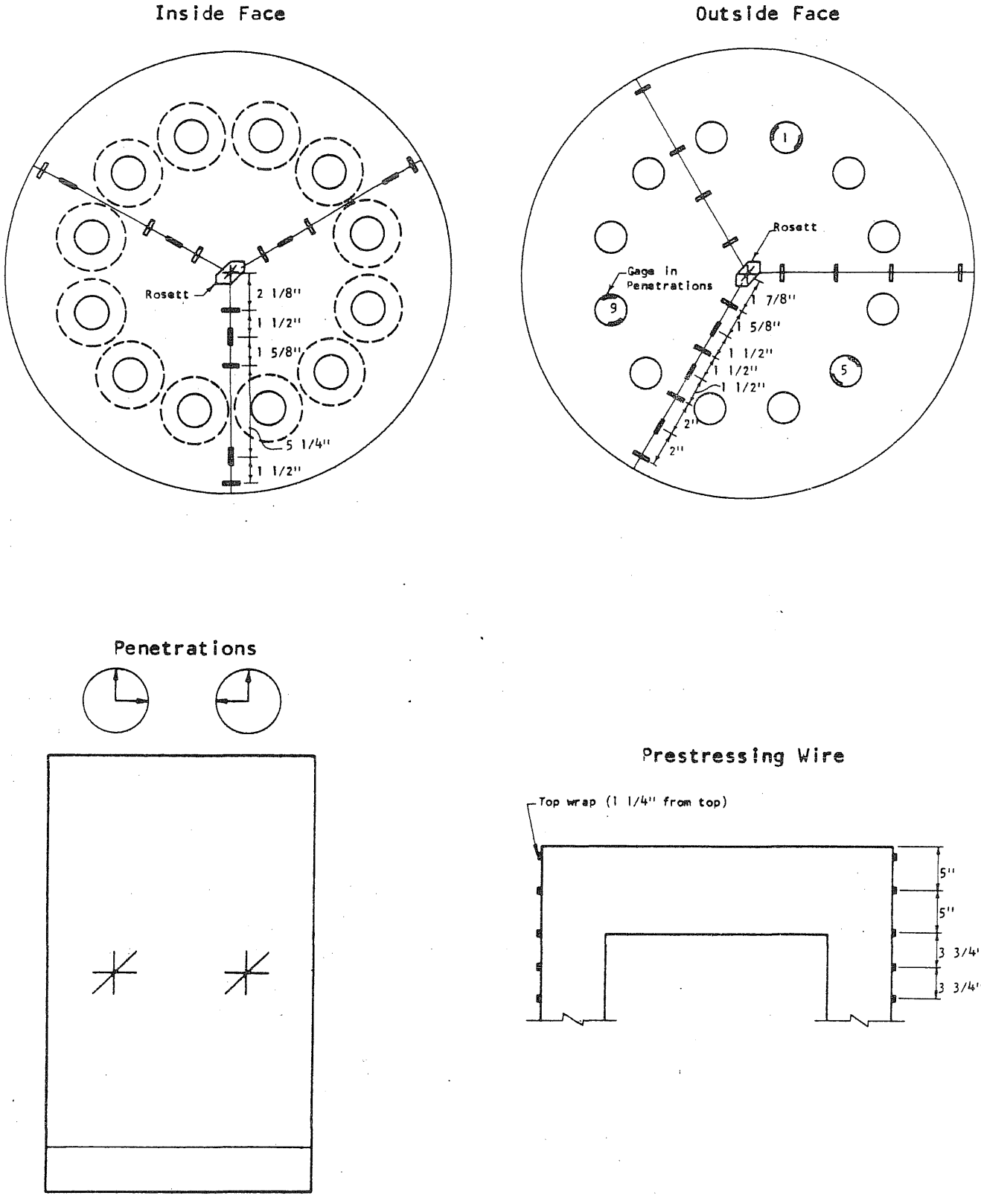

FIG. B.33 STRAIN GAGE LOCATION ON PV20

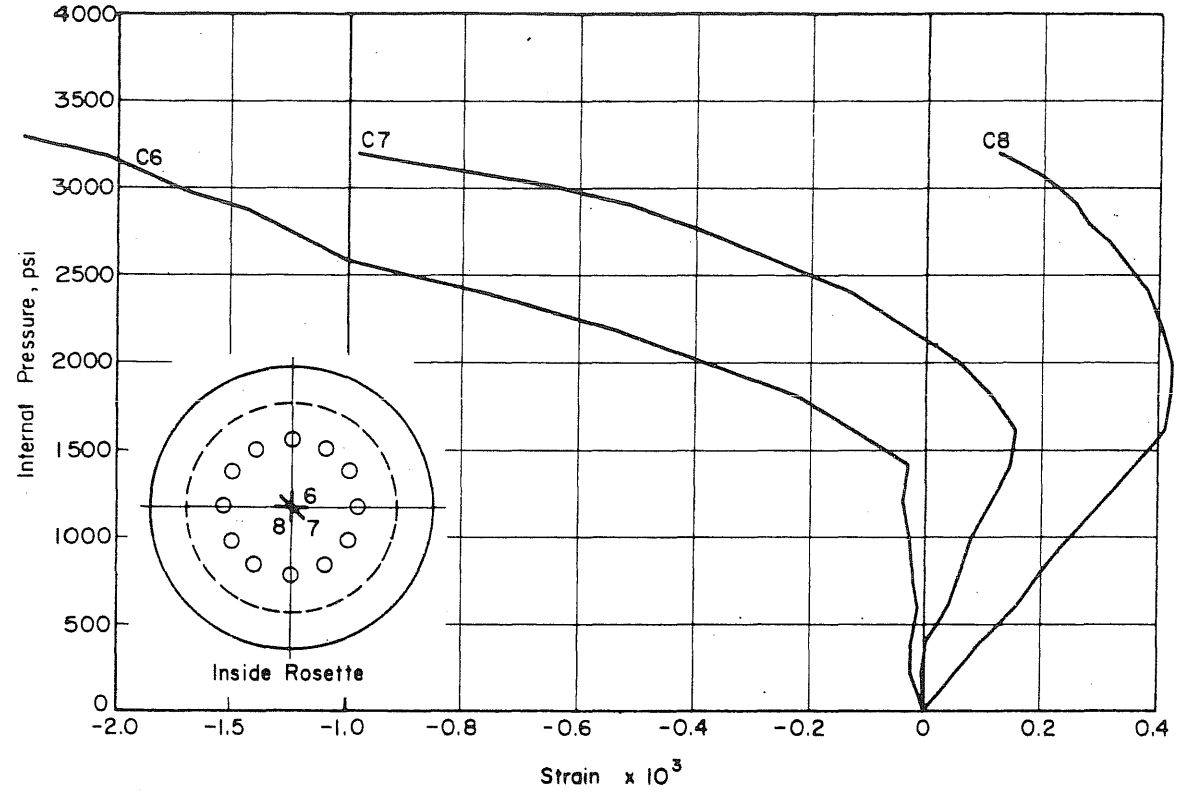

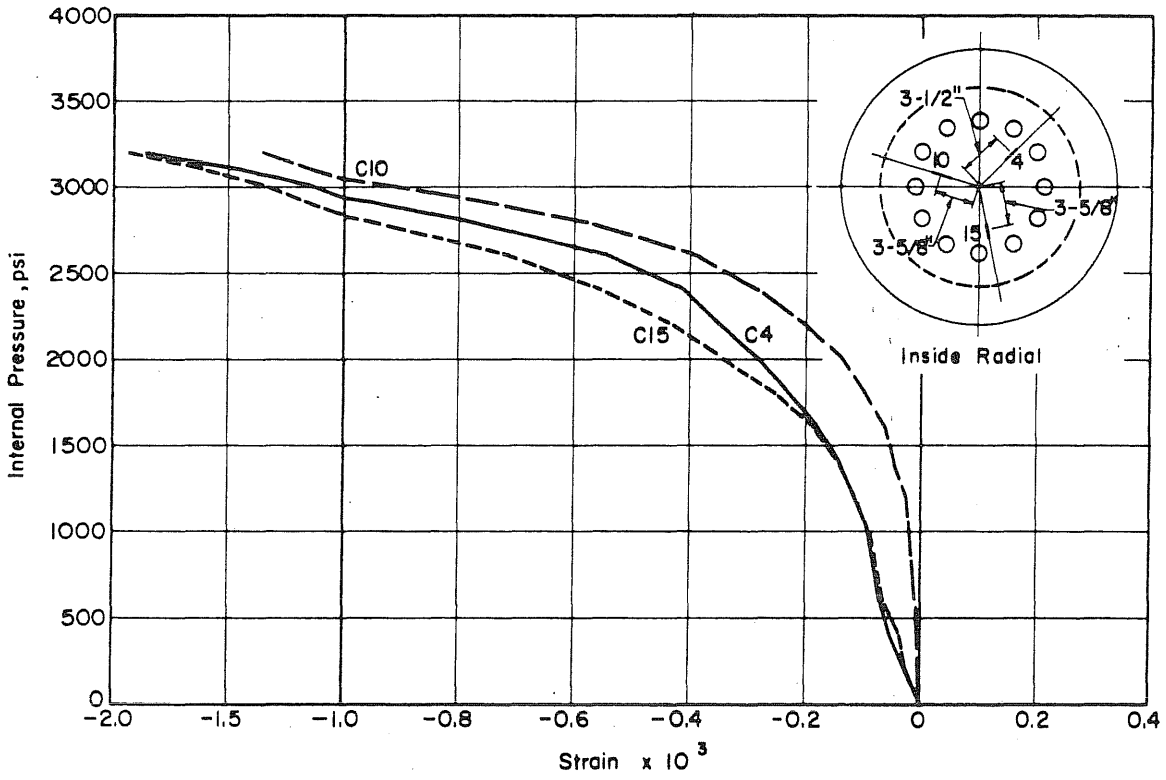

FIG. B.34 MEASURED STRAINS ON THE INSIDE FACE OF THE SLAB OF PV20

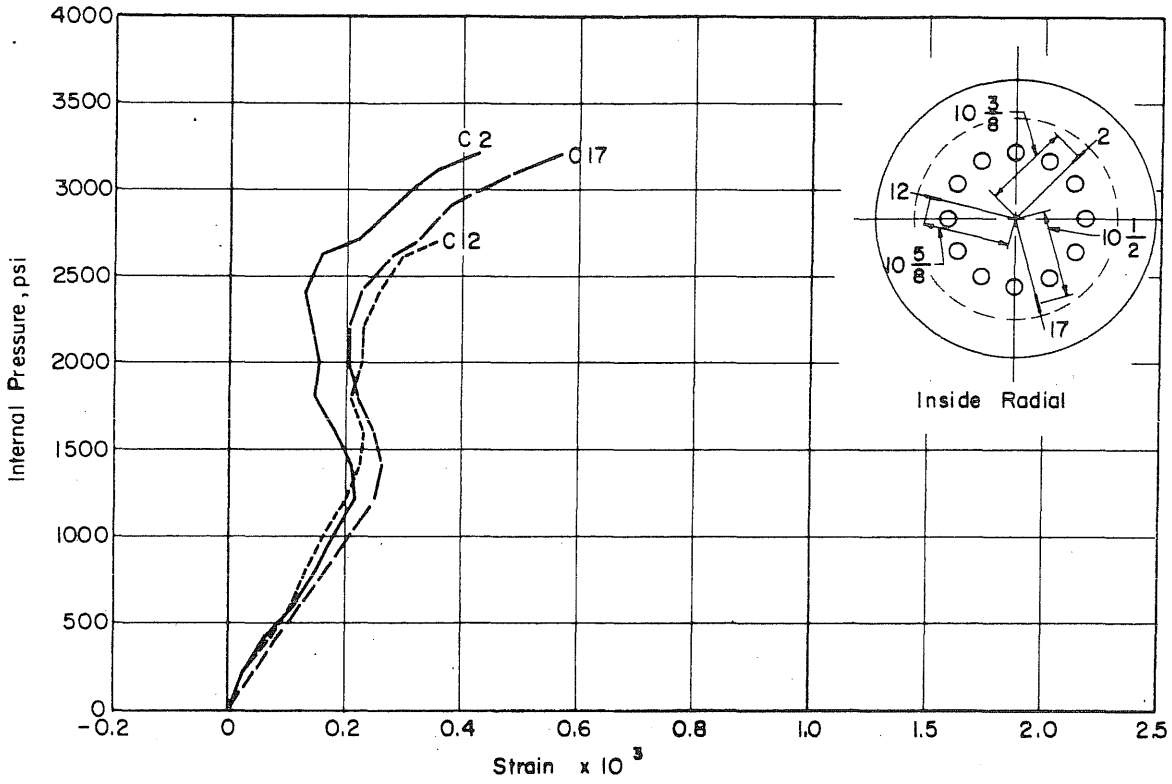

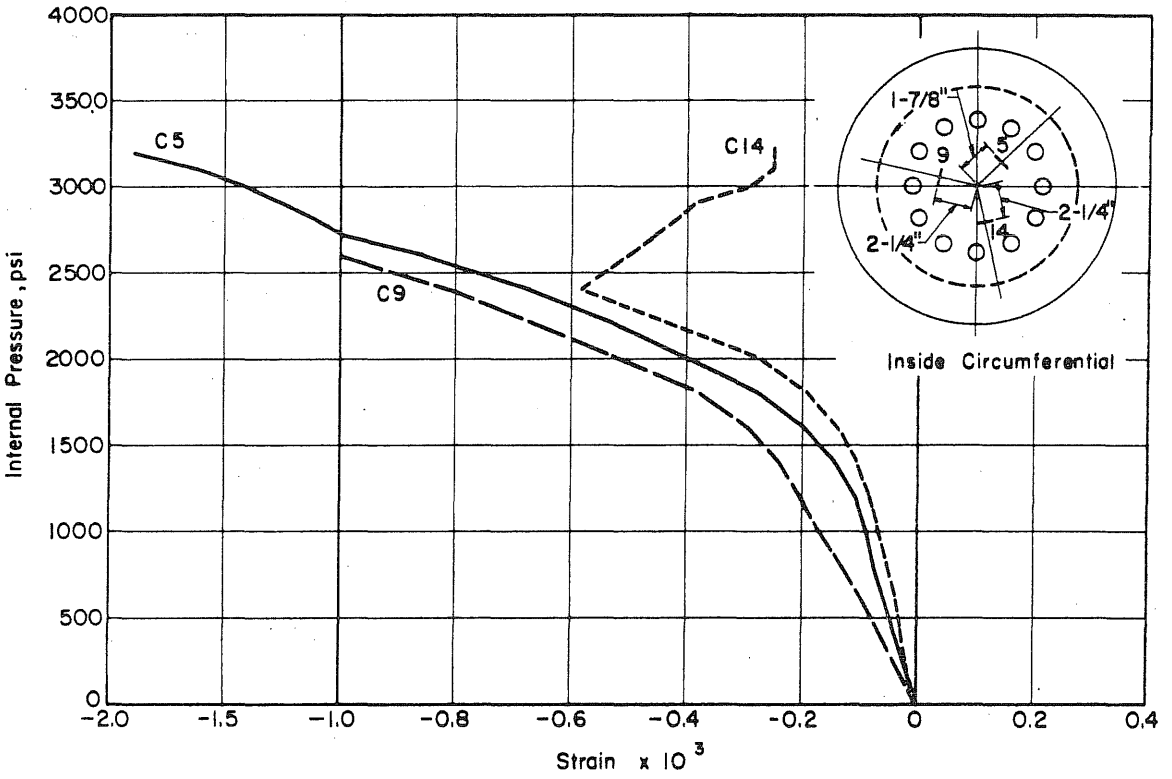

FIG. B.34 (Continued) MEASURED STRAINS ON THE INSIDE FACE OF THE SLAB OF PV20

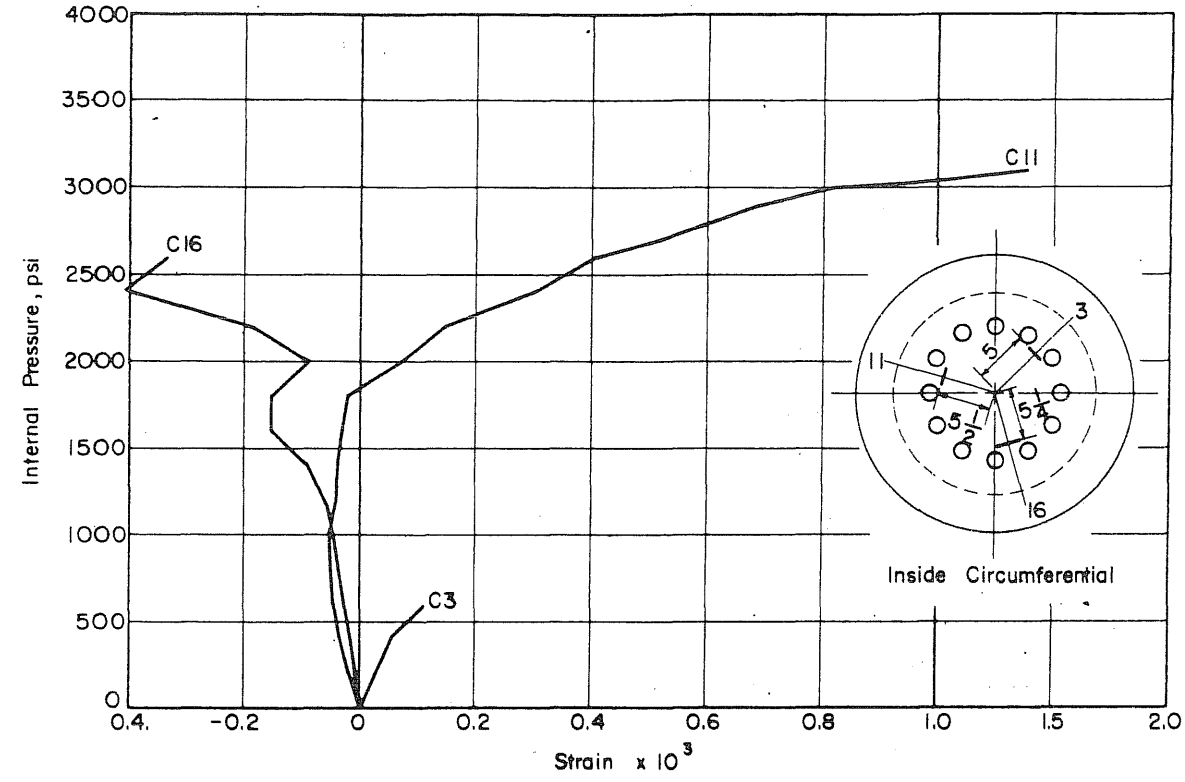

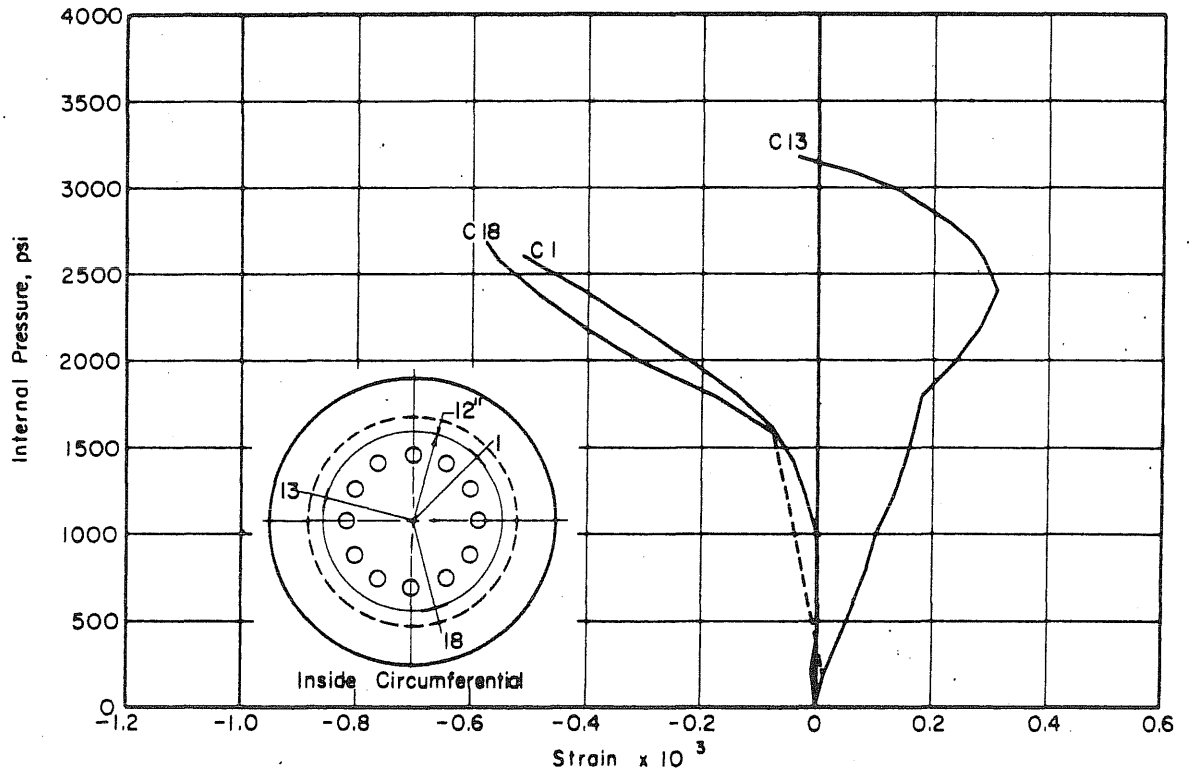

FIG. B.34 (Continued) MEASURED STRAINS ON THE INSIDE FACE OF THE SLAB OF PV20

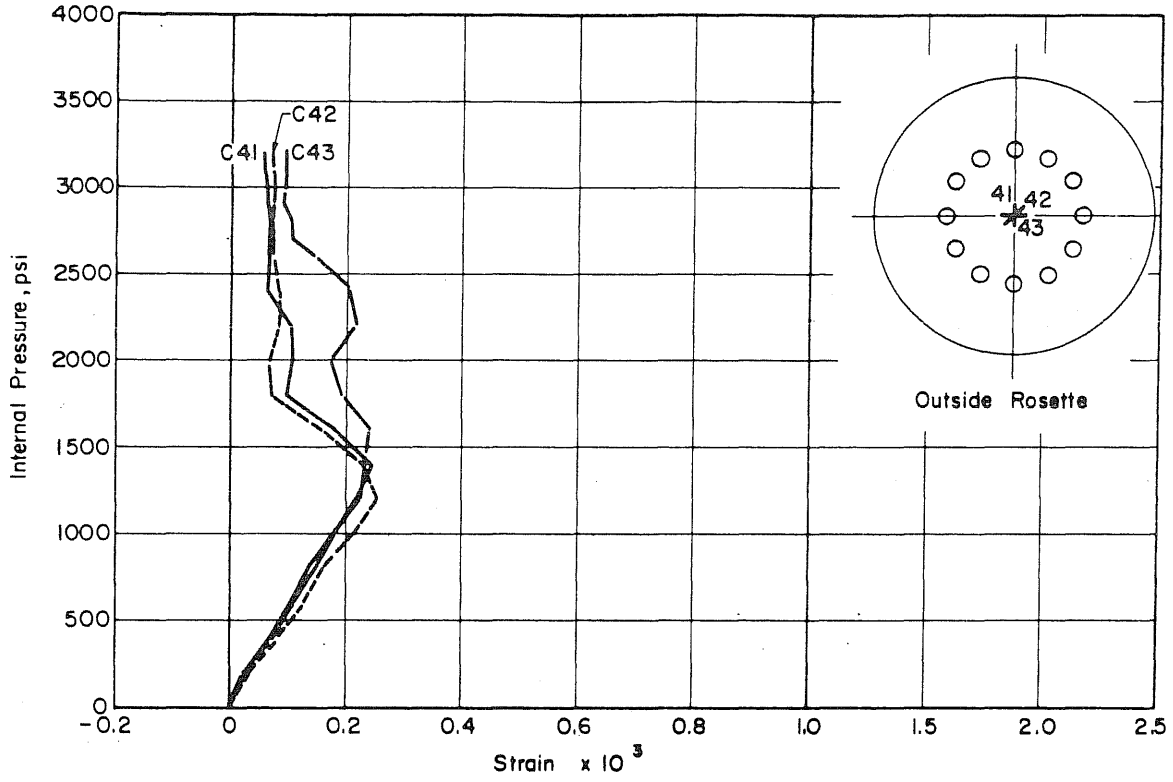

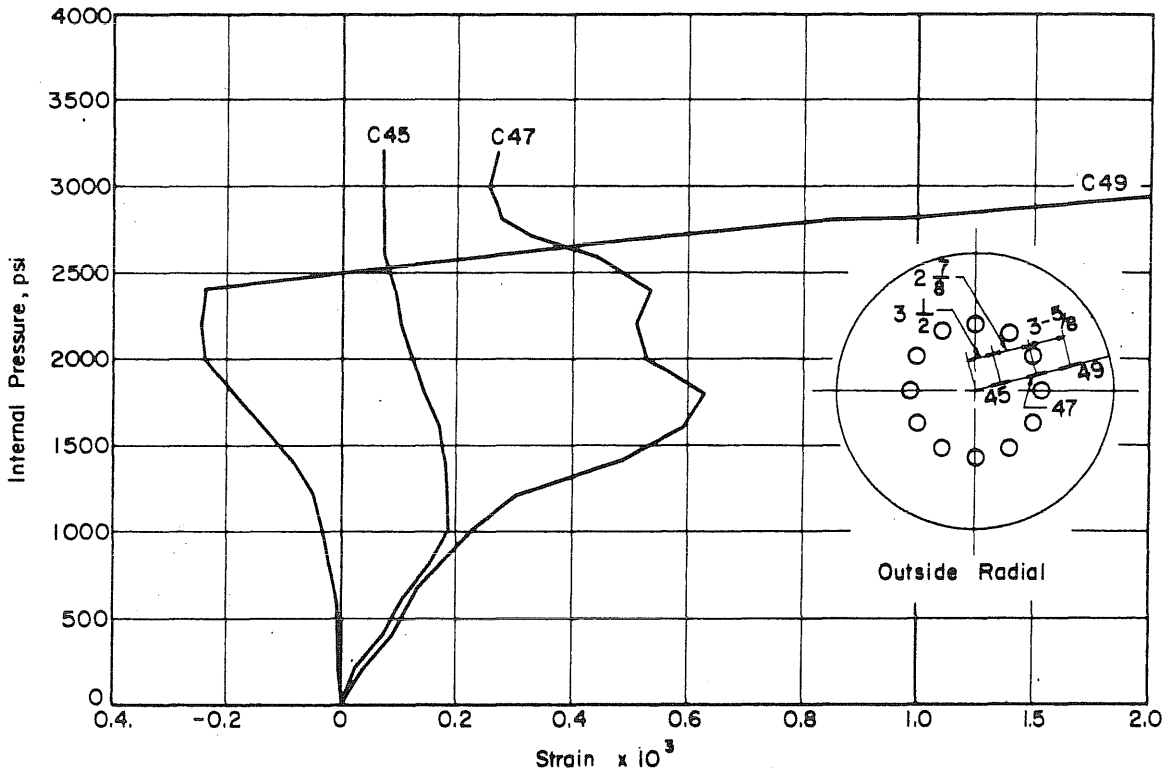

FIG. B.35 MEASURED STRAINS ON THE OUTSIDE FACE OF THE SLAB OF PV20

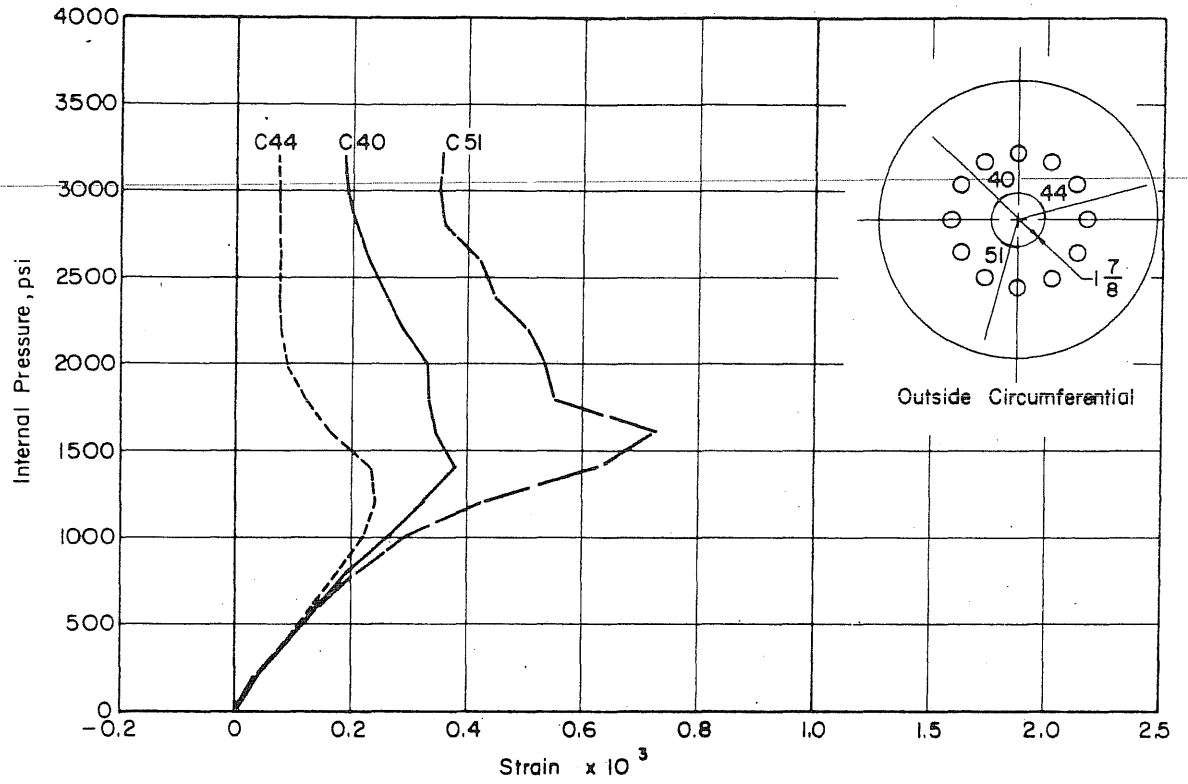

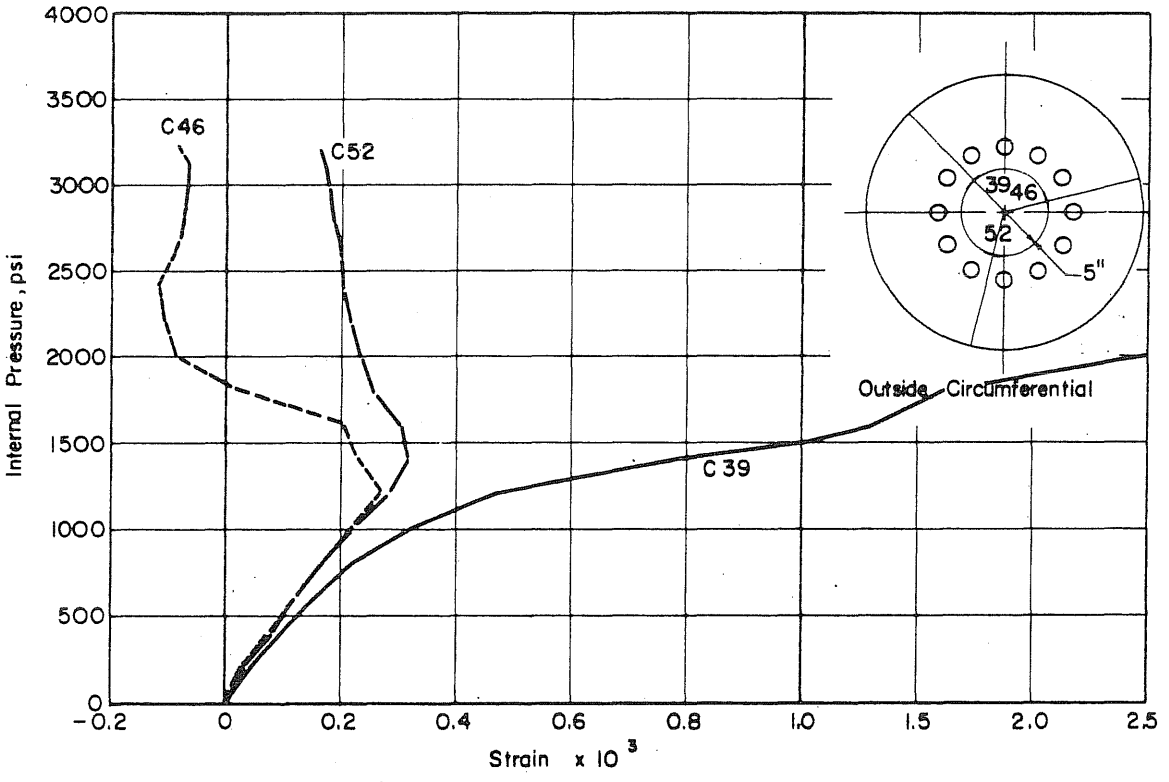

FIG. B.35 (Continued) MEASURED STRAINS ON THE OUTSIDE FACE OF THE SLAB OF PV20

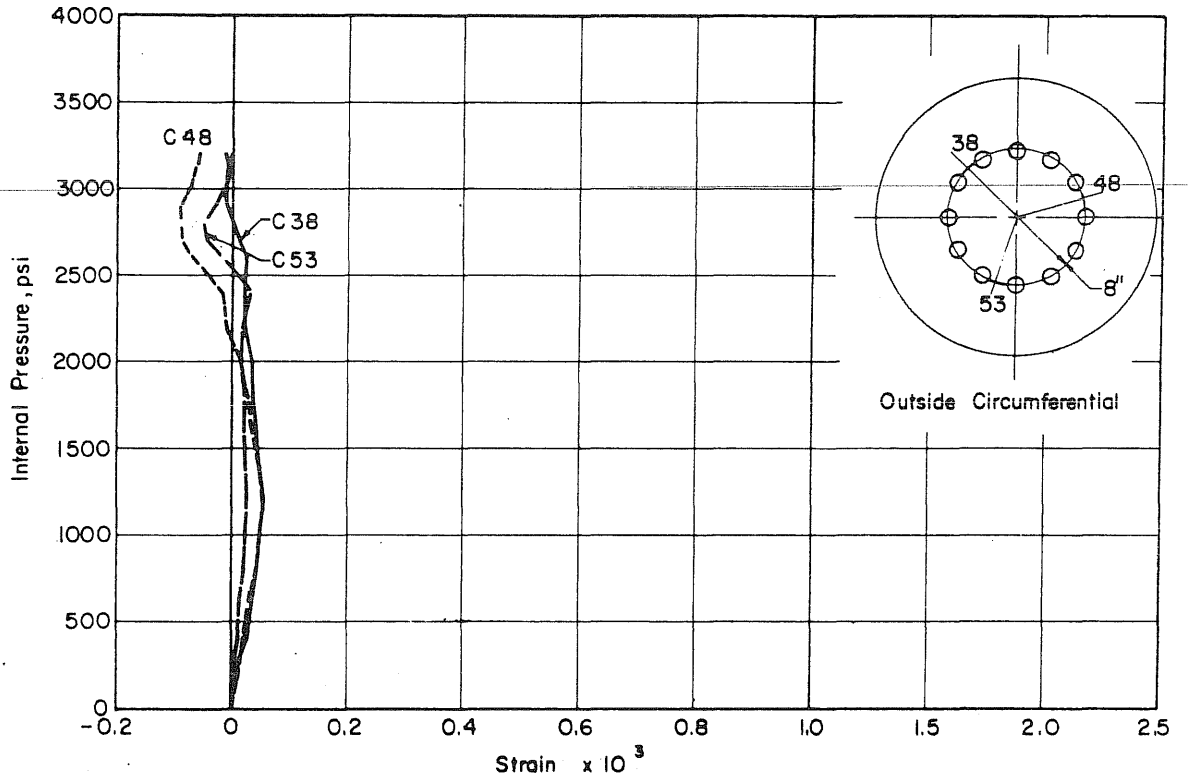

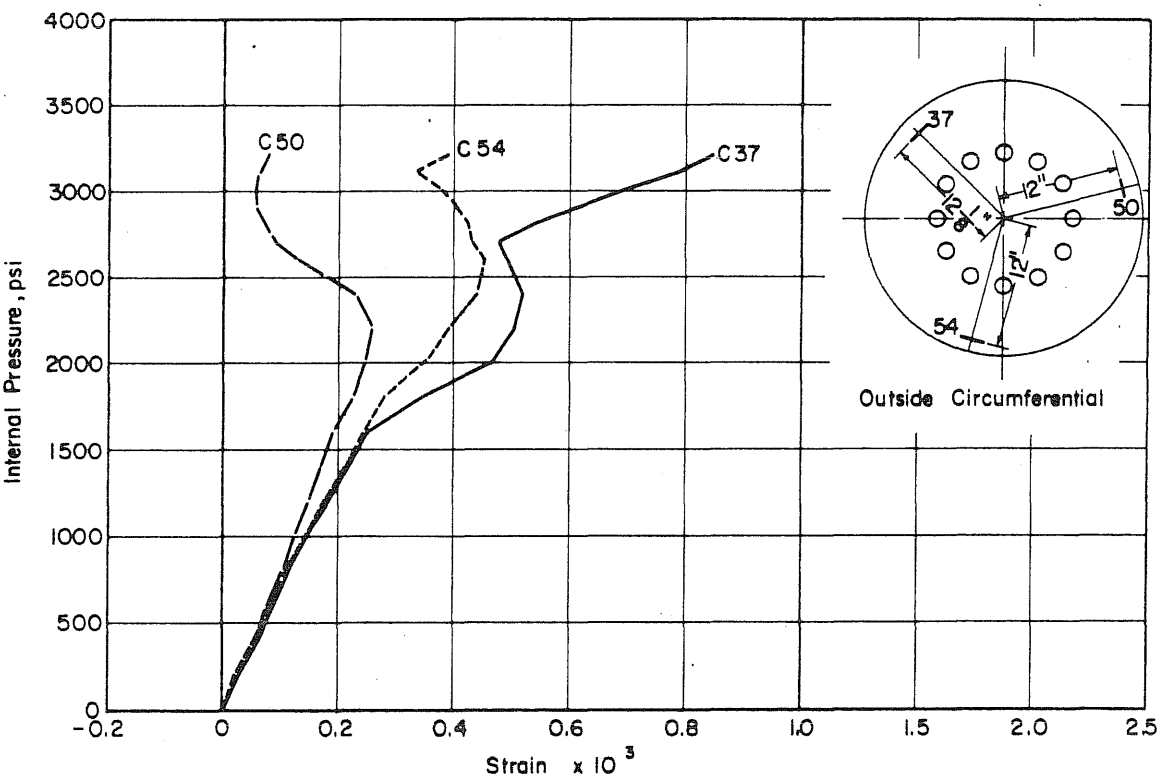

FIG. B.35 (Continued) MEASURED STRAINS ON THE OUTSIDE FACE OF THE SLAB OF PV20

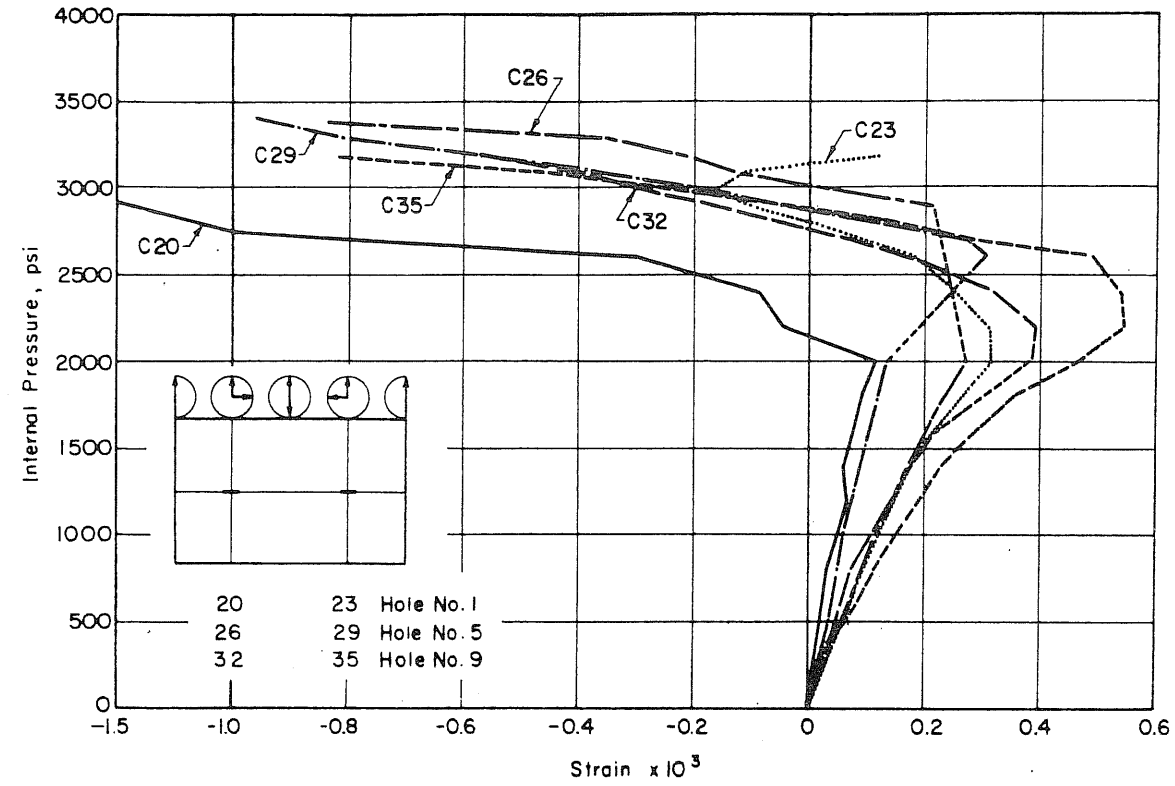

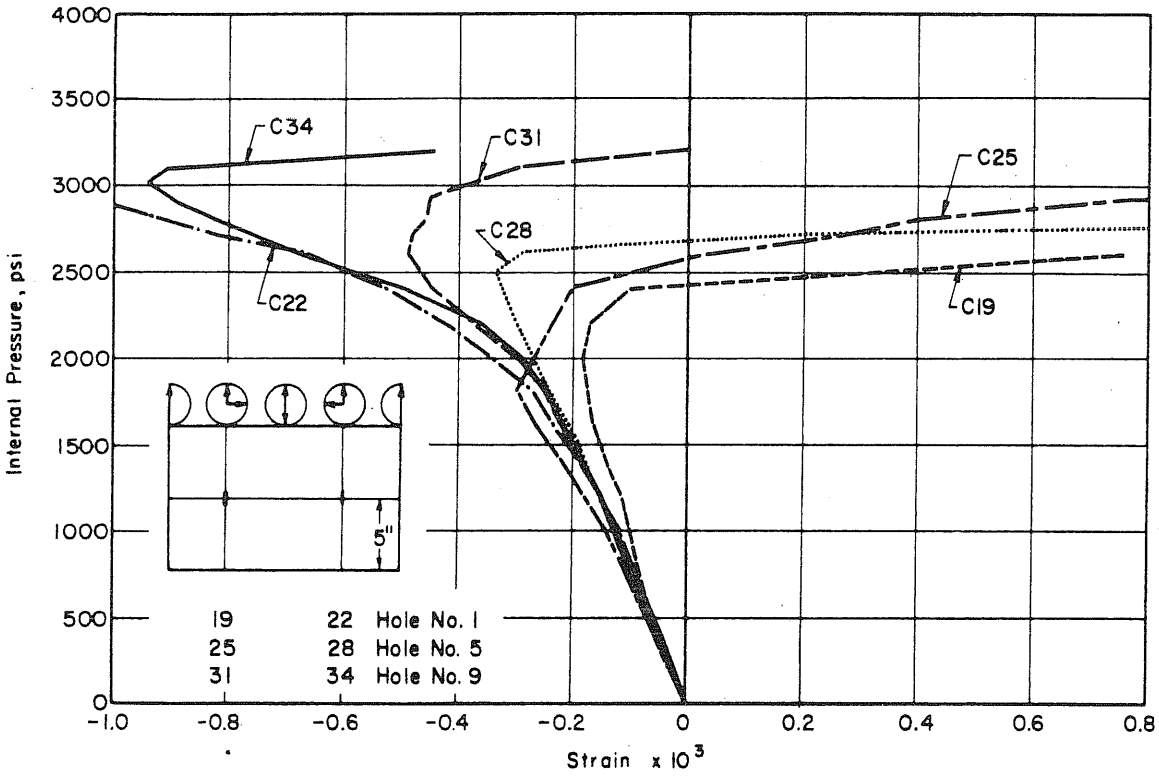

FIG. B.36 MEASURED STRAINS IN THE PENETRATIONS OF PV20

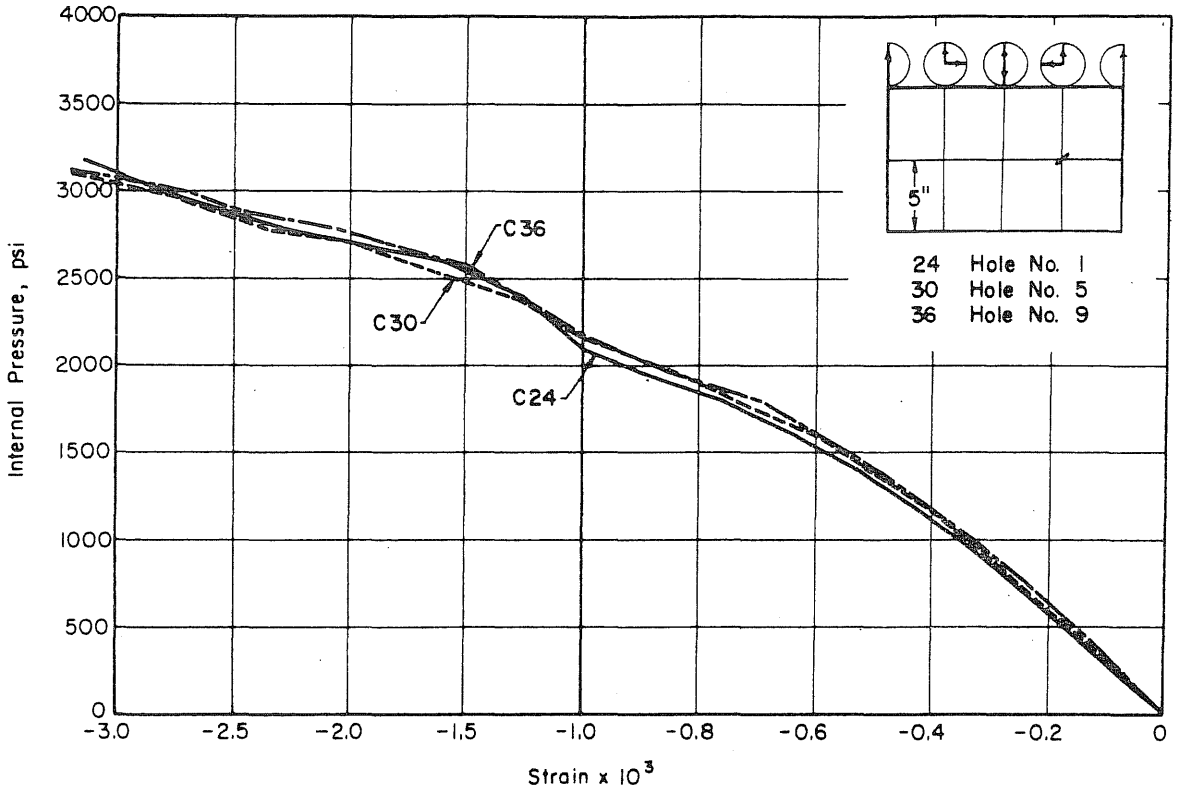

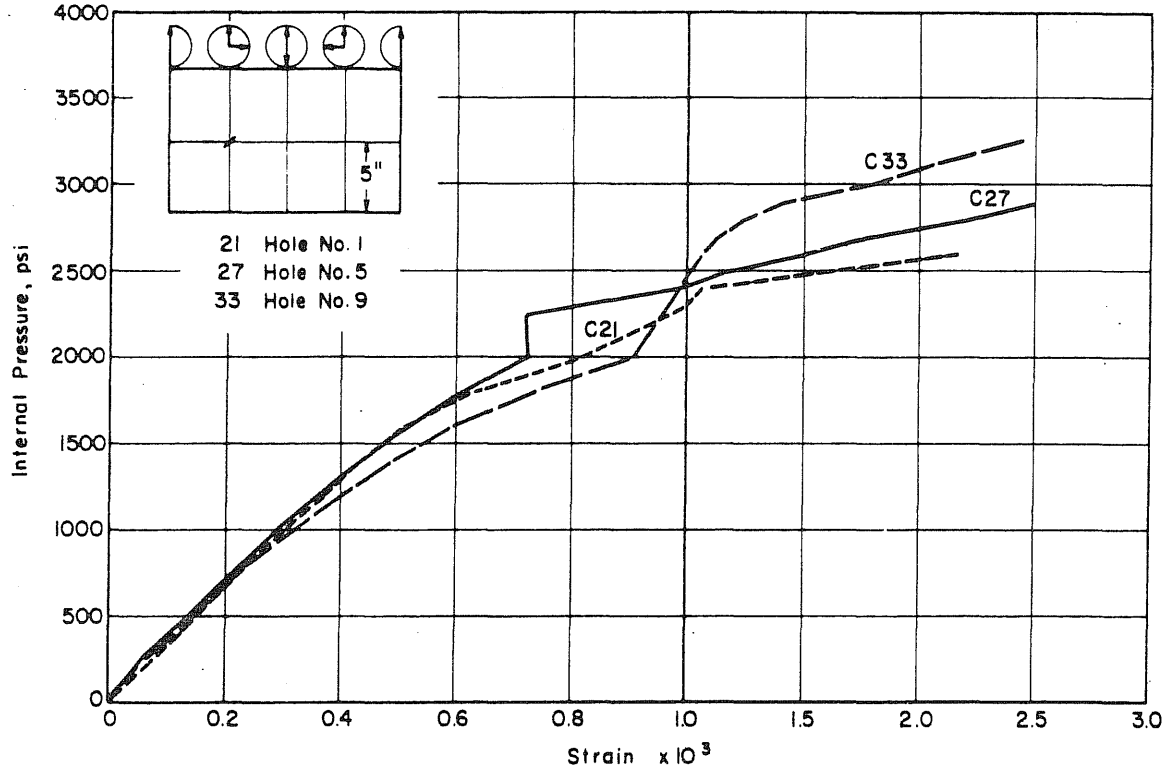

FIG. B.36 (Continued) MEASURED STRAINS IN THE PENETRATIONS OF PV20

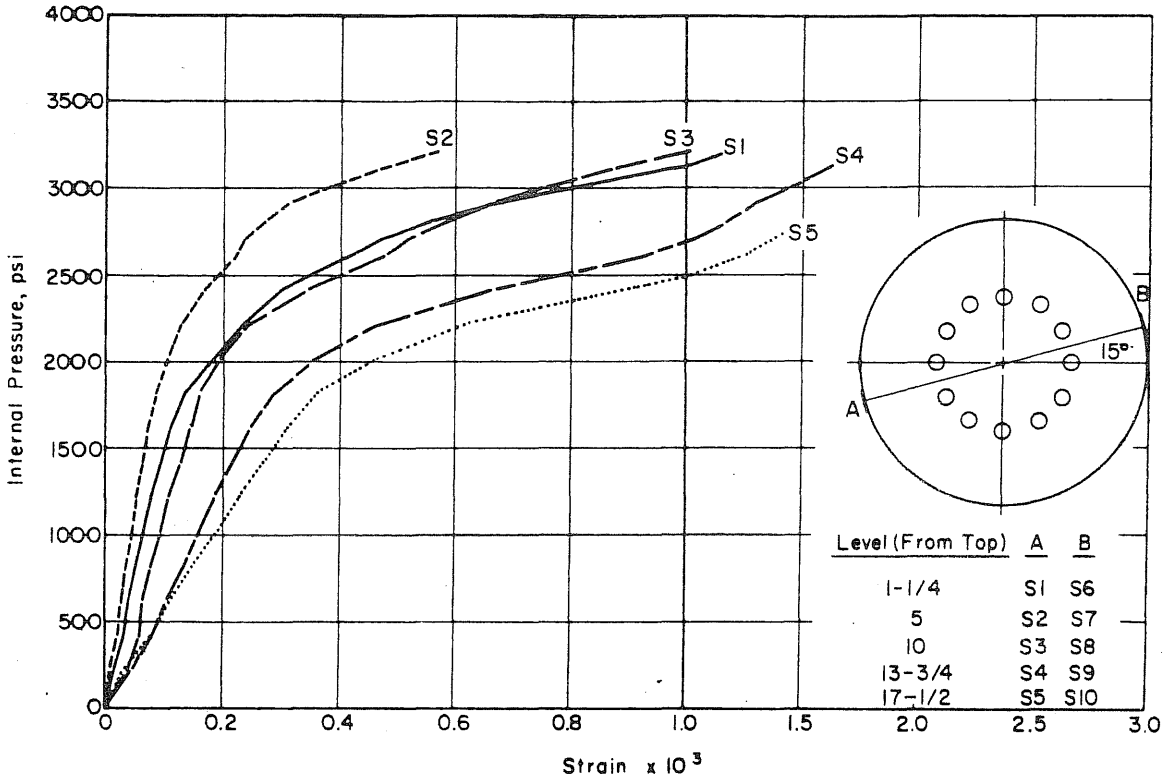

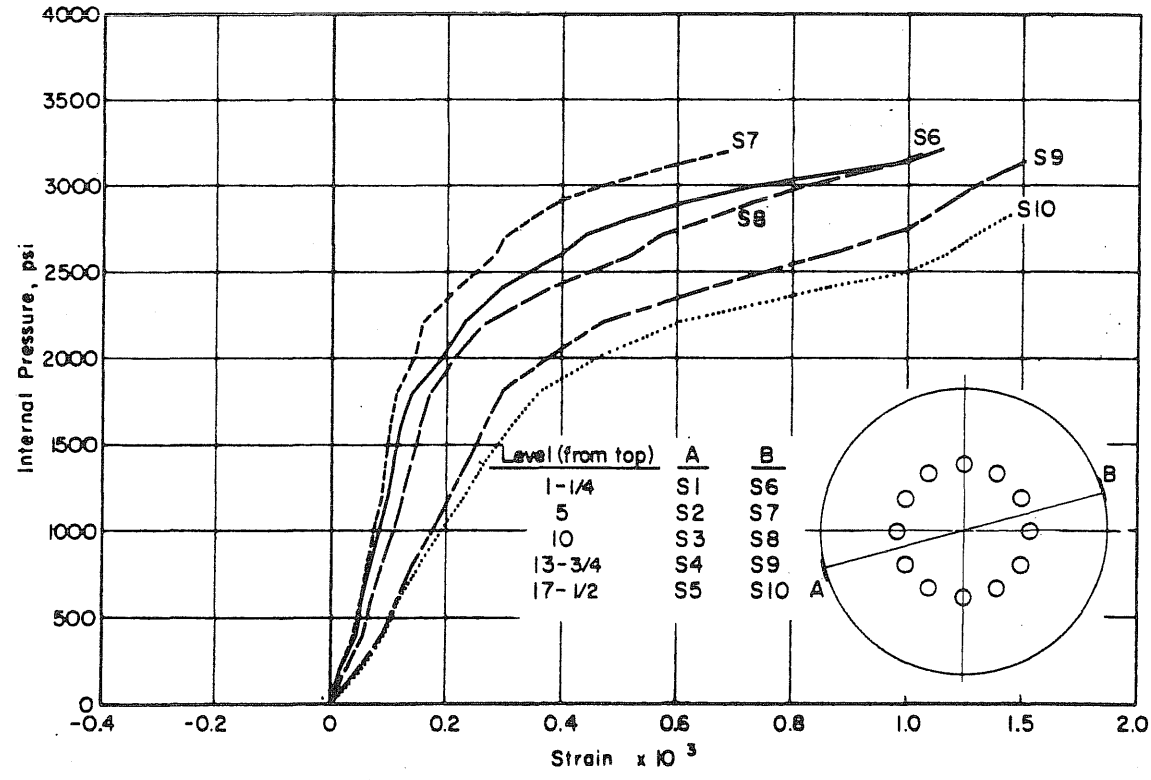

FIG. B.37 MEASURED STRAINS IN THE CIRCUMFERENTIAL PRESTRESSING WIRE OF PV20

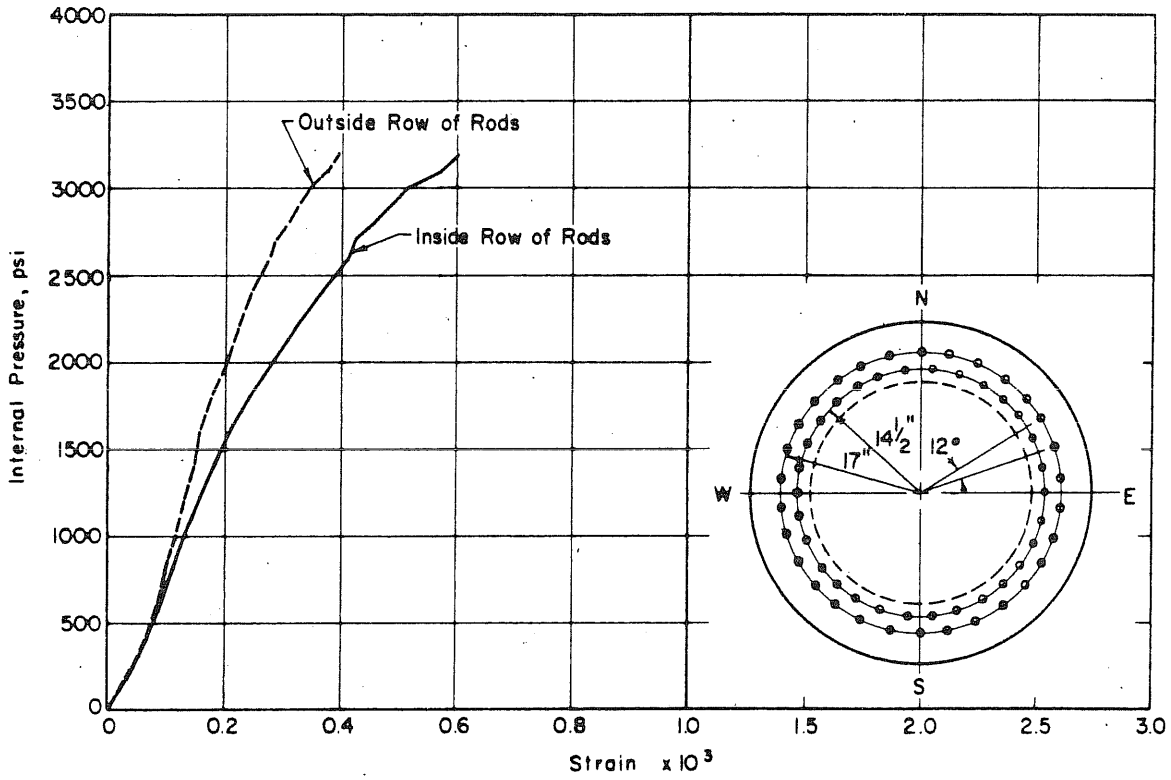

FIG. B.38 MEASURED STRAINS IN THE LONGITUDINAL PRESTRESSING RODS OF PV20

B.7 Test Vessel PV21

The course of events during this test was similar to the test of Vessel PV20 and failure occurred at 3300 psi while readings were taken.

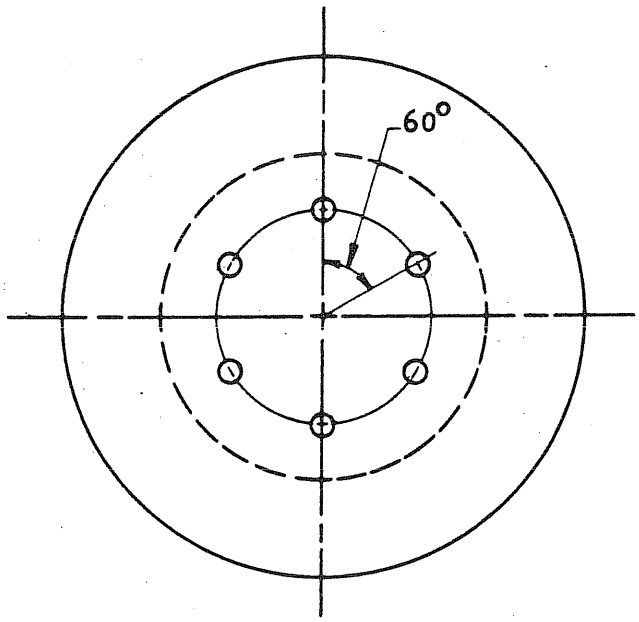

FIG. B.39 VESSEL PV21 WITH SIX 2-in. PENETRATIONS ON AN 8-in. RADIUS

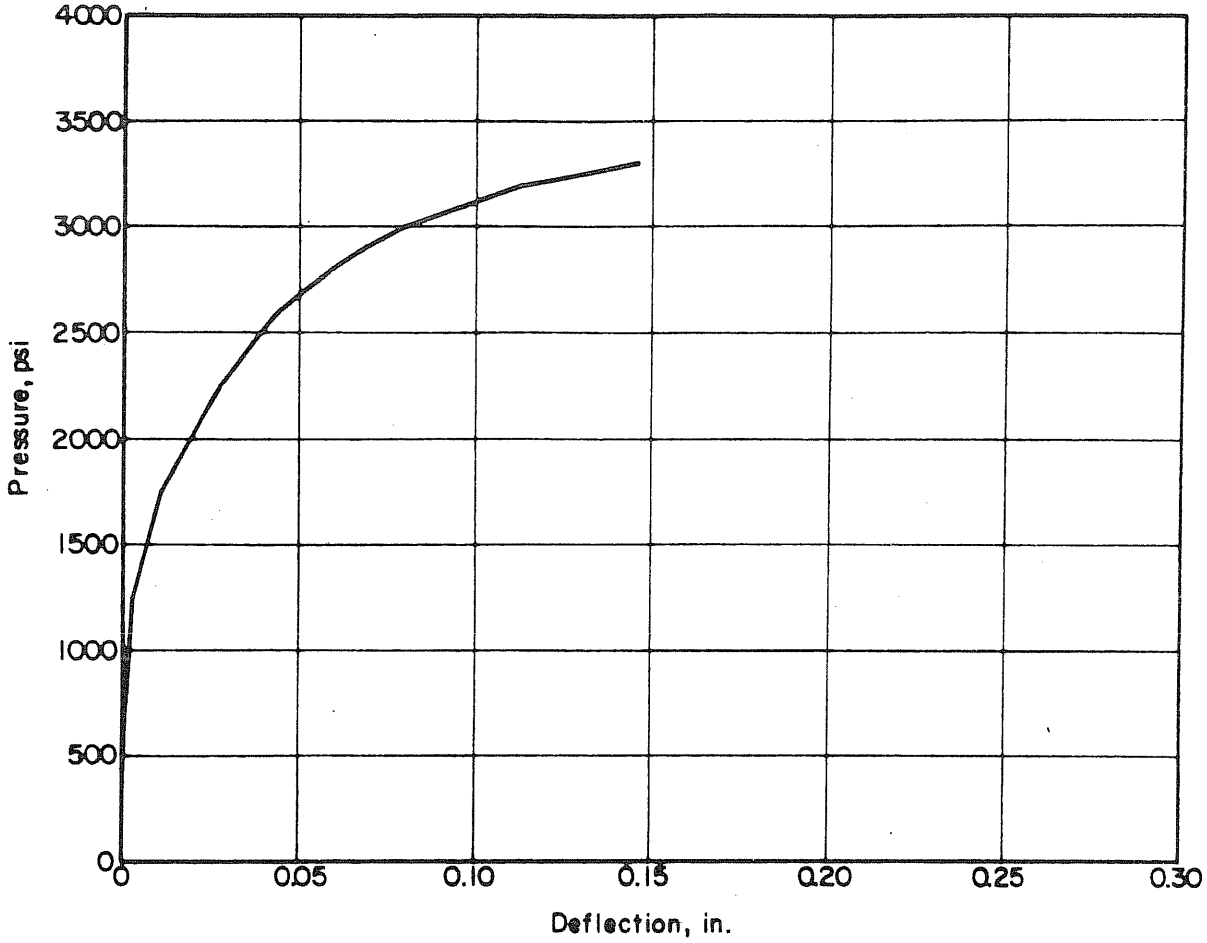

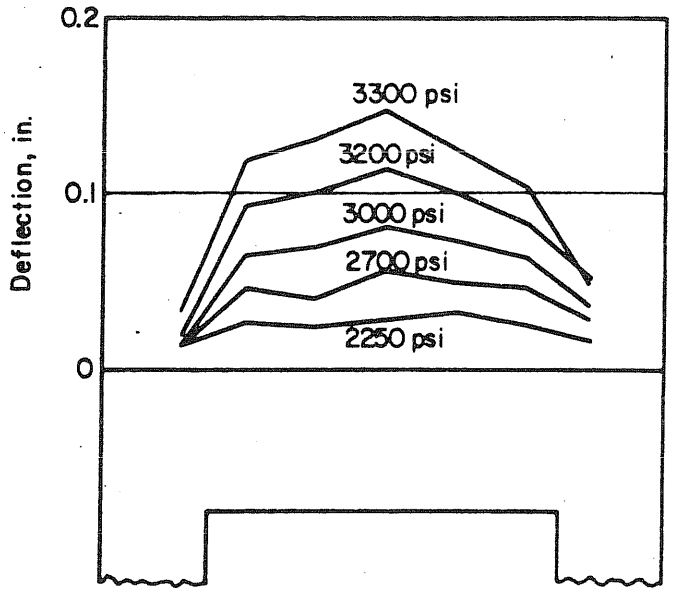

FIG. B.40 MEASURED DEFLECTION PROFILES AND DEFLECTION AT THE CENTER OF THE END SLAB OF PV21

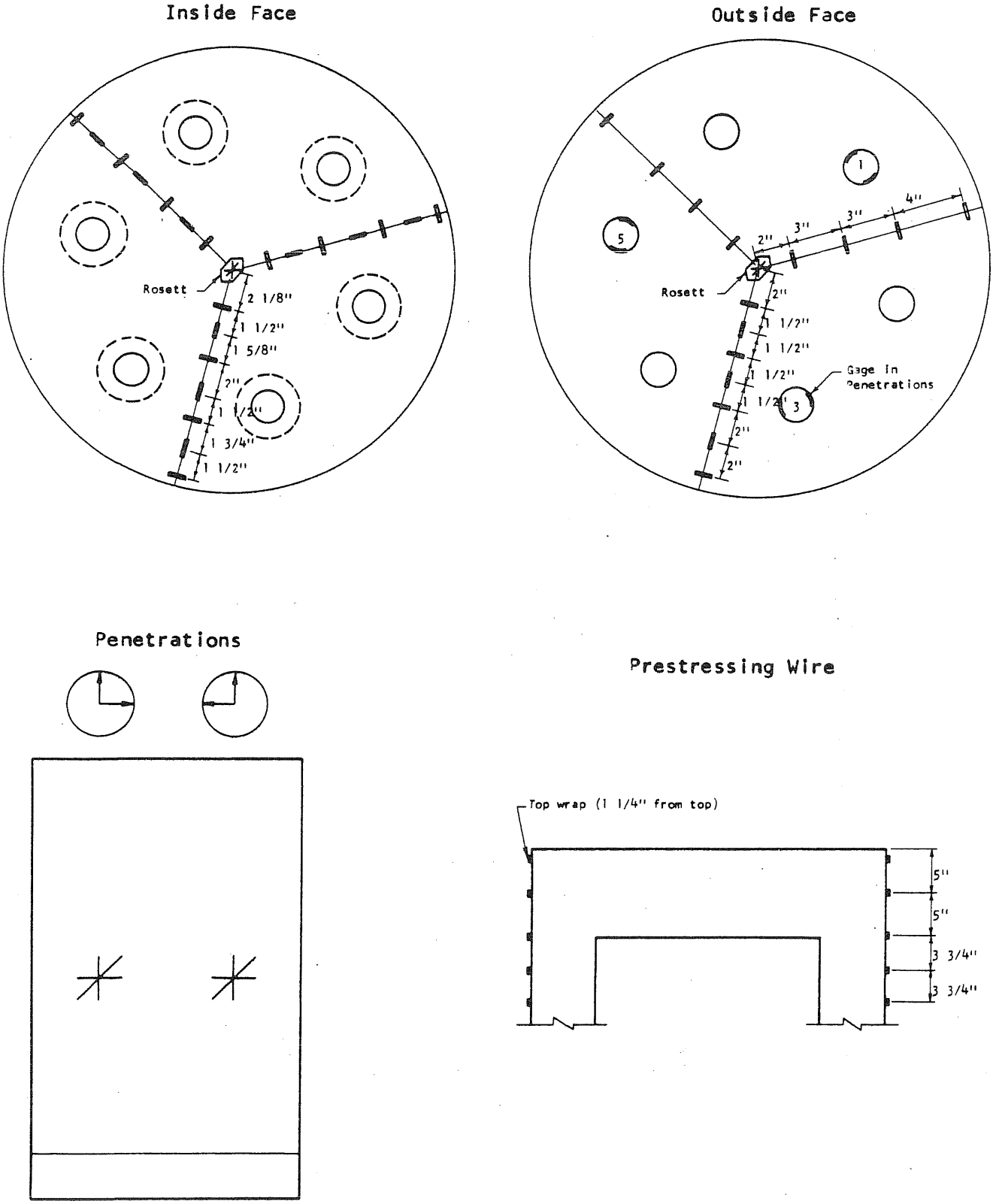

FIG. B.41 STRAIN GAGE LOCATION ON PV21

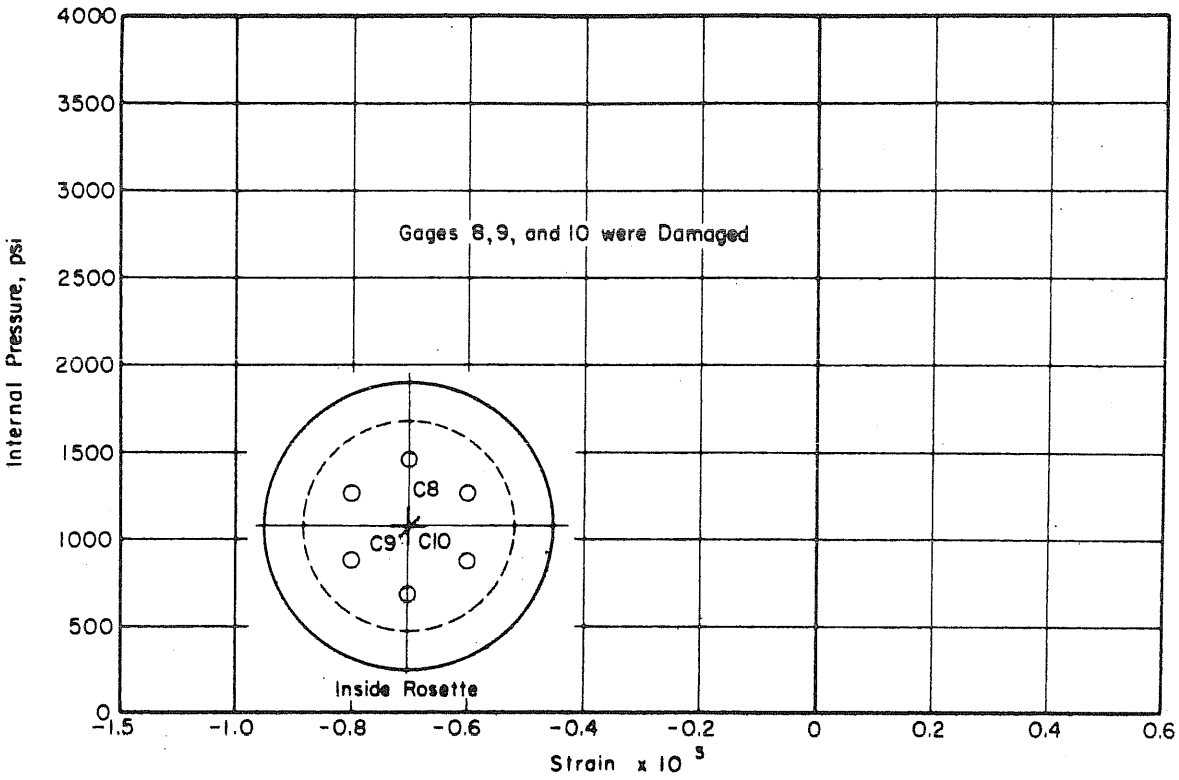

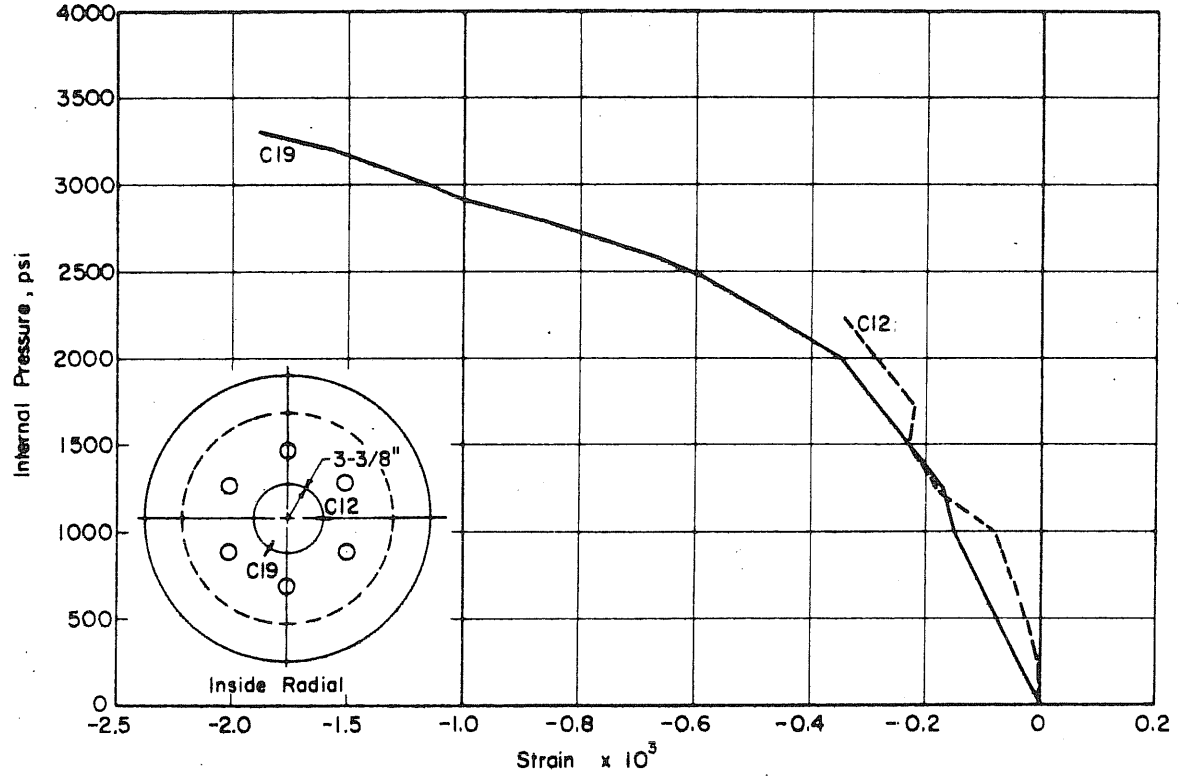

FIG. B.42 MEASURED STRAINS ON THE INSIDE FACE OF THE SLAB OF PV21

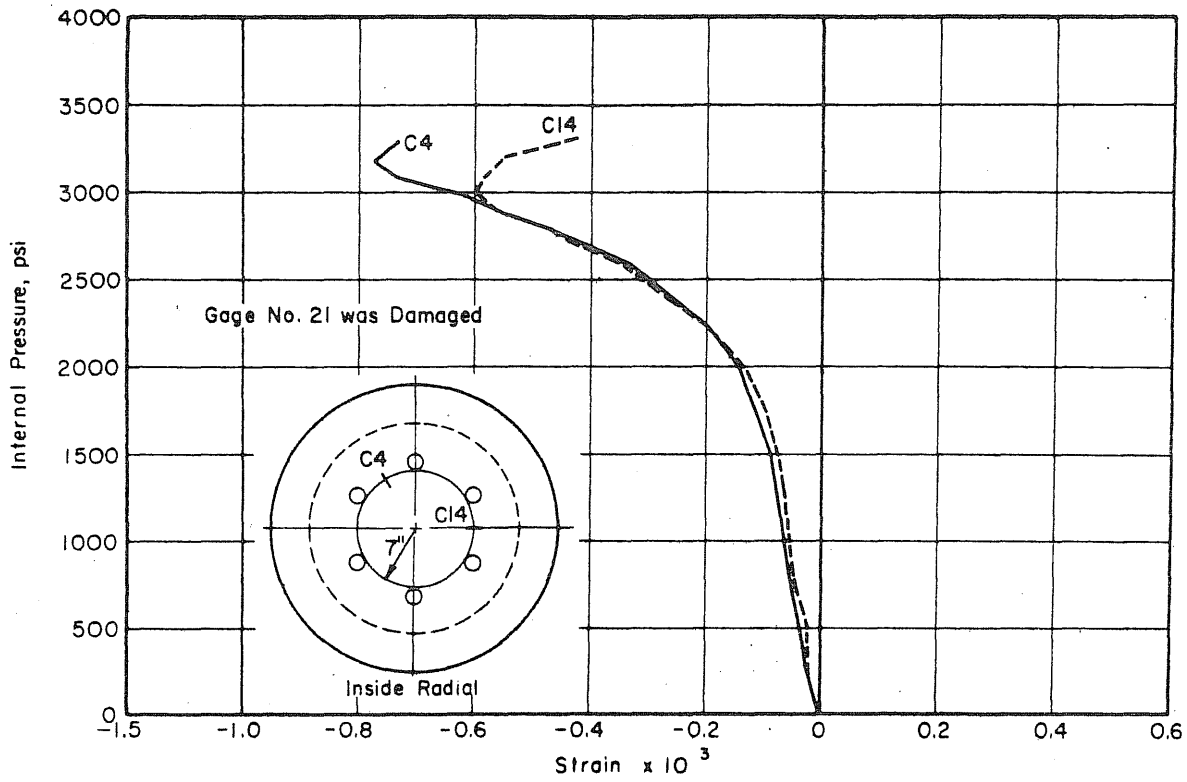

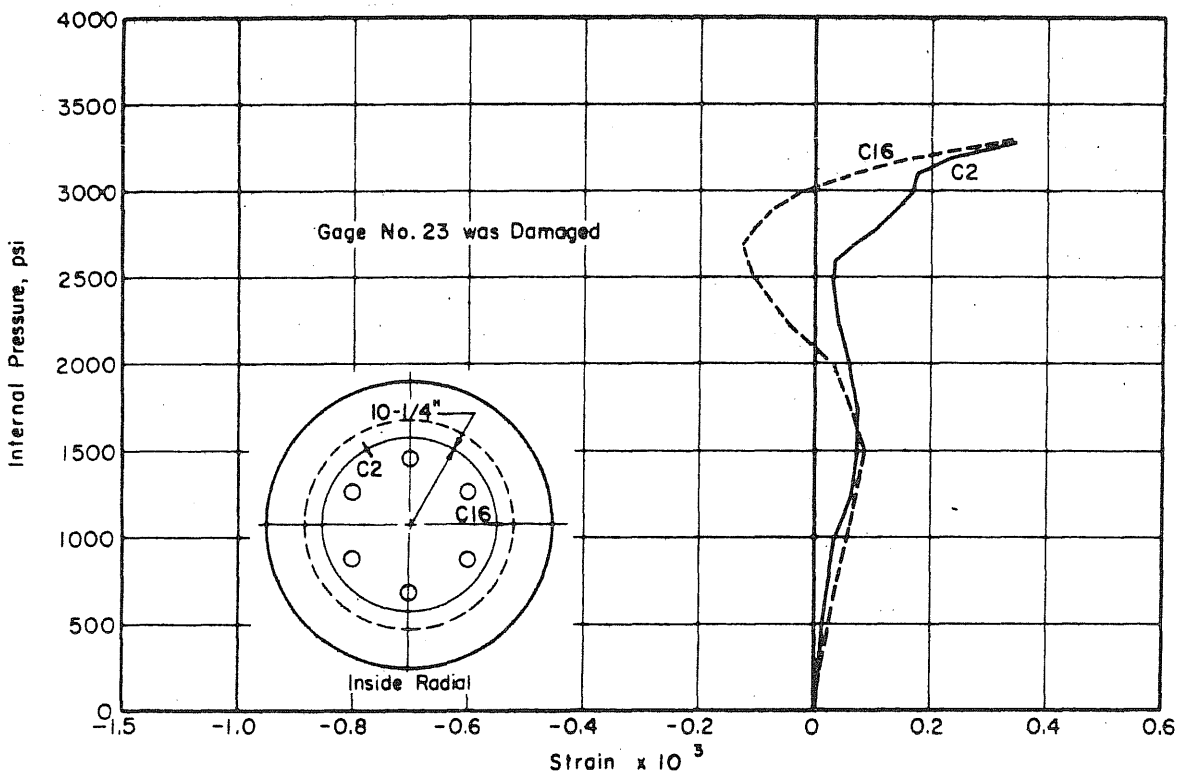

FIG. B.42 (Continued) MEASURED STRAINS ON THE INSIDE FACE OF THE SLAB OF PV21

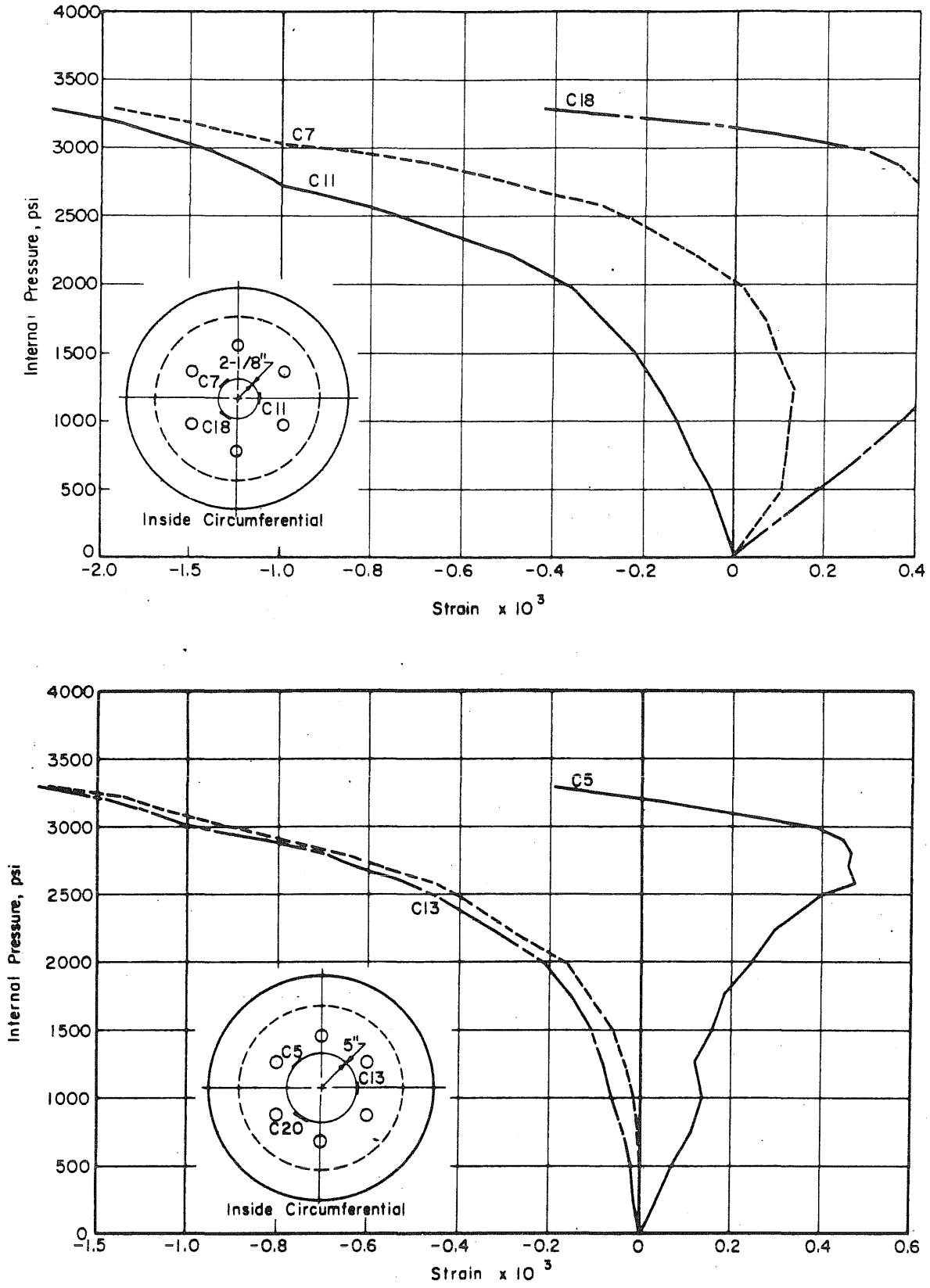

FIG. B.42 (Continued) MEASURED STRAINS ON THE INSIDE FACE OF THE SLAB OF PV21

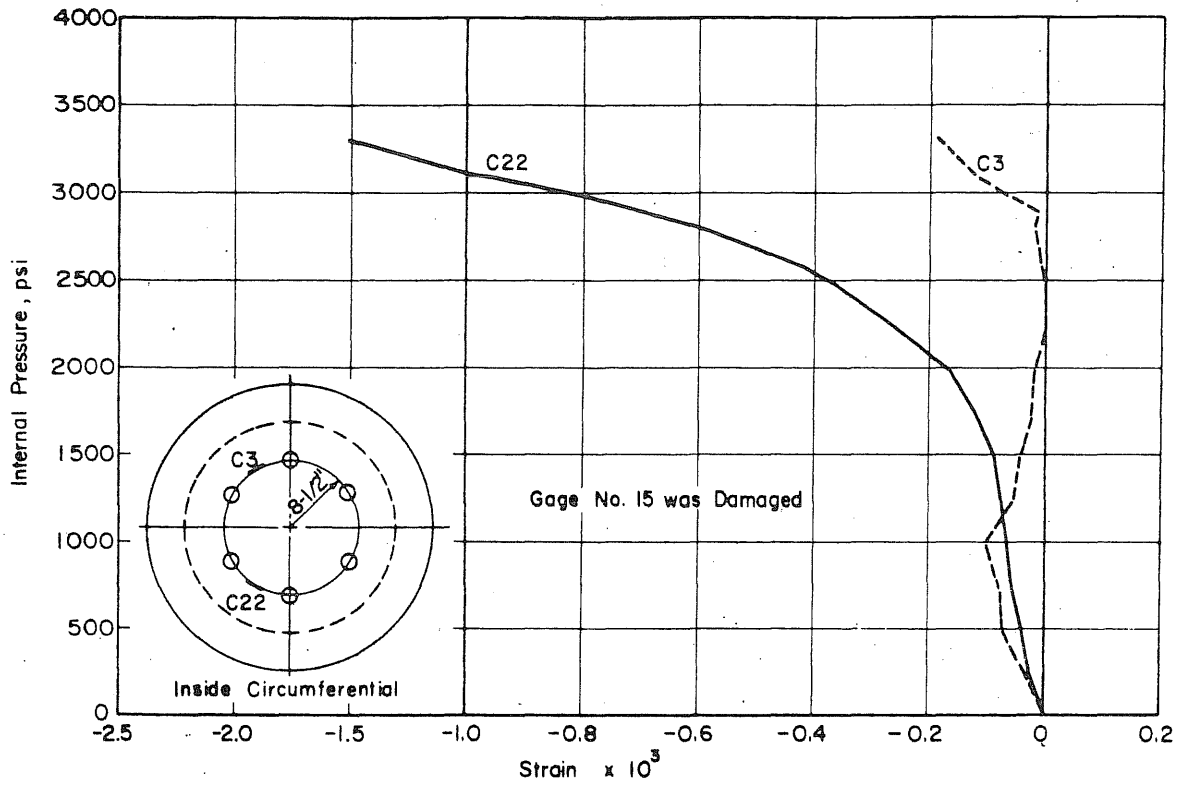

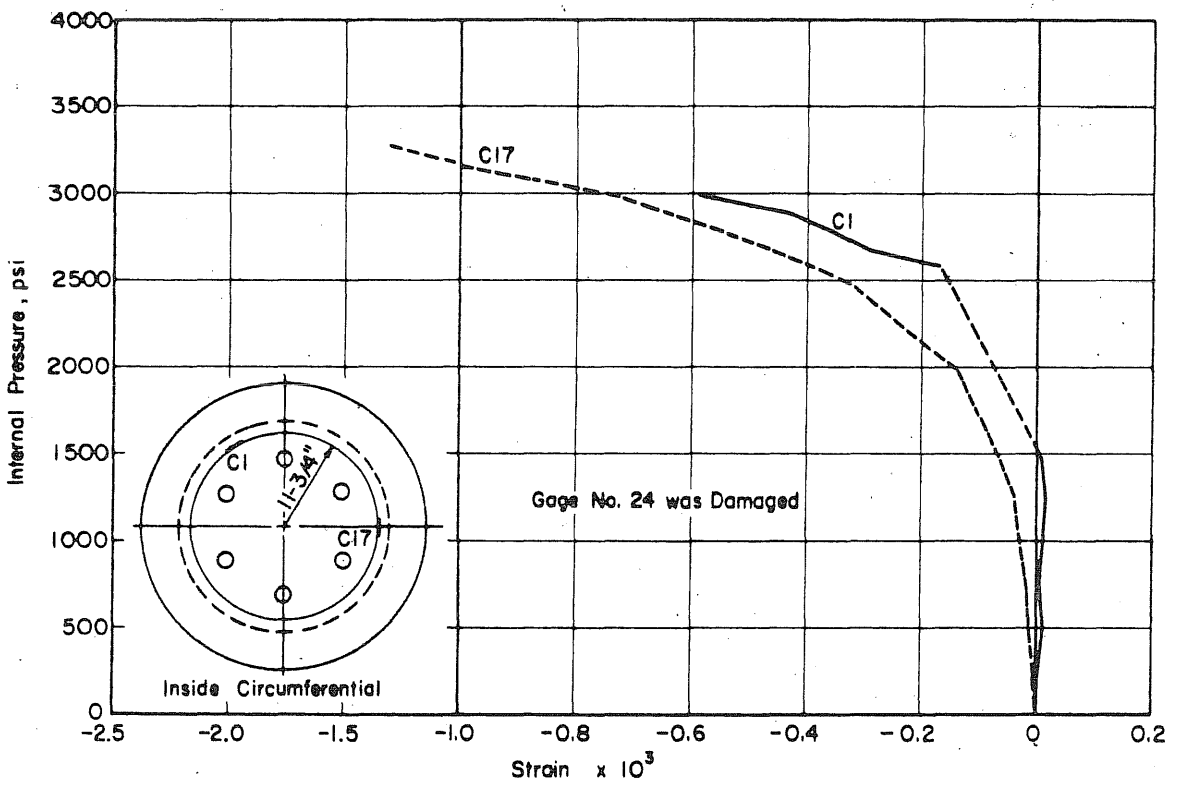

FIG. B.42 (Continued) MEASURED STRAINS ON THE INSIDE FACE OF THE SLAB OF PV21

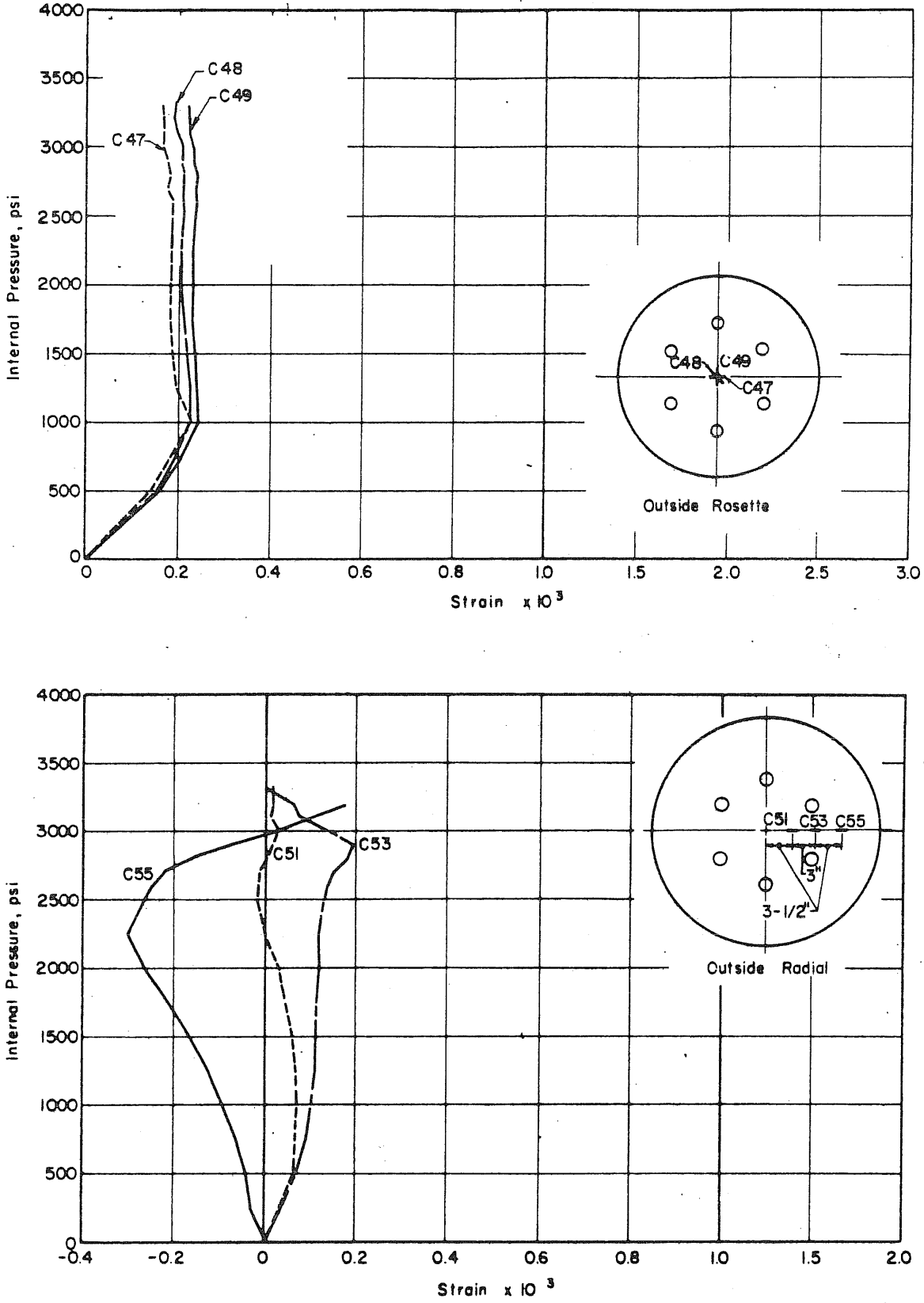

FIG. B.43 MEASURED STRAINS ON THE OUTSIDE FACE OF THE SLAB OF PV21

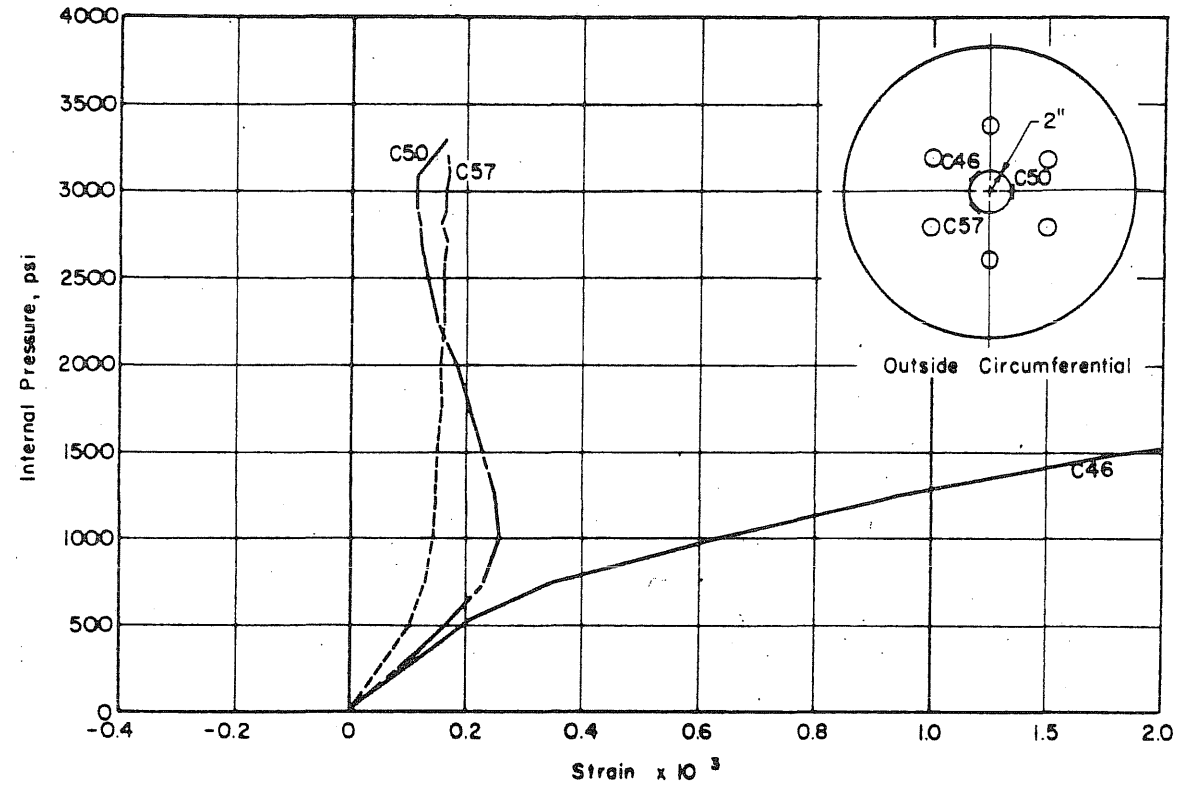

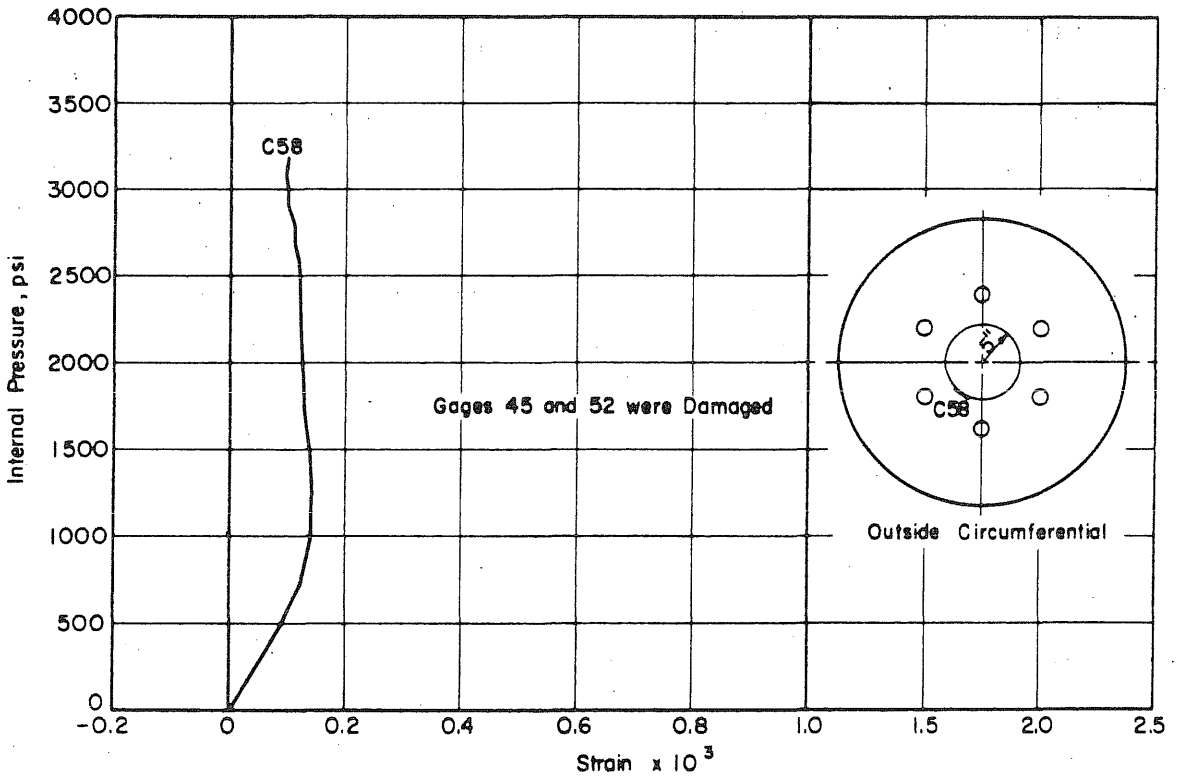

FIG. B.43 (Continued) MEASURED STRAINS ON THE OUTSIDE FACE OF THE SLAB OF PV21

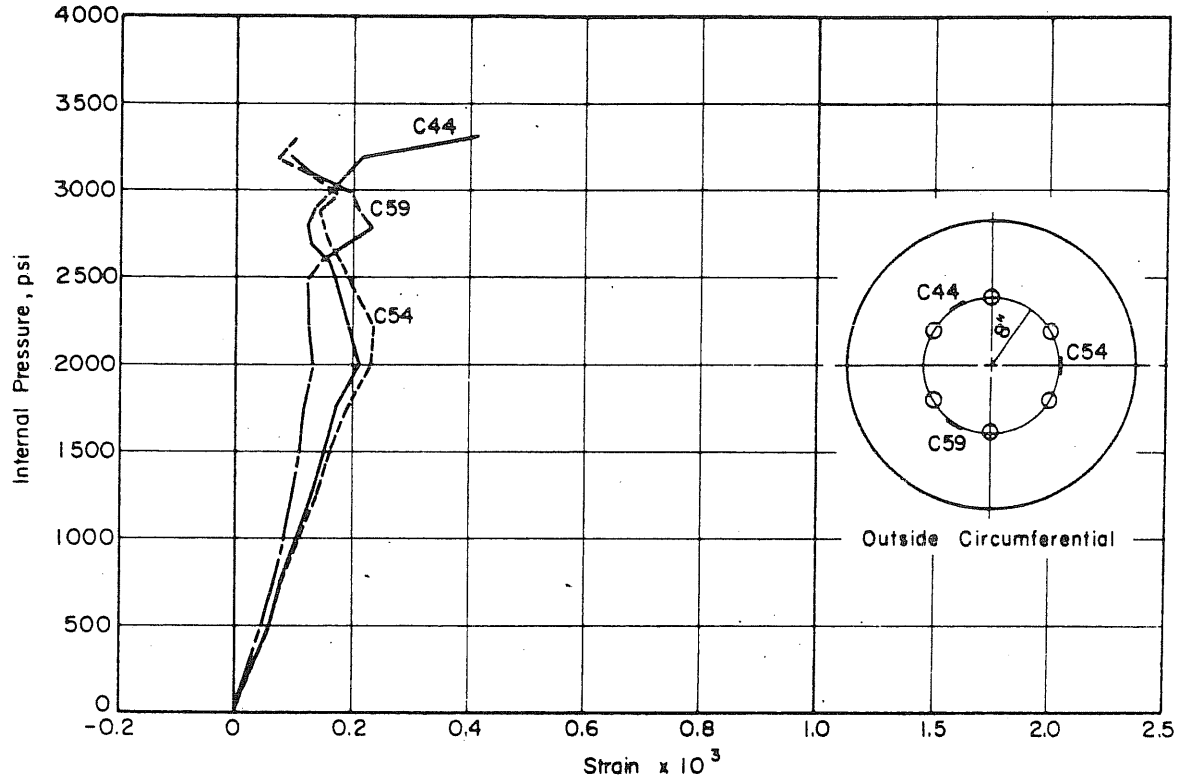

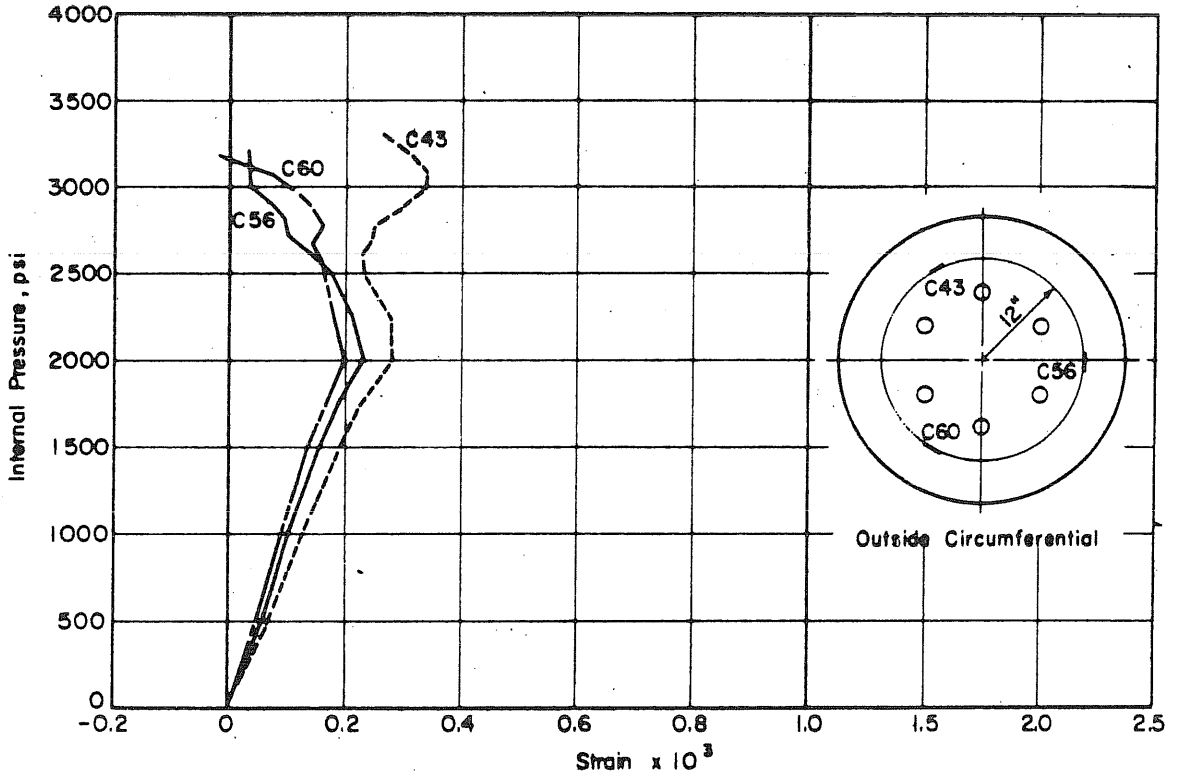

FIG. B.43 (Continued) MEASURED STRAINS ON THE OUTSIDE FACE OF THE SLAB OF PV21

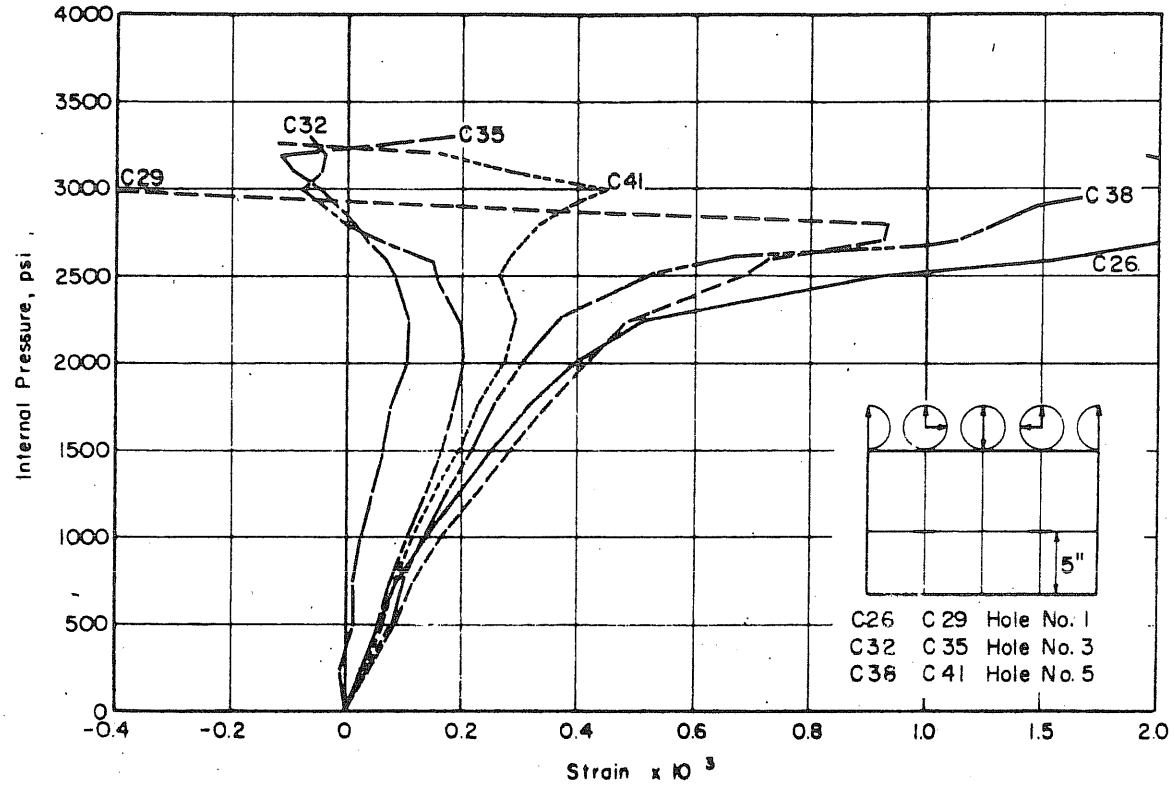

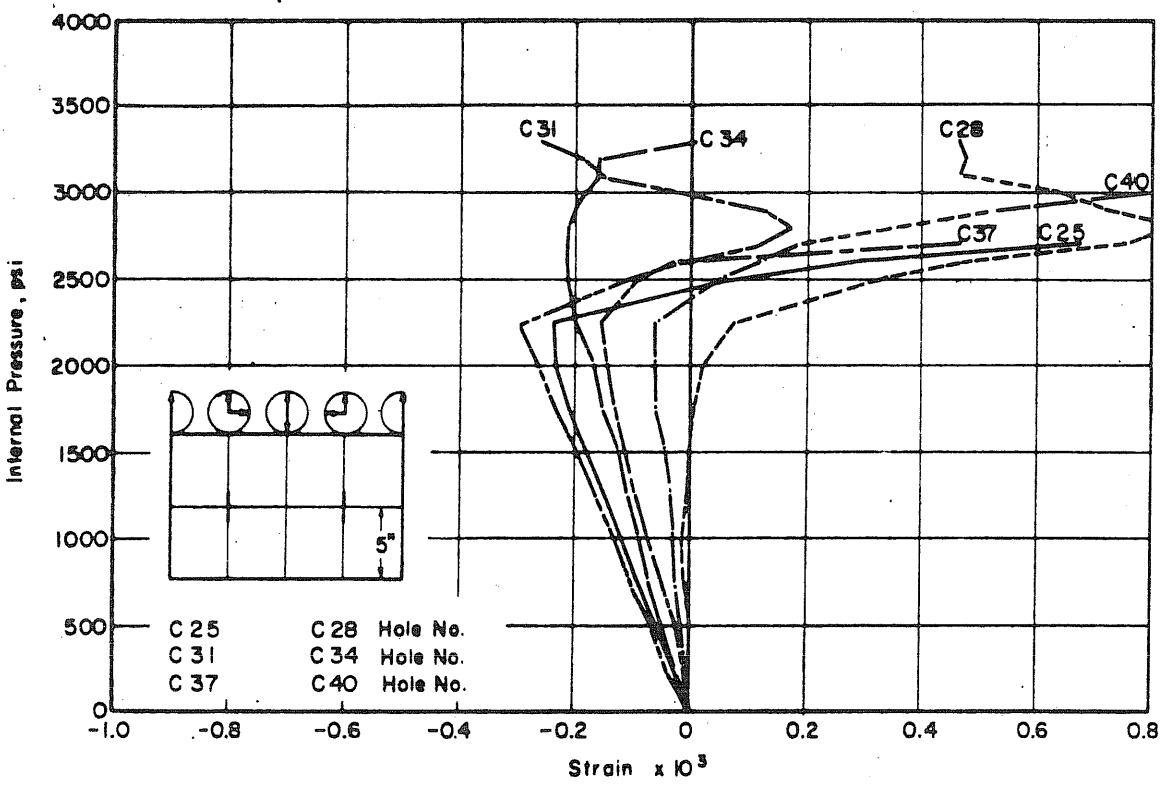

FIG. B.44 MEASURED STRAINS IN THE PENETRATIONS OF PV21

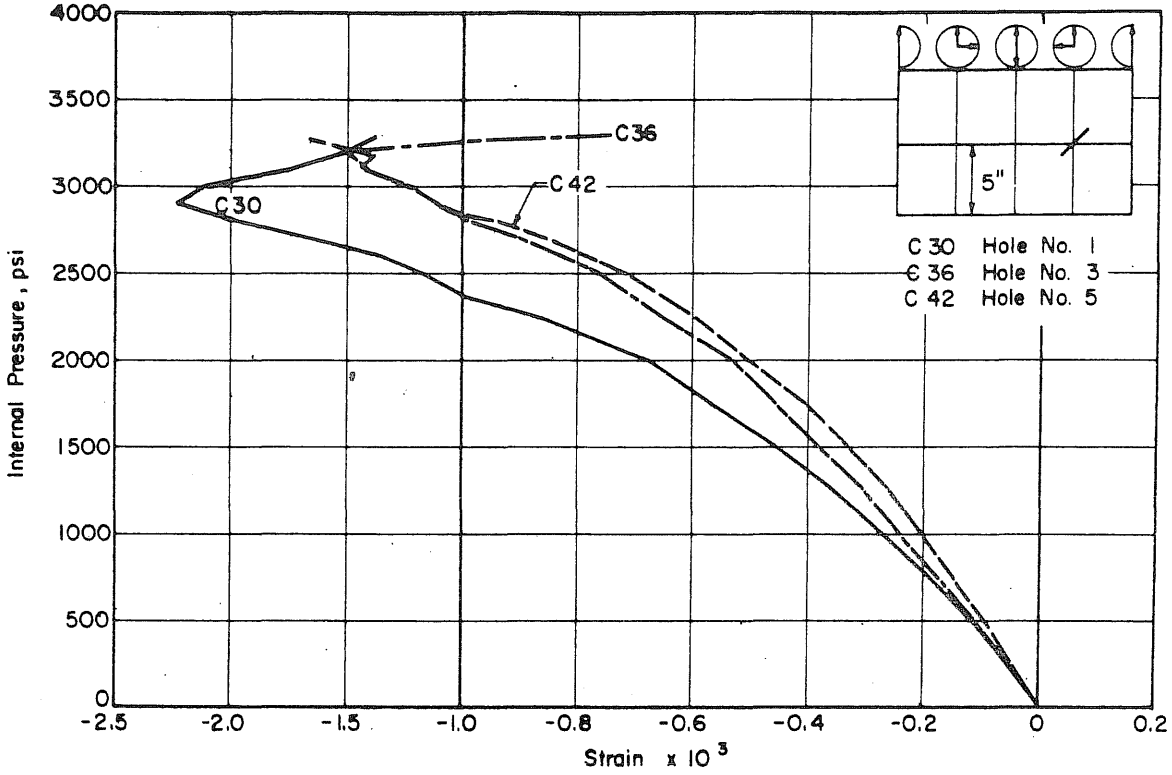

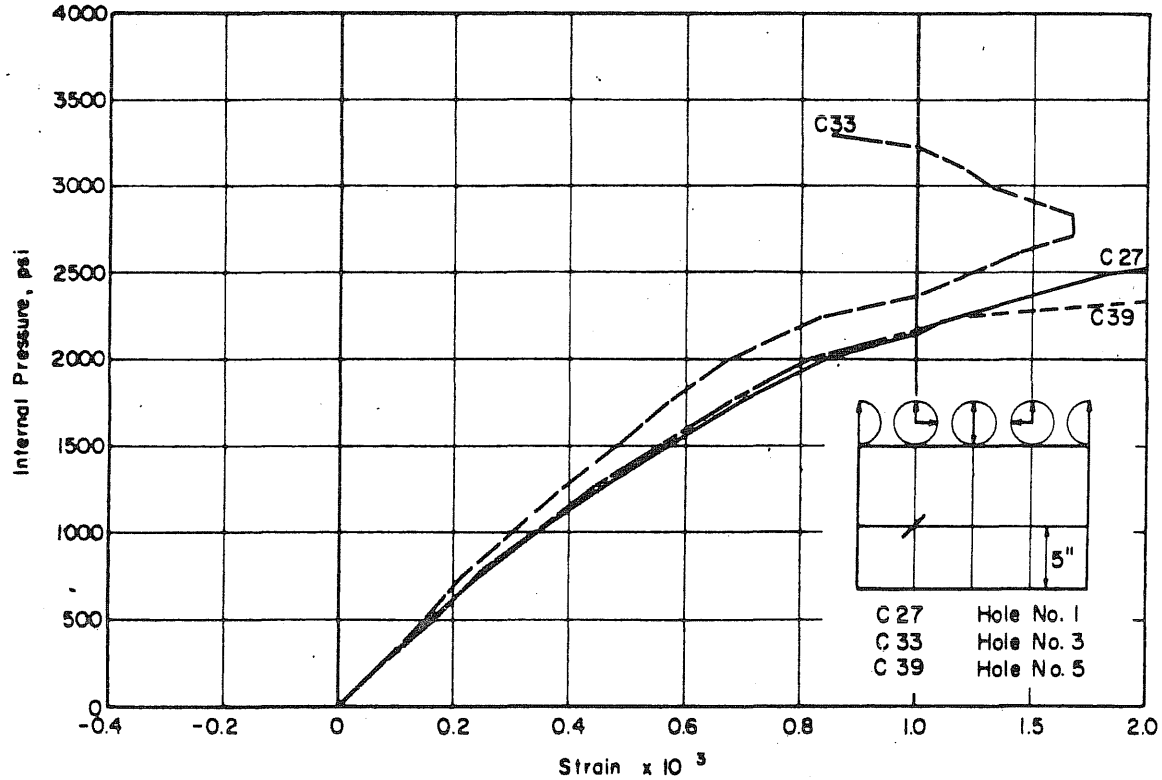

FIG. B.44 (Continued) MEASURED STRAINS IN THE PENETRATIONS OF PV21

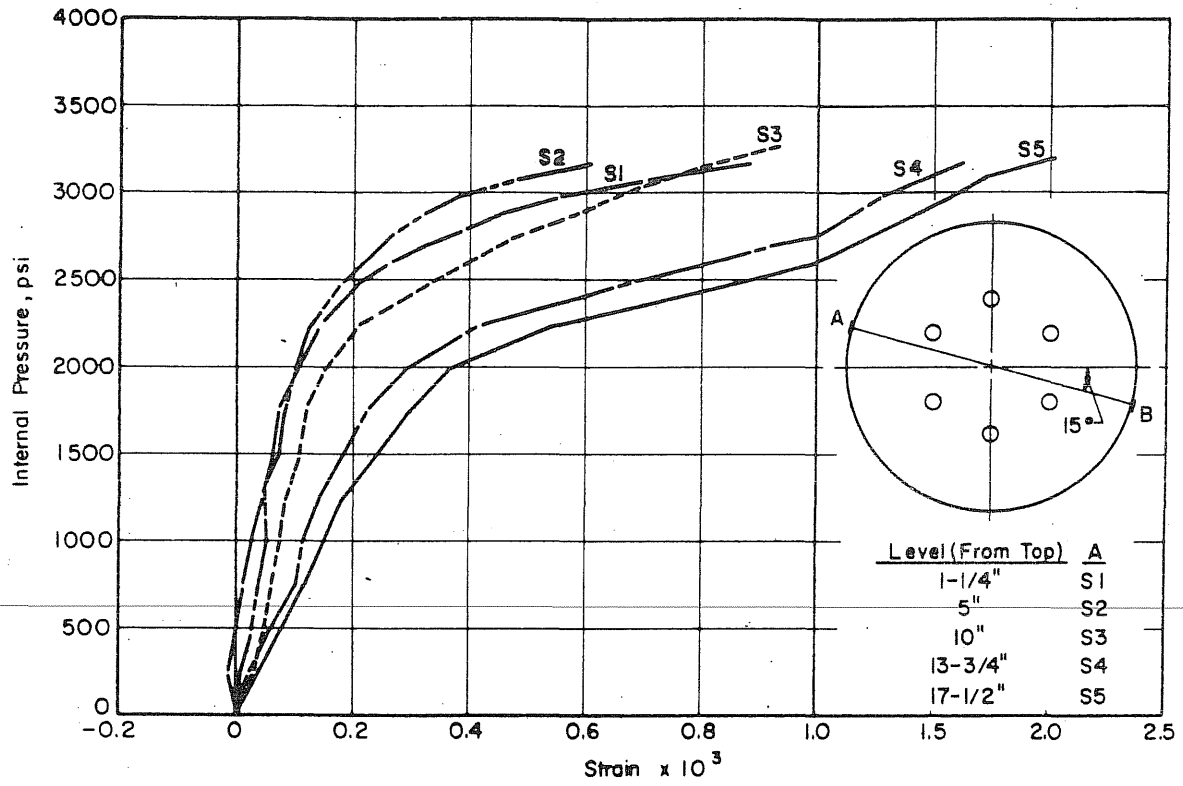

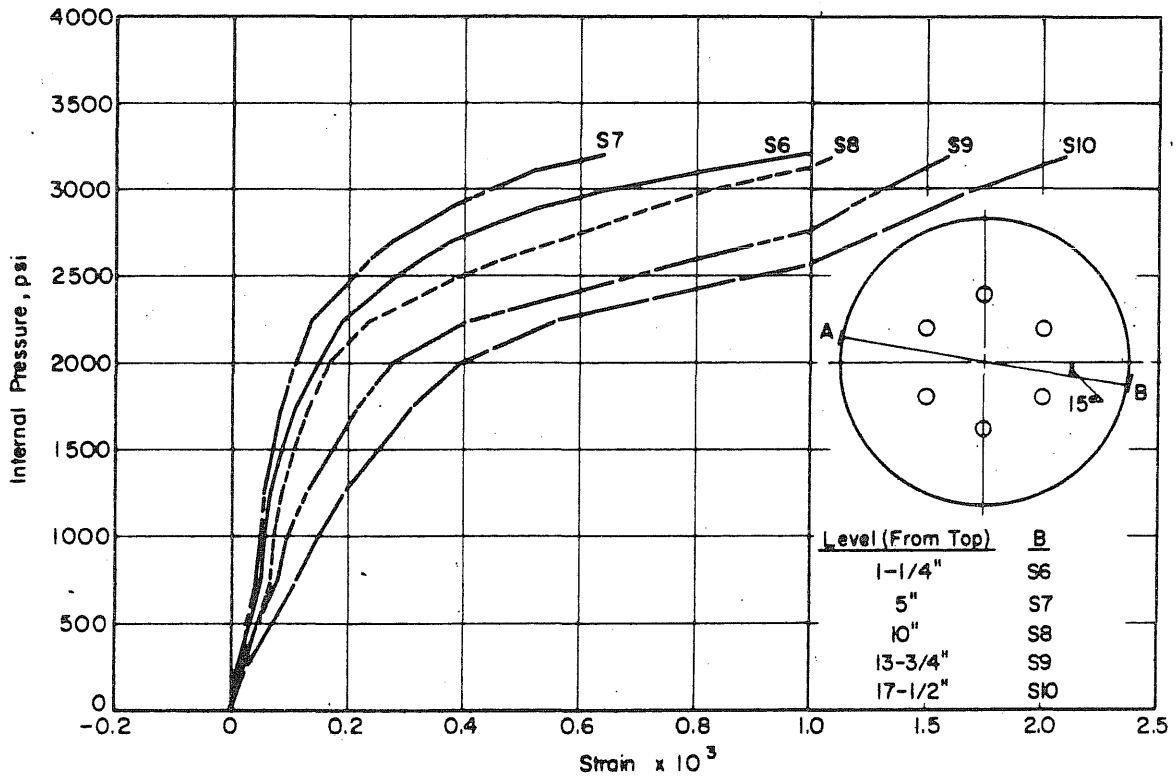

FIG. B.45 MEASURED STRAINS IN THE CIRCUMFERENTIAL PRESTRESSING WIRE OF PV21

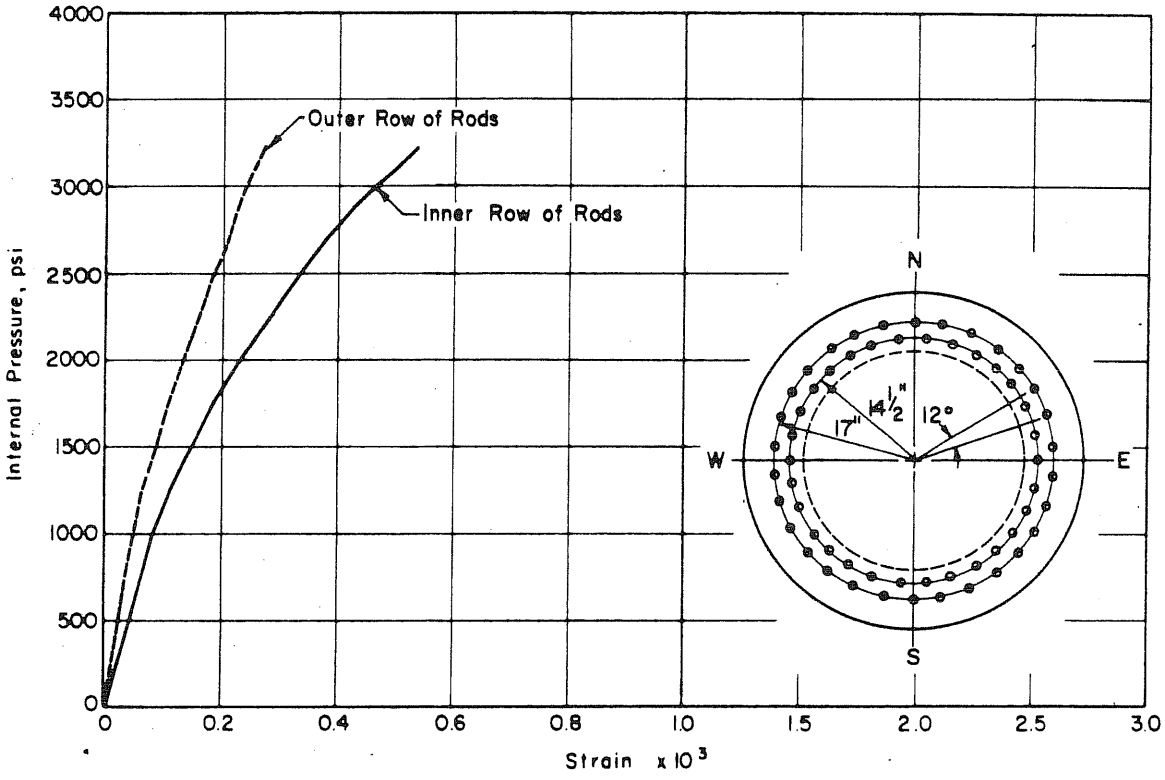

FIG. B.46 MEASURED STRAINS IN THE LONGITUDINAL PRESTRESSING RODS OF PV21

APPENDIX C: MEASURED STRAINS ON THE INSIDE FACE OF THE SLABS

C.1 Introduction

During the evaluation of the test data, problems arose in interpreting the measured strains on the inside face of the slab. Gages that were expected to record compressive strains throughout the test often indicated tensile strains, especially at low internal pressures. Possible causes to this phenomenon are discussed in this appendix.

The calculated stresses in a thin circular slab are shown in Fig. C.1. The end slab in a pressure vessel would be expected to have a similar stress distribution although the slab thickness-to-spanwidth ratio is higher. The gages at the center of the slab should record compressive strains that are higher than at any other location on the slab save for the concrete between the penetrations where local strain concentrations may yield greater strains. The analysis presented in Chapters 3 and 4, using the finite-element model supports this assumption.

The measured strains at the center of the slabs of vessels PV16 through PV20 (the corresponding gages for Vessel PV21 were out of order) are shown in Fig. C.2 - C.6. Nine gages out of fourteen read tension at low internal pressures. This phenomenon occurred in vessels with and without penetrations. Possible reasons for it are discussed in the following.

C.2 Edge Moment Caused by the Side Wall

The slab is bending under the impact of the internal pressure on the slab, causing compressive strains to develop at the center portion of the inside face of the slab. Simultaneously the internal pressure is deflecting the side wall outwards, causing a rotation of the slab-wall connection

(Fig. C.7). This results in tensile strains on the inside face of the slab. Thus there are two different sources of bending, pressure on the slab and pressure on the side wall, one causing compressive strains and the other tensile strains at the center of the inside face of the slab. It can then be argued that tensile strains developed at the center under the combined influence of the internal pressure and the side wall. However, if this was the case there should have been a more consistent trend among the gages at the center and the other gages on the inside face of the slab should have indicated a similar response. Neither was the case and the above discussion does not satisfactorily explain the strains that were measured.

C.3 Deep Beam Effect

To explain the tension at the center of the thick slab an analogy can be drawn to the tension developing at the center of a deep beam. In a deep beam the load is carried by an arch of concrete and if the beam is deep enough the arch will have less height than the beam, which will result in tensile strains at the top in the same way as in a column, Fig. C.8.

Elastic analyses for the vessels without penetrations have been carried out using both the lumped-parameter and the finite-element models. Neither of the models gave any indication of a deep beam effect, both of them predicted a linearly varying stress through the depth of the slab. To investigate if the finite-element model would show the deep beam effect and if this effect was likely to occur with the boundary conditions in the vessels, two cases were investigated using STRUDL. The investigation was limited to a beam instead of a slab and linear strain triangels were used. The most critical condition was considered to have existed in PV19 which had 2 in. penetrations

on a 4-in. radius, so a beam was chosen that was 10 in. deep and 6 in. wide, i.e. corresponding to the plug inside the penetrations, and which had a distributed load and two supports. The analysis showed that tensile stresses would develop at the top of the beam (Fig. C.9) and it is concluded that a finite-element analysis reflects the deep beam behavior.

The boundary conditions in the slab are different from the above mentioned beam. The support is provided through shear stresses along the whole cylinder that limits the slab. The same beam was used to simulate this but the support was obtained by applying parabolically distributed shear stresses along the edges (Fig. C.10). The analysis shows that the shear stresses move the arch upwards and no tensile stresses are obtained at the top.

The analysis shows that it is unlikely that the deep beam effect would occur but in case it does occur the elastic analysis using the finite-element model would indicate it.

C.4 Poisson's Effect

When the vessel is pressurized, the concrete is subjected to a compressive stress normal to the surface. The Poisson's effect causes the concrete to expand in the other directions and tensile strains are obtained. A value of 0.15 for Poisson's ratio has been assumed in the analysis. This value is relatively accurate at low stresses so this effect is included in the analysis. If the value was substantially different the analysis might be in error. However, this would then also show in the strains recorded by the other gages, which it did not.

C.5 Inplane Forces

As the vessel is pressurized the wall deflects outwards resulting in shear stresses along the boundary between the wall and the end slab (Fig. C.11). The shear stresses acting on the slab generate tensile strains along the inside face of the slab. Strain gages, applied to the prestressing wire 10 in. below the top of the slab on the outside of the vessel, will record this strain. The readings indicate that in the elastic range this strain is less than 0.0001 per 1000 psi internal pressure. This is too little to explain the tension readings of the gages at the center of the slab. Furthermore, as argued before, there is no reason why this should not be taken account for in the analytical solutions or why it should not show in the readings obtained from the other gages on the inside face of the slab.

C.6 Imperfections in Applying Gages

Before the gages are applied the surface is sandpapered and any depressions are filled with hydrocal. Thereafter the gages are attached and a 1/4-in. layer of hydrocal is applied on the inside of the slab (Fig. C.12). If the concrete is not flat under the gage, it will gradually be forced to align with the concrete surface when the pressure is applied and in doing this elongate. This process may not be completed until a high internal pressure has been reached because of the protecting layer of hydrocal.

There was usually a slight depression at the center of the slab because of the construction of the form. This depression had to be filled with hydrocal before the gages were applied. This may explain why it was mostly the gages at the center that recorded strains that were tensile and scattered.

C.7 Conclusions

The edge moment caused by the side wall, Poisson's effect and inplane forces are not satisfactory ways of explaining why some gages and especially the ones at center of the inside face of the slabs show tension, as a more consistent picture involving all the gages would then have been obtained. The deep beam effect would be most logical in explaining why it most frequently occurs to the gages at the center of the slab but analysis show this method to be unsatisfactory. The scatter in data could neither be explained by this method. The easiest and most convincing way to explain the scatter of the readings is by referring to imperfections in applying the gages. Even if this cannot be proved to have been the cause, grawer objections have to be raised against the other explanations which were discussed.

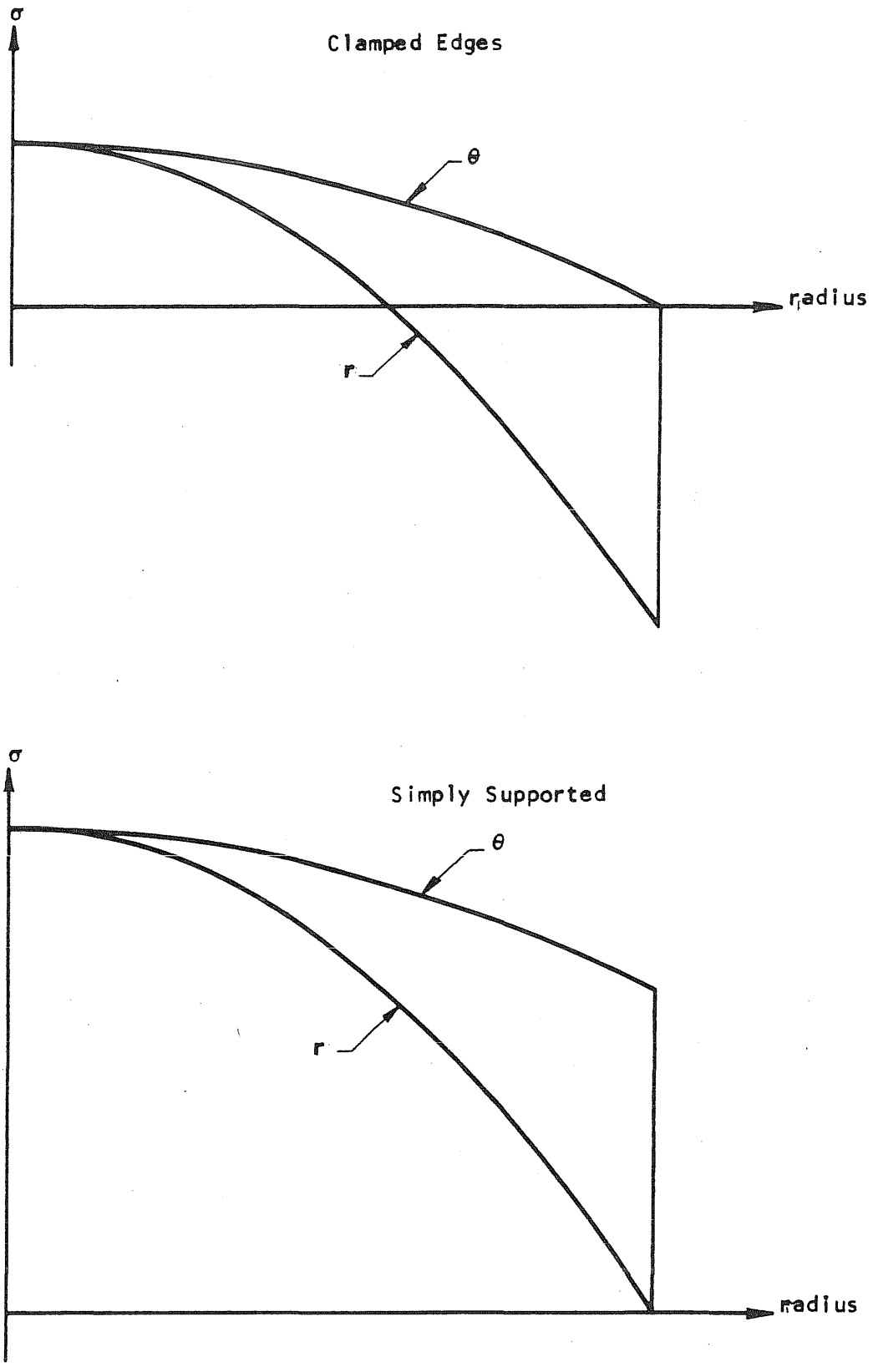

FIG. C.1 CALCULATED STRESSES IN A THIN CIRCULAR SLAB

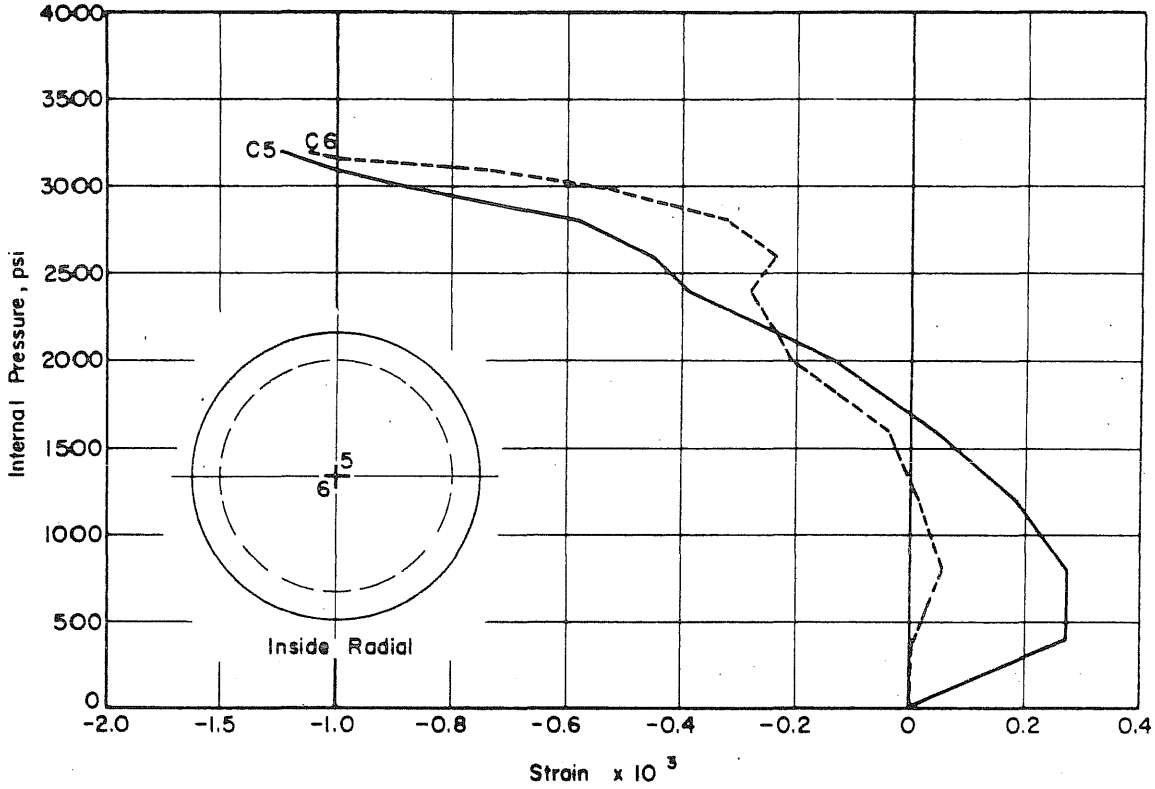

FIG. C.2 MEASURED STRAINS AT THE CENTER OF THE INSIDE FACE OF THE SLAB OF PV16

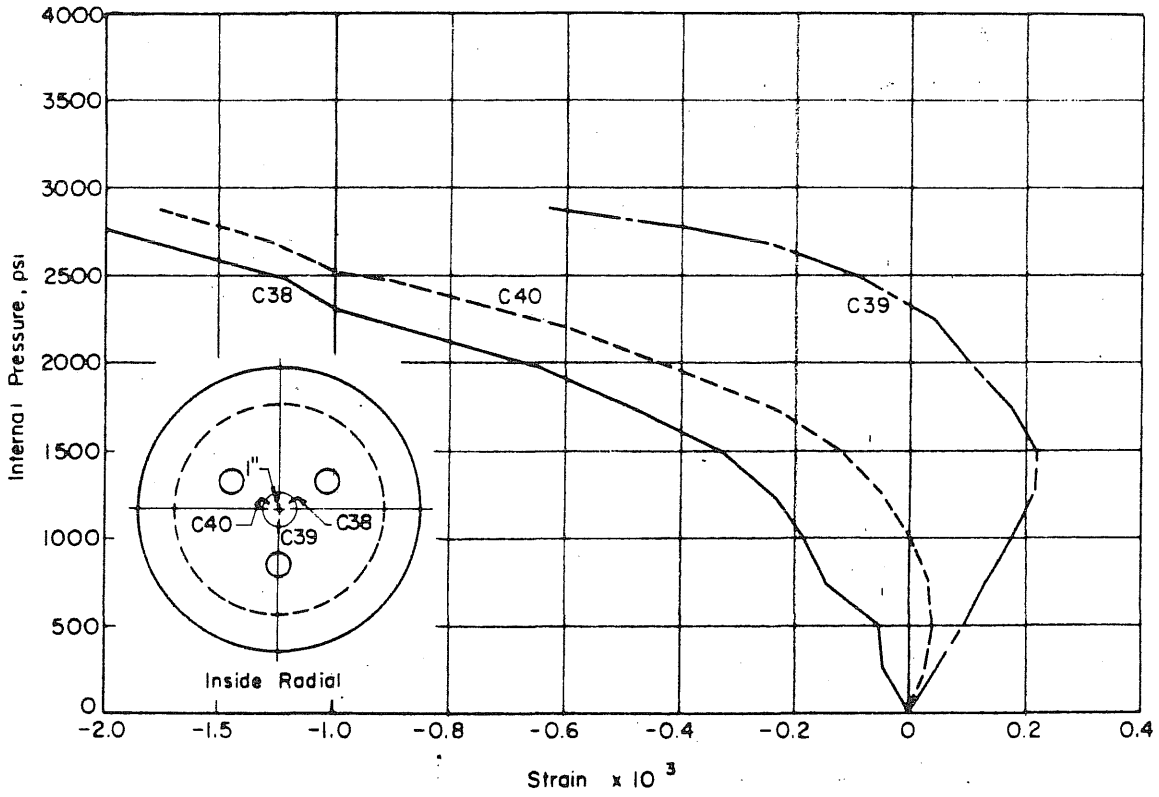

FIG. C.3 MEASURED STRAINS AT THE CENTER OF THE INSIDE FACE OF THE SLAB OF PV17

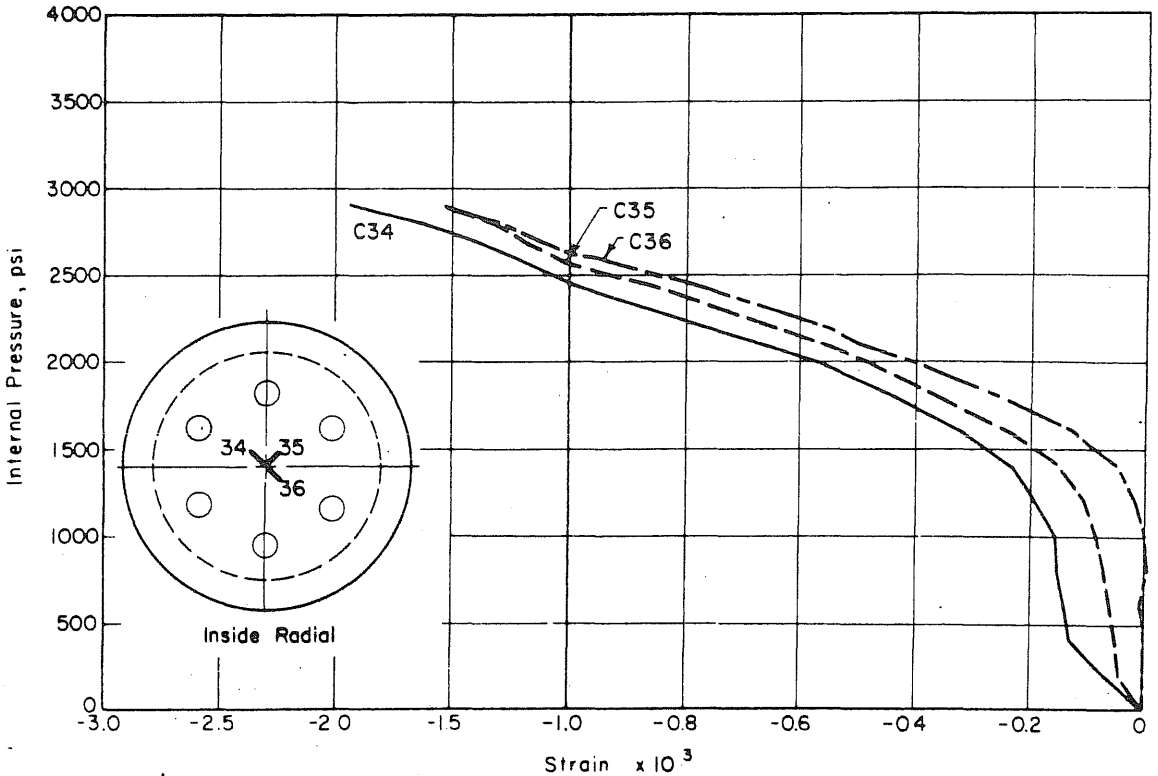

FIG. C.4 MEASURED STRAINS AT THE CENTER OF THE INSIDE FACE OF THE SLAB OF PV18

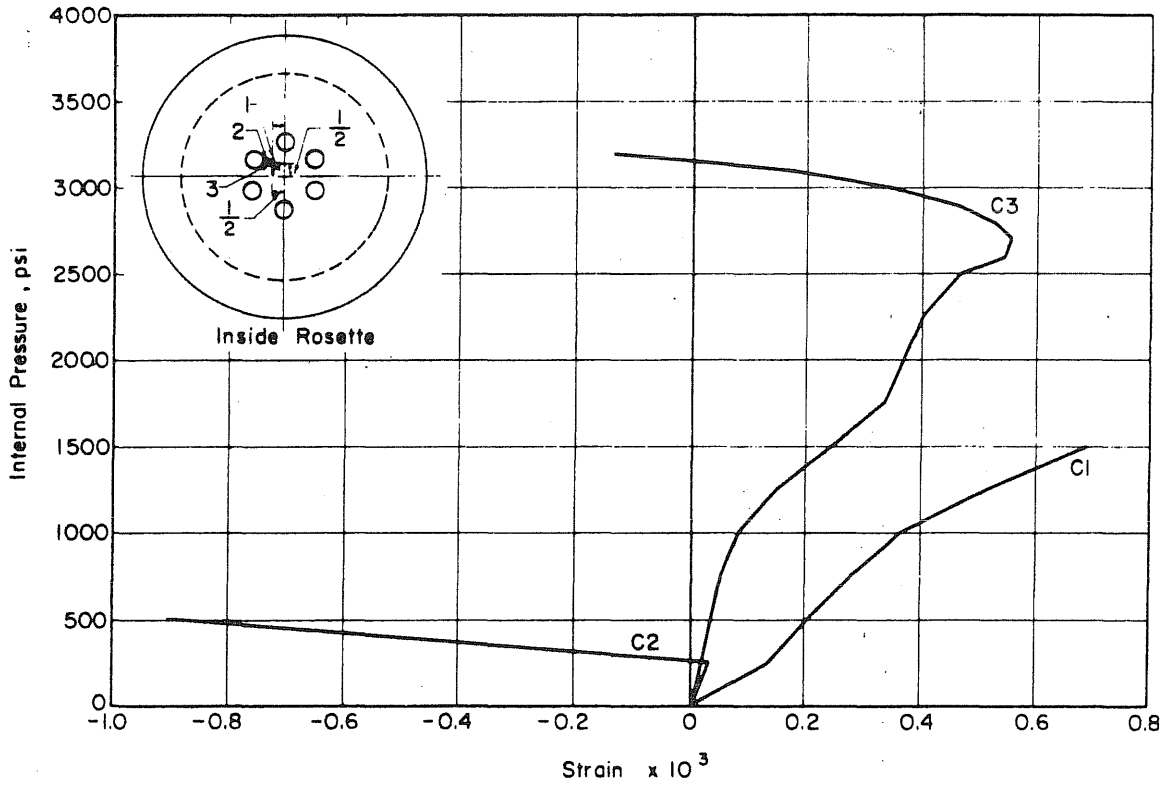

FIG. C.5 MEASURED STRAINS AT THE CENTER OF THE INSIDE FACE OF THE SLAB OF PV19

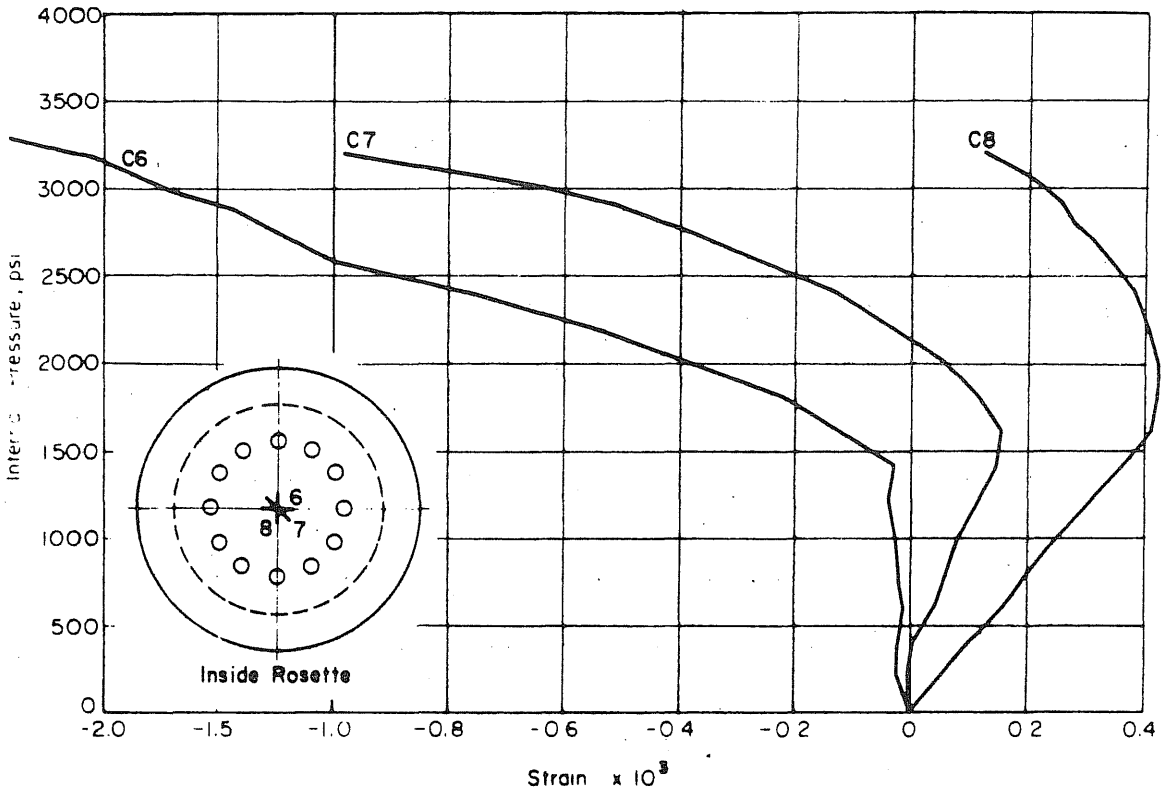

FIG. C.6 MEASURED STRAINS AT THE CENTER OF THE INSIDE FACE OF THE SLAB OF PV20

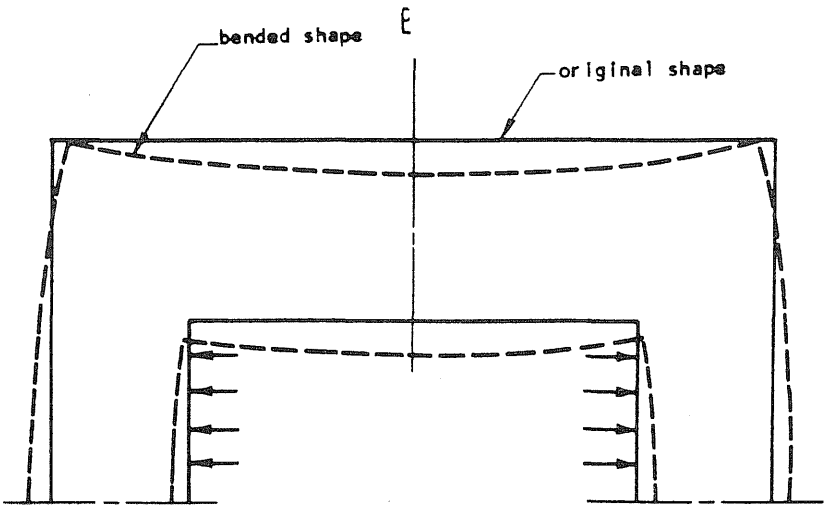

FIG. C.7 BENDING OF THE END SLAB DUE TO PRESSURE ON THE WALL

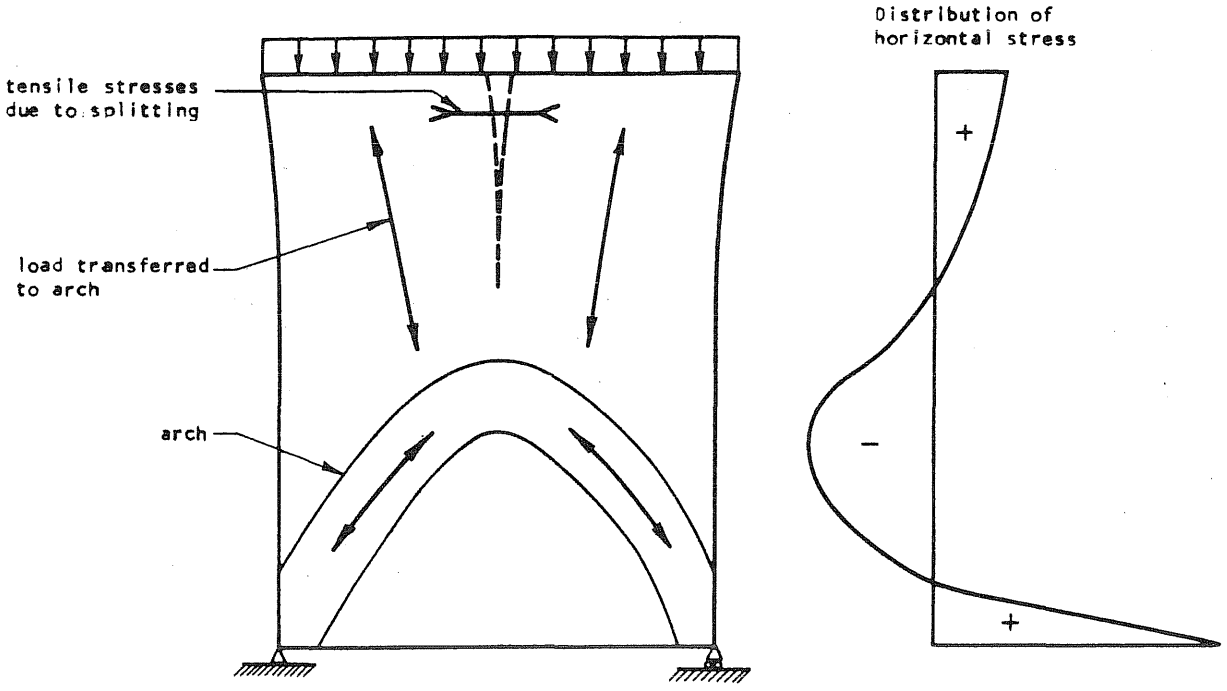

FIG. C.8 LOAD CARRYING MECHANISM OF A DEEP BEAM

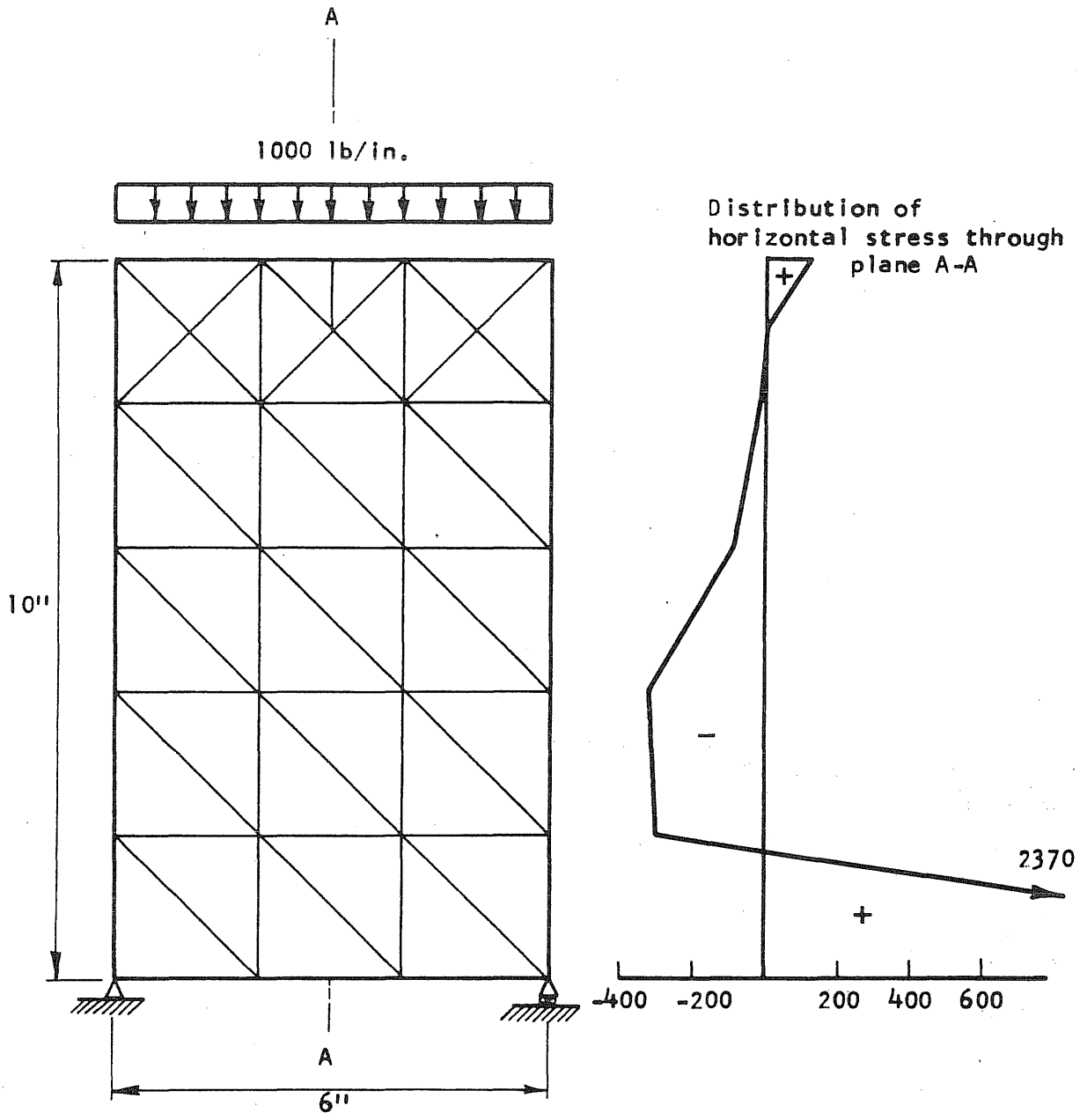

FIG. 6.9 LOADING AND SUPPORT CONDITIONS OF A DEEP BEAM AND THE CALCULATED STRESSES

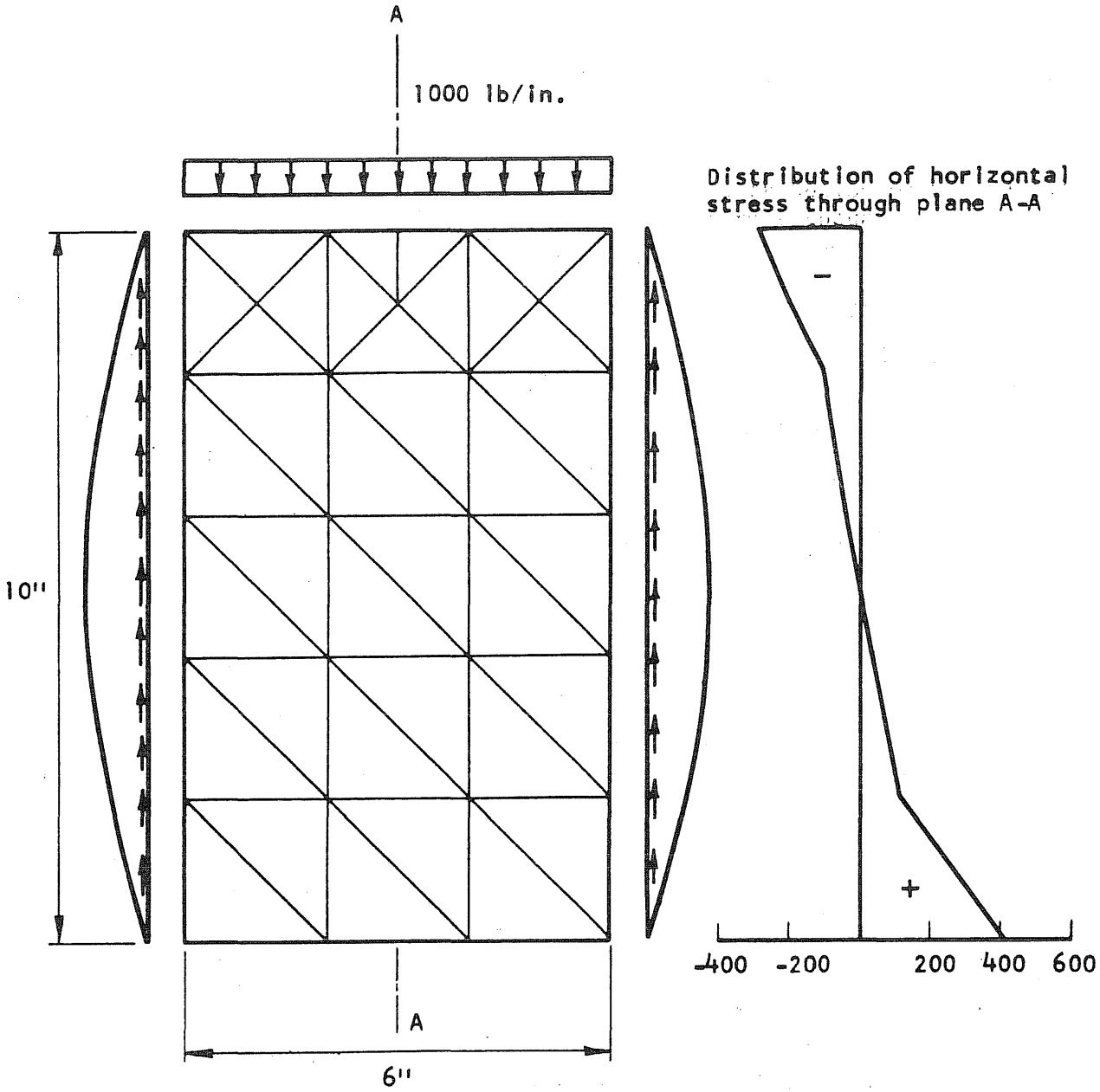

FIG. C.10 LOADING AND SUPPORT CONDITIONS OF A DEEP BEAM AND THE CALCULATED STRESSES

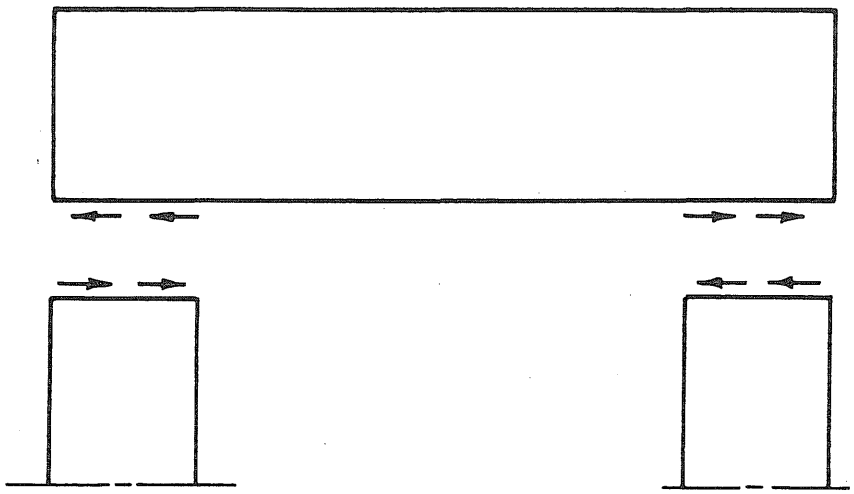

FIG. C.11 SHEAR STRESSES BETWEEN WALL AND SLAB

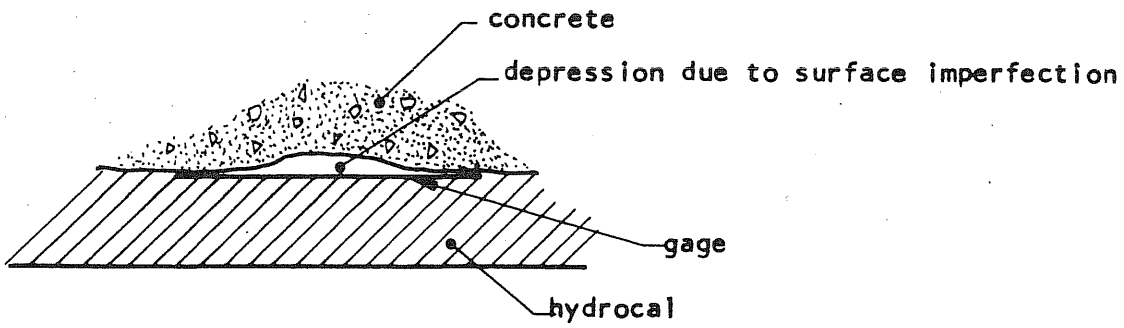

FIG. C.12 APPLICATION OF A GAGE ON AN UNEVEN SURFACE

APPENDIX D: NOTATION

d	thickness of the end slab
E	Young's modulus of elasticity
E_a	secant modulus of elasticity
G	shear modulus
r_A	distance from the center of the slab to the point where the inclined crack is assumed to initiate
r_B	distance from the center of the end slab to the inner edge of the anchorage plate
t	thickness of wall
U	strain energy
α	failure index
α_a	failure index based on average stresses at each section
α_w	maximum value of the failure index (except the nodes at the boundaries) at any section
β	solid diameter divided by total perimeter at a section
∂	depth of the cryptodome at the center
ε	strain
ν	Poisson's ratio
σ	normal stress
$\sigma_r,\sigma_z,\sigma_t$	radial, vertical and tangential stresses, respectively
$\sigma_1,\sigma_2,\sigma_3$	principal stresses
σ_o	radial prestressing stress
σ_g	internal pressure
σ_{oct}	normal stress on an octahedral plane
τ	shear stress
τ_{oct}	shear stress on an octahedral plane